KU LEUVEN

ARENBERG DOCTORAL SCHOOL
Faculty of Science

The chemical diversity of post-AGB stars in the Galaxy and the Magellanic Clouds

Kenneth De Smedt

Supervisor:
Prof. dr. H. Van Winckel

Dissertation presented in partial fulfillment of the requirements for the degree of Doctor in Science

July 2015

The chemical diversity of post-AGB stars in the Galaxy and the Magellanic Clouds

Kenneth DE SMEDT

Examination committee:
Prof. dr. G. Neyens, chair
Prof. dr. H. Van Winckel, supervisor
Prof. dr. C. Waelkens
Prof. dr. L. Decin
dr. P. Royer
dr. L. Siess
(Université Libre de Bruxelles)
dr. O. Pols
(Radboud Universiteit Nijmegen)

Dissertation presented in partial fulfillment of the requirements for the degree of Doctor in Science

July 2015

Cover image

Front cover: Infrared observations of the Small Magellanic Cloud by the Spitzer Space Telescope.

Back cover: Infrared observations of the Large Magellanic Cloud by the Spitzer Space Telescope.

These infrared observations were the basis of our sample selection of post-AGB stars in the Magellanic Clouds (see Chapter 2).

Acknowledgements

The research presented in this PhD thesis was based on funding from the Research Council of KU Leuven grant agreements GOA/2008/04 and GOA/2013/12 as well as from the Scientific Fund of Flanders (FWO) under the grants G.0703.08 and G.0470.07.

Acknowledgements
Dankwoord

Almost twenty years ago, I had my first encounter with astronomy when we learned about our Solar system in the third grade of elementary school. At that time, our Solar system still had nine official planets. This first encounter was the start of a long educational career towards astronomy. Along the run, I was a bit disappointed to learn that our Sun would never turn into a supernova but that could not temper my enthousiasm. However, when I was a bachelor student in physics, I started to doubt which master I should follow since physics counts so many fascinating aspects. Luckily, the dedicated professor of the course 'Wetenschap van de Kosmos' fully convinced me of the beautiful science of astronomy. One of the most memorable topics he explained was the visual effect of distance on stars with different sizes by comparing stars with mouses, elephants and dinosaurs. A combination of astronomy and dinosaurs, that should make everybody excited. After the two years of my master in astronomy and astrophysics, I got the golden opportunity to start a PhD thesis and prolong my astronomic adventure.

When I started this thesis, I did not expect the coming four years to pass by so quickly. Now, I approach the end of my astronomic adventure and so the completion of this manuscript. Of course, this thesis could not have been completed without the help of many. Therefore, I take here the opportunity to thank everyone who in one way or another contributed to this thesis, both in a scientific and mental way.

Hans, thank you for providing me the opportunity to continue my unfinished master thesis in the form of this PhD. Thank you for being a fantastic supervisor and motivator during the past five years. You were always there when I needed advice and motivation, and you made me more and more passionate about AGB and post-AGB stars. Thank you for the detailed reading of my extensive

texts and your recommandations to decrease the number of pages (although this thesis may not be the best example of that). Thank you for staying a good, enthousiastic promotor, even after finding out my favorite Belgian soccer team. Thank you for making me a full-fledged scientist =:-)

Lionel and Stephane, thank you for your guidance at the ULB and introducing me to the theoretical world of AGB stars. You have learned me a lot about AGB modeling during the course of my PhD, and you both made a major contribution to this thesis for which I thank you.

Thank you to the jury for the recommandations to improve my manuscript. Extra thanks go to Christoffel, who convinced me of choosing the master in astronomy with his dedictated teaching during the course 'Wetenschap van de Kosmos'.

Thanks to Amanda, Bruce, Maria, Peter, Richard and Rob for the nice conversations and/or contributions to this thesis.

Thanks to the other post-AGB team members Devika, Michel and Rajeev, for your contributions and our interesting discussions about post-AGB stars.

To Florian, Gert, Hans, Jesus, Saskia and Wim P., thank you for the support at the Mercator Telescope and for creating such a user-friendly system. Thanks to Carlos, for being my dedicated driver in La Palma and giving me an introduction to Spanish.

Thanks to the IvS system group to keep the system running for almost 100% of the time and for solving the many problems of my dedicated pc 'Dobson'.

Thank you to my generation of 'PhD buddies' Joris V. and Jonathan. Thank you Joris for being my trusted working partner for projects in the bachelor and master, and for helping me setting my first steps with Python. Thank you Jonathan, for being my project partner for 'Research Projects II' and developing my interest in post-AGB abundance determinations. Thank you both for the supporting conversations in completing our PhD manuscripts.

Thank you to my (former) office mates of the past five years: Robin, Bram, Wolfgang, Peter, Paul, Simone, Ilknur, Katrien and Marie, for creating a nice working environment and for our conversations about the universe, life (including administrative issues and the weather) and everything else.

To Marie, Ward and Rutger, thank you for all the conversations about everything and nothing.

To Timothy, thanks for the always supportive conversations and your help with asteroseismic matters. And remember, it's all going to be all right ;)

Finally, I would like to thank all IvS members for making the IvS such a wonderful place to work. Although I am not the most present person in the Coffee Room and during lunch breaks, I always enjoyed the atmosphere and conversations during receptions, Uitjes, etc. I want to thank you all for the great time at the IvS and I wish you all good luck with your future careers.

Een dikke merci aan Maarten en Veerle, Mats en Jasper. Jullie steun, sympathie en enthousiasme hebben me goed geholpen om mijn middelbare en universitaire loopbaan te voltooien. Voor dezelfde reden wil ik ook Joni bedanken, en ook om me te helpen de eerste jaren van de bachelor in de fysica te overleven.

Ik wil ook mijn grootmoeder Julienne bedanken voor alles wat ze voor me gedaan heeft, en de mentale steun die ze heeft geleverd tijdens mijn schoolcarrière. Verder wil ik ook Nico bedanken, die mij altijd kwam opvrolijken op moeilijke momenten en die zonder het te beseffen, een ongelooflijke steun is geweest en dat nu nog steeds is.

Ook een grote merci aan mijn vader, Veerle, Matthias en Sarah voor de steun en goede gesprekken, zowel in ontspannen als gestresseerde tijden.

Deze thesis had niet kunnen bestaan zonder de uitzonderlijke steun van mijn schoonfamilie. Ma en pa, heel erg bedankt om mij indertijd op te vangen en mij een plaats te geven die ik thuis kan noemen en voor jullie onvoorwaardelijke steun en liefde. Opa en oma, ook jullie bedankt voor alles wat jullie voor mij gedaan hebben en mij zo de kans te geven om deze thesis te voltooien.

Als laatste wil ik mijn gezin bedanken. Allereerst wil ik mijn trouwe viervoeter Nala bedanken om mij gezelschap te houden op die lange avonden en nachten tijdens de laatste maanden van deze thesis. Finaal wil ik mijn vrouw Jessica en mijn kinderen Steven en Laura bedanken om mij altijd de moed, hulp, begrip en liefde te geven om deze thesis tot een goed einde te brengen. De grootste sterren in mijn leven, dat zijn jullie.

Kenneth,

Leuven, September 2015

Abstract

One of the most fascinating stages in the life of low- and intermediate mass stars is the asymptotic giant branch (AGB) phase due to its strong mass loss and internal nucleosynthesis. The slow neutron capture process (*s*-process) nucleosynthesis is the origin of approximately half of all elements heavier than iron. Low-mass AGB stars are expected to be the main contributors to the cosmic carbon and *s*-process abundances. Carbon and *s*-process elements are synthesised in the AGB interior and different mixing processes transport these newly-synthesised material to the stellar surface, enriching the surface abundances. However, the physical mechanisms driving the internal AGB processes are to date poorly understood. Current AGB evolution and nucleosynthesis models are used to gain insight in the different processes, but these simulations contain large uncertainties. Observational constraints are necessary for improving our knowledge of the AGB nucleosynthesis and associated mixing processes.

Post-AGB stars are ideal testbeds for improving theoretical AGB evolution and nucleosynthesis models as the chemical composition of their photospheres display the signature of the different dredge-up processes and internal nucleosynthesis that take place during the total stellar lifetime. A systematic abundance study of optically visible post-AGB stars in a wide range in metallicity and luminosity, hence initial masses, will help to constrain AGB models. The sample of studied post-AGB stars in the Milky Way Galaxy displays a wide chemical diversity. Unfortunately, the distance to Galactic objects is unknown, hampering accurate luminosity determinations and hence initial mass estimates, which is a key parameter of AGB models. Post-AGB stars in the Magellanic Clouds do not have this distance drawback.

In this thesis, we perform detailed photospheric abundance studies of post-AGB stars in the Magellanic Clouds and the Galaxy to gain insight in the different processes that took place during the AGB phase. The known distances to the Magellanic Clouds allow to estimate the initial mass of studied post-AGB stars

and to compare the observed abundances with theoretical model predictions. A key element in our abundance studies is lead (Pb), which is the end-product of the *s*-process nucleosynthesis and hence the Pb abundance is sensitive to the different processes that take place during the TP-AGB.

Our studies show that our sample of *s*-process enriched post-AGB stars in the Magellanic Clouds are all low-mass stars with low C/O ratios and high *s*-process enrichments. Comparison with AGB model predictions shows that the observed C/O ratios are overestimated in model predictions. In addition, we find an increasing discrepancy between observed and predicted Pb abundances towards lower metallicities: for more metal-rich stars, the observed Pb abundances confirm theoretical predictions while for lower-metallicity objects, the Pb abundances are strongly overestimated.

We find a chemical diversity of post-AGB stars in the Magellanic Clouds, which is similar to the chemical diversity of their Galactic counterparts. Our abundance studies show that very similar objects with similar masses and metallicities can have large differences in *s*-process abundances. Furthermore, our abundance results confirm the mild intrinsic *s*-process enrichment of the Magellanic Clouds from previous studies. This enrichment should be taken into account when comparing observations with theoretical model predictions, which can help to improve current stellar evolution models.

Samenvatting

De asymptotische reuzentak (AGB) is één van de meest fascinerende episodes in het leven van sterren met lage en middelgrote beginmassa's. Deze fase wordt namelijk gekarakteriseerd door een sterk massaverlies en een uitgebreide interne nucleosynthese. De zogenaamde *s*-proces nucleosynthese, waarbij zware elementen gevormd worden wanneer een atoomkern neutronen vangt, is de oorsprong van ongeveer de helft van alle elementen zwaarder dan ijzer in het universum. AGB sterren met lage massa's worden aanzien als zeer belangrijke bijdragers aan de kosmische koolstof en *s*-proces abondanties. Koolstof en *s*-proces elementen worden aangemaakt in de binnenste lagen van de AGB ster, en worden vervolgens door verschillende mengprocessen naar het stellaire oppervlak gebracht. Hoewel deze scenario's algemeen aanvaard worden, zijn de fysische mechanismen achter de interne AGB processen nog niet goed begrepen. Huidige AGB evolutie- en nucleosynthesemodellen worden gebruikt om onze kennis van de verschillende AGB processen te verbeteren, maar de resulaten van deze modellen bevatten grote onzekerheden. Observaties zijn daarom noodzakelijk om onze kennis van de AGB nucleosynthese en mengprocessen te doorgronden.

Post-AGB sterren zijn ideale objecten om theoretische AGB evolutie en nucleosynthesemodellen te verbeteren, aangezien de chemische samenstelling van post-AGB fotosferen het gevolg is van de verschillende mengprocessen en interne nucleosynthese die heeft plaatsgevonden tijdens de stellaire evolutie. Een systematische abondantiestudie van optisch zichtbare post-AGB sterren die een brede waaier aan metalliciteiten en initiële massa's vertegenwoordigen, zal helpen om de verschillende parameters in AGB modellen nauwkeuriger te maken. De bestudeerde post-AGB sterren in de Melkweg hebben een zeer gevarieerde chemische diversiteit, maar de afstandsbepaling tot deze Galactische objecten is zeer onnauwkeurig. Daardoor is het niet mogelijk om de luminositeiten te bepalen en bijgevolg ook niet mogelijk om de initiële massa's, één van de belangrijkste parameters van AGB modellen, van deze objecten te schatten. Gelukkig hebben post-AGB sterren in de Magellaanse

Wolken niet deze beperking, aangezien de afstand tot de Magellaanse Wolken nauwkeurig gekend is.

In deze thesis voeren wij gedetailleerde fotosferische abondantiestudies uit van post-AGB sterren in de Magellaanse Wolken en de Melkweg, met als hoofddoel om de verschillende AGB processen beter te doorgronden. De gekende afstand tot de Magellaanse Wolken maakt het mogelijk om de initiële massa's van hun post-AGB sterren te schatten. De geobserveerde abondanties kunnen dan vergeleken worden met theoretische resultaten. Een zeer belangrijk chemisch element in onze abondantiestudies is lood (Pb). Dit element wordt beschouwd als het eindproduct van de *s*-process nucleosynthese, en de Pb abondanties zijn bijgevolg afhankelijk van de verschillende processen die plaatsvinden tijdens de AGB fase.

Onze resultaten tonen aan dat onze selectie van *s*-proces verrijkte post-AGB sterren in de Magellaanse Wolken allemaal sterren met lage massa's zijn, in combinatie met lage C/O ratio's en sterke *s*-proces verrijking. Vergelijking met de voorspelde resultaten van AGB modellen toont dat de geobserveerde C/O ratio's systematisch overschat worden. We vinden ook dat er een stijgend verschil bestaat tussen de geobserveerde en voorspelde Pb abondanties naarmate de metalliciteit daalt. De geobserveerde abondanties van de meer metaalrijke sterren in onze selectie bevestigen de voorspelde resultaten, maar naarmate de metalliciteit van de geobserveerde sterren daalt, stijgt ook het verschil tussen geobserveerde en voorspelde Pb abondanties. Voor lage metalliteiten overschatten de modellen zeer sterk de geobserveerde Pb abondanties.

We vinden ook een gevarieerde chemische diversiteit van post-AGB sterren in de Magellaanse Wolken, die sterk gelijkt op de chemische diversiteit van de Melkweg. Onze abondantiesstudies tonen dat zeer vergelijkbare objecten met vergelijkbare massa's en metalliteiten zeer verschillende *s*-proces abondanties hebben. Verder bevestigen onze abondatieresultaten de eerder bestudeerde intrinsiek milde *s*-proces verrijking van de Magellaanse Wolken. Met deze milde verrijking moet zeker rekening gehouden worden bij vergelijkingen tussen geobserveerde abondanties en theoretische model voorspellingen.

List of accronyms

2MASS	Two Micron All Sky Survey
AAT	Anglo-Australian Telescope
AGB	asymptotic giant branch
ANU	Australian National University
AU	astronomical unit
BB	black body
CO core	carbon-oxygen core
COG	curve-of-growth
CSE	circumstellar environment
DENIS	Deep Near-Infrared Survey of the Southern Sky
E-AGB	early AGB
ESO	European Southern Observatory
EW	equivalent width
FRUITY	Franec Repository of Upgraded Isotopic Tables and Yields
HBB	hot bottom burning
HERMES	High Efficiency and Resolution Mercator Echelle Spectrograph
HR diagram	Hertzsprung-Russell diagram
hs	heavy *s*-process
IR	infrared
IRAC	Infrared Array Camera
IRAS	Infrared Astronomical Satellite
ISM	interstellar medium
IvS	Instituut voor Sterrenkunde
LMC	Large Magellanic Cloud
ls	light *s*-process
LTE	local thermodynamic equilibrium
MARCS	Model Atmospheres in Radiative and Convective Scheme
MCPS	Magellanic Clouds Photometric Survey
MIPS	Multiband Imaging Photometer for Spitzer
MLT	mixing length theory

MS	main-sequence
NIST	National Institute of Standards and Technology
PAH	polycyclic aromatic hydrocarbon
PMS	pre-main sequence
PMP	partial mixing of protons
PN	planetary nebula
post-AGB	post-asymptotic giant branch
post-RGB	post-red giant branch
PPN	proto-planetary nebula
QSO	quasi-stellar objects
RGB	red giant branch
RW	reduced equivalent width
S/N	signal to noise
SAGE	Surveying the Agents of a Galaxy's Evolution
SED	spectral energy distribution
SMC	Small Magellanic Cloud
s-process	slow neutron capture process
SSO	Siding Spring Observatory
STP	spectral typing pipeline
TP-AGB	thermally pulsing AGB
TUP	third dredge-up
UV	ultraviolet
UVES	Ultraviolet and Visual Echelle Spectrograph
VLT	Very Large Telescope
WiFeS	Wide-Field Spectrograph
WD	white dwarf
YSO	young stellar object
ZAMS	zero age main sequence

Contents

Chapter 1

Introduction

In this thesis we present detailed chemical abundance studies of post-asymptotic giant branch stars (post-AGB stars) in the Milky Way Galaxy and the Magellanic Clouds. In this chapter, we start with a brief discussion about stellar evolution up to the AGB phase. Next, we describe the structural and chemical evolution of AGB stars, followed by a brief description of current theoretical AGB models. Next, we introduce post-AGB stars and present an overview of the chemical diversity of Galactic post-AGB stars. We end this chapter with our motivation and the general outline of this thesis.

1.1 Stellar evolution before the AGB in a nutshell

In this section, we briefly describe the evolution of single low- to intermediate-mass stars before the start of the AGB stage. Since this is a very broad topic to summarise in a few paragraphs, we restrict ourselves to an overall overview of the pre-AGB evolutionary stages. The main part of this section is based upon Kippenhahn et al. (2012).

1.1.1 Pre-main sequence

Single stars with initial masses between 0.8 and 8 $M_{\odot}$ (with $M_{\odot} = 1$ solar mass) follow similar evolutionary schemes. We describe the evolution of these low- to intermediate-mass stars by tracking their position through the Hertzsprung-Russell (HR) diagram. The HR diagram displays stellar luminosity

L (total energy radiated per second) versus the effective temperature $T_{\rm eff}$ (the temperature of a black body that would emit the same total amount of electromagnetic radiation as the star), both on a logarithmic scale. Fig. 1.1 shows the HR diagram with evolutionary tracks of two stars with solar composition and initial masses of 1 $M_\odot$ and 3 $M_\odot$, generated with STAREVOL (e.g. Siess 2007, and references therein). The different colored curves and letters represent the analogue evolutionary stages which will be described in this section. The respective colors and letters represent the same respective evolutionary phases for both the 1 and 3 $M_\odot$ stars, and it is clear from Fig. 1.1 that the evolutionary tracks are strongly dependent on the initial mass.

Since low-mass stars between 1 and 3 $M_\odot$ are the main topic in this thesis, we focus upon the evolution of these low-mass objects. The evolutionary tracks of heavier-mass objects with 3 $M_\odot < M_\star \leqslant 8$ $M_\odot$ are similar to those of 3 $M_\odot$, and we will not go into detail about the evolution of these heavier objects.

A star is born once it reaches the zero age main sequence (ZAMS, point a in Fig. 1.1) where it extracts most of its energy from the nuclear burning of hydrogen into helium in the stellar core. The stage before the ZAMS is called the pre-main sequence (PMS, cyan line in Fig. 1.1) during which the protostar, originating from a collapsing cloud of material, contracts until hydrogen burning is ignited. The PMS starts as soon as the protostar becomes optically visible and lasts about 10^7 years for a 1 $M_\odot$ star. During the PMS, a large amount of energy is generated due to slow gravitational contraction, which will be halted once the temperature of the stellar core is sufficient to ignite hydrogen burning and to maintain hydrostatic and thermal equilibrium. The protostar is optically thick and it radiates its energy following the general formula relating the surface luminosity to the effective temperature and surface area:

$$L = 4\pi R^2 \sigma T_{eff}^4 \tag{1.1}$$

with R the stellar radius and σ the Stefan–Boltzmann constant. Hayashi (1961) has shown that the PMS consists of two stages. During the first step, the surface temperature remains practically constant and the star moves vertically downward the HR-diagram until the internal structure of the protostar changes. It will then move towards the left. During the downward vertical movement in the HR-diagram, the luminosity due to the contraction energy is too high to reach the stellar surface solely through radiative processes like photon scattering. The star is fully convective (collective movement of material and energy) during this vertical movement, which is also called the *Hayashi track*. These Hayashi tracks are mass- and metallicity-dependent and they can be interpreted as the border between an allowed and a forbidden zone in the HR-diagram where a (proto)star to the right of its Hayashi track will rapidly change its structure and will move towards it. In the second step of the PMS, the star becomes partially

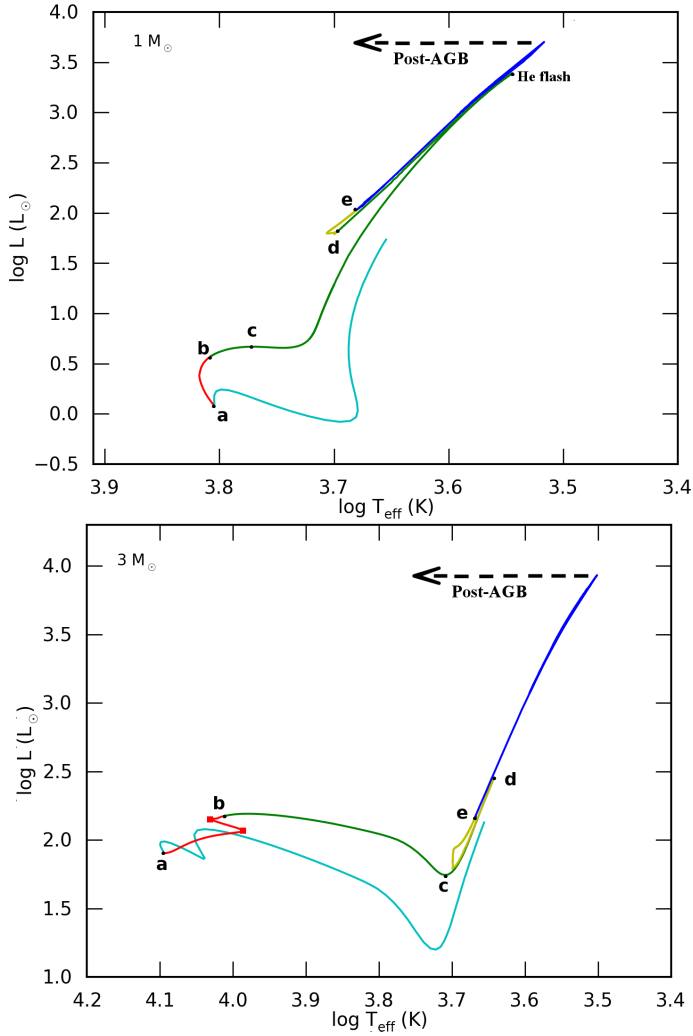

Figure 1.1: STAREVOL evolutionary tracks of two solar composition stars with initial masses of 1 $M_\odot$ (upper panel) and 3 $M_\odot$ (lower panel). The tracks cover the evolution from the pre-main sequence up to the TP-AGB, but not all thermal pulses are shown for clarity. The different colored curves and letters represent the beginning and ending of the different evolutionary phases, based upon the burning of H and He. The dashed black arrows represent the start of post-AGB evolutionary tracks.

radiative and follows the nearly horizontal Henyey-track (Henyey et al. 1955) which is characterised by a slow contraction in nearly hydrostatic equilibrium. PMS stars with $M_\star > 2\ M_\odot$ remain more radiatively stable than lower mass stars, and they are almost instantaneously on the Henyey track, largely skipping the Hayashi tracks.

During next evolutionary phases, stars will again approach their Hayashi tracks so the existence of these Hayashi tracks is important for the remaining stellar evolution.

1.1.2 From the main-sequence to the AGB

The main sequence

Once the star is born on the ZAMS, it undergoes quiescent hydrogen core burning up to 80-90% of its lifetime on the *main-sequence* (MS, red lines in Fig. 1.1). The duration of the MS depends on the stellar mass: higher mass stars will consume all the fuel in the stellar core quicker than their lower mass counterparts. For a 1 $M_\odot$ star, the MS lasts for about 10^{10} years. The shape of the evolutionary tracks of MS stars are strongly mass-dependent. The shapes are nearly identical for stars with masses from 3 up to 8 $M_\odot$, but for lower mass stars, the shapes are different. This is caused by the difference in internal structure for the different masses. These structural differences are related to convection.

MS stars have roughly the following structure: stars with masses above 1.5 $M_\odot$ have a convective core surrounded by a radiative envelope while stars with masses below 1 $M_\odot$ have a radiative core surrounded by a convective envelope. MS stars with $1\ M_\odot \leqslant M_\star \leqslant 2\ M_\odot$ have convective cores and convective outer envelopes with inbetween a radiative envelope.

MS stars with masses $M_\star \geqslant 1.3\ M_\odot$ burn central hydrogen through the strongly temperature-dependent CNO cycle which is very centrally concentrated. The convective core occupies a larger mass fraction than the hydrogen burning mass fraction and hence provides fresh hydrogen to the nuclear burning zone by mixing. As long as new hydrogen is provided to the nuclear burning zone, these stars will remain on the MS. However, the gradual decrease of the central hydrogen fraction lowers the opacity such that the convective zone shrinks. Therefore, the radiative zone moves inward which decreases the surface temperature. In addition, the mean molecular weight increases as more hydrogen is fused into helium, by which the luminosity goes up. Both these effects cause these MS stars to move in an upper right direction in the HR diagram. Once the central

hydrogen is almost depleted, the star will again start to gravitationally contract to produce energy. This overall increase in energy also increases the surface luminosity and as the stellar radius is decreasing, the surface temperature will also increase following Eq. 1.1. The star will now move up to the left in the HR-diagram until all central hydrogen is depleted (region between the red squares for the 3 $M_\odot$ star in Fig. 1.1).

For low-mass stars, the evolution is different. MS stars with $M_\star < 1.3\ M_\odot$ burn their central hydrogen through the pp chain. As the mean molecular weight increases, the luminosity of these stars will also increase but as the effective temperature is determined by the outer convective envelope, it will remain basically constant and the star will slowly move up in the HR-diagram.

Importance of convection

Stars with masses around 1.3 $M_\odot$ will gradually evolve from one structure of convection zones to the other as the different effects described above compete with each other. The exact transition mass strongly depends on the initial composition of the star and how convection is treated in stellar evolution codes that produce these theoretical evolutionary tracks like in Fig. 1.1. Although a complex matter, current stellar evolution codes implement convection in the form of a simple mixing length theory (MLT, see e.g. Chapter 7 in Kippenhahn & Weigert (1994)). MLT uses a free parameter $\alpha_{\rm MLT}$ which sets the mean free path of a convective blob in function of the pressure scale height. As this parameter can only be calibrated by observations, stellar evolution codes generally use an $\alpha_{\rm MLT}$ which is calibrated to the Sun. However, it is likely that this parameter changes for each evolutionary phase which creates large uncertainties for stellar evolution codes. Another large uncertainty considering convection is *convective overshooting*: when a convective bubble reaches the boundary layer with the radiative zone, the inertia of the bubble will cause it to penetrate the radiative zone which may have large influences on the outcomes of stellar evolution codes. Also for later evolutionary phases like the AGB, convective overshooting is poorly understood creating important uncertainties in theoretical AGB models.

Red giant branch and first dredge-up

The MS is followed by an evolutionary phase characterised by hydrogen shell burning on top of the helium core which is not yet hot enough to ignite helium burning (point b in Fig. 1.1). More massive stars ignite hydrogen shell burning in a more abrupt way than their lower-mass counterparts, as the central convection

zone during the MS mixed helium from the core in the hydrogen burning shell. Lower-mass stars do not have a convective core during the MS and thereby produce a smooth transition from central to shell hydrogen burning. The hydrogen shell-burning increases the mass of the helium core and for stars with $M_\star < 2.0\ M_\odot$, the core becomes partially electron-degenerate. This means that pressure to support self-gravity is no longer fully linked to the temperature. The pressure in the core starts to be provided by densely packed electrons which are prevented of being more compressed by the Pauli exclusion principle, while the core mass increases slowly due to hydrogen shell-burning. For most low-mass stars, this evolutionary phase with hydrogen shell burning can last a large fraction of the MS lifetime.

For more massive stars, the helium core contracts during hydrogen shell burning but it will not become degenerate since core helium burning will ignite before the core becomes degenerate. During this evolutionary stage, the surface luminosity is totally provided by the hydrogen shell-burning at the bottom of the envelope, and the star crosses the HR diagram on a very short timescale of about 0.2% of its MS lifetime towards point c in Fig. 1.1. The stellar core is heated up by contraction.

For both lower- and higher-mass stars, the core is heated up due to contraction but the surface luminosity is provided by the hydrogen shell burning. This excess in energy has difficulties in transporting itself to the surface, so a large part of this energy is used for expanding the hydrogen-rich envelope. The star now evolves to the right towards it's Hayashi track (point c in Fig. 1.1) and will strongly increase its luminosity as it keeps on expanding. The star now ascends the *red giant branch (RGB)* which occupies between 10^8 to 10^9 years for a one solar mass star. With increasing mass, the time on the RGB strongly decreases.

As the star is now ascending the HR-diagram close to its Hayashi track, the outer convective envelope occupies about 70% of the total stellar mass. The convection zone now reaches areas containing products of internal nucleosynthesis which are transported to the stellar surface. This phenomenon is called the *first dredge-up* and it transports mainly products from the CNO cycle to the stellar surface. We will discuss the first dredge-up in more detail in Sect. 1.2.2.

Horizontal branch

The way the transition from the RGB towards the next evolutionary phase takes place, strongly depends on the stellar mass. The more massive stars with $M > 2.0\ M_\odot$ will reach a central temperature of 10^8 K which will ignite central helium burning in the stellar core which has not yet become electron-degenerate. These stars have now entered a stable phase of central helium burning and hydrogen

shell burning (point d for the 3 $M_\odot$ in Fig. 1.1), and they again descend close to their Hayashi track and move towards higher effective temperatures. These stars have now entered the *horizontal branch* (yellow curves in Fig. 1.1) which lasts for about 10% of the total stellar lifetime. Once central helium has been depleted, the star will again move towards its Hayashi track, starting the next evolutionary phase.

For lower mass stars, the transition from the RGB towards the horizontal branch is more violent. Central helium burning is ignited in the electron-degenerate core. As pressure is no longer related to temperature, the material does not expand while temperature is strongly increasing due to helium burning. This creates an increasingly efficient helium burning as temperature still increases and increases the core luminosity significantly: the star undergoes a *helium flash* (see upper panel in Fig. 1.1). The thermonuclear runaway is halted once the electron-degeneracy has been lifted and the star evolves towards stable central helium burning, which starts at point d for the 1 $M_\odot$ star in Fig. 1.1 at the horizontal branch. The energy released during the helium flash is also used to expand and cool the core. This lowers the energy production in the hydrogen burning shell and therefore also the luminosity. The lower mass stars now descend close to their Hayashi track before settling on the horizontal branch. Similar to higher mass stars, the depletion of central helium starts the next evolutionary phase: *the asymptotic giant branch (AGB)* which lasts between orders of 10^5 up to 10^6 years depending on stellar mass.

1.2 AGB stars

This section gives an overview of the structural and chemical evolution of AGB stars and it is largely based on texts from Iben & Renzini (1983), Busso et al. (1999), Habing & Olofsson (2004) and Herwig (2005).

1.2.1 Structural evolution of AGB stars

At the start of the AGB, the stellar core consists out of the helium burning products carbon and oxygen. The stars have now reached point e in Fig. 1.1. As central temperatures are not high enough to initiate carbon burning, the core starts to contract and basically the same process starts over again. The stars have again reached their Hayashi tracks in the HR-diagram. During the AGB, only the most massive stars with masses of about 8 $M_\odot$ or higher will be able to initiate carbon burning. In this thesis, we mainly focus upon stars with

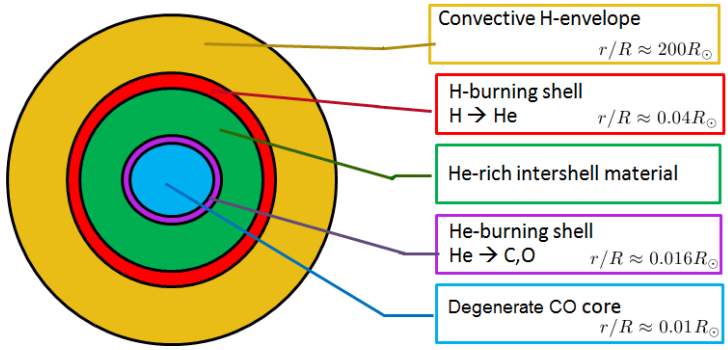

Figure 1.2: A sketch of the interior of an AGB star. The figure is not on scale. Indicated distances provide an estimated distance scale for a one solar mass AGB star.

lower masses and therefore we do not consider their evolution for the remainder of this section.

For all stars, He burning is still active but now only in the form of helium (He) shell burning. Gravitational contraction from the stellar core heats up the bottom of the He burning shell, strongly increasing the He shell-burning. As the star is on its Hayashi track, it will start to expand and ascend towards higher luminosities following its Hayashi track.

The AGB phase can be divided in two periods. The first and longest period is the *early AGB (E-AGB)* during which only He shell-burning is active. Due to the strong expansion of the outer envelope, the H-burning shell cools down and extinguishes. For stars with initial masses above 4 $M_\odot$, the large convective outer envelope can again penetrate the inner regions and transports products of internal nucleosynthesis towards the surface. These stars undergo the *second dredge-up* which is described in more detail in Sect. 1.2.2.

During the E-AGB, the mass of the CO core increases and the He-burning shell moves outwards in mass. When the He-burning shell approaches the faded H-shell, the rising temperature ignites the H-burning shell, which becomes the dominant energy source with $L_{He}/L_H \leqslant 10^{-3}$ (Iben & Renzini 1983). The star has now entered the *thermally pulsing AGB (TP-AGB)* phase. A representation of the interior of a TP-AGB star is shown in Fig. 1.2. The upper part of the blue evolutionary tracks in Fig. 1.1 represent a part of the TP-AGB phase.

Fig. 1.3 shows the structural evolution of a thermally pulsing AGB star over time, zoomed in on the small mass-coordinate with the burning shells and the

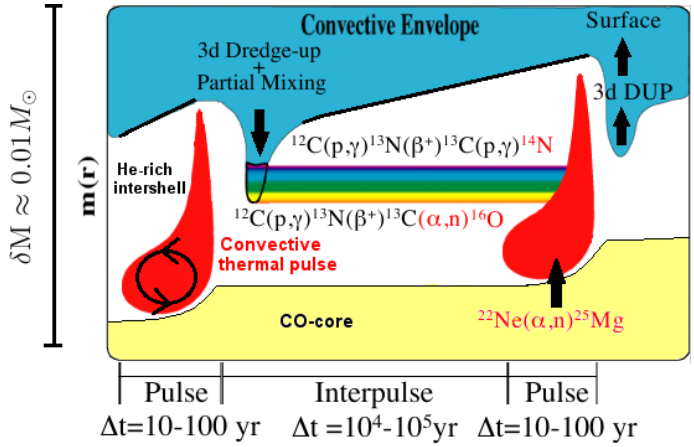

Figure 1.3: Illustration of the structure of a thermally pulsing AGB star over time, zoomed in on a small mass coordinate. The white region represents the He-rich intershell in between the convective H-envelope (blue region) and the electron-degenerate CO-core (yellow region). The bold black line at the base of the convective envelope represents the H-burning shell, the black line at the base of the intershell shows the He-burning shell. The red regions indicate convective thermal pulses. The rainbow-coloured zone represents a partial mixing zone. Important chemical reactions are shown next to the regions where they take place. Figure reproduced with permission of Stéphane Goriely.

He-rich intershell. During the TP-AGB, intervals of quiescent H-shell burning are interrupted by thermal pulses. The He-burning shell gradually moves further out in mass coordinate, reaching colder temperature layers and fades out. The H-burning shell moves outwards on top of the practically inactive He shell, increasing the mass of the He intershell with newly-synthesised He, a thin layer in radiative equilibrium in between the H- and He-burning shells (white region in Fig. 1.3). Gravitational contraction by the core increases the temperature and densities of the He-burning shell. When the shell re-ignites, a thermal pulse is started. The He-burning takes place in a thin shell which, in combination with the weight of the upper layers preventing the He-burning shell from expanding effectively, causes a thermonuclear runaway He shell flash event. This interrupts the radiative state of the He intershell and makes it almost completely convective. The thermal pulse transports away the excess of energy and thereby mixes newly-synthesised carbon and oxygen within the He-rich intershell almost up to the H-burning shell. At the end of the thermal pulse, the intershell expands and radiates away the energy produced by the temporarily effective He burning. The expansion ends the convective thermal pulse and lifts

the H-burning shell to lower temperatures where it temporarily fades out. At this point, the convective envelope penetrates the He-rich intershell to transport away the energy excess of the previously strong He-burning: this phenomenon is called the *third dredge-up*. The efficiency of the third dredge-up will strongly affect the further chemical evolution of AGB stars as described in Sect. 1.2.2.

Depending on the core mass, this cycle of thermal pulses repeats itself every 10^3 to 10^5 years. During the cycle, the strong thermal pulses, lasting for approximately an order of a hundred years, are followed by long interpulse periods with stable H-shell burning. During the TP-AGB evolution, the thermal pulses grow in strength and the interpulses become shorter. The number of thermal pulses a TP-AGB star undergoes, depends on the initial mass, metallicity and mass-loss during the TP-AGB. The star has now lost about 10 % of its mass since its birth, and it will lose almost its whole envelope mass during the TP-AGB. At the end of the TP-AGB, the star undergoes a strong dust-driven mass loss which will eventually terminate the AGB phase.

1.2.2 Chemical evolution of AGB stars

Prior to the TP-AGB

Along the MS, the chemical composition of the outer stellar envelope remains almost untouched by the nuclear fusion in the core. The only change in chemical composition of MS stars is the depletion of lithium (Li), although the mechanism behind this depletion is not fully understood (see e.g. Pace et al. 2012, and references therein). We will not elaborate on Li in MS stars in this thesis. Apart from Li, the chemical composition of the surface layer of MS stars resembles the initial composition of the star.

As already mentioned in Sect. 1.2.1, throughout the stellar life cycle the surface composition is altered by mixing events during which the large outer convective layers penetrate the deep interior regions where products of internal nucleosynthesis reside. These burning ashes are then transported by the convective envelope to the stellar surface where they alter the chemical composition of the surface. These mixing events are called dredge-ups and they can strongly change the surface composition.

The first dredge-up occurs during the ascent on the RGB (see e.g. Iben 1967) and the strength of the first dredge-up is strongly dependent on multiple factors like initial mass and metallicity. These factors determine how deep the first dredge-up will penetrate the inner regions and hence how strong it alters the surface composition. During the first dredge-up, the outer convective zone

penetrates layers with products of hydrogen burning via partial CNO processing during the MS. Therefore, the main effect of the first dredge-up is a change in surface composition of light elements with depletion of ^{12}C abundance and an increase in ^{4}He, ^{13}C and especially ^{14}N (see e.g. El Eid 1994; Lattanzio & Boothroyd 1997; Boothroyd & Sackmann 1999).

The second dredge-up occurs along the E-AGB for stars with initial masses with $M \geqslant 4\ M_{\odot}$. Similar to the first dredge-up, the outer convective envelope penetrates inner regions with the end-products of H burning via the complete CNO cycle. Therefore, the second dredge-up alters the surface abundances of the same isotopes as the first dredge-up: depletion of ^{12}C and an increase of the H-burning ashes ^{4}He, ^{13}C and ^{14}N, for which the strength of alteration is strongly dependent on initial mass (see e.g. Becker & Iben 1980; Becker 1981; Lattanzio & Boothroyd 1997).

The third dredge-up and carbon stars

During thermal pulses, He-burning ashes at the bottom of the He intershell are mixed with higher intershell layers by the convective zone generated by the strong He-shell burning (see red zones in Fig. 1.3). After a thermal pulse, the envelope expands and the inner border of the envelope will first move away from the stellar core. When the star contracts again, the inner border of the convective envelope will penetrate the He intershell which lies below the inactive H-burning shell. This mixing process is called the third dredge-up (TUP). The efficiency of the TUP is thought to increase with increasing core mass and decreasing metallicity. During TUP, the convective envelope also injects protons into the He intershell and transports material from the intershell to the stellar surface. This transported material includes the He-burning ashes, which have been previously mixed into the intershell by the convective thermal pulse. Each TUP hence mixes a certain amount of intershell material with the envelope. The He-burning ashes consist of carbon and oxygen where carbon is five to ten times more abundant than oxygen. This is because ^{12}C in the intershell is a direct product of the triple-α reactions. The latter are the almost solely providers of energy during thermal pulses, so ^{12}C is the main product of convective thermal pulses. Oxygen on the other hand is only significantly produced in the deeper radiative parts of the He shell as it requires higher temperatures to form than carbon. However, convective overshooting, which is the penetration of a convective bubble into the radiative layers at the borders of the convective zone, can transport some synthesised oxygen into the convective zone during a thermal pulse.

The transport of intershell carbon to the surface layers has a strong effect on

the C/O ratio[1] of the surface layer: with each TUP, the C/O ratio increases. The mean initial C/O ratio of a Galactic AGB star is around 0.5, reflecting the composition of the instellar medium (ISM) out of which the star was born. An oxgen-rich AGB star is also called an M star. When the C/O ratio of the star reaches unity, the star becomes a carbon or C star.

AGB stars are cool objects with typical effective temperatures between 3000 and 3500 K, for which the photospheric opacity is dominated by molecular transitions. The surface chemistry of the AGB star also determines the circumstellar chemistry and strongly impacts the mass-loss rate. Before the star becomes a carbon star, practically all carbon atoms are assumed to be locked in the CO molecule and oxgen-rich molecules such as H_2O, TiO and SiO dominate the photospheric spectra. However, when the C/O ratio exceeds unity, practically all oxygen molecules are assumed to be locked within the CO molecule and the overabundant carbon atoms can now form carbon-rich molecules like CH, C_2, CN and C_2H_2. The mass-loss driving mechanism of AGB stars is not fully understood and state-of-the-art models are not yet capable of predicting observed mass loss of AGB stars. The AGB mass-loss driving mechanism is thought to be based on momentum transfer in a dust-driven wind. AGB pulsate and therefore, they can create circumstellar regions with higher densities of molecules at an equilibrium radius where dust can form beyond the dust condensation radius. Once dust has condensed, it can efficiently capture momentum through radiation pressure which it transfers to the surrounding gas particles (see e.g. Wood (1979), Bowen (1988), Lamers & Cassinelli (1999)). The main problem in current theoretical models consists in having a high enough density at a large enough distance for dust condensation to be effective. Moreover, newly formed dust needs a large radiative cross-section to gain enough linear momentum to accelerate the wind. For C-rich stars, the carbonaceous dust can form close to the star and drive the wind. However, for O-rich stars, the driving opacity source is still not fully identified. Carbon- and oxygen-rich stars hence seem to have different mass-loss driving opacity sources. Mass loss is a key process in TP-AGB models as the envelope mass determines the number of thermal pulses and TUPs that can take place, and hence how the surface composition may alter. Unfortunately, as it is not fully understood, the implementation of mass loss in theoretical AGB models creates important uncertainties as described in Sect. 1.3.1.

The general predictions of AGB models show that only stars in a specific mass range can become C-stars. Models predict that for very low-mass stars, the convective envelope during TUP does not reach the inner region with mixed carbon from the convective thermal pulse, hence the envelope can not be enriched with carbon. Depending on the AGB model and chemical composition,

[1] This ratio expresses particle density and not mass

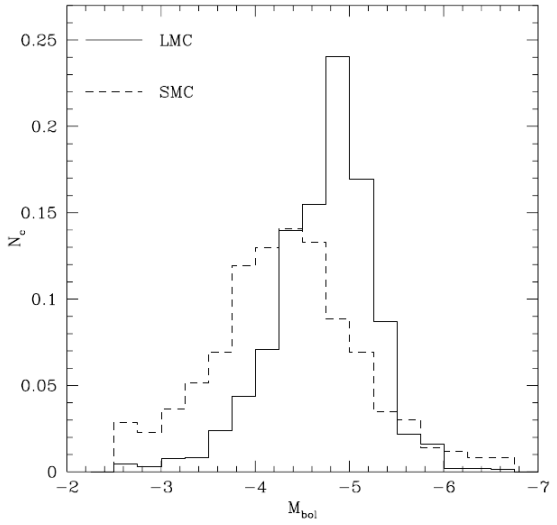

Figure 1.4: The observed carbon star luminosity functions of the LMC (solid line) and SMC (dashed line), normalised to the total number of stars. Figure from Marigo et al. (1999).

the lower mass limit for becoming a carbon star is thought to lie between 1.0 and 1.5 $M_{\odot}$ depending on metallicity.

For intermediate mass-stars, depending on chemical composition, the bottom layers of the convective envelope during the TP-AGB may reach the top layers of the H-burning shell, exposing the envelope to high temperatures (up to 10^8 K) during interpulse. This phenomenon is called hot bottom burning (HBB) and prevents intermediate-mass stars from becoming a C star (e.g. Lattanzio 2003). The He-burning ashes mixed with the convective envelope by TUP, are now processed by CNO processing at the bottom of the convective envelope and can dramatically alter the surface composition. Since the convective turn-over time of the envelope is about the order of a few years, the whole envelope is processed through the hot region a few thousand times per interpulse period (e.g. Karakas & Lugaro 2010). The dredged up ^{12}C is burned into ^{13}C which is then burned into ^{14}N, keeping the C/O ratio below unity. HBB is an important producer of ^{14}N, especially for low metallicities, and explains the absence of high-luminosity carbon stars (Boothroyd et al. 1993). However, just like TUP, HBB requires a certain envelope mass. When the mass of the envelope is low enough to cease the HBB but enough for TUP, models predictions show that the AGB star may eventually still turn into a high luminous C star but by

then the star is likely no longer optically visible as it is obscured by heavy mass-loss. Possible examples of these highly luminous carbon AGB stars have been observed in the Magellanic Clouds by van Loon et al. (1998).

Fig. 1.4 shows the observed luminosity functions of carbon stars in the Magellanic Clouds from Marigo et al. (1999). The carbon star luminosity function of the Large Magellanic Cloud (LMC) ranges from $M_{bol} = -3$ ($\pm$ 1250 $L_{\odot}$) up to $M_{bol} = -6.5$ ($\pm$ 31000 $L_{\odot}$) and peaks around $M_{bol} = -4.875$ ($\pm$ 7000 $L_{\odot}$). The carbon star luminosity function of the Small Magellanic Cloud (SMC) seems more spread with a peak around $M_{bol} = -4.375$ ($\pm$ 4500 $L_{\odot}$) and going down to $M_{bol} = -2.5$ ($\pm$ 800 $L_{\odot}$). However, the formation of such low-luminosity C stars can hardly be explained by the TUP in single AGB-stars, so it is assumed that these stars are low-mass stars that have been contaminated by the ejecta of a former AGB companion in a close binary system. The lower peak luminosity of the SMC with respect to the peak luminosity of the LMC is consistent with the lower metallicity of the SMC and the predictions that at low metallicity carbon stars are more easily formed. In addition, the number of high-luminosity carbon stars is very small which seems to confirm the efficiency of HBB to stop the the C star formation for the AGB stars with a higher mass.

1.2.3 The *s*-process nucleosynthesis in AGB stars

During the TUP, the convective envelope does not only transport material from the He intershell to the surface but also injects protons into the intershell. This forms the start of the *slow neutron capture nucleosynthesis* or *s*-process nucleosynthesis, which is the origin of approximately half of all elements heavier than iron (Gallino et al. 1998). The *s*-process creates heavy elements by neutron capture which is slow with respect to the competing β^- decay. Due to this slow process, most unstable isotopes formed by neutron capture have time to decay into more stable isotopes before the next neutron capture. Therefore, the s-process follows closely the valley of stability in the chart of isotopes as shown in Fig. 1.5. The efficiency of the *s*-process strongly depends on multiple parameters like the degree of neutron production together with the initial iron abundance of the star, which forms the seed for the creation of heavier elements. Along the *s*-process path are nuclei with closed neutron shells corresponding to magic neutron numbers N = 50, N = 82 and N = 126. Nuclei with a magic number of neutrons are very stable against neutron capture because of their low neutron capture cross-sections, and therefore they create bottlenecks in the *s*-process chain. These are consequently seen as *s*-process peaks around Sr (Z = 38), Ba (Z = 56), and Pb (Z = 82). Fig. 1.6 shows the measured and estimated neutron-capture cross-sections of heavy nuclei (A $\geqslant$ 56) on the *s*-process path for a specific neutron energy. The magic neutron numbers at N = 50, 82 and

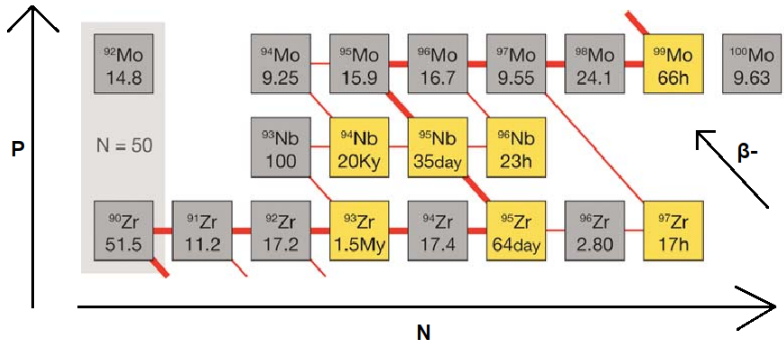

Figure 1.5: Illustration of *s*-process path through the chart of isotopes from Zr up to Mo. Left to right represents increasing number of neutrons, upwards means increasing number of protons. Stable isotopes are represented by gray squares, unstable isotopes by yellow squares. The thick red line represents the main *s*-process branch, the thin red lines represent less important branches. The numbers in the squares show the isotopic abundance fraction for the stable isotopes and the half-life time for unstable isotopes. Figure reproduced from (Herwig 2005).

126 are clearly visible because their neutron cross-sections are much lower than those of other nuclei. Also an odd-even effect is present in Fig. 1.6. Nuclei with an even atomic weight A have smaller cross-sections because the average density of resonant states in the compound nucleus is smaller than that of a nucleus with an odd atomic weight, where the captured neutron can couple in multiple ways to the unpaired nucleons. The characteristics of the cross-section curve reflect directly in the abundances, and both the *s*-process peaks and the odd-even effect are clearly visible in the solar abundance distribution of elements, shown in Fig. 1.7.

To be able to reproduce the observed s-process abundances in the Sun, it was soon realised that the s-process could not entirely take place in one single astrophysical site. Therefore, historically, the *s*-process has been separated into two components of which each has it own mean value of time-integrated neutron flux, or neutron exposure τ (Seeger et al. 1965), which is typically expressed in mbarn^{-1}. Each component is linked to a specific astrophysical site. The weak component produces nuclei with mass number A ranging from $56 < A \leqslant 90$ up to the Sr-peak and has a typical $\tau \approx 0.07$ mbarn^{-1} (Karakas & Lugaro 2010). The main component produces nuclei with $90 \leqslant A \leqslant 208$ with a mean $\tau \approx 0.3$

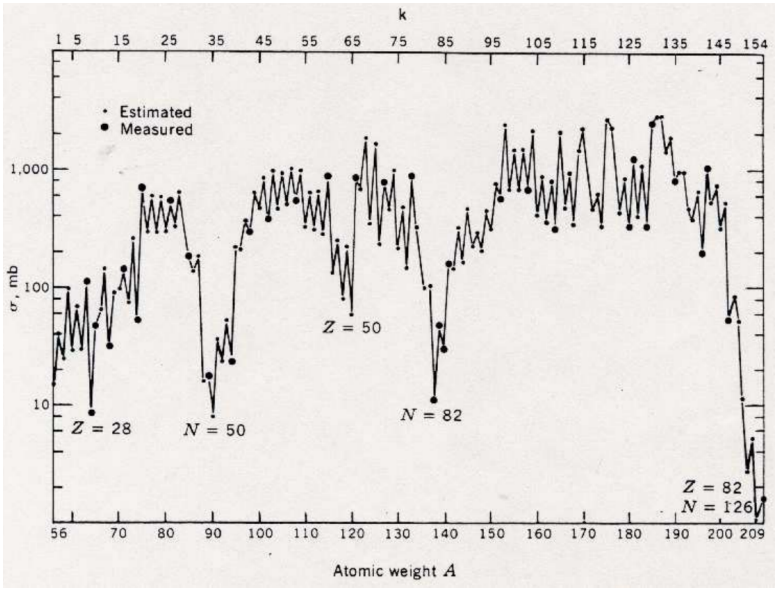

Figure 1.6: Measured and estimated neutron capture cross-sections of heavy nuclei on the *s*-process path for a neutron energy around 25 keV. The strong influence of the closed nuclear shells or magic numbers, is obvious. The cross-sections also display a strong odd-even effect representing the average level densities in the compound nucleus. Figure taken from Clayton (1983).

mbarn^{-1} for producing isotopes around the Ba-peak and reaching up to $\tau \approx 7.0$ mbarn^{-1} to produce ^{208}Pb. The weak component is thought to be mainly produced in the He and C-burning shells of massive stars (e.g. Pignatari et al. (2010)) while the main component is expected to be produced in low-mass AGB stars (e.g. Busso et al. (1999)) with large productions of ^{208}Pb in low-mass, metal-deficient AGB stars (e.g. Sneden et al. (2008)). Both the neutron and proton number of the ^{208}Pb nucleus are equal to a magic number and therefore ^{208}Pb is called 'double magic'. This implies that ^{208}Pb cannot decay and that it has a very small cross-section for neutron capture as shown in Fig. 1.6, marking it as the end-product of the *s*-process chain.

Two neutron sources are thought to be active in AGB stars. The first source is the ^{22}Ne(α,n)^{25}Mg reaction which is the dominant source in intermediate-mass stars (Truran & Iben 1977). This reaction requires high temperatures of 3.0×10^8 K which are reached at the bottom of the convective thermal pulse (see Fig. 1.3). During He burning, ^{14}N is transformed into ^{22}Ne via

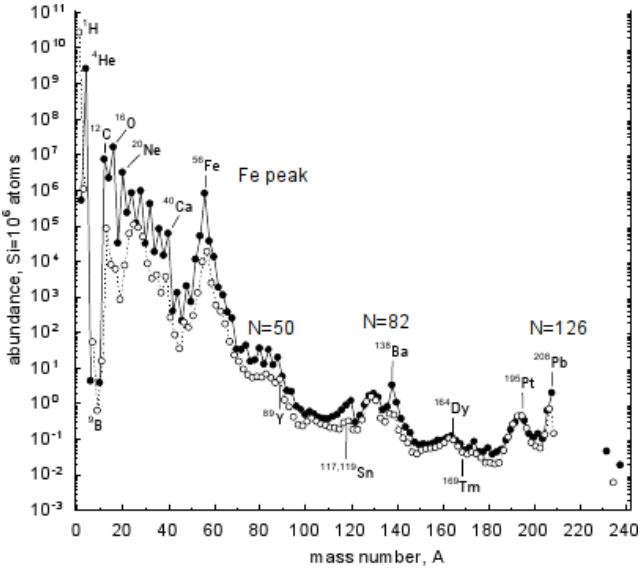

Figure 1.7: Abundance distribution of isotopes in the young solar system with respect to mass number A. Full symbols represent abundances for isotopes with even mass numbers, open symbols represent odd mass number isotopes. The *s*-process peaks are clearly visible. Figure taken from Lodders et al. (2009).

^{14}N(α,γ)^{18}F(β^+)^{18}O(α,γ)^{22}Ne. The latter element becomes a neutron source after a new α-capture. However, no more than a few percent of the ^{22}Ne is burned. During the thermal pulse, the neutrons are released in a short burst with high densities of about 10^{11} neutrons/cm^3 (Lugaro & van Raai 2008). The peak densities are only released for about a year and then followed by a neutron-density tail of a few years. As the neutron irradiation time is short, there is little time to form heavy *s*-process elements and therefore the ^{22}Ne(α,n)^{25}Mg is associated with the weak component of the *s*-process.

The second neutron source is the ^{13}C(α,n)^{16}O reaction, which is found to be the dominant neutron source in low-mass AGB stars (see e.g. Smith et al. (1987) and Gallino et al. (1998)). This reaction operates at a temperature of 9.0×10^7 K and takes place in the He-rich intershell during interpulses. After a thermal pulse, the convective hydrogen envelope penetrates the upper layers of the intershell and injects protons with decreasing number density with increasing depth. This mixing process is called *partial mixing* (see Fig. 1.3) and provides the necessary protons to transform the ^{12}C, which has been mixed throughout the intershell during the thermal pulse, into ^{13}C via ^{12}C(p,γ)^{13}N(β^+)^{13}C creating a so-called

Table 1.1: Typical properties and neutron fluxes for low- ($M < 4M_\odot$) and intermediate-mass ($4M_\odot \leqslant M < 8M_\odot$) AGB stars. The last row shows neutron exposure τ for solar metallicity stars. Table reproduced from Lugaro & van Raai (2008).

	$M < 4M_\odot$	$M > 4M_\odot$
Maximum temperature ($10^6 K$)	300	380
Intershell mass ($M_\odot$)	10^{-2}	10^{-3}
Neutron source	$^{13}C(\alpha, n)^{16}O$	$^{22}Ne(\alpha, n)^{25}Mg$
Timescale neutron fluxes (yr)	10^4	10
Maximum neutron density (n cm^{-3})	10^8	10^{11}
Neutron exposure (mbarn^{-1}, at $Z = Z_\odot$)	0.3	0.02

^{13}C-pocket. In the intershell layers where the injected proton fraction is not too high, the $^{13}C(\alpha,n)^{16}O$ reaction provides neutrons which can be captured by iron seeds to created heavy elements. However, in the upper intershell layers where the proton fraction is high, the reaction $^{13}C(p,\gamma)^{14}N$ prevents ^{13}C from acting as a neutron source (see Fig. 1.3). Moreover, the produced ^{14}N has a large $^{14}N(n,p)^{14}C$ reaction rate and hence acts as an efficient neutron poison, preventing the creation of heavy elements.

The lower layers of the partial mixing zone do not contain enough protons to form enough ^{13}C, hence the *s*-process takes only place in a small restricted region of the intershell of about 10^{-3} $M_\odot$. Although the neutron densities originating from the ^{13}C-pocket in the intershell (10^8 neutrons/cm^3) are significantly lower than neutron densities with the ^{22}Ne in intermediate-mass AGB stars, the neutron irradiation of the ^{13}C-pocket lasts thousands of years under radiative conditions during the quiescent interpulse. This provides the opportunity to create heavy elements from iron seeds and therefore, the main component of the *s*-process is associated with low-mass AGB stars. Table 1.1 provides an overview of typical parameter values associated with the neutron sources in low- and intermediate mass stars. As strong activation of the ^{22}Ne source in low-mass AGB stars is prevented by the low temperatures, a strong activation of the ^{13}C source in more massive AGB stars is prevented due to the small extent in mass of the intershell region (Lugaro & van Raai 2008) and the effect of HBB. As a general assumption, the mass of the ^{13}C-pocket is usually taken as a fraction of the intershell mass, so a smaller intershell mass leads to a smaller partial mixing zone. The relative intershell mass of intermediate mass stars is lower since thermal pulses are more frequently triggered at higher masses, creating

shorter periods for the H-burning shell to increase the mass of the intershell. Another important effect for the ^{13}C-pocket is the effect of HBB during the third dredge-up, which turns the ^{12}C and ^{13}C into ^{14}N, which may strongly diminish or even inhibit the *s*-process by the ^{13}C-pocket in the intershell for higher mass AGB stars.

The ^{12}C, which forms the origin of the ^{13}C-pocket, is not dependent on metallicity since the AGB star creates ^{12}C via the triple-α reaction so it is of primary origin. However, the number of iron seeds available for the *s*-process are of secondary origin, hence dependent on the initial metallicity of the star. Therefore, in metal-deficient AGB stars, more neutrons are available for each iron seed hence the neutron exposure increases with decreasing metallicity, assuming that the stellar structure is similar for different metallicities. Larger neutron exposures generally lead to an abundance distribution containing more species at the heavy *s*-process (hs) peak around N = 82 (including Ba, La, Ce, Nd and Sm) compared to the light *s*-process (ls) peak at N = 50 (including Sr, Y and Zr). The abundances of the heavy and light *s*-process elements are respectively averaged and defined as the heavy *s*-process index hs and the lower mass *s*-process index ls. The [hs/ls] ratio hence traces the neutron exposure, as a higher ratio indicates a higher neutron exposure. Likewise, the [hs/ls] ratio is expected to be higher in AGB stars with higher ^{13}C abundances in the ^{13}C-pocket (Herwig 2005). So generally, the maximum [hs/ls] ratios are reached at lower metallicities (Busso et al. 2001). However, as the neutron exposure increases, the total neutron flux is used to produce Pb, decreasing again the [hs/ls] ratio (see already Fig. 1.17). These large neutron exposures are expected in low-mass, metal-deficient stars that produce the strong *s*-process peak.

Due to the combination of strong mass loss with carbon and *s*-process enhancements, low-mass AGB stars are thought to be one of the main astrophysical sites of carbon and heavy *s*-elements in the interstellar medium (ISM).

1.3 AGB models

Theoretical AGB evolution and nucleosynthesis models play an important role in the interpretation of the observed abundances of AGB and their progeny, the post-asymptotic giant branch (post-AGB) stars. Since this is a wide research field, we limit our description here to some main methods and parameters used in AGB models, followed by a brief and non-complete overview of stellar evolution codes. We briefly come back to general theoretical model results in Sect. 9.1.

1.3.1 General methods

Most current AGB chemical evolutionary models are post-processing codes. First the main physical stellar structure parameters are calculated throughout stellar evolution, together with the restricted nuclear network which includes key isotopes and reactions needed to compute the stellar evolution. Thereafter, depending on the initial mass of the stellar model, a proton ingestion scheme may be imposed to create a ^{13}C-pocket (see e.g. Fishlock et al. 2014), and then the abundances of remaining isotopes are calculated. This more extensive nuclear network consists of isotopes ranging from hydrogen up to bismuth (Z=83). Recently, AGB models have been developed in which the stellar and nucleosynthetic evolution are coupled, so the nucleosynthesis is immediately calculated in each step of the evolution (Cristallo et al. 2011). Calculating the nucleosynthetic evolution requires accurate nuclear reaction rates and these are retrieved from constantly updated nuclear reaction databases like BRUSLIB (Arnould & Goriely 2006) and the JINA Reaclib Database (Cyburt et al. 2010).

As mentioned in the previous paragraph, proton ingestions are sometimes artificially imposed to create a significant ^{13}C-pocket in low-mass AGB stars. The details of the ^{13}C pocket formation mechanisms and its extent in mass in the He intershell are still unknown. Various mechanisms have been proposed like convective overshooting (Herwig et al. 1997; Herwig 2000) and deep mixing, during which material is convectively transported between the convective envelope and the radiative layers where partial H burning occurs (see e.g. Karakas 2010; Busso et al. 2010). In addition, non-convective mixing like differential rotation (e.g. Siess et al. 2004; Piersanti et al. 2013) and thermohaline mixing (e.g. Angelou et al. 2011) are currently implemented in AGB models to study their effect on the *s*-process nucleosynthesis. Also the effect of internal gravity wave mixing (Denissenkov & Tout 2003) on the *s*-process nucleosynthesis needs further exploration.

A very important parameter in AGB evolution and nucleosynthesis is the third dredge-up efficiency λ with

$$\lambda = \frac{\mathrm{M}_{dredge}}{\mathrm{M}_c} \tag{1.2}$$

where M_{dredge} is the mass of the material mixed into the convective envelope by the TUP episode and M_c is the mass growth of the core due to H-burning during the preceding interpulse period. In other words, λ represents how deep the convective envelope penetrates the intershell during the TUP. Hence $\lambda = 0$ means no material is dredged-up and $\lambda = 1$ means that the amount of dredged-up material is the same as the mass growth of the core during the interpulse. For low-mass stars (e.g. 1.0 $\mathrm{M}_\odot$), models predict that $\lambda \approx 0$, so these stars experience strong core growth during the interpulse while higher-mass (e.g.

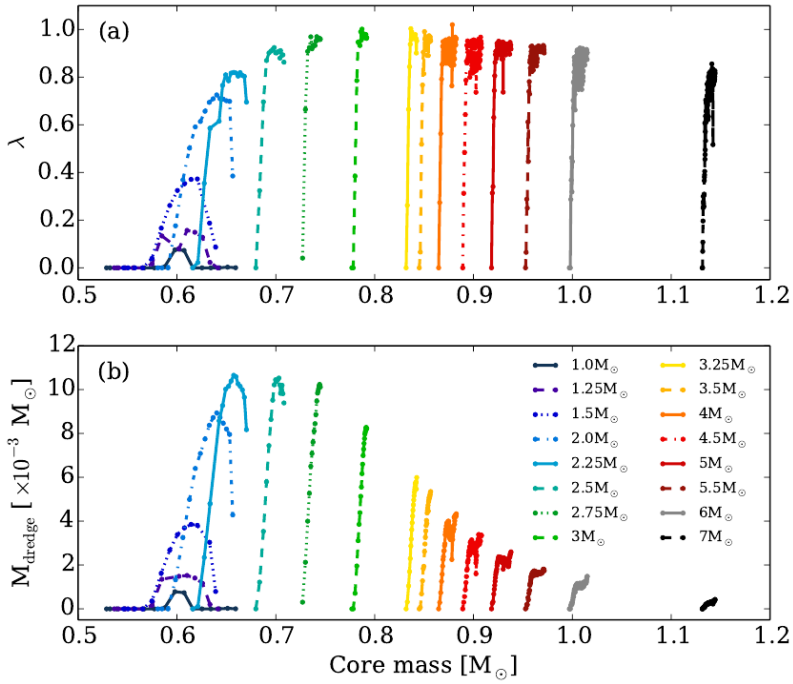

Figure 1.8: Evolution of (a) the efficiency of TUP λ and (b) M_{dredge} with core mass for different stellar masses with Z=0.001. Figure taken from Fishlock et al. (2014).

5.0 $M_\odot$) are predicted to have $\lambda \approx 1$, experiencing a minimal core growth during the interpulse (Fishlock et al. 2014). Fig. 1.8 gives an idea of the evolution of λ and M_{dredge} during the TP-AGB for different masses. During the evolution, λ can vary significantly. Therefore, λ is a key parameter for both the *s*-process and C enhancements of the surface.

If the star is C-rich, mass-loss on the TP-AGB is generated by a dust-driven stellar wind. However, the quantitative mass-loss rates during the TP-AGB have large observational and theoretical uncertainties. Moreover, because not all physical processes driving the mass loss are well understood, it is numerically impossible to include mass loss from first principles in stellar evolution codes. Therefore, the mass loss is implemented in a simplistic parametrised way. For stellar evolution before the AGB, stellar evolution codes usually use the Reimers mass loss (Reimers 1975) for which mass loss depends on the current stellar luminosity, total mass and radius of the star. The Reimers mass-loss law was

empirically determined from the mass loss of red gaints. Typical values for the Reimers mass loss range from 10^{-9} $M_{\odot}yr^{-1}$ to 10^{-4} $M_{\odot}yr^{-1}$ depending on the initial mass of the star. During the AGB phase, current AGB models use updated versions of the mass-loss prescription from Vassiliadis & Wood (1993) which can be split in two phases during the AGB based on the radial-pulsation period of the star. For periods less than $\pm$ 500 days, the mass-loss rate increases exponentially with the period until the 'superwind' phase starts. During the superwind phase, hence with periods larger than 500 days, the mass loss rate increases and reaches values of 10^{-4} $M_{\odot}yr^{-1}$.

1.3.2 Predictions of nucleosynthesis in the partial mixing zone

In this section, we describe the nucleosynthesis operating in the partial mixing zone (PMZ) and its effect on the surface abundance predictions of AGB stars. The model predictions described in this section were presented in Goriely & Mowlavi (2000) and Goriely & Siess (2005).

Nucleosynthesis in the PMZ for different proton mass fractions

To create a PMZ for their detailed study of the internal AGB nucleosynthesis, Goriely & Mowlavi (2000) artificially ingested protons in the He-rich intershell to create a PMZ with a proton mass fraction X_p^{mix} ranging from $X_p^{mix} = 10^{-6}$ up to 0.7 at the time of the third dredge-up. The resulting nucleosynthesis is than followed during the interpulse. Goriely & Mowlavi (2000) find that the nucleosynthesis is rather insensitive to the depth to which the protons are ingested. The composition of the He-rich intershell has been homogenised by the convective thermal pulse and the nucleosynthesis during the interpulse is not strongly sensitive to the temperature and density conditions at which protons are ingested. Therefore, Goriely & Mowlavi (2000) analyse the PMZ nucleosynthesis as a function of X_p^{mix}.

Fig. 1.9 shows the predicted abundance profiles of different nuclei in the PMZ at the end of an interpulse for a 1.5 $M_{\odot}$ star of solar metallicity. The shown ^{13}C abundance profile represents the obtained ^{13}C-pocket at the end of proton burning but before the $^{13}C(\alpha,n)^{16}O$ reaction starts to operate. At the end of the interpulse, ^{13}C is totally destroyed. The regime of $10^{-4} \lesssim X_p^{mix} \lesssim 4 \times 10^{-2}$ is the richest from the nucleosynthesis point of view. In this regime, ^{12}C is burned into ^{13}C by proton capture but the number of protons is not sufficient to complete the CN cycle through $^{13}C(p,\gamma)^{14}N$. This large amount of ^{13}C at the end of the the proton captures forms the so-called '^{13}C-pocket' which serves as a neutron source for the *s*-process nucleosynthesis. This ^{13}C-pocket is predicted

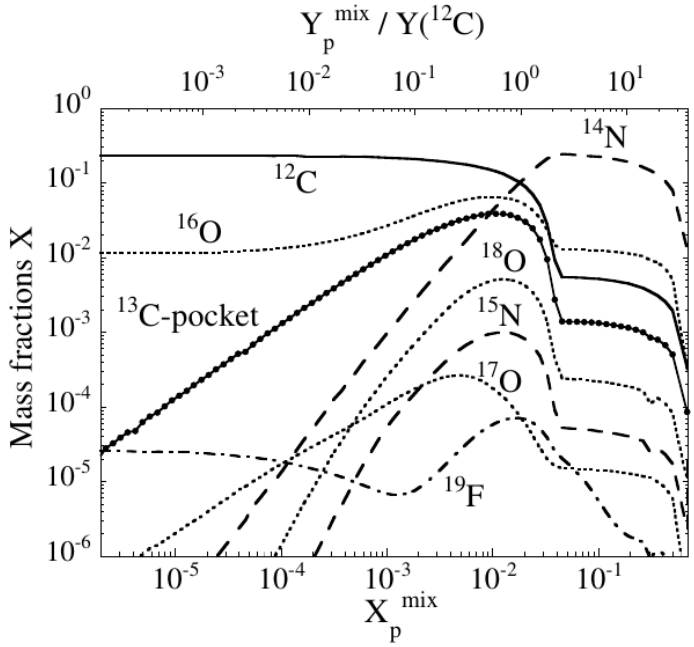

Figure 1.9: Obtained mass fractions for nuclei from C to F in the PMZ at the end of the 15th interpulse for a 1.5 $M_\odot$ star of solar metallicity. The mass fractions are expressed as a function of the mass fraction of ingested protons X_p^{mix}. The spherical dots represent the obtained ^{13}C at the end of proton burning but before the $^{13}C(\alpha,n)^{16}O$ reaction starts to operate. Figure taken from Goriely & Mowlavi (2000).

to cover a region about 5 to 20 times smaller than the total PMZ. The ^{13}C abundance which is left over after proton burning for $X_p^{mix} \backsimeq 10^{-2}$ is about fifty times higher than the ^{13}C abundance from hydrogen shell-burning. For regimes with a higher proton fraction, the full CN cycle is completed destroying ^{13}C and resulting in a large fraction of ^{14}N.

When the temperature in the PMZ increases to about 9.0×10^7 K during the interpulse, the $^{13}C(\alpha,n)^{16}O$ reaction burns ^{13}C into ^{16}O as can be seen in Fig. 1.9 and releases neutrons. The He-burning does not affect ^{14}N because its α-capture rate is too low under the thermodynamic conditions of the interpulse. The released neutrons are mainly captured by ^{14}N, ^{16}O and iron-peak elements. The neutron captures by ^{14}N and ^{16}O lead to the production of nuclei like ^{18}O, ^{15}N, ^{17}O and ^{19}F via multiple reactions. For $X_p^{mix} \lesssim 10^{-3}$, ^{14}N is not abundant enough to act as an efficient neutron poison and therefore neutrons are mainly

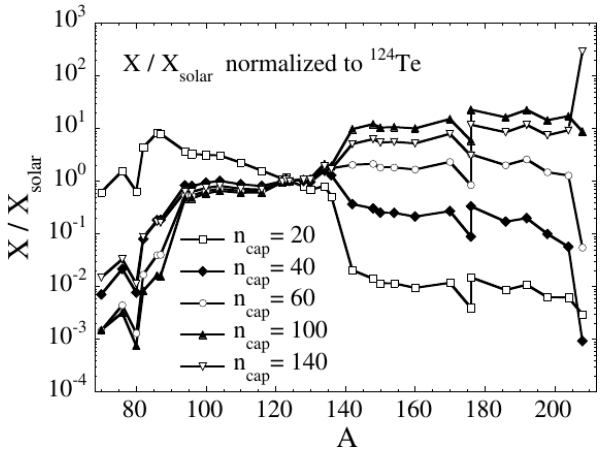

Figure 1.10: Relative abundance distribution of *s*-only nuclei for different values of $n_{\rm cap}$, the average number of neutrons captured per initial iron seed nucleus. All distributions are normalised to $\rm X/X_{\odot} = 1$ for ^{124}Te (Tellurium). Each curve is obtained from an initial proton ingestion $\rm X_p^{mix}$ range in the PMZ leading to the referred *s*-process strength $n_{\rm cap}$ (see also panel c in Fig. 1.11). Figure taken from Goriely & Mowlavi (2000).

captured by iron group nuclei leading to an efficient *s*-process nucleosynthesis.

Goriely & Mowlavi (2000) stress that the total amount of primary ^{13}C and ^{14}N produced in the intershell in Fig. 1.9 is expected to depend on metallicity. This is because the extent of the PMZ and the number of protons mixed in the intershell are expected to vary with stellar mass, metallicity and the creation mechanism of the PMZ. However, the amount of primary ^{13}C produced in a given layer is dependent only on the initial ingested proton and ^{12}C abundances in that layer. Therefore, the abundance profiles of the different nuclei in Fig. 1.9 are independent on metallicity for identical proton mixing.

A relevant quantity to represent the *s*-process strength is $n_{\rm cap}$, the average number of neutrons captured per initial iron seed nucleus. The quantity $n_{\rm cap}$ almost solely determines the *s*-process abundance distribution, apart from a few temperature-dependent branching nuclei which are dependent on the thermodynamic conditions in the PMZ. Therefore, a higher $n_{\rm cap}$ represents a strong *s*-process. Fig. 1.10 shows how the *s*-process distribution changes for different values of $n_{\rm cap}$. Low values of $n_{\rm cap}$ mainly create the weak *s*-process component with $\rm A \lesssim 90$, while the high $n_{\rm cap} = 140$ lead to a predicted overproduction of Pb. Intermediate $n_{\rm cap}$ values mainly produce elements of the

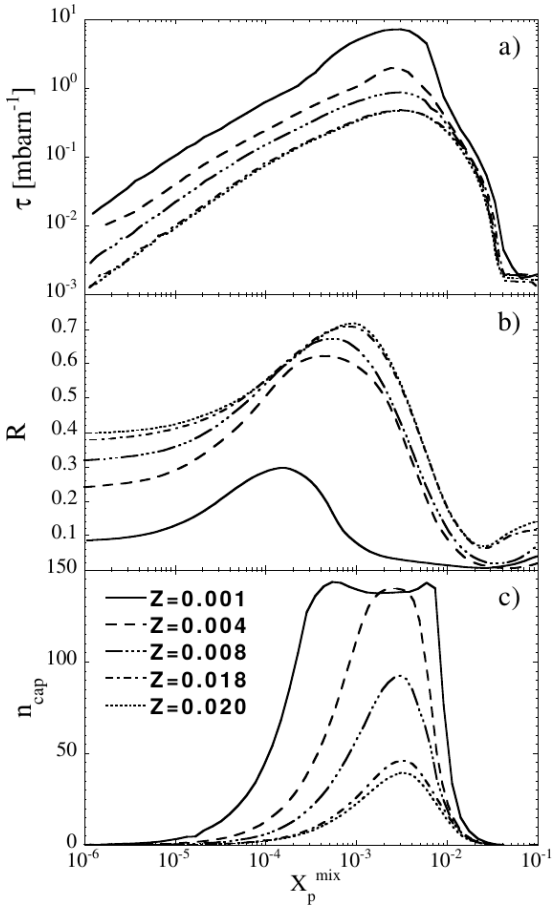

Figure 1.11: All three panels show different *s*-process quantities as a function of proton mass fraction X_p^{mix} initially mixed into the intershell for stars of different metallicities Z. Panel a shows the neutron exposure τ at the end of the interpulse period, panel b displays R: the number of neutrons captured by the heavy nuclei relative to the total released number of neutrons, and panel c represents n_{cap}: the number of neutrons captured per iron seed nucleus at the end of the interpulse period. Figure taken from Goriely & Mowlavi (2000).

main *s*-process component for $90 \lesssim A \lesssim 204$.

Other quantities to represent the efficiency of the *s*-process are the neutron exposure τ (see Sect. 1.2.3) and the number of neutrons captured by the heavy nuclei relative to the total released number of neutrons, which is expressed by

R. Fig. 1.11 displays the quantities τ, R and $n_{\rm cap}$ as a function of proton mass fraction $X_p^{\rm mix}$ for different metallicities Z. Parameters X, Y and Z are used for expressing the mass fractions of hydrogen, helium and all other remaining particles respectively, so Z $\equiv$ 1-X-Y. For a typical star, X lies in the interval [0.70,0.73] while Z typically ranges from $Z = 10^{-6}$ to $Z = 0.04$. With this definition, Z is another way to express the metallicity of a star. Contrary to the production of primary ^{13}C and ^{14}N, Fig. 1.11 shows that the *s*-process is strongly dependent on the stellar metallicity Z which is to expected, since the number of iron seed nuclei is proportional to the metallicity. Therefore, the neutron to seed abundance ratio is inversely proportional to the metallicity and $n_{\rm cap}$ increases with decreasing metallicity. As a consequence, the neutron density are also proportional to the metallicity with maximum neutron densities of 10^7 cm^3 at solar metallicities ($Z \backsimeq 0.020$) and 10^9 cm^3 at $Z = 0.001$, so the neutron exposure τ is the highest in metal-deficient stars. In contrast to this, the efficiency of neutron capture by heavy nuclei decreases with decreasing metallicities. This is due to the impact of light neutron poisons like ^{14}N which is the dominant neutron poison. A final important remark about Fig. 1.11 is that the *s*-process strength is almost independent on the thermodynamic profiles in the intershell layers since the number of neutron-captures by heavy nuclei depends on the amount of available ^{13}C, and remains insensitive to the exact temperature at which ^{13}C burns. This implies that the profiles shown in Fig. 1.11 are independent of stellar mass.

Nucleosynthesis in the PMZ for a specific ingested proton abundance profile

The results in the previous section show the interpulse nucleosynthesis predictions resulting from partial mixing of a given amount of protons in the He-rich intershell. It is expected that the partial mixing of protons becomes less efficient when going deeper into the star. Therefore, Goriely & Mowlavi (2000) adopt an ingested proton abundance profile which exponentially decreases with depth starting from $X_p^{\rm mix} = 0.7$ at the bottom of the convective envelope down to 10^{-6} at the bottom of the PMZ. The protons are ingested during the third dredge-up.

To characterise the extent of the PMZ, Goriely & Mowlavi (2000) use the parameter $\lambda_{\rm PMZ} = M_{\rm PMZ}/M_{\rm Pulse}$ with $M_{\rm PMZ}$ the mass of the PMZ and $M_{\rm Pulse}$ the mass processed by the convective thermal pulse. Remark that $\lambda_{\rm PMZ}$ is not the third dredge-up efficiency λ in Eq. 1.2. For their study, Goriely & Mowlavi (2000) assume $\lambda_{\rm PMZ} = 0.05$. Fig. 1.12 shows the *s*-process abundance distributions at the end of an interpulse phase for stars with different metallicities assuming an exponentially decreasing proton ingestion profile during the third dredge-up. All stars are expected to produce nuclei with $90 \lesssim A \lesssim 140$ with

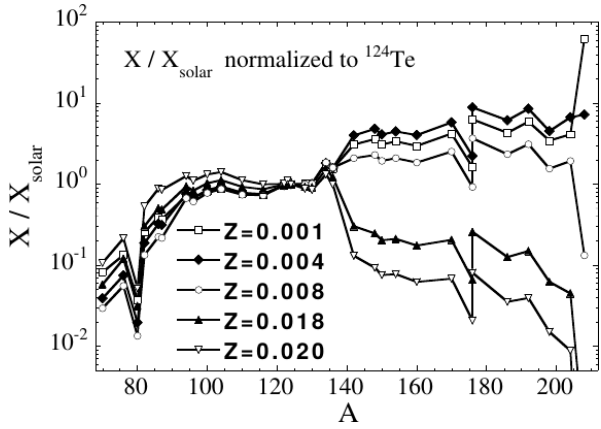

Figure 1.12: Figure similar to Fig. 1.10 representing the abundance distribution of *s*-only nuclei in the PMZ at the end of the interpulse phase for stars with different metallicities. Figure taken from Goriely & Mowlavi (2000).

a solar-like distribution. However, only stars with $Z \lesssim 0.01$ are expected to produce heavier nuclei with $140 \lesssim A \lesssim 204$ and only stars with a low metallicity of $Z < 0.004$ are expected to efficiently produce ^{208}Pb.

We remark that the PMZ nucleosynthesis results are strongly sensitive to the used cross-section rates and the used PMZ parameters like $\lambda_{\rm PMZ}$ and shape of the PMZ. Specific codes (see Sect. 1.3.6) use different PMZ parameters and often also different cross-section rates which will yield different nucleosynthesis in the intershell. Therefore, the global results of Goriely & Mowlavi (2000) are representative of the global nucleosynthesis predictions of these other stellar evolution codes, but the detailed nucleosynthesis predictions will differ depending on the used PMZ parameters and cross-section rates.

1.3.3 Surface abundance predictions

In this section, which is again based upon the results of Goriely & Mowlavi (2000), we provide an overview of the predicted effects of the internal AGB nucleosynthesis in the PMZ (Sect. 1.3.2) on the surface abundances after third dredge-up episodes. The quantitive prediction of AGB surface abundances is affected by uncertainties of the structural evolution of AGB stars as described in Sect. 1.3.5. Therefore, Goriely & Mowlavi (2000) use the basic assumptions described in the previous section together with a constant value for the dredge-up efficiency from one pulse to the next. They quantify the third dredge-up

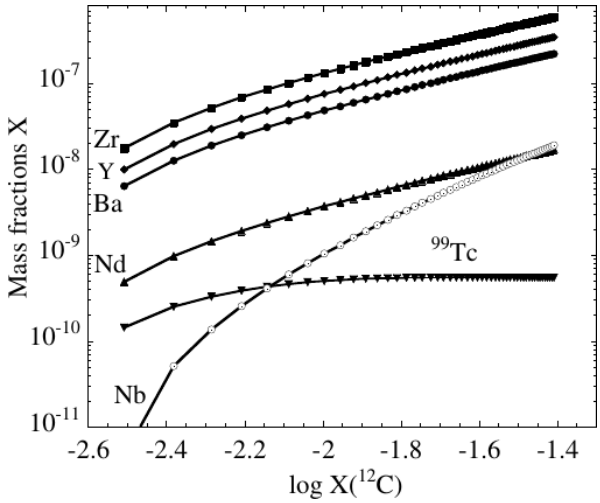

Figure 1.13: Abundance evolution of some heavy elements as a function of the ^{12}C abundance predicted at the surface of a 1.5 $M_\odot$ star of solar metallicity. The calculations are performed for a third dredge-up efficiency $\lambda_{\rm dredge} = 0.10$ and a PMZ mass extent of $\lambda_{\rm PMZ} = 0.05$. Figure taken from Goriely & Mowlavi (2000).

efficiency by the parameter $\lambda_{\rm dredge} = M_{dredge}/M_{\rm Pulse}$ with $M_{\rm dredge}$ the mass of material mixed into the convective envelope during the third dredge-up. This parameter can written in terms of the classical third dredge-up efficiency parameter λ (see Eq. 1.2) as $\lambda_{\rm dredge} = \lambda \times M_c/M_{\rm Pulse}$. Goriely & Mowlavi (2000) take a constant value of $\lambda_{\rm dredge} = 0.1$ from one pulse to the next. The obtained predictions by the efficiency of a constant dredge-up efficiency are only approximations, since the intershell conditions like temperature do vary with time during the TP-AGB and therefore influence the intershell nucleosynthesis. The upper panel of Fig. 1.8 shows that for most masses of stars, the dredge-up efficiency does not change drastically during the majority of thermal pulses. In addition, Goriely & Mowlavi (2000) assume that the AGB star undergoes a sequence of identical pulse-interpulse phases with constant envelope mass, PMZ and third dredge-up characteristics from pulse to pulse.

Fig. 1.13 shows the surface abundance evolution of some *s*-process elements during the TP-AGB for a 1.5 $M_\odot$ star of solar metallicity. Each symbol represents a different thermal pulse. The *s*-process elements Y, Zr, Ba and Nd present the same evolution pattern which corresponds to their dilution into the envelope during the third dredge-up. Therefore, the *s*-process distribution does

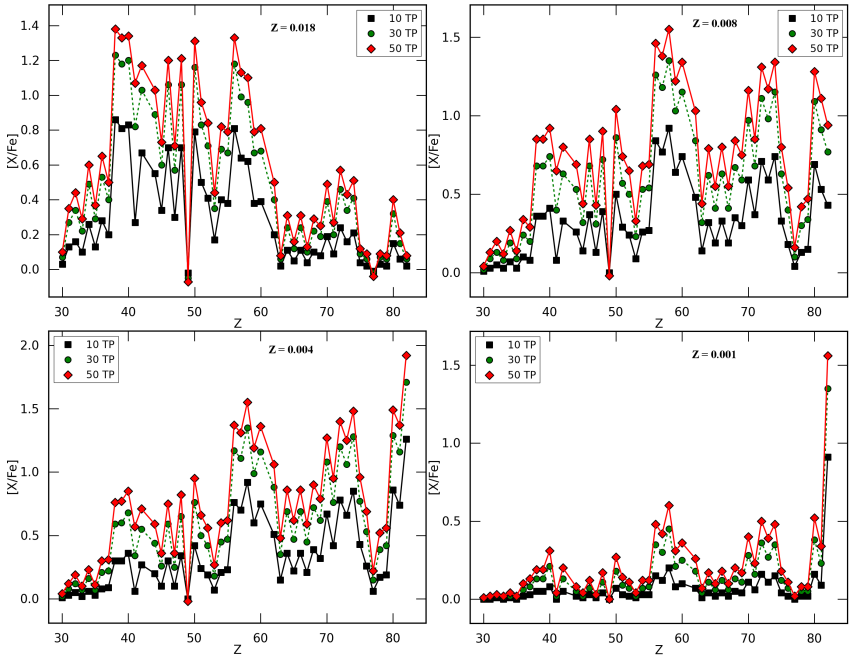

Figure 1.14: [X/Fe] results in four AGB stars of different metallicities Z. Each curve represents the s-process distribution after a specific number of thermal pulses (TP). The calculations are performed for a third dredge-up efficiency $\lambda_{\rm dredge} = 0.10$ and a PMZ mass extent of $\lambda_{\rm PMZ} = 0.05$. Figure reproduced from Table 1 in Goriely & Mowlavi (2000).

not change during the sequence of thermal pulses. This is also visible in Fig. 1.14, where the evolution of the element-over-iron ratios are shown in function of the number of thermal pulses. As described earlier, the s-process distribution is dependent on the metallicity (see Fig. 1.12) but it only moderatly changes with the number of pulses. Exceptions to this are unstable nuclei like the ^{99}Tc (technitium, Z = 43) isotope which has a half-life time of the order of the interpulse period and therefore has a constant surface mass fraction during the TP-AGB as shown in Fig. 1.13. Niobium, or Nb (Z = 41), can only be created by the decay of ^{43}Zr, which has a half-life of 1.5 million years. Therefore, the surface abundance of Nb strongly strongly rises a million years after s-process elements have been dredged-up and is anti-correlated with the Tc abundance.

Apart from metallicity, the initial mass of the AGB star is an important parameter for the structural evolution during the AGB phase because it

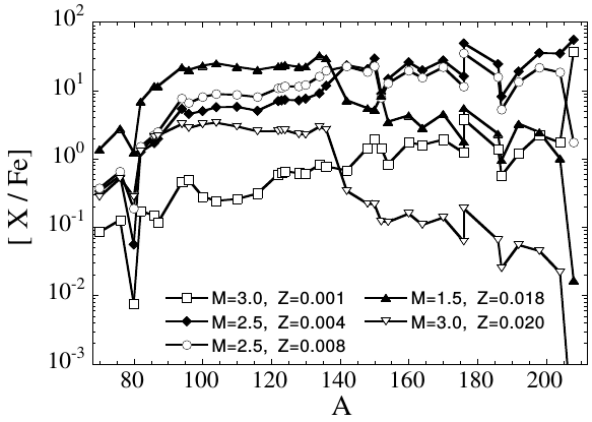

Figure 1.15: [X/Fe] surface distributions of *s*-process isotopes after a series of 30 identical thermal pulses for five AGB models of different masses and metallicities. Figure retrieved from Goriely & Mowlavi (2000).

influences the evolution of PMZ parameters like λ (see Fig. 1.8). However, the initial mass of the star does not seem to strongly influence the surface abundance distribution of *s*-process elements. Fig. 1.15 shows the surface abundance distribution of *s*-process isotopes after the onset of 30 identical thermal pulses for five AGB stars of different metallicities and masses calculated with the assumptions described above. Although these stars cover a mass range of 1.5 $M_{\odot}$, the *s*-process abundance distributions follow the distributions in Figs. 1.12 and 1.14 which are almost solely dependent on metallicity. This shows that the initial mass of the AGB star only has a marginal effect on the distribution.

Apart from the effect of metallicity and mass on the *s*-process distribution, Goriely & Mowlavi (2000) also studied the effect of the adopted proton ingestion profile in the PMZ on the surface abundances. The described predictions in Sect. 1.3.2 and this section have been calculated using an exponentially decreasing profile (see Sect. 1.3.2). To study the effect, Goriely & Mowlavi (2000) used three different abundance profiles in the PMZ as shown in Fig. 1.16 for four AGB models with different masses and different metallicities. From the 'fast' to the 'slow' profiles, only 5 to 20 % respectively of the PMZ experiences the creation of heavier elements. Except for the effect of dilution, the proton ingestion profile does not significantly affect the global *s*-process distribution. This is mainly caused by the small range in proton mass fractions X_p^{mix} over which the *s*-process occurs. So qualitatively, the shape of the proton ingestion profile is

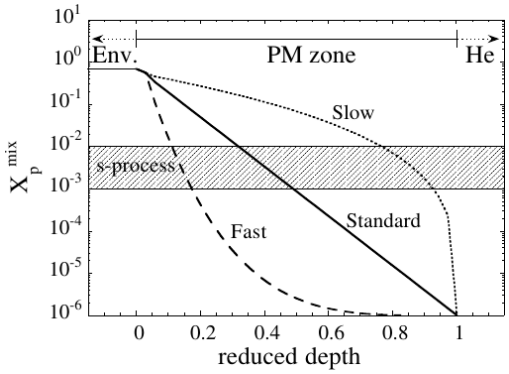

Figure 1.16: Adopted proton ingestion profiles in the PMZ located between the convective envelope and the He-burning shell. The standard profile corresponds to the exponentially decresing profile while the other profiles decrease slower or faster in depth than the standard case. The shaded area shows the main mass interval where the *s*-process takes place. Figure retrieved from Goriely & Mowlavi (2000).

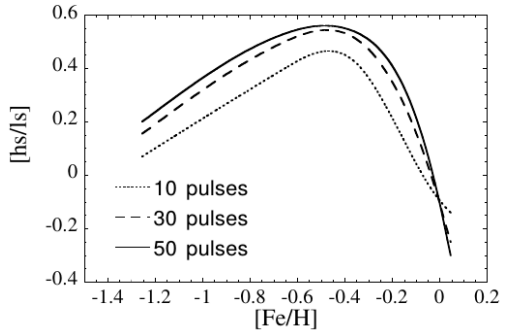

Figure 1.17: Neutron irradiation index [hs/ls] predictions as a function of stellar metallicity [Fe/H] after specific series of identical thermal pulses for the five AGB models of different masses and metallicities presented in Fig. 1.15. Figure retrieved from Goriely & Mowlavi (2000).

only moderately important for the *s*-process distribution, but quantitatively the uncertain extents of the PMZ and the third dredge-up zone affect the surface enhancements.

To end our overview of the results of Goriely & Mowlavi (2000), we show their predictions of the neutron irradiation index [hs/ls] as a function of metallicity

for different series of identical thermal pulses for the five AGB models in Fig. 1.15. They use the predictions of Ba and La to calculate the hs-index, and Sr, Y and Zr to calculate the ls-index. Fig. 1.17 shows the [hs/ls] predictions which follow a bell-shape as a function of metallicity. Although it is usually expected that [hs/ls] increases with decreasing metallicity due to the larger number of neutrons available for each iron seed nucleus, [hs/ls] decreases towards lower metallicities. This is because at lower metallicities, the hs-elements are expected to be transformed in Pb which is not included in the hs-index. The decrease of [hs/ls] towards higher metallicities follows the expected trend. Regarding the number of pulses, [hs/ls] increases faster during the initial pulses, while it becomes moderately constant at later pulses (see already Fig. 1.20).

1.3.4 General AGB model predictions with STAREVOL

Within the course of the PhD, we generated multiple stellar evolution model predictions for a grid of different masses and metallicities with the stellar evolution code STAREVOL, which is a one-dimensional Lagrangian hydrodynamic code. Detailed descriptions of the calculated physics in STAREVOL can be found in Siess et al. (2000), Siess (2006) and Palacios et al. (2006). We did not generate this grid of models with the purpose of comparing observed abundances with fine-tuned model predictions like in Chapter 3 or in e.g. Fishlock et al. (2014), but rather for learning more about the general predictions of AGB evolution models. We generated STAREVOL models for metallicities of $Z = 0.001$, $Z = 0.004$, $Z = 0.008$ and $Z = 0.02$ (= close to solar metallicity) and for initial masses of M = 1.0 $M_{\odot}$, M = 1.5 $M_{\odot}$, M = 2.0 $M_{\odot}$ and M = 3.0 $M_{\odot}$. We restricted ourselves to these parameters as they are representative of the objects studied in this thesis. The models were calculated using standard assumptions like overshooting below the convective envelope, and assuming Reimers mass loss (Reimers 1975) before the AGB and the mass loss described in Vassiliadis & Wood (1993) during the AGB. We simulated models until they stopped converging. At that point, the majority of models had remaining total masses between 0.5 and 0.7 $M_{\odot}$. Unfortunately, due to the time-constraint of a PhD, we could not yet analyse this grid of models in detail. We remark that our generated STAREVOL model results contain the evolution of stellar structure and abundances of light elements like C, N and O but not for the *s*-process elements which have to be calculated via post-processing. Of all our calculated STAREVOL models, we have the predicted *s*-process abundances for our 1.5 $M_{\odot}$, 2.0 $M_{\odot}$ and 3.0 $M_{\odot}$ model results with $Z = 0.001$, which were kindly provided by S. Goriely. A detailed analysis of the remaining model grid is for future study (see Sect. 9.1.1).

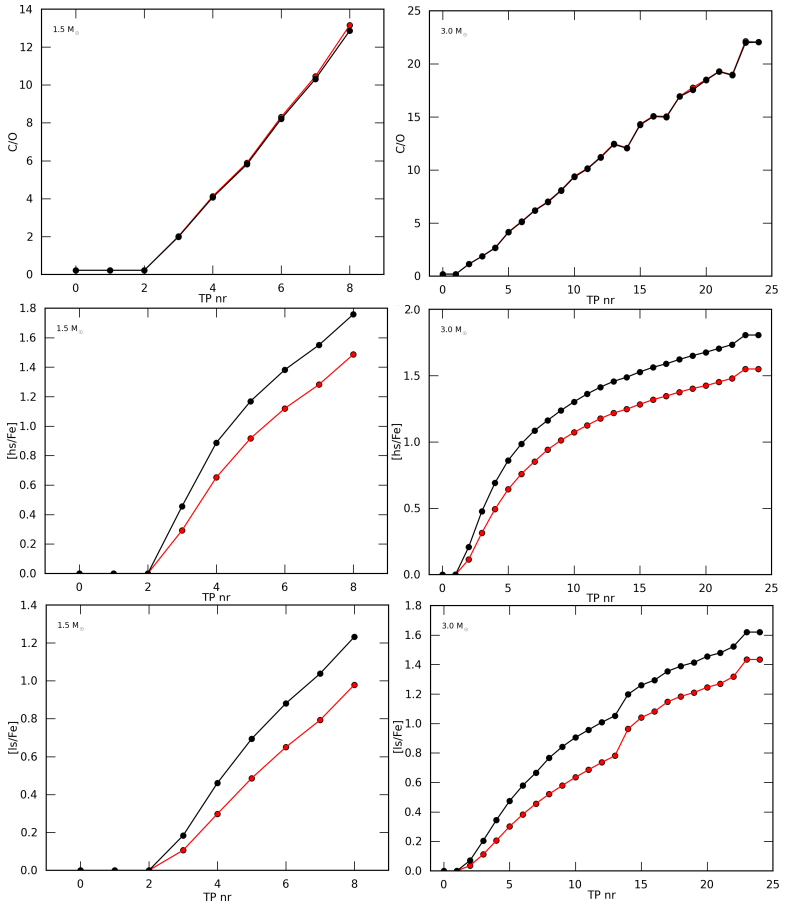

Figure 1.18: Evolution of the C/O ratio, [hs/Fe] and [ls/Fe] with each thermal pulse for a STAREVOL 1.5 $M_\odot$ (left column) and a 3.0 $M_\odot$ (right column) model with $Z = 0.001$. The red and black curves indicate the results for partial mixing zones covering 5% and 10 % respectively of the extent of the thermal pulse.

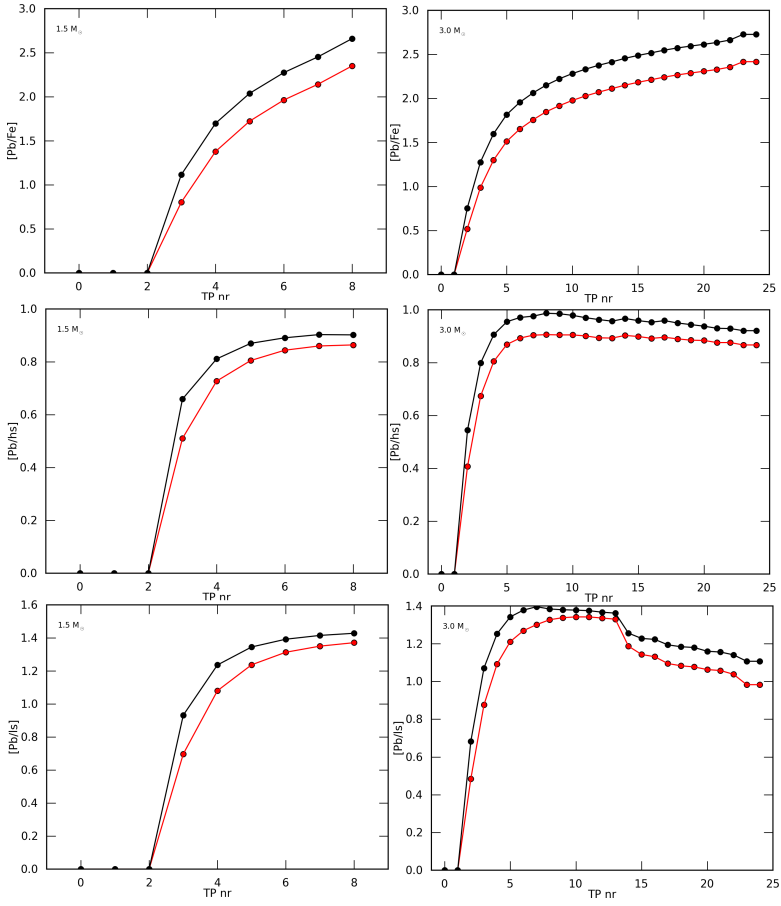

Figure 1.19: Similar to Fig. 1.18, but with evolution of [Pb/Fe], [Pb/hs] and [Pb/ls].

The main difference between the STAREVOL model predictions and those of Goriely & Mowlavi (2000) in the previous sections is that the STAREVOL predictions take into account the variation with time of intershell characteristics like temperature, density and PMZ and third dredge-up parameters along the AGB. These variations partly affect the internal nucleosynthesis. Also other simplified assumptions by Goriely & Mowlavi (2000) are transformed in a more realistic format within STAREVOL, but the main results of Goriely & Mowlavi (2000) remain valid. Here, we present some of our general model predictions with STAREVOL.

General λ results:
We will not elaborate on the general stellar structure results of the model grid, but we remark that these are similar to the results of model studies like in Fishlock et al. (2014). Here, we restrict our discussion to the third dredge-up parameter λ (see Eq. 1.2). We find the same behavior of λ as in Fig. 1.8 for our different $Z = 0.001$ model results. Comparison of the λ results for the different STAREVOL models shows that the mean λ decreases with increasing metallicity, hence less efficient dredge-ups for higher metallicities are predicted. The 1.0 $M_\odot$ models undergo multiple thermal pulses, but only the $Z = 0.001$ and $Z = 0.004$ models have two and one dredge-ups respectively. The model predictions also show the generally expected increase of the number of thermal pulses with increasing initial mass.

***S*-process indices for $Z = 0.001$:**
Figs. 1.18 and 1.19 show the evolution for each thermal pulse of the C/O ratio, the *s*-process indices [hs/Fe] and [ls/Fe], and the Pb indices of the 1.5 $M_\odot$ and 3.0 $M_\odot$ STAREVOL models. The *s*-process related indices are calculated using a partial mixing of protons model with a simple exponentially decreasing profile of mixed protons as described in Goriely & Mowlavi (2000). Each panel in Figs. 1.18 and 1.19 shows two curves, corresponding to two different sizes of the PMZ. The red dots represent the results for a PMZ which corresponds to 5 % of the extent of the preceding thermal pulse (hence $\lambda_{\rm PMZ} = 0.05$), the black dots represent the same but for $\lambda_{\rm PMZ} = 0.1$. These relative extents are kept constant during the calculation of the different pulses. We remark that the 2.0 $M_\odot$ results are similar to the 1.5 $M_\odot$ results.

The C/O ratio results in the upper panels of Fig. 1.18 show a strong increase once the third dredge-up is activated. The final C/O ratios of both models are much higher than observed C/O ratios in *s*-process enriched post-AGB stars (see e.g. second column in Table 6.8). The extend of the PMZ has only a neglible effect on the C/O ratio. The *s*-process indices [hs/Fe] and [ls/Fe] strongly increase once the third dredge-up is activated. For [ls/Fe], there is a larger increase at thermal pulse 14 for the 3.0 $M_\odot$ model, which is caused by the activation of the ^{22}Ne(α,n)^{25}Mg reaction, which mainly produces ls-elements.

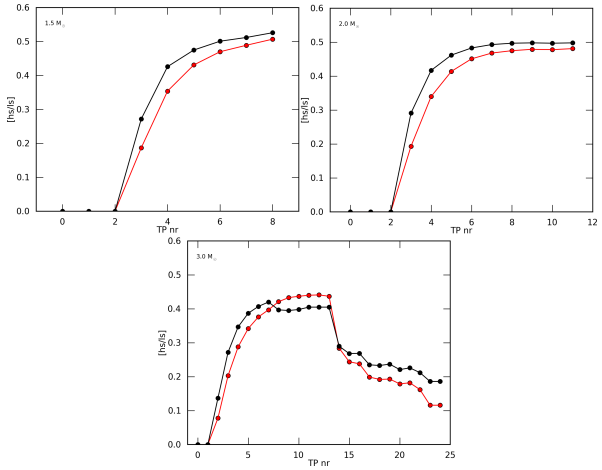

Figure 1.20: Similar to Fig. 1.18, but with evolution of [hs/ls]. The 2.0 $M_\odot$ model is included for clarity.

For the *s*-process indices, the extent of the PMZ has a clear effect since the intershell zone where the *s*-process can take place is larger. In Fig. 1.19, [Pb/Fe] follows the same trend as [hs/Fe], but it is higher due to the low metallicity since more neutrons are available for each iron nucleus. After a few dredge-ups, [Pb/hs] becomes approximately constant. For [Pb/ls], the strong increase of [ls/Fe] after pulse 14 due to the activation of the ^{22}Ne, is clearly visible for the 3.0 $M_\odot$ model. The permanent triggering of the ^{22}Ne source during following thermal pulses causes [Pb/ls] to decrease.

Fig. 1.20 shows the evolution of the neutron irradiation index [hs/ls] with thermal pulse number for the three AGB models. It is clear that [hs/ls] evolves towards a constant value for an increasing number of thermal pulses. For the 3.0 $M_\odot$ model, the effect of the ^{22}Ne source is clearly visible, gradually reducing the [hs/ls] index with increasing number of pulses. Before the activation of the ^{22}Ne source, [hs/ls] also evolved towards a constant value for the 3.0 $M_\odot$ model.

In the previous section, we showed that the initial mass of the AGB star only has a moderate influence on the *s*-process distribution. However, Figs. 1.18, 1.19 and 1.20 show that after a select number of pulses, the ^{22}Ne neutron source is activated in the 3.0 $M_\odot$ model. This strongly influences the final surface abundance distribution as shown in Fig. 1.21. For Z $\gtrsim$ 45, all three models have comparable abundance distributions with somewhat higher abundances for the 3.0 $M_\odot$ model while for most elements with Z $\lesssim$ 45, the elements in the 3.0 $M_\odot$ model are clearly more abundant than the lower mass stars. This implies

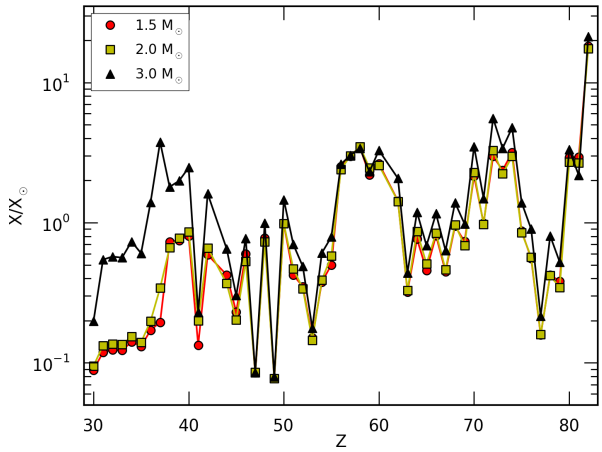

Figure 1.21: Surface abundance distribution with respect to the solar abundances for our three Z=0.001 AGB models with different masses. The effect of the ^{22}Ne neutron source is clearly visible for elements with Z $\lesssim$ 45 in the 3.0 M$_\odot$ model. Only the surface abundances for the $\lambda_{\rm PMZ} = 0.05$ models are shown since those of $\lambda_{\rm PMZ} = 0.1$ are very similar.

a much lower final surface [hs/ls] value for the 3.0 M$_\odot$ model as shown in Fig. 1.20. We can therefore conclude that, although small initial mass differences will almost not change the *s*-process abundance distribution, it is important to have an initial mass estimate of the AGB star to take into account the possible activation of the ^{22}Ne neutron source when comparing observed abundances with predictions.

As a final remark, we would like to stress the importance of taking into account the evolution of intershell characteristics like temperature and density throughout the AGB evolution. The predictions for the 3.0 M$_\odot$ model with Z = 0.001 of Goriely & Mowlavi (2000) in Fig. 1.15 do not show any contribution of the ^{22}Ne neutron source, in contrast to our results. This is because their intershell parameters do not evolve during the AGB evolution while these parameters do evolve in our STAREVOL models, eventually creating the appropiate thermodynamic conditions for activation of the ^{22}Ne reaction. This shows the importance of realistic assumptions in AGB modeling. Unfortunately, there are still multiple poorly understood processes taking place during the AGB, inducing uncertainties in AGB model predictions.

1.3.5 Uncertainties in AGB models

Many TP-AGB processes are currently still poorly understood and they create uncertainties in AGB model predictions. The most important ones are convective overshooting which influences the border regions between zones in convective and radiative equilibrium, and hence also the creation of the ^{13}C-pocket in the intershell. Also the efficiency of the TUP, which determines the enrichment of the stellar surface with carbon and *s*-process elements, is not well understood together with the need of extra mixing processes in the form of rotation or thermohaline mixing.

In addition, the physical driving mechanisms of TP-AGB mass loss also impose uncertainties on AGB nucleosynthesis predictions. One of the implications of the uncertain TP-AGB mass loss is the effect of the last thermal pulse for the final surface abundances. The strongly-reduced envelope mass determines when the star evolves towards the post-AGB. When the star loses just enough mass during the last thermal pulse to evolve towards the post-AGB, this last pulse will not be followed by a third dredge-up and hence an extra final enhancement. This has important implications for the final absolute surface abundances because any dredged-up elements after the last thermal pulse will create large enrichments in the diluted envelope. The envelope mass during the final third dredge-up is hence crucial for the final surface abundances.

A last and a very important poorly understood TP-AGB process is the physical mechanism for creating a PMZ from which the ^{13}C-pocket originates. To date, stellar evolution models still artificially impose PMZs using prescriptions which differ between the AGB evolution codes but which strongly influence the outcome of the *s*-process nucleosynthesis predictions.

The previous paragraphs show that observational constraints of the photospheric abundances of AGB stars are necessary to improve our knowledge of the physical processes taking place during the TP-AGB. Unfortunately, the study of elemental abundances in AGB photospheres is difficult (see e.g. Abia et al. 2008) due to the dominance of molecular transitions in the outer AGB layers, the often dynamic pulsating atmospheres creating dust-driven mass loss and the difficult interpretation of chemical studies since stars with different initial masses and metallicities occupy the same region in the HR diagram. Fortunately, the progeny of AGB stars are ideal probes for accurate elemental abundance studies.

1.3.6 Stellar evolution codes

Currently, there exist numerous stellar evolution codes, both open source and private. In this thesis, we make use of two different stellar evolution codes. The first stellar evolution code is STAREVOL, which was introduced in Sect. 1.3.4. The second stellar evolution code is the Mount Stromlo Stellar Evolution code, a one-dimensional stellar evolution code for which detailed descriptions can be found in Karakas et al. (2002), Lugaro et al. (2004), Karakas & Lattanzio (2007) and Karakas (2010). We will also make comparisons with AGB nucleosynthesis models from the online-database FRUITY[2] (Franec Repository of Upgraded Isotopic Tables and Yields, Cristallo et al. (2011)). Other recent stellar evolution codes are described in Stancliffe et al. (2011), Marigo et al. (2013), Cristallo et al. (2014), Bisterzo et al. (2014) and Lugaro et al. (2015).

1.4 Post-AGB stars

At the end of the TP-AGB, the envelope mass is strongly reduced down to about 0.05 $M_\odot$ or lower due to the strong mass loss. The star now evolves towards high temperatures at an almost constant luminosity (see Figs. 1.1 and 1.22). This is because the surface layer is gradually heating up due to the proximity of the stable burning thin H-shell which produces the luminosity. The star has now entered the *post-asymptotic giant branch* (post-AGB) phase. In this section, which is largely based on the texts from Van Winckel (2003) and van Aarle et al. (2011), we first describe the evolution of post-AGB stars, followed by the chemical diversity of Galactic post-AGB stars.

1.4.1 Evolution

Typical luminosities for post-AGB stars range from 10^3 to a few 10^4 $L_\odot$ while the post-AGB transition time (time to cross the HR-diagram, see e.g. Fig. 1.22) ranges from about 30 years for the most massive objects to 10^5 years for the least massive objects. These much longer transition times for low-mass stars create an observational bias towards low-mass post-AGB stars. When the stellar effective temperature reaches about 30 000K, the radiated photons of the central star are capable of ionising the circumstellar material which becomes a planetary nebula (PN). However, not all post-AGB stars become PNe. The most massive post-AGB stars cross the HR diagram so fast that they are still embedded in their AGB dusty envelope at the start of the PN

[2]http://fruity.oa-teramo.inaf.it/

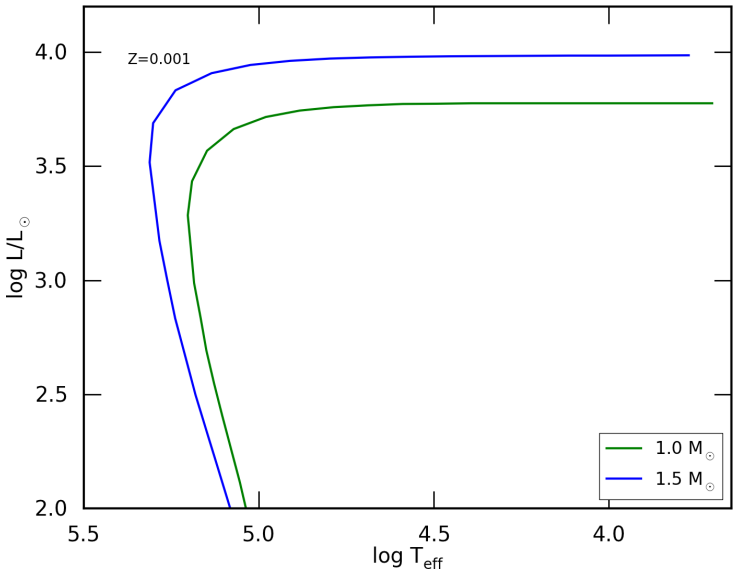

Figure 1.22: Evolutionary post-AGB tracks of Vassiliadis & Wood (1994) for two metal-deficient stars (Z =0.001) with initial masses of 1.0 $M_\odot$ and 1.5 $M_\odot$.

phase. For the least massive post-AGB stars, the transition time is so slow that the circumstellar material is already too dispersed when the energetic ionising photons are finally created, hence no PN is expected for these objects. At the end of the PN stage, hydrogen shell burning ceases and the central temperatures are not high enough to initiate carbon burning in the electron-degenerate CO core. The star has become a CO *white dwarf* with masses between $\sim$ 0.5 - 1.0 $M_\odot$, which steadily cools down and follows the white dwarf cooling track in the HR diagram (see Fig 1.22).

Evolutionary post-AGB tracks in the HR diagram have been published for a wide range of initial masses and metallicities (Schönberner 1983; Vassiliadis & Wood 1994; Blöcker 1995). Unfortunately, these post-AGB tracks are not computed from first principles and their main uncertainties are linked to the poorly understood AGB mass-loss mechanisms. Moreover, the currently available post-AGB tracks (Vassiliadis & Wood 1994; Blöcker 1995) were calculated more than two decades ago, they are hence not updated with current opacity tables which are needed for more up-to-date mass-loss rates. The AGB mass-loss rates for calculating the post-AGB tracks in Vassiliadis & Wood (1994) are based on empirical determinations of AGB stars in Vassiliadis & Wood (1993). The AGB mass-loss rates for the calculation of the Blöcker (1995) post-AGB tracks

are based upon the numerical results of Bowen (1988) for the atmospheres of pulsating O-rich AGB stars. The calculated length of the AGB evolution depends on the mass loss during the TP-AGB, which determines the internal structure of the remnant object. This internal structure determines the core mass at the end of the TP-AGB and hence also the length of the post-AGB phase. For instance, the mass-loss prescriptions during the AGB by Vassiliadis & Wood (1994) are in general lower than those of Blöcker (1995) resulting in a more massive WD for the same initial mass. In addition, the lower mass-loss prescriptions during the post-AGB by Vassiliadis & Wood (1994) result in longer transition times.

The phase of the thermal pulse cycle during the start of the post-AGB phase is also important. Regarding the different burning phases during the thermal pulse cycle, it can be expected that about 70% of the post-AGB stars are burning hydrogen, 15% is burning helium and another 15% are burning both (e.g. Blöcker 2001). If the post-AGB phase starts at more than 90% of the thermal pulse cycle, hence close to the start of a new thermal pulse, conditions are optimal to expect a thermal pulse during the post-AGB phase or PN, or even during the WD phase when H shell-burning has already ceased (Herwig et al. 1999). A thermal pulse during the post-AGB or PN stage is called a 'late thermal pulse' while a thermal pulse on the WD cooling track is called a 'very late thermal pulse'. These pulses inflate again the envelope and create a *born-again* AGB star hence the star crosses again the HR diagram towards the AGB (e.g. Schönberner 1979; Iben 1984)). These objects evolve so fast that this stellar evolution phase can be observed on a human timescale. For some objects, the late thermal pulses may occur multiple times before reaching the WD cooling track (e.g. Blöcker 1995). The occurrence of (very) late thermal pulses seems not so rare as it is expected that about 10% of all AGB stars will undergo one.

There exists observational evidence of these fast-evolving objects of which the three most famous examples are FG Sge, V605 Aql and V4334 Sgr, the latter also being known as Sakurai's object. These objects display strong temperature changes from about 5000K to about 50 000K in a human lifetime (FG Sge and V605 Aql) and drastic abundance changes (V4334 Sgr) (see e.g. Schönberner 2008; Gallino et al. 2011; Lau et al. 2011, and references therein). Late and very late thermal pulses may also help to explain the peculiar abundances of the Wolf-Rayet central stars of some PNe and the very hot H-deficient PG1159 stars (e.g. Gallino et al. 2011; Werner et al. 2011; Kepler et al. 2014, and references therein).

1.4.2 The circumstellar environment

The circumstellar environment (CSE) of post-AGB stars is well suited for the study of mass loss during the AGB phase. The CSE of post-AGB stars, which are often also called proto-planetary nebulae (PPNe) in multiple studies, display a wide variety in shape and structure in thermal emission and in scattered light. There exist numerous studies about the CSEs of post-AGB stars including mid-IR studies focusing upon the symmetry braking of the CSE nebula between the AGB and PN phase (e.g. Lagadec et al. 2011; Bujarrabal et al. 2013), radiative transfer and structure studies of circumbinary discs around post-AGB stars (e.g. Hillen et al. 2014) and far-IR studies about the chemical composition of the post-AGB CSEs (e.g. Hrivnak et al. 2009; Wesson et al. 2010; Zhang et al. 2013). The recent Atacama Large Millimeter Array (ALMA) of the European Southern Observatory (ESO) in Chili will definitely play an important role for a better understanding of AGB and post-AGB CSEs. Although a very interesting and important topic of post-AGB evolution, we will not further elaborate on the shaping of post-AGB CSEs in this thesis. As the chemical compositions of the surface and circumstellar environment are related, we will often link observed IR features to the surface composition and evolutionary status of the stars.

Spectral energy distributions

Based upon the shape of the spectral energy distributions (SEDs) and more specifically the behavior in the near-IR, the optically visible Galactic post-AGB stars can be roughly divided into two groups (see Fig. 1.23). The first group consists of post-AGB stars with a double-peaked SED of which the peak at longer wavelengths corresponds to the detached expanding, circumstellar AGB remnant envelope. These envelopes contain cooling dust and gas (left panel in Fig. 1.23). Depending on the strength of the circumstellar reddening, the stellar photosphere is directly visible or obscured in the optical light by the circumstellar material. Some Galactic post-AGB stars have SEDs completely dominated by thermal emission of dust due to the complete obscuration of the photosphere by a strong equatorial density enhancement, or torus (e.g. Meixner et al. 1999; Ueta et al. 2000).

The second group consists of post-AGB stars with a strong excess in the near-IR, indicating hot dust close to the central star. These SEDs correspond to a disc rather than an expanding envelope (De Ruyter et al. 2006). It is now well established that this indicates the presence of a stable compact circumbinary disc (e.g. De Ruyter et al. 2006; Deroo et al. 2007; Gielen et al. 2011; Hillen et al. 2013, 2014; Bujarrabal et al. 2015), therefore the specific characteristics

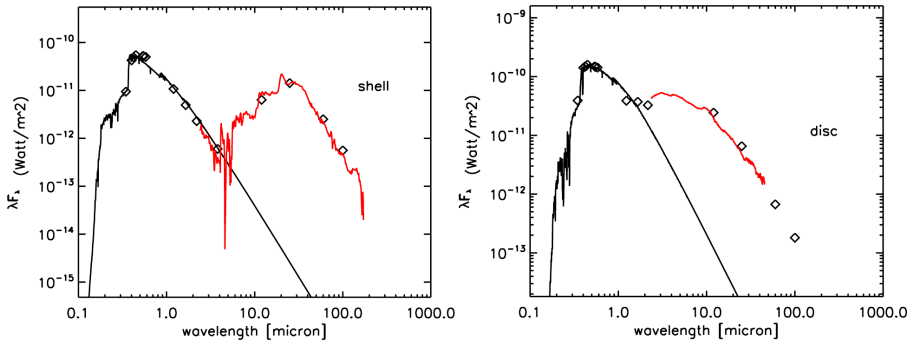

Figure 1.23: SEDs of Galactic post-AGB stars. The left panel shows HD 56126, a C-rich star with a double-peaked SED. The right panel displays the O-rich 89 Her which has a typical disc SED. Diamonds represent dereddened photometry, the full black lines the best fitting photospheric Kurucz models and the full red lines represents the ISO spectra. Figure reproduced from van Aarle et al. (2011).

of the SED are closely related to the binary nature of the central star (Van Winckel et al. 2009).

Chemistry of the circumstellar environment

Based upon observations of the IRAS satellite, Kwok et al. (1989) found that Galactic objects with an observed solid-state emission feature at 21 μm turned out to be carbon-enriched post-AGB stars. These objects are appropriately called *21 μm objects*. Later photospheric abundance studies also revealed that these stars have undergone strong *s*-process enrichments (Klochkova 1995; Van Winckel & Reyniers 2000; Reddy et al. 2002). The strength of the 21 μm feature strongly varies for individual sources although the profile remains relatively constant (Volk et al. 1999). To date, the feature has currently been observed in the circumstellar material of a small number of galactic and extra-galactic objects, the carrier of this dust feature is to date still unknown although several suggestions have been made such as particles composed of SiC and amorphous SiO_2, FeO or polycyclic aromatic hydrocarbons (PAHs) (see e.g. Posch et al. 2004; Sloan et al. 2014). The 21 μm feature is specific for C-rich post-AGB stars since it is not observed in C-rich AGB stars and C-rich PNe (Hrivnak et al. 2008b, 2009). Other typical components in the CSE of C-rich post-AGB stars are CO, C_2, CS, CN, C_2H_2, MgS and SiC. In some objects, the strong emission of PAHs can be detected.

Oxygen-rich post-AGB stars have a different chemistry of the CSE with typical molecules like CO, H_2O, OH, CO_2, SiO, TiO together with dust which mainly contains amorphous and crystalline silicates. However, large carbonaceous molecules have been detected around post-AGB binaries with stable oxygen-rich circumbinary discs (e.g. Gielen et al. 2011). This indicates that additional processing must occur to explain the presence of these large carbonaceous molecules. A possible explanation is the destruction of CO molecules in the CSE by e.g. photodissociation after which the released carbon combine into large carbonaceous molecules.

1.4.3 Chemical diversity in Galactic post-AGB stars

The chemical composition of post-AGB stars reflects the chemical alterations the star has undergone during the stellar lifetime: the initial chemical composition has been altered by possible dredge-up processes which have polluted the surface layers with newly-synthesised material from the stellar interior. Post-AGB photospheres are very useful for studying the chemical abundances of the individual elements and to gain insight in the different processes that took place during stellar evolution, including the AGB TUP and *s*-process nucleosynthesis. While the photospheres of AGB stars are dominated by molecular transitions, hampering the study of individual elements, post-AGB photospheres peak in the optical spectrum and are dominated by atomic transitions. This renders the possibility to study the abundances of a wide range of elements ranging from CNO up to lead (Pb). Also, unlike AGB stars, post-AGB stars often do not undergo any high-amplitude pulsations and do not suffer strong mass loss, making an accurate determination of the atmospheric parameters possible (see Chapter 2). In addition, post-AGB stars have ended the TP-AGB (although a late thermal pulse is still possible), so their current position in the HR-diagram can be compared with evolutionary post-AGB tracks (Sect. 1.4.1) while the positions of TP-AGB stars in the HR-diagram overlap for different initial masses and metallicities. These features make post-AGB stars useful probes for constraining AGB evolution and nucleosynthesis models.

Photospheric abundance studies of Galactic post-AGB stars show a wide chemical diversity. Due to the very short duration of the post-AGB phase for higher masses, the observational bias of post-AGB stars is towards lower masses. Because of the old age of these stars, the general expectation is to encounter post-AGB stars at subsolar metallicities together with altered abundances due to the different dredge-up episodes during the stellar lifetime. For low-mass stars with an intial mass $M_i \gtrsim 1.5$ $M_\odot$, this includes a global CNO enhancement with respect to iron, a C/O ratio > 1, and a global *s*-process enhancement with respect to the solar abundances. Only a minor fraction ($\pm$

25%, Rao et al. 2012) of the observed Galactic post-AGB stars display these CNO and *s*-process enhancements. The majority of Galactic post-AGB stars display no enrichment at all or even show some degree of depletion of refractory elements in their spectra, for which elements with high dust condensation temperatures are systematically underabundant (see page 32). This chemical anomaly is limited to objects with a disc and hence binaries (e.g. Gezer et al. 2015). Only a very limited number of Galactic post-AGB objects show mild *s*-process enrichment. An overview of studied *s*-process enriched, non-enriched and depleted post-AGB stars in the Milky Way Galaxy can be found in e.g Van Winckel (2003) and Rao et al. (2012) and references therein.

Before discussing the different degrees of *s*-process enrichment, we briefly discuss the difference between 'intrinsic' and 'extrinsic' enrichment. When a star is enriched by *s*-process elements which were synthesised in its core, we call it 'intrinsically enriched'. Extrinsic *s*-process enrichment occurs in binary systems when a star is polluted by material from its evolved companion which passed through the TP-AGB phase. Hence the observed *s*-process elements in an 'extrinsically enriched' object were not created by the object itself, but by the companion which is now a white dwarf.

S-process enrichment in Galactic post-AGB stars

Since the first discovery of strong *s*-process lines in HD 56126 by Klochkova (1995), several abundance studies of the photospheric chemical composition of post-AGB stars have been published. Although the *s*-process elements in strongly *s*-process post-AGB stars still occur in trace amounts in absolute abundance, they can create large spectral line features in optical spectra. An example of this is shown in the lower spectrum of Fig. 1.24, where two spectral lines of the *s*-process elements zirconium (Zr, Z=40) and lanthanum (La, Z=57) are clearly present and form a spectral blend. Typically, elemental abundances in *s*-process abundance studies are expressed relative to iron ([el/Fe][3]), as iron forms the seed for the creation of heavy elements. This provides a clear signature of *s*-process enrichment with respect to solar abundances as shown in Fig. 1.25, where the element-over-iron ratios of two strongly *s*-process enriched stars are displayed. The strong enrichment is translated in [el/Fe] $\gg 0$ for elements with Z $\geqslant$ 38.

However, individual abundance studies of post-AGB stars lack homogeneous atomic data in the sense that individual studies throughout time use different solar abundances. In addition, the uncertain oscillator strengths (gf-values)

[3] $[X/Y] = \log_{10}\left(\frac{N_X}{N_Y}\right)_{star} - \log_{10}\left(\frac{N_X}{N_Y}\right)_{\odot}$ with $\log_{10}(N_H) = 12.00$ dex

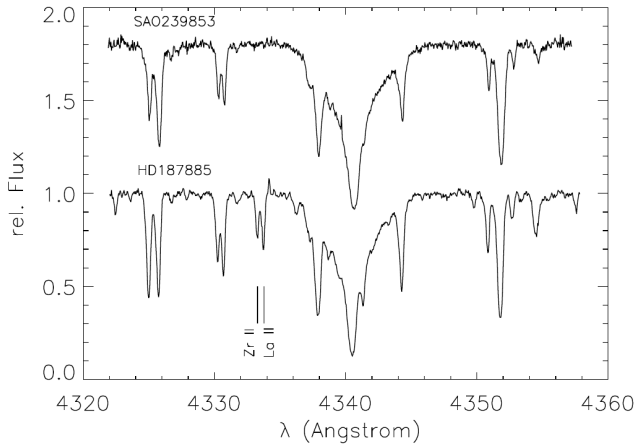

Figure 1.24: Comparison between the spectral Hγ regions of two post-AGB stars with similar SEDs and photospheric properties. The O-rich SAO 239853 does not show s-process enrichment while the C-rich HD 187885 does. Figure retrieved from Van Winckel et al. (1996b).

have direct influence on the final abundance results. When using different solar abundances, the gf values should also be scaled to the used solar abundances. There exist differences of up to 0.3-0.5 dex in gf values for the same atomic lines between different atomic line databases, hampering a quantitative comparison with theoretical AGB model computations.

Studies of Galactic *s*-process enriched post-AGB stars have shown that there is no observational evidence of a correlation between the degree of *s*-process enhancement and the metallicity as shown in Fig. 1.26. In contrast, these studies observationally confirm the connection between *s*-process and C-enrichment while non-enriched objects are O-rich which indeed links the C/O ratio with an efficient TUP. Furthermore, the metallicity range of observed Galactic *s*-process enriched post-AGB ranges from [Fe/H] = -0.2 to -1.0 dex which points to low initial masses. The observed Galactic *s*-process enriched post-AGB stars are hence metal-poor post-carbon stars.

One of the most striking observational evidence of chemical diversity of Galactic post-AGB stars is the large difference in enrichment for post-AGB stars with similar photospheric parameters and similar SEDs. A well illustrating example of this diversity is presented in Fig. 1.24, where the spectra of two stars with similar SEDs and photospheric properties are shown. These stars are nearly identical, but only the lower-spectrum star is *s*-process enriched. Also within the

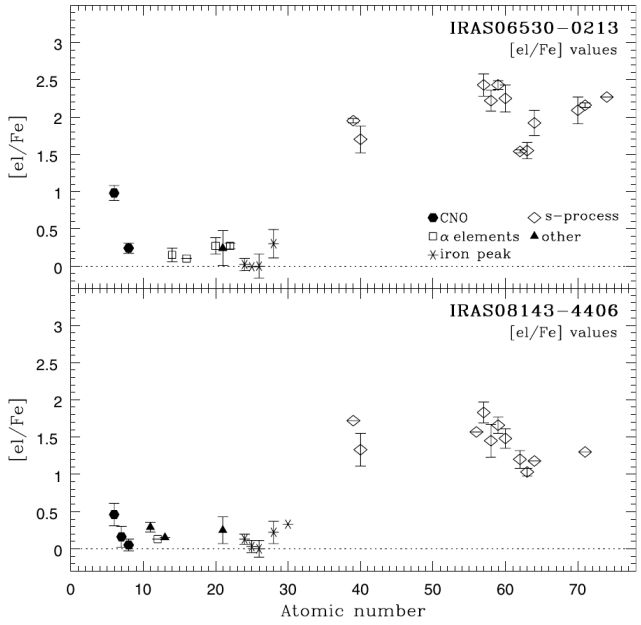

Figure 1.25: The abundances of two strongly *s*-process enriched post-AGB stars, relative to the iron abundance. The error bars represent line-to-line scatter while the dotted line represents [el/Fe] = 0. Both stars have similar atmospheric parameters and metallicity. Figure retrieved from Reyniers et al. (2004).

group of *s*-process enriched post-AGB stars, the differences in enhancement can be large as shown in Fig. 1.25 where both stars have approximately the same atmospheric parameters and metallicities, but the enrichment of IRAS 06530-0213 is clearly higher than the one of IRAS 08143-4406. Assuming that these stars have similar low initial masses, such abundance differences for stars with similar masses and metallicities can be explained by a spread in both *s*-process nucleosynthesis efficiency, hence the properties of the created ^{13}C-pocket, and the TUP efficiency. Another possible explanation is that both stars had similar TUP and *s*-process nucleosynthesis efficiency, but a different envelope mass during the last thermal pulse which translates in a different dilution factor.

In a strict homogeneous study by Van Winckel & Reyniers (2000), there appears to be a clear correlation between the *s*-process overabundance and the neutron irradiation, expressed by the [hs/ls]-ratio which was introduced in Sect. 1.2.3. The lower panel of Fig. 1.26 shows this correlation and points to a strong connection between TUP and the partial mixing in the intershell which creates

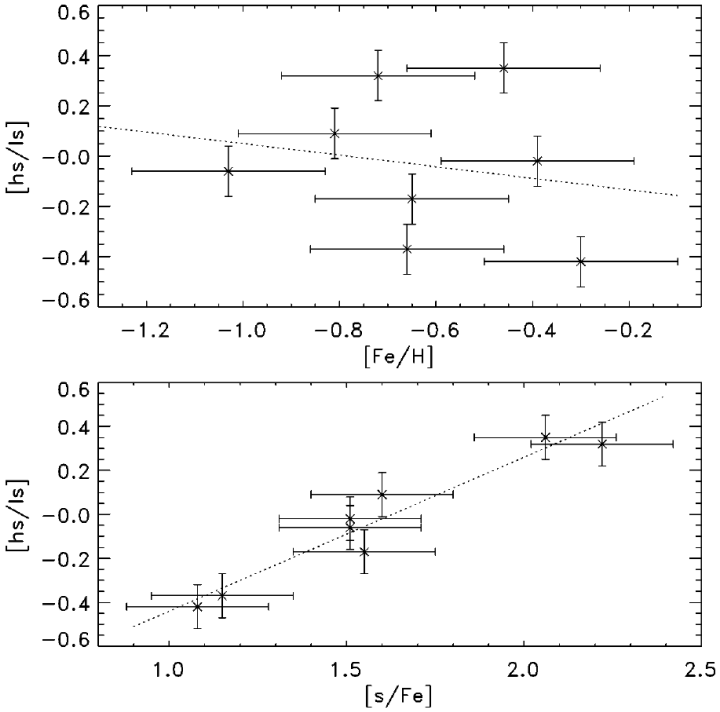

Figure 1.26: *Upper panel:* [hs/ls] (= neutron irradiation) as a function of metallicity in a homogeneous study of *s*-process enriched post-AGB stars. The dotted line represents the least squares fit with a correlation coefficient of -0.19. *Lower panel:* [hs/ls] as a function of total *s*-process enrichment. The dotted line represents the least squares fit with a correlation coefficient of +0.96. Figure retrieved from Van Winckel (2003).

the ^{13}C-pocket.

For strong neutron irradiation, the formation of heavy elements up to Pb are expected (Goriely & Mowlavi 2000; Busso et al. 2001). In the Milky Way Galaxy, the theoretically expected overabundances of Pb, for which Pb is overabundant with respect to the other *s*-elements, is to date only observed in Galactic metal-deficient, cool, extrinsically enriched objects (see e.g. Van Eck et al. 2001, 2003; Aoki et al. 2001; Behara et al. 2010). However, not all Galactic metal-deficient, cool, extrinsically enriched objects display the strong Pb overabundance (Aoki et al. 2001; Van Eck et al. 2003). To date, strong Pb overabundances have not been detected in Galactic intrinsically enriched post-AGB stars. However,

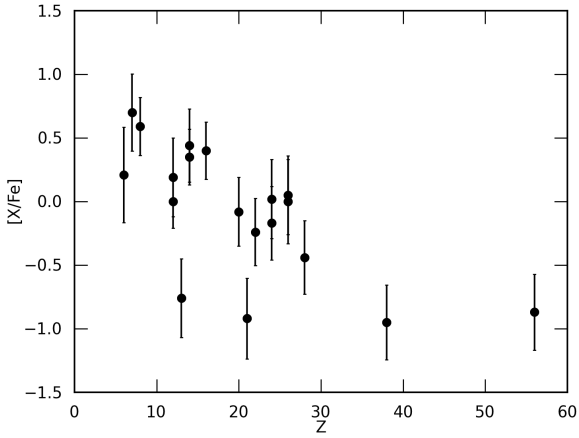

Figure 1.27: Abundance profile of the O-rich post-AGB star HD 133656 which does not show any signs of *s*-process enrichment or depletion. Figure reproduced from the abundance results in Van Winckel et al. (1996a).

other heavy elements like Gd (Z=64), Yb (Z=70), Lu (Z=71) and W (Z=74) have been clearly observed in some objects (e.g. Reyniers & Van Winckel 2003; Reyniers et al. 2004).

The majority of Galactic post-AGB stars ($> 50\%$) do not show any signs of *s*-process enrichment and are O-rich. An example abundance pattern of such a post-AGB star is shown in Fig. 1.27. The abundance pattern shows a [O/Fe] $>$ [C/Fe] and the two observed *s*-process elements Sr (Z=38) and Ba (Z=56) have [el/Fe] < 0, which indicates no *s*-process enrichment. These O-rich objects display a metallicity range of [Fe/H] = -0.3 to -1.0 dex, similar to their C-rich counterparts. The circumstellar O-rich dust points to the absence of efficient TUP. Hence there exists a strong chemical dichotomy for the large majority of Galactic post-AGB stars: a post-AGB is either C-rich combined with strong *s*-process enrichments or it is O-rich and does not display any signs of *s*-process enrichment at all. Only a very limited number of mild *s*-process enriched objects have been detected to date (e.g. Rao et al. 2012, and references therein).

Whether the current distribution of strongly, mildly and non *s*-process enriched objects is real or caused by a bias in selection criteria is still a matter of debate and needs further study.

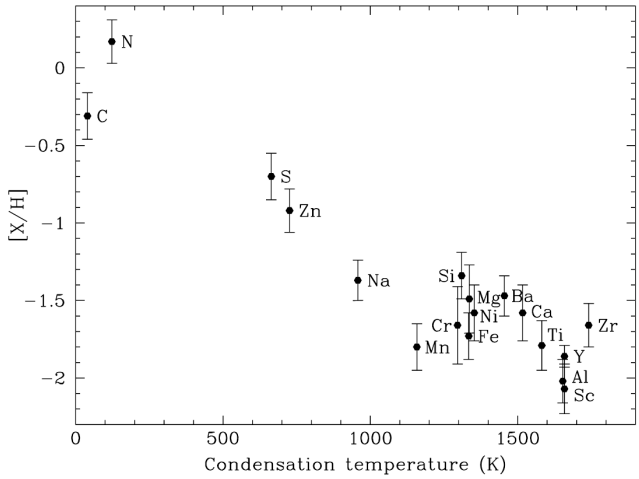

Figure 1.28: Example of a typical abundance pattern for a depleted star (HD 46703). The abundances are plotted with respect to the condensation temperature of each individual element, which is the temperature at which half of the particles of the element are condensed onto dust grains, under the assumption of chemical equilibrium, at a constant pressure of 10^{-4} bar in a solar mixture (Lodders et al. 2009). Figure retrieved from Hrivnak et al. (2009).

Depleted post-AGB stars

Apart from *s*-process enriched and non-enriched objects, the sample of studied Galactic post-AGB stars contains a group of stars displaying strong deficiencies of not only *s*-process elements but also for other elements like Fe, Mg and Si while other abundances like C, N, O and zinc (Zn) are not affected. This phenomenon is called depletion and a typical depletion pattern in shown in Fig. 1.28.

The physical processes behind the observed depletion pattern can be explained by following the suggestion of Venn & Lambert (1990) who found a similarity between the depletion pattern and the chemical pattern of the gas-phase abundances of the ISM. Bond (1991) proposed that the iron in depleted stars is selectively removed by dust formation. This received strong support by the detection of high [Zn/Fe] ratios in depleted objects (e.g. Van Winckel et al. 1992, 2002; Hrivnak et al. 2008a). As Zn and Fe have a similar nucleosynthetic origin, but with Zn having a much lower condensation temperature (Lodders et al. 2009), it appears that the depletion pattern has a chemical origin rather than a nucleosynthetic one. The depletion starts with a chemical fractionation

caused by the formation of dust in the CSE where the gas of refractory elements is captured in dust particles, which is then followed by a re-accretion of the circumstellar gas. As post-AGB photospheres are too hot to form dust, Waters et al. (1992) proposed that the most favourable conditions for depletion to occur is when the circumstellar dust is trapped in stable long-lived discs while the gas is re-accreted onto the star. Since the *s*-process elements are refractory, the chemical composition of the circumstellar dust renders the best evidence for any AGB enrichment instead of the photosphere, where any signs of a possible nucleosynthetic history are lost.

As depletion requires stable long-lived discs, it is linked to binarity and this is well established by observations of depleted post-AGB binaries with circumbinary discs (see e.g. Van Winckel et al. 1995, 1999; Maas et al. 2002; Van Winckel et al. 2009; Hrivnak et al. 2009). So far, depletion has only been observed in disc sources (Gezer et al. 2015).

1.5 Motivations and outline

This thesis is part of a larger project in which we study Galactic and extragalactic post-AGB stars to improve our knowledge of the physical processes during the final stages of stellar evolution (e.g. Reyniers et al. 2004; Gielen et al. 2011; van Aarle et al. 2011, 2013; Kamath et al. 2014; Hillen et al. 2014; Gorlova et al. 2014; Kamath et al. 2015, accepted).

In our introduction, we show that, although the general scheme of the final stellar evolutionary phases of low- and intermediate mass stars is generally acknowledged, there is no understanding of different important physical processes that take place during these evolutionary phases. The main problems are related to the poor knowledge of mass-loss mechanisms during the AGB phase and the internal evolution of TP-AGB stars like the creation of the ^{13}C-pocket and the efficiency of mixing processes (see Sect. 1.3.1). Therefore, the outcome of current theoretical AGB evolution and nucleosynthesis models contain large uncertainties. Observational constraints are necessary to further improve our knowledge of the AGB nucleosynthesis and corresponding mixing processes.

Post-AGB stars are ideal testbeds for improving theoretical AGB evolution and nucleosynthesis models since the chemical composition of their photospheres display the different dredge-up processes that take place during the total stellar lifetime. A systematic abundance study of optically visible post-AGB stars in a wide range of metallicities and luminosities, hence initial masses, will help to constrain AGB model parameters.

The sample of studied Galactic post-AGB stars displays a wide chemical diversity, but unfortunately the distances to these objects are unknown. Therefore it is not possible to determine accurate luminosities and hence initial masses of Galactic post-AGB stars since their position in the HR-diagram is determined by their initial mass. Moreover, although displaying a broad range in photospheric composition, the known sample of Galactic post-AGB stars is rather limited due to the short transition times, which hinder the creation of a significant statistical sample. Furthermore, it remains unclear whether the chemical diversity of the known Galactic sample represents the total class of post-AGB stars. These shortcomings make it difficult to link observations with theoretical model predictions, and how the different model predictions fit in the broader context of stellar evolution.

Post-AGB stars in the Magellanic Clouds do not have the drawback of the unknown distances of their Galactic counterparts since we know the distances to the Magellanic Clouds.

The main subject of this thesis are the systematic photospheric abundance studies of post-AGB stars in the Galaxy and the Magellanic Clouds. With known distances of 50 kpc (Storm et al. 2011) and 61 kpc (Hilditch et al. 2005) for the LMC and SMC respectively, the Magellanic Clouds provide the opportunity to determine the luminosities and hence estimate the initial masses of these stars. Since we can accurately determine the metallicity and moderatly estimate the initial mass of these objects, we can directly compare the photospheric abundances with theoretical AGB nucleosynthetic model predictions. For the determination of initial post-AGB masses, we prefer the use of the theoretical post-AGB tracks of Vassiliadis & Wood (1994) covering a range in metallicities while the tracks of Blöcker (1995) only represent solar mixture.

An important part of our photospheric abundance studies is the study of Pb in intrinsically *s*-process enriched post-AGB stars, both in the Galaxy and the Magellanic Clouds. As Pb is the final product of the *s*-process nucleosynthesis, the Pb abundance is sensitive to the different processes that occur during the TP-AGB. To date, Pb has only been detected in extrinsically *s*-process enriched stars in the Galaxy. The same is true for extra-galactic stars with the exception of MACHO 47.2496.8, an intrinsically s-process enriched post-AGB stars in the LMC (Reyniers et al. 2007a). And, although the distances to the Galactic post-AGB stars are unknown, a systematic study of Pb for different metallicities will help to gain insight in the different processes that took place in these stars.

The outline of the thesis is as follows. In Chapter 2, we discuss the selection of our sample of Galactic and extra-galactic post-AGB stars together with an overview of the instruments and tools that are used for our studies. An extensive chemical abundance study of the highly *s*-process enriched SMC star

J004441.04-732136.4 is presented in Chapter 3, followed by an abundance study of Pb in *s*-process enriched post-AGB stars in the Magellanic Clouds in Chapter 4. Then, we present the abundance study of two strongly *s*-process enriched post-AGB stars in the LMC in Chapter 5. Next we present a homogeneous abundance study of Pb in *s*-process enriched post-AGB stars in the Milky Way Galaxy in Chapter 6. Thereafter, we present the chemical abundances of a mildly *s*-process enriched post-AGB star in the LMC in Chapter 7. In the final two chapters, we present our overall conclusions of this thesis followed by a discussion of the future prospects in this research topic.

Chapter 2

Sample selection and general methodology

Due to their known distances, post-AGB stars in the Magellanic Clouds are useful testbeds for constraining theoretical AGB evolution and nucleoynthesis models. Therefore, a large part of this thesis focusses on chemical abundance studies of Magellanic Cloud post-AGB stars.

In this chapter, we introduce the Magellanic Clouds (MCs) and how we selected the MC and Galactic post-AGB stars for our research. In addition, we also provide an overview of chemical abundance studies of post-AGB stars in the Large Magellanic Cloud which were published before and during the creation of this thesis. We then describe the instruments which were used for observing the high-resolution spectral data for our research and we end with an introduction on chemical abundance studies.

2.1 The Magellanic Clouds

The Magellanic Clouds are two satellite galaxies of the Milky Way Galaxy and they were named after the Portuguese navigator Ferdinand Magellan, whose crew described them during the first voyage around the world in the 16th century. Both galaxies can be seen from the Southern hemisphere and they lie about 22° apart in the sky near the south celestial pole.

The Large Magellanic Cloud (LMC) is classified as a barred Magellanic Spiral

Figure 2.1: IR observations of the LMC (left panel) and SMC (right panel) by the NASA's Spitzer Space Telescope (Werner et al. 2004). The IR light is colour-coded: blue shows the light at 3.6 μm which generally indicates the presence of older stars, green shows organic dust at 8.0 μm and red highlights cold dust at 24 μm. Figures retrieved from http://www.spitzer.caltech.edu

(SBm, de Vaucouleurs & Freeman 1972) because of its bar-like feature embedded in a disc and its single spiral arm. The LMC has a diameter of about 4.3 kpc and a height of about 500 pc. It is roughly 100 times less massive than the Milky Way Galaxy with a mass of about 10^{10} $M_{\odot}$ and it lies at a distance of about 50 kpc (Keller & Wood 2006; Reid & Parker 2010; Storm et al. 2011) to the centre of the Milky Way Galaxy. It has a low mean metallicity of $\sim$-0.5 dex (e.g. Geisler et al. 2009; Lapenna et al. 2012) and a mean radial velocity of +262 km/s (van der Marel et al. 2002).

The Small Magellanic Cloud (SMC) is classified as an irregular galaxy but is assumed to have been a disrupted barred galaxy as it contains a central bar structure. It has a diameter of about 2.2 kpc and is roughly 150 times less massive than the Milky Way Galaxy with a mass of about 7×10^9 $M_{\odot}$. It lies at a distance of about 60 kpc (Keller & Wood 2006) and it has a low mean metallicity of $\sim$-0.7 dex (Luck et al. 1998). It has a mean radial velocity of +160 km/s (Richter et al. 1987).

The irregular form of both galaxies is a possible result of tidal interactions between the Milky Way Galaxy and the MCs. Proof of the interaction between the MCs is found in a bridge of gas connecting both galaxies. The common envelope of neutral hydrogen suggests that they are gravitationally bound. Like most irregular galaxies, the MCs are rich in gas and dust as shown in Fig.

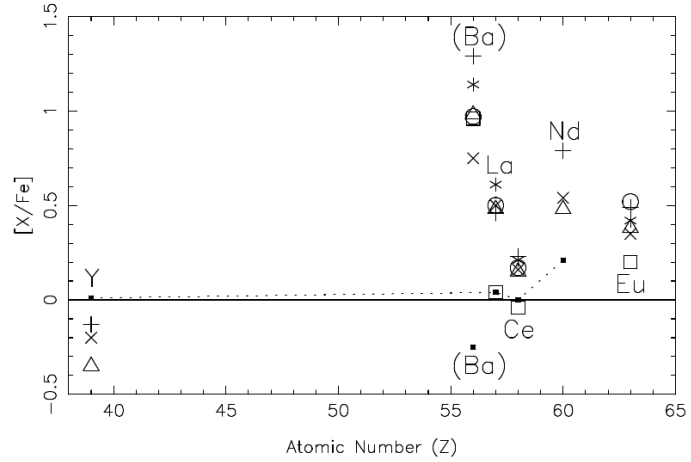

Figure 2.2: Element over iron ratios for some *s*-process elements in SMC red giant stars. Each symbol denotes a different red giant. The small filled square denotes the abundances of the Galactic red giant Arcturus for comparison. Figure retrieved from Hill (1997).

2.1, and are hence ideal star-formation sites. A famous example of an active star-formation region is the Tarantula Nebula in the LMC.

2.1.1 Chemical properties of the Magellanic Clouds

When comparing the chemical abundance results of MC post-AGB stars with the predictions of AGB nucleosynthesis models, it is important to take into account the intrinsic chemical enrichment of *s*-process elements in the MCs. It is observationally well established that the heavy *s*-process (hs) elements are enhanced in non-evolved MC stars. Older studies already found that generally, the hs-elements around Z=56 show slight enhancements between $0 <$ [el/Fe] $\leqslant 0.5$ dex while the light *s*-process elements do not show any enhancement or even show slight deficiencies (see e.g. Spite et al. 1986; Russell & Bessell 1989; Luck & Lambert 1992; Spite et al. 1993; Hill 1997; Luck et al. 1998; Hill 1999; Gonzalez & Wallerstein 1999). This enhancement of hs-elements is not present in the Galaxy and is hence linked to the MCs. Fig. 2.2 shows the [el/Fe] results of six red giants spread over the SMC together with the Galactic red giant Arcturus (small filled square) for comparison from Hill (1997). The figure shows the enhancement of hs-elements for MC giants with respect to Arcturus while the ls-element Y is slightly deficient. The Ba abundances in

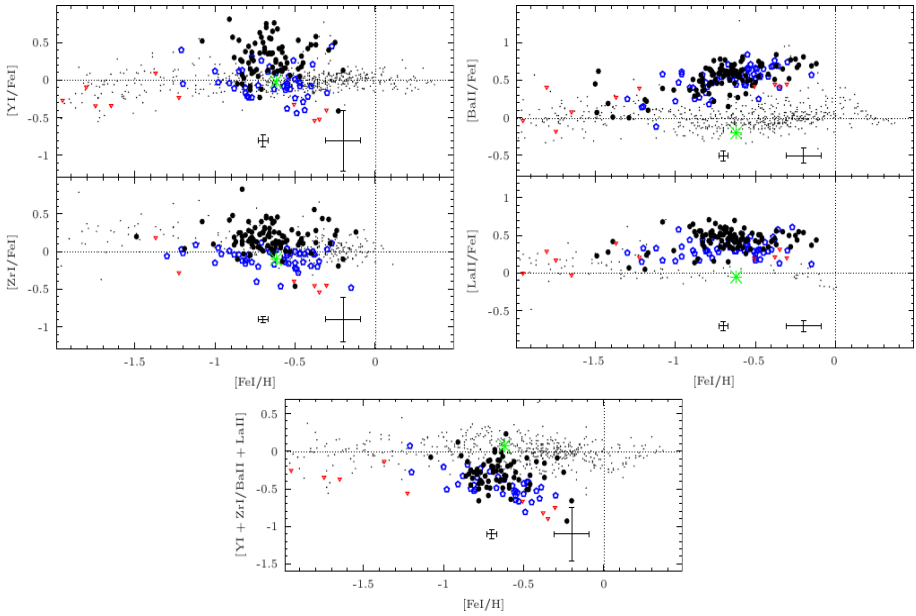

Figure 2.3: [el/Fe] results of ls- and hs-elements from Van der Swaelmen et al. (2013, and references therein). Black filled dots present LMC bar abundances, blue open pentagons abundances of the LMC inner disc, small black dots represent Galactic abundances, red triangles the abundances in globular LMC clusters and the green asterisk represent the abundances of Arcturus. Figures reproduced from Van der Swaelmen et al. (2013).

Fig. 2.2 are mostly based upon saturated lines, and may be overestimated. A comparison between the hs-element enhancements in MC giants in these studies shows that the hs-elements are generally more enhanced in the SMC. The mean hs-element enrichments of the LMC and SMC are about +0.3 dex and +0.5 dex respectively.

More recent abundance studies of LMC giants by Mucciarelli et al. (2008, 2010) and Van der Swaelmen et al. (2013) show similar results. The abundance results of Mucciarelli et al. (2008, 2010) for four intermediate-age and three old globular clusters show slight deficiencies for Y while elements like La and Nd are enhanced. They find that cerium (Ce, Z=58) is almost not enhanced while other hs-elements are enhanced. Van der Swaelmen et al. (2013) performed similar abundance studies of a large sample of LMC field red giant stars located in the disc and the bar. They find that the abundances of barium (Ba, Z=56) and lanthanum (La, Z=57) increase with increasing metallicity (right panel of Fig.

2.3) while the abundances of the ls-elements yttrium (Y, Z=39) and zirconium (Zr, Z=40) basically remain constant over the observed metallicity range (left panel of Fig. 2.3). They also find that the LMC bar shows higher enrichments in Y and Zr than the inner LMC disc while this is not true for Ba and La. Van der Swaelmen et al. (2013) assume that these observed differences may be an effect of the metallicity of the AGB stars producing the *s*-process elements. They attribute the Y and Zr abundance differences between the LMC bar and disc to a recent episode of stellar formation in the bar a few Gyr ago (see e.g. Olszewski et al. 1996; Bekki & Tsujimoto 2012). This generated more metal-rich AGB stars, for which the production of ls-elements is favoured. However, this stellar formation will also generate more massive AGB stars where the creation of ls-elements is also favoured. Therefore, the abundance difference between Y and Zr in the LMC bar and disc should be attributed to the combination of metallicity and mass of the AGB stars which produced these elements.

The lower panel of Fig. 2.3 shows that the [ls/hs] ratio of the LMC is lower than the ratio of the Galaxy (small black dots in Fig. 2.3), which implies that the LMC has a higher enhancement of hs-elements. This indicates that the AGB stars which dominated the LMC enrichment were more metal-poor than those of the Galaxy.

Unfortunately, we do not find similar extensive abundance studies like in Mucciarelli et al. (2008, 2010) and Van der Swaelmen et al. (2013) for the SMC, but we assume that it displays a similar [hs/ls] behavior. There may however be differences in intrinsic galactic enrichment between the MCs as studies show that the SMC experienced a more continuous star formation throughout time (e.g. Cignoni et al. 2012) while the LMC experienced a long epoch between 12 and 5 Gyr ago with almost no star formation (e.g. Harris & Zaritsky 2009).

2.2 Post-AGB selection in the Magellanic Clouds

The Magellanic Cloud post-AGB stars that are studied in this thesis were selected from the resulting catalogues of surveys which made use of the IR photometry of the Spitzer Space Telescope and low-resolution spectra to identify post-AGB stars. In this section, we briefly describe the different surveys from which our sample of Magellanic Cloud stars are selected.

2.2.1 The Spitzer SAGE surveys

The Spitzer survey of the Small Magellanic Cloud (Spitzer S^{3}MC Bolatto et al. 2007) provided the basis of the first selection of post-AGB stars in the SMC. This survey resulted in a point source catalogue with over 400 000 sources with photometry of the Infrared Array Camera (IRAC Fazio et al. 2004) at 3.6, 4.5, 5.8 and 8.0 μm and of the Multi-band Imaging Photometer for Spitzer (MIPS Rieke et al. 2004) at 24, 70 and 160 μm. The S^{3}MC catalogue was later included in the SAGE-SMC catalogues, where SAGE-SMC stands for 'Surveying the Agents of Galaxy Evolution in the Tidally Stripped, Low Metallicity Small Magellanic Cloud' (Gordon et al. 2011). The observed SAGE-SMC region also contains the observed S^{3}MC subregion and the datapoints of the S^{3}MC survey were reprocessed which showed that there were some small systematic errors on the S^{3}MC datapoints. For the construction of the SAGE-SMC catalogue, the Spitzer photometry was bandmerged with photometry of the Two Micron All Sky Survey 2MASS (2MASS Skrutskie et al. 2006). The SAGE-SMC catalogue and the analogue SAGE-LMC catalogue for the LMC (Meixner et al. 2006) are used for the construction of catalogues of optically visible post-AGB candidates in the Magellanic Clouds by van Aarle et al. (2011) and Kamath et al. (2015) for the LMC (see Sect. 2.2.2) and by Kamath et al. (2014) for the SMC (see Sect. 2.2.3).

2.2.2 Search for post-AGB stars in the LMC

Two different catalogues of optically visible post-AGB candidates in the LMC were constructed by van Aarle et al. (2011) and Kamath et al. (2015). We briefly discuss the construction of these two catalogues.

Search for post-AGB stars in the LMC by van Aarle et al. (2011)

The text in this section is based upon the study 'The optically bright post-AGB population of the LMC' by van Aarle et al. (2011).

The initial selection of post-AGB candidates by van Aarle et al. (2011) was based upon the IR photometry in the SAGE-LMC catalogue. They first imposed a colour selection which was inspired by the knowledge of Galactic sources to avoid background galaxies, extreme AGB stars, which are strongly dust-enshrouded AGB stars (Blum et al. 2006), and red supergiants, but to select suspected SED shell and disc sources.

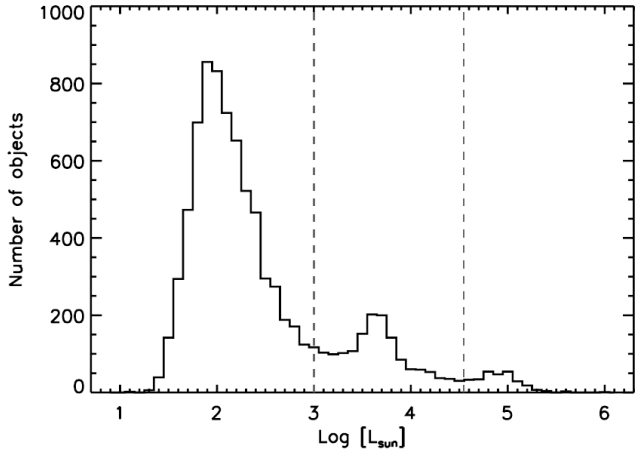

Figure 2.4: Histogram of the integrated luminosities by black body fitting. The vertical dashed lines represent a lower and upper limit for the luminosities of post-AGB stars between 1000 and 35 000 $L_\odot$ respectively. Figure retrieved from van Aarle et al. (2011).

The IR photometry of the remaining selection was then bandmerged with optical photometry of the $UBVR$ CCD survey of the Magellanic Clouds (Massey 2002), the LMC stellar catalogue of Zaritsky et al. (2004) and the Guide Star Catalog, Version 2.3.2 (GSC2.3) (Lasker et al. 2008). The combined photometry allowed van Aarle et al. (2011) to estimate the luminosities of central objects by fitting up to three black bodies to all photometry without applying reddening, which means correcting the observed photometry for possible scattering by dust. The resulting luminosity distribution of the remaining sample stars are shown in Fig. 2.4. van Aarle et al. (2011) kept the objects with luminosities between the vertical dashed lines, representing luminosities of 1000 and 35 000 $L_\odot$ which are typical post-AGB luminosities based upon the predictions of Blöcker (1995). It is expected that objects with $L < 1000$ $L_\odot$ are most probably young stellar objects (YSOs) while objects with $L > 35000$ $L_\odot$ are most probably massive supergiants, although it is clear in Fig. 2.4 that the distribution tails of the three different peaks overlap, so pollution by YSOs and supergiants is still possible in the remaining sample.

To reject possible intruders like YSOs, massive supergiants, PNe and foreground stars, van Aarle et al. (2011) performed a cross-correlation with catalogues of these other known types of objects in the LMC. Low-resolution spectra of the ANU Telescope at Siding Spring Observatory (SSO) in Australia and the Radcliffe Telescope at the South African Astronomical Observatory were

obtained for the remaining objects in the selection. After rejection of the clear non-post-AGB objects, the low-resolution spectra were used to determine the spectral types of the remaining objects. The spectral types were then used to determine the reddening of the photometry and calculate more accurate luminosities. Based upon the shape of their SED, the remaining objects were categorised as shell, disc or unclear in the catalogue[1] of van Aarle et al. (2011) which contains 1407 post-AGB candidates.

Search for post-AGB stars in the LMC by Kamath et al. (2015)

The text in this section is based upon the study 'Optically Visible Post-AGB Stars, Post-RGB Stars and Young Stellar Objects in the Large Magellanic Cloud' by Kamath et al. (2015) which is accepted for publication in MNRAS.

Kamath et al. (2015) adopted the initial sample selected by van Aarle et al. (2011) for an extensive spectroscopic survey to identify post-AGB, YSOs and post-RGB candidates in the LMC. The latter objects have similar mid-IR excesses, stellar parameters and SEDs as post-AGB stars but their luminosities, ranging from 100 - 2500 $L_{\odot}$ and hence also masses and radii, are much lower than those expected for post-AGB stars. Since RGB stars are known to have luminosities < 2500 $L_{\odot}$, it is expected that these objects are evolved dusty post-RGB stars. These objects were identified for the first time by Kamath et al. (2014) in an extensive survey of the Small Magellanic Cloud for the identification of post-AGB stars and YSOs (see Sect. 2.2.3). Due to the unknown distances and hence luminosities, post-RGB stars have not yet been identified in the Galaxy. This indicates that some of the identified Galactic post-AGB stars may very well be post-RGB stars.

Low-resolution spectra were obtained with the AAOmega double beam multifibre spectrograph (Sharp et al. 2006) mounted on the 3.9m Anglo Australian Telescope at SSO. The AAOmega allows for a simultaneous observation of 392 targets, including the targets needed for calibration, over a 2 degree field. A total of 2106 objects were observed from a total of 8626 candidates due to limited observational time. Fig. 2.5 shows the 2 degree fields in the LMC that were used in the survey of Kamath et al. (2015). The spectra of about 558 objects had too low signal so these were rejected leaving a total of 1548 individual objects.

From preliminary spectral classification, Kamath et al. (2015) could remove intruders with similar mid-IR excesses as post-AGB stars like M stars, C stars, PNe and background galaxies. Also objects with spectra dominated by emission

[1] http://vizier.cfa.harvard.edu/viz-bin/VizieR?-source=J/A+A/530/A90

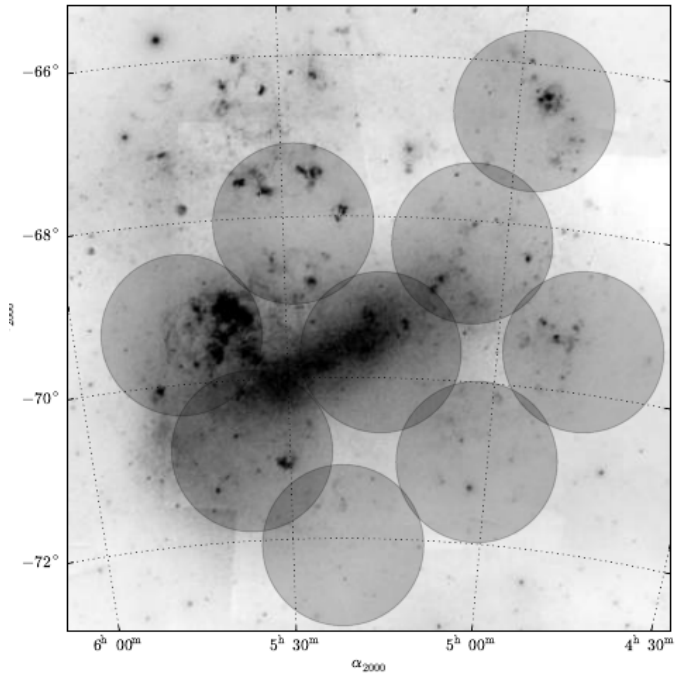

Figure 2.5: A Digitalised Sky Survey image of an 8 degree field of view centered on the LMC. The circles represent the observed 2 degree fields in the LMC covered in the survey of Kamath et al. (2015). Figure retrieved from Kamath et al. (2015).

lines were removed from the sample although they may be hot post-AGB/post-RGB stars or YSOs. They will be studied in a following publication.

Kamath et al. (2015) developed a fully automated spectral typing pipeline (STP) to simultaneously determine the stellar parameters effective temperature $T_{\rm eff}$, surface gravity log g and metallicity [Fe/H] . The STP matched each individual observed spectrum to a library of synthetic spectra, to find the minimum rms deviation over a restricted $T_{\rm eff}$, log g and [Fe/H] grid. Synthetic spectra were obtained from the Munari synthetic library (Munari et al. 2005). Based upon the spectral type of the star, different spectral regions were used for the spectral fitting. Fig. 2.6 shows an example of a spectral typing result. A total of 581 candidates were spectroscopically analyzed by STP.

Thereafter, the reddening of the candidate objects is determined by estimating the difference between the intrinsic colours (determined from the $T_{\rm eff}$ of the

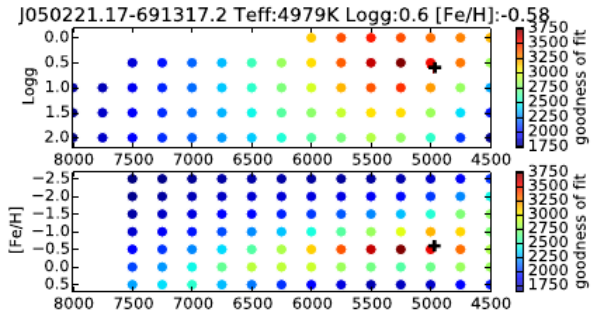

Figure 2.6: Example of a spectral typing result using Munari templates. The results are for the LMC star J050221.17-691317.2 which will be studied in detail in Chapter 7. The plots show the inverse rms distribution (= goodness of fit) in the T_{eff}- log g and T_{eff}- [Fe/H] space with the red plus indicating the final interpolated value. Figure retrieved from Kamath et al. (2015).

spectral fitting) and the measured colours. 85 objects were removed from the sample in this step, as they did not have the required optical photometry. Thereafter, Kamath et al. (2015) calculated the photospheric luminosity (L_{ph}) of the central stars by applying a bolometric correction for the preferred model atmospheres corresponding to each individual candidate normalised to the dereddened V magnitude and combining this with the distance to the LMC. They used the same photometry as van Aarle et al. (2011) and also added WISE photometry (The Wide-field Infrared Survey Explorer Wright et al. 2010) in the 3.4, 4.6, 12 and 22 μm bands for the construction of their SEDs.

Then, the derived atmospheric parameters (T_{eff}, surface gravity log g and metallicity [Fe/H]), the reddening E(B-V) and the derived photospheric luminosity were used for characterizing the remaining 496 candidates. Very luminous objects with $L_{ph} \geqslant 35000$ $L_{\odot}$ were rejected and will be analyzed in a future study. Disentangling post-AGB/post-RGB candidates from YSO candidates is difficult as these objects have similar T_{eff} and L_{ph} together with similar IR colours and dust excesses. Kamath et al. (2015) devised a criterion based on surface gravity log g of the central star. For the same luminosity, the mass of a YSO will be 15 to 20 times that of a corresponding post-AGB/post-RGB star, which leads to a mean difference of about 1.3 dex in log g between post-AGB/post-RGB and YSOs. However, an important remark is that of all atmospheric parameters, log g has the highest uncertainty since log g least affects the spectra with respect to T_{eff} and [Fe/H]. Therefore, there remains a degree of uncertainty in the classification method. High-resolution spectra are needed to confirm the nature of the individual objects.

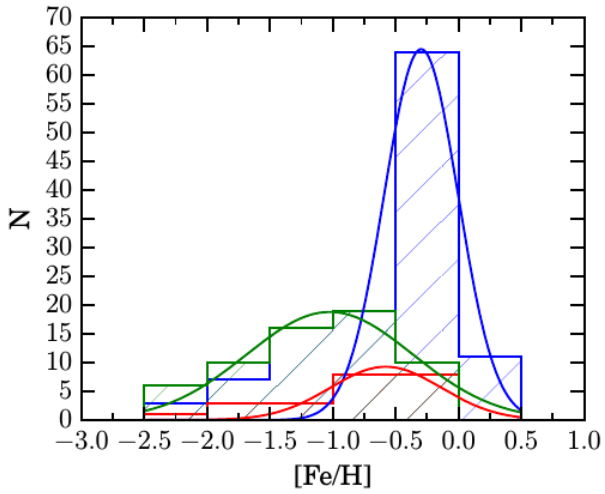

Figure 2.7: Histogram showing the [Fe/H] distribution for the post-AGB (red), post-RGB (green) and YSO candidates (blue). The coloured curves denote the individual Gaussian fits to the respective histograms. Figure retrieved from Kamath et al. (2015).

After the distinction of the 162 YSO candidates, the distinction between the remaining 154 post-AGB and post-RGB was made by using the luminosity criterion $L_{ph}/\mathrm{L}_{\odot} > 2500$ for post-AGB stars and $L_{ph}/\mathrm{L}_{\odot} \leqslant 2500$ for post-RGB stars. This resulted in a final sample of 35 post-AGB candidates and 119 post-RGB candidates. Fig. 2.7 shows the metallicity distribution of the sample of post-AGB, post-RGB and YSO candidates. The histogram shows the expected distribution as post-AGB/post-RGB stars are old to intermediate age populations, and are hence more metal-poor than the YSOs. Based upon their SED IR shapes, Kamath et al. (2015) divide the final sample of post-AGB and post-RGB into shell, disc or 'uncertain' sources. Of the 35 post-AGB objects, this resulted in 10 shell-sources, 23 disc-sources and 2 of uncertain SED type. Similarly, the 119 post-RGB objects resulted in 23 shell-sources, 56 disc-sources and 40 of uncertain SED type.

Kamath et al. (2015) expect post-RGB stars to be in binary systems, since the single-star mass loss that occurs during the RGB phase is insufficient to remove the hydrogen-rich envelope and to produce the dusty post-RGB star (e.g. Vassiliadis & Wood 1993). Therefore, the only way to create large amounts of mass loss followed by the evolution off the RGB is via binary interactions (e.g. Han et al. 1995; Heber 2009).

Although the final catalogue of optically visible post-AGB stars in the LMC of Kamath et al. (2015) contains 35 post-AGB candidates, with possible polluters like luminous YSOs and probably some post-AGB candidates that may have been classified as post-RGB or YSO, Kamath et al. (2015) remark that this survey is not complete. This is caused by the used colour crition in van Aarle et al. (2011) which does not include older post-AGB/post-RGB stars with expanding shells. Also, due to the optically visible criterion ($V < 20$ mag), faint and heavily dust-enshrouded post-AGB stars are not included in the survey.

2.2.3 Search for post-AGB stars in the SMC

The text in this section is based upon the study 'Optically visible Post-AGB/RGB stars, and young stellar objects in the Small Magellanic Cloud: candidate selection, spectral energy distributions and spectroscopic examination' by Kamath et al. (2014). The SMC survey was performed before the similar LMC survey in Sect. 2.2.2

The initial selection of Kamath et al. (2014) was based upon photometry of the SAGE-SMC survey (Gordon et al. 2011). Additional optical photometry was added from the Magellanic Clouds Photometric Survey (MCPS, Zaritsky et al. 2002)) and the Deep Near-Infrared Survey of the Southern Sky catalogue (DENIS, Epchtein et al. 1997)) together with additional mid-IR WISE photometry.

Kamath et al. (2014) used similar colour criteria as in van Aarle et al. (2011) and Kamath et al. (2015), with some additional criteria to account for the lower luminosity of SMC objects as the distance to the SMC is larger than for the LMC. A total of five selection criteria are imposed to remove intruders like extreme AGB stars, massive supergiants and low-mass YSOs from the sample. The main difference between the selection criteria of the LMC survey in Kamath et al. (2015) and the SMC survey in Kamath et al. (2014) was the 24 μm depth of the Spitzer survey in the SMC which was too shallow. Therefore, the 24 μm flux could not be used for selecting SMC sources. The SMC colour selection criteria resulted in an initial sample of 1194 objects.

Low-resolution spectra were obtained with the AAOmega double beam multifibre spectrograph mounted on the 3.9m Anglo Australian Telescope at SSO. Four different 2 degree fields were observed which resulted in low-resolution spectra of 801 unique candidates. Fig. 2.8 presents the 2 degree fields in the SMC used for the survey. After rejection of spectra with too low signal or technical errors, the current sample contained a total of 621 individual objects.

As the colour selection criteria for the construction of the initial sample were

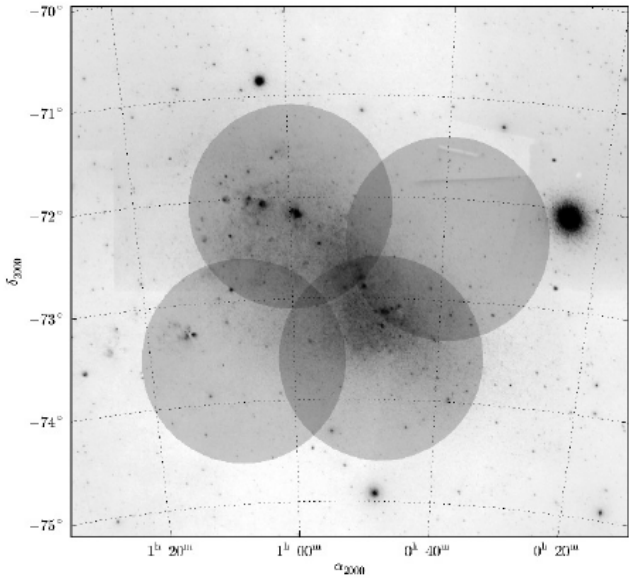

Figure 2.8: A Digitalised Sky Survey image of an 5 degree field of view centered on the SMC. The four circles represent the observed 2 degree fields in the SMC covered in the survey of Kamath et al. (2014). Figure retrieved from Kamath et al. (2014).

not too restrictive, the sample was polluted by objects with similar IR excesses like post-AGB/post-RGB stars. By spectral classification by eye, objects like M stars, C stars, PNe, background galaxies and YSOs were removed from the sample. Also objects with strong emission lines and strong UV continuum fluxes were removed from the sample, as these are characteristic features of hot post-AGB/post-RGB stars or hot YSOs. These objects will be studied in future work. After removal of all these objects, the sample contained 103 objects.

The spectroscopic analysis of the remaining sample objects was performed using the STP described in Sect. 2.2.2. Fig. 2.9 shows the results of the SMC star J004441.04-732136.4, which is studied in Chapter 3. The STP provides the atmospheric parameters $T_{\rm eff}$, log g and [Fe/H]. Based upon the STP results, the log g criterion described in Sect. 2.2.2 results in a divided sample of 63 post-AGB/post-RGB candidates and 40 YSO candidates. Also the reddening and photospheric luminosity L_{ph} were calculated the same way as described in Sect. 2.2.2. The disentanglement of post-AGB and post-RGB stars was again based upon the luminosity criterion of $L_{ph}/{\rm L}_{\odot} > 2500$ for post-AGB stars

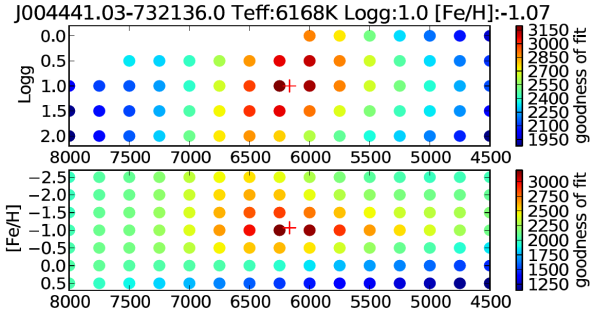

Figure 2.9: Example of a spectral typing result using Munari templates. The results are for the SMC star J004441.04-732136.4 which will be studied in detail in Chapter 3. The plots show the inverse rms distribution (= goodness of fit) in the $T_{\rm eff}$ - log g and $T_{\rm eff}$ - [Fe/H] space with the red plus indicating the final interpolated value. Figure retrieved from Kamath et al. (2014).

and $L_{ph}/L_{\odot} \leqslant 2500$ for post-RGB stars. This resulted in a final sample of 21 post-AGB candidates and 42 post-RGB candidates. The metallicity distribution of the post-AGB/post-RGB candidates and YSO candidates is presented in Fig. 2.10. The figure shows a similar trend as Fig. 2.7, with lower metallicities for the older post-AGB/post-RGB stars. As expected, the mean metallicities of both SMC distributions are lower than those of the LMC.

The post-AGB/post-RGB sample was divided into shell-, disc- and uncertain-sources based upon the shapes of their SEDs. Of the final 63 post-AGB/post-RGB candidates, 27 are disc-sources, 6 are shell-sources and 30 have uncertain SED types. The majority of disc-sources are post-RGB candidates while almost all shell-sources are post-AGB candidates. The resulting catalogue is available online[2]. Similar to the LMC survey, the colour selection criteria did not include older post-AGB/post-RGB stars with old and cool expanding shells nor faint and heavily dust-enshrouded post-AGB stars.

2.3 Sample selection of post-AGB stars

2.3.1 Timeline of this thesis w.r.t. surveys

The different surveys described in Sect. 2.2 provided the sample of MC stars used in this thesis. At the start of this thesis, some SMC post-AGB stars were

[2]http://vizier.cfa.harvard.edu/viz-bin/VizieR?-source=J/MNRAS/439/2211

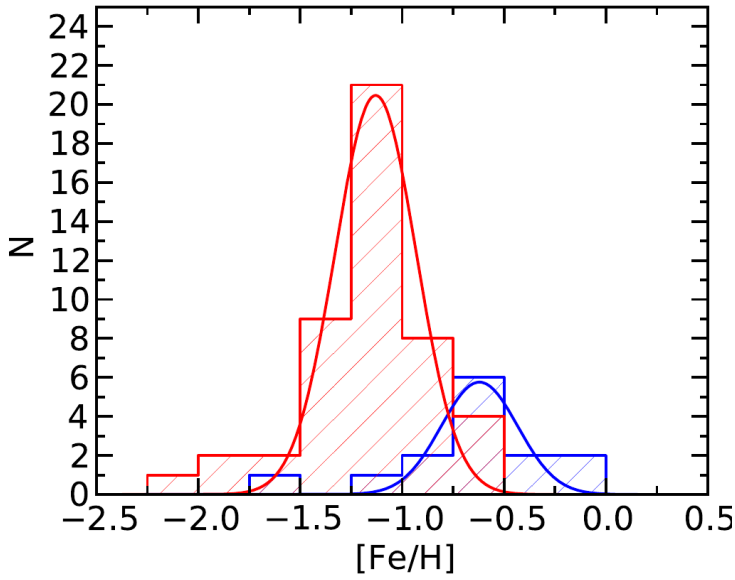

Figure 2.10: Histograms with the metallicity distribution of post-AGB/RGB (red) and YSO (blue) candidates of the SMC survey of Kamath et al. (2014). Red and blue curves represent Gaussian fits to the respective histograms. Figure retrieved from Kamath et al. (2014).

already observed with the high-resolution UVES spectrograph (see Sect. 2.5). The survey of optically visible post-AGB stars in the LMC by van Aarle et al. (2011) was already completed. The surveys of Kamath et al. (2014) and Kamath et al. (2015) were ongoing and finished during the course of the PhD. Based upon the results of these three surveys, a second selection of MC candidates was observed with UVES at the end of the first year of this thesis. We initialised the project for a homogeneous abundance study of Pb in Galactic *s*-process enriched objects in the third year of this thesis. New observations were obtained from the UVES and HERMES (see Sect. 2.5) spectrographs during the third and last year of this work. In the next two sections, we will briefly describe the selection of post-AGB stars of this work.

The ultimate goal of this research is to come to detailed studies of post-AGB stars covering a whole luminosity range as well as metallicity range. This will provide stringent tests on AGB evolution and nucleosynthesis models. We describe now the individual objects which we selected for detailed studies and how the thesis is structured.

2.3.2 SMC and LMC objects discussed in this thesis

J004441.04-732136.4, the subject post-AGB star of Chapter 3, is catalogued as a post-AGB candidate by the SMC survey of Kamath et al. (2014), described in Sect. 2.2.3. This star has a typical post-AGB shell SED and also the calculated luminosity by Kamath et al. (2014) is typical for post-AGB stars. The low-resolution spectra, used for the STP, also showed signatures of strong *s*-process lines which was later confirmed by the obtained high-resolution UVES spectra. In addition, J004441.04-732136.4 is also identified as a 21 μm object by Volk et al. (2011) which makes this an ideal candidate for C- and *s*-process enrichment based upon Galactic 21 μm sources (see Sect. 1.4.2).

Due to their strong *s*-process enrichment, J004441.04-732136.4 and three LMC post-AGB stars from van Aarle et al. (2013), J050632.10-714229.8, J052043.86-692341.0 and J053250.69-713925.8, are selected for a Pb abundance study of MC objects in Chapter 4. The three objects in van Aarle et al. (2013) were selected based upon their shell SEDs and in addition, Volk et al. (2011) detected a strong 21 μm feature for J052043.86-692341.0.

The selection of the LMC objects in Chapters 5 and 7 is based upon their shell SEDs, typical for post-AGB stars. In addition, the high-resolution spectra of the two post-AGB stars in Chapter 5, J051213.81-693537.1 and J051848.86-700246.9, display strong *s*-process lines. To our knowledge, no mid-IR spectroscopy exists of these objects for the detection of a strong 21 μm feature. The high-resolution spectra of J050221.17-691317.2, the subject star of Chapter 7, do not show signs of strong *s*-process. But since J050221.17-691317.2 has a typical post-AGB luminosity, we selected it for a detailed abundance study.

2.3.3 Galactic objects discussed in this thesis

The interesting results of our study of Pb in *s*-process enriched MC stars in Chapters 4 and 5 inspired us to perform a similar study of Pb in Galactic *s*-process enriched post-AGB stars. We first selected all Galactic post-AGB stars which gave prove of strong *s*-process enrichment in previous abundance studies (see e.g. Rao et al. 2012, and references therein). For these stars, we checked the availability of high-resolution UVES and HERMES spectra covering the spectral region around 4057.807 Å, which is the wavelength of the strongest Pb I line between 3500 and 10000 Å. If available, we required a S/N of at least 25 around the Pb I line region. This resulted in three stars for which the data was available in the ESO archive[3]. For the remaining stars of our list, we checked the possibility of observing these stars with the UVES and

[3]http://archive.eso.org/eso/eso_archive_main.html

Table 2.1: Overview of our sample of Galactic stars in Chapter 6. The third column shows the instrument used for the observations, the fourth column displays whether the object is identified as 21 μm object and the last column provides an overview of previous abundance studies.

IRAS	Other name	instrument	21 μm	literature
05113+1347	-	UVES	Yes	1
05341+0852	-	UVES	Yes	2
06530-0213	-	UVES	No	3
07134+1005	HD56126	HERMES	Yes	2
07430+1115	-	UVES	No	4
08143-4406	-	UVES	No	3
08281-4850	-	UVES	No	5
13245-5036	-	UVES	Yes	-
14325-6428	-	UVES	Yes	5
14429-4539	-	UVES	Yes	-
17279-1119	HD158616	UVES	No	6
19500-1709	HD187885	HERMES	Yes	2
22223+4327	V448Lac	HERMES	Yes	2,6
22272+5435	HD235858	HERMES	Yes	1

References: [1]Reddy et al. (2002), [2]Van Winckel & Reyniers (2000), [3]Reyniers et al. (2004), [4]Reddy et al. (1999), [5]Reyniers et al. (2007b), [6]Rao et al. (2012)

HERMES spectrograph within the available time frame of this thesis. We also excluded those objects which resulted in very long observing times for reaching a S/N of at least 25 at 4000 Å. This resulted in an approved ESO programme (ESO number 094.D-0067, PI K. De Smedt). At that moment, the total sample contained 12 Galactic *s*-process enriched stars covering a metallicity range from [Fe/H] $\approx$ -0.3 to -1.0 dex and multiple 21 μm objects.

We added two extra objects to the sample, IRAS 13245-5036 and IRAS 14429-4539, for which Cerrigone et al. (2011) detected clear 21 μm features. This provides us the opportunity to add two new objects to the small sample of identified Galactic *s*-process enriched post-AGB stars. This results in the total sample of fourteen Galactic stars that is listed in Table 2.1.

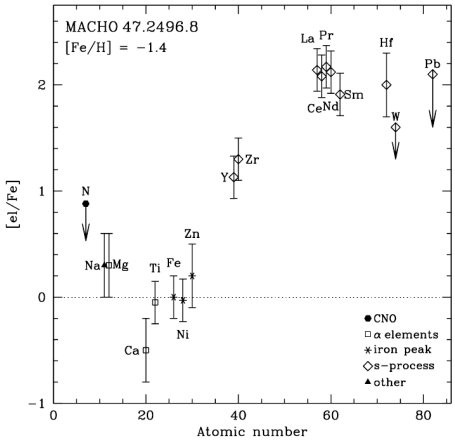

Figure 2.11: [el/Fe] results for MACHO47.1496.8 from Reyniers et al. (2007a). Down arrows indicate derived abundance upper limits. Figure retrieved from Reyniers et al. (2007a).

2.4 Chemical diversity in the LMC: pilot studies

In this section, we provide a short overview of previous chemical studies of post-AGB stars in the LMC. To our knowledge, similar studies have not yet been performed for post-AGB stars in the SMC. The different abundance studies show that LMC post-AGB stars display a similar chemical diversity as their Galactic counterparts.

2.4.1 *S*-process enrichment

The first confirmation about the existence of *s*-process enriched post-AGB stars in the Magellanic Clouds was provided by Reyniers et al. (2007a) who studied MACHO 47.2496.8. They found a low metallicity of [Fe/H] = -1.4 and strong *s*-process enhancements (see Fig. 2.11). They also derived an upper limit of [Pb/Fe] < 2.1, ruling out the predicted Pb overabundance with respect to the hs-elements for metal-poor stars. In addition, they found a C/O ratio lower limit of C/O > 2 and $^{12}C/^{13}C = 200 \pm 25$. The latter isotopic ratio indicates the efficiency of the TUP as a large transport of ^{12}C from the stellar interior to the surface is expected during an efficient TUP, hence resulting in high $^{12}C/^{13}C$. By integrating under the dereddened SED, Reyniers et al. (2007a) found a typical post-AGB luminosity of 5000 $L_{\odot}$.

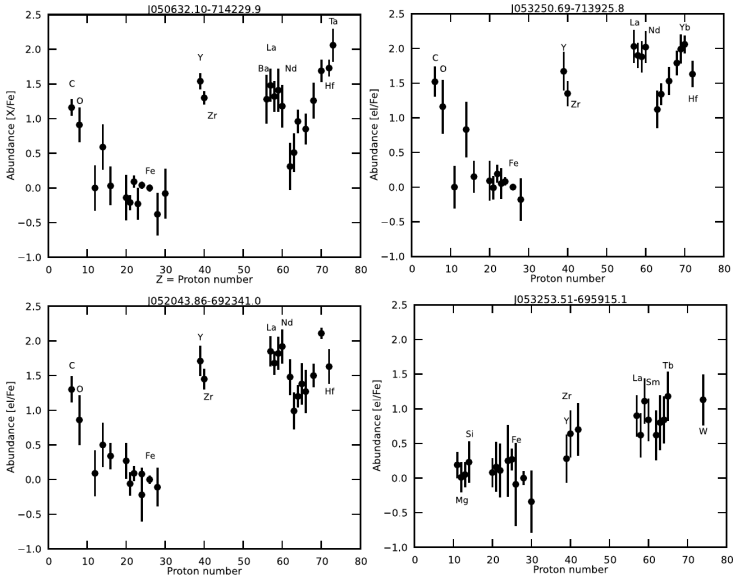

Figure 2.12: Elements over iron ratios of the four LMC post-AGB candidates studied by van Aarle et al. (2013). All four objects show s-process enrichment. Figure reproduced from van Aarle et al. (2013).

A more recent abundance study of post-AGB stars in the LMC was done by van Aarle et al. (2013), who studied four post-AGB candidates: J050632.10-714229.9 (J050632), J053250.69-713925.8 (J053250), J052043.86-692341.0 (J052043) and J053253.51-695915.1 (J053253). K. De Smedt has contributed to this study. All four objects display *s*-process enrichment in different degrees (Fig. 2.12) and have shell SEDs (Fig. 2.13). J050632, J053250 and J052043 have low-metallicities of [Fe/H] $\approx$ -1.2 dex while J053253 has [Fe/H] $\approx$ -0.5 dex. The first three objects also have luminosities ranging from 4700 up to 5700 $L_{\odot}$ and comparison with the post-AGB tracks of Vassiliadis & Wood (1994) in the HR diagram reveals that all objects have low initial masses ranging from about 1 to 1.5 $M_{\odot}$.

This is not the case for J053253 with a low luminosity of 1150 $L_{\odot}$. van Aarle et al. (2013) assume that J053253 is an extrinsically enriched star. However, the survey of Kamath et al. (2015) classified this object as a YSO, based upon their imposed log g criterion. The YSO origin of this object is corroborated by the fact that in the [hs/ls] versus [s/Fe] diagram, hence the neutron irradiation versus mean *s*-process enrichment, J053253 is a clear outlier as shown in the upper panel in Fig. 2.14). As the LMC is intrinsically enriched in hs-elements (see

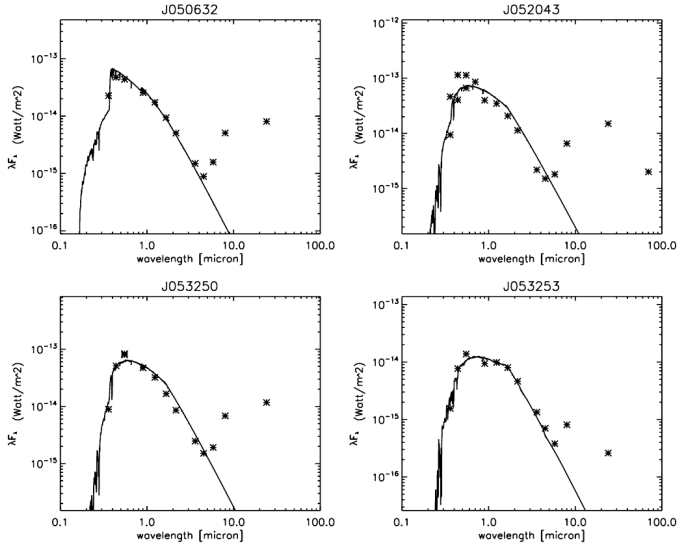

Figure 2.13: SEDs of the four post-AGB candidates of van Aarle et al. (2013) from which this figure was retrieved. The stars represent dereddened photometry and the black lines are the rescaled atmosphere models.

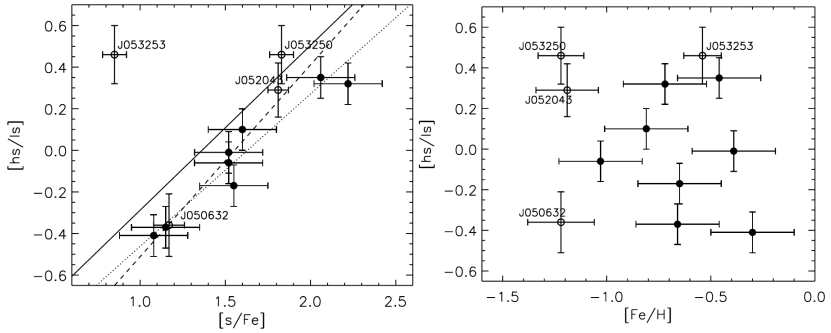

Figure 2.14: *Left panel:* Correlation between total *s*-process enrichment and [hs/ls]. Open circles indicate objects from van Aarle et al. (2013), closed circles are Galactic objects from Van Winckel & Reyniers (2000) an Reyniers et al. (2004). The full lines gives the least-squares fit for all objects, the dashed line for all objects except J053253 and the dotted line for all closed circle objects. *Right panel:* Similar to the left panel, but for [Fe/H] versus [hs/ls]. Figure reproduced from van Aarle et al. (2013).

Sect. 2.1.1), it is indeed likely that J053253 is a YSO rather than a post-AGB star as described in Kamath et al. (2015).

To perform a general comparison with theoretical AGB models, van Aarle et al. (2013) used the nucleosynthetic AGB models from the online-database FRUITY[4] (FUll-Network Repository of Updated Isotopic Tables & Yields Cristallo et al. 2011). As the assumed evolutionary nature of J053253 by van Aarle et al. (2013) is not correct, we do not include it in the discussion of the results. For the three remaining post-AGB stars, van Aarle et al. (2013) use the results of FRUITY models with initial masses of 1.5 $M_{\odot}$ and $Z = 0.001$. Comparison between the abundance results of the three post-AGB stars of van Aarle et al. (2013) with the FRUITY models reveal that C is generally overpredicted while O is underpredicted resulting in a C/O ratio which is approximately a factor 20 higher than observed. For J052043 and J053250, the strongest enriched post-AGB stars, the hs-element abundances are well reproduced while the ls-element abundances are underestimated by about 0.2 dex. Therefore, [hs/ls] is somewhat overpredicted by the models. For J050632, the model underestimates the ls abundances and overestimates the hs abundances. van Aarle et al. (2013) conclude that, although J050632, J052043 and J053250 are intrinsically enriched post-AGB stars with similar metallicity and luminosity, they display strong differences in *s*-process enrichment. This implies that AGB models should be individually adapted to match observed abundance patterns.

2.4.2 Discs and depletion

Depletion is the phenomenon where stellar photospheres show strong deficiencies in abundances of elements with high condensation temperatures, and which is linked to circumbinary discs. We refer to Sect. 1.4.3 and Fig. 1.28 for a more detailed explanation about depletion.

Reyniers & Van Winckel (2007) performed the first abundance study of an extra-galactic post-AGB star named MACHO 82.8405.15. This luminous post-AGB star is part of a binary system and displays a clear depletion pattern (see lower right panel of Fig. 2.15) with a detected metallicity of [Fe/H] = -2.6. MACHO 82.8405.15 probably had an initial iron content of subsolar composition. The SED shape of MACHO 82.8405.15 indicates hot dust close to the central star, hence the presence of a circumbinary disc as shown in the lower right panel of Fig. 2.15).

In another study, Gielen et al. (2009) studied the abundances of three other MACHO objects which all showed different degrees of depletion (see Fig. 2.15).

[4]http://fruity.oa-teramo.inaf.it/

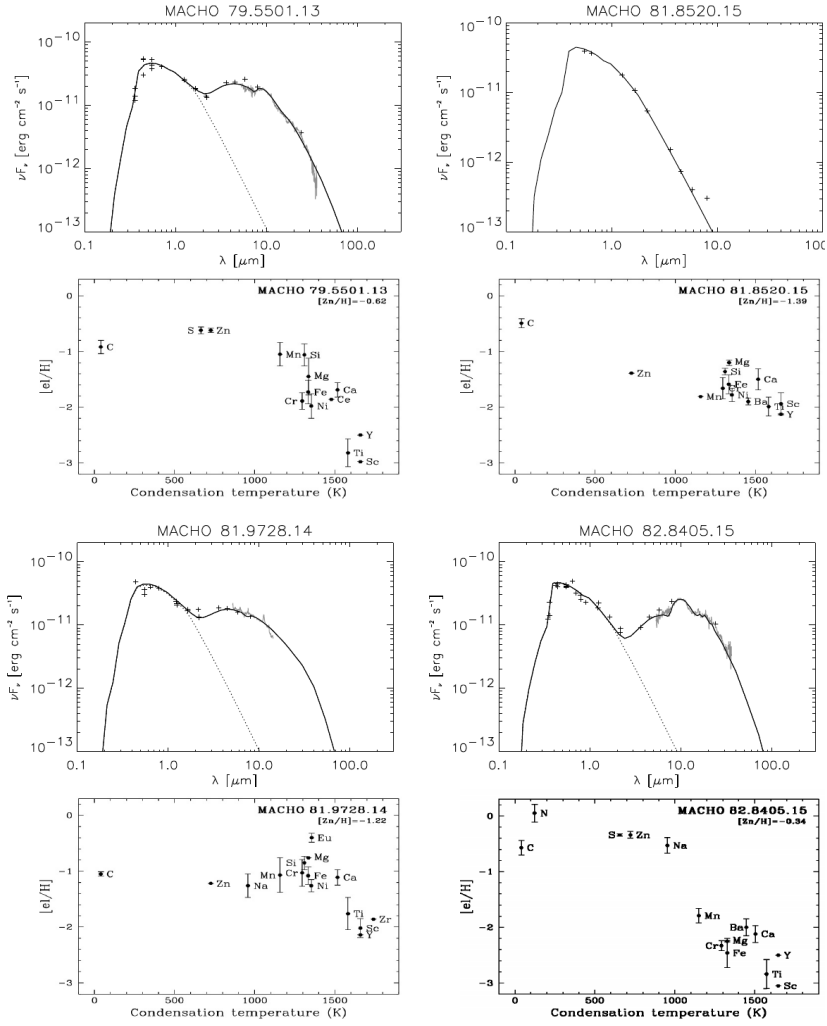

Figure 2.15: First and third row: SEDs of the three MACHO objects studied by Gielen et al. (2009) and MACHO 82.8405.15 from Reyniers & Van Winckel (2007). Triangles represent dereddened photometry, the black line is the best-fitting atmosphere model. The light gray overplotted spectra are Spitzer-IRS spectra. Second and fourth row: Abundance profiles versus condensation temperature of the three MACHO objects studied by Gielen et al. (2009) and MACHO 82.8405.15 from Reyniers & Van Winckel (2007). Figure reproduced from Gielen et al. (2009).

MACHO 79.5501.13 and MACHO 82.8405.15 of Reyniers & Van Winckel (2007) have high [Zn/H] values of about -0.62 and -0.34 dex respectively and show strong depletion patterns. MACHO 81.8520.15 and MACHO 81.9728.14 have low [Zn/H] of -1.39 and -1.22 dex respectively and only show clear depletion at higher condensation temperatures. However, Zn also seems affected by depletion in MACHO 81.8520.15 so the gas-dust separation affected also the cooler dust regions. The SEDs in Fig. 2.15 show that three out of four SEDs display hot dust close to the central star, which indicates the presence of circumstellar discs. MACHO 81.8520.15 does not display a clear IR excess but the depleted photosphere testifies that such a disc must be, or must have been, present around this object. According to Gielen et al. (2009), a possible explanation of the SED and abundance combination of MACHO 81.8520.15 is a very evolved and processed disc from which the original gas content has been cleared and which now still contains trace amounts of dust. More photometric or spectroscopic data at long wavelengths is necessary to learn more about the CSE of this star.

2.4.3 Other studies

Apart from optical chemical abundance studies, there exist multiple mid-IR and far-IR studies about the chemistry of the circumstellar environment (CSE) of post-AGB candidates in the LMC. Here, we briefly discuss three such studies.

Volk et al. (2011) performed a study of the 21 μm in MCs based upon mid-IR Spitzer spectra. They obtained IR spectra of 15 LMC and 2 SMC post-AGB stars and detected large differences in the strength of the 21 μm features of the different objects. One of these objects is J004441.04-732136.4, which was included in this thesis based upon its strong 21 μm feature.

A more recent example of a post-AGB CSE study is the detection of polycyclic aromatic hydrocarbons (PAHs) by Matsuura et al. (2014) around post-AGB candidates. They suggest that PAHs are gradually processed while the central stars evolve from post-AGB phase to planetary nebulae, changing their composition before PAHs are incorporated into the interstellar medium. They remark that, although some metallicity dependence of PAH spectra exists, the the spectral characteristics of PAHs for LMC and Galactic post-AGB stars are more dependent on the evolutionary status of the central object than on the metallicity.

A final study to remark is the SAGE-Spec Spitzer Legacy programme by Woods et al. (2011). This study presents the classification of 197 point sources observed with the Infrared Spectrograph on the Spitzer Space Telescope. The authors use a decision-tree method of object classification based on infrared spectral features, continuum and spectral energy distribution shape, bolometric luminosity, cluster

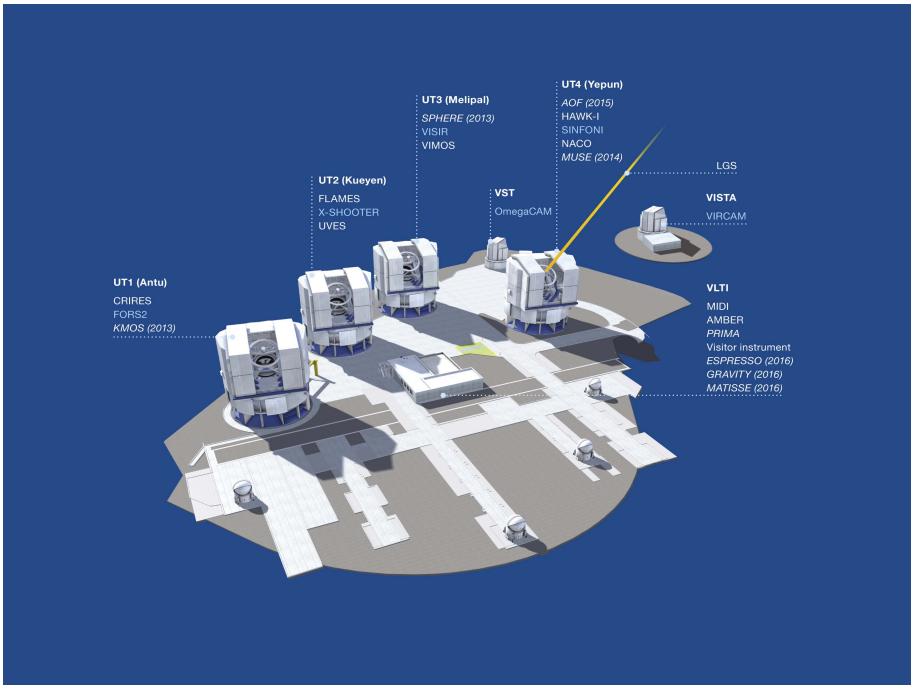

Figure 2.16: Current overview of the instruments on the VLT in Paranal, Chili. Figure retrieved from http://www.eso.org/sci/facilities/paranal/instruments/overview.html.

membership and variability information, which is used to classify the SAGE-Spec sample of point sources. They find a wide variety of objects, including 23 post-AGB candidates. This selection includes the three MACHO objects studied in Gielen et al. (2009).

2.5 Observations and instruments

The thesis deals with the determination of the chemical composition of stellar photospheres on the basis of high-resolution optical spectra. In this section, we provide an overview of the instruments used for obtaining the high-resolution spectra of our sample of post-AGB stars.

2.5.1 UVES and the VLT

UVES[5] is the high-resolution spectrograph of the Very Large Telescope (VLT)[6] of the European Southern Observatory (ESO) in Paranal, Chile. The VLT consists of four Unit Telescopes with main mirrors of 8.2m diameter and four movable 1.8m diameter Auxiliary Telescopes. The telescopes can work together, to form a giant 'interferometer', the ESO Very Large Telescope Interferometer (VLTi). Also two survey telescopes are present in Paranal: the 4m visible and infrared VISTA and the 2.6m optical VST. Each one of the UT provides one Cassegrain and two Nasmyth focus stations for facility instruments. In addition each UT is equipped with a Coude focus station from which the light can be coherently combined in the interferometric focus. Currently, 11 instruments including 2 interferometric instruments are operational and offered for science observations (see Fig. 2.16).

UVES, or the Ultraviolet and Visuelle Echelle Spectrograph (Dekker et al. 2000), is located at the Nasmyth B focus of UT2 (Kueyen). It is a cross-dispersed echelle spectrograph designed to operate with high efficiency from the atmospheric cut-off at 300 nm to the long wavelength limit of the CCD detectors at about 1100 nm. To this aim, the light beam from the telescope is split in two arms within the instrument, corresponding to the wavelength regions from UV to Blue, and from Visual to Red. Each arm is equipped with CCD detectors, with one CCD in the blue arm and a mosaic of two CCDs in the red arm, allowing the simultaneous observation of three different wavelength ranges. The two arms can be operated separately, or in parallel via a dichroic beam splitter. The resolving power is about 40,000 when a 1-arcsec slit is used. The maximum resolution is 80 000 and 110 000 in the Blue and the Red Arm respectively, classifying UVES as a high-resolution spectrograph. Three image slicers are also available to obtain high resolving power without excessive slit losses. The instrument is built for maximum mechanical stability and allows for accurate wavelength calibration. The combination of UVES with the 8.2m diameter UT2 makes this the ideal instrument to obtain high-resolution spectra of post-AGB stars in the Magellanic Clouds and the Galaxy.

The UVES spectra used in this thesis were observed during the following ESO observation programmes: 066.D-0171, 073.D-0241, 084.D-0932, 088.D-0433 and 094.D-0067.

[5]Largely based upon http://www.eso.org/sci/facilities/paranal/instruments/uves.html
[6]Largely based upon http://www.eso.org/public/teles-instr/vlt/

Figure 2.17: The 1.2m Mercator telescope at the Roque de los Muchachos Observatory on La Palma.
Figure retrieved from http://www.mercator.iac.es/instruments/telescope/.

2.5.2 HERMES and the Mercator Telescope

HERMES[7], or High Efficiency and Resolution Mercator Echelle Spectrograph (Raskin et al. 2011), is a spectrograph for the 1.2m Mercator telescope[8] (Fig. 2.17) at the Roque de los Muchachos Observatory on La Palma. The primary mirror's diameter measures 1.2 m and in combination with the secondary mirror of 0.3 m, this semi-automatic telescope has a focal length of 14.4 m. There is also a tertiary flat mirror which can occupy several positions, at 45 degrees of the telescopes optical axis to deviate the light to the Nasmyth focal stations and a park position outside the optical beam to let the light pass to the Cassegrain focus.

HERMES is mounted in a temperature-controlled room and is fibre-fed from the Nasmyth A focal station through an atmospheric dispersion corrector. HERMES features a fixed wavelength setting of 377-900 nm in a single exposure, with a choice of observing modes: a high resolution mode or a simultaneous wavelength reference mode with spectral resolutions of 85 000 and 62 000 respectively. Although mainly used for asteroseismology and binarity studies, the high-resolution and efficiency make HERMES also ideal for accurate abundance studies of Galactic optically bright post-AGB stars.

[7]Largely based upon http://www.mercator.iac.es/instruments/hermes/
[8]http://www.mercator.iac.es/instruments/telescope/

2.6 Introduction to chemical abundance studies

In this section, we provide a general introduction to chemical abundance studies as these are frequently performed in this work.

2.6.1 Model atmospheres

The descriptions in this section are partly based upon texts from Gray (2005).

2.6.2 What are model atmospheres?

Model atmospheres basically simulate the upper stellar layers from which optical radiation escapes, hence the stellar photosphere. These model atmospheres are tables of numbers representing the temperature, density, opacity and other parameters versus the *optical depth* at a reference wavelength. The optical depth τ_ν is a dimensionless parameter representing the optical thickness of layers and is hence a measure of transparency.

Current standard model atmospheres are calculated using some basic assumptions which simplify calculations. Without going in too much detail, we list here the general basic assumptions of standard model atmospheres:

- Standard model atmospheres are *plane-parallel*: the photosphere is thin relative to the curvature of the star. This means that a beam of photons intersects the different stellar outer layers at the same angle whereas in the spherical case, the beam of photons will intersect the different layers at another angle from the radial direction. The spherical case is hence more complex.
- Standard model atmospheres are *homogeneous*: the chemical composition is the same in all photospheric layers.
- Standard model atmospheres are in *hydrostatic equilibrium*: the photosphere is not undergoing any large-scale accelerations comparable to the surface gravity, and there is no dynamically significant mass loss.
- Standard model atmospheres are in *local thermal equilibrium*: this is explained in detail in the next section.
- Standard model atmospheres are *time-independent*: they represent the stellar photosphere at a certain moment during stellar evolution.

- Standard model atmospheres are in *radiative equilibrium*: there are no sources or sinks of energy in the photosphere, so the energy generated in the core of the star is hence flowing outward to the outer boundary. This means that the wavelength-integrated flux is constant at each depth.
- Standard model atmospheres have a depth independent microturbulent velocity: the microturbulent velocity (see Sect. 2.6.7) is constant over the photosphere.

A model atmosphere is determined by four atmospheric parameters: the effective temperature $T_{\rm eff}$, surface gravity $\log g$, the metallicity and the microturbulent velocity ξ_t (see next sections). Accurate abundance calculations can only be performed when these four atmospheric parameters are well determined (see Sect. 2.6.3). In this thesis, we make use of the model atmospheres of Kurucz (Castelli & Kurucz 2004; Kurucz 1970, and references therein) and the MARCS (Model Atmospheres in Radiative and Convective Scheme) model atmospheres (Gustafsson et al. 2008).

Local thermodynamic equilibrium

The majority of model atmospheres are calculated under the assumption of local thermodynamic equilibrium (LTE). In LTE, the mean free path of a particle is much smaller than the distance over which temperature changes. Therefore, the particle will undergo many collisions with other particles before reaching a region with a different temperature. The velocity distribution of the gas particles can therefore be described by a Maxwell-Boltzmann distribution:

$$\frac{n(v)}{N_{\rm total}}{\rm d}v = \left(\frac{m}{2\pi kT}\right)^{\frac{3}{2}} 4\pi v^2 {\rm e}^{-\frac{mv^2}{2kT}}{\rm d}v \tag{2.1}$$

which describes the number of particles of mass m with a velocity amplitude between v and $v + {\rm d}v$, with T the local temperature. An example of a Maxwell-Boltzmann distribution is shown in Fig. 2.18 and is a Gaussian distribution. The maximum represents the most probable velocity $v_{mp} = \sqrt{2kT/m}$, the mean velocity $v_{rms} = \sqrt{3kT/m}$. The number of atoms or molecules occupying a specific excited energy state can be expressed by the Boltzmann equation

$$\left[\frac{n_{r,s}}{N_r}\right]^{\rm LTE} = \frac{g_{r,s}}{U_r} e^{-\frac{\chi_{r,s}}{kT}} \tag{2.2}$$

with

- $n_{r,s}$ = number density in excitation level s of ionisation level r;

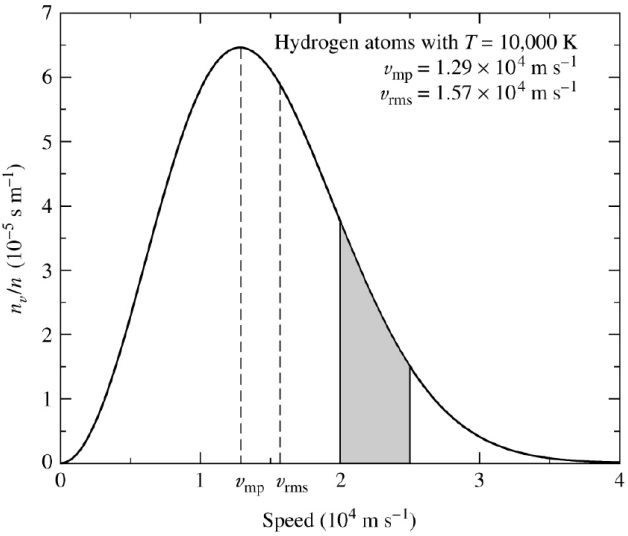

Figure 2.18: The Maxwell-Boltzmann distribution in LTE of hydrogen atoms at a temperature of 10000K. The most probable (v_{mp}) and mean (v_{rms}) velocities are indicated. Figure retrieved from Carroll & Ostlie (1996).

- $N_r = \sum_s n_{r,s}$, the number density of all atoms in ionisation state r;
- $g_{r,s}$ = statistical weight, or degeneracy, of level s of ionisation state r. In angular momentum-spin couplings, the g-factors are (2J+1) with J the total angular momentum quantum number;
- $\chi_{r,s}$ = the excitation energy of level s of the ionisation state r as measured from the ground state (r,0), so $\chi_{r,s} \equiv E_{r,s}$ - $E_{r,0}$;
- U_r the partition function of ionisation state r which is given by $U_r \equiv \sum_s g_{r,s} \mathrm{e}^{-\chi_{r,s}/kT}$. The partition function is the weighted sum of the number of ways the atom or ion can arrange its electrons with the same energy, hence higher energy configurations receive less weight due to $\chi_{r,s}$ in the exponential.

The distribution over the excited states in Eq. 2.2 is only sensitive to temperature. We remark that the thermal velocity in Eq. 2.1 will be a source of line-broadening due to the Doppler effect: atoms and ions with a given velocity will absorb and emit photons at slightly different frequencies than the ones at rest due to the Doppler effect. The microscopic distribution of these velocities will create the smearing of the line-profile.

Another assumption for LTE is that the distribution of different ionisation is given by the Saha equation

$$\left[\frac{N_{r+1}}{N_r}\right]^{\mathrm{LTE}} = \frac{\Phi(T)}{P_e} \tag{2.3}$$

with

$$\Phi(T) = 0.665\frac{U_{r+1}}{U_r}T^{\frac{5}{2}}10^{-5040\chi/kT}. \tag{2.4}$$

The Saha equation represents the ratio between ions of subsequent ionisation levels. P_e is the electron pressure with $P_e = N_e kT$. Notice that in the ionisation equation, both temperature and pressure are important. For increasing pressure with the same temperature, it will be more difficult to liberate electrons from ions.

Non-LTE calculations do not follow the assumption that level populations of atoms are only dependent on temperature and pressure. This introduces a great deal of additional complexity in which the microphysics and accurate atomic data are needed as well as detailed computations of the level populations. The level populations can be computed assuming statistical equilibrium such that the net level population is not changed. This means that all processes leading to an increase of a population n_i, are balanced by a net effect of all processes depopulating the level. The main difficulty for calculating non-LTE model atmospheres is that the large number of equations are coupled and depend on the radiation field, which again depends on the populations. The rate equations must therefore be solved at the same time as the radiative transfer equations for all relevant frequencies. The calculation of non-LTE models is hence complex. In our abundance studies, we will only use LTE atmosphere models.

2.6.3 Abundance determinations

The *curve of growth* (COG) is a plot of line strength, expressed as the equivalent width, as a function of column density of absorbers N_i. The column density is the number of photon absorbers per unit area along a beam of photons. The equivalent width W_λ of an absorption line is defined as the width, in wavelength units, of a rectangular strip of spectrum having the same area as the absorption line. In other words, it is the width which a line would have if the intensity of the line were zero everywhere for a similar energy. The equivalent width W_λ is expressed by

$$W_\lambda = \int_{-\infty}^{\infty}(1 - \mathrm{e}^{-\tau_\lambda})\mathrm{d}\lambda \tag{2.5}$$

In an optically thin approximation with $\tau \ll 1$ and a very cold homogeneous slap in front of a star:

$$\frac{W_\lambda}{\lambda} = \frac{\pi e^2}{m_e c} \frac{\lambda}{c} N_i g f \tag{2.6}$$

with e the electron charge, m_e the electron mass and gf the *oscillator strength*. Basically, the oscillator strength gf is a dimensionless quantity representing the probability of absorption or emission of a photon between energy levels of an atom or molecule. The COG of Eq. 2.6 is a straight line as $W_\lambda \sim N_i$. This simplified approach can not be used for more optically thick layers for which a more complex radiative transfer needs to be calculated. We remark that the division of W_λ by λ in Eq. 2.6 is customary because it normalises Doppler-dependent phenomena like thermal broadening.

Column density, which expresses the number of absorbers per unit surface, can also be expressed in absolute abundances, which expresses the number of atoms of an element. The abundances are scaled to hydrogen for which a typical abundance $\log \epsilon(\mathrm{H}) = 12$ is assumed. Theoretical COGs are used to model the relation between equivalent width and abundance for a specific spectral line with all other parameters fixed. Here, we will not go into the computational details but instead, we show how column density, hence abundances, are related to equivalent width using Fig. 2.19. The small gray and yellow line lie on the linear part of the COG, hence $W_\lambda \sim N_i$. As the line strength increases, the line centre (or Doppler core) becomes 'black', as all light is removed from the spectral line profile, and an increase in abundance does not drastically change the equivalent width. This type of lines are strongly saturated and they lie on the flat part of the COG. Examples of such lines are the red, blue and orange lines. These lines are hence no reliable abundance indicators. For very strong lines, the core of the line is saturated but for increasing optical depth, the Lorentz wings (having a Lorentz profile) become dominant. For these lines, $W_\lambda \propto \sqrt{\lambda^2 N_i}$. Examples of such lines are the purple and black lines in Fig. 2.19. The theoretical COG shows that abundance determinations should preferably be performed using weak spectral lines which lie on the linear part of the COG.

Fig. 2.19 shows that the vertical position of the flat part of the curve growth is dependent on the Doppler width b, which is a combination of the thermal and microturbulent velocity. The latter parameter unites all possible velocity fields other than thermal velocity acting on a microscopic scale. We come back to the microturbulent velocity in Sect. 2.6.7. Remark that the theoretical Doppler widths in Fig. 2.19 are very large to clearly show the effect of microturbulent velocity. Observed Doppler widths typically range between a few up to about ten km/s.

However, observationally we do not know the column density or abundance, so

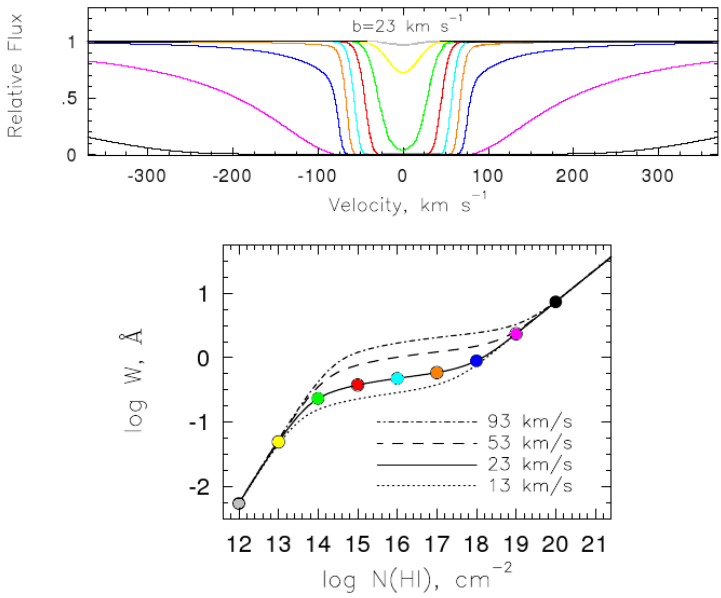

Figure 2.19: Theoretical curve of growth (COG, lower panel) for different line strengths of a specified spectral line (upper panel). The different curves in the lower panel represent COGs with different Doppler widths b. The upper panel shows the spectral line for different column densities, each with a different colour. These same colours represent the position of the respective column density in the lower panel for Doppler width b = 23 km/s. Figure retrieved from Charlton & Churchill (2000).

empirical COGs show $\log(W_\lambda/\lambda)$ as a function of $\log(gf\lambda)$. We use an empirical COG following the approach of Milne and Eddington to show which parameters are crucial for abundance determinations. This Milne-Eddington approach assumes:

- The source function, which is the frequency-dependent ratio of emission over absorption, is linear with optical depth
- LTE
- The line profile function and ratio between the absorption coefficients of the line and continuum are independent of optical depth in the atmosphere.

The empirical COG equation then becomes

$$\log\left(\frac{W_\lambda}{\lambda}\right) = \log\left(\frac{\pi e^2}{m_e c^2}\frac{1}{U}\frac{N_{ion}}{N_{el}}N_H A_0\right) + \log(gf\lambda) - \theta_\chi + \log(A_{el}) - \log(\alpha_\nu^c) \tag{2.7}$$

The left part of the equation is the direct observable equivalent width. The first term on the right-hand-side contains the Saha equation term N_{ion}/N_{el}, partition function U, the number of hydrogen particles N_H and the constant A_0, a parameter to describe the flux contrast between line and continuum. The Saha term expresses the population rate of a specific ionic state of an element to all available ionisation states of that element. The second term on the right-hand side contains the oscillator strength gf. The third parameter θ_χ represents the excitation temperature (see Eq. 2.2), which combines the temperature of an atmospheric layer with the excitation potential of the lower energy level of the line. The fourth parameter represents the elemental abundance (A_{el}) and the last term represents the continuum opacity. Abundance determinations hence require a large amount of input which are provided by model atmospheres (temperature, pressure, optical depth, ...) and by spectral linelists which contain detailed atomic data like rest wavelengths, lower excitation potential energies and oscillator strengths. Unfortunately, the oscillator strengths of many spectral lines can not be determined accurately and are hence a source of large uncertainties. A small change in oscillator strength can significantly change the corresponding abundance. Therefore, the effects of uncertain log gf values should be taken into account in abundance studies.

Although a curve of growth analysis provides a good physical insight in what the important parameters are for abundance determinations, they are now rarely used. Current abundance determination codes use the distribution over the different excitation and ionisation stages by the local application of the Saha and Boltzmann equations to determine the abundances of species in the stellar photosphere. Theoretical equivalent widths are then computed by integrating over the stellar atmosphere and compared to the observed equivalent widths to determine the abundances. Preferably, only weak lines are used for abundance determinations as their equivalent widths scale linearly with the abundance as they lie on the linear part of the COG (see Fig. 2.19). These lines are formed deep in the stellar photospheres. The very large majority of determined abundances in this thesis are therefore based upon weak lines.

In principle, only one spectral line is enough to determine the abundance of an element. However, the population of an excited state (expressed by Eq. 2.2) can be small for specific energy levels with respect to all other available excited states. The derived abundance will then not be accurate as it is based upon an energy level which is only marginally populated. The same is true

for ionisation levels which are only marginally populated. Therefore, the most accurate abundances are calculated using weak spectral lines of the dominant excitation and ionisation levels. The individual abundances for the different spectral lines of the same element represent the typical abundance uncertainty.

A final important remark about abundance determination is that absolute abundance determinations are not fully accurate when they are based on a one-dimensional LTE analysis of the spectra. In addition, extra uncertainties are created by inaccurate oscillator strengths and the individual atmospheric parameters (see next section). Given all the strengths and uncertainties, relative abundances, which quantify the difference in abundance between two similar stars with the same global parameters, are much more reliable than absolute abundance determinations.

2.6.4 Atmospheric parameter determinations

Abundance results depend upon the used model atmosphere. Therefore, we must first determine the preferred model atmosphere which resembles best the observed stellar photosphere in effective temperature, surface gravity, microturbulent velocity and metallicity. To determine the parameters of a model atmosphere, we use the abundances of elements covering a wide range in lower excitation potential and with two present ionisation levels, to determine the atmospheric parameters. For stars with intermediate spectral types A, F and G, iron is usually the preferred element for the atmospheric parameter determination.

2.6.5 Effective temperature

Together with the metallicity, the effective temperature $T_{\rm eff}$ has the strongest effect on stellar spectra. The effective temperature is constrained using an excitation analysis which compares the strength of lines with very different excitation levels of a given ion, with the strength expected for a given atmosphere model. The temperature dependence is reflected by the Boltzmann factor in Eq. 2.7. Therefore, for higher temperatures, we expect a higher overall excitation distribution of the ions. By obtaining the abundances of spectral lines with very different excitation levels for the same ion, the effective temperature is constrained by imposing that the abundance is independent of excitation potential. By performing excitation analyses for a range of effective temperatures, the effective temperature with the smallest correlation between excitation potential and abundances is the preferred effective temperature. Fig. 2.21 shows an example excitation analysis for different effective temperatures,

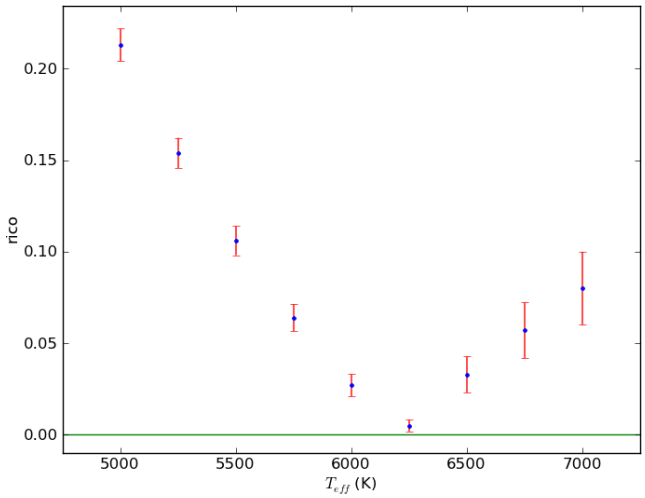

Figure 2.20: Overview of the correlations in Fig. 2.21. The preferred effective temperature is $T_{eff} = 6250$ K.

Fig. 2.20 shows the corresponding correlations between abundance and excitation potential for the different effective temperatures.

2.6.6 Surface gravity

The surface gravity $\log g$ of our sample of stars is determined by imposing that the ions of an element have equal abundances, e.g. the abundance of Fe I and Fe II should be equal. The Saha equation in Eq. 2.7 is pressure dependent (see Eq. 2.3). With increasing pressure, it is less likely that electrons are released. Therefore, once a good temperature estimate is obtained, the surface gravity is constrained by comparing the abundances of the different ions of the same element for different model surface gravities. Two different ionic states are needed and for the stars of intermediate spectral type, these are typically the neutral and firstly-ionised states.

2.6.7 Microturbulent velocity

The microturbulent velocity unites all possible velocity fields other than the thermal velocity that act on a microscopic scale. The quantification of the microturbulent velocity ξ_t is illustrated by the lower panel of Fig. 2.19. The

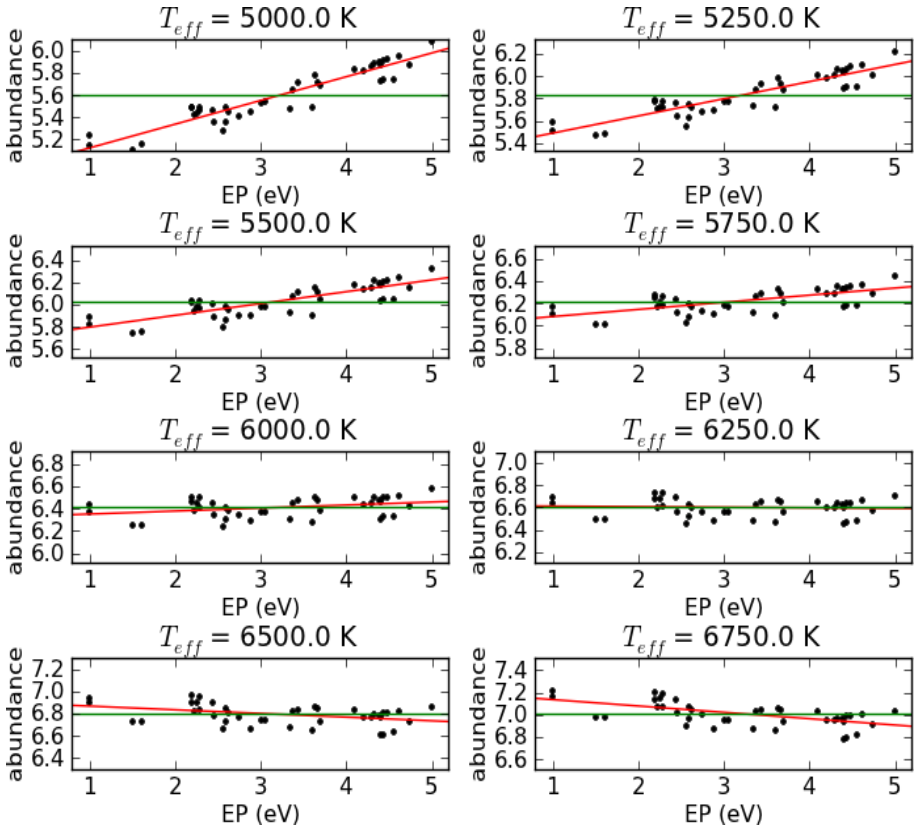

Figure 2.21: Excitation analyses for different effective temperatures for a specific star. Black dots represent the abundances of different Fe I lines, the red line represents the correlation between excitation potential (EP) and the abundances. The green represents a correlation of zero.

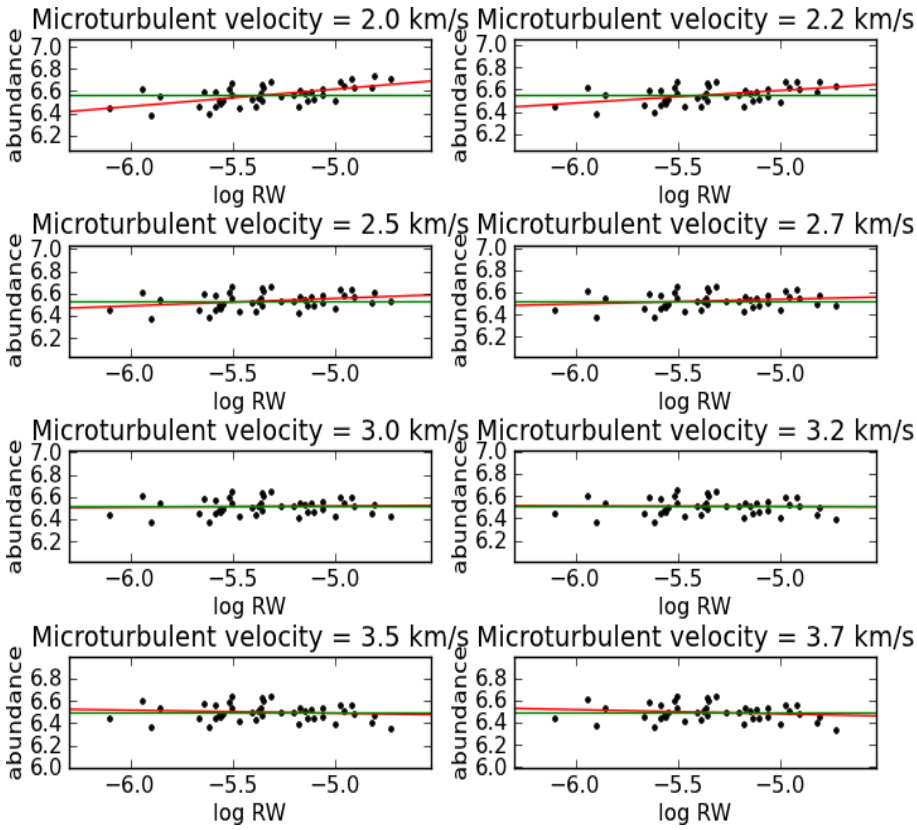

Figure 2.22: Study of the correlations between reduced equivalent width (RW) and abundances for different microturbulent velocities for a specific star. Symbols and lines are the same as in Fig. 2.21.

microturbulent velocity determines the start of the flat part of the COG, which influences derived abundances of strong lines, but not those of weaker lines. Therefore, the microturbulent velocity is constrained by imposing that the abundances of both weak and stronger lines, which are close to the saturation limit, are the same. This is done by a similar analysis as for the effective temperature in Fig. 2.21, but instead of correlation with lower excitation potential, the correlation between reduced equivalent width (RW = W_λ/λ) and abundances is analysed as presented in Fig. 2.22. The microturbulent velocity has the least influence on stellar spectra and should hence be determined once an accurate temperature and gravity have been obtained.

2.6.8 Metallicity

The metallicity is the automatic end result of the determination of the three other atmospheric parameters. In this work, we use as metallicity [Fe/H] which is generally a good indicator of the mean metallicity. We use the solar abundance of $\log \epsilon_\odot(\mathrm{Fe}) = 7.50$ of Asplund et al. (2009).

2.7 PyMOOG

We conclude this chapter by introducing PyMOOG, our self-written Python-wrapper around the LTE abundance calculation routine MOOG by C. Sneden (1973). MOOG computes abundances by an iterative processes in which theoretical equivalent widths (EWs) of single lines are computed for different abundances and matched to the observed EWs. As described in Sect. 2.6.3, abundance determinations require a large amount of input. MOOG hence requires multiple input files, like model atmospheres and atomic data, and a general input file which provides MOOG the input paths and appropriate commands to perform the required calculations. Apart from abundance determinations of observed spectral lines, MOOG is also able to determine the theoretical equivalent widths of a given set of spectral lines for a specific model atmosphere and input abundance. In the same context, MOOG can also calculate synthetic spectra. Each of these commands require specific input from the general input file which differs for each command. In addition, before MOOG can be used for the abundance determination of measured spectral lines, the observed EWs must first be determined using other means. The EW determination and manual construction of the required input files of MOOG can be become very time-consuming when a large number of ions, and therefore a large number of individual spectral lines, needs to be studied. We have written

PyMOOG to strongly diminish the time needed for EW calculations and the construction of required input files.

PyMOOG is a Python wrapper around MOOG, which implies that PyMOOG itself does not perform any abundance calculations. Instead, PyMOOG first creates the necessary input files and then runs MOOG via a shell command. Thereafter, it reads in the necessary input from the MOOG generated output files. PyMOOG currently does not have a GUI, but instead interacts via the shell and via interactive Python plots.

The two available model atmosphere libraries included in PyMOOG are the LTE plane-parallel Kurucz atmosphere models of Castelli & Kurucz (2004) and the LTE spherical MARCS models described in Gustafsson et al. (2008), both with solar-scaled metallicities. It is possible to interpolate between the available atmosphere model grids in $T_{\rm eff}$ and log g. The effective temperature of available models ranges from 3500 K up to 50000 K, the surface gravities range from 0.0 up to 5.0 dex. These models were calculated for an [Fe/H] range from -2.5 up to 0.5 dex. The preferred metallicity and microturbulent velocity for calculation with MOOG are implemented as input in the model atmosphere input file. MOOG can handle microturbulent velocities below 10 km/s.

PyMOOG also includes atomic linelists for a wide range of elements, ranging from helium (He, Z=2) up to uranium (U, Z=92) from the Vienna Atomic Line Database (VALD Kupka et al. 1999). The VALD linelists are combined with a list of lines that has been gathered at the Instituut voor Sterrenkunde (IvS) for the chemical analysis of A, F and G type stars (Van Winckel & Reyniers 2000), and which is regularly updated. It is possible to use the combined linelists of VALD and the IvS, or only the VALD linelists. The combination of linelists provides atomic data of about 135 individual ions and covers a wavelength range from 3000 Å up to 11 000 Å. For most elements, linelists of the neutral and in a lesser extent the firstly-ionised state are included. For some heavy elements like neodymium (Nd, Z=60) and europium (Eu, Z=63), the second ionisation level is also included. Also linelists of the National Institute of Standards and Technology (NIST Kramida et al. 2013) are included, albeit only for comparison of abundance results for the corresponding VALD and IvS lines. This is because the number of spectral lines and ions covered by NIST is much lower compared to VALD.

PyMOOG requires normalised spectra for the measurements of observed EWs as MOOG can only calculate normalised synthetic spectra. The observed spectra can be in fits or ascii files, and the user can choose the wavelength ranges included in the abundance determination. The EWs of spectral lines are measured with the use of interactive plots that center on the required spectral line. The user marks the wavelength range and continuum position

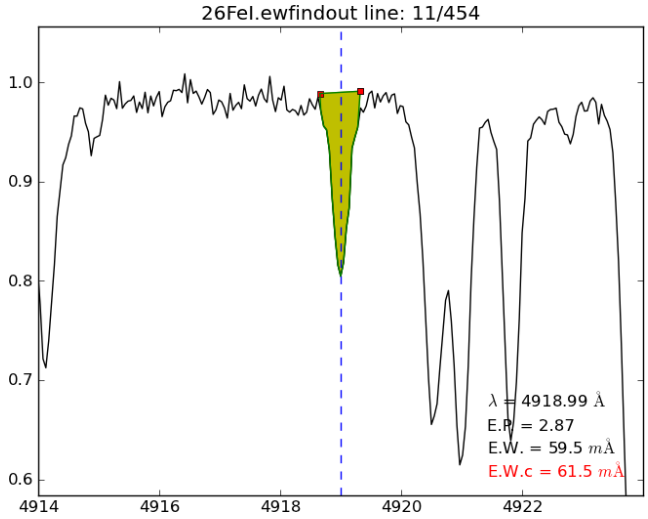

Figure 2.23: Screenshot of the interactive plot of PyMOOG with the EW measurement of an Fe I line of the post-AGB star HD 56126. Red dots indicate the two points selected by the user to mark the edges of the spectral line, the yellow surface represents the measured EW (E.W.c.). The lower right of the figure displays rest wavelength λ (marked with the vertical dashed line), excitation potential E.P., the theoretically predicted EW (E.W.) and the calculated EW (E.W.C.) in red. At the top, the ion and the number of spectral lines are displayed.

of the spectral line, specified by two points, after which the EW of the line is calculated by direct integration of the surface below the line between the two points. Fig. 2.23 shows an example of an EW measurement in PyMOOG.

PyMOOG has two modules, one for atmospheric parameter determination based upon the lines of one element, and one for abundance determinations of all other elements once the stellar atmosphere parameters are determined.

2.7.1 Atmospheric parameter determination in PyMOOG

For the atmospheric parameter determination, the user chooses an element with a large number of spectral lines with a broad excitation energy range and spectral lines of two different ions. This can be any available element but Fe is a common choice. We use Fe in the remainder of this paragraph as the example element with which the atmospheric parameters are determined. As not all Fe

lines in the linelist will display line features for a specific model atmosphere, the theoretical EWs of all Fe lines within the specified wavelength ranges are calculated with MOOG. Then, all Fe lines with a theoretical EW within a user-specified EW range are selected. The user can then measure the EW of any of these lines. Once the user has calculated the EWs of Fe lines of choice for both the Fe I and Fe II lines, the effective temperature is calculated using the method described in Sect. 2.6.5. At the start of the program, the user can specify whether the neutral or first ionisation state needs to be used for the $T_{\rm eff}$ determination. Thereafter, the surface gravity is determined using both ions as described in Sect 2.6.6. If the derived log g differs from the entry log g of the initial model, the effective temperature is determined again using the newly derived log g. Then, the microturbulent velocity is determined using the method described in Sect. 2.6.7. A last iteration is performed for all atmospheric parameters using the newly determined parameters from the previous iterations. The preferred atmospheric parameters are summarised in an output file, together with the number of lines used and the abundances of both Fe I and Fe II. If the atmospheric parameters are determined using a different element then Fe, the user is advised to rerun the atmospheric parameter determination for Fe using the previously determined parameters as initial atmosphere model to determine [Fe/H] if possible.

After the first temperature and log g iteration, the user has the possibility to add, remove or correct certain spectral lines from the list used for parameter determination. The user needs to specify an allowed standard deviation for the line-to-line scatter, within which all individual line abundances should lie. This allowed standard deviation is typically 0.2 dex. When at least one line deviates from the allowed standard deviation, the user has the possibility to recalculate EWs after which a new iteration starts for the appropriate parameter.

The atmospheric parameter determination can be run individually for Kurucz and Marcs model atmospheres, or simultaneously. In case the atmospheric parameter determination is run simultaneously, the atmospheric parameters are first determined for one model atmosphere and then for the other. The linelist created before the atmospheric parameter determination is then used for both model atmospheres, as the measured EWs are independent of the used atmosphere model.

To confirm the derived atmospheric parameters, an extra script is provided for comparison between synthetic spectra, based upon the used spectral lines and the derived atmospheric parameters, and the observed spectrum. These synthetic spectra are generated by MOOG but of course, these synthetic spectra display solar-scaled abundances, adapted to the derived metallicity. Therefore, when Fe is used for atmospheric parameter determination, the spectral lines of all other elements will not fit optimally as their individual abundances are

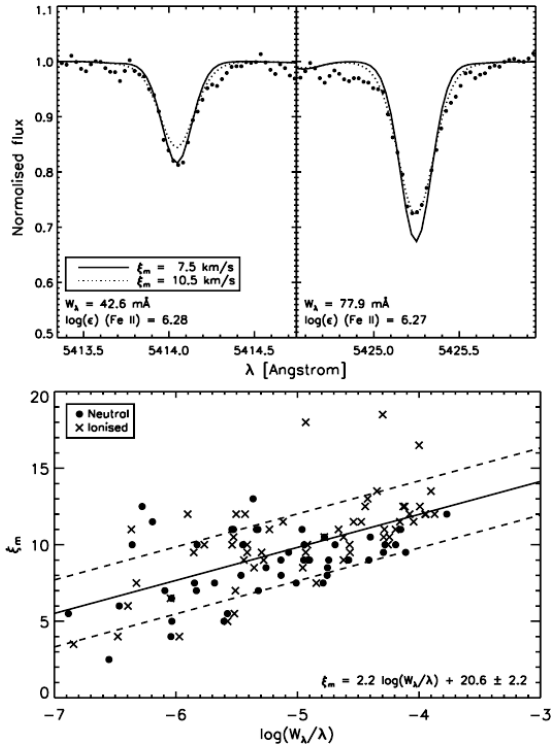

Figure 2.24: Illustration of the necessity of different values of macroturbulence at different reduced EWs. The upper panel displays two Fe II lines from the spectrum of J050632.10-714229.8 from the same spectral region and with a similar derived abundance from their measured EW. However, their macroturbulent velocity differs by 3 km/s. The lower panel shows the macroturbulent velocity of J050632.10-714229.8 as a function of reduced EW. The dashed lines represent the standard deviation on the mean trend. Figures retrieved from van Aarle et al. (2013).

unknown. In addition, synthetic spectra require extra input for effects like rotational velocity or macroturbulence which change the shape of the line profile, but not the measured EW. Macroturbulence includes the effects of turbulence cells in the photosphere which are large enough such that photons remain within the cells from the time of creation until they escape the stellar photosphere. Each of these cells provides a complete spectrum, which is Doppler shifted corresponding to the velocity of the cell. When viewing all these turbulent cells simultaneously, the observed spectral lines are broadened. Each spectral line needs an individual macroturbulent velocity. In abundance studies of post-AGB stars by Reyniers et al. (2004) and van Aarle et al. (2013), the authors find correlations between the reduced equivalent width (W_λ/λ) and macroturbulent velocity which differ for each star. Fig. 2.24 shows the need of different macroturbulent velocities for different spectral lines in the upper panel and an example of a correlation between reduced EW and macroturbulent velocity in the lower panel for one of the sample stars in van Aarle et al. (2013). Since post-AGB stars are large objects, they have low surface rotational velocities and the effect of macroturbulence becomes important for comparison with synthetic spectra.

2.7.2 Abundance determination in PyMOOG

Once all atmospheric parameters are determined, the abundances of all other available ions can be determined. An input file lists all ions that will be studied. Similar to the atmospheric parameter determination, the module starts with the selection of spectral lines with theoretical EWs within a specific EW range. Since not all elements are always solar-scaled, like C and *s*-process elements in enriched post-AGB stars, the theoretical abundances for which the theoretical EWs are calculated can be increased or lowered to reproduce expectations. While the program is running, new ions can be added and theoretical EWs can be recalculated for updated abundances.

Once all spectral lines for the different ions have been selected, the program provides an overview of all ions in the input file that have spectral lines with theoretical EWs within the specified EW range. The selection procedure may take some minutes depending on the number of requested ions and wavelength range. Once the selection procedure is finished, it does not have to be rerun when restarting the program unless this is requested.

Each ion is studied individually. From the list of available ions, the user can choose the ion he/she wants to study after which an interactive plot appears to measure the EWs similar to the atmospheric parameter determination. Thereafter, the elemental abundance is determined with MOOG, and the mean

and individual abundance results of the spectral lines are shown. The user can then add, remove or recalculate spectral lines of the specific ion, or add the deduced abundance to the list of confirmed abundance results. The last step is necessary since it is not always possible to determine accurate abundance results for each ion in the list of available ions.

It is possible to generate synthetic spectra with the deduced abundance results. These synthetic spectra use the abundances included in the list of confirmed abundance results. For elements without confirmed abundances, the initial abundances used for the theoretical EW calculations are included in the synthetic spectra. It is also possible to plot the [el/H] and [el/Fe] results of the ions included in the list of confirmed abundance results.

Once the abundances of all required ions have been determined, it is possible to run an error analysis of all abundances included in the list of confirmed abundances. This error analysis includes the abundance uncertainties due to line-to-line scatter and atmospheric parameters. The uncertainties on the atmospheric parameters need to be entered manually and are typically for post-AGB stars $T_{\rm eff}$ ± 125 to 250 K, log g ± 0.25 to 0.5 dex and ξ_t ± 0.25 to 0.5 km/s. PyMOOG then performs abundance determinations with the atmosphere models at the edge of the uncertainty intervals for all ions in the list of confirmed abundance results. The total uncertainty $\sigma_{\rm tot}$ of [X/H] is then the quadratic sum of the errors due to line-to-line scatter ($\sigma_{\rm l2l}$) and errors due to atmospheric parameter uncertainties ($\sigma_{{\rm T}_{eff}}$, $\sigma_{\rm logg}$, σ_{ξ_t}):

$$\sigma_{\rm tot} = \sqrt{\left(\frac{\sigma_{\rm l2l}}{\sqrt{N_{\rm ion}}}\right)^2 + (\sigma_{{\rm T}_{eff}})^2 + (\sigma_{\rm logg})^2 + (\sigma_{\xi_t})^2}. \quad (2.8)$$

The total uncertainty $\sigma_{\rm [XFe]tot}$ of [X/Fe] is then the quadratic sum of the errors due to line-to-line scatter ($\sigma_{\rm l2l}$), errors due to atmospheric parameter uncertainties ($\sigma_{{\rm T}_{eff}}$, $\sigma_{\rm logg}$, σ_{ξ_t}) and the Fe abundance error ($\sigma_{\rm Fe}$):

$$\sigma_{\rm [XFe]tot} = \sqrt{\left(\frac{\sigma_{\rm l2l}}{\sqrt{N_{\rm ion}}}\right)^2 + (\sigma_{{\rm T}_{eff}})^2 + (\sigma_{\rm logg})^2 + (\sigma_{\xi_t})^2 + \left(\frac{\sigma_{\rm Fe}}{\sqrt{N_{\rm Fe}}}\right)^2}. \quad (2.9)$$

The error analysis will create folders with the individual abundance results for the different atmosphere models, and provides plots and files with a summary of these results. If C and O are derived, the C/O ratio is also included in the error analysis.

2.7.3 Abundance determinations in this thesis

PyMOOG was used for the abundance determinations in Chapters 4 (only Pb), 5, 6 and 7. The abundance determinations in Chapter 3 are done with MOOG, following the same methods as with PyMOOG, and the EW measurements were performed with the command driven environment ESO-MIDAS[9] (version 04FEB).

This chapter provided information on the target selection as well as a general introduction to the determination of abundances on the basis of high-resolution spectra. As small lines are best tracers of the chemical content of stellar photospheres, the spectra need to be of high S/N where a typical value of S/N > 100 is to be aimed at. In the blue spectral regions, this is often not reached. In the following chapters, we describe several detailed studies of individual objects.

[9]http://www.eso.org/sci/software/esomidas/

Chapter 3

The extreme *s*-process enrichment of the SMC post-AGB star J004441.04-732136.4

This chapter was originally published as:

Post-AGB stars in the SMC as tracers of stellar evolution: the extreme s-process enrichment of the 21 μm star J004441.04-732136.4.

K. De Smedt, H. Van Winckel, A. I. Karakas, L. Siess, S. Goriely, P. R. Wood

Astronomy & Astrophysics, Vol. 541, A67, 2012

ABSTRACT

Context: This paper is part of a larger project in which we want to focus on the still poorly understood Asymptotic Giant Branch (AGB) third dredge-up processes and associated *s*-process nucleosynthesis.

Aims: We confront accurate spectral abundance analyses of post-AGB stars in both the Magellanic Clouds, to state-of-the-art AGB model predictions. With this comparison we aim at improving our understanding of the 3rd dredge-up phenomena and their dependencies on initial mass and metallicity.

Methods: Because of the well constrained distance with respect to Galactic post-AGB stars, we choose an extra-galactic post-AGB star for this contribution, namely the only known 21 μm object of the Small Magellanic Cloud (SMC): J004441.04-732136.4 . We used optical UVES spectra to perform an accurate spectral abundance analysis. With photometric data of multiple catalogues we construct a spectral energy distribution and perform a variability analysis. The results are then compared to predictions of tailored theoretical chemical AGB evolutionary models for which we used two evolution codes.

Results: Spectral abundance results reveal J004441.04-732136.4 to be one of the most *s*-process enriched objects found up to date, while the photospheric C/O ratio of 1.9 ± 0.7, shows the star is only modestly C-rich. J004441.04-732136.4 also displays a low [Fe/H] = -1.34 $\pm$ 0.32, which is significantly lower than the mean metallicity of the SMC. From the SED, a luminosity of $7600 \pm 200 L_{\odot}$ is found, together with E(B-V) = 0.64 $\pm$ 0.02. According to evolutionary post-AGB tracks, the initial mass should be $\approx 1.3 M_{\odot}$. The photometric variability shows a clear period of 97.6 $\pm$ 0.3 days. The detected C/O as well as the high *s*-process overabundances (e.g. [Y/Fe] = 2.15, [La/Fe] = 2.84) are hard to reconcile with the predictions. The chemical models also predict a high Pb abundance, which is not compatible with the detected spectrum, and a very high $^{12}C/^{13}C$, which is not yet constrained by observations. The predictions are only marginally dependent on the evolution codes used.

Conclusions: By virtue of their spectral types, favourable bolometric corrections as well as their constrained distances, post-AGB stars in external galaxies offer unprecedented tests to AGB nucleosynthesis and dredge-up predictions. We focus here on one object J004441.04-732136.4, which is the only known 21 μm source of the SMC. We show that our theoretical predictions match the *s*-process distribution, but fail in reproducing the detected high overabundances and predict a high Pb abundance which is not detected. Additionally, there remain serious problems in explaining the observed pulsational properties of this source.

AUTHOR CONTRIBUTIONS

K. De Smedt performed the spectral analysis, the SED analysis (including luminosity calculation and initial mass determination) and the frequency analysis. The bulk of the text was written by K. De Smedt with the assistance of H. Van Winckel. The theoretical predictions of the Mount Stromlo evolutionary models were calculated by A. I. Karakas who also wrote the corresponding section. The STAREVOL predictions were calculated by L. Siess and S. Goriely who also wrote the corresponding section. The derived stellar pulsation period was examined by P.R. Wood.

3.1 Introduction

The final evolution of low- and intermediate-mass stars is a fast transition from the Asymptotic Giant Branch (AGB) over the post-AGB transit towards the Planetary Nebula Phase (PN), before the stellar remnant cools down as a White Dwarf (WD). Although this scheme may be generally acknowledged, there is no understanding from first principles of different important physical processes that govern these evolutionary phases. The main shortcomings are related to the lack of understanding of the mass-loss mechanisms and mass-loss evolution along the AGB ascent, the subsequent shaping processes of the circumstellar shells, and the lack of fundamental understanding of the internal chemical evolution of these stars (Habing & Olofsson 2003; Herwig 2005).

Here we focus on the poorly understood AGB 3rd dredge-up phenomenon, during which products of the internal nucleosynthesis are brought to the surface of the star. This is mainly ^{12}C as the primary product of the triple alpha reaction, but also the products of neutron-capture synthesis. There are two main neutron sources in AGB stars: 1) the ^{22}Ne(α,n)^{25}Mg reaction which is activated at temperatures of $T \gtrsim 300 \times 10^6$K, and 2) the ^{13}C($\alpha$,n)^{16}O reaction, which is activated at much lower temperatures of $T \gtrsim 90 \times 10^6$K. Observational and theoretical evidence has shown that the ^{13}C(α,n)^{16}O reaction is the main neutron source in low-mass AGB stars of $\approx 1 - 3 M_\odot$ (Straniero et al. 1995; Gallino et al. 1998; Abia et al. 2002).

Synthesis by the s-process in AGB stars is an important contributor to the cosmic abundances past the iron peak and these stars are also thought to be very important contributors to the total carbon and nitrogen enrichment (e.g.

Romano et al. 2010; Kobayashi et al. 2011). Post-AGB photospheres bear witness to the total chemical changes accumulated during the stellar lifetime.

In recent years, theoretical models of these internal nucleosynthesis and photospheric enrichment processes gained enormously in sophistication: extensive nuclear networks with updated cross-sections were included (e.g. Cristallo et al. 2011, 2009; Karakas 2010; Church et al. 2009); non-convective mixing such as differential rotation and thermohaline mixing have been implemented (e.g. Siess et al. 2003; Siess 2007; Stancliffe et al. 2007; Angelou et al. 2011); the effect of deep mixing or extra mixing processes have been critically evaluated (e.g. Karakas et al. 2010; Busso et al. 2010) and overshoot regimes have been explored in more detail in order to explain the extent of the ^{13}C pocket (Herwig 2005). All these processes involve great uncertainties and observational data are required to calibrate them.

Accurate determination of photospheric abundances in AGB stars is difficult (e.g. Abia et al. 2008, and references therein). First of all, the photosphere is dominated by molecular opacity, making the mere detection of trace elements over a wide range of atomic masses difficult. Moreover, AGB stars often have dynamic atmospheres caused by pulsations which develop into dust driven winds. Finally, chemical results of AGB stars are difficult to interpret, because stars with different initial mass and metallicity occupy the same region in the Hertzsprung-Russell diagram (HR-diagram).

Post-AGB stars do not have these drawbacks: First, their atmospheres do not show the large amplitude pulsations as well as the large mass-loss rates that characterise evolved AGB atmospheres. Second, their photospheres are hotter, so atomic transitions prevail. This allows to quantify the abundances in post-AGB stars for a very wide range of elements, from CNO up to the most heavy *s*-process elements, well beyond the Ba peak (e.g. Van Winckel & Reyniers 2000; Reyniers & Van Winckel 2003).

During the past decade it has been realised that Galactic post-AGB stars are chemically much more diverse than anticipated (e.g. Van Winckel 2003). Some post-AGB stars are indeed the most s-process enriched objects known to date (e.g. Reyniers et al. 2004), while others are not enriched at all. A distinct subclass of Galactic post-AGB stars is formed by the so-called *21 μm objects* displaying a strong solid-state feature around 21 μm (Kwok et al. 1989) in their IR spectra. The carrier of this feature still needs to be identified, although several suggestions have been discussed in literature (e.g. Posch et al. 2004). The feature is only detected in post-AGB Carbon stars (e.g. Hrivnak et al. 2008b, 2009) and till now not yet in spectra of normal carbon stars nor in carbon-rich planetary nebula (Volk et al. 2011). The chemical studies of Galactic 21 μm stars show that they display strong overabundances of *s*-process

elements with a wide range of neutron capture efficiencies (Van Winckel & Reyniers 2000; Reddy et al. 2002; Reyniers & Van Winckel 2003; Reyniers et al. 2004). The poorly known distances and hence luminosities and masses of the limited Galactic post-AGB sample hamper, however, the interpretation of the variety of abundances in the broader theoretical context of stellar (chemical) evolution.

We therefore initiated a project to exploit our newly identified large sample of post-AGB stars in the Large Magellanic Cloud (van Aarle et al. 2011) and in the Small Magellanic Cloud (Kamath et al. 2011), to study the *s*-process production and associated 3rd-dredge-up processes. The unique spectral characteristics of post-AGB stars, together with the new large sample, covering a wide range in luminosities and metallicities, with well constrained distances, means that these objects provide unprecedented direct tests for the theoretical structure and enrichment models of solar-mass stars. In this contribution, we focus on the object J004441.04-732136.4 (hereafter abbreviated to J004441.04) which is the only object of the Small Magellanic Cloud (SMC) known to date in which the 21 μm feature is identified (Volk et al. 2011). The paper is organised as follows: In Sect. 3.2 we discuss the observational data of J004441.04. Sect. 3.3 describes the spectral analyses performed to determine the atmospheric parameters as well as the accurate photospheric composition. The spectral energy distribution (SED) of J004441.04 is analysed in Sect. 3.4 followed by the determination of the initial mass in Sect. 5. We then used two state-of-the-art evolution codes coupled to post-processing codes to compute the predicted chemical signature of this object in Sect. 3.6. The discussion and conclusions are given in Sect. 3.7.

3.2 Data

3.2.1 Photometric data

Photometric data from the Magellanic Cloud Photometric Survey (MCPS, Zaritsky et al. (2002)), the Deep Near-Infrared Survey (DENIS, Fouqué et al. (2000)), the Two Micron All Sky Survey (2MASS,Cutri et al. (2003)) and the Spitzer S^3MC survey (Bolatto et al. 2007) are used for the construction of the spectral energy distribution (SED) of J004441.04 in Sect. 3.4. A summary of the absolute photometric datapoints is given in Table 3.1. The MCPS, 2MASS and DENIS data were taken in a timespan of 2 years (1997 till 1999) while the Spitzer data were acquired in 2004 and 2005. For the variability analysis, we used the Optical Gravitational Lensing Experiment II (OGLE II) lightcurve (Szymanski 2005; Udalski et al. 1997) obtained in the I filter.

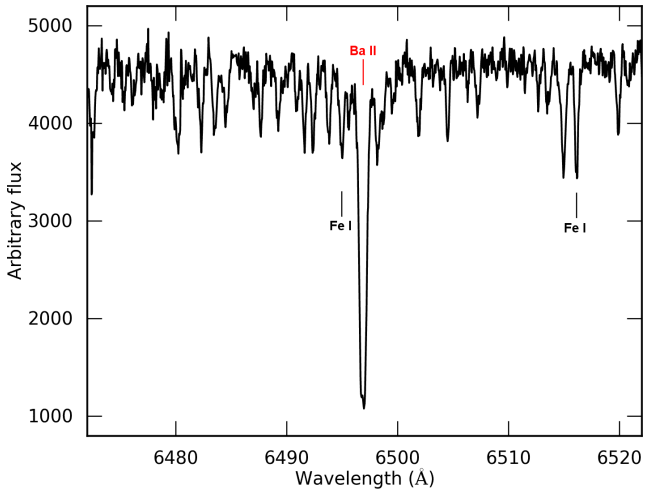

Figure 3.1: Not-normalised UVES spectrum of J004441.04, centered around the Ba II line at 6496.897 Å. The spectrum is set to rest velocity.

3.2.2 Spectroscopic data

We use high-resolution spectra obtained with the Ultraviolet and Visual Echelle Spectrograph (UVES, Dekker et al. (2000)), which is the echelle spectrograph mounted on the 8m UT2 Kueyen Telescope of the Very Large Telescope (VLT) array at the Paranal Observatory of ESO in Chili. Multiple spectra of J004441.04 were obtained on the same day within a time span of approximately two hours. We used the dichroic beam-splitter resulting in a wavelength coverage from approximately 3280 to 4530 Å for the blue arm of UVES, and from approximately 4780 to 5770 Å and from 5800 to 6810 Å for the lower and upper part of the mosaic CCD chip respectively. Each wavelength range was observed three times with an exposure time of 2871 seconds each.

The UVES reduction pipeline was used for the reduction of the spectra. This includes the standard steps of extracting frames, determining wavelength calibration and applying this scale to flat-field divided data. Also cosmic clipping was included in the reduction.

All spectra were normalised by fitting in small spectral windows, fifth order polynomials through interactively defined continuum points. Once all three subspectra of the same wavelength range are normalised, the weighted mean subspectrum was determined. These mean subspectra are then again merged into one normalised spectrum and this is used for the spectral abundance

Table 3.1: Photometric data used for the SED of J004441.04. A standard error of 0.05 mag is assumed for the SED study. IRAC and MIPS are instruments of the Spitzer satellite.

band	survey	mag	F_ν (Jy)
V	MCPS	15.96	1.573×10^{-3}
I	MCPS	14.46	5.635×10^{-3}
I_c	DENIS	14.44	4.260×10^{-3}
J	DENIS	13.62	6.310×10^{-3}
K	DENIS	12.94	4.194×10^{-3}
J	2MASS	13.63	5.635×10^{-3}
H	2MASS	13.23	5.216×10^{-3}
K_S	2MASS	13.02	4.128×10^{-3}
[3.6]	IRAC	12.33	3.976×10^{-3}
[4.5]	IRAC	11.90	3.434×10^{-3}
[5.8]	IRAC	10.39	1.010×10^{-2}
[8.0]	IRAC	8.344	3.459×10^{-2}
[24]	MIPS	5.141	5.998×10^{-2}

determination.

Unfortunately, the signal-to-noise ratio (S/N) is too poor for a large part of the blue spectrum (wavelength range 3280 to 4200 Å) making these wavelength ranges unusable for an accurate spectral abundance analysis hence they are not used for the study of J004441.04. Except for these bluer wavelength ranges, an overall S/N around 100 is obtained.

3.3 Spectral analyses

It is useful to compare the spectrum of J004441.04 with Galactic post-AGB stars. In Fig. 3.2 and 3.3 we compare a small spectral part of J004441.04 with the same spectral range of two Galactic post-AGB stars. The lower spectrum is from the Galactic post-AGB star IRAS06530-0213 (hereafter abbreviated to IRAS06530). This is a post-AGB star with a metallicity of [Fe/H] = -0.46 and $T_{\rm eff}$ = 7250 K and it is recognised to be the star with the highest *s*-process overabundances known to date (Reyniers et al. 2004). The upper spectrum is from the non-enriched Galactic star HD112374 = HR 4912 (Lambert et al. 1983; Giridhar et al. 1997). This star has a similar spectral type and a metallicity of [Fe/H]= -1.1. The normalised spectra are brought to the same velocity scale

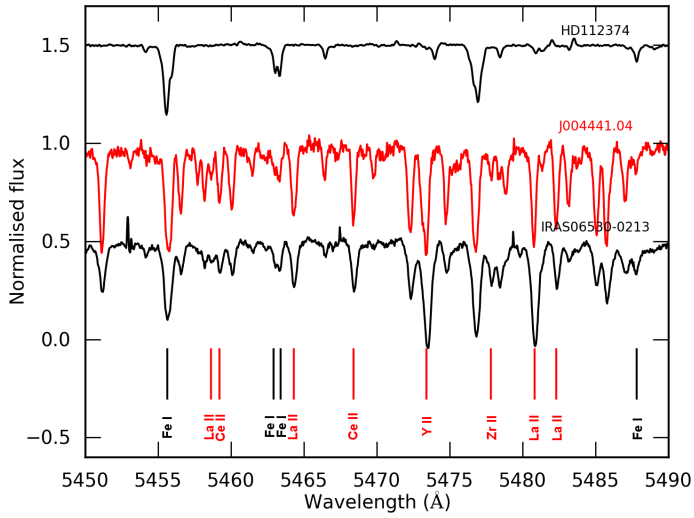

Figure 3.2: Comparison of the normalised spectra of J004441.04 (middle), IRAS 06530 (lower) and HD112374 (upper). The upper and lower spectra have been shifted in flux for clarity. Red and black vertical lines mark positions of *s*-nuclei and non *s*-nuclei respectively. For more information, see text.

and offset for clarity. Red and black vertical lines mark positions of *s*-nuclei and non *s*-nuclei respectively. It is remarkable that the spectra of J004441.04 are very similar to IRAS06530-0213 which illustrates its high *s*-process overabundance. We therefore choose the used line list of IRAS06530 in Reyniers et al. (2004) for quantified relative spectral analyses.

3.3.1 General methods

Both the atmospheric parameter determination and the abundance determination are performed using the same routines. The local thermal equilibrium (LTE) Kurucz-Castelli atmosphere models (Castelli & Kurucz 2004) are used in combination with the LTE abundance calculation routine MOOG (version July 2009) by C. Sneden (1973). Non-LTE effects are not taken into account for the spectral analyses of J004441.04.

The equivalent width (EW) of lines are measured via direct integration and abundances are computed by an iterative process in which the theoretical EWs of single lines are computed for a given abundance and matched to the observed EWs. Blended lines are avoided as much as possible. To check whether lines

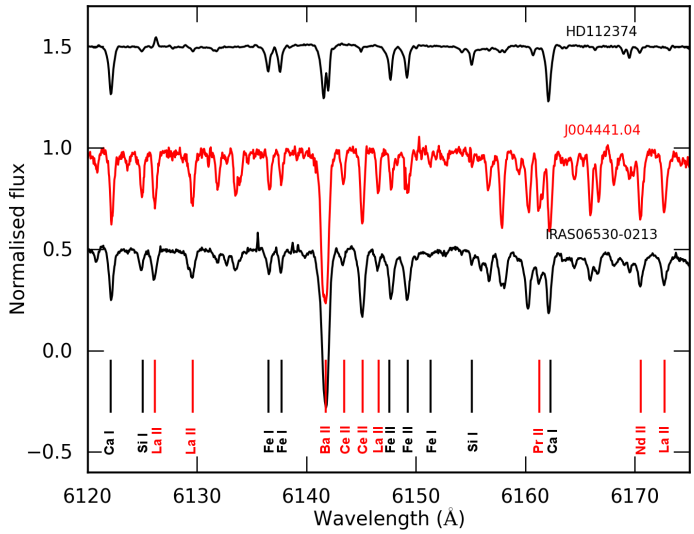

Figure 3.3: Comparison of the normalised spectra of J004441.04 (middle), IRAS 06530 (lower) and HD112374 (upper). The upper and lower spectra have been shifted in flux for clarity. Red and black vertical lines mark positions of *s*-nuclei and non *s*-nuclei respectively.

are part of blends with other identified lines, synthetic spectra are modelled with MOOG using Vienna Atomic Line Database (VALD) linelists (Kupka et al. 1999) and compared to the stellar spectra.

In order to identify lines, the radial velocity of J004441.04 is estimated by fitting a Gaussian curve to a number of identified atomic lines to determine their central wavelength. Using the equation of the Doppler shift, this results in a heliocentric radial velocity v = 148 ± 3 km/s which is accurate enough for line identification purposes. The useful line identification tool of Lobel (2006) was used for the first identifications. The heliocentric radial velocity of the SMC is in average 160 km/s (Richter et al. 1987) and the velocity of J004441.04 confirms the membership of the SMC.

3.3.2 Atmospheric parameter determination

The atmospheric parameters are derived using Fe I and Fe II lines and the standard spectroscopic methods: the effective temperature T_{eff} is derived by imposing the iron abundance, derived from individual Fe I lines, to be

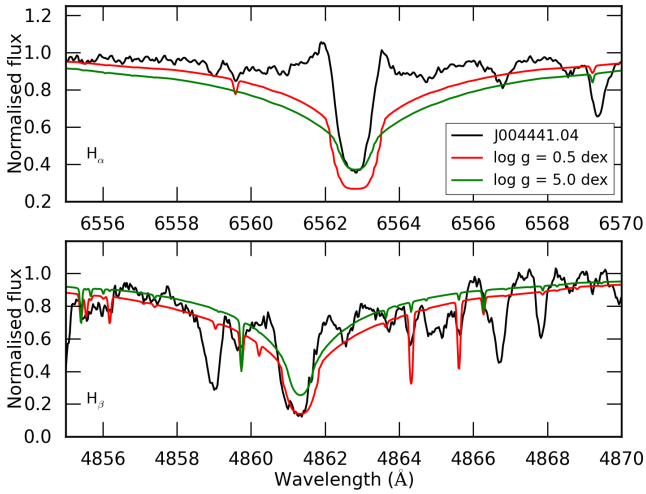

Figure 3.4: Comparison between Balmer lines of J004441.04 with synthetic models of Coelho et al. (2005) with different log g. The upper panel shows H_α, the lower panel shows H_β. The black spectrum represents J004441.04, the red and green spectrum are synthetic spectra with a log g of 0.5 and 5.0 dex respectively. For more information, see text.

independent of lower excitation potential; surface gravity log g is derived by imposing ionization equilibrium between the iron abundance of individual Fe I and Fe II; the microturbulent velocity ξ_t is derived by imposing the iron abundance from individual Fe I lines to be independent of reduced equivalent width (RW). For these analysis, 17 Fe I and 4 Fe II lines are used. Due to the high *s*-process enrichment of J004441.04, the number of useful non-blended Fe lines for the atmospheric determination is limited, especially for Fe II.

The results for the different atmospheric parameters are shown in Table 3.2 and lie in the range of typical post-AGB parameter values. The iron abundance for the determined atmospheric parameters is a good estimate of the overall chemical composition [M/H] which is in this case [Fe/H] = -1.34 ± 0.32 (dex). The abundance error of ± 0.32 is the total error including the line to line scatter and the uncertainties by the used atmospheric model which will be further discussed in Sect. 3.3.3. The low iron abundance of J004441.04 with respect to the mean metallicity of the SMC of [Fe/H] ≈ -0.7 (Luck et al. 1998) classifies J004441.04 as a low-metallicity star which are generally acknowledged as astrophysical production sites of heavy *s*-nuclei provided the third dredge-up (TDU) takes place.

Table 3.2: Determined atmospheric parameters of J004441.04

$T_{\rm eff}$ (K)	6250 ± 250
log g (dex)	0.5 ± 0.5
ξ_t (km/s)	3.5 ± 0.5
[M/H] (dex)	-1.34 ± 0.32

An attempt was made to determine the surface gravity of J004441.04 by fitting synthetic spectra to its Balmer lines H_α and H_β at 6562.8 Å and 4861.3 Å respectively. The comparison between the Balmer wings of the synthetic models with different log g and J004441.04 would provide an estimate of the surface gravity of J004441.04. However, this method is not usable for J004441.04, since its Balmer wings display emission lines as shown in Fig. 3.4. The upper panel shows the comparison between H_α lines, the lower panel shows H_β. The black spectrum represents J004441.04, the red and green spectrum are synthetic spectra of Coelho et al. (2005) with a log g of 0.5 and 5.0 dex respectively. Both panels display emission in the wings of both Balmer lines of J004441.04 which are most probably caused by ongoing mass loss. Also the strong enrichment of J004441.04 makes it impossible to fit the Balmer wings, since J004441.04 displays multiple strong atomic lines which are not included in the synthetic spectra. This is especially clear in the lower panel of Fig. 3.4.

The atmospheric parameters can be checked using results on other species only when the number of lines for that species is significant. Unfortunately, most species only have two, three or four useful lines (see already Table 3.3) due to the high number of blends. Fe I is the only neutral ion with single lines covering a large range in excitation potential. Fe is also the only element for which a useful number of lines of different ions is found. Therefore, the microturbulent velocity ξ_t is the only parameter which can be checked using another species than Fe: although the used number of lines of La II, Ce II and Nd II is small, they do provide a mean to check the derived ξ_t. This ξ_t check with La II and Ce II yields $\xi_t = 3.5$ km/s and Nd II gives $\xi_t = 3.0$ km/s , which confirms the found microturbulent velocity.

3.3.3 Abundance determination

With our preferred model atmosphere as basis, we started with a full but strictly relative abundance analysis and limited ourselves first to the lines used in the spectral analyses of IRAS 06530-0213.

We used mainly isolated non-blended, non-saturated lines and the individual atomic lines are all double-checked via a spectrum synthesis to investigate the possible presence of unresolved blends. N lines with EWs larger than 3 Å are not found and are not used due to possible confusion with noise in the spectrum. A redder spectrum will be needed for the N abundance determination.

Unfortunately, at these high overabundances, all Sr and Ba lines are heavily saturated making accurate abundance determination of these two most famous *s*-process species impossible (Figs. 3.1 and 3.3). The other s-process abundances come from isolated single lines except for those species where all detectable lines turned out to be blended. These specific blends were fitted by creating synthetic spectra in MOOG using VALD line lists of specific wavelength ranges. The resulting fits for Eu II and Gd II are shown in Fig. 3.6 for the Eu II line at 6437.640 Å in the upper panel and the Gd II line at 5733.852 Å in the lower panel. The black spectrum is the spectrum of J004441.04, the colored spectra are synthetic spectra with different abundances of the studied element. The Eu II line at 6437.640 Å is part of a blend with a very weak Y II line at 6437.169 Å, the Gd II line is part of a blend with a relatively strong Ce II line at 5733.692 Å. Fig. 3.5 shows the spectrum synthesis of the W II line at 5104.432 Å. The black spectrum is J004441.04, the colored spectra are synthetic spectra with different W abundances. This W II line forms a blend with a Sm II line at 5104.479 Å which is indicated in the figure. The positions of lines unknown to VALD are indicated with '?' proving that there are still a large number of lines that need to be identified in this highly enriched object.

The next step in the process was to constrain abundances for elements which have no isolated single lines. We used VALD line lists to predict the equivalenth widths for all lines of a given element by assuming a strong overabundance. For each element we then choose the strongest line in our observed spectrum and fitted this line with synthetic spectra of MOOG, analog to the Eu II and Gd II abundances so with appropriate input abundances of all elements which we could quantify previously. Unfortunately, also here the strong overabundances of *s*-process elements create spectral lines which are unknown to VALD linelists making abundance determinations difficult because of possible blends of unknown origin. Using the synthetic spectrum method, we estimated abundances for Mg I and Zn I together with the *s*-process elements Dy II, Er II, Yb II, Lu II and Hf II. Afterwards, we determined the EW of each used line in order to perform an error analysis on the derived abundances. For the abundance determination of O, we did not use the forbidden O I lines at 6300 and 6363 Å as they are part of an identified and unidentified blend respectively. After the abundance determination, we performed a spectral synthesis of the 6300 Å line using the derived O abundance which rendered a good fit. As forbidden lines are not sensitive to non-LTE effects (see e.g. Kiselman 2002), this is a confirmation of

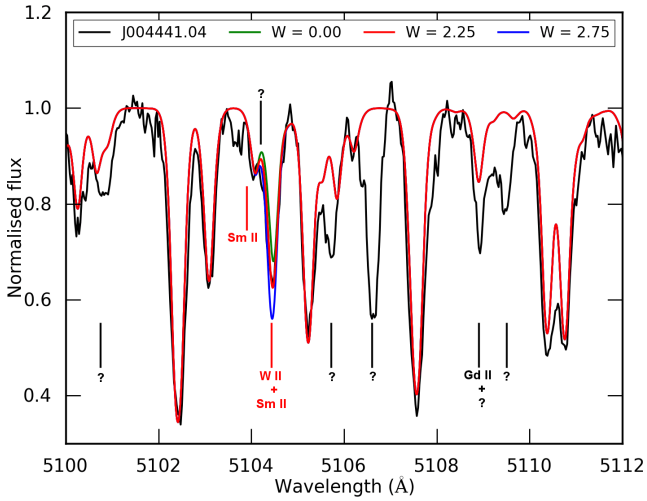

Figure 3.5: Spectrum synthesis of the W II line at 5104.432 Å. The black spectrum is J004441.04, the colored spectra are synthetic spectra with different W abundances. The Sm II line at 5104.080 Å, which forms a blend with W II, is indicated together with some atomic lines which are not included in the line list. For more information, see text.

the obtained high oxygen abudance.

The final abundance results of J004441.04 are shown in Table 3.3 where N represents the number of lines used for the abundance determination of the species, the full line list used for the abundance determination is listed in Appendix A. Solar abundances are taken from Asplund et al. (2009), uncertanties in log ϵ and log $\epsilon_{\odot}$ due to line-to-line scatter are given by σ_{ϵ} and $\sigma_{\epsilon_{\odot}}$ respectively. The sensitivity of [X/Fe] to uncertainties in the line-to-line scatter, effective temperature, surface gravity and microturbulent velocity are given by $\sigma_{[X/Fe]}$, $\sigma_{T_{eff}}$, σ_{logg} and σ_{ξ_t} respectively. The combined uncertainty in [X/Fe] due to the above described sensitivity is represented by σ_{tot}. Elemental abundances derived via synthetic spectrum fitting are indicated in an italic font in Table 3.3. We remark again that non-LTE effects are not taken into account in the abundance determination of the different species. Although the abundances of some useful elements for nucleosynthesis studies cannot be determined, Table 3.3 still contains quantified abundances of a wide range of *s*-elements.

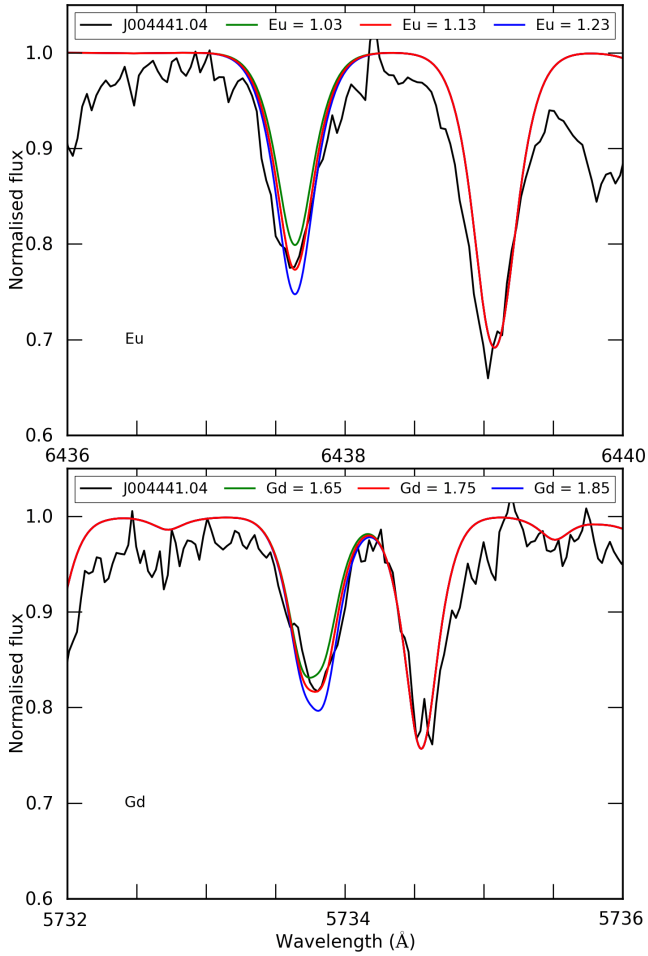

Figure 3.6: Spectrum synthesis of Eu II (top) and Gd II (bottom) lines at 6437.640 Å and 5733.852 Å respectively. The black spectrum is J004441.04, the colored spectra are synthetic spectra with different abundances of the studied element. For more information, see text.

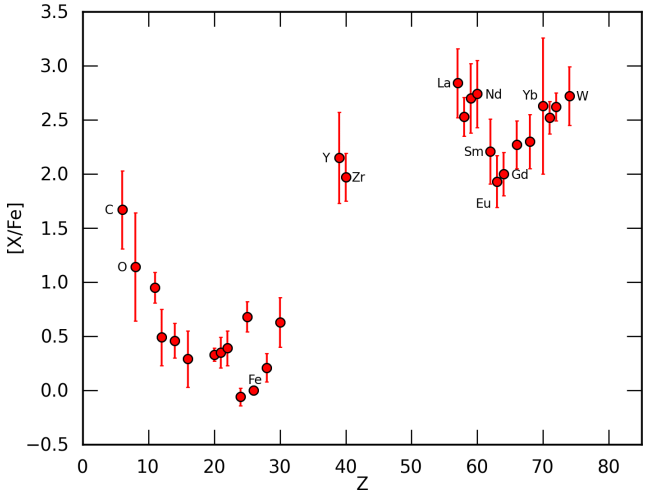

Figure 3.7: [X/Fe] results of J004441.04, the errorbars represent the total uncertainty σ_{tot}. Some elements are labelled for clarity. For more information, see text.

3.3.4 Abundance results

The [X/Fe] results of Table 3.3 are plotted in Fig. 3.7, the errorbars represent the total uncertainty σ_{tot}. For clarity some elements are labelled. The figure illustrates well the post-carbon star signature of J004441.04, with a C enrichment and very strong *s*-process enrichment. The C/O ratio is 1.9 ± 0.7. The uncertainties of the model atmosphere has the biggest impact on the accuracy of this ratio. J004441.04 is a post-AGB Carbon star with a C/O larger than one, but only mildly so.

Concerning the available α-elements Mg, Si, S, Ca and Ti, the simple mean of the [X/Fe] is $[\alpha/\mathrm{Fe}] = +0.4$. Such an enhancement is normal for Galactic objects in this metallicity range as a consequence of galactic chemical evolution and would not point to an intrinsic enhancement. However, it is not clear whether this relation also holds for the SMC.

The extreme *s*-process abundances point to a very effective dredge-up. With [Y/Fe] = +2.2 and [La,Ce,Pr,Nd/Fe] all inbetween 2.5 and 2.8 the *s*-process overabundance is extreme. Also the *s*-process overabundances of elements well beyond the Ba peak are high. The abundance results show that J004441.04 is the strongest *s*-process enriched extra-galactic object studied to date.

Table 3.3: Abundance results of J004441.04 together with the calcuted errors due to line to line scatter and uncertainties of the chosen atmosphere model. N represents the number of lines used for the abundance determination of the species. Uncertainties in log ϵ and log $\epsilon_\odot$ due to line-to-line scatter are given by σ_ϵ and $\sigma_{\epsilon_\odot}$ respectively. $\sigma_{[X/Fe]}$, $\sigma_{T_{eff}}$, σ_{logg} and σ_{ξ_t} represent the sensitivity of [X/Fe] to uncertainties in the line-to-line scatter, effective temperature, surface gravity and microturbulent velocity respectively. σ_{tot} represents the total uncertainty of [X/Fe] due to the line-to-line scatter and model uncertainties. Solar abundances are retrieved from Asplund et al. (2009). Abundances of elements indicated with italicised text are determined via synthetic spectra fitting. For more information, see text.

Species	N	log $\epsilon \pm \sigma_\epsilon$	log $\epsilon_\odot \pm \sigma_{\epsilon_\odot}$	[X/Fe] $\pm \sigma_{tot}$	$\sigma_{[X/Fe]}$	$\sigma_{T_{eff}}$		$\sigma_{\log g}$	σ_{ξ_t}	
						+250 K	-250 K	+0.5 dex	+0.5 km/s	-0.5 km/s
C I	6	8.76 ± 0.10	8.43 ± 0.05	1.67 ± 0.36	0.14	-0.23	0.24	0.11	0.02	-0.02
O I	3	8.49 ± 0.09	8.69 ± 0.05	1.14 ± 0.50	0.13	-0.35	0.32	0.12	0.02	-0.05
Na I	2	5.85 ± 0.08	6.24 ± 0.04	0.95 ± 0.14	0.12	-0.08	0.06	-0.02	0.01	-0.03
Mg I	*1*	*6.75 ± 0.20*	*7.60 ± 0.04*	*0.49 ± 0.26*	*0.22*	*-0.11*	*0.05*	*-0.05*	*0.02*	*-0.04*
Si I	2	6.63 ± 0.01	7.51 ± 0.03	0.46 ± 0.16	0.09	-0.11	0.07	-0.05	0.02	-0.04
S I	2	6.07 ± 0.13	7.12 ± 0.03	0.29 ± 0.26	0.16	-0.17	0.15	0.03	0.02	-0.04
Ca I	4	5.33 ± 0.03	6.34 ± 0.04	0.33 ± 0.06	0.09	-0.03	0.03	0.01	0.00	0.00
Sc II	3	2.18 ± 0.08	3.15 ± 0.04	0.35 ± 0.14	0.15	0.08	-0.08	0.01	-0.01	0.01
Ti II	3	4.02 ± 0.21	4.95 ± 0.05	0.39 ± 0.16	0.25	0.06	-0.05	0.01	-0.02	0.01
Cr II	3	4.26 ± 0.04	5.64 ± 0.04	-0.06 ± 0.08	0.13	-0.02	0.00	-0.02	0.01	-0.02
Mn I	2	4.77 ± 0.11	5.43 ± 0.04	0.68 ± 0.14	0.14	-0.07	0.01	-0.05	0.01	-0.04
Fe I	17	6.16 ± 0.07	7.50 ± 0.04	0.00 ± 0.03	0.11	0.00	0.00	0.00	0.00	0.00
Fe II	4	6.18 ± 0.11	7.50 ± 0.04	0.00 ± 0.08	0.17	0.00	0.00	0.00	0.00	0.00
Ni I	4	5.09 ± 0.17	6.22 ± 0.04	0.21 ± 0.13	0.19	-0.05	0.01	-0.04	0.03	-0.04
Zn I	*1*	*3.85 ± 0.20*	*4.56 ± 0.05*	*0.63 ± 0.23*	*0.22*	*-0.06*	*0.00*	*-0.04*	*-0.01*	*0.00*
Y II	2	3.04 ± 0.03	2.21 ± 0.05	2.15 ± 0.42	0.13	0.26	-0.08	0.20	-0.13	0.19
Zr II	2	3.23 ± 0.11	2.58 ± 0.04	1.97 ± 0.22	0.17	0.13	-0.08	0.07	-0.06	0.07
La II	9	2.62 ± 0.13	1.10 ± 0.04	2.84 ± 0.32	0.18	0.23	-0.14	0.09	-0.08	0.10
Ce II	8	2.79 ± 0.13	1.58 ± 0.04	2.53 ± 0.18	0.18	0.12	-0.12	-0.01	-0.02	0.01
Pr II	2	2.10 ± 0.01	0.72 ± 0.04	2.70 ± 0.32	0.12	0.23	-0.18	0.02	-0.06	0.06
Nd II	7	2.84 ± 0.10	1.42 ± 0.04	2.74 ± 0.31	0.16	0.24	-0.17	0.03	-0.05	0.07
Sm II	2	1.85 ± 0.04	0.96 ± 0.04	2.21 ± 0.30	0.13	0.22	-0.16	0.05	-0.05	0.07

Table 3.3: Continued.

Species	N	log $\epsilon \pm \sigma_\epsilon$	log $\epsilon_\odot \pm \sigma_{\epsilon_\odot}$	[X/Fe] $\pm \sigma_{tot}$	$\sigma_{[X/Fe]}$	$\sigma_{T_{eff}}$		$\sigma_{\log g}$	σ_{ξ_t}	
						+250 K	-250 K	+0.5 dex	+0.5 km/s	-0.5 km/s
Eu II	*1*	*1.13 ± 0.10*	*0.52 ± 0.04*	*1.93 ± 0.24*	*0.16*	*0.10*	*-0.13*	*-0.06*	*-0.04*	*0.04*
Gd II	*1*	*1.75 ± 0.10*	*1.07 ± 0.04*	*2.00 ± 0.20*	*0.16*	*0.05*	*-0.10*	*-0.04*	*0.00*	*-0.02*
Dy II	*1*	*2.05 ± 0.20*	*1.10 ± 0.04*	*2.27 ± 0.22*	*0.12*	*0.11*	*-0.16*	*-0.05*	*-0.01*	*-0.01*
Er II	*1*	*1.90 ± 0.20*	*0.92 ± 0.05*	*2.30 ± 0.25*	*0.24*	*0.04*	*-0.07*	*-0.04*	*0.01*	*-0.02*
Yb II	*1*	*2.15 ± 0.20*	*0.84 ± 0.11*	*2.63 ± 0.63*	*0.26*	*-0.02*	*-0.01*	*-0.04*	*0.57*	*0.00*
Lu II	*1*	*1.30 ± 0.20*	*0.10 ± 0.09*	*2.52 ± 0.15*	*0.15*	*0.02*	*-0.06*	*-0.03*	*-0.04*	*0.06*
Hf II	*1*	*2.15 ± 0.20*	*0.85 ± 0.04*	*2.62 ± 0.13*	*0.12*	*0.03*	*-0.08*	*-0.03*	*0.00*	*-0.01*
W II	*1*	*2.25 ± 0.20*	*0.85 ± 0.12*	*2.72 ± 0.27*	*0.26*	*0.02*	*-0.07*	*-0.04*	*-0.01*	*-0.01*

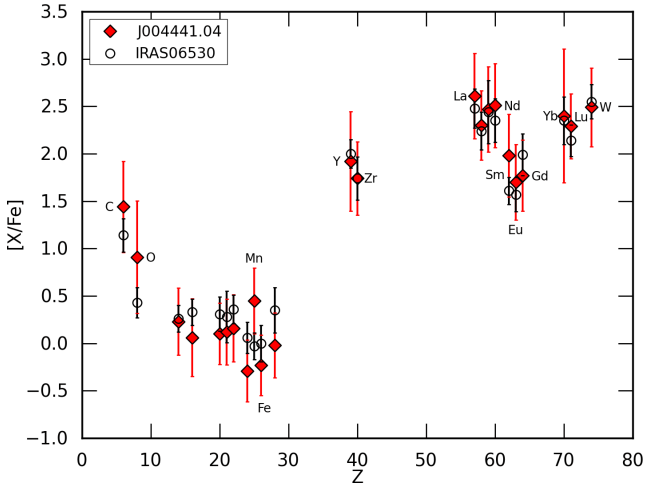

Figure 3.8: Comparison of [X/Fe] results for J004441.04 and IRAS 06530 (Reyniers et al. 2004) scaled to [Zr/Fe]. Some elements are labelled for clarity. The red errorbars of J004441.04 ratios are the total uncertainty while for IRAS 06530, the black errorbars represent line-to-line scatter. For more information, see text.

Fig. 3.7 shows a stronger overabundance of the heavy *s*-process component (magic neutron number 82) around La and Ce with respect to the light *s*-process component (magic neutron number 50) around Y and Zr which indicates an effective ^{13}C pocket for the production of heavy elements.

To get a good comparative view of the *s*-process nucleosynthesis of J004441.04 and IRAS 06530, we scale the [Zr/Fe] result of J004441.04 to the [Zr/Fe] result of IRAS 06530 making both [Zr/Fe] values overlap. This difference between the [Zr/Fe] results is then added to the ratios of J004441.04.

The results of this scaling are shown in Fig. 3.8 in which the red diamonds are the [X/Fe] results of J004441.04, open circles represent the results of IRAS 06530. The red errorbars of J004441.04 ratios represent the total uncertainty in [X/Fe] while for IRAS 06530, the black errorbars represent only the line-to-line scatter taken from Reyniers et al. (2004). Some elements are labelled for clarity. Despite a metallicity difference, Fig. 3.8 clearly shows that both objects have very similar *s*-process abundance patterns. With a C/O ratio of 2.8 and 1.9 respectively, also the C/O ratio of IRAS 06530 and J004441.04 are very similar. The same abundance trends can be found for the lighter elements where only Mn displays a strong difference. Following the index definitions of Reyniers

et al. (2004), we find an intrinsic index [hs/ls] = +0.5 and [s/Fe] = 2.4. In these indices, hs stands for high-mass *s*-process elements around the Ba peak and ls for elements around the Sr peak. We quantified the Ba abundance using the observed Nd abundance. This places J004441.04 in the upper right corner of the upper panel in Fig. 7 of Reyniers et al. (2004) confirming the correlation between the total enrichment of *s*-process elements and the [hs/ls] index. The results of J004441.04 corroborate the finding that there is no clear correlation between metallicity and the [hs/ls] index in the metallicity range sampled by post-AGB stars (Reyniers et al. 2004).

3.4 Spectral energy distribution

The spectral energy distribution (SED) of J004441.04 and its assumed distance provide the opportunity of determining its luminosity. The photometric data of Table 3.1 are used for the SED construction of J004441.04. For post-AGB objects in the SMC, we need to take into account three possible sources of reddening.

The first one is reddening by interstellar dust in the Milky Way Galaxy (MW) towards the SMC. Schlegel et al. (1998) derived the extinction towards the SMC by galactic dust to be small with an average of E(B-V) = 0.037 mag.

The second possible reddening source is reddening in the SMC itself. Fig. 3.9 shows the MW (green) and SMC (blue) extinction curves which are taken from Cardelli et al. (1989) and Gordon et al. (2003) respectively. The lines indicate the extinction of the different photometric bands of Table 3.1. The SMC curve only contains values at filter wavelengths explaining the strange behavior. Since both J and K bands almost overlap, only one of them is indicated in the figure. The extinction in the wavelength range used for the SED of J004441.04 is approximately the same for both the MW and the SMC. The largest difference between both reddening laws are shown in the J and K bands. The extinction is small for these IR bands, making that the different reddening laws hardly differ in the wavelength regime of interest. Because of the strong resemblance between the MW and SMC curve in the used wavelength range, we use the reddening law of the MW to determine the reddening in the SMC.

The third extinction cause is reddening by the circumstellar dust envelope of the post-AGB object itself. We applied a dereddening assuming that the wavelength dependency of the circumstellar extinction is similar to the interstellar medium (ISM) extinction law of the MW.

We determined the total reddening by applying a χ^2 minimalisation on the fit

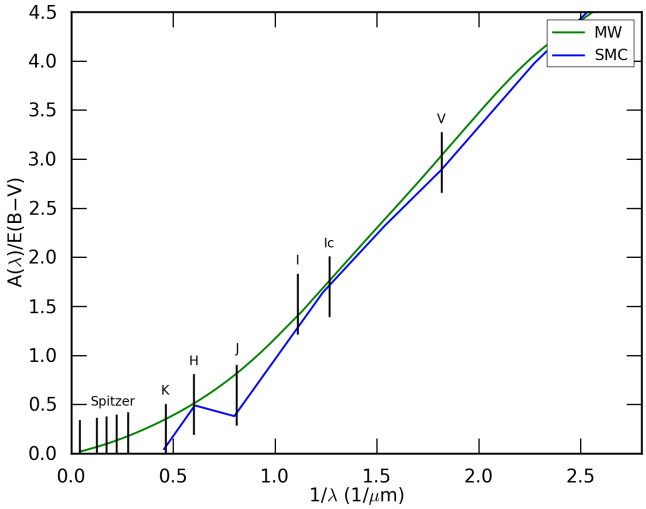

Figure 3.9: Extinction curves of the MW (green) and the SMC (blue). The position of the photometric bands used for the SED of J004441.04 are indicated. The MW extinction curve is taken from Cardelli et al. (1989), the SMC extinction curve from Gordon et al. (2003). The SMC curve only contains values at filter wavelengths explaining the strange behavior.

Table 3.4: SED results of J004441.04 using a distance of 61 kpc.

E(B-V)	0.64 ± 0.02
L ($L_\odot$)	7600 ± 200
$L_{IR}/L_\star$	0.34 ± 0.01

between the scaled model atmosphere and the dereddened broadband fluxes. A Monte Carlo simulation is used to determine the error on E(B-V) for 1000 arrays with a normal distribution of the original flux. For J004441.04, this results in an E(B-V) of 0.64 ± 0.02.

The SED of J004441.04 is shown in Fig. 3.10 together with the IR spectrum of J004441.04 which was used in Volk et al. (2011) to identify the object as a 21 μm source. Squares indicate the dereddened fluxes, triangles indicate original (reddened) fluxes and the black line represents the scaled atmospheric Kurucz model (see 3.2).

J004441.04 has a clear double-peaked SED where the left peak represents the

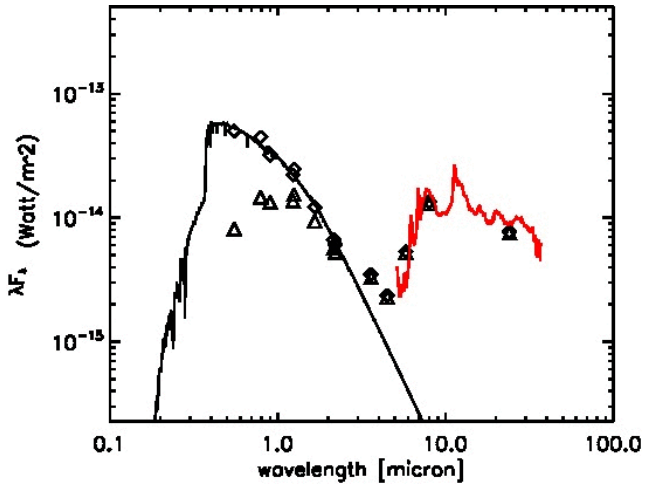

Figure 3.10: SED of J004441.04. Squares indicate the derived dereddened flux, triangles indicate original flux. The black line represents the Kurucz atmosphere model used to fit the photometry of J004441.04. The red spectrum is the IR spectrum which is used in Volk et al. (2011).

stellar photosphere and the right peak is the IR excess created by radiation of dust grains in the ejected AGB mass envelope (Fig. 3.10). By integrating the surface of the scaled Kurucz model, the luminosity of J004441.04 can be obtained assuming the distance to the SMC is approximately the distance to J004441.04. We use a distance of 61 kpc (Hilditch et al. 2005) to determine the luminosity which results in a photospheric luminosity of 7600 ± 200 $L_\odot$ where the luminosity error is again determined via Monte Carlo simulations. The luminosity ratio of the IR excess and the photosphere can give some information about the strength of the circumstellar reddening. The IR luminosity is simply determined by integrating the surface of the IR excess. The resulting luminosity ratio $L_{IR}/L_\star$ is 0.34 ± 0.01 so about 34% of the radiation emitted by the star is absorbed and re-emitted by dust in the circumstellar envelope contributing to reddening. We can assume the visible galactic extinction A_V can be approximated to $A_V \approx 3.1 \cdot$ E(B-V) and via Fig. 3.9 we can assume the V band extinction of the MW and SMC are approximately the same. The deduced E(B-V) of 0.64 ± 0.02 makes that roughly 20% of the original photosphere flux reaches the observer and the other 80% of the photosphere flux is absorbed or scattered outside the line-of-sight. Comparing this with the luminosity ratio $L_{IR}/L_\star = 0.34 \pm 0.01$ indicates that there is a significant contribution of the ISM extinction in the SMC and/or that there is deviation from spherical symmetry in the

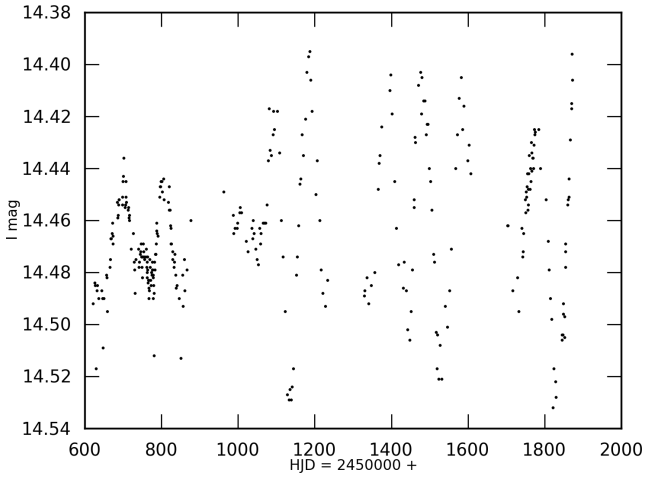

Figure 3.11: OGLE lightcurve of J004441.04 in the I band. For more information, see text.

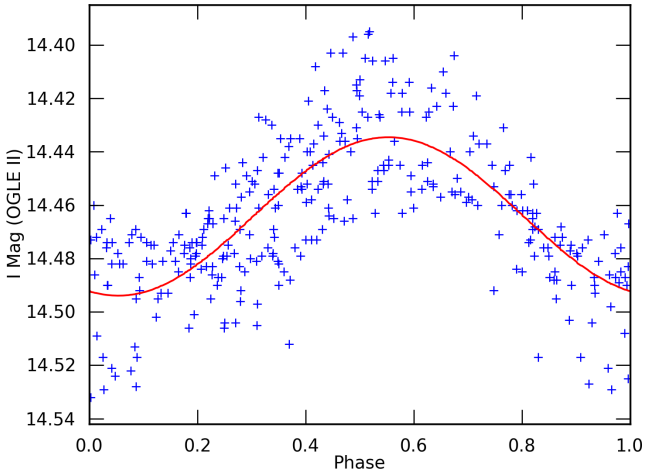

Figure 3.12: Phase diagram with the lightcurve of J004441.04 (blue crosses) folded over the dominant frequency of 97.6 ± 0.3 days (red line).

circumstellar shell.

Post-AGB stars pass through the Cepheid II instability strip and J004441.04 is no exception. The variability in the I filter is displayed in Fig. 3.11. A frequency

analysis of this light curve provides a dominant period of 97.6 ± 0.3 days which is plotted in a phase diagram in Fig. 3.12. Blue crosses are the individual light curve points of Fig. 3.11 and it is clear from Fig. 3.12 that this is indeed the dominant period. Amplitude modulation is clearly apparent in Fig. 3.11. As the amplitude of the variability is rather small (maximum ±0.15 mag in I), the use of stable atmosphere models for the spectral analyses is still appropriate.

We attempted to use the observed period of 97.6 days to constrain the parameters of J004441.04 under the assumption that this is a pulsation. The linear pulsation code of Wood (1976) and its updates as described in Kamath et al. (2010) was used to examine the pulsation period of the fundamental mode in stellar models with luminosities of 7600, 10000, 15000 and 18000 $L_\odot$ and $T_{\rm eff}$ values between 4700 and 6300 K. The stellar mass was obtained from a linear fit between L and M for the two post-AGB tracks of Vassiliadis and Wood (1994) for an abundance of Z=0.001. The composition of the models was assumed to be X=0.75 and Z=0.001.

For our derived $T_{\rm eff}$ of 6250 K for J004441.04, the pulsation period of all these models is too small, typically near 50 days. This is about half the observed period. A much cooler effective temperature is required in order to obtain a model with the observed period of 97.6 days. At the luminosity L = 7600 $L_\odot$ (our estimated value), a fundamental mode period of 97.6 days occurs at $T_{\rm eff} \sim 4830$ K while at the highest luminosity investigated (18000 $L_\odot$) a fundamental mode period of 97.6 days occurs at $T_{\rm eff} \sim 5010$ K. In addition, models with $T_{\rm eff}$ near 6250 K are pulsationally stable in modes with periods greater than 20 days while those with $T_{\rm eff}$ near 4900 K are unstable. The pulsation periods are relatively insensitive to composition (X=0.10 was tried) and the adopted mass.

The $T_{\rm eff}$ value of $\sim$ 4900K required to get the correct pulsation period is, however, incompatible with the spectrum of J004441.04. There are two possible explanations for this discrepancy. Firstly, it is possible that the pulsation models are wrong. These stars are truely extreme: in the inner one third of the star radiation provides 90% of the pressure supporting the exterior envelope. The stars are difficult to analyse but all the relevant physics is included so there should be no obvious problem. The metal abundances in the envelope are non-standard so that the solar-scaled abundances used will lead to errors in the opacity. This is more likely to affect the stability of the models than the periods. It is not obvious that the pulsation models have significant incomplete physics.

If the pulsation models give the correct periods, then a second explanation for the discrepancy is required. Here we raise the possibility that the observed periodicity is not a pulsation but it could be due to other surface phenomena

like rapid rotation of a spotted star or an orbiting companion. With our adopted T_{eff} and L values, and with a stellar mass of 0.65 $M_{\odot}$, the breakup period is $\sim$ 94 days, very close to the observed period. So if rotation is an explanation for the variability, the star must be rotating at near-breakup velocity, which is again incompatible with the detected broadening of the spectral lines, unless we happen to look along the rotation axes. The angle between the line-of-sight and the rotation axes should, in that case, be lower than 10°. Also, models indicate that a strong rotation and rotational shear in the intershell, may mix ^{14}N into the ^{13}C pocket hence impact on the efficiency of the *s*-process nucleosynthesis (Herwig et al. 2003; Siess et al. 2004). Considering the other possibility, an orbiting companion or dust cloud would have to be very close to the surface of J004441.04. The SED shows no indication of a hot dust excess (Fig. 3.10). All these possibilities do seem very unlikely. We are therefore unable to provide a satisfactory explanation for the observed periodicity in J004441.04.

3.5 Initial mass determination

Before comparing the results of J004441.04 with theoretical nucleosynthetic models, its initial mass (mass at the zero-age main-sequence) needs to be estimated. Both metallicity and initial mass are fundamental parameters for the calculation of models.

We use the evolutionary post-AGB tracks of Vassiliadis & Wood (1994) to obtain an accurate estimate of the initial mass. The choice of these tracks is based upon the metallicity: these authors calculated tracks for a metallicity of Z = 0.001 corresponding to the found metallicity of J004441.04. Unfortunately, the Vassiliadis & Wood (1994) tracks start at an effective temperature of $T_{eff} = 10^4$ K and hence do not include the 6250 K of J004441.04. However, the luminosity of post-AGB stars remains approximately constant during their transit through the HR diagram, allowing linear extrapolation between log T_{eff} and log $L/L_{\odot}$ towards lower temperatures. The need for extrapolation to lower temperatures may indicate that J004441.04 is in the beginning stage of the post-AGB phase.

Fig. 3.13 shows the position of J004441.04 in the HR diagram together with the 1.5 $M_{\odot}$ (red line) and 1.0 $M_{\odot}$ (green line) evolutionary tracks of Vassiliadis & Wood (1994) for Z = 0.001. Based upon this figure, we estimate an initial mass of M $\simeq$ 1.3 $M_{\odot}$ for J004441.04. The tracks for Z=0.001 predict a mass for the current post-AGB star of 0.65 $M_{\odot}$. With the derived T_{eff} and L, the radius is 75 $R_{\odot}$, and log g = 0.5 also gives M=0.65 $M_{\odot}$ which is consistent with the tracks.

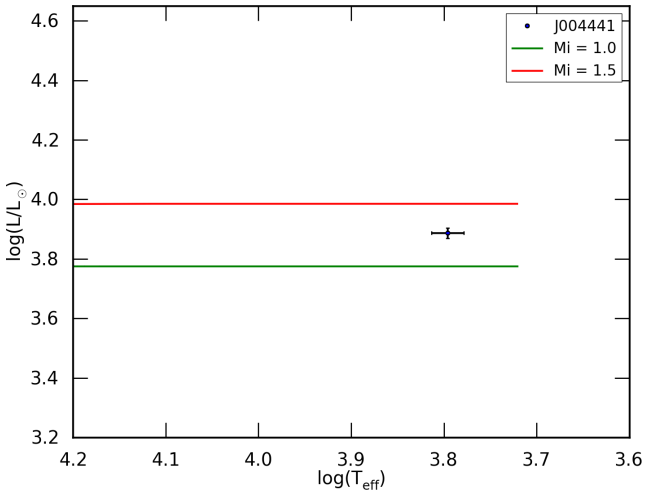

Figure 3.13: J004441.04 positioned in the HR diagram based upon the results in this paper. The red and green lines respectively represent the 1.5 $M_{\odot}$ and 1.0 $M_{\odot}$ evolutionary tracks of Vassiliadis & Wood (1994) for Z = 0.001.

3.6 AGB chemical models

We compare the observed abundance results with predictions from two independent stellar evolution codes, with which we calculated models of a 1.3$M_{\odot}$ star of [Fe/H] = -1.4.

3.6.1 Mount-Stromlo Evolutionary predictions

One of the AGB evolutionary models was calculated using the same version of the stellar evolution code described in Karakas (2010, and references therein), which uses the Vassiliadis & Wood (1993) mass-loss rate on the AGB, and includes the addition of C and N-rich low-temperature opacities tables from Lederer & Aringer (2009). Convective overshoot is used to induce the third dredge-up (TDU) in the 1.3$M_{\odot}$, $Z = 0.0006$ model. The TDU is the inward movement of the convective envelope into regions processed by partial He-burning during a thermal instability (see Herwig 2005, for a recent review). Some form of overshoot is required because low-mass models computed previously with the same code shows little or no TDU for masses $\lesssim 2\,M_{\odot}$ at solar metallicity. We calculate one stellar evolution sequence of a 1.3$M_{\odot}$ model star with a scaled-solar initial abundance pattern with Z = 0.0006.

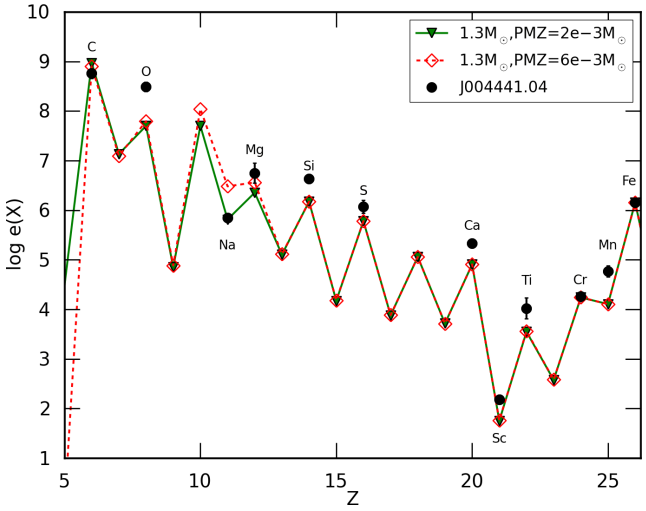

Figure 3.14: The predicted abundance of elements lighter than Fe, in $\log \epsilon(\mathrm{X})$, as a function of atomic number, Z, for a 1.3 $\mathrm{M}_{\odot}$ model of $Z = 0.0006$ ([Fe/H] = -1.4). Abundances are sampled at the tip of the AGB, after the last computed thermal pulse. Included are the approximate locations (in proton number, Z) of some key elements. Predictions are shown for two values of the parameter $\mathrm{M}_{\mathrm{mix}} = 2 \times 10^{-3}$ (points connected by the solid green line) and $6 \times 10^{-3}\,\mathrm{M}_{\odot}$ (points connected by the red dashed line). This parameter determines the size of the ^{13}C pocket and *s*-process enrichment, see text for details. The derived abundance of the post-AGB star J004441.04 is shown with error bars.

We include overshoot by extending the position of the base of the convective envelope by 1.0 pressure-scale height. We do not vary this free parameter for this study, noting that the final predicted carbon abundance of $\log \epsilon(\mathrm{C}) = 8.90$ is already 40% higher than the observed carbon abundance of $\log \epsilon(\mathrm{C}) = 8.76$. The final predicted luminosity of the stellar model at the tip of the AGB is $8400\,\mathrm{L}_{\odot}$, which is achieved after 14 thermal pulses. The observed luminosity of $7600\,\mathrm{L}_{\odot}$ is reached after 12 thermal pulses. It would be possible to match the observed luminosity at the tip of the AGB by either increasing the mass-loss rate or increasing the amount of overshoot.

The *s*-process abundance predictions were calculated using the post-processing nucleosynthesis code and full network of 320 species described in Lugaro et al. (2012), with reaction rates taken from the JINA REACLIB library (Cyburt et al. 2010). For the initial composition we used the solar distribution of abundances from Asplund et al. (2009) scaled down to [Fe/H]=-1.4. Solar abundances of

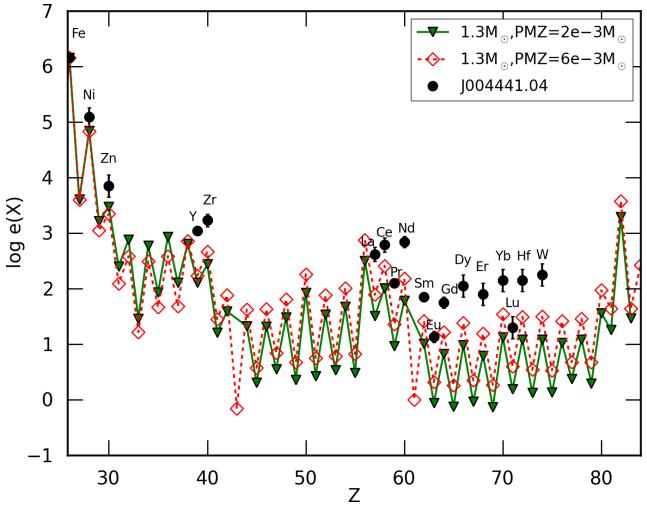

Figure 3.15: Same as Fig. 3.14 except for elements heavier than Fe.

C, N, O, Ne, Mg, Si, S, Ar, and Fe are the pre-solar nebula values from Table 5 of Asplund et al. (2009); F is the meteoritic value of $\log \epsilon(F)_{\odot} = 4.42$ from Table 1 of the same paper (chosen because it has a lower uncertainty), and for many of the elements heavier than Fe we use the meteoritic values for the solar abundances (e.g., Sr, Eu, Pb). No α-enhancement was used at this stage.

In order to obtain an enrichment of *s*-process elements, we artificially introduce some protons into the top of the He-intershell. Note that this has become standard practice for the simple reason that there is not enough ^{13}C in the H-burning ashes of AGB stars to make it an efficient neutron source. Recent studies investigating the formation of the ^{13}C pocket by various mechanisms have found that the proton abundance in the intershell decreases monotonically (e.g., Cristallo et al. 2009). We apply the assumption that the proton abundance in the intershell decreases monotonically from the envelope value of $\simeq 0.7$ to a minimum value of 10^{-4} at a given point in mass located below the base of the envelope. We do this in the same manner as described in Alves-Brito et al. (2011) and Kamath et al. (2012).

This *partially mixed zone* (or PMZ) is required in order to facilitate the formation of a ^{13}C pocket which allows neutrons to be released by the ^{13}C(α,n)O^{16} reaction (Straniero et al. 1995; Gallino et al. 1998; Goriely & Mowlavi 2000; Herwig 2005). The mass of the proton profile is a free parameter which we set as a constant mass. We adopt two choices for the extent of the partially mixed proton zone: 1) PMZ = 0.002M$_{\odot}$ (green solid line in Figs. 3.14 and 3.15), and

2) PMZ = 0.006$M_\odot$ (red dashed line in Figs. 3.14 and 3.15).

In Figs. 3.14 and 3.15 we show the abundances derived for J004441.04 in this work along with nucleosynthesis predictions from this model. The main point of this comparison is to show that a standard, initial scaled-solar abundance pattern used in the stellar model produce *s*-process overabundances that are *not* compatible with the derived abundances for J004441.04. The main shortcomings are that:

- While the predicted C overabundance is only 40% higher than the observed value, the predicted O overabundance is too low. This makes that the C/O prediction is ∼18, which is clearly in contrast to the detected value of 1.9±0.7. An initial alpha enhanced enrichment of [O/Fe] = +0.4, still makes the final O abundance too small and the high [O/Fe] = 1.14 indicates that the star has dredged-up a considerable amount of oxygen, above the level found in the stellar model of [O/Fe] = 0.35 dex.
- The total overabundances of the *s*-process nuclei are clearly too low;
- While the predicted *s*-process *distribution* is very similar to the observed one, the predicted Pb abundance is significantly higher than the observed upper limit (see Sect. 3.6.3 and Fig. 3.17).

Note also that the final predicted $^{12}C/^{13}C$ ratio is extremely high at ≈ 1800. An observational constraint on the isotopic ratios is not possible with the wavelength coverage we have at present, but this should be certainly a priority in our next observational season.

It is plausible that at the low metallicity of [Fe/H] = −1.34, J004441.04 evolved from an initially α-enhanced composition. This would explain the discrepancy between the predicted and observed Si, S and Ca abundances.

3.6.2 STAREVOL

To test the uncertainties associated with stellar modeling, an additional 1.3$M_\odot$, [Fe/H]=-1.4 model was computed with the STAREVOL code (e.g. Siess 2007, and references therein). The initial composition is slightly different, scaled solar according to Cunha et al. (2006) which is based upon the Asplund et al. (2005) composition with neon enhanced by nearly a factor of 2. This change in the neon abundance was required to reproduce a correct seismic solar structure. As before, we do not consider α- enhancement and, with our reference composition, the star has a metallicity Z=0.0044. We use the Reimers mass loss rate with $\eta = 0.5$ up to the beginning of the AGB phase and then switch to the Vassiliadis

& Wood (1993) prescription. The effect of CO opacities is modeled using the analytical fits described in Marigo (2002). Overshooting is also included at the base of the convective envelope but no overshoot from the flash-driven convection zone into the CO core is taken into account. We use the diffusive approach of Herwig et al. (1999) with $f_{over} = 0.02$. Similar to the Stromlo model, this AGB model experiences 15 thermal pulses and the TDU starts at pulse number 6. Considering the small overshoot parameter, the amount of dredged-up material is rather limited and, except for pulse number 9, $\lambda \lesssim 0.06$ (where λ is the ratio of the dredged-up mass to the intershell mass increase between 2 consecutive pulses). At the tip of the AGB, the stellar luminosity is $9400\,L_{\odot}$. As previously mentioned, this value can be lowered if a higher mass loss rate is used.

The STAREVOL network includes 55 species and allows an accurate treatment of the nucleosynthesis up to ^{37}Cl (for details, see Siess & Arnould (2008)). In this code, mixing and nuclear burning are solved simultaneously, once the structure has converged. For the *s*-process nucleosynthesis, we use the post-processing code as described in Goriely & Siess (2001) which includes about 547 nuclei up to Po with all relevant nuclear (n-, p-, α-captures), weak (electron captures, -decays) and electromagnetic (photodisintegration) interactions. Nuclear reaction rates are taken from the updated Nuclear Astrophysics Library of the Brussels University (BRUSLIB, available at `http://www.astro.ulb.ac.be/bruslib`). Following Goriely & Mowlavi (2000), a PMZ of about half the mass extension of the pulse (i.e some $6 - 10 \times 10^{-3}$M$_{\odot}$) is introduced below the convective envelope at the time of the TDU. In this PMZ, the proton profile decreases exponentially from the envelope mass fraction down to 10^{-6} allowing for the formation of a substantial ^{13}C pocket.

The results of the post-processing calculations are shown by the blue line in Fig.3.16. The model has the same basic shortcoming, namely an oxygen enrichment ([O/Fe] =0.13) too weak by a factor of ∼10 but a carbon enrichment ([C/Fe]=1.42) compatible with the observed value. As illustrated in Fig.3.16, the surface *s*-process enrichment is also too low with respect to the observations. The *s*-process abundance pattern itself is in good agreement except again for Pb (see Sect. 3.6.3).

At the end of the AGB evolutionary phase, we are left with a relatively small convective envelope of less than 0.05 M$_{\odot}$. If we assume that our star model experiences a very last thermal pulse with a deep TDU, a substantial surface pollution follows and a good agreement with the observations can be achieved (red-solid line in Fig.18). This last-pulse modeling corresponds to a post-processing calculation identical to those characterizing the previous TDU episodes but for which the TDU is just assumed to extend to about 7×10^{-3} M$_{\odot}$ deep into the C-rich region, i.e about half of the pulse mass is now diluted

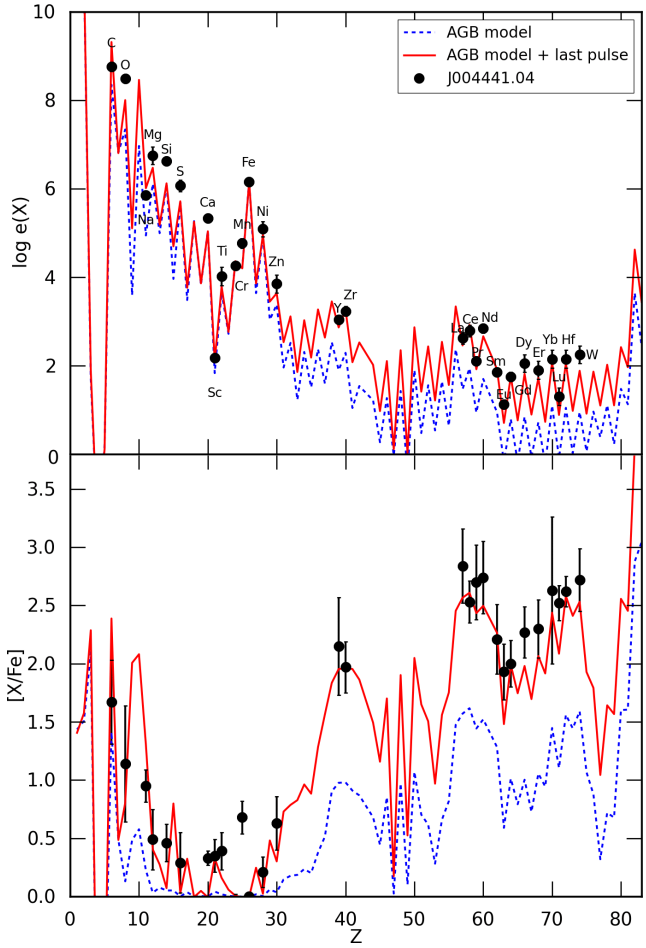

Figure 3.16: Predicted elemental distribution in log ϵ (top) and [X/Fe] (bottom panel) as a function of the atomic number Z for a $1.3 M_{\odot}$,[Fe/H] = -1.4 model computed with STAREVOL. In each panel, the blue-dashed line corresponds to the post-processed AGB model including 15 thermal pulses and the red line shows the results expected from the occurrence of an additional final thermal pulse followed by a deep TDU.

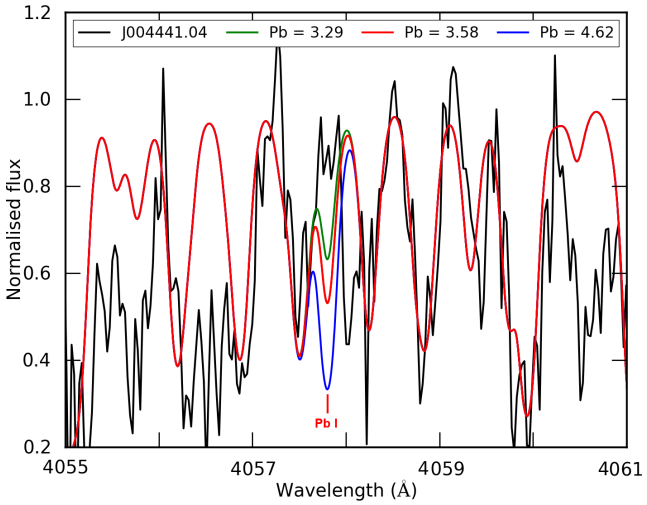

Figure 3.17: Pb I line region in the spectrum of J004441.04 compared with model predictions. In green, the Mount Stromlo model prediction (Section 6.1) and in red and blue the predictions obtained by the STAREVOL code (Section 6.2).

into the envelope. This improved fit to the observation is due to the small remaining envelope mass ($M_{env} < 0.05 M_{\odot}$) which limits the dilution of the dredged-up material. The observed distribution of *s*-process elements can be nicely reproduced except for Pb which, in both simulations, is overproduced (see Sect. 3.6.3), as classically done in all *s*-process simulations at low-metallicity (Goriely & Mowlavi 2000). Concerning the light elements, this last dredge-up brings significantly more C, O, F, Ne and Na to the surface. The C is now in disagreement with the observations but on the other hand, we can reproduce the oxygen enrichment, yielding a similar C/O$\sim$ 20 as before. We also note that the underabundance of the α-elements Si, S and Mn remains. It is interesting to see how the use of different abundances units, namely $\log(\epsilon)$ and [X/Fe] can be misleading. Finally, note that within the *s*-process model adopted here, the partial mixing of protons into the C-rich region also leads to a significant production of F, Ne and Na (see e.g Goriely & Mowlavi (2000)) which is also the case for the Mount-Stromlo models as shown in Fig. 3.18. The estimated abundance of Na by the models is seen in Fig. 3.18 to be in rather good agreement with observation. It would be extremely valuable to confirm observationally the predicted F overproduction of about 2 dex. Unfortunately, at these photospheric temperatures, F has no suitable lines in the sampled spectrum and its abundance can not be quantified.

3.6.3 Pb discrepancy

Figs. 3.15, 3.16 and 3.18 clearly show that current stellar evolution codes predict strong Pb overabundances for J004441.04. The strongest predicted Pb line in our sampled spectral range is 4057.807 Å. Unfortunately, this spectral region has a low S/N preventing an accurate Pb abundance determination. We focused on this spectral region and looked carefully on the three exposures. We obtained a weighted average of the three UVES spectra and then confronted this final spectrum with spectral synthesis models. We used the Pb abundances predicted by the chemical models in Fig. 3.17. The black spectrum is the normalised weighted mean spectrum of J004441.04, the green spectrum displays the predicted Pb abundance of the Mount-Stromlo model with PMZ = $0.006 M_{\odot}$, the red and blue spectrum represent the STAREVOL predictions with the blue spectrum the model with a last thermal pulse. Although the stellar spectrum is of poor quality, it is clear from Fig. 3.17 that the predicted strong line is not present in the stellar spectrum. From Fig. 3.17 we estimate an upper Pb abundance of 3.00 for J004441.04. Unfortunately we do not have a spectrum of IRAS 06530 in this spectral domain. In the late thermal pulse scenario (Fig. 3.18), the predicted Pb abundance becomes very large, which is incompatible with the detected spectrum. To reduce the production of Pb, the neutron in the PMZ production must be reduced. Partial pollution of the ^{13}C pocket by ^{14}N induced by rotational mixing (e.g. Herwig et al. 2003; Siess et al. 2004) may be needed to solve this problem but this will need a detailed investigation which is outside the scope of this paper.

3.7 Discussion and Conclusion

We presented a detailed analysis of J004441.04, the only known 21 μm object of the SMC. This metal poor star ([Fe/H] = -1.34 ± 0.32), turns out to be among the most *s*-process enriched stars known to date while displaying only a moderate C/O ratio of 1.9 ± 0.7. The atmospheric parameters ($T_{eff} = 6250 \pm 250$, log g = 0.5 ± 0.5) combined with the luminosity of 7600 ± 200 $L_{\odot}$ as well as the pulsation period of 97.6 ± 0.3 days, show that we witness the post-AGB phase of a star of low initial mass. This initial mass is estimated to be $\simeq 1.3$ $M_{\odot}$. Our findings on an extra-Galactic source corroborate the conclusion that 21 μm stars are post-Carbon stars. Although of lower metallicity, the object displays very similar overabundances as the most *s*-process rich post-AGB star known in our Galaxy (IRAS 06530-0213).

Our AGB model predictions are based on model calculations which include a forced overshoot of the convective boundary as well as an artificial inclusion of

a proton profile into the intershell. We used two independent codes for these predictions. For comparsion, we also included in Fig. 3.18 the nearest model in the coarser grid of models by Cristallo et al. (2011) (1.5 $M_{\odot}$, Z = 0.001) which yields similar discrepancy like our two models.

While the predicted C overabundance is compatible with the observations, the predicted O abundance is significantly lower resulting in a predicted C/O ratio of ∼20 which is clearly too high. More oxygen could be dredged-up in the models, if one includes additional overshooting below the thermal pulse, as shown by Herwig (2000).

While the models fit the *s*-process distribution well, as depicted in Fig. 3.18, the absolute abundances are not well matched. In our late thermal pulse scenario, we assume that a thermal pulse occurred with dredge-up and a limited dillution by the remaining reduced envelope mass. In this model, the very high overabundances are matched better. A noticeable exception is that the predicted Pb abundance is much larger than the detected upper limit (Fig. 3.17). A higher S/N spectrum in the region of Pb lines is needed to better quantify the Pb abundance which would yield an ever stronger test on the nucleosynthesis but our spectrum is incompatible with such high Pb abundance. With the data at hand, no isotopic ratio could be determined yet but the predicted $^{12}C/^{13}C$ of $\sim$ 1800 is extremely high. The nearest model in the coarser grid of models by Cristallo et al. (2011) yields similar discrepancy with even a higher predicted C/O ratio and $^{12}C/^{13}C$ values.

Our calculations demonstrate that there is only a weak dependency of the theoretical predictions on the adopted stellar evolution code.

It is interesting to compare the abundance pattern of J004441.04 with the patterns observed in peculiar metal poor stars like the CEMP-*s*/*r* stars, that is, a carbon-enhanced metal-poor star with enrichments in both *s* and *r*-process elements (see discussions in Beers & Christlieb 2005; Jonsell et al. 2006; Sneden et al. 2008; Lugaro et al. 2012). According to the definition given in Jonsell et al. (2006), CEMP-*s*/*r* stars have [Eu/Fe]>1 and [Ba/Eu]>0. The post-AGB star J004441.04 satisfies all of these criteria. It is carbon rich with [C/Fe] = 1.67 and [Ba/Eu] > 0, using the [Ba/Fe] = 2.67 estimated earlier. The estimated Ba (or observed La, which is a good proxy for elements at the second *s*-process peak) and Eu abundances put this star well into the region of the [Eu/Fe]–[Ba/Fe] plane occupied by the CEMP-*s*/*r* stars (see Fig. 5 from Lugaro et al. 2012). Abundance wise, J004441.04 could be seen as a more metal rich analogue of the CEMP-*s*/*r* stars. However, unlike many of the stars within the CEMP-*s*/*r* class, the distribution of heavy elements in J004441.04 is similar to that of a pure *s*-process, except for the anomalously low Pb abundance. What is unusual about J004441.04 is how the star obtained such large enrichments of heavy

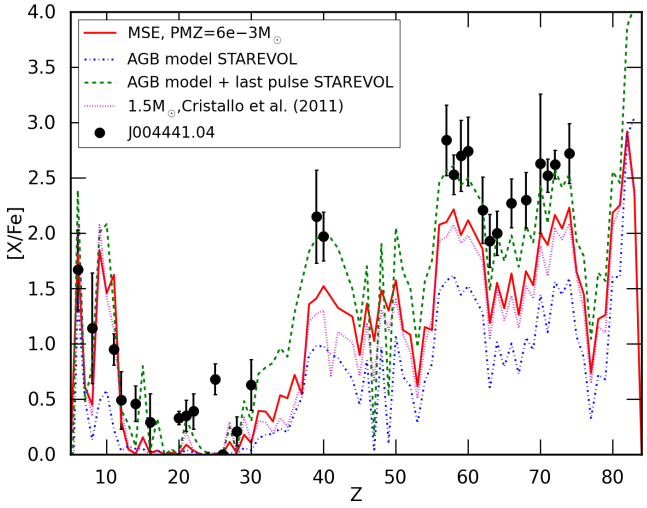

Figure 3.18: The abundance pattern of J004441.04 in comparison with the model predictions. In red, the Mount Stromlo model (Sect. 3.6.1), in blue the predictions obtained by the STAREVOL code (Sect. 3.6.2), the green dashed curve is computing assuming a late thermal pulse with deep dredge-up occurs when the dilution is small. The magenta line is the 1.5 $M_{\odot}$, Z = 0.001 model of Cristallo et al. (2011).

elements, while keeping the C/O ratio low.

It is fair to say that many of the chemical, physical and pulsational properties of the interesting SMC post-AGB star J004441.04 are, as yet, unaccounted for by our model predictions. This study is the first of a series in which we aim at a systematic study of post-AGB stars in the Magellanic clouds. These objects with constrained distances will provide unprecedented and systematic tests of the AGB model predictions, complementary to the limited study of AGB stars (e.g. de Laverny et al. 2006; Abia et al. 2011) for which much lower overabundances are detected. The ultimate aim of this programme is to make progress in the understanding of the complex interplay between mixing, nucleosynthesis and mass-loss which characterise the final evolution of solar-like stars.

Chapter 4

Pb in *s*-process enriched post-AGB stars in the Magellanic Clouds

This chapter was originally published as:

The lead discrepancy in intrinsically *s*-process enriched post-AGB stars in the Magellanic Clouds.

K. De Smedt, H. Van Winckel, D. Kamath, A. I. Karakas, L. Siess, S. Goriely, P. R. Wood

Astronomy & Astrophysics, Vol. 563, L5, 2014

ABSTRACT

Context: Our understanding of the *s*-process nucleosynthesis in asymptotic giant branch (AGB) stars is incomplete. AGB models predict, for example, large overabundances of lead (Pb) compared to other *s*-process elements in metal-poor low-mass AGB stars. This is indeed observed in some extrinsically enhanced metal-poor stars, but not in all. An extensive study of intrinsically *s*-process enriched objects is essential for improving our

knowledge of the AGB third dredge-up and associated *s*-process nucleosynthesis.

Aims: We compare the spectral abundance analysis of the SMC post-AGB star J004441.04-732136.4 with state-of-the-art AGB model predictions with a main focus on Pb. The low S/N in the Pb line region made the result of our previous study inconclusive. We acquired additional data covering the region of the strongest Pb line.

Methods: By carefully complementing re-reduced previous data, with newly acquired UVES optical spectra, we improve the S/N of the spectrum around the strongest Pb line. Therefore, an upper limit for the Pb abundance is estimated from a merged weighted mean spectrum using synthetic spectral modeling. We then compare the abundance results from the combined spectra to predictions of tailored AGB evolutionary models from two independent evolution codes. In addition, we determine upper limits for Pb abundances for three previously studied LMC post-AGB objects.

Results: Although theoretical predictions for J004441.04-732136.4 match the *s*-process distribution up to tungsten (W), the predicted very high Pb abundance is clearly not detected. The three additional LMC post-AGB stars show a similar lack of a very high Pb abundance.

Conclusions: From our study, we conclude that none of these low-mass, low-metallicity post-AGB stars of the LMC and SMC are strong Pb producers. This conflicts with current theoretical predictions.

AUTHOR CONTRIBUTIONS

K. De Smedt determined the Pb abundance upper limits of all four Magellanic Cloud post-AGB stars. All authors, and especially H. Van Winckel and L. Siess, contributed to the content and phrasing of the final text. The referred theoretical AGB model prediction and hence contributions of co-authors, are the same as in Chapter 3.

4.1 Introduction

During the asymptotic giant branch (AGB), stars undergo thermal pulses that may be followed by third dredge-ups during which freshly synthesized products are brought into the envelope, among them the carbon and *s*-process elements. Theoretical and observational evidence shows that the main neutron source in low-mass AGB stars (1-3 $M_{\odot}$) is the $^{13}C(\alpha,n)^{16}O$ reaction (Straniero et al. 1995; Gallino et al. 1998; Abia et al. 2002). It is widely accepted that the ^{13}C pocket originates in a region where protons from the H-rich convective envelope are mixed into the He-rich intershell after a thermal pulse. However, the physical mechanisms of both third dredge-up and partial mixing in the intershell remain poorly understood.

The *s*-process nucleosynthesis is predicted to depend strongly on metallicity while the ^{12}C component, hence the ^{13}C neutron source, in the intershell are of primary origin. In metal-deficient environments ([Fe/H] < -1), in proportion, more neutrons are available for each iron seed resulting in larger overabundances of heavy *s*-process elements with respect to lighter ones ([hs/ls]). However, to date no clear relation has been observed between [hs/ls] and metallicity (see e.g. Fig 10 in van Aarle et al. (2013)) in post-AGB stars. The end product of the *s*-process nucleosynthesis chain is the double magic lead ^{208}Pb isotope, which is predicted to have large overabundances with respect to other s-elements in metal-poor conditions (see Gallino et al. (1998),Goriely & Mowlavi (2000) and (Lugaro et al. 2012, and references therein)). The detection of metal-deficient objects with strong Pb enhancement by e.g. Van Eck et al. (2001, 2003) and Behara et al. (2010) confirm these predictions. However, some low-metallicity extrinsically *s*-process enriched objects (i.e. binaries) were found without strong Pb overabundance (Aoki et al. 2001; Van Eck et al. 2003). These are just a few illustrations that show that our understanding of the *s*-process nucleosynthesis is limited. Additional systematic observations are required to deduce *s*-process distributions, including Pb abundances, to improve our understanding of the third dredge-up and AGB nucleosynthesis mechanisms (e.g. Herwig 2005, and references therein).

In De Smedt et al. (2012) (paper I), we performed an extensive spectral abundance analysis of the Small Magellanic Cloud (SMC) post-AGB object J004441.04-732136.4 (hereafter abbreviated to J004441). As a 21 μm source (Volk et al. 2011), J004441 shows very strong *s*-process enhancement combined with a low metallicity of [Fe/H] = -1.34 ± 0.32 and a modest C/O ratio of 1.9 ± 0.7. A luminosity of 7600 ± 200 $L_{\odot}$ was derived with the known distance to the SMC. Comparison of the position of J00441 in the HR diagram to evolutionary post-AGB tracks of Vassiliadis & Wood (1994) resulted in an estimated initial mass of approximately 1.3 $M_{\odot}$. Based upon the initial mass and metallicity, different theoretical models were calculated with two independent

stellar evolution codes, namely the Mount-Stromlo Evolutionary code (Karakas 2010, and references therein) and the STAREVOL code (e.g. Siess 2007, and references therein). The theoretical predictions match the *s*-process distribution but fail to reproduce the high overabundances and the modest C/O ratio. All models predict strong Pb overabundances but unfortunately, the strongest spectral Pb line at 4057.807 Å was only covered by a very low S/N spectrum, preventing an accurate Pb abundance determination with the data of Paper I. We therefore reanalysed the Pb abundance of J004441 using a newly obtained UVES spectrum which is described in this letter.
In addition, we determine upper limits for the Pb abundances for three Large Magellanic Cloud (LMC) post-AGB objects. Accurate spectral abundance studies of these objects have been conducted by van Aarle et al. (2013), but Pb was not included in their analysis. Comparison of the different Pb enhancements will provide insight into the intrinsic enrichment of metal-poor, low-mass AGB objects.
In the following section, we report on the new data and Section 3 describes our analysis and abundance determination. We compare the results of J004441 with model predictions in Section 4, followed by analyses of the Pb abundances for the LMC objects in Section 5. We end with a brief discussion.

4.2 Observations and data reduction

We use high-resolution spectra obtained with the UVES spectrograph (Dekker et al. 2000) mounted on the VLT. Apart from the UVES spectra used in Paper I, we obtained a new UVES spectrum with an exposure time of 1500 seconds. The dichroic beam splitter was used, which provided a wavelength coverage from approximately 3760 to 4985 Å for the blue arm and 6705 to 8513 Å and 8663 to 10420 Å for the lower and upper parts of the mosaic CCD chip, respectively. This results in a wavelength range overlap with the Paper I spectra of 3760 to 4530 Å, 4780 to 4985 Å, and 6705 to 6810 Å.
Reduction of the UVES data is performed using the Reflex environment. In an attempt to optimize the S/N of the blue spectra, the new blue spectrum is reduced using different settings for the slit length and wavelength bin size in the reduction pipeline. Then the S/N of the different spectra are determined by computing the standard deviation obtained in different continuum regions in the wavelength range from 4800 Å to 4950 Å. This wavelength range is present in both the old and new spectra. For the new data, the best S/N was found for the standard parameter settings in the pipeline. Based upon the S/N results for the new data, the spectra of Paper I are also reduced again using the standard parameter settings in the pipeline.

Table 4.1: Determined atmospheric parameters of J004441 in Paper I and three LMC objects of van Aarle et al. (2013).

	J004441	J050632	J052043	J053250
$T_{\rm eff}$ (K)	6250 ± 250	6750 ± 250	5750 ± 250	5500 ± 250
log g (dex)	0.5 ± 0.5	0.5 ± 0.5	0.0 ± 0.5	0.0 ± 0.5
ξ_t (km/s)	3.5 ± 0.5	3.0 ± 0.5	3.0 ± 0.5	3.0 ± 0.5
[Fe/H] (dex)	-1.34 ± 0.32	-1.22 ± 0.18	-1.15 ± 0.20	-1.22 ± 0.19
$L/L_\odot$	7600 ± 200	5400 ± 700	8700 ± 1000	6500 ± 1000

The different blue spectra are then merged into a weighted mean spectrum. The weights are based upon the S/N quality. A small spectral window of 50 Å around the strongest 4057.807 Å Pb line is then normalized by fitting a fifth order polynomial through interactively defined continuum points. The final S/N of this combined spectrum is ~ 25 in the region of the Pb line.
The velocity correction for the new data is exactly the same as for the previous data hence a heliocentric radial velocity of 148 ± 3 km/s is applied. This constant velocity suggests J004441 to be either a single star or a binary in a wide orbit.

4.3 Spectral analysis of Pb in J004441

For clarity, Table 4.1 shows the atmospheric parameters of J004441 (determined in Paper I), together with the derived parameters of three LMC objects from van Aarle et al. (2013), which is discussed below. We assume [Fe/H] as an accurate value of the mean metallicity of the stars. For all objects, we redid neither the atmospheric parameter determination nor the abundance analysis of already determined elements.
The merged spectrum quality is sufficient to determine an upper limit of the Pb abundance using the region around the 4057.807 Å line. We used an LTE Kurucz-Castelli atmosphere model (Castelli & Kurucz 2004) with the atmospheric parameters shown in Table 4.1, combined with the LTE abundance calculation program MOOG (Sneden 1973) and VALD linelists (Kupka et al. 1999). The studied elemental abundances in Paper I, together with an overall metallicity [M/H] = -1.34 dex, are included in the spectral synthesis fit of the Pb line. Possible non-LTE effects are not taken into account.
Figure 4.1 displays the spectral synthesis fits to the Pb line in J004441. The coloured spectra represent different abundance values for Pb with all other

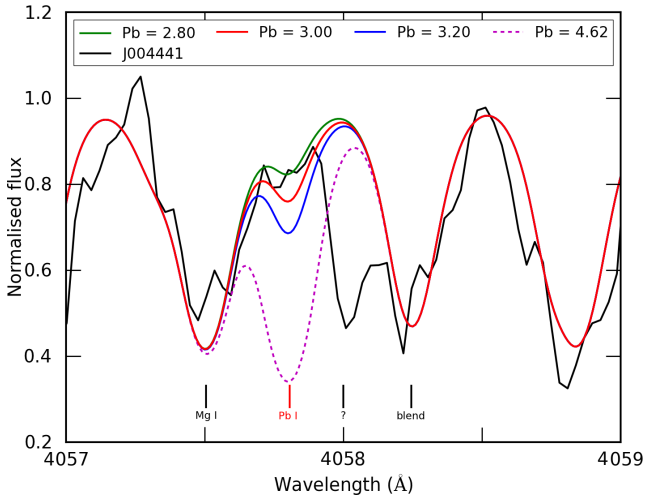

Figure 4.1: Upper limit Pb abundance determination of J004441 using spectrum synthesis. The black spectrum is J004441 while coloured spectra represent synthetic spectra with different Pb abundances. Full coloured lines are used for the upper limit Pb abundance determination, the dashed magenta line represents the line when assuming an Pb abundance as predicted by the best fitting AGB model (see Sect. 4). The question mark indicates the position of an unidentified spectral line.

elemental abundances constant. The upper limit for the Pb abundance is derived by comparison with the full coloured lines. It is difficult to determine the continuum level accurately. The fit of the Mg I line to the left of the Pb line and the blended line at 4058.2 Å are used as estimates of the continuum position. The question mark in Fig.4.1, indicates the wavelength position of a spectral line which remains unidentified despite our efforts. Manually increasing the input abundance of all available elements in the region of this line did not change the synthetic spectrum, so we conclude that this line is not present in the VALD linelist. In strongly *s*-process enhanced photospheres, the mere line identification is often problematic (e.g. Reyniers et al. 2002). Considering the strong *s*-process enrichment of J004441, this line is probably an unidentified *s*-process spectral line. The identification of this spectral line is essential for constraining a more accurate Pb abundance, and it allows us to set an upper limit for the Pb abundance around $\log_\epsilon$ (Pb) = 3.0 ($\log_\epsilon$ (H) = 12.0).
To test the abundance fit, we replaced the VALD Pb line in the VALD linelist by the analogue Pb line from the NIST Atomic Spectra Database (Kramida et al. 2013) and the Pb line analogue from the Pb line list used in Van Eck et al. (2003).

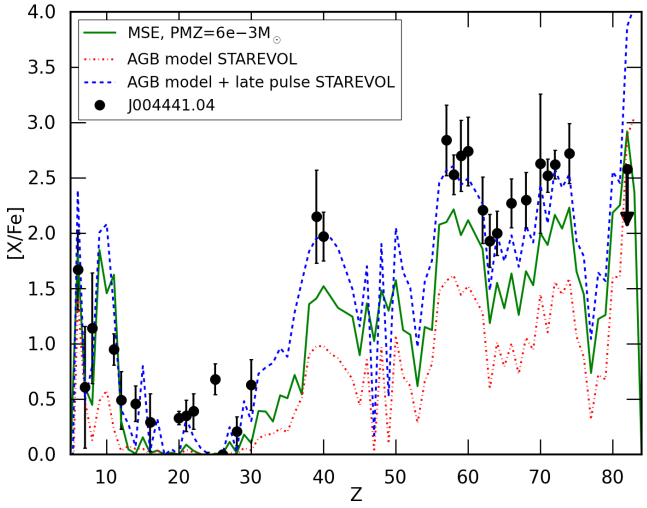

Figure 4.2: Comparison of the J004441 abundance ratios with model predictions. Black dots represent the [X/Fe] results of J004441, the green line represents the Mount Stromlo (MSE) model, red and blue dashed lines show STAREVOL code predictions with the latter including a late thermal pulse with a deep dredge-up when dilution is small. The [Pb/Fe] result is indicated with a down arrow, representing an upper limit.

The oscillator strengths (log gf) for the VALD, NIST, and Van Eck linelists for the Pb line are -0.17, -0.18 and -0.22, respectively, while the excitation potential is 1.32 eV for all linelists. This results in a maximal abundance difference of 0.05 dex, which is neglible with respect to the uncertainty due to the continuum position. Also the isotopic Pb line list of Van Eck et al. (2003) was fitted assuming solar isotope ratios and obviously resulted in an even lower Pb abundance upper limit, which seems improbable considering the Pb abundance discrepancy in Sect. 4.4. We therefore adopt a Pb abundance of $\log_\epsilon(\mathrm{Pb}) = 3.0$ for comparison with AGB models.

The nitrogen (N) abundance is also derived using spectral synthesis. In Paper I, no clear N lines were detected in the optical part of the spectra. However, the new spectra cover a wider wavelength range towards the IR, displaying clear unblended N lines. Based upon the analysis of five spectral lines, we find $\log_\epsilon$ (N) = 7.10 ± 0.32 where the error contains model, line-to-line scatter, and non-LTE uncertainties. We apply a non-LTE correction of 0.3 dex as found in Lyubimkov et al. (2011) to similar objects and adopt this value as the non-LTE uncertainty.

Table 4.2: [s/Fe] results for specific s-elements of the studied objects.

	[La/Fe]	[Ce/Fe]	[Nd/Fe]	[Pb/Fe]
J004441	2.84 ± 0.32	2.53 ± 0.18	2.74 ± 0.31	<2.58
J050632	1.48 ± 0.25	1.33 ± 0.23	1.18 ± 0.31	<1.52
J052043	1.85 ± 0.24	1.68 ± 0.20	1.92 ± 0.26	<1.40
J053250	2.03 ± 0.26	1.91 ± 0.20	2.02 ± 0.24	<1.70

4.4 AGB chemical models

We compare the newly derived abundance results with model predictions from two independent stellar evolution codes of Paper I. Both codes calculated models for a 1.3 $M_{\odot}$ star of [Fe/H] = -1.4 for which the calculated AGB tip luminosities are somewhat higher than the observed luminosity. The luminosities can be fine-tuned by increasing the mass-loss rate, but this should not alter the predicted abundance profiles.

The observed abundances compared to model predictions are shown in Fig. 4.2 where different coloured lines represent different model predictions. The derived [Pb/Fe] upper limit of J004441 is indicated with a down arrow. The Mount-Stromlo Evolutionary (MSE) predictions (Karakas 2010, and references therein) are calculated for a metallicity of Z = 0.0006, while both STAREVOL code predictions (e.g. Siess 2007, and references therein) have a reference composition of Z = 0.0044 (see Paper I) and are calculated using the same parameter values. The red STAREVOL model includes a late thermal pulse combined with a deep dredge-up, resulting in substantial surface pollution due to the low convective envelope mass. A detailed description of the conclusions drawn from Fig. 4.2 for C, O, and s-elements except Pb, is given in Paper I and will not be repeated in this letter.

The dashed magenta line in Fig. 4.1 is computed using the [Pb/Fe] = 4.62 as predicted from the best fitting AGB model in Fig. 4.2 and clearly shows that such a high Pb abundance is incompatible with our spectrum. Figure 4.2 also indicates that the Pb overabundance is similar to that of the other heavy *s*-process peak elements (La, Ce and Nd around Z=60). The newly derived N abundance (Z = 7) fits the different model predictions well.

4.5 LMC objects

To expand the sample of studied Pb abundances in *s*-process enriched post-AGB stars, Pb abundance upper limits are derived for three LMC objects studied by van Aarle et al. (2013) (Paper II). These three objects are J050632.10-714229.8, J052043.86-692341.0, and J053250.69-713925.8, hereafter respectively abbreviated to J050632, J052043, and J053250. For the Pb abundance analysis, we use the normalized spectra of Paper II. For J052043, two studies were conducted in Paper II of which we use the spectra observed in December (J052043_b in Paper II). Table 4.1 shows the atmospheric parameters of the three objects. All objects are found to be metal-poor and to have initial masses below 1.5 $M_{\odot}$. In none of the objects is the Pb line clearly detected.
Similar to the study of J004441, spectral synthesis is used for the Pb abundance determinations of the three LMC objects. Table 4.2 lists the [s/Fe] determinations for Ba-peak elements, along with the Pb abundance upper limits. The shown abundance results of the three LMC objects are derived in Paper II, except for Pb. For none of the objects is the [Pb/Fe] uncertainty larger than 0.08 dex due to model uncertainties. The [s/Fe] results for all studied s-elements of the different objects are shown in the upper panel of Fig. 4.3. For a given metallicity, the overabundances depend on the amount of dilution in the envelope mass. Therefore, the lower panel of Fig. 4.3 shows the [s/Fe] results scaled to [La/Fe] of J052043 to show the *s*-process distribution of the different stars independent of dilution. From Table 4.2 and Fig. 4.3, we conclude that for J004441 and J050632, the Pb upper limit overabundance is similar to the overabundances of the Ba-peak elements, while for J052043 and J053250, Pb is modestly underabundant with respect to Ba-peak elements.

4.6 Discussion and conclusion

Using additional spectra of J004441, an *s*-process rich post-AGB star in the SMC, we obtained an upper limit of the Pb abundance. With [Pb/Fe] < 2.58, Pb shows a similar or smaller overabundance than the *s*-process elements of the Ba-peak. However, this upper limit is much smaller than predicted by our specific AGB models. The latter were tuned to the initial mass and metallicity of the object and focussed on a fit through the obtained overabundances of the Zr- and Ba-peak elements. This discrepancy is real and not due to the poor S/N of the spectrum. The *s*-process predictions of the tuned AGB models, based on successive thermal pulses with associated partial mixing and dredge-ups are not able to reproduce the low Pb abundance.
The [Pb/Fe] results for the three LMC objects are similar to J004441: there is

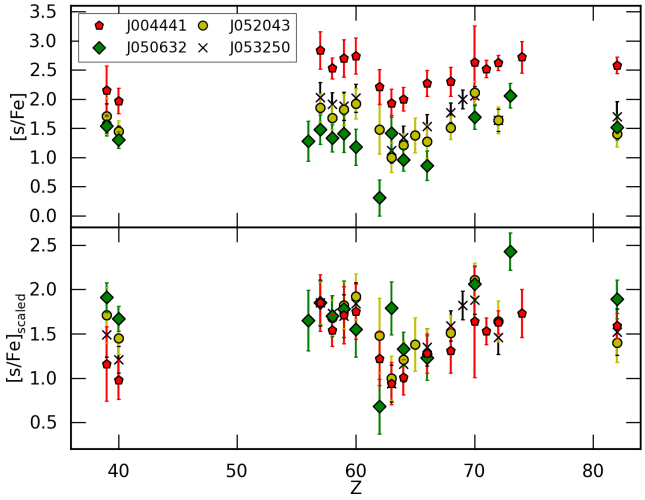

Figure 4.3: Upper panel: Overview of [s/Fe] for the different objects. The values at Z=82 represent the derived Pb abundance upper limits. Lower panel: [s/Fe] for the different objects scaled to [La/Fe] at Z=57.

no predicted high Pb overabundance relative to the Ba-peak elements. Although having a strong *s*-process enrichment, the four low-mass, metal-deficient post-AGB stars of the Magellanic clouds all show the absence of the theoretically predicted strong Pb overabundances. This trend is similar to what is observed in some, but not all, extrinsically enriched objects in Aoki et al. (2001) and Van Eck et al. (2003). Current AGB models based on a ^{13}C-pocket arising from diffusive overshooting at the base of the convective envelope during the third dredge-up have problems reproducing the observed low Pb abundances in metal poor stars, the spread in [hs/ls] at a given metallicity and/or the C/O ratios. This clearly indicates that some physical ingredients are missing in the description of this process. To improve the situation, we need to obtain full abundance patterns of many post-AGB stars in both the LMC and SMC, so that we can identify systematics in the observed patterns. Simultaneously, we need to explore alternative processes to explain the derived abundance profiles. In this study, we used the diffusive approach to form the ^{13}C pocket, but the partial mixing of protons below the envelope may not be diffusive in essence but rather advective. For instance, when adopting a new mixing algorithm, Straniero et al. (2006) were able to generate a more massive ^{13}C pocket and consequently produce higher *s*-process surface enrichments in better agreement with observations. Rotation is also a key physical ingredient that may have a strong impact on the synthesis of *s*-elements. Depending on the degree

of shear, the *s*-process nucleosynthesis can be completely inhibited (see e.g. Langer et al. (1999), Herwig et al. (2003) and Siess et al. (2004)) or partially activated (Piersanti et al. 2013). Also the effect of internal gravity wave mixing (Denissenkov & Tout 2003) on the *s*-process nucleosynthesis still needs to be explored.

Additional work, both theoretically assisted by direct hydrodynamical simulations and observational with systematic abundance determinations of a whole population of post-AGB stars with well constrained distances and a spread in metallicity, is needed to better constrain the *s*-process mechanisms.

Chapter 5

Detailed abundance study of two post-AGB stars in the LMC

This chapter is accepted for publication in Astronomy & Astrophysics, under the name:

Chemical abundance study of two strongly *s*-process enriched post-AGB stars in the LMC: J051213.81-693537.1 and J051848.86-700246.9

K. De Smedt, H. Van Winckel, D. Kamath, P. R. Wood

ABSTRACT

Context: This paper is part of a larger project in which we systematically study the chemical abundances of extra-galactic post-asymptotic giant branch (post-AGB) stars. The aim of our programme is to derive chemical abundances of stars covering a large range in luminosity and metallicity with the ultimate goal to test, constrain and improve our knowledge of the poorly understood AGB phase, especially the third dredge-up mixing processes and associated

s-process nucleosynthesis.

Aims: Post-AGB photospheres are dominated by atomic lines and display the effects of internal chemical enrichment processes over the entire stellar lifetime. In this paper, we study two carefully selected post-AGB stars, J051213.81-693537.1 and J051848.86-700246.9, in the Large Magellanic Cloud (LMC). Both objects show signs of *s*-process enhancement. The combination of favourable atmospheric parameters for detailed abundance studies and their known distances (and hence luminosities and initial masses), make these objects ideal probes of the AGB third dredge-up and *s*-process nucleosynthesis by providing observational constraints for theoretical AGB models.

Methods: We use high-resolution optical UVES spectra to determine accurate stellar parameters and subsequently perform detailed elemental abundance studies of post-AGB stars. Additionally, we use available photometric data covering optical and IR bands to construct spectral energy distributions for reddening and luminosity determinations. We then estimate initial masses from theoretical post-AGB tracks.

Results: We obtained accurate atmospheric parameters for J051213.81-693537.1 ($T_{\rm eff}$ = 5875 ± 125 K, log g = 1.00 ± 0.25 dex, [Fe/H]= −0.56 ± 0.16 dex) and J051848.86-700246.9 ($T_{\rm eff}$ = 6000 ± 125 K, log g = 0.50 ± 0.25 dex, [Fe/H]= −1.06 ± 0.17 dex). Both stars show extreme *s*-process enrichment associated with relatively low C/O ratios of 1.26 ± 0.40 and 1.29 ± 0.30 for J051213-693537.1 and J051848-700246.9 respectively. We could only derive upper limits of the lead (Pb) abundance. These upper limits show a possible very slight Pb overabundance with respect to heavy *s*-elements for J051213-693537.1, while J051848-700246.9 shows an upper limit of the Pb abundance similar to [hs/Fe]. Comparison with theoretical post-AGB evolutionary tracks in the HR-diagram reveals that both stars have low initial masses between 1.0 and 1.5 $M_{\odot}$.

Conclusions: This study adds to the results obtained so far on a very limited number of *s*-process enriched stars in the Magellanic Clouds. With the addition of the two stars in this study, we find an increasing discrepancy between observed and predicted Pb abundances towards lower metallicities of the studied *s*-process rich post-AGB stars in the Magellanic Clouds. The more metal-rich J051213-693537.1 fits well the theoretical Pb abundance predictions, while the five other objects with [Fe/H] < 1, including J051848-700246.9, have much lower Pb overabundances than predicted. In all objects found so far, including the objects in this study, the C/O ratio is very moderate due to the

enhancement of O as well as C. We find that all *s*-process rich stars in the LMC and SMC studied till now, cluster in the same region of the HR-diagram and are associated with low-mass stars with a low metallicity on average. We corroborate the published lack of correlation between the metallicity and the neutron irradiation, while the neutron exposure ([hs/ls]) is strongly correlated with the third dredge-up efficiency ([s/Fe]). These correlations seem to hold in our Galaxy as well as in the Magellanic Clouds.

AUTHOR CONTRIBUTIONS

K. De Smedt reduced the data and performed the full analysis of both stars. The bulk of the text was written by K. De Smedt with the assistance of H. Van Winckel, D. Kamath and P. R. Wood. All authors contributed to the content, layout and phrasing of the final text.

5.1 Introduction

Post-asymptotic Giant Branch (post-AGB) stars are low- to intermediate-mass stars ($M \leqslant 8M_{\odot}$) in a transient evolutionary phase between the Asymptotic Giant Branch (AGB) and the White Dwarf (WD) phase. In single stars, a superwind mass-loss terminates the AGB phase after which the star evolves on to the post-AGB phase, eventually cooling down as a white dwarf. During the AGB phase, the endproducts of internal chemical processes like C,N,O and *s*-process elements are transported to the stellar surface by multiple dredge-up events, called the third dredge-up (TDU). The *s*-process synthesis in AGB stars is an important contributor to the cosmic abundances past the iron peak and these stars are also expected to be important contributors to the cosmic carbon and nitrogen enrichment (e.g Romano et al. 2010; Kobayashi et al. 2011).

Photospheric spectra of AGB stars are dominated by molecular bands and they are often veiled by circumstellar dust making it difficult to study abundances of individual elements (e.g. Abia et al. 2008). However, post-AGB spectra are dominated by atomic transitions allowing extensive abundance studies of individual elements. Their photospheres bear witness to the total chemical

changes accumulated during the stellar lifetime, making them ideal tracers for the study of AGB nucleosynthesis and associated TDUs.

Chemical studies of Galactic post-AGB stars show a large variety of chemical abundance patterns (e.g. Van Winckel 2003, and references therein). Only about 25% of the studied Galactic post-AGB stars display strong *s*-process enrichment (e.g. Rao et al. 2012, and references therein). Although stars in the Galactic sample of post-AGB stars are well studied, their unknown distances hamper accurate luminosity determinations and hence accurate initial mass estimates which are a key parameter in constraining single star evolution and nucleosynthesis AGB models.

One way to overcome this distance problem, is to study post-AGB stars in the Magellanic Clouds. The distances to the Magellanic Clouds are well known, with the LMC at a distance of about 50 kpc (Keller & Wood 2006; Reid & Parker 2010; Storm et al. 2011) and the SMC at a distance of about 60 kpc (Keller & Wood 2006). Furthermore, the Magellanic Cloud stars generally have lower mean metallicities than their Galactic counterparts, with a mean metallicity of $\sim$-0.5 dex for the LMC (e.g. Geisler et al. 2009; Lapenna et al. 2012) and $\sim$-0.7 dex for the SMC (Luck et al. 1998). This allows for the study of post-AGB stars in a broad metallicity range.

Therefore, we initiated a larger project in which we search for post-AGB stars in the Magellanic Clouds and then use these objects to study the poorly understood AGB TDUs and *s*-process nucleosynthesis. van Aarle et al. (2011) and Kamath et al. (2015, accepted), provide catalogues of spectroscopically verified optically visible post-AGB candidates in the Large Magellanic Cloud (LMC) and Kamath et al. (2014) provides a catalogue of spectroscopically verified optically visible post-AGB candidates in the Small Magellanic Cloud (SMC).

In this paper, we present the detailed chemical study of two newly identified LMC post-AGB candidates that were carefully selected (based on their stellar parameters and spectral features) from our optically visible post-AGB LMC catalogues.

Our previous abundance studies of strongly *s*-process enriched post-AGB stars in the Magellanic Clouds by De Smedt et al. (2012), van Aarle et al. (2013) and De Smedt et al. (2014) show that there are still large decrepancies between observed abundances and theoretical predictions. The biggest discrepancies are related to the C/O ratio since observationally derived C/O ratios are small in comparison to the theoretical predictions. The theoretical carbon abundance is often overestimated, whereas the derived oxygen abundance is larger than predicted. Also lead (Pb, Z=82), which is considered to be the end product of the *s*-process chain due to its double magic number, is strongly overestimated

Table 5.1: Overview of observations. 'Exp. Time' represents the exposure time. The Red arm is the combination of the lower and upper part of the mosaic CCD chip. V represents the visual magnitude.

Object name (IRAC)	Exp. time (s) Blue arm	Exp. time (s) Red arm	V mag
J051213.81-693537.1	6 × 1500	6 × 1500	15.7
J051848.86-700246.8	1 × 1500	2 × 1500	15.5

by theoretical models as shown in De Smedt et al. (2014).

We describe the observations and data reduction of both objects in Sect. 5.2. Detailed abundance analysis of the obtained spectra is presented in Sect. 5.3 followed by the discussion of the abundances in Sect. 5.4. Luminosity determinations and initial mass estimates are presented in 5.5. We discuss the neutron irradiation of our sample stars in Sect. 5.6. Finally, we end with a brief discussion and conclusions in Sect. 5.7.

5.2 Observations and data reduction

We obtained high-resolution spectra using the UVES echelle spectrograph (Dekker et al. 2000), mounted on the 8m UT2 Kueyen Telescope of the VLT array at the Paranal Observatory of ESO in Chili. We selected the dichroic beam-splitter resulting in a wavelength coverage for the blue arm from approximately 3280 to 4530 Å, and in the red arm for the lower and upper part of the mosaic CCD chip from approximately 4780 to 5770 Å and from 5800 to 6810 Å respectively. A slit width of 1 arcsecond was used as compromise between spectral resolution and slit-loss minimalisation. An overview of the observations is given in Table 5.1. For J051848.86-700246.8 (hereafter abbreviated to J051848), only one blue spectrum was available due to an instrumental error. For J051213.81-693537.1 (hereafter abbreviated to J051213), two additional spectra were also obtained but due to the significant lower quality with respect to the six other spectra, these two spectra are not used for this study. The spectra of each object were obtained in one night and in one large time interval.

The data was reduced using the UVES pipeline (version 5.3.0) in the Reflex environment of ESO [1]. This reduction includes the standard steps of extracting frames, determining wavelength calibration, applying this scale to flat-field

[1] https://www.eso.org/sci/software/reflex/

divided data and cosmic-clipping. The standard reduction parameters of the UVES pipeline were used as these gave the best signal-to-noise (S/N) of the final spectra.

After reduction, weighted mean spectra were calculated for the three wavelength ranges. Since all spectra were taken in small time intervals, no velocity corrections were needed for calculating the weighted mean. These weighted mean spectra were then divided into subspectra, each with a fixed wavelength range of 120 Å for which the first and last 10 Å overlapped with the previous and subsequent spectra. Each of these subspectra was normalised individually by fitting fifth order polynomials through interactively defined continuum points. All subspectra were then again merged into one large spectrum which is used for the spectral analysis. In the wavelength regions where the subspectra overlapped, the mean flux was calculated.

We note that the wavelength range from 3280 to about 3900 Å has a poor S/N making it unsuitable for accurate spectral analysis. We therefore did not use this spectral region in the analysis. The mean S/N in the remaining wavelength range of the blue spectrum is about 25 for both stars. The red spectra have a higher mean S/N between 80 and 100. The high resolution of the UVES spectra permits accurate radial velocity determinations by using the positions of spectral lines. Line positions are measured by fitting a Gaussian through the measured line profiles, line identification is based upon the rest wavelengths from the VALD database Kupka et al. (1999). We find a radial velocity of 227.8 $\pm$ 1.9 km/s for J051848 and a radial velocity of 284.3 $\pm$ 1.0 km/s for J051213. Both radial velocities are consistent with the average radial velocity of the LMC, which is approximately 270 km/s (van der Marel et al. 2002).

5.3 Spectral analyses

A visual inspection of the UVES spectra immediately shows the very strong *s*-process enrichment for both objects. The panels in Fig. 5.1 show different wavelength regions of J051213 and J051848. Both figures also show the corresponding spectral region of J004441.04-732136.4 (J004441), which is a strongly *s*-process enhanced SMC post-AGB star (De Smedt et al. 2012). All three objects have similar atmospheric parameters except for the metallicity as described in Sect. 5.3.1. Both J051213 and J051848 display strong Ba II (lower panel in Fig 5.1) and Y II (upper panel in Fig 5.1) lines, a clear indication of *s*-process enrichment. Although J051213 and J051848 are members of the LMC, while J004441 is an SMC object, they have similar spectra.

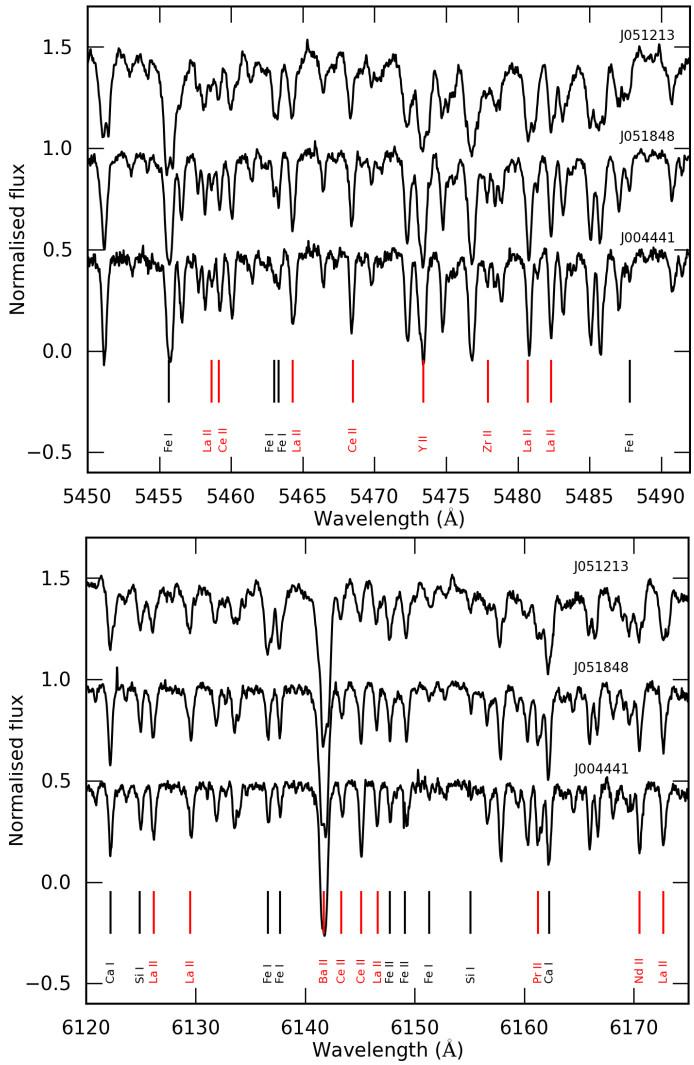

Figure 5.1: Comparison of the normalised spectra of J051213 (upper spectrum), J051848 (middle spectrum) and J004441 (lower spectrum) for two different wavelength ranges. The upper and lower spectra have been shifted in flux for clarity and all spectra are shifted to a zero velocity. Red and black vertical lines mark positions of *s*-nuclei and non *s*-nuclei respectively. See text for more information.

The spectral analyses includes atmospheric parameter and abundance determination. We use PyMOOG, our own Python wrapper around the local thermal equilibrium (LTE) abundance calculation routine MOOG (version June 2014 Sneden 1973). For the analyses of our two LMC stars, we use the LTE Kurucz-Castelli atmosphere models (Castelli & Kurucz 2004). As with the radial-velocity determination, spectral lines are identified using linelists from the VALD database (Kupka et al. 1999). We combine the VALD linelists with a list of lines that has been gathered at the Instituut voor Sterrenkunde for the chemical analysis of A, F and G stars (Van Winckel & Reyniers 2000). The linelists implemented in PyMOOG cover a wavelength range from 3000 up to 11000 Å. This covers the full wavelength coverage of the UVES spectra, and allows for the identification of spectral lines of about 160 ions ranging from He (Z=2) up to U (Z=92). We included neutral and firstly ionised ions for most of the elements. For some *s*-process elements, the second ionisation is included although the effective temperatures of the two sample stars in this study are too low for these ionisations.

The equivalent width (EW) of spectral lines are measured interactively with PyMOOG. The EWs are calculated by direct integration. The abundances are computed by an iterative process in which the theoretical EWs of single lines are computed for given abundances and matched to the observational EWs. For our analysis, we avoided blended lines as much as possible. Synthetic spectra were used for checking whether used spectral lines are part of blends with other identified lines.

5.3.1 Atmospheric parameters

The atmospheric parameters are determined using the atmospheric parameter determination module in PyMOOG. We use linear interpolation to calculate atmospheric models which are within the parameter steps of the Kurucz-Castelli models. For the determination of the effective temperature and surface gravity $\log g$, we use parameter steps of 125 K and 0.5 dex respectively. For the microturbulent velocity, we choose steps of 0.2 km/s.

To derive the atmospheric parameters we use Fe I and Fe II lines. The effective temperature $T_{\rm eff}$ is determined by enforcing the iron abundance, derived from the individual Fe I lines, to be independent of lower excitation potential. We choose Fe I lines for this purpose since the available Fe II lines do not cover an appropiate range in lower excitation potential. The surface gravity $\log g$ is determined by enforcing ionisation equilibrium between the individual Fe I and Fe II abundances. The microturbulent velocity ξ_t is derived by enforcing

Table 5.2: Determined atmospheric parameters of J051213 and J051848. The errors for [Fe/H] include line to line scatter and model uncertainty. N_{FeI} and N_{FeII} show the number of lines used for Fe I and Fe II respectively.

Object	J051213	J051848
T_{eff} (K)	5875 ± 125	6000 ± 125
$\log g$ (dex)	1.00 ± 0.25	0.50 ± 0.25
ξ_t (km/s)	3.0 ± 0.2	2.8 ± 0.2
[FeI/H]	-0.56 ± 0.16	-1.06 ± 0.17
[FeII/H]	-0.56 ± 0.15	-1.03 ± 0.14
N_{FeI}	53	35
N_{FeII}	13	9

the iron abundance from individual Fe I lines to be independent of reduced equivalent width which we define in this contribution as EW/λ.

The individual atmospheric parameter results together with the number of used individual spectral lines are shown in Table 5.2. The indicated uncertainties of [FeI/H] and [FeII/H] are the total errors on the iron abundances which includes line-to-line scatter and the atmospheric parameter uncertainties as described below in Sect. 5.3.2. The metallicity of J051213 is similar to the mean LMC metallicity of -0.4 dex, while J051848 has a significantly lower metallicity.

Both stars are of spectral type F and have low surface gravities confirming their evolved nature. The effective temperatures of both stars could be determined accurately. Kamath et al. (2015) estimate stellar parameter for J051848, based on low-resolution spectra. We find that the derived stellar parameters of our study and those of Kamath et al. (2015) agree well within the estimated errors.

5.3.2 Abundance determination

We use the derived atmospheric parameters in Table 5.2 for the abundance determination using PyMOOG. We mainly use isolated non-blended, non-saturated lines but due to the rich spectra with strong enhancements this is a challenge. However, with spectral synthesis, we determine the abundances of ions which can only be found in blends. Lines with EWs smaller than 5 mÅ are not used as they may be confused with noise in the spectra.

Only a few carbon and oxygen lines are available for abundance determination because most of the lines are severly blended. For J051213, where only one

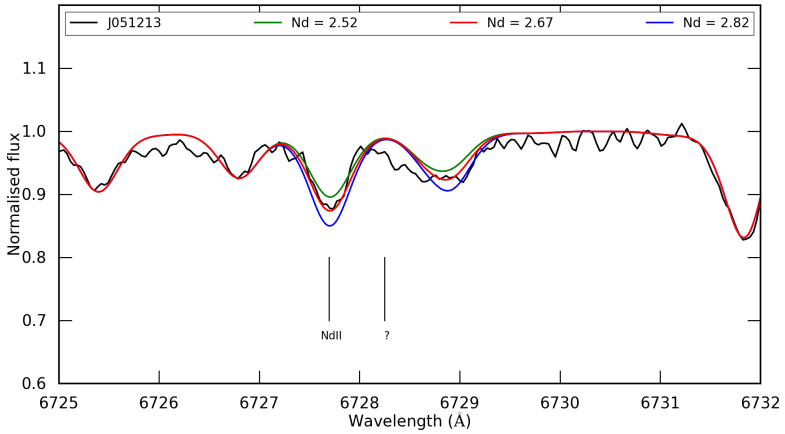

Figure 5.2: Spectrum synthesis of the Nd II line at 6727.695 Å for J051213. The black spectrum is the observed spectrum, the colored spectra represent synthetic spectra with different Nd abundances. The position of the Nd line is indicated. For more information, see text.

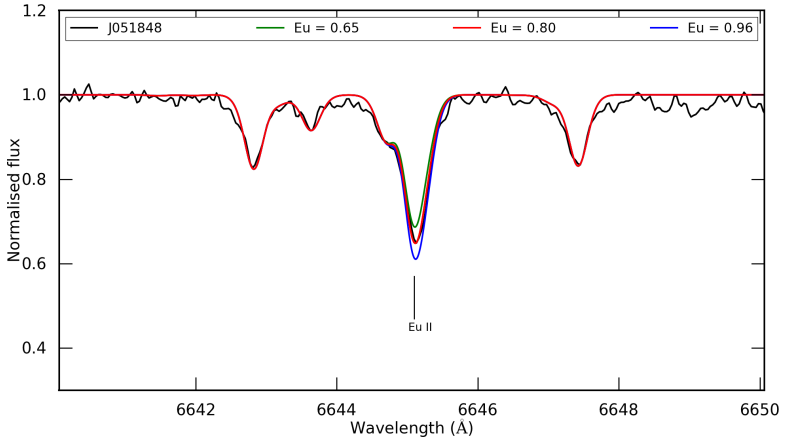

Figure 5.3: Spectrum synthesis of the Eu II line at 6645.064 Å for J051848. The black spectrum is the observed spectrum, the colored spectra represent synthetic spectra with different Eu abundances. The position of the Eu line is indicated. For more information, see text.

spectral line was available for both the C and O abundances, these abundances were determined using spectral synthesis. The O abundance of J051213 is determined using the forbidden [O I] line at 6300 Å which is part of a fully identified blend. This line is not sensitive to non-LTE effects (e.g. Kiselman 2002). For J051848, we found four useful lines for carbon and two non-forbidden O I lines. For both stars, nitrogen lines larger than 5 mÅ are not found in the available wavelength coverage of the UVES spectra.

The spectra of both objects allowed abundance determinations of many elements past the iron peak. Unfortunately, all available Sr and Ba lines are heavily saturated hampering accurate abundance determinations for these two *s*-process elements. Most of the other studied *s*-elements abundances are determined from multiple, unblended lines. Apart from the light *s*-process (ls) peak elements Y and Zr, and heavy *s*-process (hs) peak elements La, Ce, Pr and Nd, we find abundances for heavier elements like gadolinium (Gd, Z=64), dysprosium (Dy, Z=66), erbium (Er, Z=68), thulium (Tm, Z=69), luthetium (Lu, Z=71) and hafnium (Hf, Z=72).

To illustrate our analyses, in Fig. 5.2, we show the comparison between synthetic spectra with different Nd abundances for J051213 around the Nd II line at 6727.695 Å. The red line represents the best synthetic fit to the observations. The figure shows that our derived abundances reproduce well the observed spectral lines. A similar fit for the Eu II line at 6645.064 Å for J051848 is shown in Fig. 5.3.

Pb is a very important tracer of the *s*-process nucleosynthesis. Unfortunately, at the photospheric conditions of our stars, the useful Pb lines are in the very blue. Due to the low S/N around the strongest Pb I line at 4057.807 Å, it is difficult to determine accurate lead (Pb, Z=82) abundances for both sample stars, therefore we prefer to determine Pb abundance upper limits. For J051213, the S/N is poor as can be seen in Fig. 5.4. The combination of many unidentified spectral lines, i.e. lines not included in the linelists, and the poor S/N make it difficult to determine the position of the continuum. For some unidentified lines, we mark the positions indicated with question marks.

For J051848, the S/N is higher, but again many unidentified lines are present in the spectral region (as shown in Fig. 5.5). For both stars, we use the spectral blended lines at 4057.5, 4058.3, 4058.8 and 4059.9 Å to estimate the position of the continuum at the Pb I line by eye. With our adopted local continuum positions, small Pb line features are present in the observed spectra as the dashed lines represent synthetic spectra without the Pb I line at 4057.807 Å.

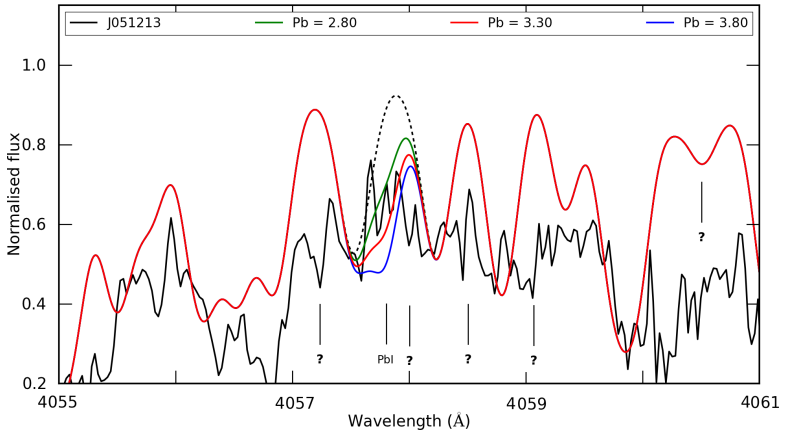

Figure 5.4: Spectrum synthesis of the Pb I line at 4057.807 Å for J051213. The black spectrum is the observed spectrum of J051213, the colored spectra represent synthetic spectra with different Pb abundances. The dashed black line shows the synthetic spectrum if no Pb would be present. Positions of unidentified spectral lines are indicated by question marks. For more information, see text.

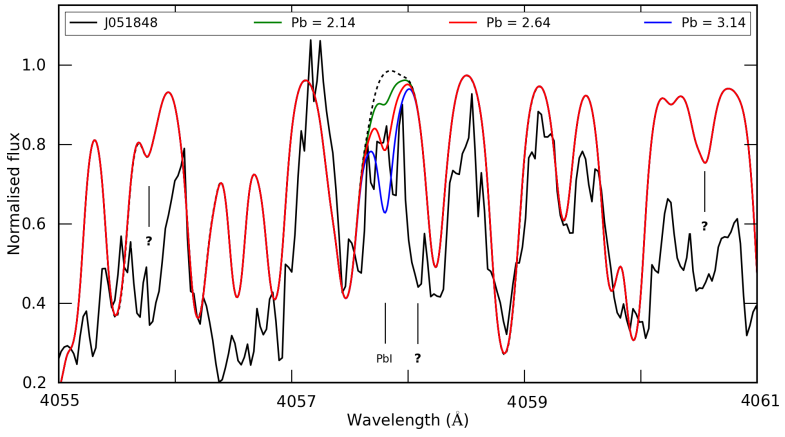

Figure 5.5: Spectrum synthesis of the Pb I line at 4057.807 Å for J051848. The black spectrum is the observed spectrum, the colored spectra represent synthetic spectra with different Pb abundances. The dashed black line shows the synthetic spectrum if no Pb would be present. Positions of unidentified spectral lines are indicated by question marks. For more information, see text.

Table 5.3: Abundance results of J051213.81-693537.1 and J051848.86-700246.9. The table lists for each ion the used number of lines (N) for the abundance determination, the determined abundance (log ϵ), the uncertainty of this abundance due to line-to-line scatter (σ_{121}), the element over iron ratio ([X/Fe]) and total uncertainty (σ_{tot}). The total uncertainty σ_{tot} includes line-to-line scatter and atmospheric parameter uncertainty (see text for details). The last column lists the solar abundances from Asplund et al. (2009). We impose a standard deviation of 0.20 dex for all ions for which the abundance was derived using spectrum synthesis or for which only one line is available. The abundances of Pb and Th are upper limits.

	J051213					Sun	J051848				
	$T_{\rm eff}$ = 5875 K			ξ_t = 3.0 km/s			$T_{\rm eff}$ = 6000 K			ξ_t = 2.8 km/s	
	log g = 1.00 dex			[Fe/H] = -0.56 dex			log g = 0.50 dex			[Fe/H] = -1.03 dex	
Ion	N	log ϵ	σ_{121}	[X/Fe]	σ_{tot}	log $\epsilon_\odot$	N	log ϵ	σ_{121}	[X/Fe]	σ_{tot}
C I	1	8.75	0.20	0.88	0.26	8.43	4	8.61	0.13	1.21	0.16
O I	1	8.65	0.20	0.52	0.26	8.69	2	8.50	0.05	0.84	0.19
Mg I	1	7.00	0.20	-0.04	0.24	7.60	2	6.73	0.07	0.19	0.12
Al I	1	6.60	0.20	0.71	0.25	6.45					
Si I	4	7.32	0.05	0.37	0.18	7.51					
S I	2	6.51	0.03	-0.05	0.13	7.12	1	6.46	0.20	0.37	0.25
Ca I	11	6.00	0.09	0.22	0.09	6.34	8	5.56	0.08	0.28	0.08
Ca II	1	6.00	0.20	0.22	0.24	6.34					
Sc II	3	2.93	0.03	0.34	0.10	3.15	6	2.30	0.08	0.18	0.11
Ti I	2	4.69	0.07	0.30	0.13	4.95					
Ti II	7	4.62	0.13	0.23	0.11	4.95	4	4.12	0.08	0.20	0.11
V I	1	3.91	0.20	0.54	0.25	3.93					
V II	2	3.91	0.04	0.54	0.14	3.93					
Cr I	4	5.20	0.07	0.12	0.10	5.64	6	4.70	0.07	0.12	0.08
Cr II	7	5.16	0.11	0.08	0.10	5.64	12	4.78	0.07	0.17	0.08
Mn I	1	4.69	0.20	-0.18	0.24	5.43					
Fe I	53	6.94	0.10	0.00	0.06	7.50	35	6.44	0.07	0.00	0.05
Fe II	13	6.94	0.09	0.00	0.07	7.50	9	6.47	0.12	0.00	0.10
Ni I	4	5.75	0.08	0.09	0.12	6.22	8	5.22	0.10	0.06	0.10
Cu I						4.19	1	3.53	0.20	0.40	0.23
Zn I	1	4.22	0.20	0.22	0.29	4.56	1	3.78	0.20	0.25	0.29

Table 5.3: Continued.

	J051213					Sun	J051848				
	$T_{\rm eff}$ = 5875 K			ξ_t = 3.0 km/s			$T_{\rm eff}$ = 6000 K			ξ_t = 2.8 km/s	
	$\log g$ = 1.00 dex			[Fe/H] = -0.56 dex			$\log g$ = 0.50 dex			[Fe/H] = -1.03 dex	
Ion	N	$\log \epsilon$	σ_{121}	[X/Fe]	σ_{tot}	$\log \epsilon_\odot$	N	$\log \epsilon$	σ_{121}	[X/Fe]	σ_{tot}
Y II	5	3.13	0.11	1.48	0.13	2.21	6	2.79	0.12	1.61	0.15
Zr II	2	3.20	0.02	1.18	0.10	2.58	2	2.85	0.05	1.30	0.13
La II	6	2.52	0.13	1.98	0.13	1.10	7	2.55	0.11	2.48	0.20
Ce II	6	2.91	0.12	1.89	0.13	1.58	5	2.37	0.07	1.82	0.13
Pr II	6	1.96	0.06	1.80	0.13	0.72	11	1.75	0.05	2.06	0.14
Nd II	14	2.67	0.10	1.81	0.13	1.42	14	2.69	0.10	2.30	0.16
Sm II	1	1.70	0.20	1.30	0.24	0.96	2	1.80	0.12	1.87	0.18
Eu II	2	0.98	0.07	1.02	0.13	0.52	2	0.81	0.12	1.32	0.17
Gd II						1.07	10	1.75	0.12	1.71	0.12
Dy II	2	2.00	0.20	1.46	0.21	1.10	4	1.91	0.09	1.84	0.12
Er II	2	1.90	0.20	1.54	0.22	0.92	1	1.63	0.20	1.74	0.26
Tm II						0.10	1	1.20	0.20	2.13	0.24
Lu II						0.10	3	1.16	0.08	2.08	0.15
Hf II						0.85	1	1.84	0.20	2.02	0.25
Pb I	1	< 3.30		< 2.11		1.75	1	< 2.62		< 1.93	
Th II	1	< 1.35		< 1.89		0.02					

5.4 Abundance results

The complete abundance analysis results of both objects are presented in Table 5.3. The spectral lines used for these analyses are listed in Appendix B.

Based upon the ionisation potential of the corresponding ion, the element over iron ratios ([X/Fe]) in Table 5.3 are calculated using Fe I or Fe II. If the ionisation potential of an ion is below the ionisation potential of Fe I, the abundance of Fe I is used for calculating [X/Fe]. If the ionisation potential exceeds the ionisation potential of Fe I, Fe II is used for calculating [X/Fe]. The same principle is also used for calculating the total error of [X/Fe]. The errors were determined using the method described in Deroo et al. (2005). The uncertainties due to the atmospheric parameters are calculated by determining the abundances of a certain ion for atmospheric models with $T_{\rm eff}$ plus and minus 125 K, models with $\log g$ plus and minus 0.25 dex and microturbulent velocity plus and minus 0.2 km/s (see Table 5.2). The uncertainty in microturbulent velocity can have important effects for ions which are only determined by large lines like Y II. The total uncertainties are then the quadratic sum of the uncertainties of the mean due to line-to-line scatter ($\sigma_{\rm l2l}$), uncertainties due to atmospheric parameters ($\sigma_{{\rm T}_{eff}}$, $\sigma_{\rm logg}$, σ_{ξ_t}) and the Fe abundance uncertainty ($\sigma_{\rm Fe}$):

$$\sigma_{\rm tot} = \sqrt{\left(\frac{\sigma_{\rm l2l}}{\sqrt{N_{\rm ion}}}\right)^2 + (\sigma_{{\rm T}_{eff}})^2 + (\sigma_{\rm logg})^2 + (\sigma_{\xi_t})^2 + \left(\frac{\sigma_{\rm Fe}}{\sqrt{N_{\rm Fe}}}\right)^2}.$$

The scaling to Fe I or Fe II based upon ionisation potential strongly decreases the [X/Fe] uncertainty of certain ions with respect to using only Fe I or only Fe II for all [X/Fe] calculations.

The [X/Fe] results in Table 5.3 are plotted in Fig. 5.6.

5.4.1 Carbon and oxygen

Both stars are carbon enhanced. The uncertainties of C and O for J051213 are large since only one line could be used for the abundance determinations. Both ions are also strongly sensitive to changes in effective temperature. We find [C/Fe] values of about 0.9 and 1.2 for J051213 and J051848, respectively and [O/Fe] values of about 0.5 and 0.8, respectively. This results in moderate C/O ratios of only 1.26 ± 0.40 for J051213 and 1.29 ± 0.30 for J051848, which are a combination of relatively low C enhancements as well as relatively high O enhancements. Based upon their abundances (Fig. 5.6) and their luminosities (see Sect. 5.5), both stars are carbon-enhanced post-AGB stars but the C/O ratios are not very large.

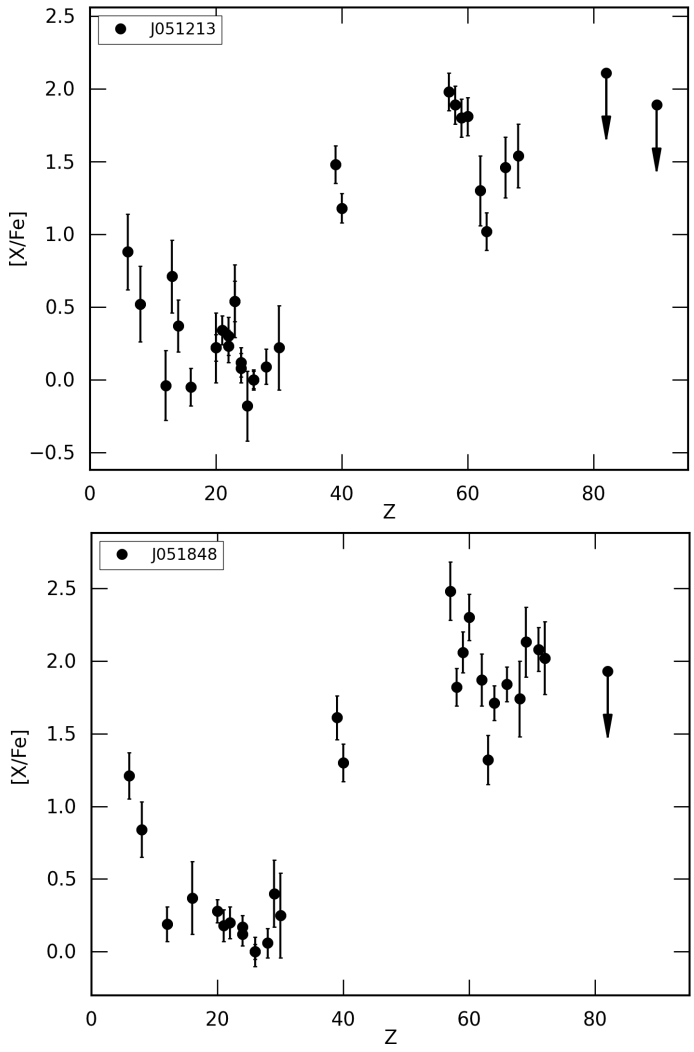

Figure 5.6: [X/Fe] results of J051213 (upper panel) and J051848 (lower panel). The errors bars represent the total uncertainties $\sigma_{\rm tot}$. The abundances of Pb (Z=82) and Th (Z=90) are upper limits and marked with down-arrows.

5.4.2 Alpha-elements

Concerning the available α-elements Mg, Si, S, Ca and Ti, the mean of [X/Fe] is $[\alpha/\mathrm{Fe}] = +0.14$ and $[\alpha/\mathrm{Fe}] = +0.26$ for J051213 and J051848 respectively. For J051848, no Si abundance was available. With respect to Galactic abundances, these α-element abundance are slightly deficient but they fall within the expected abundance ranges for the LMC, consistent with their respective metallicities (e.g Van der Swaelmen et al. 2013; Pompéia et al. 2008).

5.4.3 *s*-process elements

The *s*-process elements can be subdivided into three groups. This division is based upon the number of neutrons in the nuclei. The first group are the light *s*-process (ls) elements around neutron magic number 50 ($Z \sim 38$) with elements like Sr, Y and Zr. For both stars, we were able to measure Y and Zr only. The second group are the heavy *s*-process (hs) elements around magic neutron number 82 ($Z \sim 58$) with elements like Ba, La, Ce, Pr, Nd and Sm. The last group consists out of one element which is the double magic ion ^{208}Pb, which has a magic neutron number of 126 and a magic proton number of 82. Due to its double magic state, ^{208}Pb is accepted as the end product of *s*-process nucleosynthesis.

The [X/Fe] results in Fig. 5.6 display strong enrichment in both stars, confirming their post third dredge-up status. Especially J051848 displays strong enhancements for La (Z=57) and Nd (Z=60), two typical *s*-process elements of Ba peak. Also the *s*-elements of the Sr peak are enriched, albeit less strongly then the Ba-peak elements. The abundances of elements past the hs peak are strongly enhanced in both stars.

For J051213, we find a Pb abundance upper limit which is similar to the overabundances of the Ba-peak elements. For J051848, we find that the Pb upper abundance limit is lower than the abundance ratios of La and Nd, and similar to the Ce (Z=58) abundance ratio.

An overview of the C/O ratio, metallicity, α-element enhancement and the observational indices used for describing *s*-process overabundances and distributions (See Sect. 5.6) are listed in Table 5.4.

Table 5.4: Overview of the C/O ratio, metallicity, α-element enrichment, s-process indices and Pb abundance upper limits for J051213 and J051848.

Object	C/O	[Fe/H]	[α/Fe]	
J051213	1.26 ± 0.40	-0.56 ± 0.15	0.14 ± 0.07	
J051848	1.29 ± 0.30	-1.03 ± 0.14	0.26 ± 0.08	
Object	[ls/Fe]	[hs/Fe]	[s/Fe]	[hs/ls]
J051213	1.33 ± 0.08	1.74 ± 0.08	1.61 ± 0.06	0.41 ± 0.12
J051848	1.46 ± 0.10	2.12 ± 0.08	1.90 ± 0.07	0.66 ± 0.13

Table 5.5: Estimated luminosity and reddening of J051213 and J051848.

Object	J051213	J051848
E(B-V)	0.69 ± 0.03	0.44 ± 0.02
L ($L_\odot$)	6700 ± 200	6250 ± 200

5.5 Luminosity and initial mass determination

5.5.1 Spectral energy distributions and luminosities

The spectral energy distributions (SEDs) and known distance to the LMC allow us to determine the luminosities of our sample stars and estimate their initial masses (Sect. 5.5.2). The photometric data for constructing the SEDs are retrieved from the following catalogues: the UBVR CCD Survey of the Magellanic Clouds (Massey 2002), the 2MASS 6X catalogue (Cutri et al. 2003), the Deep Near-Infrared Survey (DENIS,Fouqué et al. (2000)), the WISE All-Sky Data catalogue (Cutri et al. 2012) and the Spitzer SAGE survey of the LMC (Meixner et al. 2006).

For our sample post-AGB stars, we assume three sources to contribute to the reddening. The first source is reddening by interstellar dust in the Milky Way Galaxy towards the LMC. Schlegel et al. (1998) find a relatively small extinction towards the LMC of E(B-V) = 0.075 mag. The second source is reddening by interstellar dust in the LMC. We assume similar extinction laws in the LMC and Milky Way Galaxy and use the Galactic extinction curves of Cardelli et al. (1989) to determine reddening in the LMC. The third source of reddening is caused by circumstellar dust of the post-AGB object itself. We assume the

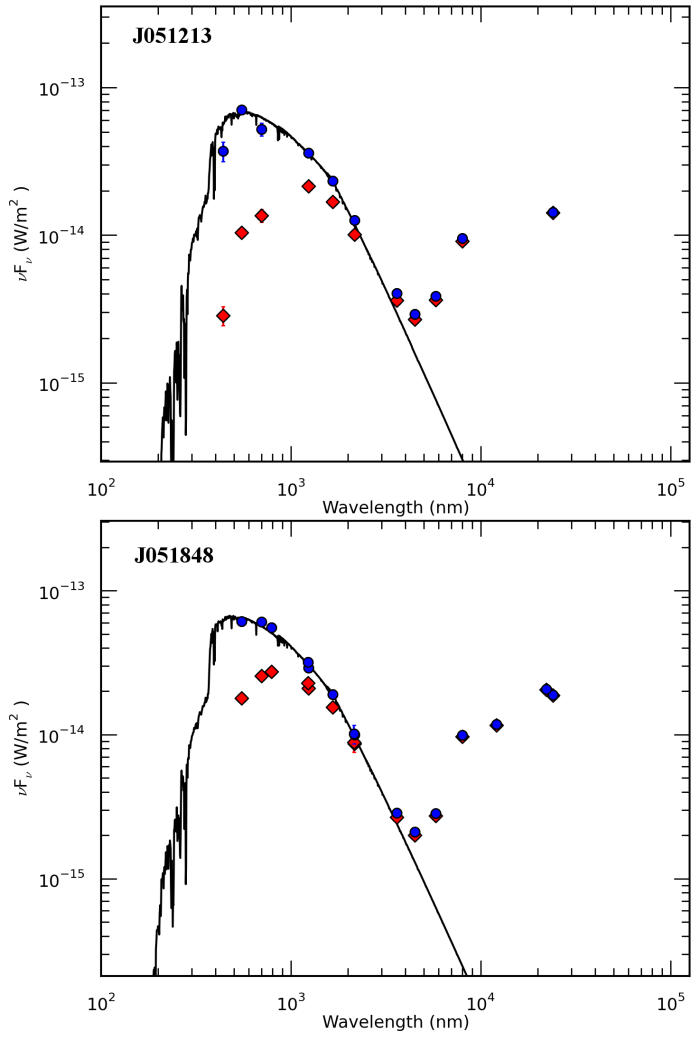

Figure 5.7: SEDs of J051213 (upper panel) and J051848 (lower panel). Red diamonds symbolise the red, original photometry, blue circles represent the dereddened photometry. The black lines represent the scaled Kurucz atmosphere models.

circumstellar extinction has the same wavelength dependency as the Galactic extinction law.

The total dereddening is determined by applying a χ^2 minimalisation on the fit

between the dereddened broadband fluxes and the appropiate Kurucz model atmospheres which are used for the abundance determination. For the scaled model of J051213, we have linearly interpolated between available models to obtain our preferred atmosphere model. The error on E(B-V) is determined by a Monte Carlo simulation of 100 arrays with a normal distribution of the original flux. The luminosities are calculated by integrating the surface of the scaled Kurucz models and applying a distance of 50 kpc to the LMC (e.g. Keller & Wood 2006; Reid & Parker 2010). The errors on the luminosity are determined by a Monte Carlo simulation, similar to the error derivation of the reddening. The estimated luminosity and reddening results of both the sample stars are listed in Table 5.5. The constructed SEDs are shown in Fig. 5.7.

The SEDs in Fig. 5.7 are double peaked, indicating a circumstellar dust envelope originating from the strong mass-loss during the AGB (Van Winckel 2003). We find a signficant reddening value for both stars, especially J051213 has a high line-of-sight extinction of E(B-V) $\approx$ 0.7. This extinction is dominated by the circumstellar extinction given the evidence for dusty circumstellar envelopes of these objects. The derived luminosities in Table 5.5 are within the expected luminosity range for post-AGB stars and they agree well with the post-TDU nature of these objects.

5.5.2 Initial mass estimates

Two key parameters in state-of-the-art evolution and nucleosynthetic AGB models are the metallicity and initial stellar mass. We use the post-AGB evolutionary tracks of Vassiliadis & Wood (1994) to obtain an estimate of the initial masses of our sample stars. We compare the positions of the sample stars with those of the theoretical tracks in the Hertsprung-Russell (HR) diagram in Fig. 5.8. We have also included the positions of three other *s*-process enriched LMC post-AGB stars J050632.10-714229.9, J052043.86-692341.0 and J053250.69-713925.8 (van Aarle et al. 2013) and the *s*-process enriched SMC post-AGB star J004441.04-732136.4 (De Smedt et al. 2012). For all stars, we use the theoretical tracks that were calculated for a metallicity which corresponded the most to the derived metallicities of the individual objects. The theoretical tracks from Vassiliadis & Wood (1994) start at an effective temperature of 10^4 K which is higher than the derived temperatures of the shown stars. Since the luminosity of post-AGB stars remains approximately constant when crossing the HR-diagram, we have used linear extrapolation between log $T_{\rm eff}$ and log $L/L_{\odot}$ to extrapolate towards lower temperatures.

We find that the *s*-process enriched post-AGB stars included in Fig. 5.8 have low masses below about 1.5 $M_{\odot}$. We find that strong *s*-process enrichment is

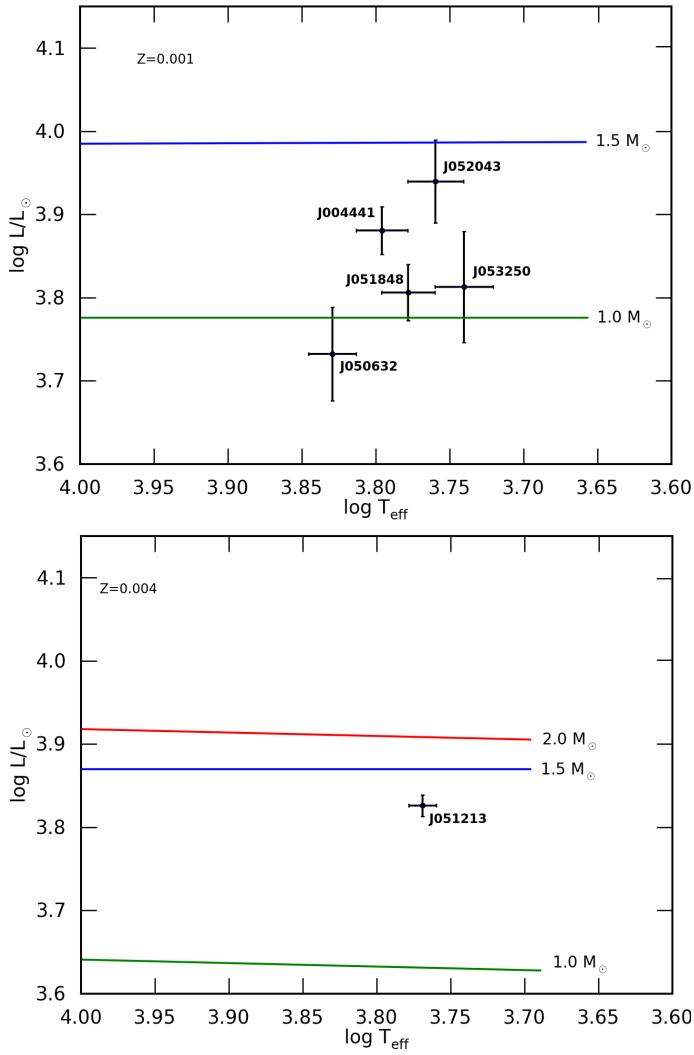

Figure 5.8: Comparison of our sample stars and four other *s*-process enriched Magellanic Cloud post-AGB stars. The displayed evolutionary tracks are from Vassiliadis & Wood (1994) with a metallicity of Z=0.001 in the upper panel and Z=0.004 in the lower panel. The mass corresponding to each track is indicated. For more information, see text.

linked to low initial masses in all studied sources till now (De Smedt et al. 2012; van Aarle et al. 2013).

We remark that our initial mass estimates depend on the applied mass-loss rate history on the AGB, and the theoretical post-AGB tracks of Vassiliadis & Wood (1994) used for the initial mass estimates, are determined using the at that time deduced initial-final mass relations.

5.6 Neutron irradiation

The *s*-process distributions and *s*-process overabundances are typically represented by four observational indices: [ls/Fe], [hs/Fe], [s/Fe] and [hs/ls]. Unfortunately, the elemental abundances used for the calculations of these indices vary in literature. To have a significant statistical sample, we include the abundance results from Van Winckel & Reyniers (2000) and Reyniers et al. (2004) for Galactic objects in the *s*-process index study. For the ls-index, we follow the suggestion from Busso et al. (1995) and use the mean of the relative abundances of Y and Zr. For the hs-index, normally the Ba abundance is used, but since an accurate Ba abundance study is hampered by the strong saturated Ba lines in *s*-process enriched objects, we replace the Ba abundance by the Ce abundance which can be determined accurately in enriched objects. The hs-index is then the mean of the relative abundances of La, Ce, Nd and Sm. Our four *s*-process indices are:

$$[\text{ls/Fe}] = \frac{[\text{Y/Fe}] + [\text{Zr/Fe}]}{2}$$

$$[\text{hs/Fe}] = \frac{[\text{La/Fe}] + [\text{Ce/Fe}] + [\text{Nd/Fe}] + [\text{Sm/Fe}]}{4}$$

$$[\text{s/Fe}] = \frac{[\text{Y/Fe}] + [\text{Zr/Fe}] + [\text{La/Fe}] + [\text{Ce/Fe}] + [\text{Nd/Fe}] + [\text{Sm/Fe}]}{6}$$

$$[\text{hs/ls}] = [\text{hs/Fe}] - [\text{ls/Fe}]$$

Since we use a non-standard element selection for the hs index calculations, we list the four *s*-process indices of all stars in our *s*-process indices analysis in Table 5.6. This includes Galactic object from Van Winckel & Reyniers (2000) and Reyniers et al. (2004), and Magellanic Cloud objects from this paper, De Smedt et al. (2012) and van Aarle et al. (2013). For objects IRAS 04296+3429, IRAS 19500-1709 and J053250.69-713925.8, no Sm abundance could be determined. To estimate the Sm abundance for these objects, we scale the abundance of Sm to the abundance of Nd, which is the element with an atomic mass closest to

Table 5.6: Overview of the four *s*-process indices of the stars in Figs. 5.9 and 5.10.

Object	[Fe/H]	C/O	[ls/Fe]	[hs/Fe]	[s/Fe]	[hs/ls]
IRAS 04296+3429[a]	-0.62 ± 0.20		1.66 ± 0.12	1.34 ± 0.07	1.45 ± 0.06	-0.32 ± 0.14
IRAS 05341+0852[a]	-0.85 ± 0.20	1.4 ± 0.3	1.92 ± 0.08	2.30 ± 0.07	2.17 ± 0.05	0.38 ± 0.11
IRAS 06530-0213[b]	-0.46 ± 0.20	2.8 ± 0.3	1.82 ± 0.09	2.11 ± 0.07	2.02 ± 0.05	0.29 ± 0.11
IRAS 07134+1005[a]	-1.00 ± 0.20	1.0 ± 0.3	1.55 ± 0.17	1.36 ± 0.07	1.43 ± 0.07	-0.19 ± 0.18
IRAS 08143-4406[b]	-0.39 ± 0.20	1.3 ± 0.3	1.52 ± 0.15	1.49 ± 0.07	1.50 ± 0.07	-0.03 ± 0.16
IRAS 19500-1709[a]	-0.60 ± 0.20	1.1 ± 0.3	1.38 ± 0.11	0.90 ± 0.07	1.06 ± 0.06	-0.48 ± 0.13
IRAS 22223+4327[a]	-0.31 ± 0.20	1.2 ± 0.3	1.55 ± 0.10	1.25 ± 0.09	1.35 ± 0.07	-0.30 ± 0.14
IRAS 23304+6147[a]	-0.79 ± 0.20	2.9 ± 0.3	1.55 ± 0.10	1.50 ± 0.09	1.52 ± 0.07	-0.05 ± 0.14
J004441.04-732136.4[c]	-1.34 ± 0.17	1.9 ± 0.7	2.06 ± 0.10	2.58 ± 0.10	2.40 ± 0.10	0.52 ± 0.10
J050632.10-714229.9[d]	-1.15 ± 0.17	1.5 ± 0.3	1.42 ± 0.07	1.07 ± 0.14	1.19 ± 0.09	-0.35 ± 0.15
J051213.81-693537.1[e]	-0.56 ± 0.15	1.3 ± 0.4	1.33 ± 0.08	1.74 ± 0.08	1.61 ± 0.06	0.41 ± 0.12
J051848.86-700246.9[e]	-1.03 ± 0.14	1.3 ± 0.3	1.46 ± 0.10	2.12 ± 0.08	1.90 ± 0.07	0.66 ± 0.13
J052043.86-692341.0[d]	-1.15 ± 0.17	1.6 ± 0.9	1.67 ± 0.12	1.85 ± 0.10	1.79 ± 0.08	0.19 ± 0.16
J053250.69-713925.8[d]	-1.22 ± 0.11	2.5 ± 0.7	1.51 ± 0.16	1.94 ± 0.10	1.80 ± 0.08	0.43 ± 0.19

[a] Galactic object, from Van Winckel & Reyniers (2000). For C/O, we assume an uncertainty of 0.3 dex.
[b] Galactic object, from Reyniers et al. (2004). For C/O, we assume an uncertainty of 0.3 dex.
[c] SMC object, from De Smedt et al. (2012).
[d] LMC object, from van Aarle et al. (2013).
[e] LMC object, from this paper.

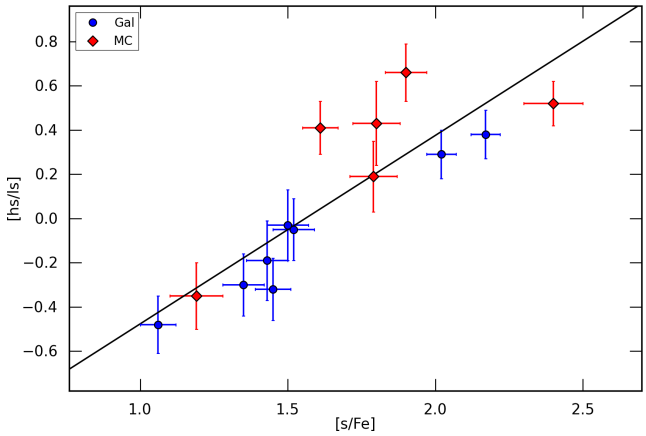

Figure 5.9: Correlation between the total enrichment in *s*-process elements and the [hs/ls] index for the stars listed in 5.6. Galactic objects are represented by blue circles, Magellanic Cloud objects are represented by red diamonds. The full line shows the least-squares fit to all data points.

Sm and included in the hs index. We use the AGB nucleosynthesis models from the online-database FRUITY[2] (Franec Repository of Upgraded Isotopic Tables and Yields Cristallo et al. 2011) and use the models with metallicities closest to the respective star's metallicity. We choose a standard mass of 1.5 $M_{\odot}$ based upon our estimated initial mass results for the Magellanic Cloud objects (see Sect. 5.5.2)

Van Winckel & Reyniers (2000), Reyniers et al. (2004) and van Aarle et al. (2013) find a strong correlation between [s/Fe] and [hs/ls] indices in Galactic and Magellanic Cloud objects, for which elements with high [s/Fe] generally show a higher [hs/ls] ratio. We add three objects (our two sample stars and J004441 from De Smedt et al. 2012) to this relation (see Fig. 5.9). We find that these three objects confirm the correlation between [s/Fe] and [hs/ls] with a correlation coefficient of 0.86. The [s/Fe] index represents the third dredge-up efficiency, although it is also influenced by the mass-loss history during the AGB phase and the envelope mass during TDUs. Note that the [hs/ls] index represents neutron irradiation, the number of neutrons which are available for each iron seed nucleus. Generally, an overabundance of hs-elements with respect to ls-elements is expected in low-mass and low-metallicty AGB stars (1-3 $M_{\odot}$) in which the $^{13}C(\alpha,n)^{16}O$ is expected to be the main neutron source for the *s*-process (e.g. Straniero et al. 1995; Gallino et al. 1998;

[2]http://fruity.oa-teramo.inaf.it/

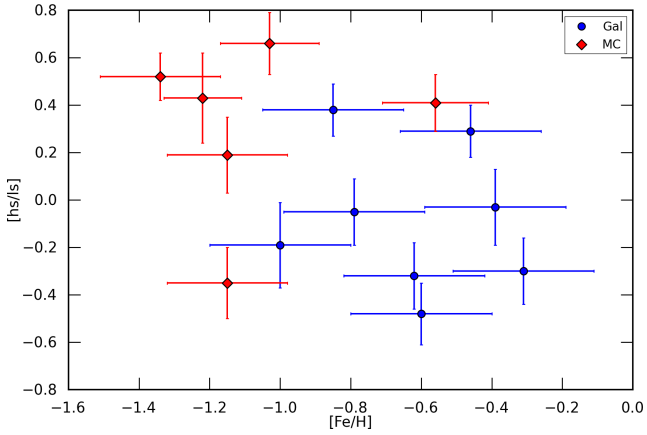

Figure 5.10: The absence of correlation between the metallicity [Fe/H] and the [hs/ls] index for all stars listed in 5.6. Symbols and the line are similar to Fig. 5.9. There is no clear correlation between metallicity and this range of metallicities.

Abia et al. 2002; Cristallo et al. 2011; Karakas & Lattanzio 2014). In heavier AGB stars, the ^{22}Ne(α,n)^{25}Mg reaction is dominant which mainly produces ls-elements. Of all the Magellanic Cloud objects listed in Table 5.6, all objects have low initial masses and an overabundance of hs with respect to ls, except J050632.10-714229.9.

As described above, the [hs/ls] index is expected to increase with decreasing metallicity due to a larger number of neutrons for each iron seed, assuming that the diffusion of protons in the He-rich intershell is totally independent of metallicity. In Fig. 5.10, which also includes our sample stars and J004441, there is no clear correlation between [Fe/H] and [hs/ls].

Low-mass, low-metallicity stars are expected to have high overabundances of Pb with respect to the hs-elements. The AGB models predict the ^{13}C neutron source to be of primary origin, which means that it is independent of the initial metallicity. For similar models with different metallicity, the neutron production is predicted to be similar, but the number of available Fe seeds is different. Per Fe seed nucleus, there are more neutrons available at low metallicity. This results in the creation of heavier *s*-elements. Since Pb is the expected end-product of the *s*-process nucleosynthesis, high Pb abundances are expected in metal-poor stars.

In order to compare our Pb abundance results to mean theoretical predictions,

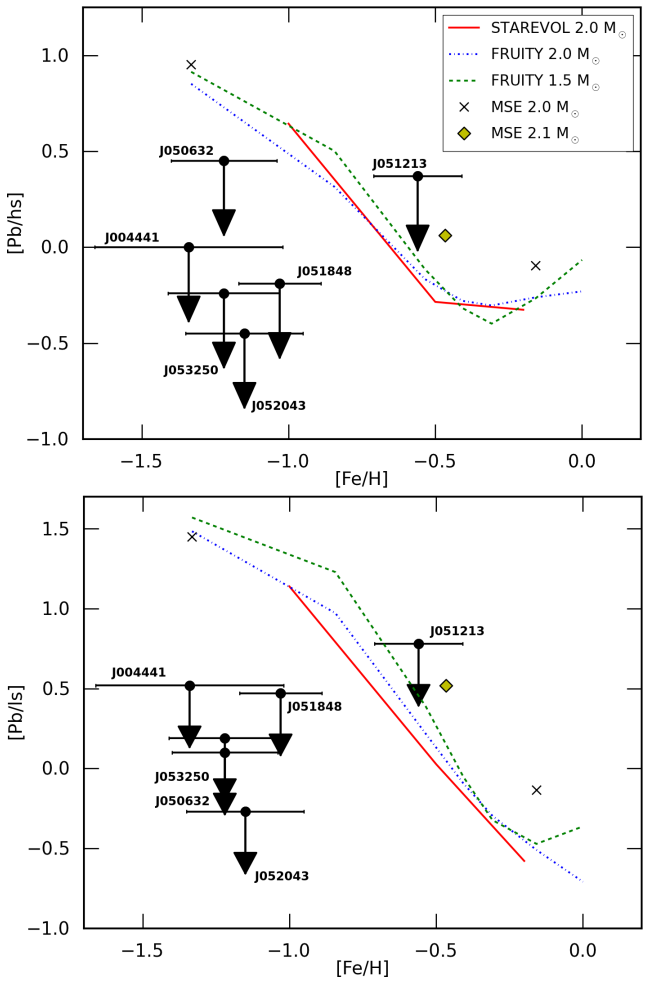

Figure 5.11: Overview of the observed [Pb/hs] (upper panel) and [Pb/ls] (lower panel) upper limits of *s*-process enriched post-AGB stars in the Magellanic Clouds from this study and De Smedt et al. (2014). The observed abundance upper limits are plotted together with the [Pb/hs] and [Pb/ls] predictions of the 2.0 $M_{\odot}$ STAREVOL models (red full line),the 2.0 $M_{\odot}$ and 2.1 $M_{\odot}$ Mount Stromlo models (black crosses and yellow diamond respectively) and the 1.5 and 2.0 $M_{\odot}$ FRUITY models (green dashed and blue dot-dashed lines respectively). The black horizontal lines represent the [Fe/H] uncertainty of the displayed stars. The position of each star is indicated with the first part of its 2MASS name. For more information, see text.

we obtained predicted values from different AGB evolution and nucleosynthesis codes. For this comparison, we use [Pb/hs] ([Pb/Fe] - [hs/Fe]) and [Pb/ls] ([Pb/Fe] - [ls/Fe]), which represent the overabundance of Pb with respect to the other *s*-process elements. Fig. 5.11 shows the comparison between the observed [Pb/hs] (upper panel) and [Pb/ls] (lower) upper limits, together with 2.0 $M_{\odot}$ model predictions of the STAREVOL code (Siess 2007, and references therein) for metallicities of [Fe/H] = -1.0, -0.5 and -0.2 dex (red full line), Mount-Stromlo Evolutionary code (MSE) predictions (Fishlock et al. 2014; Karakas 2010, and references therein) for [Fe/H] $\approx$ -1.3 and -0.15 dex for 2.0 $M_{\odot}$ models (black crosses) and [Fe/H] $\approx$ -0.5 dex for a 2.1 $M_{\odot}$ model (yellow diamond), and the publicly-available 2.0 $M_{\odot}$ model predictions of FRUITY (Cristallo et al. 2011) within a metallicity range from [Fe/H] = -1.5 up to 0.0 dex (blue point-dashed line) for seven different metallicities. Due to the limited number of available metallicities within the shown metallicity ranges, the STAREVOL and FRUITY curves in Fig. 5.11 are not smooth. We remark that, although all stars in Fig. 5.11 have estimated initial masses between 1.0 and 1.5 $M_{\odot}$ (see De Smedt et al. 2012; van Aarle et al. 2013, and Sect. 5.5.2), it is justified to make a comparison with 2.0 $M_{\odot}$ model predictions since the differences between the 1.5 and 2.0 $M_{\odot}$ FRUITY model predictions is only marginal.

Fig. 5.11 shows that the predictions fit well the observed Pb abundance upper limit of J051213 but strongly overestimate the Pb overabundances of the lower metallicity stars. There is an increasing discrepancy between predicted and observed Pb abundances towards lower metallicities. A larger sample of post-AGB stars with derived Pb abundances is required to confirm the observed discrepancy towards lower metallicities. More research is clearly needed to explain the consistent low Pb abundances in *s*-process enriched low-metallicity post-AGB stars. This is beyond the scope of this study.

5.7 Conclusions

We aim at understanding the chemical diversity displayed by post-AGB stars and here we focus on *s*-process rich objects. With detailed studies of a well sampled grid of post-AGB objects covering a wide range in luminosity (hence core-mass and initial mass) and metallicity, we aim to build-up a systematic set of constraints on AGB models. These will help us to understand the physical processes related to AGB nucleosynthesis and mixing. To obtain these constraints, we study newly discovered post-AGB stars in the Magellanic Clouds. Due to their known distances, accurate luminosity and hence initial mass estimates can be made which is contrary to the situation for Galactic peers.

Here, we report on a detailed chemical study of two *s*-process enriched optically visible post-AGB stars in the LMC. The objects were carefully selected from our low-resolution surveys (van Aarle et al. 2011; Kamath et al. 2015, accepted). Our high-resolution spectral data reveal very rich spectra, literally swamped with atomic lines of *s*-process elements. We quantified that both objects belong to the most *s*-process rich objects known to date despite their similarly low C/O ratios. The metallicity difference between both stars is about 0.5 dex.

With the addition of our two sample stars, all *s*-process enhanced post-AGB stars in the LMC and SMC studied till now cluster in the same region of the HR-diagram. All are associated with the latest evolutionary phase of low-mass stars with, on average, low metallicity.

We also confirm the correlation between [hs/ls] and [s/Fe] for *s*-process enriched post-AGB stars and find that both Galactic and Magellanic Cloud objects follow the same relation. The neutron exposure as traced by [hs/ls] is correlated with the overall *s*-process overabundances, as traced by [s/Fe]. [s/Fe] is also determined by the amount of dredged-up intershell material and the envelope dilution. In addition, we strengthen and confirm that there is no clear correlation between neutron irradiation and metallicity. Furthermore, we find an increasing discrepancy between observed and predicted Pb overabundances towards lower metallicities: the higher metallicity J051213 with [Fe/H] $\approx$ -0.56 dex fits well the model predictions, while J051848 and other Magellanic Cloud objects from previous studies display much lower [Pb/hs] and [Pb/ls] results than predicted.

Our current and future research involves expanding our survey of chemical studies in the Magellanic Clouds to construct a grid that cover a larger and well-sampled range in luminosity (hence initial mass) and metallicity. We intend to use this grid of constraints to finetune AGB models and therefore the underlying physics of nucleosynthesis and mixing.

Chapter 6

Pb abundances in Galactic *s*-process enriched post-AGB stars

This chapter is submitted as:

Study of Pb abundances in Galactic *s*-process enriched post-AGB stars

K. De Smedt, H. Van Winckel, D. Kamath, L. Siess, S. Goriely, A. I. Karakas, R. Manick

Astronomy & Astrophysics, in prep., 2015

ABSTRACT

Context: This paper is part of a larger project in which we systematically study the chemical abundances of Galactic and extra-galactic post-asymptotic giant branch (post-AGB) stars. The goal at large is to provide improved observational constraints to the models of the complex interplay between the AGB *s*-process nucleosynthesis and the associated mixing processes.

Aims: Lead (Pb) is the final product of the *s*-process nucleosynthesis and is predicted to have large overabundances with respect to other *s*-process elements in AGB stars of low metallicities. However, Pb abundance studies of *s*-process enriched post-AGB stars in the Magellanic Clouds show a discrepancy between observed and predicted Pb abundances. The determined upper limits based on spectral studies are much lower then what is predicted. In this paper, we focus specifically on the Pb abundance of 14 Galactic *s*-process enhanced post-AGB stars, to check whether the same discrepancy is present in the Galaxy as well. Among these 14 objects, 2 were not yet subject to a detailed abundance study in the literature.

Methods: We use high-resolution UVES and HERMES spectra for detailed spectral abundance studies of our sample of Galactic post-AGB stars. None of the sample stars display clear Pb lines, and we only deduce upper limits of the Pb abundance by using spectrum synthesis in the spectral ranges of the strongest Pb lines.

Results: We do not find any clear evidence of Pb overabundances in our sample. The derived upper limits are strongly correlated with the effective temperature of the stars with increasing upper limits for increasing effective temperatures. We obtain stronger Pb constraints on the cooler objects. Moreover, we confirm the *s*-process enrichment and carbon enhancement of two unstudied 21 μm sources IRAS 13245-6428 and IRAS 14429-4539. The mildly *s*-process enhanced post-AGB star IRAS 17279-1119 is part of a binary system and may be the long sought precursor of extrinsic Ba stars.

Conclusions: Stars with $T_{\rm eff} > 7500$ K do not provide strong constraints on the Pb abundance as the strongest line in the optical spectrum will only be detectable at unrealistically high Pb atmospheric abundances. Combining the Pb abundance results from this study with abundances from our previous studies, we conclude that the discrepancy between theory and observation increases towards lower metallicities. For all stars with [Fe/H] > -0.7 dex, the model predictions are complient with the deduced upper limits on the Pb abundances. For stars with [Fe/H] < -0.7 dex, however, the model predictions overestimate the Pb abundances with respect to the other *s*-process elements. All objects, except IRAS 17279-1119, confirm the relation between neutron exposure [hs/ls] and third dredge-up efficiency [s/Fe] whereas no relation between metallicity and neutron exposure is detected within the metallicity range of our total sample ($-1.4 <$ [Fe/H] < -0.2). The mild enrichment of IRAS 17279-1119 can probably be attributed to a cut-off of the AGB evolution due to binary interactions. To our knowledge, IRAS 17279-1119 is the first

s-process enhanced Galactic post-AGB star known in a binary system and is a possible precursor of the extrinsic Ba dwarf stars.

AUTHOR CONTRIBUTIONS

K. De Smedt initiated this study of Pb in Galactic objects, performed the sample selection, retrieved and reduced all spectral data, performed the full spectral analysis of all objects and constructed the SED of IRAS 17279-1119. H. Van Winckel and R. Manick performed the radial velocity study of IRAS 17279-1119. The large majority of the text is written by K. De Smedt, with the assistance of all co-authors.

6.1 Introduction

The final evolution of low- to intermediate mass single stars ($M \lesssim 7\ M_{\odot}$) is characterised by a fast transition from the Asymptotic Giant Branch (AGB) over the post-AGB track towards the planetary nebula phase. During late stages of AGB evolution, convective thermal pulses (TPs) occur in the intershell, which are possibly followed by third dredge-ups (TDUs) which transport newly-synthesised material from the stellar interior to the surface. The main dredged-up element is ^{12}C as primary product of the triple alpha reaction. AGB stars are thought to be very important contributors to the total carbon and nitrogen enrichment of galaxies (e.g. Romano et al. 2010; Kobayashi et al. 2011).

Apart from ^{12}C, the TDU also brings elements created by neutron synthesis to the stellar surface. The slow-neutron capture process (or *s*-process) is the origin of approximately half of all cosmic abundances past the iron peak. It is generally acknowledged that the ^{13}C(α,n)^{16}O reaction is the main neutron source in low-mass AGB stars (1-3 $M_{\odot}$) (e.g. Straniero et al. 1995; Gallino et al. 1998; Mowlavi et al. 1998; Abia et al. 2002; Karakas & Lattanzio 2014; Neyskens et al. 2015). It is also widely accepted that a ^{13}C-pocket is produced by transport of protons from the convective envelope into the He-rich intershell. The neutrons created in the ^{13}C-pocket by the alpha capture reaction, can then be used for the creation of heavy elements by the slow neutron capture process (*s*-process). Although observations confirm that heavy elements can indeed

be created by AGB stars, the physical mechanisms behind the AGB internal nucleosynthesis and associated dredge-up processes are poorly understood.

The end product of the *s*-process nucleosynthesis chain is the doubly magic ^{208}Pb isotope, which is predicted to have large overabundances with respect to other *s*-elements in metal-poor conditions, i.e. [Fe/H] smaller than -1.0 dex (see e.g. Gallino et al. 1998; Goriely & Mowlavi 2000; Lugaro et al. 2012, and references therein). These predictions are confirmed in some extrinsically enriched metal-poor objects, where strong Pb enhancements are indeed observed (e.g. Van Eck et al. 2001, 2003; Behara et al. 2010). These objects were polluted with matter from an evolved binary companion when it passed the TP-AGB phase but which is now a white dwarf. However, not all metal-deficient objects with *s*-process enrichment show this strong Pb overabundance (e.g. Aoki et al. 2001; Van Eck et al. 2003) in contrast to the predictions.

AGB photospheres are dominated by molecular transitions which hinder the study of individual elements (e.g. Abia et al. 2008). This problem does not occur in post-AGB stars, for which the photospheres are hotter, and dominated by atomic transitions. Their spectra allow for extensive chemical studies of individual elements. Post-AGB atmospheres display the outcome of chemical enrichment from internal nucleosynthesis and dredge-up processes during the entire stellar evolution. This makes post-AGB stars ideal probes to study AGB nucleosynthesis (Van Winckel 2003).

In our recent studies of post-AGB stars in the Magellanic Clouds (van Aarle et al. 2011; Kamath et al. 2014, 2015), we focussed on the intrinsic *s*-process enriched post-AGB star J004441.04-732136.4 (J004441) in the Small Magellanic Cloud (SMC) (De Smedt et al. 2012, 2014). In De Smedt et al. (2014), we compared the observed abundance results with fine-tuned, theoretical state-of-the-art AGB models. Although this star is metal-poor and strongly *s*-process enriched, we found a strong discrepancy between the observed and predicted Pb overabundance. The best fitting model overestimates the Pb overabundance by more than 2 dex. Moreover, the same Pb discrepancy was detected in three other metal-deficient post-AGB stars in the LMC (De Smedt et al. 2014). This low Pb content was also detected by Reyniers et al. (2007a) for the LMC star MACHO 47.2496.8. For all of these objects with intrinsic enrichment, the upper limits of the Pb abundances are equal or smaller than the overabundances of the other *s*-elements. In Chapter 5, we found a similar discrepancy for two newly identified *s*-process enriched post-AGB stars in the LMC. We concluded that the low Pb abundance seems to be a common feature in *s*-process rich post-AGB stars in the Magellanic Clouds. Furthermore, we find that all the objects studied till now have low initial masses which, in combination with low metallicities, strongly contradicts theoretical nucleosynthetic predictions of Pb.

In this contribution, we extend our Pb studies and focus on the Galactic *s*-process rich post-AGB stars. In combination with the studied Magellanic Cloud objects, we aim at a systematic study of the behaviour of Pb in post-AGB stars covering a wide range of metallicities. Another key parameter for evolutionary and nucleosynthetic AGB modeling is the initial mass. Unfortunately, we are not able to perform accurate initial mass estimates for Galactic objects as the distances to these objects are highly uncertain. By studying the general behaviour of Pb in Galactic *s*-process enriched post-AGB we provide new constraints for the models of AGB nucleosynthesis and associated processes.

The selection of our Galactic sample stars and the observations are described in Sect. 6.2. The spectral analyses are discussed in Sect. 6.3 followed by the abundance results of all elements lighter than Pb in Sect. 6.4. The abundance results of Pb are presented in Sect. 6.5. The neutron irradiation of our sample of stars is discussed in Sect. 6.5.1. In Sect. 6.6, we specifically focus upon the evolutionary status of one of the sample stars IRAS 17279-1119. We end this paper with the conclusions in Sect. 6.7.

6.2 Sample selection and observations

Our sample consists of 12 Galactic post-AGB stars which are known to be *s*-process rich, and two new post-AGB candidates, IRAS 13245-5036 and IRAS 14429-4539, for which no abundance studies have been reported yet. The majority of the already studied Galactic post-AGB stars are 21 μm objects, named after the strong solid-state feature at 21 μm (Kwok et al. 1989). To date, all 21 μm objects are acknowledged to be post-AGB stars with carbon and *s*-process enhancements in their photospheres (e.g. Hrivnak et al. 2009). Since both IRAS 13245-5036 and IRAS 14429-4539 are post-AGB candidates with a clear 21 μm feature (Cerrigone et al. 2011), we have added these stars to our sample.

We use high-resolution spectra of two different spectrographs. The first spectrograph is the Ultraviolet and Visual Echelle Spectrograph (UVES, Dekker et al. (2000)), the echelle spectrograph mounted on the 8m UT2 Kueyen Telescope of the VLT array at the Paranal Observatory of ESO in Chili. The second spectrograph is the High Efficiency and Resolution Mercator Echelle Spectrograph (HERMES, (Raskin et al. 2011)), the spectrograph mounted on the 1.2m Mercator telescope at the Roque de los Muchachos Observatory on La Palma.

For all objects, we first checked whether optical high-resolution spectra with sufficient signal-to-noise (S/N) around 4058 Å, the spectral region of the

Table 6.1: Overview of the sample: Name(s), observational logs, references of previous studies and radial velocities.

IRAS	Other name	Date	UT start	Exp. time[a] (s)	Telescope+ Spectrograph	References	r_v (km/s)
05113+1347[d]		2014-10-07	07:55	Blue: 1 × 2676	VLT + UVES	1	6 ± 2
		2014-11-23	05:03	Blue: 1 × 2676	VLT + UVES		5 ± 1
				Red: 2 × 1200	VLT + UVES		5 ± 1
05341+0852[d]		2014-10-06	07:52	All: 1 × 1826	VLT + UVES	2	28 ± 1
		2014-10-06	08:28	All: 1 × 1826	VLT + UVES		28 ± 1
06530-0213		2014-12-24	04:03	All: 1 × 2427	VLT + UVES	3	52 ± 1
		2014-12-24	04:50	All: 1 × 2427	VLT + UVES		52 ± 1
07134+1005[d]	HD 56126	2014-09-05	05:50	1 × 920	Mercator + HERMES	2	92 ± 1
		2014-09-08	05:39	1 × 1000	Mercator + HERMES		94 ± 1
07430+1115		2014-12-24	05:33	Blue: 1 × 2176	VLT + UVES	4	41 ± 2
				Red: 2 × 1000	VLT + UVES		41 ± 1
08143-4406[b]		2001-01-16	06:41	Blue437: 2 × 1800	VLT + UVES	3	52 ± 2
		2001-01-16	07:16	Red860: 3 × 500	VLT + UVES		52 ± 1
		2001-02-01	04:21	Red: 1 × 1800	VLT + UVES		52 ± 1

[1]Reddy et al. (2002), [2]Van Winckel & Reyniers (2000), [3]Reyniers et al. (2004), [4]Reddy et al. (1999), [5]Reyniers et al. (2007b), [6]Rao et al. (2012)

[a] Exposure times of UVES spectra are split up into three categories: Exposure times for the Blue arm, Red arm or both arms, the latter is indicated with 'All'. Terms 'Blue' and 'Red' refer to observations with the Blue390 and Red580 setting. For older observations, the Blue437 and Red860 settings have also been used.

[b] For more information about these observations, see Reyniers (2002).

[c] For more information about the observations of IRAS 14325-6428, see Reyniers et al. (2007b).

[d] Identified 21 μm source.

Table 6.1: Continued.

IRAS	Other name	Date	UT start	Exp. time[a] (s)	Telescope+ Spectrograph	References	r_v (km/s)
08281-4850		2015-01-25	04:18	All: 1 × 2400	VLT + UVES	5	117 ± 1
		2015-01-25	03:47	All: 1 × 2600	VLT + UVES		116 ± 1
		2015-01-31	02:39	All: 1 × 2116	VLT + UVES		117 ± 1
13245-5036[d]		2015-03-06	04:53	All: 1 × 346	VLT + UVES		54 ± 1
14325-6428[c]		2004-05-13	07:13	Blue437: 1 × 1800	VLT + UVES	5	-83 ± 1
				Red860: 1 × 1800	VLT + UVES		-83 ± 1
		2004-05-13	06:39	Red: 1 × 1800	VLT + UVES		-82 ± 1
14429-4539[b,d]		2001-02-03	08:24	Red: 1 × 1800	VLT + UVES		0 ± 2
			08:55	Red: 1 × 1200	VLT + UVES		0 ± 2
		2001-02-06	07:53	Red: 1 × 1800	VLT + UVES		0 ± 2
		2001-02-12	07:54	Blue437: 3 × 2000	VLT + UVES		4 ± 2
				Red860: 3 × 2000	VLT + UVES		4 ± 2
17279-1119	HD158616	2014-09-18	00:00	All: 1 × 65	VLT + UVES	6	62 ± 1
19500-1709[d]	HD187885	2009-07-16	00:20	2 × 2000	Mercator + HERMES	2	15 ± 1
22223+4327[d]	V448 Lac	2009-07-31	02:50	4 × 1800	Mercator + HERMES	2,6	-41 ± 1
22272+5435[d]	HD235858	2014-08-29	01:55	3 × 720	Mercator + HERMES	1	-38 ± 1

strongest identified Pb I line, were already available for UVES in the ESO archive and for HERMES in the archive of the Institute of Astronomy (KULeuven). If not, we requested and performed observations for those objects for which a S/N of 25 around 4058 Å would be reached within an hour.

All objects, observational details and previous abundance studies are listed in Table 6.1. The last column shows the radial velocity of the observed spectra.

6.2.1 UVES spectra

The UVES spectra obtained in the period 2014-2015 (see Table 6.1) were observed using the same setting. We selected the dichroic beam-splitter resulting in a wavelength coverage for the blue UVES arm from approximately 3280 to 4530 Å, and for the lower and upper part of the mosaic CCD chip from approximately 4780 to 5770 Å and from 5800 to 6810 Å respectively. A slit width of 1 arcsecond was used to gain an optimal compromise between spectral resolution and slit-loss minimalisation.

For IRAS 08143-4406, we use the reduced UVES spectra from Reyniers et al. (2004) for our analysis. These spectra were observed with different settings, resulting in two sets of spectra representing different wavelength coverages. There is a time gap of 16 days between the observations of both sets of data. This gap was large enough to observe significant changes in the photosphere of IRAS 08143-4406, resulting in two different sets of atmospheric parameters in the analysis by Reyniers et al. (2004). The UVES spectra of post-AGB candidate IRAS 14429-4539 were obtained using the same settings as for IRAS 08143-4406. For details about the observations of IRAS 08143-4406 and IRAS14429-4539, we refer to Reyniers (2002). For IRAS 14325-6428, we use the observed spectra described in Reyniers et al. (2007b) for the spectral analysis.

All UVES spectra in Table 6.1, except for IRAS 08143-4406 and IRAS 14429-4539, were reduced using the UVES pipeline in the Reflex environment of ESO [1]. The reduction scheme includes extraction of frames, determinations of wavelength calibration and applying this scale to flat-field divided data. Cosmic clipping was also included. We choose the standard reduction parameters of the UVES pipeline as these gave the best signal-to-noise (S/N) ratio of the final spectrum. The spectra of IRAS 08143-4406 and IRAS 14429-4539 were already reduced with older versions of the UVES pipeline.

[1] https://www.eso.org/sci/software/reflex/

6.2.2 HERMES spectra

All HERMES spectra are obtained in high-resolution mode ($\lambda/\Delta\lambda = 85.000$). These spectra cover a wavelength range from about 3770 Å up to about 9000 Å, although some gaps in the spectra are present at large wavelengths, as the reddest orders are too long for the CCD. The specific reduction pipeline of HERMES (Raskin et al. 2011) includes similar steps as the UVES pipeline, and is used for the full reduction of the spectra.

6.2.3 Normalisation and merging

When necessary, the individual reduced spectra of each object are first corrected for radial velocity differences (see Table 1). For UVES spectra, the radial velocities are determined by using the positions of individual spectral lines. For HERMES spectra, the radial velocities are determined using a cross-correlation routine specific to the HERMES pipeline (Raskin et al. 2011).

Thereafter, weighted mean spectra are calculated for the individual wavelength ranges of UVES and for the total HERMES spectra. For the normalisation of the spectra we subdivided the weighted mean spectra into fixed wavelength ranges of 120 Å where the first and last 10 Å overlap with the previous and subsequent spectral parts. Specific care was taken as to conserve the Balmer profiles during the normalisation procedure. Each subspectrum is normalised individually by fitting a fifth order polynomial through interactively defined continuum points. After the individual normalisations, all normalised subspectra are then merged into one large spectrum which is used for the spectral abundance studies.

6.3 Spectral analyses

Figs. 6.1, 6.2 and 6.3 presents the spectral region around the Ba II line at 6141.813 Å together with the identification of several spectral lines. Each figure corresponds to a different range in effective temperature $T_{\rm eff}$ (see Sect. 6.3.1): Fig. 6.1 shows our sample stars with $T_{\rm eff} < 7000$ K, Fig. 6.2 shows sample stars with $7000\ {\rm K} \leqslant T_{\rm eff} < 8000$ K and Fig. 6.3 shows the sample stars with $T_{\rm eff} \geqslant 8000$ K. The figures illustrate how the number of strong spectral lines decreases with increasing effective temperature for all elements.

The overall S/N of the red spectra of UVES (see Table 6.1) and the optical spectral regions of HERMES is very high and ranges from 80 to 200. We perform a comparative systematic analysis of all objects and hence decide not

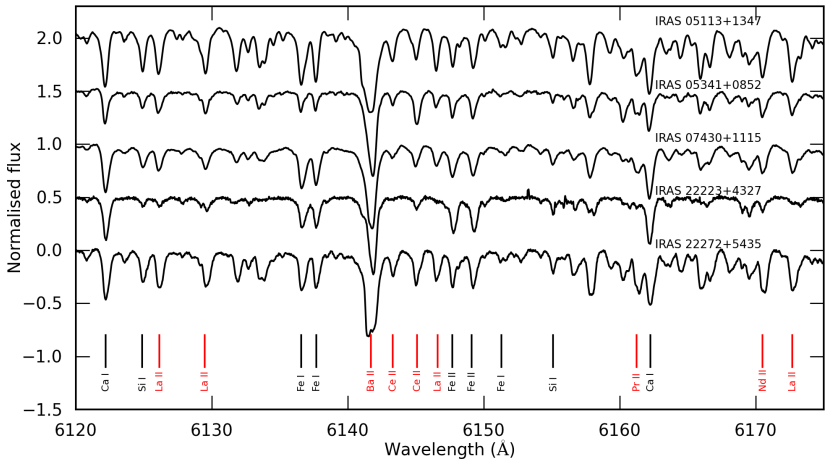

Figure 6.1: Comparison of the normalised spectra of all sample stars with T_{eff} < 7000 K. The spectra have been shifted in flux for clarity and all spectra are shifted to zero velocity. Red and black vertical lines mark positions of *s*-nuclei and non *s*-nuclei respectively. For more information, see text.

to rely on the previous results in the literature, but perform an independent full spectral analysis using the same method for all objects. Depending on the temperature of the star, the S/N of spectra below 3700 Å are too poor for both spectrographs, so these regions are not used for our analysis. For the UVES data, we use the full red spectral region sampled in our setting as well as the spectral region from 3900 Å onwards. For hotter stars, we could extend this region towards bluer wavelengths.

In this contribution we focus on Pb but unfortunately, the optical spectrum of Pb is poor in spectral lines for the typical atmospheric parameters of our sample stars. The strongest Pb I lies in the blue part of the spectrum (λ4057.807 Å), a spectral region with low S/N and a large number of blends. For some hotter stars, the strongest line of Pb II at 5608.853 Å will be used to constrain the Pb abundance. To investigate the possible strength of Pb, we calculated which input [Pb/H] abundance is needed to create a spectral line of 5 mÅ. The latter is the lower limit for distinguishing spectral lines from noise in the spectra. Fig. 6.4 shows these theoretical Pb abundances for different effective temperatures and for [Fe/H] = -1.0 dex and [Fe/H] = -0.2 dex. These abundances are calculated for a $\log g$ = 1.5 dex for all stars with T_{eff} < 9250 K and for log g = 2.0 dex for 9250 and 9500 K. Fig. 6.4 shows that the needed Pb abundance for a spectral line detection increases significantly with rising temperature. The figure also shows that the effect of metallicity is negligible in the temperature

Table 6.2: Model atmospheres of the sample of stars. The errors for [Fe/H] include line to line scatter and model uncertainty (see Sect. 6.3.2). N_{FeI} and N_{FeII} show the number of lines used for Fe I and Fe II respectively.

Object	T_{eff} (K) ± 125	$\log g$ (dex) ± 0.25	ξ_t (km/s) ± 0.25	[FeI/H]	[FeII/H]	N_{FeI}	N_{FeII}
IRAS 05113+1347	5500	0.50	5.00	-0.49 ± 0.15	-0.54 ± 0.17	21	11
IRAS 05341+0852	6750	1.25	3.50	-0.70 ± 0.15	-0.54 ± 0.11	47	20
IRAS 06530-0213	7375	1.25	4.00	-0.38 ± 0.20	-0.32 ± 0.11	24	54
IRAS 07134+1005	7250	0.50	3.25	-0.96 ± 0.31	-0.91 ± 0.20	42	32
IRAS 07430+1115	6000	1.00	3.25	-0.31 ± 0.15	-0.35 ± 0.15	43	17
IRAS 08143-4406[a]	7000	1.50	5.50	-0.45 ± 0.16	-0.43 ± 0.11	17	8
IRAS 08143-4406[b]	7250	1.50	5.00	-0.37 ± 0.17	-0.36 ± 0.11	70	23
IRAS 08281-4850	7875	1.25	5.50	-0.29 ± 0.31	-0.26 ± 0.11	44	23
IRAS 13245-5036	9500	2.75	4.50	-0.35 ± 0.20	-0.30 ± 0.10	21	41
IRAS 14325-6428	8000	1.00	5.75	-0.55 ± 0.33	-0.56 ± 0.10	26	58
IRAS 14429-4539	9375	2.50	4.75	-0.26 ± 0.21	-0.18 ± 0.11	26	52
IRAS 17279-1119	7250	1.25	3.00	-0.51 ± 0.19	-0.64 ± 0.12	44	30
IRAS 19500-1709	8000	1.00	6.00	-0.58 ± 0.42	-0.59 ± 0.10	33	32
IRAS 22223+4327	6500	1.00	4.75	-0.32 ± 0.14	-0.30 ± 0.11	80	25
IRAS 22272+5435	5750	0.50	4.25	-0.77 ± 0.14	-0.77 ± 0.12	35	24

[a] Results of the Blue437 and Red860 observations of IRAS 08143-4406 in Table 6.1.
[b] Results of the Red580 observations of IRAS 08143-4406 in Table 6.1.

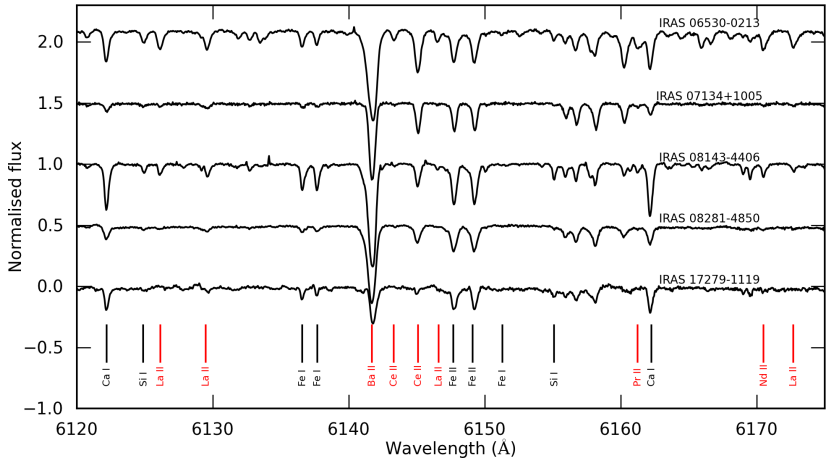

Figure 6.2: Similar to Fig. 6.1, but for the sample stars with 7000 K $\leqslant T_{\rm eff} <$ 8000 K.

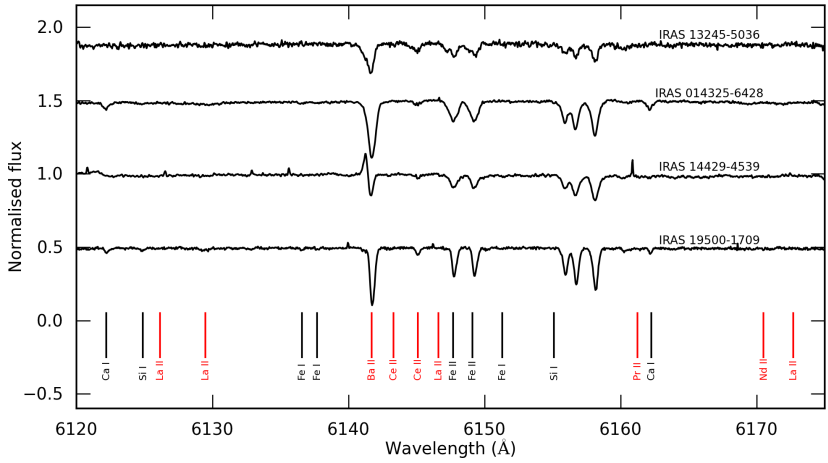

Figure 6.3: Similar to Figs. 6.1 and 6.2, but for the sample stars with $T_{\rm eff} \geqslant$ 8000 K.

and metallicity range of the programme stars.

In order to trace Pb we have to synthesise the spectral regions around the Pb lines and hence we need a complete set of abundances. For these, we used the spectral regions with good S/N. We use the same methods for the atmospheric

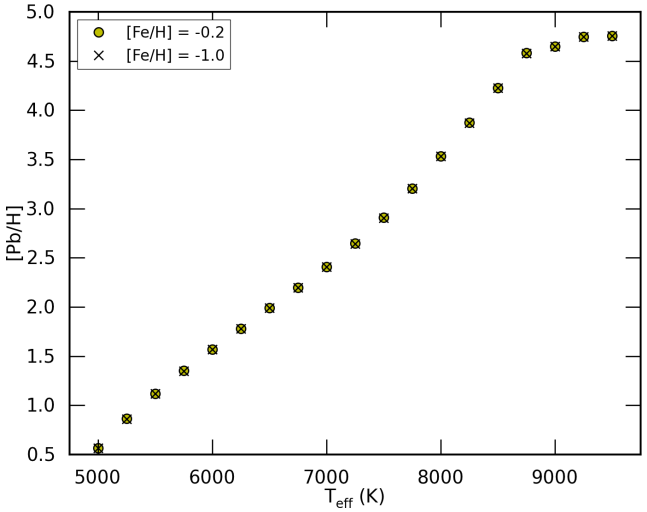

Figure 6.4: Overview of [Pb/H] needed to obtain a Pb I or Pb II spectral line of 5 mÅ for different temperatures and metallicities. For more information, see text.

parameter determinations and abundance studies for all programme stars. Then, we used these abundances to make detailed spectral synthesis spectra in the regions of the strongest Pb lines. In this way, we obtained the best constraints on the Pb abundances.

We have written a Python wrapper (PyMOOG) around the local thermal equilibrium (LTE) abundance calculation routine MOOG (version June 2014 Sneden 1973) which is combined with LTE Kurucz-Castelli atmosphere models (Castelli & Kurucz 2004). Spectral line identification is based on linelists from the VALD database (Kupka et al. 1999) in combination with a list of spectral lines that has been gathered at the Institute of Astronomy (KULeuven) for the chemical analysis of A, F and G stars (Van Winckel & Reyniers 2000). The implemented linelists cover a wavelength range from 3000 up to 11000 Å, covering the full wavelength coverage of the UVES and HERMES spectra. We have included linelists for about 160 ions ranging from helium (He, Z=2) up to uranium (U, Z=92). Neutral and firstly ionised lines are available for most elements. For some *s*-elements, the second ionisation is also included and will be used for the spectral abundance studies of the hottest stars in the sample.

The equivalent width (EW) of spectral lines are interactively measured via direct integration in PyMOOG. The abundances are computed via an iterative

process in which the theoretical EWs of single lines are computed for given abundances and matched to the observed EWs. Blended lines are avoided as much as possible, although for some species, we could sometimes only use blended lines in our strongly *s*-process enriched stars.

6.3.1 Atmospheric parameters

The atmospheric parameters are determined using Fe I and Fe II lines in the standard spectroscopic method: the effective temperature $T_{\rm eff}$ is determined by imposing the iron abundance to be independent of lower excitation potential; surface gravity $\log g$ by imposing ionisation equilibrium between the individual Fe I and Fe II abundances; microturbulent velocity by imposing the iron abundance to be independent of reduced equivalent width which we define as EW/λ.

To decrease the abundance uncertainty imposed by the stepsize of the atmospheric parameters, we use linear interpolation to calculate atmospheric models which lie within the parameter steps of the Kurucz-Castelli models. We choose temperature steps of 125 K, surface gravity steps of 0.25 dex and microturbulent velocity steps of 0.25 km/s.

The individual atmospheric parameter results for the sample of stars are listed in Table 6.2. The shown uncertainties for [FeI/H] and [FeII/H] include both line-to-line scatter and atmospheric parameter uncertainties as described below in Sect. 6.3.2. Similar to Reyniers et al. (2004), we have determined the atmospheric parameters separately for the different spectra sets of IRAS 08143-4406 (see Sect. 6.2). Within the time gap between the observations, the spectral lines of IRAS 08143-4406 had changed significantly, resulting in different sets of atmospheric parameters. These changing spectral line shapes are expected as post-AGB stars cross the Population II Cepheid instability strip during their evolution hence pulsations may strongly change the atmospheric parameters. For the other stars, the spectral lines did not show any visible changes within the time of the observations.

Typically, the uncertainties for Fe I lines are larger than those of Fe II because of the larger sensitivity of Fe I lines to temperature. For the two new 21 μm post-AGB stars IRAS 13245-5036 and IRAS 14429-4539, we find higher temperatures and higher surface gravities with respect to the other sample stars, which points to a more evolved phase of the post-AGB evolutionary stage.

Table 6.3: Abundance results of IRAS 05113+1347, IRAS 05341+0852, IRAS 07430+1115 and IRAS 22272+5435.

		IRAS05113 [Fe/H] = -0.49					IRAS05341 [Fe/H] = -0.54					IRAS07430 [Fe/H] = -0.31					IRAS22272 [Fe/H] = -0.77				
Ion	log $\epsilon_\odot$	N	log ϵ	σ_{121}	[X/Fe]	σ_{tot}	N	log ϵ	σ_{121}	[X/Fe]	σ_{tot}	N	log ϵ	σ_{121}	[X/Fe]	σ_{tot}	N	log ϵ	σ_{121}	[X/Fe]	σ_{tot}
C I	8.43	6	8.87	0.11	0.65	0.16	16	8.73	0.10	1.03	0.10	6	8.87	0.06	0.79	0.13	14	8.71	0.07	1.05	0.12
O I	8.69	1	8.49	0.20	0.01	0.27	2	8.71	0.07	0.75	0.11	2	8.64	0.20	0.30	0.22	2	8.55	0.02	0.63	0.09
Na I	6.24	2	5.88	0.01	0.17	0.12	1	6.00	0.20	0.46	0.23	2	6.20	0.09	0.27	0.12	2	5.90	0.00	0.42	0.09
Mg I	7.60	1	7.20	0.20	0.13	0.24	1	6.88	0.20	-0.02	0.24	2	7.26	0.01	-0.03	0.11	3	6.75	0.20	-0.08	0.17
Al I	6.45											2	6.37	0.13	0.24	0.15	1	6.07	0.20	0.39	0.23
Si I	7.51	4	7.23	0.06	-0.07	0.20	5	7.04	0.10	0.26	0.18	5	7.52	0.13	0.36	0.19	4	7.06	0.05	0.32	0.16
S I	7.12	1	6.97	0.20	0.06	0.25	3	6.65	0.09	0.25	0.15	2	6.69	0.02	-0.08	0.13	2	6.64	0.02	0.28	0.11
Ca I	6.34	3	5.66	0.03	-0.14	0.10	7	5.83	0.05	0.20	0.08	7	6.03	0.09	-0.0	0.08	8	5.81	0.10	0.24	0.08
Ca II	6.34						3	5.97	0.09	0.36	0.12						1	5.79	0.20	0.22	0.24
Sc II	3.15	6	2.87	0.09	-0.08	0.13	6	2.72	0.09	0.30	0.09	4	3.00	0.06	0.20	0.10	3	2.75	0.20	0.37	0.18
Ti I	4.95	4	4.47	0.09	0.05	0.13						5	4.90	0.11	0.27	0.11	2	4.50	0.05	0.32	0.10
Ti II	4.95	3	4.41	0.05	-0.34	0.12	2	4.50	0.20	0.28	0.19	9	4.86	0.09	0.26	0.09	2	4.47	0.03	0.29	0.11
V I	3.93	3	3.71	0.11	0.32	0.15						1	4.00	0.20	0.38	0.24					
V II	3.93											2	3.99	0.03	0.41	0.13	2	3.21	0.03	0.05	0.11
Cr I	5.64	4	5.02	0.03	-0.09	0.10	2	4.99	0.06	0.05	0.12	2	5.20	0.02	-0.13	0.09	4	4.91	0.06	0.03	0.08
Cr II	5.64						10	5.03	0.06	0.12	0.07	6	5.16	0.07	-0.13	0.08	9	4.94	0.06	0.06	0.07
Mn I	5.43	1	4.60	0.20	-0.3	0.24						2	4.96	0.06	-0.15	0.11	1	4.58	0.20	-0.08	0.22
Mn II	5.43						1	5.40	0.20	0.70	0.22						1	4.60	0.20	-0.06	0.22
Fe I	7.50	21	6.96	0.11	0.00	0.08	47	6.80	0.10	0.00	0.06	43	7.19	0.08	0.00	0.05	35	6.73	0.07	0.00	0.05
Fe II	7.50	10	7.29	0.13	0.00	0.11	20	6.77	0.07	0.00	0.05	17	7.15	0.08	0.00	0.06	24	6.73	0.08	0.00	0.05

Notes: For each ion, the table lists the used number of lines (N) for the abundance determination, the determined abundance (log ϵ), the uncertainty on this abundance due to line-to-line scatter (σ_{121}), the element over iron ratio ([X/Fe]) and the total uncertainty on [X/Fe] (σ_{tot}) which includes line-to-line scatter and atmospheric parameter uncertainty (see text for details).

The solar abundances (log $\epsilon_\odot$) in the second column are retrieved from Asplund et al. (2009).

For all elemental abundances determined via only one spectral line or via spectrum synthesis, we adopt a line-to-line scatter of 0.20 dex.

Table 6.3: Continued.

		IRAS05113 [Fe/H] = -0.49					IRAS05341 [Fe/H] = -0.54					IRAS07430 [Fe/H] = -0.31					IRAS22272 [Fe/H] = -0.77				
Ion	log $\epsilon_\odot$	N	log ϵ	σ_{121}	[X/Fe]	σ_{tot}	N	log ϵ	σ_{121}	[X/Fe]	σ_{tot}	N	log ϵ	σ_{121}	[X/Fe]	σ_{tot}	N	log ϵ	σ_{121}	[X/Fe]	σ_{tot}
Co I	4.99	2	4.59	0.01	0.13	0.13															
Ni I	6.22	5	5.78	0.10	0.10	0.11	6	5.81	0.06	0.29	0.08	11	5.89	0.12	-0.01	0.09	8	5.66	0.07	0.21	0.07
Cu I	4.19	1	3.94	0.20	0.28	0.24	1	4.25	0.20	0.76	0.23	2	3.92	0.07	0.05	0.12	1	3.80	0.20	0.37	0.22
Zn I	4.56	1	4.15	0.20	-0.2	0.32						1	4.46	0.20	0.25	0.28	1	4.06	0.20	0.27	0.29
Y II	2.21	2	3.30	0.20	1.29	0.22	4	3.47	0.10	1.98	0.12	1	3.25	0.20	1.39	0.24	4	3.14	0.08	1.69	0.12
Zr II	2.58	3	3.73	0.11	1.36	0.15	2	3.61	0.06	1.76	0.10	2	3.45	0.12	1.22	0.15	3	3.35	0.08	1.54	0.11
La II	1.10	6	2.69	0.16	1.80	0.16	8	2.82	0.08	2.45	0.11	11	2.50	0.12	1.75	0.12	6	2.65	0.20	2.32	0.15
Ce II	1.58	4	3.18	0.10	1.80	0.14	5	3.12	0.06	2.27	0.10	5	2.71	0.09	1.47	0.11	4	2.66	0.06	1.84	0.11
Pr II	0.72	6	2.20	0.14	1.68	0.16	7	2.27	0.09	2.28	0.14	11	1.94	0.13	1.57	0.14	13	1.81	0.07	1.86	0.13
Nd II	1.42	8	2.88	0.05	1.66	0.13	23	3.18	0.11	2.49	0.13	17	2.64	0.08	1.57	0.12	7	2.61	0.05	1.96	0.13
Sm II	0.96	3	2.10	0.09	1.34	0.16	2	1.99	0.12	1.76	0.16	4	2.05	0.13	1.43	0.15	3	1.67	0.09	1.47	0.14
Eu II	0.52	2	1.21	0.10	0.90	0.16	2	1.25	0.09	1.46	0.14	2	0.98	0.07	0.81	0.13	2	0.89	0.06	1.14	0.12
Gd II	1.07	3	2.29	0.09	1.43	0.16	2	2.17	0.08	1.82	0.12	3	2.00	0.07	1.28	0.13	13	1.99	0.12	1.69	0.16
Tb II	0.30											1	1.70	0.20	1.75	0.27					
Dy II	1.10	2	2.34	0.01	1.44	0.14	2	2.25	0.20	1.88	0.20	2	2.18	0.00	1.43	0.13	8	2.13	0.09	1.80	0.11
Er II	0.92	4	2.15	0.07	1.43	0.14	2	2.23	0.05	2.04	0.12						3	1.74	0.04	1.58	0.10
Yb II	0.84						1	2.50	0.20	2.39	0.24						1	2.00	0.20	1.93	0.24
Lu II	0.10	2	1.34	0.20	1.45	0.23	2	1.74	0.01	2.36	0.12	1	0.85	0.20	1.10	0.25	2	1.25	0.20	1.92	0.21
Hf II	0.85	2	2.19	0.09	1.55	0.16	1	2.15	0.20	2.02	0.23						2	1.85	0.20	1.77	0.19
W II	0.85						1	3.07	0.20	2.95	0.25						1	2.30	0.20	2.21	0.25

Table 6.4: Abundance results of IRAS 06530-0213, IRAS 22223+4327 and both observations of IRAS08143-4406. The list of IRAS08143 BLUE437 contains the results for the Blue437 and Red860 spectra, the list of IRAS08143 RED580 shows the results for the Red580 spectra (see Sect. 6.2).

		IRAS06530 [Fe/H] = -0.32					IRAS08143 BLUE437 [Fe/H] = -0.43					IRAS08143 RED580 [Fe/H] = -0.36					IRAS22223 [Fe/H] = -0.30				
Ion	log $\epsilon_\odot$	N	log ϵ	σ_{12l}	[X/Fe]	σ_{tot}	N	log ϵ	σ_{12l}	[X/Fe]	σ_{tot}	N	log ϵ	σ_{12l}	[X/Fe]	σ_{tot}	N	log ϵ	σ_{12l}	[X/Fe]	σ_{tot}
C I	8.43	10	8.94	0.07	0.83	0.13	15	8.71	0.06	0.71	0.10	11	8.74	0.09	0.67	0.12	19	8.72	0.06	0.59	0.07
N I	7.83						7	7.41	0.30	0.01	0.22						2	7.68	0.30	0.15	0.21
O I	8.69	6	8.72	0.08	0.35	0.11						3	8.52	0.04	0.19	0.13	5	8.70	0.06	0.31	0.13
Na I	6.24	1	6.32	0.20	0.46	0.22						2	6.35	0.08	0.48	0.11	2	6.20	0.04	0.28	0.08
Mg I	7.60	1	7.22	0.20	-0.0	0.23	4	7.21	0.06	0.05	0.09	2	7.22	0.04	-0.01	0.10	1	7.30	0.20	0.02	0.22
Al I	6.45						2	6.40	0.01	0.40	0.09	1	6.42	0.20	0.34	0.22	2	6.10	0.04	-0.03	0.09
Si I	7.51	2	7.34	0.13	0.15	0.22	4	7.54	0.06	0.46	0.17	7	7.66	0.08	0.51	0.18	14	7.42	0.10	0.21	0.17
Si II	7.51	1	7.36	0.20	0.17	0.24															
P I	5.41						1	5.80	0.20	0.82	0.26										
S I	7.12	3	7.00	0.05	0.21	0.18	7	7.10	0.08	0.41	0.14	3	7.10	0.01	0.34	0.15	5	6.94	0.08	0.12	0.12
Ca I	6.34	12	6.18	0.09	0.22	0.09	3	6.15	0.07	0.26	0.09	12	6.16	0.09	0.18	0.08	8	6.01	0.08	-0.01	0.07
Ca II	6.34	2	6.08	0.01	0.06	0.10						4	6.11	0.07	0.13	0.10	3	6.00	0.07	-0.04	0.10
Sc II	3.15	5	3.15	0.03	0.33	0.09						2	3.09	0.04	0.30	0.10	4	2.95	0.10	0.10	0.11
Ti I	4.95						5	5.03	0.13	0.53	0.11	5	5.06	0.07	0.47	0.09					
Ti II	4.95	5	4.79	0.05	0.16	0.09						5	5.01	0.09	0.42	0.10	5	4.54	0.12	-0.11	0.11
V II	3.93						2	3.75	0.01	0.25	0.12	1	3.74	0.20	0.17	0.24	4	3.64	0.17	0.01	0.15
Cr I	5.64	2	5.45	0.03	0.19	0.09	4	5.33	0.07	0.13	0.09	4	5.41	0.11	0.13	0.11	6	5.22	0.11	-0.1	0.09
Cr II	5.64	11	5.36	0.07	0.04	0.07	2	5.31	0.06	0.10	0.11	13	5.31	0.06	0.03	0.07	11	5.29	0.06	-0.05	0.06
Mn I	5.43	2	4.99	0.20	-0.07	0.19	3	5.05	0.03	0.07	0.08	2	5.05	0.20	-0.02	0.19	2	4.98	0.03	-0.13	0.08
Mn II	5.43						1	5.08	0.20	0.08	0.23	1	5.05	0.20	-0.01	0.23					
Fe I	7.50	54	7.12	0.08	0.00	0.05	17	7.05	0.08	0.00	0.06	70	7.13	0.08	0.00	0.04	80	7.18	0.06	0.00	0.04
Fe II	7.50	24	7.18	0.08	0.00	0.06	8	7.07	0.10	0.00	0.10	23	7.14	0.09	0.00	0.06	25	7.20	0.07	0.00	0.05

Notes: Same as for Table 6.3.

Table 6.4: Continued.

		IRAS06530 [Fe/H] = -0.32					IRAS08143 BLUE437 [Fe/H] = -0.43					IRAS08143 RED580 [Fe/H] = -0.36					IRAS22223 [Fe/H] = -0.30				
Ion	log $\epsilon_\odot$	N	log ϵ	σ_{121}	[X/Fe]	σ_{tot}	N	log ϵ	σ_{121}	[X/Fe]	σ_{tot}	N	log ϵ	σ_{121}	[X/Fe]	σ_{tot}	N	log ϵ	σ_{121}	[X/Fe]	σ_{tot}
Co II	4.99																1	4.71	0.20	0.02	0.23
Ni I	6.22	5	6.07	0.05	0.23	0.08	13	6.06	0.08	0.28	0.07	4	6.08	0.05	0.22	0.08	13	5.87	0.07	-0.03	0.06
Ni II	6.22	1	6.15	0.20	0.25	0.23															
Cu I	4.19	1	4.39	0.20	0.58	0.22						1	4.32	0.20	0.50	0.22	1	4.09	0.20	0.22	0.22
Zn I	4.56	1	4.70	0.20	0.46	0.30						1	4.60	0.20	0.40	0.29	3	4.36	0.09	0.10	0.19
Y II	2.21	2	3.79	0.11	1.91	0.16	3	3.63	0.04	1.85	0.11	2	3.65	0.02	1.80	0.12	3	3.24	0.08	1.33	0.11
Zr II	2.58	2	3.86	0.04	1.60	0.10	5	3.85	0.13	1.70	0.12	4	3.85	0.10	1.63	0.11	3	3.63	0.06	1.35	0.10
Mo II	1.88																1	2.89	0.20	1.31	0.23
Ba II	2.18						1	3.45	0.20	1.70	0.27						1	2.89	0.20	1.01	0.26
La II	1.10	7	3.06	0.05	2.28	0.16	18	2.47	0.05	1.80	0.11	14	2.46	0.10	1.72	0.14	14	1.87	0.11	1.07	0.12
Ce II	1.58	10	3.31	0.12	2.05	0.15	7	2.61	0.04	1.46	0.11	5	2.56	0.10	1.35	0.14	5	2.30	0.10	1.02	0.13
Pr II	0.72	5	2.75	0.07	2.35	0.19	6	2.15	0.07	1.85	0.16	9	2.10	0.09	1.74	0.17	5	1.44	0.07	1.02	0.15
Nd II	1.42	16	3.31	0.07	2.21	0.18	12	2.70	0.06	1.71	0.14	19	2.67	0.09	1.61	0.16	13	1.96	0.11	0.85	0.15
Sm II	0.96	2	2.25	0.04	1.61	0.17	16	1.90	0.04	1.37	0.12	6	1.91	0.08	1.31	0.15	8	1.25	0.10	0.59	0.14
Eu II	0.52	2	1.56	0.01	1.36	0.17						2	1.10	0.01	0.94	0.14	2	0.78	0.14	0.56	0.16
Gd II	1.07	5	2.59	0.11	1.84	0.13	8	2.00	0.06	1.36	0.09	2	2.02	0.01	1.31	0.11	1	1.67	0.20	0.90	0.23
Dy II	1.10																1	1.80	0.20	1.00	0.24
Er II	0.92	2	2.88	0.07	2.29	0.15	2	2.20	0.20	1.71	0.20	1	2.20	0.20	1.64	0.24	1	1.18	0.20	0.56	0.23
Tm II	0.10	1	1.45	0.20	1.67	0.24															
Yb II	0.84	1	2.72	0.20	2.21	0.25	1	2.15	0.20	1.74	0.25	1	2.12	0.20	1.64	0.25					
Lu II	0.10	3	1.85	0.20	2.07	0.19						1	1.00	0.20	1.26	0.25					
Hf II	0.85	1	2.43	0.20	1.91	0.22															
W II	0.85	1	2.98	0.20	2.45	0.25						1	2.15	0.20	1.66	0.25	1	1.45	0.20	0.90	0.25

Table 6.5: Abundance results of IRAS 07134+1005, IRAS 08281-4850, IRAS 17279-1119 and IRAS 19500-1709.

		IRAS07134 [Fe/H] = -0.91					IRAS08281 [Fe/H] = -0.26					IRAS17279 [Fe/H] = -0.64					IRAS19500 [Fe/H] = -0.59				
Ion	log $\epsilon_\odot$	N	log ϵ	σ_{121}	[X/Fe]	σ_{tot}	N	log ϵ	σ_{121}	[X/Fe]	σ_{tot}	N	log ϵ	σ_{121}	[X/Fe]	σ_{tot}	N	log ϵ	σ_{121}	[X/Fe]	σ_{tot}
C I	8.43	47	8.68	0.08	1.16	0.22	16	8.91	0.05	0.75	0.21	17	8.36	0.09	0.47	0.14	15	8.82	0.06	0.99	0.33
N I	7.83	3	7.50	0.30	0.57	0.19						1	7.27	0.30	-0.07	0.35	3	7.65	0.30	0.41	0.17
O I	8.69	9	8.59	0.06	0.81	0.19	5	8.54	0.06	0.12	0.11	2	8.39	0.05	0.24	0.16	8	8.81	0.04	0.72	0.09
Na I	6.24						1	6.65	0.20	0.70	0.22	2	6.25	0.05	0.52	0.11					
Mg I	7.60	4	6.89	0.06	0.26	0.13	3	7.38	0.09	0.07	0.10	2	7.25	0.06	0.16	0.12	2	7.31	0.01	0.29	0.07
Mg II	7.60																3	7.29	0.00	0.28	0.10
Al I	6.45																1	5.51	0.20	-0.36	0.21
Si I	7.51						2	7.50	0.20	0.25	0.31	6	7.33	0.10	0.36	0.20	1	7.03	0.20	0.11	0.49
Si II	7.51											1	7.33	0.20	0.36	0.26	2	7.01	0.06	0.10	0.13
S I	7.12	1	6.59	0.20	0.38	0.35	3	7.24	0.03	0.38	0.24	2	6.91	0.02	0.33	0.18					
K I	5.03	2	4.68	0.07	0.61	0.12															
Ca I	6.34	11	5.44	0.05	0.07	0.11	5	6.29	0.08	0.25	0.15	7	6.00	0.07	0.17	0.09	3	6.08	0.06	0.32	0.23
Ca II	6.34	3	5.47	0.03	0.04	0.18	2	6.18	0.03	0.10	0.16	1	6.00	0.20	0.20	0.25	3	5.92	0.08	0.18	0.26
Sc II	3.15	8	2.41	0.06	0.17	0.09	5	3.19	0.04	0.30	0.13	7	2.71	0.09	0.10	0.12	8	2.78	0.11	0.23	0.22
Ti I	4.95											3	4.62	0.06	0.18	0.12					
Ti II	4.95	24	4.18	0.09	0.14	0.08	12	4.74	0.04	0.05	0.09	16	4.65	0.13	0.24	0.10	33	4.54	0.09	0.19	0.14
V II	3.93	5	3.32	0.10	0.30	0.11	1	3.68	0.20	0.02	0.24	5	3.92	0.10	0.53	0.13	11	3.62	0.10	0.28	0.12
Cr I	5.64	3	4.70	0.14	0.03	0.16	1	5.40	0.20	0.05	0.22	2	5.17	0.03	0.04	0.11	3	5.12	0.10	0.06	0.11
Cr II	5.64	14	4.85	0.09	0.12	0.10	12	5.33	0.05	-0.05	0.06	13	5.14	0.11	0.04	0.10	24	5.14	0.10	0.10	0.07
Mn I	5.43	2	4.56	0.04	0.10	0.09											2	4.75	0.03	-0.09	0.09
Mn II	5.43	4	4.52	0.08	0.00	0.16						2	5.03	0.10	0.13	0.15	5	4.91	0.04	0.07	0.06
Fe I	7.50	42	6.53	0.07	0.00	0.05	44	7.21	0.07	0.00	0.04	44	6.99	0.10	0.00	0.06	33	6.92	0.06	0.00	0.04
Fe II	7.50	32	6.59	0.09	0.00	0.06	23	7.24	0.07	0.00	0.05	30	6.96	0.13	0.00	0.08	32	6.91	0.03	0.00	0.03

Notes: Same as for Table 6.3.

Table 6.5: Continued.

		IRAS07134 [Fe/H] = -0.91					IRAS08281 [Fe/H] = -0.26					IRAS17279 [Fe/H] = -0.64					IRAS19500 [Fe/H] = -0.59				
Ion	$\log \epsilon_\odot$	N	$\log \epsilon$	σ_{12l}	[X/Fe]	σ_{tot}	N	$\log \epsilon$	σ_{12l}	[X/Fe]	σ_{tot}	N	$\log \epsilon$	σ_{12l}	[X/Fe]	σ_{tot}	N	$\log \epsilon$	σ_{12l}	[X/Fe]	σ_{tot}
Co I	4.99											2	4.28	0.14	-0.2	0.17					
Co II	4.99																1	4.70	0.20	0.31	0.22
Ni I	6.22	5	5.34	0.08	0.09	0.09						4	6.13	0.11	0.43	0.12	3	5.79	0.08	0.15	0.08
Ni II	6.22	1	5.32	0.20	0.01	0.26	2	5.90	0.20	-0.06	0.19	4	6.07	0.07	0.39	0.11	2	5.80	0.07	0.18	0.09
Zn I	4.56											1	4.25	0.20	0.23	0.31					
Y II	2.21	12	2.97	0.12	1.67	0.13	7	3.66	0.06	1.72	0.19	10	2.38	0.12	0.71	0.12	11	3.02	0.11	1.40	0.29
Zr II	2.58	15	3.28	0.09	1.61	0.09	12	3.74	0.10	1.42	0.11	10	2.82	0.11	0.77	0.12	22	3.32	0.10	1.34	0.19
Mo II	1.88	1	2.68	0.20	1.71	0.27	1	3.35	0.20	1.73	0.23						2	2.88	0.08	1.60	0.12
Ba II	2.18	2	3.09	0.02	1.82	0.30	1	3.80	0.20	1.88	0.36	1	2.80	0.20	1.16	0.31	1	3.00	0.20	1.42	0.49
La II	1.10	29	2.04	0.09	1.85	0.24	17	2.70	0.11	1.87	0.28	7	1.48	0.13	0.92	0.17	5	1.87	0.09	1.37	0.43
Ce II	1.58	41	2.27	0.11	1.59	0.20	21	2.85	0.08	1.54	0.24	11	2.02	0.10	0.98	0.15	7	2.28	0.12	1.29	0.39
Pr II	0.72	5	1.43	0.08	1.62	0.31	3	2.40	0.20	1.94	0.34	5	1.35	0.11	1.17	0.21					
Nd II	1.42	29	2.14	0.08	1.63	0.29	15	2.83	0.09	1.67	0.30	8	1.64	0.07	0.75	0.19	5	2.31	0.03	1.48	0.44
Sm II	0.96	13	1.49	0.07	1.44	0.26						3	1.46	0.08	1.03	0.19					
Eu II	0.52	2	0.20	0.20	0.59	0.32	2	1.00	0.20	0.74	0.33						1	1.10	0.20	1.18	0.48
Gd II	1.07	6	1.33	0.08	1.17	0.19	2	1.98	0.02	1.18	0.18						2	1.52	0.18	1.05	0.34
Dy II	1.10	2	1.14	0.20	0.95	0.28	1	1.90	0.20	1.06	0.33										
Er II	0.92	2	1.41	0.00	1.40	0.22	1	2.19	0.20	1.54	0.30										
Lu II	0.10	4	0.80	0.20	1.61	0.22	1	1.30	0.20	1.46	0.25	1	0.50	0.20	0.94	0.27	2	0.64	0.10	1.13	0.21
Hf II	0.85						2	2.35	0.20	1.76	0.20	1	1.04	0.20	0.72	0.25	1	1.53	0.20	1.27	0.25

Table 6.6: Abundance results of IRAS 13245-5036, IRAS 14325-6428 and IRAS 14429-4539.

		IRAS13245 [Fe/H] = -0.30					IRAS14325 [Fe/H] = -0.56					IRAS14429 [Fe/H] = -0.18				
Ion	$\log \epsilon_\odot$	N	$\log \epsilon$	σ_{121}	[X/Fe]	σ_{tot}	N	$\log \epsilon$	σ_{121}	[X/Fe]	σ_{tot}	N	$\log \epsilon$	σ_{121}	[X/Fe]	σ_{tot}
C I	8.43	4	8.70	0.00	0.57	0.21	24	9.06	0.10	1.18	0.23	3	8.93	0.08	0.68	0.23
N I	7.83						7	7.45	0.30	0.18	0.20					
O I	8.69	5	8.65	0.12	0.26	0.13	10	8.70	0.06	0.57	0.09	6	8.82	0.04	0.31	0.12
Na I	6.24						1	6.50	0.20	0.81	0.22					
Mg I	7.60	5	7.16	0.07	-0.09	0.09	4	7.51	0.05	0.47	0.08	3	7.32	0.04	-0.01	0.09
Mg II	7.60	2	7.20	0.07	-0.11	0.11	5	7.37	0.13	0.33	0.14	3	7.29	0.03	-0.13	0.10
Al I	6.45	1	5.75	0.20	-0.35	0.23	1	5.70	0.20	-0.2	0.21	2	5.89	0.01	-0.3	0.09
Al II	6.45											1	5.97	0.20	-0.3	0.26
Si I	7.51	1	7.19	0.20	-0.02	0.33	1	6.85	0.20	-0.1	0.38	1	7.10	0.20	-0.23	0.33
Si II	7.51	3	7.19	0.07	-0.02	0.12	2	6.83	0.00	-0.12	0.18	1	7.15	0.20	-0.18	0.25
S I	7.12						1	7.20	0.20	0.64	0.32					
Ca I	6.34						5	6.23	0.10	0.44	0.21					
Ca II	6.34						2	6.26	0.03	0.48	0.20					
Sc II	3.15	6	3.29	0.11	0.44	0.18	11	2.97	0.11	0.38	0.19	8	3.38	0.12	0.41	0.20
Ti II	4.95	22	4.96	0.10	0.31	0.12	28	4.57	0.07	0.18	0.12	42	5.03	0.10	0.26	0.12
V II	3.93	2	3.73	0.03	0.10	0.11	11	3.60	0.09	0.23	0.12	4	3.99	0.09	0.24	0.13
Cr I	5.64						3	5.28	0.09	0.19	0.10					
Cr II	5.64	11	5.44	0.07	0.10	0.07	22	5.19	0.07	0.11	0.05	28	5.51	0.09	0.05	0.07
Mn I	5.43						1	4.94	0.20	0.06	0.23					
Mn II	5.43											2	5.30	0.04	0.05	0.10
Fe I	7.50	21	7.15	0.10	0.00	0.07	26	6.95	0.06	0.00	0.04	26	7.24	0.09	0.00	0.06
Fe II	7.50	41	7.20	0.06	0.00	0.04	58	6.94	0.06	0.00	0.04	52	7.32	0.09	0.00	0.05

Notes: Same as for Table 6.3.

Table 6.6: Continued.

		IRAS13245 [Fe/H] = -0.26					IRAS14325 [Fe/H] = -0.56					IRAS14429 [Fe/H] = -0.64				
Ion	log $\epsilon_\odot$	N	log ϵ	σ_{121}	[X/Fe]	σ_{tot}	N	log ϵ	σ_{121}	[X/Fe]	σ_{tot}					
Ni I	6.22						3	5.78	0.06	0.12	0.08					
Ni II	6.22	4	5.93	0.07	0.01	0.09	4	5.74	0.10	0.08	0.10	4	5.97	0.10	-0.07	0.11
Y II	2.21	11	3.31	0.04	1.40	0.23	10	2.99	0.12	1.34	0.26	10	3.15	0.10	1.13	0.25
Zr II	2.58	17	4.00	0.08	1.72	0.15	17	3.18	0.12	1.16	0.16	13	3.86	0.10	1.46	0.17
Ba II	2.18	1	4.00	0.20	2.12	0.34	1	3.10	0.20	1.48	0.42					
La II	1.10	3	3.02	0.10	2.22	0.28	7	1.85	0.06	1.31	0.35	4	2.61	0.11	1.69	0.29
Ce II	1.58	4	3.40	0.20	2.12	0.28	3	2.29	0.20	1.27	0.35					
Pr III	0.72	2	2.83	0.08	2.41	0.11										
Nd II	1.42						2	2.25	0.20	1.39	0.40					
Nd III	1.42	12	3.30	0.07	2.18	0.07						15	2.94	0.09	1.70	0.08
Sm II	0.96						1	1.75	0.20	1.35	0.41					
Eu II	0.52						1	0.75	0.20	0.79	0.41					
Gd II	1.07						1	1.76	0.20	1.25	0.34					
Dy II	1.10						1	1.48	0.20	0.94	0.39					
Dy III	1.10	1	2.79	0.20	1.99	0.23										
Lu II	0.10						1	0.85	0.20	1.31	0.28					
Hf II	0.85						1	1.53	0.20	1.24	0.25	1	2.54	0.20	1.87	0.25

6.3.2 Abundance determination

The abundance analysis of the individual programme stars is performed with our preferred atmospheric parameter sets listed in Table 6.2. We only use spectral lines with EWs smaller than 150 mÅ, as stronger lines are saturated. We also avoid spectral lines with EWs smaller than 5 mÅ as these may be confused with noise in the spectra.

Ideally, we would only use isolated lines but the strong enrichments and/or high metallicities of the programme stars make this difficult. Therefore, we use spectrum synthesis to check if suspicious spectral lines are part of identified blends. For some elements, we could only determine the abundance using spectral synthesis.

The number of spectral lines for the carbon abundance determination varies strongly with temperature, while for oxygen only a limited number of spectral lines is available in the temperature range of the programme stars. For almost all stars, the O abundances are determined from the high excitation oxygen multiplet at 6156 Å and/or the forbidden oxygen lines at 6300 and 6363 Å. The latter lines are not affected by possible non-LTE effects (see e.g. Kiselman 2002). For some stars with HERMES spectra, we could determine the nitrogen abundances for spectral lines in the wavelength range between 7000 and 9000 Å. These lines are known to be non-LTE sensitive, however, and therefore we apply the temperature-sensitive non-LTE corrections of Lyubimkov et al. (2011) (see Sect. 6.4).

The number of lines available for elements ranging from sodium (Na, Z=11) up to sulphur (S, Z=16) is limited. Therefore, these abundances can not be determined in all stars. For the iron-peak elements, ranging from calcium (Ca, Z=20) up to zinc (Zn, Z=30), we find a wide range of elemental abundances for the majority of stars.

In all programme stars, we find spectral lines of *s*-process elements of the strontium-peak (Sr, Z=38) and barium-peak (Ba, Z=56), respectively known as the light *s*-process (ls) elements and heavy *s*-process (hs) elements. Unfortunately, we could not determine the abundance of Sr in any object as the available Sr lines are always strongly saturated. For the other ls elements yttrium (Y, Z=39) and zirconium (Zr, Z=40), we find useful spectral lines in each object to determine their abundance. For some stars, we also detect one or two lines for molybdenum (Mo, Z=42).

For the hs elements, we can always determine the abundances of lanthanum (La, Z=57) and neodymium (Nd, Z=60), and for most of the stars, strong cerium (Ce, Z=58) lines are present. In a few objects, we are able to determine the

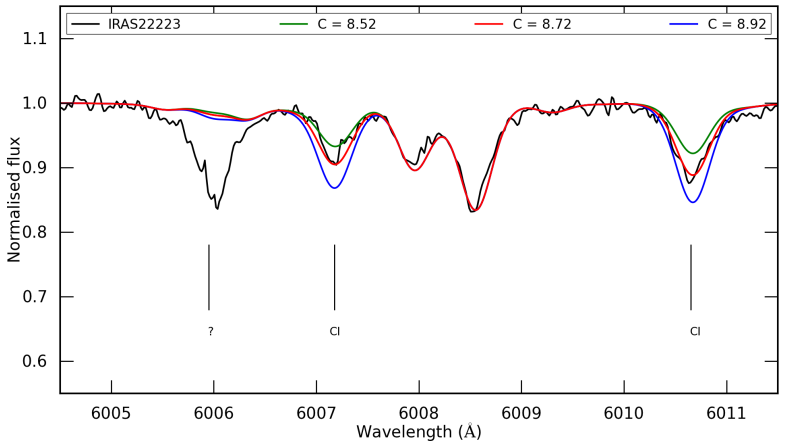

Figure 6.5: Spectrum synthesis of the C I lines at 6007.176 and 6010.675 Å for IRAS 22223+4327. The black spectrum is the observed HERMES spectrum, the colored spectra represent synthetic spectra with different C abundances. The red line represents the determined C abundance, the green and blue spectra represent synthetic spectra with a C abundance of -0.2 dex and +0.2 dex respectively. For more information, see text.

abundance of Ba using a weak Ba II line. In the other stars, the available Ba lines are highly saturated. We can also determine the abundances of a range of elements beyond the Ba-peak like europium (Eu, Z=63), gadolinium (Gd, Z=64), dysprosium (Dy, Z=66), erbium (Er, Z=68), ytterbium (Yb, Z=70), luthetium (Lu, Z=71), hafnium (Hf, Z=72) and tungsten (W, Z=74). Most of the abundances of these elements are determined using spectral synthesis.

6.4 Abundance results till Z $<$ 82 for all sample stars

The abundance results of the different programme stars are listed in Tables 6.3 to 6.6, each table contains stars of similar effective temperatures. The corresponding [X/Fe] results are plotted in Figs. 6.8, 6.9 and 6.10. An overview of the lines used for these analyses can be found in 15 catalogues which are available at CDS[2]. The abundance results for Pb are discussed in Sect. 6.5.

[2]A link to the catalogues

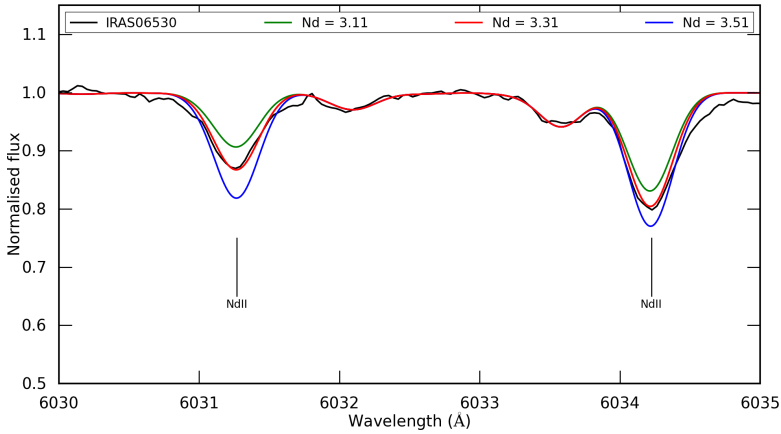

Figure 6.6: Spectrum synthesis of the Nd II lines at 6031.270 and 6034.228 Å for IRAS 06530-0213. The black spectrum is the observed UVES spectrum, the colored spectra represent synthetic spectra with different Nd abundances. The red line represents the determined Nd abundance, the green and blue spectra represent synthetic spectra with a Nd abundance of -0.2 dex and +0.2 dex respectively. For more information, see text.

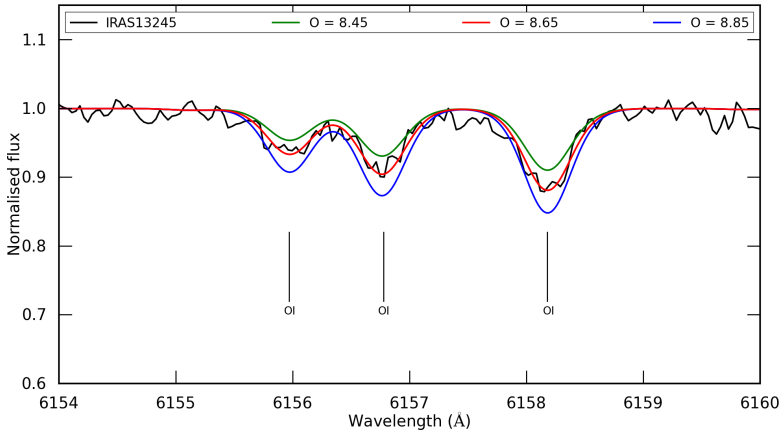

Figure 6.7: Spectrum synthesis of the O I triplet at 6156 Å for IRAS 13245-5036. The black spectrum is the observed UVES spectrum, the colored spectra represent synthetic spectra with different O abundances. The red line represents the determined O abundance, the green and blue spectra represent synthetic spectra with an O abundance of -0.2 dex and +0.2 dex respectively. For more information, see text.

The total errors $\sigma_{\rm tot}$ in Tables 6.3 to 6.6 are calculated following the methodology of Deroo et al. (2005). The errors due to atmospheric parameter uncertainties are calculated by determining the elemental abundances for atmospheric models with an effective temperature $T_{\rm eff}$ $\pm$125 K, surface gravity $\log g \pm 0.25$ dex and microturbulent velocity $\xi_t \pm 0.25$ km/s with respect to the preferred value. We include microturbulent velocity in our error analysis despite the fact that for most ions, the associated error is only of the order of a few 0.01 dex. However, for some ions for which only relatively strong spectral lines are available like Y II, the error due to microturbulence can increase to about 0.1 dex.

The total uncertainty $\sigma_{\rm tot}$ on [X/Fe] is then the quadratic sum of the error on the mean (the line-to-line scatter $\sigma_{\rm l2l}$ divided by the square root of the number of lines used), atmospheric parameter uncertainties ($\sigma_{T_{eff}}$, $\sigma_{\rm logg}$, σ_{ξ_t}) and the Fe abundance error ($\sigma_{\rm Fe}$):

$$\sigma_{\rm tot} = \sqrt{\left(\frac{\sigma_{\rm l2l}}{\sqrt{N_{\rm ion}}}\right)^2 + (\sigma_{T_{eff}})^2 + (\sigma_{\rm logg})^2 + (\sigma_{\xi_t})^2 + \left(\frac{\sigma_{\rm Fe}}{\sqrt{N_{\rm Fe}}}\right)^2}.$$

We assume an intrinsic uncertainty of 0.2 dex for all elemental abundances which are determined by only one line or via spectrum synthesis. This error is a substitute of the line-to-line scatter determined for elements with more useful lines. The [X/Fe] abundances are calculated using the Fe ion with an ionisation potential closest to the ionisation potential of the studied ion. In other words: if the ionisation potential of an ion is below the ionisation potential of Fe I, the Fe I abundance is used for calculating [X/Fe]. If the ionisation potential exceeds the ionisation potential of Fe I, the abundance of Fe II is used instead.

In Tables 6.3 to 6.6, all elemental abundances were double-checked by comparing each spectral line with synthetic spectra with the determined abundances. Examples of such comparisons are shown in Figs. 6.5, 6.6 and 6.7. Fig. 6.5 shows a spectrum synthesis check for the determined C abundance of IRAS 22223+4327. The red synthetic spectrum computed using the determined elemental abundances, fits well the observed spectrum except for the strong spectral line at 6006 Å. To investigate its identification, we artificially increased the abundances of all elements with spectral lines in this spectral region, but none could produce the observed absorption. This shows that the linelists are not complete for our strongly s-process enriched stars, the spectra of which are swamped with transitions of s-process elements. Also, for other stars and different spectral regions, we find spectral lines not included in the linelists.

Fig. 6.6 shows a spectrum synthesis check of the determined Nd abundance of IRAS 06530-0213 for the Nd II lines at 6031.270 and 6034.228 Å, confirming the high Nd abundance of IRAS 06530-0213. The spectrum synthesis of the high excitation O I triplet at 6156 Å of IRAS 13245-5036 is shown in Fig.

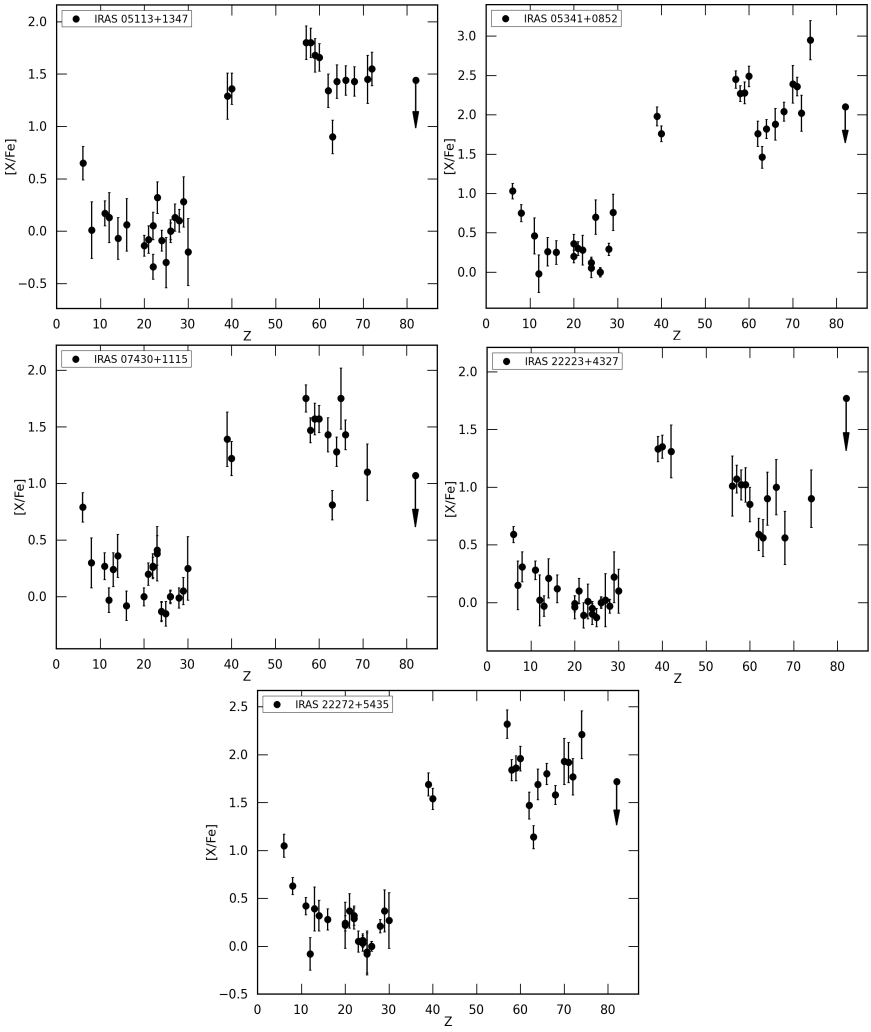

Figure 6.8: Element-over-iron ratios for the programme stars with $T_{eff} < 7000$ K. The down-arrow at Z=82 displays the adopted Pb abundance upper limits. For more information, see text.

6.7 and shows a good agreement between observations and the determined O abundances.

We briefly discuss the derived abundances followed by the comparison between our determined results and those of previous studies. In Sect. 6.5, we discuss

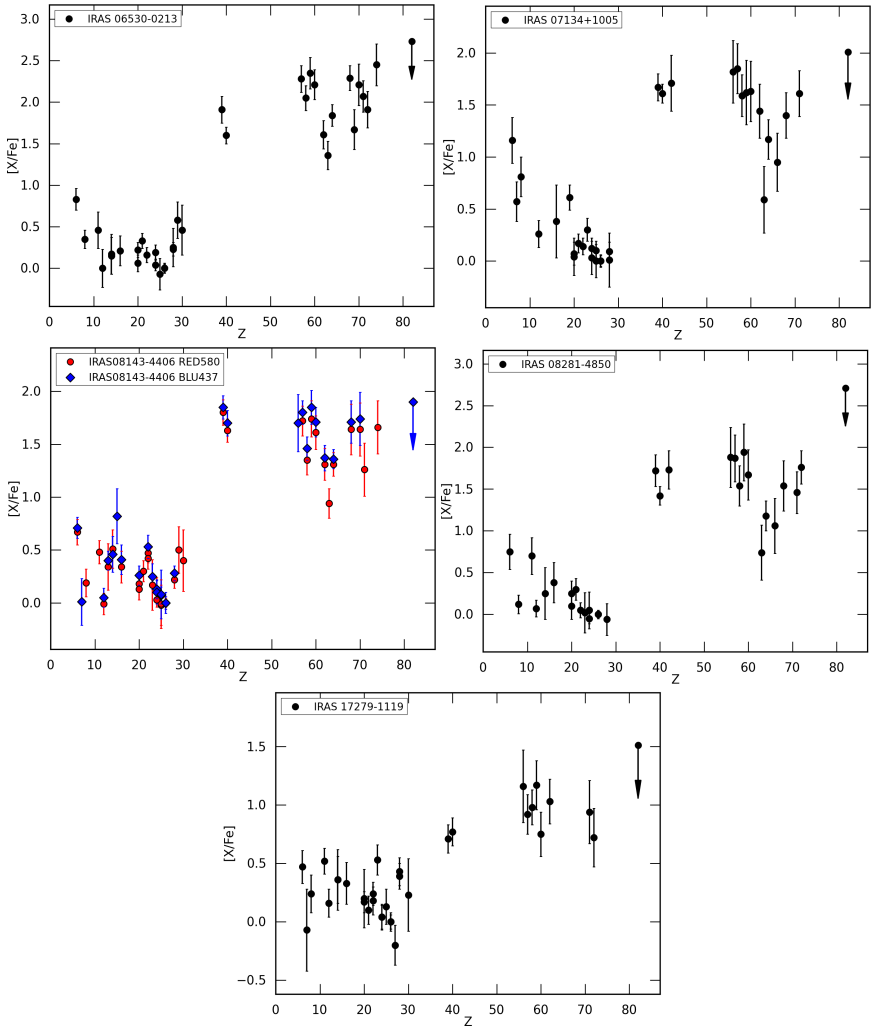

Figure 6.9: Element-over-iron ratios for the programme stars with 7000 K $\leqslant$ $T_{\rm eff}$ $<$ 8000 K. The down-arrow at Z=82 displays the adopted Pb abundance upper limits. For IRAS 08143-4406, the abundance results of both observational settings are shown. For more information, see text.

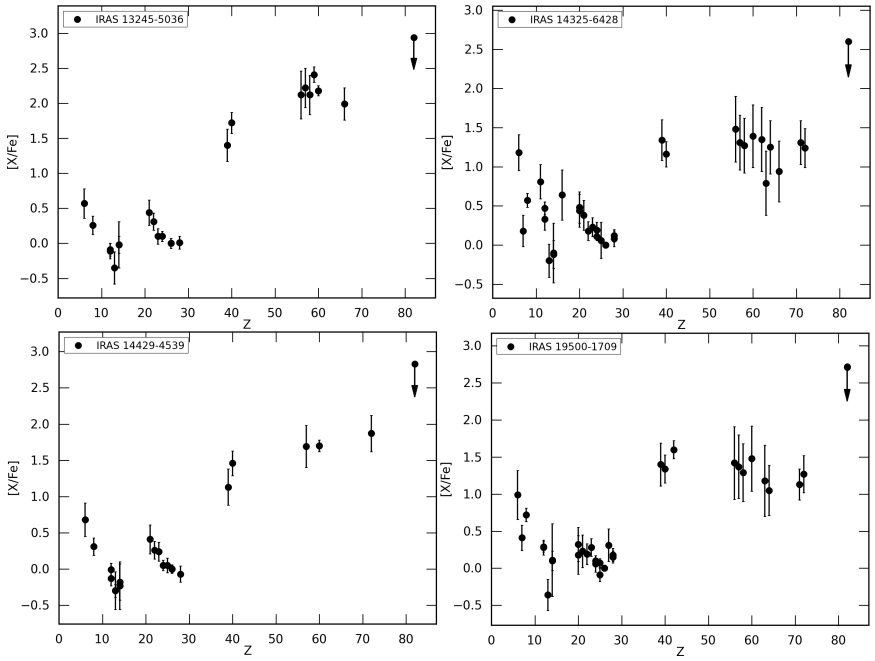

Figure 6.10: Element-over-iron ratios for the programme stars with $T_{\rm eff} \geqslant 8000$ K. The down-arrow at Z=82 displays the adopted Pb abundance upper limits. For more information, see text.

specifically the derived Pb abundances.

6.4.1 CNO-elements

For all programme stars, we can determine the carbon and oxygen abundances. The C/O ratios range from about 1.0 up to 2.5 and are listed in the second column of Table 6.8. The errors on the C/O ratios in Table 6.8 include line-to-line scatter and atmospheric model uncertainties. They can become significant due to the strong temperature sensitivity of the available C and O lines within the temperature range of the sample stars. The two new post-AGB stars IRAS 13245-5036 and IRAS 14429-4539 display C/O ratios of about 1.1 and 1.3 respectively. This also confirms the observation that the 21 μm feature is only detected around carbon-rich post-AGB stars.

For six of the stars, we could determine nitrogen abundances using non-LTE sensitive spectral lines between 7000 and 9000 Å. We applied non-LTE corrections to the LTE N abundances following the temperature-dependent corrections of Fig. 4 in Lyubimkov et al. (2011), which shows a larger correction for higher temperatures. We adopted the following corrections: for IRAS 22223+4327, we use a correction of -0.3 dex; for IRAS 08143-4406, we apply a correction of -0.4 dex; for IRAS 07143+1005 and IRAS 17279-1119 we apply corrections of -0.5 dex and for IRAS 14325-6428 and IRAS 19500-1709, we use corrections of -0.65 dex and -0.7 dex respectively. These corrections are already included in the listed results of Tables 6.4, 6.5 and 6.6. Given the uncertainties on the non-LTE correction, we assume a somewhat ad-hoc line-to-line scatter of 0.3 dex for all N abundance determinations.

6.4.2 *s*-process elements

The two new post-AGB stars, IRAS 13245-5036 and IRAS 14429-4539, show strong s-process enrichments with a stronger overabundance of the hs elements with respect to the ls elements. Although both stars have similar atmospheric parameters, we could only determine a limited set of *s*-process elements for IRAS 14429-4539 due to the lower metallicity. The *s*-process enrichments confirm the evolved nature of both stars. This corroborates the finding that the stars displaying the 21 μm feature are all s-process rich and carbon-rich post-AGB stars which are the likely decendents of AGB Carbon stars.

We confirm that all other programme stars show *s*-process enhancements for both the ls and hs elements, with significant differences between the objects. IRAS 17279-1119 displays a mild s-process enrichment with most of the *s*-process elements having an [X/Fe] < 1.0 dex, while the two strongest enriched objects, IRAS 05341+0852 and IRAS 06530-0213, have high *s*-process [X/Fe] abundances reaching up to 2.5 dex. For IRAS 08143-4406, the abundances derived from the two observational settings are similar (upper right panel of Fig. 6.9).

Apart from the different levels of enrichment, we also find different abundance distributions. For IRAS 08143-4406, IRAS 14325-6428, IRAS 19500-1709 and IRAS 22223+4327, the enrichment of the ls elements Y and Zr is higher or similar to that of the hs elements, while for the other stars the situtation is reversed. We will go into more detail about the hs/ls behaviour in Sect. 6.5.1.

For those objects with Mo determination, we find that Mo has similar enhancements as Y and Zr. The elements with $Z > 62$ are also enriched and their abundance distributions strongly vary from star to star, to a level comparable to or less than that of the hs elements.

6.4.3 Comparison with previous studies

In Appendix D, we provide the comparison between our abundance results and those of previous abundance studies (see second-last column of Table 6.1). For IRAS 13245-5036 and IRAS 14429-4539, there are no available data in literature. We remark that previous studies used different linelists and solar abundances which can explain small differences between ours and previous determinations. Especially, changes in oscillator strength log gf can significantly impact the individual spectral line abundances.

6.5 Pb abundance results

For each star, we use an artificially high abundance to theoretically predict which optical Pb line (Pb I or Pb II) will be the strongest for a specific set of atmospheric parameters. We then select the Pb line which gives the largest predicted EW. For some stars, both Pb lines result in a similar theoretical EW, so we can use both lines to constrain the Pb abundance.

Depending on the effective temperature of the sample stars, the Pb abundaces are probed either using the strongest Pb I line at 4057.807 Å or Pb II line at 5608.853 Å. As the Pb I line lies in a low S/N region with many spectral blends and the Pb II line is generally very small so that it can be confused with noise in the spectrum, none of the sample stars display a clear Pb line feature from which an accurate Pb abundance can be derived. Therefore, we can only determine upper limits on the Pb abundance.

We generate synthetic spectra for the spectral region of the Pb line, including all the derived abundances, listed in Tables 6.3 to 6.6. We use the synthetic spectral lines to estimate the local position of the continuum at the Pb line. The lowest Pb abundance for which the synthetic spectrum fully includes the observed spectral blend at the Pb line, is adopted as upper limit of the Pb abundance.

Examples of our method are illustrated in Figs. 6.11, 6.12 and 6.13 for three different sample stars.

Fig. 6.11 shows the Pb abundance determination of IRAS 22223+4327 using the Pb I line at 4057.807 Å. For stars with lower temperatures and/or high metallicities, this spectral region contains many spectral blends. The S/N in this blue region is generally only between 20 and 30. We use the identified spectral blends at 4057.5 Å and 4058.9 Å to estimate the position of the continuum and then use different synthetic Pb abundances to determine the upper limit.

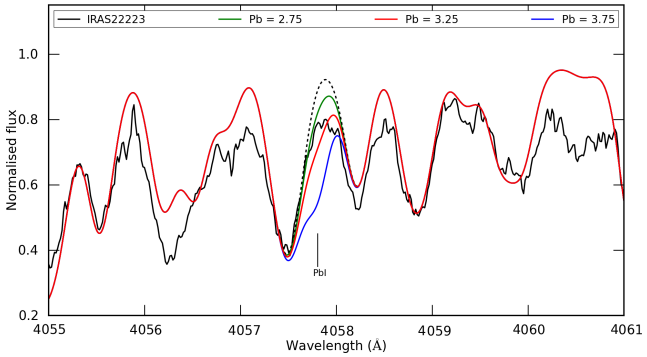

Figure 6.11: Spectrum synthesis of the Pb I line at 4057.807 Å for IRAS 22223+4327. The black spectrum is the observed HERMES spectrum, the colored spectra represent synthetic spectra with different Pb abundances. The red line represents the adopted Pb abundance upper limit, the green and blue represent the adopted abundance upper limit -0.5 dex and +0.5 dex respectively. The dashed black line shows the synthetic spectrum if no Pb would be present. For more information, see text.

For each figure the red synthetic spectra represent our adopted abundance upper limit and the dashed black lines show synthetic spectra without any Pb contribution included.

In case of IRAS 22223+4327, there is no clear contribution from Pb. The blue synthetic spectrum in Fig. 6.11 provides a full observed feature around 4057.807 Å but generates a large contribution to the blend with the line at 4057.5 Å, which is not observed in the spectrum. Therefore, we adopt an upper limit of the Pb abundance for IRAS 22223+4327 which creates only a contribution to the blend which is still compliant with the observed spectrum. Fig. 6.11 also shows that there are a number of spectral lines in this region which are not included in the linelists. The line features at 4056.2 Å and 4060.5 Å are examples. Moreover, for stars with $T_{\rm eff} < 7500$ K and [Fe/H] > 0.5 dex, we can not reproduce the blended line at 4058.2 Å at the red side of the Pb I line, which would otherwise be a major factor for constraining the local continuum position.

The Pb abundance determinations of IRAS 06530-0213 are presented in Fig. 6.12. The upper panel shows the determination via the Pb I line at 4057.807 Å, the lower panel shows the same for the Pb II line at 5608.853 Å. Also for this star, we do not detect a clear Pb I line and we use the spectral blends at 4057.5 and 4058.9 Å to estimate the position of the continuum. We adopt

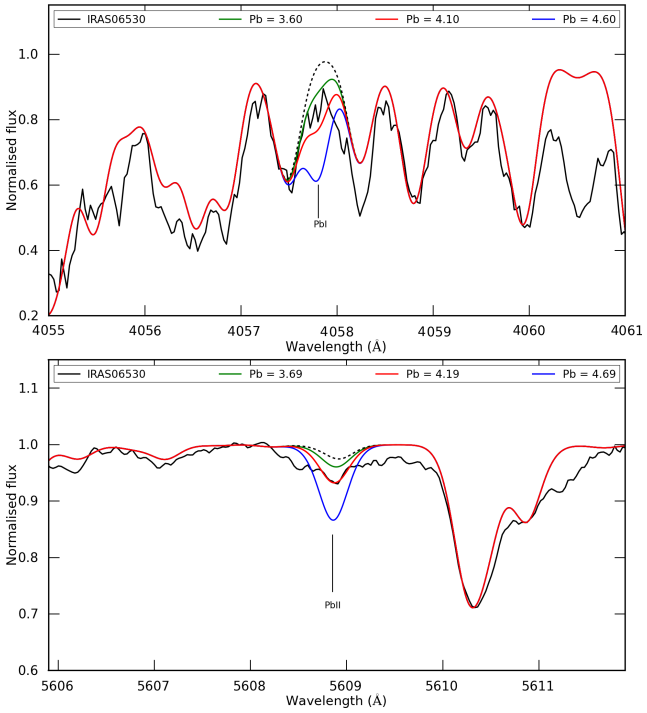

Figure 6.12: Spectrum synthesis of the Pb I line at 4057.807 Å (upper panel) and of the Pb II line at 5608.853 Å (lower panel) for the UVES spectra of IRAS 06530-0213. Lines and symbols are similar to Fig. 6.11. For more information, see text.

a Pb abundance which generates a synthetic Pb line which fully incorporates the observed line feature at 4057.807 Å. For the Pb II line at 5608.853 Å, we use the continuum between 5606.3 and 5608 Å in combination with the blend at 5610.3 Å to estimate the position of the continuum at 5608.853 Å. The Pb II line lies in a spectral region where the continuum is affected by a blend of small unidentified spectral lines, ranging from 5608 up to 5610 Å. The observed spectrum lies below the continuum of the synthetic spectra. To make sure this feature is real, we checked the individual observed spectra of IRAS 06530-0213 in Table 6.1 and found the feature to be present in both observations. We also compared with the old observations from Reyniers et al. (2004) and also there too, this broad feature is present. We therefore expect this depression to be real. This is likely a set of unresolved small lines. For the Pb II line, we adopt a Pb abundance which fits the observed spectrum. However, comparison with

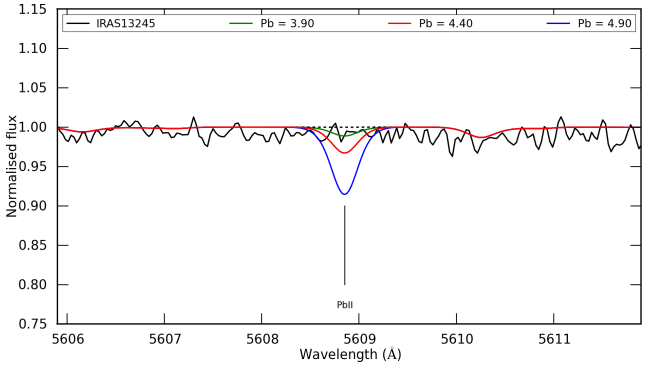

Figure 6.13: Spectrum synthesis of the Pb II line at 5608.853 Å for the UVES spectrum of IRAS 13245-5036. Lines and symbols are similar to Fig. 6.11. For more information, see text.

the spectra of Reyniers et al. (2004) suggest that the small line at 5608.853 Å in the broad feature between 5608 and 5610 Å is not significant as it is not seen in the older spectra. Due to this possibility, in combination with the lower upper limit found for the Pb I line, we adopt the limit for the Pb I line as the upper limit of the Pb abundance for IRAS 06530-0213.

Fig. 6.13 shows the Pb abundance determination for IRAS 13245-5036 using the Pb II line at 5608.853 Å. We do not detect any Pb II line feature for this star, and therefore we adopt an upper limit of the Pb abundance which creates a synthetic Pb II line which lies slightly below the observed spectrum. The Pb I line at 4057.807 Å would need a significantly higher Pb abundance than the adopted upper limit based on the Pb II line. Therefore, we only consider the upper limit based on the Pb II line.

The determinations of the upper limits on the Pb abundances of all other programme stars are presented and discussed in Appendix C. We do not detect strong Pb lines for any of the fourteen *s*-process enriched post-AGB stars. For the remaining part of the paper, we will therefore refer to the Pb upper limit abundances as Pb_{up}. In Table 6.7, we list the individual Pb upper limit abundance results for the Pb I and Pb II line of the programme stars. The element-over-iron ratios corresponding to the adopted Pb abundance are shown in Figs. 6.8, 6.9 and 6.10, indicated with down-arrows. The last six rows display the results of De Smedt et al. (2014) and Chapter 5 for six carbon and *s*-process enhanced post-AGB stars in the Magellanic Clouds and will be used in the analysis of the neutron irradiation in Sect. 6.5.1.

Table 6.7: Pb abundance upper limits Pb_{up} of the programme stars, together with the Pb indices [Pb_{up}/hs] and [Pb_{up}/ls] and the effective temperature. We adopt the solar Pb abundance of log ϵ(Pb) = 1.75 dex from Asplund et al. (2009). The abundances of Pb I and Pb II are determined via the 4057.807 Å and 5608.853 Å spectral lines respectively. The last six rows display the Pb_{up} results of six post-AGB stars in the Magellanic Clouds from De Smedt et al. (2014) and Chapter 5.

Object	[Fe/H]	log ϵ(PbI_{up})	[PbI_{up}/Fe]	log ϵ($PbII_{up}$)	[$PbII_{up}$/Fe]	[Pb_{up}/hs]	[Pb_{up}/ls]	T_{eff} (K)
IRAS 05113+1347	-0.49	< 2.65	< 1.44			< -0.21	< 0.11	5500
IRAS 05341+0852	-0.54	< 3.15	< 2.10			< -0.14	< 0.23	6750
IRAS 06530-0213	-0.32	< 4.10	< 2.73	< 4.19	< 2.76	< 0.69	< 0.98	7375
IRAS 07134+1005	-0.91	< 2.79	< 2.01			< 0.38	< 0.37	7250
IRAS 07430+1115	-0.31	< 2.50	< 1.07			< -0.48	< -0.23	6000
IRAS 08143-4406[a]	-0.43	< 3.20	< 1.90			< 0.32	< 0.13	7000
IRAS 08281-4850	-0.26	< 4.20	< 2.74	< 4.20	< 2.71	< 1.13	< 1.14	7875
IRAS 13245-5036	-0.26			< 4.40	< 2.94	< 0.91	< 1.38	9500
IRAS 14325-6428	-0.56			< 3.79	< 2.60	< 1.27	< 1.35	8000
IRAS 14429-4539	-0.64			< 4.40	< 2.83	< 1.36	< 1.54	9375
IRAS 17279-1119	-0.64	< 2.75	< 1.51			< 0.59	< 0.77	7250
IRAS 19500-1709	-0.59	< 3.89	< 2.72			< 1.38	< 1.35	8000
IRAS 22223+4327	-0.30	< 3.25	< 1.82			< 0.94	< 0.48	6500
IRAS 22272+5435	-0.77	< 2.70	< 1.72			< -0.18	< 0.11	5750
J004441.04-732136.4	-1.34	< 3.00	< 2.58			< 0.00	< 0.52	6250
J050632.10-714229.8	-1.22	< 2.05	< 1.52			< 0.45	< 0.10	6750
J052043.86-692341.0	-1.15	< 2.00	< 1.40			< -0.45	< -0.27	5750
J053250.69-713925.8	-1.22	< 2.23	< 1.70			< -0.24	< 0.19	5500
J051213.81-693537.1	-0.56	< 3.30	< 2.11			< 0.37	< 0.78	5875
J051848.86-700246.9	-1.03	< 2.62	< 1.93			< -0.19	< 0.47	6000

[a] Determined via the Blue437 spectra of IRAS 08143-4406.

6.5.1 Discussion

The lack of accurate distance determinations to the fourteen programme stars hinders accurate luminosity determinations, which prevents to estimate the core masses and constrain the initial masses. Therefore, the comparison of our abundance results with tailored, state-of-the-art theoretical AGB evolution and nucleosynthesic models is difficult. Given the subsolar metallities we expect that the majority of the fourteen sample stars will have low initial masses (M $\leqslant$ 2.0 $M_{\odot}$). Future distance determinations will be essential to confirm this assumption.

6.5.2 Abundance results versus general predictions

In this section, we will compare our derived Pb_{up} results with AGB model predictions obtained for a star of 2 $M_{\odot}$. We remark that the *s*-process in present AGB models is almost not sensitive to the initial stellar mass for these low-mass AGB stars.

Different observational indices are commonly used for representing *s*-process distributions and *s*-process overabundances namely [ls/Fe], [hs/Fe], [s/Fe] and [hs/ls]. The elements that are included for the calculation of these indices vary between authors. Here, we calculate the indices with the same elements as in Chapter 5. For the ls index, we take the mean of the relative abundances of Y and Zr; For hs, we compute the mean of the relative abundances of La, Ce, Nd and Sm. The [hs/Fe] and [ls/Fe] of the programme stars in this paper are listed in Table 6.8. The index [s/Fe] is the mean of the relative abundances of the elements for the ls and hs indices and the index [hs/ls] is calculated according to [hs/Fe]-[ls/Fe]. The latter index, [hs/ls], is an indicator of the neutron irradiation if the *s*-process takes place in radiative shells (Gallino et al. 1998; Busso et al. 2001). Larger neutron irradiations result in the creation of heavier *s*-process elements, hence [hs/ls] $>$ 0. Indices [Pb/hs] ([Pb/Fe] - [hs/Fe]) and [Pb/ls] ([Pb/Fe] - [ls/Fe]) then represent the overabundance of Pb with respect to the other *s*-process overabundances. The third and second last column of Table 6.7 show the [Pb_{up}/hs] and [Pb_{up}/ls].

We were unable to determine the abundances of Ce for IRAS 14429-4539 and Sm in four hotter stars. To estimate the Ce and Sm abundances for these objects, we scale the abundance of Ce and Sm respectively to the abundance of La and Nd, elements with an atomic mass closest to Ce and Sm. For scaling, we make use of the AGB nucleosynthesis models from the online-database FRUITY[3] (Franec Repository of Upgraded Isotopic Tables and Yields,Cristallo

[3]http://fruity.oa-teramo.inaf.it/

Table 6.8: Overview of the C/O ratio, the metallicity and s-process indices for our sample of stars.

Object	C/O	[Fe/H]	[ls/Fe]	[hs/Fe]	[s/Fe]	[hs/ls]
IRAS 05113+1347	2.42 ± 0.40	-0.49 ± 0.15	1.33 ± 0.13	1.65 ± 0.07	1.54 ± 0.07	0.32 ± 0.15
IRAS 05341+0852	1.06 ± 0.30	-0.54 ± 0.11	1.87 ± 0.08	2.24 ± 0.06	2.12 ± 0.05	0.37 ± 0.10
IRAS 06530-0213	1.66 ± 0.39	-0.32 ± 0.11	1.75 ± 0.09	2.04 ± 0.08	1.94 ± 0.06	0.29 ± 0.13
IRAS 07134+1005	1.24 ± 0.29	-0.91 ± 0.20	1.64 ± 0.13	1.63 ± 0.20	1.63 ± 0.14	-0.01 ± 0.24
IRAS 07430+1115	1.71 ± 0.30	-0.31 ± 0.15	1.30 ± 0.14	1.55 ± 0.06	1.47 ± 0.06	0.25 ± 0.15
IRAS 08143-4406[a]	1.66 ± 0.39	-0.43 ± 0.11	1.77 ± 0.08	1.58 ± 0.06	1.65 ± 0.05	-0.19 ± 0.11
IRAS 08281-4850	2.34 ± 0.42	-0.26 ± 0.11	1.57 ± 0.11	1.58 ± 0.12	1.58 ± 0.09	0.01 ± 0.17
IRAS 13245-5036	1.11 ± 0.30	-0.30 ± 0.10	1.56 ± 0.14	2.03 ± 0.11	1.88 ± 0.09	0.47 ± 0.18
IRAS 14325-6428	2.27 ± 0.40	-0.56 ± 0.10	1.25 ± 0.15	1.33 ± 0.19	1.30 ± 0.14	0.08 ± 0.24
IRAS 14429-4539	1.29 ± 0.26	-0.18 ± 0.11	1.29 ± 0.15	1.47 ± 0.10	1.41 ± 0.08	0.18 ± 0.08
IRAS 17279-1119	0.94 ± 0.22	-0.64 ± 0.12	0.74 ± 0.08	0.92 ± 0.09	0.86 ± 0.07	0.18 ± 0.12
IRAS 19500-1709	1.02 ± 0.17	-0.59 ± 0.10	1.37 ± 0.29	1.34 ± 0.30	1.35 ± 0.21	-0.03 ± 0.41
IRAS 22223+4327	1.04 ± 0.22	-0.30 ± 0.11	1.34 ± 0.07	0.88 ± 0.07	1.03 ± 0.05	-0.46 ± 0.10
IRAS 22272+5435	1.46 ± 0.26	-0.77 ± 0.12	1.61 ± 0.08	1.90 ± 0.07	1.80 ± 0.05	0.28 ± 0.11

[a] C/O ratio is calculated from the results of the Red580 observations of IRAS 08143-4406, other results are calculated from the results of the Blue437 observations.

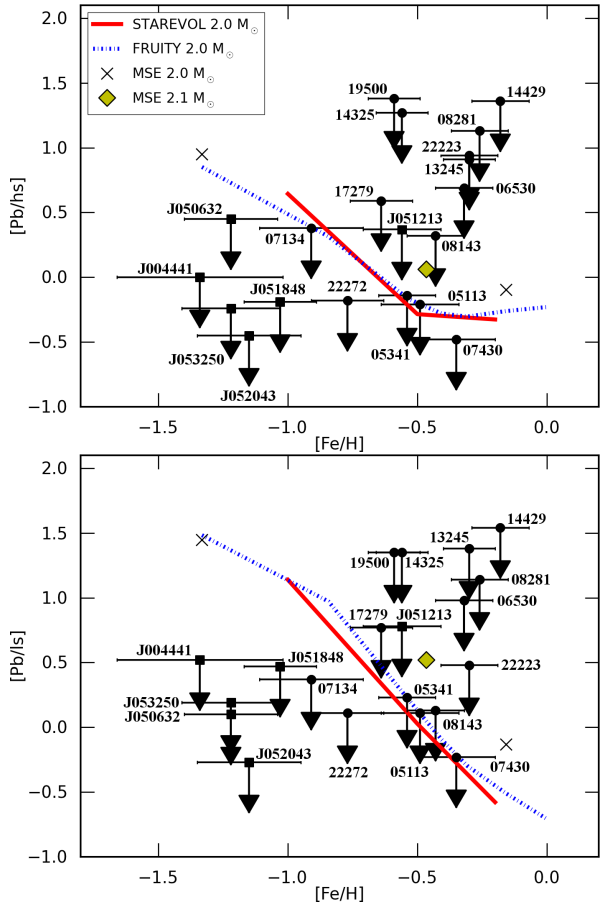

Figure 6.14: The observed [Pb_{up}/hs] (upper panel) and the [Pb_{up}/ls] (lower panel) versus [Fe/H] results of the Galactic sample stars of this study (black circles) and the Magellanic Cloud stars in De Smedt et al. (2014) and Chapter 5 (black squares). The observed abundance upper limits are plotted together with the [Pb/hs] and [Pb/ls] predictions of the 2.0 $M_\odot$ STAREVOL models (red full line), the 2.0 $M_\odot$ and 2.1 $M_\odot$ Mount Stromlo models (MSE, black crosses and yellow diamond respectively) and the 2.0 $M_\odot$ FRUITY models (blue dot-dashed line). The black horizontal lines represent the [Fe/H] uncertainty of the displayed stars. The position of each star from this study is indicated with the first numbers of its IRAS name, for Magellanic Cloud stars from De Smedt et al. (2014) and Chapter 5, the first part of the 2MASS name is used.

et al. (2011)), which covers a wide metallicity range, and use the models with metallicities closest to the metallicity of the star. We use an initial mass of 1.5 $M_\odot$ for the FRUITY models.

The [s/Fe] results in Table 6.8 indeed confirm the strong *s*-process enhancements of the sample stars with [s/Fe] $\geqslant$ 1.0 except for IRAS 17279-1119 with [s/Fe] = 0.86 dex, which is mildly *s*-process enriched (0.0 < [s/Fe] < 1.0 dex). IRAS 22223+4327 and IRAS 08143-4406 have [hs/ls] < 0. IRAS 07134+1005, IRAS 08281-4850, IRAS 14325-6428 and IRAS 19500-1709 have [hs/ls] $\approx$ 0 while the remaining eight stars, including the mildly enriched IRAS 17279-1119, have [hs/ls] > 0.

The dominant neutron source in low-mass AGB stars is expected to be the ^{13}C(α,n)^{16}O reaction during the radiative interpulse phase, leading to [hs/ls] > 0 at subsolar metallicities -1.2 dex $\lesssim$ [Fe/H] $\lesssim -0.1$ dex (Goriely & Mowlavi 2000). In heavier AGB stars, the ^{22}Ne(α,n)^{25}Mg reaction becomes the dominant neutron source resulting in [hs/ls] < 0 (e.g. Goriely & Mowlavi 2000; Goriely & Siess 2004; Karakas et al. 2012). In intermediate-mass AGB stars (M > $\sim$ 4 $M_\odot$), the ^{22}Ne(α,n)^{25}Mg reaction within the convective thermal pulse may dominate the neutron production if the temperature at the base of the pulse reaches some 3.5×10^8 K. In this case, the production of light *s*-process elements is favoured because of the convective nature of the region where the neutron irradiation takes place and the [hs/ls] index tends to be negative.

We compare the adopted Pb_{up} results with the [Pb/hs] and [Pb/ls] predictions of AGB evolution and nucleosynthesis models as in Chapter 5. The upper panel of Fig. 6.14 shows the derived [Pb_{up}/hs] vs [Fe/H] results of the post-AGB stars in this study, together with the results of *s*-process enriched post-AGB stars in the Magellanic Clouds in Chapter 5. The lower panel of Fig. 6.14 is similar but for [Pb_{up}/ls] vs [Fe/H]. The observed results are compared to the 2.0 $M_\odot$ model predictions of the STAREVOL code (Goriely & Siess 2004; Siess 2007, and references therein), the 2.0 $M_\odot$ and 2.1 $M_\odot$ Mount-Stromlo Evolutionary (MSE) predictions (Fishlock et al. 2014; Karakas 2010, and references therein) and the 2.0 $M_\odot$ model predictions of FRUITY (Cristallo et al. 2011). The MSE, STAREVOL and FRUITY predictions are rather insensitive to the initial stellar mass and show the global expected behaviour of [Pb/hs] and [Pb/ls] as a function of [Fe/H] in our present understanding of the *s*-process nucleosynthesis in AGB stars. For the clarity of Fig. 6.14, we have omitted the 1.5 $M_\odot$ FRUITY model predictions since the differences between the 1.5 $M_\odot$ and 2.0 $M_\odot$ models are small.

For the higher metallicity stars with [Fe/H] > -0.7 dex, the model predictions are well within the observed Pb_{up} results, while for stars with [Fe/H] < -0.7 dex the discrepancy between observations and predictions become larger as the

metallicity decreases. This trend is also confirmed by stars with well constrained Pb_{up} results such as IRAS 05113+1347, IRAS 05341+0852, IRAS 06530-0213 and IRAS 22223+4327 covering an [Fe/H] range from -0.8 to -0.3 dex. For IRAS 07430+1115, the [Pb_{up}/hs] result falls within the predicted limits.

In addition, it is not surprising to see that the Pb_{up} results of the hottest stars in the sample lie high above the model predictions in Fig. 6.14. As expected from Fig. 6.4, the very high Pb_{up} results for these stars are more related to temperature than to visible Pb line features. Therefore, we consider these Pb_{up} as poorly constraint. We conclude that stars with $T_{eff} > 7500$ K without significantly high Pb abundances are not useful for comparison with theoretical Pb abundance predictions. However, these hot stars remain useful for C/O ratio and other *s*-element comparisons.

6.5.3 Correlations

Previous studies have shown that there is no correlation between metallicity and neutron irradiation. According to the models, the [hs/ls] index is expected to increase with decreasing metallicity up to [Fe/H] $\sim$ -0.4 dex after which it strongly decreases towards higher metallicities (e.g. Goriely & Mowlavi 2000). With the addition of our new results, we confirm that this is not observed: in the lower panel of Fig. 6.15 we illustrate the absence of this expected correlation between metallicity and [hs/ls]. This implies that the total neutron irradiation is not (only) dependent on metallicity in our metallicity range.

In the upper left panel of Fig. 6.15, we show the correlation between [hs/Fe] and [ls/Fe] for our sample stars, the Magellanic Cloud post-AGB stars in van Aarle et al. (2013); De Smedt et al. (2014) and Chapter 5, and for two additional Galactic *s*-process enriched post-AGB stars from Reyniers et al. (2004). It is clear that both *s*-process indices are correlated and a high [ls/Fe] generally implies also a strong enhancement in [hs/Fe]. The spread is, however, large and this indicates that the different objects were subject to a variable neutron irradiation, irrespective of the dilution of the atmosphere.

In previous studies, Reyniers et al. (2004) and van Aarle et al. (2013) identified a strong correlation between [s/Fe] and the [hs/ls] index in Galactic and Magellanic Cloud objects. Strongly enriched objects, for which there has been a low dilution of the enriched material with the envelope material, were also subject to strong neutron irradiations and hence showed a high [hs/ls]. This correlation is confirmed in Chapter 5. Here, we add/update the results of our fourteen programme stars to the previously used sample. The resulting [s/Fe] and [hs/ls] correlation is shown in the upper right panel of Fig. 6.15 where two correlations are shown. The dashed line represents the correlation between the [s/Fe] vs

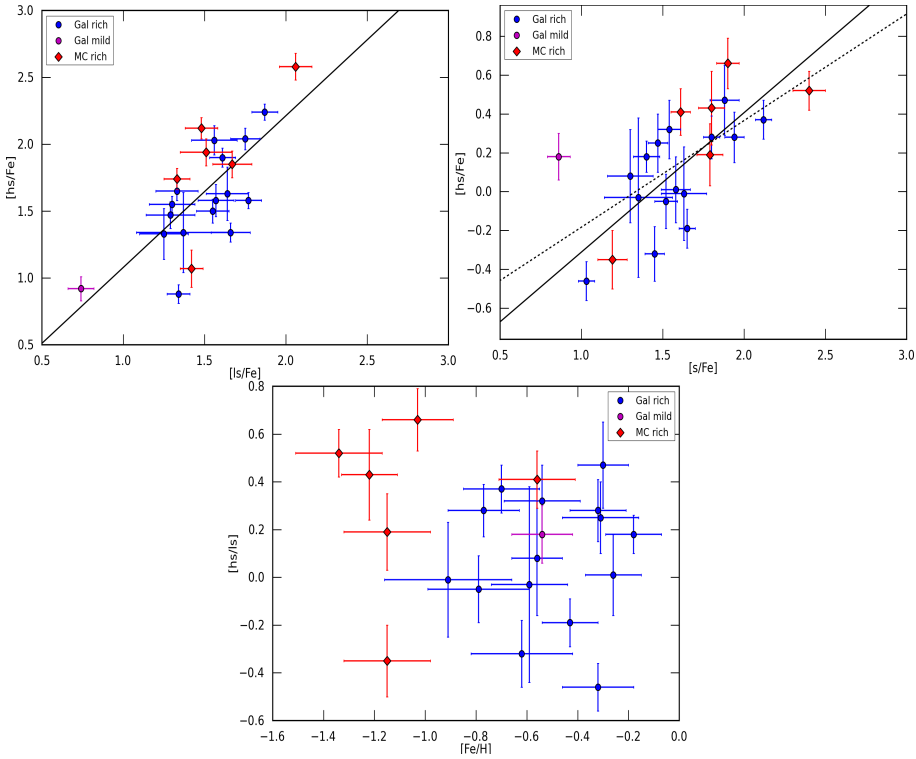

Figure 6.15: Upper left panel: Correlation between the *s*-process indices [hs/Fe] and [ls/Fe] for our sample stars and Magellanic Cloud stars from De Smedt et al. (2014) and Chapter 5. Also included are the results of two Galactic *s*-process enriched stars from Reyniers et al. (2004): IRAS 04296+3429 and IRAS 23304+6147. Galactic objects are represented by blue (= strongly-enriched) and purple (= mildly-enriched) circles, Magellanic Cloud objects are represented by red diamonds. Upper right panel: Similar to upper panel but for the correlation between the total enrichment in *s*-process elements [s/Fe] and the [hs/ls] index. The dashed line shows the least-squares fit to all results, the full line shows the fit for all stars except for IRAS 17279-1119 (purple circle). Lower panel: Similar to the upper panel but for the correlation between the metallicity [Fe/H] and the [hs/ls] index. For more information, see text.

[hs/ls] results for all stars in the plot, the full line represents the correlation without the inclusion of IRAS 17279-1119. We choose these two correlations as IRAS 17279-1119 has [s/Fe] < 1 dex whereas the other stars have [s/Fe] $\geqslant$ 1 dex. The correlation of the full and dashed lines in the upper right panel of Fig. 6.15 are 0.75 and 0.65 respectively. The second result shows that the inclusion of the mildly enhanced IRAS 17279-1119 already moderately lowers the correlation for all objects. This infers a different *s*-process history for IRAS 17279-1119 with respect to the other programme stars (see Sect. 6.6).

6.6 IRAS 17279-1119

IRAS 17279-1119 has only a mild s-process enrichment (see lower right panel of Fig. 6.9) and is an outlier in the upper right panel of Fig. 6.15, so in this section we focus specifically on this object.

Fig. 6.16 shows the spectral energy distribution (SED) of IRAS 17279-1119. The photometric data for constructing the SED is retrieved from the following catalogues: the General Catalogue of Photometric Data (GCPD Mermilliod et al. 1997), the All-sky compiled catalogue of 2.5 million stars (Kharchenko 2001), the 2MASS All-Sky Catalog of Point Sources (Cutri et al. 2003), the WISE All-Sky Data catalogue (Cutri et al. 2012), the AKARI/IRC mid-infrared all-sky survey (Ishihara et al. 2010) and the IRAS catalogue of Point Sources (Helou & Walker 1988).

Fig. 6.16 shows both the original raw photometric points (red diamonds) as well as the dereddened data (blue dots). For Galactic objects, we consider two possible reddening sources. The first source is reddening by interstellar dust in the Galaxy towards IRAS 17279-1119. The second source is reddening by the circumstellar dust of IRAS 17279-1119 itself. For both sources, we use the Galactic extinction curves of Cardelli et al. (1989) to determine the reddening. The total reddening is determined by applying a χ^2 minimalisation on the fit between the dereddened broadband fluxes and our preferred Kurucz model atmosphere which we used for the abundance study of IRAS 17279-1119. The error on the total reddening E(B-V) is determined by a Monte Carlo simulation of 100 arrays with a normal distribution of the original flux. We find a total reddening of E(B-V) $= 0.76 \pm 0.02$ for IRAS 17279-1119.

The SED displayed in Fig. 6.16 indicates an excess starting at 2 micron indicating the thermal emission of dust near the dust-sublimation temperature and therefore close to the central star. It is now well established that this traces the presence of a stable compact circumbinary disc (e.g. De Ruyter et al. 2006; Deroo et al. 2007; Gielen et al. 2011; Hillen et al. 2013, 2014; Bujarrabal et al.

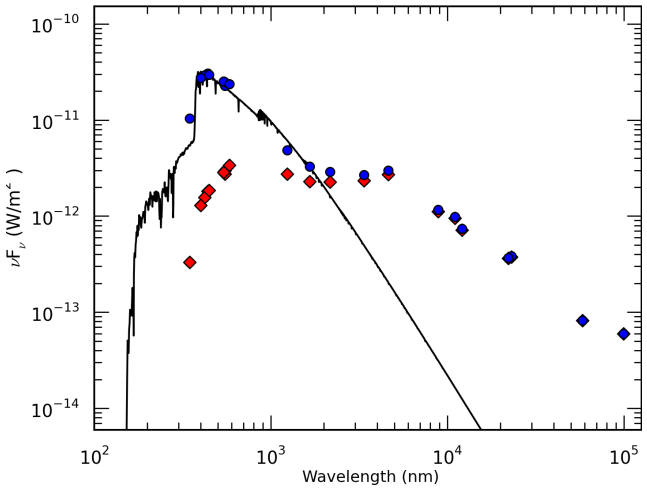

Figure 6.16: SED of IRAS 17279-1119. Red diamonds represent the red, original photometry, blue circles represent the dereddened photometry. The black line is the scaled Kurucz atmosphere model.

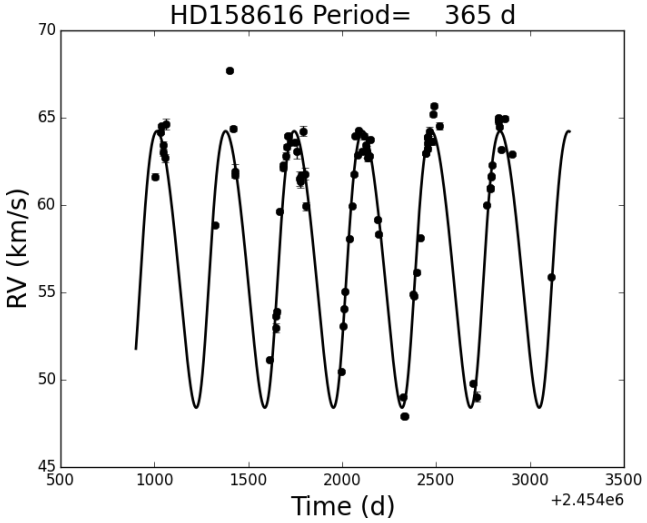

Figure 6.17: Radial velocity orbit of IRAS 17279-1119. Black circles represent the observed radial velocities, the black curve is the sine-fit to the orbit. For more information, see text.

Table 6.9: Orbital elements of IRAS 17279-1119.

		σ
Period (d)	365.0	1.0
e	0.0 (forced)	
K (km s^{-1})	7.92	0.44
γ (km s^{-1})	56.8	0.5
a sin i (A.U.)	0.27	0.02
f(M) ($M_\odot$)	0.026	0.004
RMS residuals ($km\,s^{-1}$)	1.8	

2015; Gezer et al. 2015). The specific characteristics of the spectral energy distribution are closely related to the binary nature of the central star (Van Winckel et al. 2009).

We obtained radial velocity monitoring data with the HERMES spectrograph, (Raskin et al. 2011) mounted on the 1.2 meter Mercator telescope in the framework of our large programme on evolved binaries (Van Winckel et al. 2010; Gorlova et al. 2013). In total we obtained 85 radial velocity measurements starting on 19/06/2009 covering a total timespan of 2211d. We also used the ASAS (Pojmanski & Maciejewski 2004) photometry to study the photometric behaviour. The photometry consists of 788 datapoints covering a timespan of 3156d. Many of the variables near the Population II Cepheid instability strip have complex lightcurves in which several modes are excited with periods close to each other so that beating effects are easily detectable (Kiss et al. 2006). IRAS 17279-1119 is no exception and periods of 90, 87 and 83 days are found in the photometry using a S/N criterion of 4 in the fourier transform. Unfortunately, our photometric series do not overlap in time with the radial velocity series.

We detect orbital motion (see Fig 6.17) with an orbital period of exactly 1 year. The orbital solution is clear with a fractional variance reduction of 91% in the fit. In Table 6.9 we list the orbital data. We cover in total close to 6 cycles, but as the period is close to one year, the phase coverage is not ideal. Nonetheless the orbital detection is clear.

With an 'a sin i' of only 0.27 AU, it is clear that the current orbit is too small to accomodate a TP-AGB star whose radius is expected to be 1-2 AU. The object must have experienced strong binary interaction when on the AGB. The mass function gives a constraint on the mass of the companion provided the mass of the primary and the inclination are known. As the primary is a post-AGB star, it is fair to assume the mass is a typically white dwarf mass of 0.6 $M_\odot$. Assuming a most probable inclination of 60 degrees, the mass of the companion

is only 0.3 $M_{\odot}$. With an inclination of 30 degrees, this becomes 0.6 $M_{\odot}$. As there are no symbiotic activities, we suggest that the companion is non-evolved.

To our knowledge, IRAS 17279-1119 is the first *s*-process rich post-AGB star discovered to be in a spectroscopic binary. If, during the binary interaction phase, there was mass transfer of enriched material to the secondary, the companion accreted *s*-process rich gas. This object seems therefore a precursor of extrinsically enrichd stars. These are binaries in which the observed *s*-process rich component was polluted by material expelled from its companion star when it passed the AGB evolutionary phase and which is now a white dwarf (see Jorissen et al. 1998). IRAS 17279-1119 may very well be the first detected precursor of the Ba dwarfs, given the low mass of the companion.

6.7 Conclusions

In this paper, we presented a homogeneous abundance study of a sample of fourteen Galactic *s*-process enriched post-AGB stars with the aim to determine Pb abundances. Our results confirm that two newly identified 21 μm sources IRAS 13245-5036 and IRAS 14429-4539 are indeed carbon and *s*-process enriched and we confirm the post-AGB nature of both objects. Furthermore, we find a strong chemical diversity for the sample stars ranging from only a mild *s*-process enrichment up to strong *s*-process enrichment.

None of the sample objects display clear distinctive Pb lines in their spectra and therefore we can only determine Pb abundance upper limits (Pb_{up}). These Pb abundance upper limits are determined using synthetic spectra. Comparison with theoretical spectra reveals that some of the cooler stars in the sample display visible contributions of Pb in the unresolved blends. Because of the low S/N, it is impossible to determine the contribution and hence abundance accurately.

For the hotter stars with $T_{eff} > 7500$ K, there are no visible Pb line contributions in the spectra. Therefore, these Pb_{up} results are poorly constrained which makes hot post-AGB stars without drastically high Pb abundances not useful for the Pb comparison with theoretical AGB nucleosynthesis predictions.

Comparison of observed Galactic Pb_{up} abundances with theoretical *s*-process calculations of ~ 2.0 $M_{\odot}$ stellar models confirm the results of Magellanic Cloud stars from De Smedt et al. (2014) and Chapter 5. For metallicities with [Fe/H] $>$ -0.7 dex, the predicted Pb abundances are well within the observed Pb_{up} results, while there exists an increasing discrepancy towards lower metallicities. Additional research is necessary to explain this trend.

We confirm that there is no correlation between neutron irradiation and metallicity in the metallicity range probed here which is a confirmation of previous studies.

We confirm the correlation between [hs/ls] and [s/Fe] indicating the connection between strong neutron irradiation and the overall photospheric enrichments. The mildly *s*-process enriched IRAS 17279-1119 does not follow this correlation because the orbital elements suggest that an evolutionary cut-off from the AGB was forced prematurely due to binary interaction: the current orbit is too small to accomodate an AGB star with a typical luminosity. In addition, IRAS 17279-1119 is to our knowledge the first confirmed *s*-process rich post-AGB star in a binary system.

In summary, we find an increasing discrepancy between observed and predicted Pb abundances towards lower metallicities. All objects with a metallicity [Fe/H] < -0.7 dex show Pb upper limits which are lower than the predicted Pb abundances. Contrary to the Magellanic Cloud samples, the distances to the Galactic sample stars are poorly known and hence it is difficult to constrain their current core masses but also their initial masses. Distance estimates are hence necessary to connect the determined abundance results with tailored theoretical predictions in detail. The GAIA distance determinations will be crucial in this respect.

Chapter 7

The mild *s*-process enrichment in the LMC: J050221.17-691317.2

The research results in this chapter will be published in a forthcoming paper.

7.1 Introduction

In this chapter, we discuss the abundance study of a mildly *s*-process enriched post-AGB star in the LMC: J050221.17-691317.2. In Sect. 7.2, we briefly discuss the selection of this object for this study followed by the details of the observations in Sect. 7.3. The spectral analysis of this object is explained in detail in Sect. 7.4 followed by the abundance results in Sect. 7.5. The luminosity and initial mass are determined in Sect. 7.6 followed by a discussion of the neutron irradiation in Sect. 7.7. We end this chapter with the conclusions in Sect. 7.8.

7.2 Sample selection

J050221.17-691317.2, hereafter abbreviated to J050221, was selected as a post-AGB candidate in the surveys of van Aarle et al. (2011) and Kamath et al.

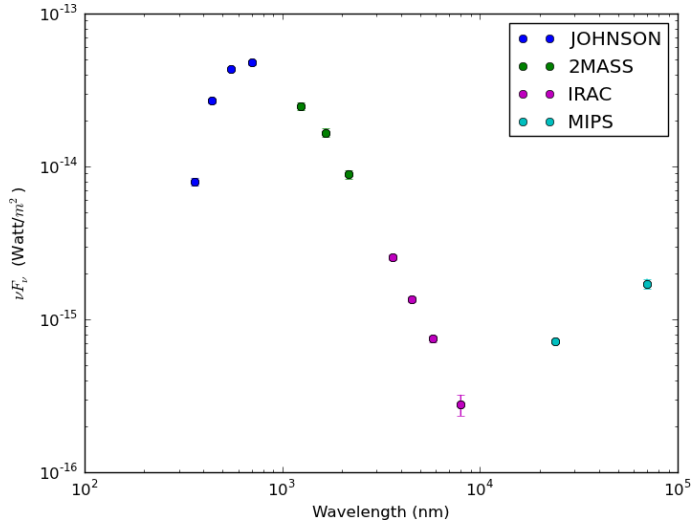

Figure 7.1: SED of the observed photometry of J050221. The Johnson photometry is obtained from Massey (2002), 2MASS photometry of Cutri et al. (2012), and IRAC and MIPS photometry from Meixner et al. (2006).

(2015) (see Chapter 2). Based on its SED, both surveys catalogued J050221 as post-AGB candidate with an expanding shell of dust, indicating a past mass-loss. The SED of J050221, with only the raw data, is shown in Fig. 7.1. van Aarle et al. (2011) found a luminosity of about 11300 $L_\odot$ and a reddening of E(B-V) = 0.36 ± 0.05. Kamath et al. (2015) found a much lower luminosity of about 5000 $L_\odot$ and a small reddening of E(B-V) = 0.02 ± 0.04. The similarity between the SED of J050221 and the SEDs of the two *s*-process enriched LMC post-AGB stars of Chapter 5 is large. The STP result of Kamath et al. (2015) resulted in an effective temperature of about 5250 K, a low log g of 0.5 dex and [Fe/H] ≈ -0.6 dex which is close to mean LMC metallicity of -0.5 dex (e.g. Geisler et al. 2009; Lapenna et al. 2012). All these results indeed make J050221 an ideal post-AGB candidate, and therefore J050221 was selected to be observed with high-resolution spectroscopy. Once the high-resolution UVES spectra (see Sect. 7.3) were obtained, comparison with the spectra of the enriched LMC post-AGB star J051213 from Chapter 5 (see already Fig. 7.2) suggests J050221 to have no or mild *s*-process enhancements. Therefore, J050221 is chosen for an extensive abundance study.

7.3 Observations

J050221 is observed using the high-resolution UVES echelle spectrograph (Dekker et al. 2000), mounted on the 8m UT2 Kueyen Telescope of the VLT array at the Paranal Observatory of ESO in Chili. Observations were performed using the dichroic beam-splitter which results in a wavelength coverage for the blue arm from approximately 3280 to 4530 Å and in the red arm for the lower and upper part of the mosaic CCD chip from approximately 4780 to 5770 Å and from 5800 to 6810 Å respectively. We choose a slit width of 1 arcsecond to gain an optimal compromise between spectral resolution and slit-loss minimalisation. Two exposures were performed with an exposure time of 1500 s in the night of November 28th in 2011.

The observed spectra are reduced using the UVES pipeline (version 5.3.0) in the Reflex environment of ESO [1]. This reduction includes the standard steps of extracting frames, determining wavelength calibration, applying this scale to flat-field divided data and cosmic-clipping. For spectra reduced within the Reflex environment, the standard reduction parameters of the UVES pipeline were used as these result in the best signal-to-noise (S/N).

Once reduced, the weighted mean spectra are created for the three different wavelength regions. The weighted mean spectra are then divided into subspectra with a fixed wavelength range of 120 Å where the first and last 10 Å overlap with the previous and subsequent spectra. Each subspectrum is then normalised individually by fitting a fifth order polynomial through interactively defined continuum points. Then, all subspectra are merged into one large spectrum, which is used for the spectral analysis. During merging, the mean flux was calculated for the overlapping spectral regions of the subspectra. The final spectra have a mean S/N of 90 in the red spectra and a S/N ranging from 25 to 45 in the blue spectrum in the wavelength regions above 4000 Å.

7.4 Spectral analysis

Fig. 7.2 shows the spectral region around the Ba II line at 6141.813 Å for the normalised UVES spectra of J050221 and the *s*-process enriched post-AGB star J051213.81-693537.1 (J051213) from Chapter 5. Both stars have similar atmospheric parameters and metallicities (see Sect. 7.4.1), but a different *s*-process enrichment. J050221 displays some spectral lines of *s*-process elements, but these lines are much weaker than those of J051213.

[1] https://www.eso.org/sci/software/reflex/

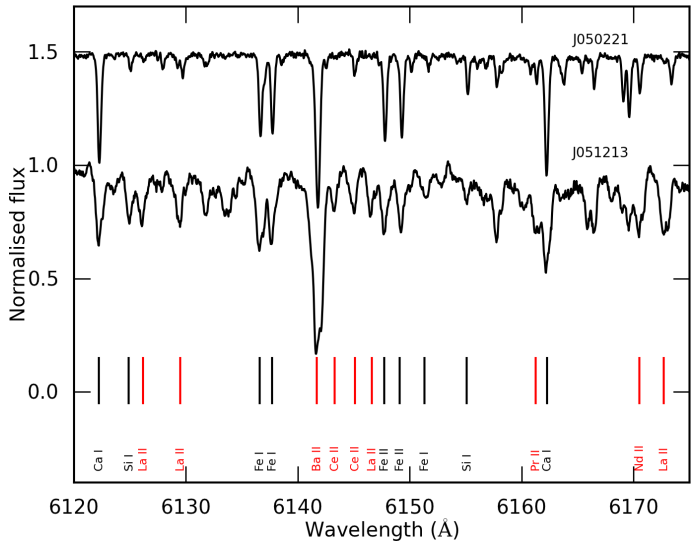

Figure 7.2: Comparison of the spectra of J050221 with the spectrum of the *s*-process enriched J051213 from Chapter 5. The spectra have been shifted in flux for clarity and set to zero-velocity. Red and black vertical lines mark positions of *s*-nuclei and non-*s*-nuclei respectively.

The high-resolution UVES spectra in Fig. 7.2 allows for accurate radial velocity determinations by using the positions of spectral lines. Line positions are measured by fitting a Gaussian through the measured line profiles, the line identification is based upon the rest wavelengths from the VALD database (Kupka et al. 1999). We derive a radial velocity of 253 $\pm$ 2 km/s for J050221, which is consistent with the mean average radial velocities of 262 km/s (van der Marel et al. 2002) for the LMC.

We use PyMOOG for the spectral analysis of J050221. We use the plane parallel LTE Kurucz-Castelli atmosphere models (Castelli & Kurucz 2004) and the spherical LTE MARCS atmosphere models (Gustafsson et al. 2008) to make a comparative abundance study between both model types. The spectral analysis of both model atmospheres are performed independently. For our analysis, we avoid blended lines as much as possible. When the abundance of an ion can only be determined by using blended lines, we use synthetic spectra for the abundance analysis. These synthetic spectra are calculated using the Kurucz model atmospheres. We did not include non-LTE effects in our spectral analyses and also did not include molecular lines.

Table 7.1: Model atmosphere results of J050221. The errors for [Fe/H] include line-to-line scatter and all model atmosphere uncertainties (see Sect. 7.4.2). A total of 89 Fe I and 31 Fe II lines are used for the atmospheric parameter determination.

	Kurucz	Marcs
$T_{\rm eff}$ (K)	6250 ± 125	6375 ± 125
log g (dex)	1.00 ± 0.25	1.50 ± 0.25
ξ_t (km/s)	3.00 ± 0.25	3.25 ± 0.25
[FeI/H]	-0.50 ± 0.14	-0.51 ± 0.14
[FeII/H]	-0.54 ± 0.13	-0.42 ± 0.10

7.4.1 Atmospheric parameter determination

The atmospheric parameters of J050221 are determined using both Fe I and Fe II lines and the standard spectroscopic methods. We determine the effective temperature $T_{\rm eff}$ by imposing the iron abundance to be independent of lower excitation potential. We choose the Fe I lines for our temperature determination as the lower excitation potential range for Fe II lines is not broad enough for accurate temperature determinations. We determine the surface gravity log g by imposing ionisation equilibrium between the individual Fe I and Fe II abundances. The microturbulent velocity ξ_t is determined by imposing the iron abundance to be independent of the reduced equivalent width (= EW/λ). Similar to the effective temperature determination, we choose Fe I lines for the microturbulent velocity determination.

We decrease the parameter steps of the Kurucz and Marcs atmosphere models using linear interpolation to calculate atmospheric models which lie within the parameter steps. We do not do any extrapolation. We choose temperature steps of 125 K, surface gravity steps of 0.25 dex and microturbulent velocity steps of 0.25 km/s.

As the EWs of lines are independent of the used atmospheric model, we use the same selection of iron lines for both atmospheric parameter determinations with the Kurucz and Marcs model atmospheres. The atmospheric parameter determinations of the J050221 are listed in Table 7.1. The listed errors of the Fe abundances include line-to-line scatter and atmospheric parameter uncertainties. The atmospheric parameters are determined by a large number of Fe lines. For both atmosphere models, we find similar post-AGB like parameters including metallicity.

7.4.2 Abundance determination

We use the derived atmospheric parameters in Table 7.1 for the abundance determinations.

The spectrum of J050221 does not display much blended lines and therefore we mainly use isolated non-blended lines. The abundances of ions which can only be found in blends are determined using spectral synthesis (see e.g. Figs. 6.5, 6.6 and 6.7). For all stars, we first perform the abundance determination with the Kurucz model and then we use the same selected lines for the analysis with the Marcs model. We do not use lines with EWs smaller than 5 mÅ as they may be confused with spectral noise.

Due to its relatively high temperature, we find seven spectral lines for the carbon abundance determination. The oxygen abundance is determined using the oxygen triplet at 6156 Å. The forbidden oxygen lines are not used as they are part of unidentified blends. We do not detect any visible nitrogen line feature in available spectral regions.

We can determine the elemental abundances of light elements ranging from sodium (Na, Z=11) up to sulphur (S, Z=16). We can also determine the elemental abundances for many iron-peak elements, ranging from calcium (Ca, Z=20) up to zinc (Zn, Z=30).

We find a relatively large number of lines for determining the abundances of the light *s*-elements (ls-elements) yttrium (Y, Z=39) and zirconium (Zr, Z=40). For the heavy *s*-elements (hs-elements), we are able to determine the abundances of typical elements like lanthanum (La, Z=57), cerium (Ce,Z=58), praesodymium (Pr, Z=59), neodymium (Nd, Z=60) and samarium (Sm, Z=62). In addition, we detect a non-saturated barium (Ba, Z=56) II line at 4166 Å, providing the opportunity to determine an accurate Ba abundance. For the europium (Eu, Z=63) abundance determination, we can use the typical spectral lines at 6437.640 and 6645.064 Å.

Regarding the heavy elements with $Z > 63$, we can only use one spectral line to determine the abundances of gadolinium (Gd, Z=64), dysprosium (Dy, Z=66) and luthetium (Lu, Z=71). These abundances are determined using spectral synthesis. J050221 does not display a visible Pb I line feature at 4057.807 Å, and therefore we do not determine the Pb abundance. However, we detect a clear thorium (Th, Z=90) line feature at 4019.129 Å, which is part of an identified blend. As the Th line is part of a large blend, we use spectral synthesis to determine a Th abundance upper limit.

Table 7.2: Abundance results of J050221. For each ion, we list the used number of lines (N), the determined abundance (log ϵ), the uncertainty of log ϵ due to line-to-line scatter (σ_{l21}), the element-over-iron ratio ([X/Fe]) and the total uncertainty on [X/Fe] (σ_{tot}). The latter uncertainty includes line-to-line scatter and atmospheric parameter uncertainty. The solar abundances in the second column are retrieved from Asplund et al. (2009)

		J050221									
		Kurucz [Fe/H] = -0.50					Marcs [Fe/H] = -0.51				
Ion	log $\epsilon_\odot$	N	log ϵ	σ_{l21}	[X/Fe]	σ_{tot}	N	log ϵ	σ_{l21}	[X/Fe]	σ_{tot}
C I	8.43	7	7.80	0.20	-0.09	0.17	6	7.87	0.01	-0.14	0.11
O I	8.69	3	8.46	0.06	0.31	0.17	3	8.51	0.07	0.24	0.17
Na I	6.24	2	6.00	0.00	0.26	0.11	2	6.00	0.01	0.27	0.12
Mg I	7.60	1	7.20	0.20	0.10	0.23	1	7.19	0.20	0.10	0.23
Al I	6.45	2	6.06	0.02	0.11	0.11	2	6.07	0.01	0.13	0.12
Si I	7.51	11	7.29	0.08	0.32	0.17	11	7.29	0.08	0.20	0.14
Si II	7.51	1	7.30	0.20	0.34	0.25	1	7.32	0.20	0.23	0.26
S I	7.12	3	6.89	0.07	0.31	0.13	3	6.92	0.07	0.23	0.13
Ca I	6.34	12	6.05	0.14	0.21	0.10	12	6.02	0.14	0.19	0.10
Ca II	6.34	4	6.03	0.07	0.23	0.12	4	6.12	0.05	0.20	0.12
Sc II	3.15	7	2.54	0.10	-0.07	0.11	7	2.69	0.09	-0.03	0.11
Ti I	4.95	2	4.63	0.12	0.18	0.16	2	4.67	0.11	0.23	0.15
Ti II	4.95	3	4.63	0.01	0.23	0.11	3	4.75	0.04	0.22	0.12
V I	3.93	3	3.35	0.16	-0.08	0.17	3	3.40	0.17	-0.02	0.17
V II	3.93	7	3.42	0.10	0.04	0.12	7	3.60	0.10	0.09	0.12
Cr I	5.64	4	5.34	0.10	0.20	0.11	4	5.34	0.07	0.21	0.10
Cr II	5.64	15	5.29	0.08	0.20	0.08	15	5.40	0.08	0.19	0.08
Mn I	5.43	3	5.04	0.13	0.11	0.14	3	5.06	0.14	0.14	0.14
Mn II	5.43	2	4.96	0.08	0.08	0.13	2	5.09	0.08	0.09	0.14
Fe I	7.50	89	7.00	0.09	0.00	0.05	89	6.99	0.11	0.00	0.05
Fe II	7.50	31	6.96	0.11	0.00	0.07	31	7.08	0.12	0.00	0.07
Co I	4.99	2	4.39	0.12	-0.1	0.15	2	4.39	0.15	-0.09	0.17
Ni I	6.22	8	5.73	0.10	0.01	0.09	8	5.74	0.12	0.03	0.11
Cu I	4.19	2	3.56	0.01	-0.13	0.10	2	3.60	0.03	-0.08	0.12
Zn I	4.56	1	3.80	0.20	-0.21	0.29	1	3.83	0.20	-0.31	0.27

Table 7.2: Continued.

		J050221									
		Kurucz [Fe/H] = -0.50					Marcs [Fe/H] = -0.51				
Ion	log $\epsilon_\odot$	N	log ϵ	$\sigma_{\rm l2l}$	[X/Fe]	σ_{tot}	N	log ϵ	$\sigma_{\rm l2l}$	[X/Fe]	σ_{tot}
Y II	2.21	8	1.81	0.10	0.14	0.12	8	1.98	0.10	0.20	0.12
Zr II	2.58	7	2.09	0.12	0.06	0.12	7	2.27	0.11	0.11	0.12
Ba II	2.18	1	2.14	0.20	0.50	0.28	1	2.25	0.20	0.49	0.26
La II	1.10	13	1.17	0.15	0.62	0.15	13	1.34	0.14	0.67	0.14
Ce II	1.58	11	1.57	0.09	0.53	0.12	11	1.74	0.10	0.58	0.12
Pr II	0.72	4	0.83	0.05	0.66	0.16	4	1.01	0.04	0.72	0.16
Nd II	1.42	18	1.51	0.09	0.63	0.14	18	1.67	0.08	0.67	0.13
Sm II	0.96	4	0.76	0.07	0.35	0.15	4	0.94	0.06	0.40	0.14
Eu II	0.52	2	0.48	0.06	0.50	0.14	2	0.64	0.06	0.54	0.14
Gd II	1.07	1	1.05	0.20	0.52	0.24	1	1.24	0.20	0.59	0.25
Dy II	1.10	1	0.75	0.20	0.19	0.26	1	0.94	0.20	0.27	0.26
Lu II	0.10	1	-0.07	0.20	0.38	0.26	1	0.11	0.20	0.44	0.26
Th II[a]	0.02	1	< 0.06		< 0.59		1	< 0.26		< 0.66	

[a] The determined Th abundance is an upper limit.

7.5 Abundance results

The Kurucz and Marcs model abundance results of J050221 are listed in Table 7.2. An overview of the spectral lines used for the analysis is provided in Appendix F.

We impose a line-to-line scatter of 0.2 dex for all elemental abundances in Table 7.2 that have been determined using only one spectral line or by using synthetic spectra. We do not mention errors for the upper abundance limit of Th. For the calculation of the element-over-iron ratios, we use the Fe ion for which the ionisation potential lies closest to the ionisation potential of the studied ion. The same principle is used for calculating the total errors $\sigma_{\rm tot}$ of the [X/Fe] results which include both line-to-line scatter and uncertainties by atmospheric parameters (see Eq. 2.9).

7.5.1 Kurucz versus Marcs results

The [X/Fe] results of J050221 in Table 7.2 are plotted in Fig. 7.3 for both atmospheric models. There are no significant differences between the Kurucz

and Marcs model results which follow a similar abundance distribution. We find that the Marcs model results in slightly higher abundances than the Kurucz model. For all ions, the largest difference between derived Kurucz and Marcs absolute abundances is 0.2 dex, while the largest difference in [X/Fe] results is 0.12 dex (error bars not included). This shows the need for comparing relative abundances instead of absolute abundances as described in Sect. 2.6.3. As the abundance differences between both models are relatively small, we will not discuss the individual model results in the further discussion of the abundance results, but the common abundance distribution.

7.5.2 Elements with Z $<$ 38

In Table 7.2, a remarkable feature is a negative [C/Fe] $\approx$ -0.1 dex and a positive [O/Fe] $\approx$ +0.3 dex for J050221. This results in a low C/O ratio of about 0.2 (see Table 7.4), indicating no carbon enhancements for J050221. For the calculation of [α/Fe], we used the [X/Fe] results of magnesium (Mg, Z=12), silicon (Z=14), sulphur (S, Z=16), calcium (Ca, Z=20) and titanium (Ti, Z=22). We find moderate α-element enhancements of about 0.2 dex (see Table 7.4), which correspond to the expected LMC [α/Fe] for this metallicity (e.g. Van der Swaelmen et al. 2013). We are able to detect the abundances of the iron-peak elements ranging from Ca up to zinc (Zn, Z=30). For about half of these elements, we are able to determine the abundances of two ions which confirm the use of our preferred atmosphere models.

7.5.3 Heavier elements

Fig. 7.3 and Table 7.4 show a very small enhancement of the ls-elements Y and Zr around Z = 40 with [ls/Fe] $\approx$ +0.1 dex, and a mild *s*-process enrichment for the hs-elements around Z = 56 with [hs/Fe] $\approx$ +0.55 dex. We speak of mild *s*-process enrichment when the mean [X/Fe] of the *s*-process elements lies between zero and one: $0 < [s/\mathrm{Fe}] \leqslant 1$. For the hs-elements, the [Ba/Fe] = +0.5 dex is similar to the results of the other hs-elements. We find that [Eu/Fe] $>$ [Sm/Fe], while in *s*-process enriched post-AGB stars Eu is generally underabundant with respect to Sm. Heavy elements with Z $>$ 63 have similar or lower abundance ratios with respect to the hs-elements. The adopted Th abundance upper limit is somewhat higher than the mean [hs/Fe].

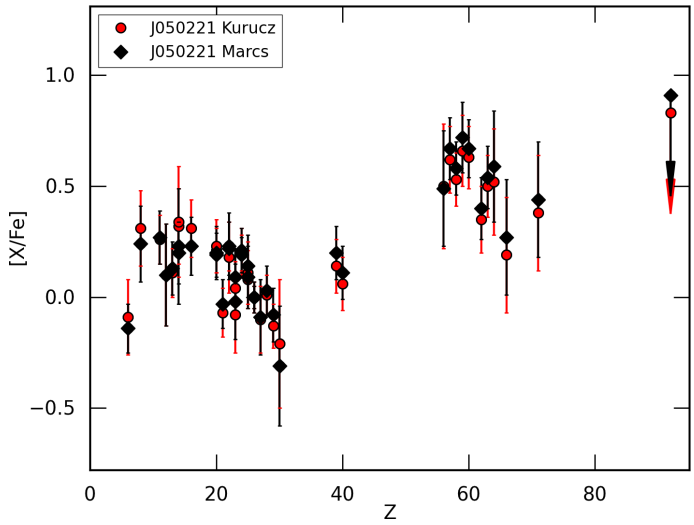

Figure 7.3: Element-over-iron ratios of J050221 for the Kurucz (red dots) and Marcs (black diamonds) model atmospheres in Table 7.2. The down-arrow indicates the abundance upper limit of Th. Errorbars represent the total errors $\sigma_{\rm tot}$.

7.6 Luminosity and initial mass

The atmospheric parameter determination and the known distance to the LMC allow us to calculate the luminosity and estimate the initial mass of J050221.

7.6.1 Luminosity determination

We use the photometry in Fig. 7.1 to construct the SED of J050221 by using our preferred Kurucz atmosphere model. For the calculation of the reddening of J050221, we assume the three possible sources of reddening described in Sect. 5.5.1. We use the Galactic extinction curves of Cardelli et al. (1989) to calculate the total reddening. We apply a χ^2 minimalisation on the fit between the dereddened broadband fluxes and the preferred Kurucz model atmosphere to calculate the total reddening. The reddening uncertainties are calculated using a Monte Carlo simulation for 100 arrays with a normal distribution of the original flux. We determine the luminosity by integrating the surface of the scaled Kurucz models and applying a distance of 50 kpc. Errors for the luminosity are also calculated using a Monte Carlo simulation for 100 arrays

Table 7.3: SED results of J050221 using a distance of 50 kpc.

E(B-V)	0.18 ± 0.02
L ($L_\odot$)	6700 ± 300

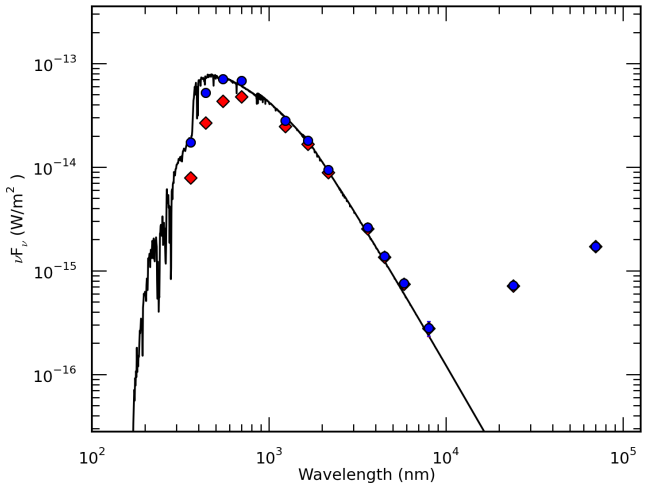

Figure 7.4: Constructed SED of J050221. Red diamonds represent the original reddened photometry from Fig. 7.1, blue circles represent the dereddened fluxes. black lines represent the best-fitting scaled Kurucz model atmosphere.

with a normal distribution of the original flux. Table 7.3 lists the SED results of J050221, the newly constructed SED is presented in Fig. 7.4. The determined luminosity is a typical post-AGB luminosity and lies in between the determined luminosities by van Aarle et al. (2011) and Kamath et al. (2015), who also found different atmospheric parameters and hence used different atmosphere models to determine the luminosity.

7.6.2 Initial mass estimate and HR diagram

With the determined effective temperature and luminosity, we are able to estimate the initial mass of J050221. Fig. 7.5 shows the position of J050221 in the HR diagram together with the theoretical post-AGB tracks of Vassiliadis & Wood (1994). We choose the Z = 0.004 tracks as this metallicity corresponds the most to the derived metallicity of J050221. Fig. 7.5 also shows the position

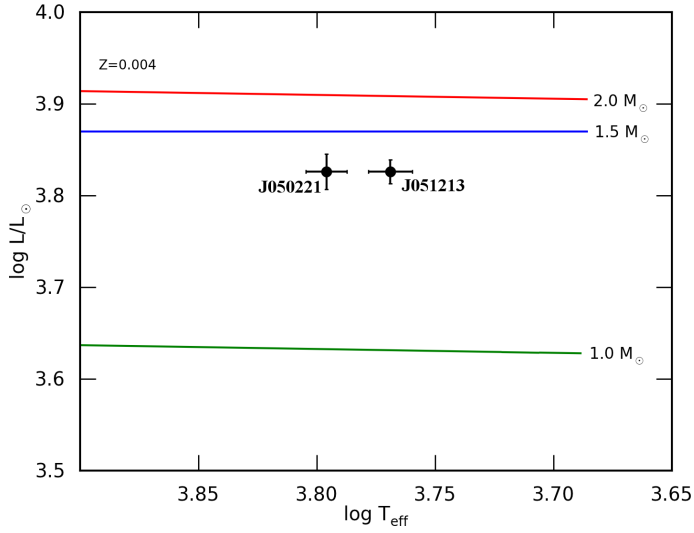

Figure 7.5: Position of J050221 in the HR-diagram compared to theoretical post-AGB tracks of Vassiliadis & Wood (1994). The representative initial mass of each track is shown at the right end. Also the position of the strongly *s*-process enriched LMC post-AGB star J051213.81-693537.1 (J051213, Chapter 5) is shown.

of J051213 (T_{eff}= 5875 K, log g = 1.00 dex, ξ_t = 3.0 km/s, [Fe/H] $\approx$ -0.55 dex) from Chapter 5, which has similar atmospheric parameters and luminosity like J050221. Both stars have low initial masses around 1.5 $M_\odot$ and similar metallicities but very different abundances: while J050221 only displays mild *s*-process enrichment, J051213 is strongly *s*-process enriched (see Chapter 5).

Fig. 7.6 shows the position of J050221 and the *s*-process enriched post-AGB stars from De Smedt et al. (2012), van Aarle et al. (2013) and Chapter 5. Although a strongly different level of *s*-process enrichment, J050221 occupies a similar position in the HR-diagram as the other stars. We can therefore conclude that the position in the HR-diagram is not a clear indicator of the level of *s*-process enrichment.

7.7 Neutron irradiation

To quantify the *s*-process distributions and *s*-process overabundances of J050221, we use the typical four observational indices of previous chapters: [ls/Fe], [hs/Fe],

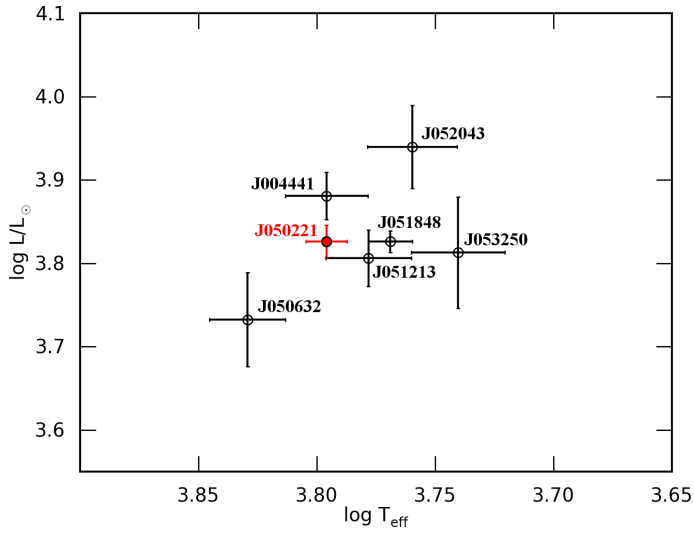

Figure 7.6: Position in the HR-diagram of J050221 and the *s*-process enriched post-AGB stars from De Smedt et al. (2012), van Aarle et al. (2013) and Chapter 5.

Table 7.4: Overview of the C/O ratio, metallicity and α- and *s*-process indices of J050221.

	Kurucz	Marcs
C/O	0.22 ± 0.08	0.23 ± 0.04
[Fe/H]	-0.50 ± 0.14	-0.51 ± 0.14
[α/Fe]	0.22 ± 0.07	0.19 ± 0.07
[ls/Fe]	0.10 ± 0.08	0.15 ± 0.08
[hs/Fe]	0.53 ± 0.07	0.58 ± 0.07
[s/Fe]	0.39 ± 0.05	0.44 ± 0.05
[hs/ls]	0.43 ± 0.11	0.43 ± 0.11

[s/Fe] and [hs/ls]. The different *s*-process indices of J050221 are listed in Table 7.4 for both the Kurucz and Marcs model atmospheres. As expected from the results of Table 7.2, the indices are similar for both model atmospheres. The [s/Fe] results indeed show a mild *s*-process enhancement with a high [hs/ls]. The very low C/O ratio of J050221 does not testify of any efficient third dredge-up, which is also needed for *s*-process enhancements.

This is also confirmed by the position of J050221 in the [hs/ls] versus [s/Fe] diagram in the upper panel of Fig. 7.7. This object (cyan diamond) does not follow the correlation defined by the post dredge-up objects. J050221 is too rich in hs-elements to follow this correlation. The same is true for the mildly *s*-process enhanced IRAS 17279-1119 (purple dot) of Chapter 6. The lower panel of Fig. 7.7, representing [hs/ls] versus [Fe/H] of the same stars as the upper panel, again shows no signs of correlation.

Based upon the result of the upper panel of Fig. 7.7, we assume that the mild *s*-process enrichment of J050221 reflects the initial chemical composition of the gas cloud from which it originates, hence the local intrinsic *s*-process abundances of the LMC at its place of birth. Therefore the *s*-process elements observed in the photosphere of J050221 are not created by the star itself. Comparison with the observed *s*-process elements in red giants by Van der Swaelmen et al. (2013) indeed suggest this scenario as described in Sect. 2.1.1.

This scenario imposes two important consequences with respect to post-AGB stars in the Magellanic Clouds. The first is the strong resemblance in atmospheric parameters, SED shapes, luminosities and hence initial masses between J050221 and the other *s*-process enriched post-AGB stars in the Magellanic Clouds in this thesis, especially with J051213. These similarities suggest that these stars should have followed a similar evolution but the observed surface abundances of J050221 contradicts this assumption. It is also possible that J050221 is a binary star and therefore followed a different evolution than J051213. However, the similarity between the SED of J050221 and the SEDs of intrinsically *s*-process enriched post-AGB stars in the Magellanic Clouds in the previous chapters seem to rule out binarity. More research in the form of fine-tuned stellar evolutionary models are necessary to explain the large abundance difference between similar stars like J050221 and J051213. The chemical diversity in post-AGB stars is larger than theoretical AGB models can account for.

The second important remark is the mild *s*-process enrichment of the LMC in hs-elements. In Galactic objects, *s*-process overabundances are an indicator of an evolved nature of the observed object, or its invisible binary companion which, during its AGB phase, enriched the observed star. The latter are so-called barium stars and are hence extrinsically enriched. The very low C/O ratio of J050221 (C/O $\ll$ 1.0) seems to rule out extrinsic enrichment.

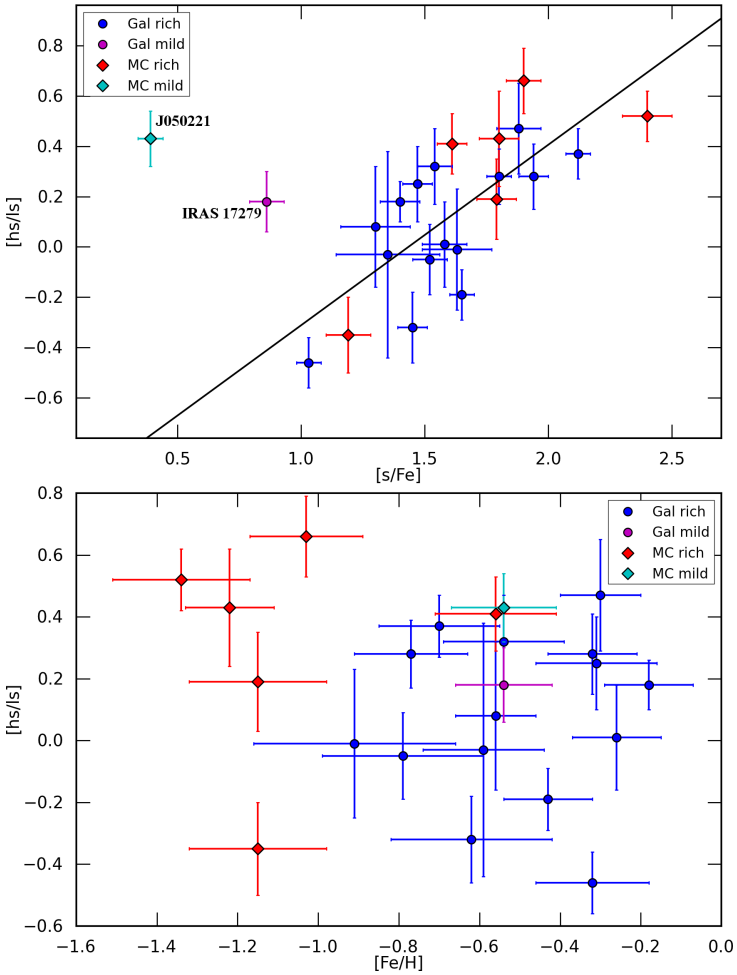

Figure 7.7: Upper panel: Correlation between the total enrichment in *s*-process elements and the [hs/ls] index of all *s*-process enriched Magellanic Cloud stars in this thesis from De Smedt et al. (2012), van Aarle et al. (2013), Chapter 5 and this chapter, and the Galactic post-AGB stars from Chapter 6. Enriched Galactic objects are represented by blue dots, enriched Magellanic Cloud objects are represented by red diamonds. The black line represents the least-squares fit to all enriched objects. The purple dot represents the mildly-enriched IRAS 17279-1119, the cyan diamond represents J050221. Lower panel: Similar to the upper panel but for the correlation between the metallicity [Fe/H] and the [hs/ls] index.

Also, about 1% of Galactic RGB stars are barium stars, and if we assume a similar population in the Magellanic Clouds, the chance of observing a barium star in its post-AGB evolution is very small. Nevertheless, contrary to observed *s*-process overabundances in Galactic objects, observed mild *s*-process overabundances in LMC objects are not an indicator of an evolved nature due to the intrinsic *s*-process enrichment of the galaxies themselves. Since both Magellanic Clouds show intrinsic *s*-process enhancement, we conclude that this intrinsic enrichment must be subtracted from observed *s*-process abundances to know the stellar intrinsic *s*-process enrichment. However, as the intrinsic *s*-process element abundances increased throughout the evolution of the galaxies, which is translated in increasing *s*-process abundances towards higher metallicities (see Fig. 2.3), the subtracted intrinsic abundances should be adapted to the respective metallicity of the observed star. In addition, there exists a spread in metallicity and *s*-process abundances in the LMC, as shown in Fig. 2.3 where different mean Y and Zr abundances are observed in the LMC bar and LMC disc. Therefore, the subtracted intrinsic abundances are also dependent on the region of birth of the observed star.

Nevertheless, for the strongly *s*-process enriched post-AGB stars in the Magellanic Clouds, the effect of subtracting any galactic intrinsic enrichment from the observed abundances would be negligible. For example, an intrinsic enrichment of [La/Fe] = +0.5 dex in the SMC would lower the observed [La/Fe] = +2.84 dex of J004441.04-732136.4 (Chapter 3) by only 0.002 dex (= 2.84 - $\log(10^{2.84}\text{-}10^{0.5})$). However, for a mildly enriched object with an observed [La/Fe] = +1.00 dex, an intrinsic galactic enrichment of [La/Fe] = +0.5 dex would lower the observed [La/Fe] by about 0.17 dex. Therefore, the intrinsic galactic enrichment becomes more important for objects with lower *s*-process enrichments.

7.8 Conclusions

In this chapter, we performed a detailed abundance study of the LMC post-AGB star J050221.17-691317.2. Our abundance analysis shows that J050221 displays mild *s*-process enrichment with almost no overabundances for the ls-elements and mild overabundances for the hs-elements, combined with a very low C/O ratio. The shell-shaped SED results in a typical post-AGB luminosity and comparison with theoretical post-AGB tracks reveals that J050221 has a low estimated initial mass, similar to the strongly *s*-process enriched post-AGB stars in the Magellanic Clouds studied in the previous chapters. J050221 also occupies the same region in the HR diagram as the enriched post-AGB stars, which shows that the position in the HR diagram is no indicator of the level of

enrichment. We find that the mild enrichment of J050221 resembles the local chemical composition of the LMC at the time and place of birth of J050221. Therefore, we conclude that these intrinsic galactic enhancements should be subtracted from observed *s*-process abundances in LMC stars.

We conclude that J050221 is likely *not* a post dredge-up object and hence not enriched during its AGB evolution. As objects with similar metallicities and initial masses occupying the same region in the HR diagram are found to be much stronger *s*-process enriched than J050221, we conclude that post-AGB stars in the Magellanic Clouds are chemically very diverse.

Chapter 8

Conclusions

Although the general evolutionary scheme of single low-mass AGB stars is understood, there is no understanding from first principles of different physical processes that govern this evolutionary phase. In this thesis, we focus upon the poorly understood AGB *s*-process nucleosynthesis and corresponding mixing processes. Post-AGB photospheres bear witness of the internal nucleosynthesis and mixing processes that occurred during the full stellar lifetime. The Galactic sample of post-AGB stars displays a wide chemical diversity but, due to the lack of accurate distance measurements and hence accurate luminosity determinations, the observed abundances of these stars can not be compared to finetuned stellar evolution and nucleosynthesis model predictions. To overcome the distance problem, we study post-AGB stars in the Magellanic Clouds, which are selected from previous surveys, to gain insight in the different internal physical processes governing the AGB phase.

In Chapter 3, we present a detailed abundance study of the low-mass, metal-deficient SMC post-AGB star J004441.04-732136.4 (J004441). This object has very strong *s*-process enhancements but a moderate C/O ratio. Comparison between the observed abundances and finetuned theoretical model predictions reveals that models can well reproduce the observed abundance distribution but neither the moderate C/O ratio nor the upper limit of the observed Pb abundance, which does not show a Pb overabundance with respect to the other *s*-elements. Due to the low S/N around the spectral region of the observed Pb line, the discrepancy between observed and predicted Pb abundances can not yet be confirmed in Chapter 3.

The new observations of J004441 in Chapter 4 confirm this observed Pb discrepancy. The best fitting model of the other *s*-process elements overestimates

the observed Pb abundance upper limit by about 2.0 dex. In addition, three other *s*-process enriched low-mass, metal-poor LMC post-AGB stars also do not bear witness of any Pb overabundance with respect to the other *s*-elements.

The abundance analysis of two newly identified LMC post-AGB stars in Chapter 5 display the same trends: low C/O ratios, strong *s*-process enhancements but no indications of strong Pb overabundances with respect to the other *s*-process elements. This lack of Pb overabundances is expected in the more metal-rich J051213.81-693537.1 with [Fe/H] $\approx$ -0.6 dex, but not in the more metal-poor J051848.86-700246.9 with [Fe/H] $\approx$ -1.0 dex. We hence detect an increasing discrepancy between observed and predicted Pb abundances towards lower metallicities.

To confirm the observed Pb discrepancy trend, we perform a homogeneous abundance study of fourteen Galactic *s*-process enriched post-AGB stars with a main focus on Pb in Chapter 6. Comparison between predicted Pb abundances and observed Pb abundance upper limits indeed confirm the observed discrepancy which starts around [Fe/H] $\approx$ -0.7 dex. In addition, we find that the mildly enriched IRAS 17279-1119 is member of a binary system, and most probably suffered an early cut-off from its AGB evolution due to binary interactions.

In Chapter 7, we present the abundance results of the mildly *s*-process enhanced LMC post-AGB star J050221.17-691317.2 (J050221). Apart from having very different abundances, J050221 is very similar to the *s*-process enriched Magellanic Cloud post-AGB stars, including its position in the HR diagram which is hence no indicator for C and *s*-process enrichment. Comparison with the abundance results of red giants in the Magellanic Clouds lets us conclude that the *s*-process abundances of J050221 represent the intrinsic LMC abundances.

By combining the main results of the individual chapters in this work, we summarise the following main conclusions:

We find a wide chemical diversity for post-AGB stars in the Magellanic Clouds which is similar to the diversity of their Galactic counterparts. Despite the large differences in enrichments, ranging from strong *s*-process enrichment with moderate carbon enrichment down to mild *s*-process enrichment with no carbon enhancement, the observed Magellanic Cloud post-AGB stars in this thesis are all low-mass stars and occupy the same region in the HR diagram. Therefore, the position in the HR diagram is not sufficient to disentangle objects with differing enrichments.

The intrinsic galactic enrichments of the Magellanic Clouds should be taken into account when studying the *s*-process nucleosynthesis in the Magellanic Clouds. The contribution of these intrinsic galactic enrichments depends upon

the age ($\sim$ metallicity) and region of the observed stars.

Theoretical AGB evolution and nucleosynthesis models are able to reproduce the observed abundance distributions of strongly *s*-process enriched post-AGB stars but are not able to reproduce the observed low C/O ratios and Pb abundance upper limits. The observed C/O ratio is generally overestimated by the models due to an overestimated carbon abundance and a strongly underestimated oxygen abundance. We find an increasing discrepancy between predicted and observed Pb abundances towards lower metallicities starting from about [Fe/H] = -0.7 dex. Additional research is needed to explain this phenomenon.

We confirm the correlation between neutron irradiation [hs/ls] and mean *s*-process enrichment [s/Fe] for strongly *s*-process enriched post-AGB stars. Mildly enhanced objects do not follow this correlation. We also find that there is no correlation between neutron irradiation [hs/ls] and metallicity [Fe/H].

Chapter 9

Future prospects

To end this thesis, we provide insights in ongoing and future work in the addressed research fields presented in this work. In Sect. 9.1, we discuss our ongoing work with the stellar evolution code STAREVOL and we describe the main questions for future theoretical modeling. In Sect. 9.2, we discuss the preliminary results of non-post-AGB objects in our sample of post-AGB candidates. In Sect. 9.3, we end with observational future prospects of post-AGB stars.

9.1 Prospects in theoretical modeling

9.1.1 Studies with STAREVOL

As described in Sect. 1.3.4, we generated multiple stellar evolution model predictions for a grid of different masses and metallicities with the stellar evolution code STAREVOL (see e.g. Siess 2007, and references therein). We gave a brief overview of the main results for the dredge-up parameter λ (Eq. 1.2) and described in more detail the surface abundance predictions for three AGB models with metallicity $Z = 0.001$ and masses 1.5, 2.0 and 3.0 $M_{\odot}$. In addition, we also generated models for the same masses but for metallicities $Z = 0.004$, $Z = 0.008$ and $Z = 0.02$. Also 1.0 $M_{\odot}$ were generated. We remark that these models were created with the purpose of learning more about the general predictions of AGB evolution models and not for detailed abundance comparisons between observations and fine-tuned model predictions like in Chapter 3. Due to the time-constraint of a PhD, we could not yet analyse

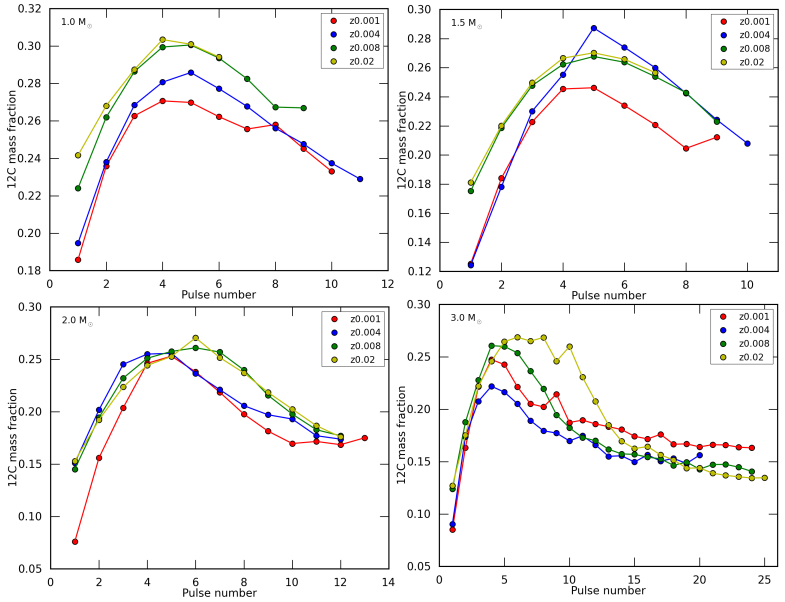

Figure 9.1: Mass fraction of ^{12}C in thermal pulses for STAREVOL models with different masses and metallicities.

this grid of models in detail. However, analysis of the evolution of the ^{12}C mass fraction in the convective thermal pulses for our model grid revealed an unexpected evolution for the different AGB models.

^{12}C mass fraction in thermal pulses:
Fig. 9.1 shows the evolution of the ^{12}C mass fraction within the convective thermal pulses for our different generated STAREVOL models. The ^{12}C mass fraction of each thermal pulse was measured during the maximum extent of the convective thermal pulse in the mean mass coordinate between bottom of the convective pulse and the mass coordinate of the deepest extent of the convective envelope during the third dredge-up. The overall mass within the intershell, and hence convective thermal pulses, consists mainly out of ^{4}He, and then ^{12}C and ^{16}O. Fig. 9.1 shows that for all masses and metallicities, the ^{12}C mass fraction first increases before it decreases again. For the 2.0 and 3.0 M$_{\odot}$ models, the ^{12}C mass fraction eventually becomes approximately constant. To date, it is not clear why the ^{12}C mass fraction follows this behavior during the TP-AGB and why there are large mass fraction differences for the different metallicities of the same initial mass. As the seed of the ^{13}C-pocket in the intershell, this ^{12}C mass fraction behavior during the TP-AGB has important consequences on

the predicted *s*-process abundances, and knowing the mechanism behind this phenomenon will help us gain insight in the AGB nucleosynthesis.

We have searched for the mechanism causing the behavior of ^{12}C in thermal pulses by studying the reaction rates of the triple α-reaction (which creates ^{12}C) and the ^{12}C(α,γ)^{16}O reaction (which destroys ^{12}C and creates ^{16}O) during the different thermal pulses and interpulses. However, based upon the reaction rates, the ^{12}C(α,γ)^{16}O is only marginally triggered during the thermal pulses where the ^{12}C mass fraction drops. We recently found that the decreased ^{12}C mass fractions in Fig. 9.1 are combined with an increase in the ^{4}He mass fraction while the ^{16}O fraction only marginally increases. Since ^{4}He is produced by H shell-burning during the TP-AGB during the interpulse, more research is necessary to study the evolution of the ^{12}C and ^{4}He mass fractions during the interpulses. The current obtained model calculations have too large time steps to plot in detail the evolution of the mass fractions during the interpulse. Therefore, recalculations of the interpulses with smaller time steps are necessary to study this evolution in detail.

9.1.2 General theoretical prospects

The final predicted C/O ratios in the upper panels in Fig. 1.18 confirm that the observed C/O ratios in *s*-process enriched post-AGB stars, which typically lie between C/O = 1 and C/O = 2.5, are much lower than predicted. To date, it is not clear why the observed C/O ratios are so low. A general comparison with theoretical models shows that the observed C/O ratios are already reached after the first or second third dredge-up episode, and keeps increasing during following dredge-ups. More research is needed to solve the observed low C/O ratios which may include higher initial O abundances or higher fractions of dredged-up O. The latter may be realised by experimenting with convective overshooting at the top of the degenerate core, which may mix more O in the intershell during a thermal pulse.

As the expected end-product of the *s*-process chain, the Pb abundance is sensitive to the different processes that occur during the TP-AGB. The results in Fig. 6.14 show that the predicted Pb overabundances for *s*-process enriched post-AGB stars with [Fe/H] $\lesssim$ -0.7 are too high, and difference between observations and predictions increases towards lower metallicities. Since the final Pb abundance depends upon the created ^{13}C-pockets during interpulses, the exploration of building mechanisms of the ^{13}C-pockets are necessary for reproducing the low observed Pb abundances. Also the effects of alternative mixing processes like rotation (e.g. Siess et al. 2004; Piersanti et al. 2013) or the effects of internal gravity wave mixing (Denissenkov & Tout 2003) should be explored. Another

interesting scenario to explore is the effect of proton-ingestion episodes (PIEs) in a convective thermal pulse (Lugaro et al. 2015).

In addition, the large differences in *s*-process abundances for stars with similar initial masses, metallicities and atmospheric parameters like J050221.17-691317.2 and J051213.81-693537.1 (see e.g. Fig. 7.2) can not be explained by the current AGB models. There is no knowledge of any mechanisms included in AGB models which may explain the large abundance differences, so further research is needed to solve this phenomenon.

A last but very important topic for further study of theoretical stellar evolution models is mass loss for which the physical driving mechanisms are not well understood. Since the total accumulated mass loss determines the duration of the TP-AGB, it also influences the number of thermal pulses and dredge-ups and hence the predicted C/O ratio and *s*-process abundances as well as the core mass and the final luminosity of the post-AGB evolutionary phase. For example, a change in the implementation of mass loss between an old and the current version of STAREVOL, resulted in a significant decrease of the number of thermal pulses for a 3 $M_{\odot}$ model with Z = 0.02: the model generated with the older mass loss implementation underwent 30 thermal pulses more than the recent model. The large difference is explained by the much higher mass loss for the recent model. In addition, while both models had similar initial C/O ratios around 0.25, the final C/O ratios differed by about 3.7 with a C/O = 4.8 for the old model and a C/O = 1.1 for the new model. This clearly shows the need of accurate mass-loss prescriptions in theoretical AGB models.

Mass loss is also very important for the calculation of theoretical post-AGB tracks, which we use for our initial mass estimates. Since the theoretical post-AGB tracks of Vassiliadis & Wood (1994) and Blöcker (1995) are based upon empirical results, old opacity tables and the deduced initial-final mass relations at that time period, there is a strong need in updated theoretical post-AGB tracks to make the initial mass estimates much more accurate. A possible source for updated post-AGB tracks could be the stellar evolution code package MESA[1], but more study is needed to check whether the current MESA calculations are able to accurately reproduce the AGB and post-AGB evolutionary phase.

In summary, there are still many processes which need more future detailed study to gain insight in the AGB evolution and nucleosynthesis, and the observable effects in the subsequent post-AGB phase.

[1]Modules for Experiments in Stellar Astrophysics, http://mesa.sourceforge.net/

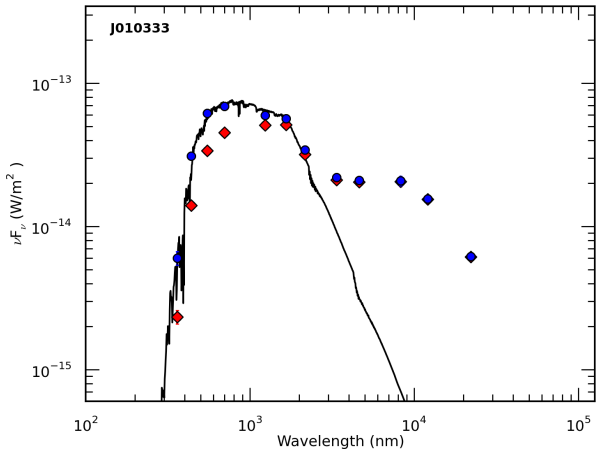

Figure 9.2: Spectral energy distribution of J010333.93-724405.3. Red diamonds show the original reddened photometric fluxes, blue circles the dereddened fluxes. The black line represents the best-fitting scaled Kurucz model atmosphere.

9.2 Abundance study of non-post-AGB intruders in the post-AGB sample

Apart from the analysed post-AGB stars in the previous chapters, our sample of post-AGB candidates in the Magellanic Clouds with high-resolution UVES spectra also contains objects which are not post-AGB stars. These objects were selected based upon their post-AGB-like properties in the surveys of van Aarle et al. (2011), Kamath et al. (2014) and Kamath et al. (2015). We performed abundance studies of six of these objects. In the first part of this section, we briefly elaborate on the results of one of these objects: J010333.93-724405.3, which is an SMC object. In the second part, we summarise the results of all six objects.

9.2.1 J010333.93-724405.3

Fig. 9.2 shows the SED of J010333.93-724405.3 (J010333), which shows a strong excess in the near-IR and hence indicates the presence of a circumstellar disc (see e.g. right panel of Fig. 1.23). The STP and SED results of J010333 in Kamath et al. (2014) are typical for a post-AGB star, with a log $g = 0.0$ dex and luminosity of about 10500 $L_\odot$. Based upon these results and the SED shape in Fig. 9.2, J010333 was selected for observations with UVES.

Table 9.1: Model atmosphere results of J010333. The errors for [Fe/H] include line-to-line scatter and all model atmosphere uncertainties. A total of 31 Fe I and 15 Fe II lines are used for the atmospheric parameter determination.

	Kurucz	Marcs
$T_{\rm eff}$ (K)	4500 ± 125	4500 ± 125
log g (dex)	1.00 ± 0.25	0.75 ± 0.25
ξ_t (km/s)	2.25 ± 0.25	2.50 ± 0.25
[FeI/H]	-0.54 ± 0.22	-0.54 ± 0.22
[FeII/H]	-0.54 ± 0.22	-0.57 ± 0.27

The obtained UVES spectra were observed with the same settings as for J004441.04-732136.4 in Chapter 3. We obtained two Blue, one RedL and two RedU spectra for J010333, each with a total exposure time of 2250 s. These spectra were reduced in a similar way as the studied post-AGB stars in the previous chapters. At first glance, the high resolution spectra revealed no indications of strong *s*-process enrichment but also seemed to rule out strong depletion, which is often detected in Galactic post-AGB stars with discs (e.g. Gezer et al., 2015, submitted). Similar to J050221.17-691317.2 (J050221) in Chapter 7, we performed spectral analyses with PyMOOG for both Kurucz and Marcs model atmospheres. The atmospheric parameter results of J010333 are listed in Table 9.1. Both atmosphere models result in similar parameters: a low surface gravity and a metallicity which is somewhat higher than the mean SMC metallicity of -0.7 dex (Luck et al. 1998).

Thereafter, we performed a detailed abundance study using the preferred atmosphere models. The abundance results of J010333 are presented in Fig. 9.3. Like for J050221 in Chapter 7, the abundance results are very similar for both model atmospheres. J010333 has a low C/O ratio around 0.40, a low enrichment of ls-elements with [ls/Fe] $\approx$ 0.15 dex and a mild enrichment of hs-elements with [hs/Fe] $\approx$ 0.55 dex.

The study of the SED of J010333 in Fig. 9.2 resulted in a reddening of E(B-V) = 0.21 ± 0.02 and a luminosity of L = 12400 ± 300 $L_{\odot}$. In order to confirm the post-AGB nature of J010333, we used the combination of derived atmospheric parameters and luminosity to calculate the current stellar mass. As described in Sect. 2.2.2, Kamath et al. (2014) used a log g criterion to disentangle post-AGB/post-RGB objects from young stellar objects (YSOs). For the same luminosity, YSOs have a higher mass and hence log g than post-AGB

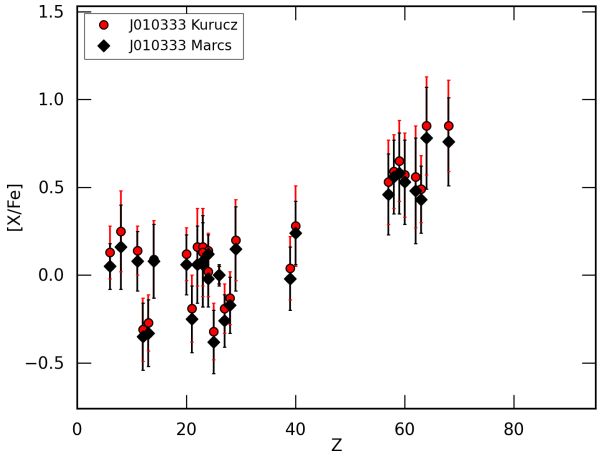

Figure 9.3: [X/Fe] results of J010333, with the Kurucz model results represented by red circles and the Marcs model results with black circles.

stars. We calculate the current stellar mass using

$$\mathrm{M} = \frac{g\mathrm{R}^2}{\mathrm{G}} \tag{9.1}$$

with M expressed in kg, R in meter and G = 6.673 × 10^{-11} m s kg^{-1}. The current stellar radius can be determined using the luminosity:

$$\mathrm{R} = \sqrt{\frac{\mathrm{L}}{4\pi\sigma\mathrm{T}_{\mathrm{eff}}^4}} \tag{9.2}$$

with R expressed in meter, L in Watt, T_{eff} in K and σ = 5.66956 × 10^{-8} W m^{-2} K^{-4}. The gravitational acceleration g is calculated using $g = 10^{\log g}/100$ (expressed in m s^{-2}). This results in a current mass of 12.3 ± 7.2 $M_\odot$. Since post-AGB stars have expected current masses around 0.6 $M_\odot$, this current mass result indicates that J010333 is a YSO instead of a post-AGB star. We remark that the effect of log g on the current mass determination is significant, and a small change in surface gravity can strongly alter the current mass estimate (see already Table 9.2) which is also translated in the large errors of the current mass calculations. This implies that J010333 is likely a very luminous YSO since typical expected Galactic YSO luminosities lie around 500 $L_\odot$. Kamath et al. (2014) and Kamath et al. (2015) have found multiple of these objects in their Magellanic Cloud survey. The eventual YSO nature of J010333 also implies that the found *s*-process abundances represent the intrinsic enrichment

Table 9.2: . Current mass results of different stars in the post-AGB sample. The evolved nature of the first six stars in unknown, while the three last stars are confirmed post-AGB stars from previous chapters. L represents the luminosity, M_c shows the current mass results for the preferred Kurucz models, the fourth and fifth column show the current mass results for the same Kurucz atmosphere models but with log g -0.25 and +0.25 dex respectively.

Object	L ($L_\odot$)	M_c ($M_\odot$)	M_c -0.25 ($M_\odot$)	M_c +0.25 ($M_\odot$)
J010056	10000 ± 300	35.0 ± 20.6	22.0 ± 12.9	68.7 ± 40.4
J010324	28700 ± 2000	25.5 ± 15.0	15.9 ± 9.4	49.9 ± 29.4
J010333	12400 ± 300	12.3 ± 7.2	6.3 ± 3.7	19.3 ± 11.5
J010929	3500 ± 100	2.8 ± 1.6	1.4 ± 0.8	4.3 ± 2.5
J045623	10300 ± 300	13.6 ± 7.7	6.8 ± 4.0	21.6 ± 12.6
J052221	3900 ± 100	1.7 ± 1.0	1.1 ± 0.7	3.6 ± 2.1
J050221	6700 ± 300	1.8 ± 1.0	1.0 ± 0.6	3.2 ± 1.8
J051213	6700 ± 200	2.3 ± 1.3	1.4 ± 0.8	4.4 ± 2.6
J051848	6250 ± 200	0.6 ± 0.4	0.4 ± 0.2	1.1 ± 0.7

of the SMC at the place and time of birth of J010333, similar to J050221 in the LMC.

9.2.2 Other objects

Apart from J010333, we also analysed five other Magellanic Cloud objects with disc-shaped SEDs. Three out of five objects are SMC stars: J010056.97-715551.1 (J010056), J010324.36-723803.7 (J010324) and J010929.81-724820.8 (J010929). The two LMC stars are J045623.23-692748.9 (J045623) and J052221.13-655551.6 (J052221). Similar to J010333, these objects have low surface gravities and typical metallicities of their host galaxies. The abundance results of these stars all show mild enrichments with [hs/Fe] = 0.5 to 0.7 dex and [ls/Fe] = 0.1 to 0.6 dex, and C/O ratios $\lesssim 1$. The SED studies of these objects reveal a wide luminosity range from L = 3500 to 29000 $L_\odot$ as listed in Table 9.2. The derived current masses (M_c) of these objects, together with the effect of changing log g by -0.25 and +0.25 dex are shown in the third, fourth and fifth column of Table 9.2 respectively. The bottom three rows of Table 9.2 show the results for the studied post-AGB stars J051213.81-693537.1 (J051213) and J051848.86-700246.9 (J051848) from Chapter 5 and J050221 from Chapter 7.

The wide range of luminosities in Table 9.2 translates in a wide range of initial masses. Table 9.2 also shows the strong effect of the uncertainty of log g. The

three confirmed post-AGB stars all show low current masses while the other six objects have low and high current masses. The high mass objects can not be post-AGB stars, and we find that the spectra of three of the four objects with $M_c > 2.0$ $M_\odot$ (J010324, J010333 and J045623) display small lithium (Li, Z=3) lines at 6708 Å. Li can be an indicator of a YSO nature, but it can also be linked to hot bottom burning which occurs during the TP-AGB in stars with $M \geqslant 4.0$ $M_\odot$. J052221, which has a low current mass, displays a strongly-saturated Li line. The most heavy object, J010056, does not show any Li nor does J010929. We remark that none of the studied post-AGB stars in this work display any Li lines. In addition, we remark that J010324 and J010929 display TiO emission features in their optical spectra, which have been studied by Wood et al. (2013). Apart from TiO emission in these two stars, none of the objects display any clear emission features except for H_α, displaying emission in the wings or showing P Cygni profiles. These six objects cover a wide range of spectral features and they will be studied in more detail in the near future to identify the nature of these objects. Massive YSOs should be rare and they should be linked to starforming regions. We therefore also need to study the local environment of the objects. Optical visible very massive YSOs are not expected (see discussion on the birthline in Kamath et al. (2014, 2015). Based upon the similar enrichments, we assume that the abundances of these six objects all reflect the intrinsic *s*-process enrichment of their host galaxies. The [hs/ls] versus [s/Fe] reveals that none of these six objects follow the observed correlation of *s*-process enriched post-AGB stars, as shown in the upper panel of Fig. 9.4. All mildly *s*-process enriched objects in Fig. 9.4 cluster in the same region of the [hs/ls] versus [s/Fe] diagram and have too high hs-element enrichments to follow the correlation of heavy *s*-process enriched post-AGB stars. The low panel of Fig. 9.4 shows that the mild enrichment is not correlated with metallicity.

Apart from these six objects, we have also obtained high-resolution spectra of other intruders like a C-star, a luminous YSO with clear emission lines and a hydrogen-poor star with strong emission lines. We also have spectra of hot A- and B-type stars, but these objects will be studied in future research.

9.3 General observational prospects

Based upon the results of Kamath et al. (2014) and Kamath et al. (2015), a new sample of post-AGB candidates in the Magellanic Clouds have been observed with UVES. These spectra provide the opportunity to expand our currently limited sample of post-AGB stars in the Magellanic Clouds. Hopefully this

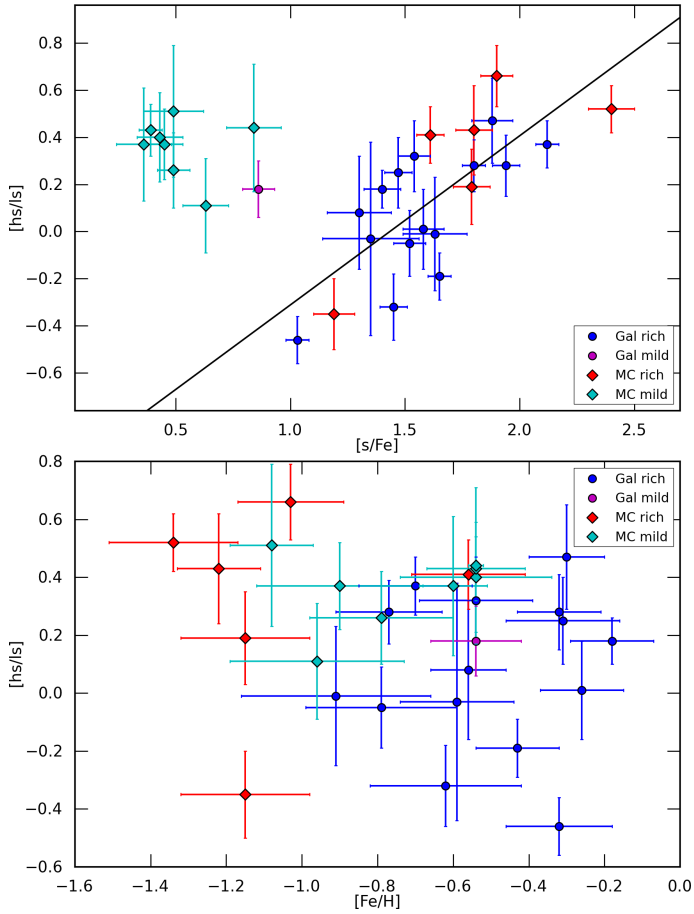

Figure 9.4: Upper panel: Correlation between the total enrichment in *s*-process elements and the [hs/ls] index for our total sample stars of studied post-AGB stars in this work and the six additional stars of Table 9.2. Galactic objects are represented by blue (= strongly-enriched) and purple (= mildly-enriched) dots, Magellanic Cloud objects are represented by red diamonds. The dashed line shows the least-squares fit to the results of the *s*-process enriched post-AGB stars. The mild enriched objects all cluster in the same region. Lower panel: Similar to the upper panel but for the correlation between the metallicity [Fe/H] and the [hs/ls] index.

sample will increase our metallicity and luminosity range, which will help to better constrain the parameters of AGB evolution and nucleosynthesis models.

As a final remark, we mention the GAIA mission[2], which provides the opportunity to measure accurate distances towards Galactic objects, including post-AGB stars. The luminosities and hence initial mass estimates of Galactic post-AGB stars will improve our insights in the wide chemical diversity of post-AGB stars.

[2]http://sci.esa.int/gaia/

Appendix A

Atomic data used for the spectral analysis in Chapter 3

Table A.1: Details of all spectral lines used for the spectral analysis of J004441.04-732136.4 in Chapter 3. EWs indicated with SS are calculated using synthetic spectra.

ion	Z	wavelength (Å)	EP (eV)	log gf	EW (mÅ)
C I	6	6655.517	8.54	-1.94	56.0
C I	6	6012.225	8.64	-2.00	48.8
C I	6	6014.834	8.64	-1.59	71.0
C I	6	6016.444	8.64	-1.83	74.6
C I	6	5551.578	8.64	-1.90	53.2
C I	6	6002.987	8.65	-2.17	39.3
O I	8	6155.971	10.74	-0.67	18.7
O I	8	6454.444	10.74	-1.08	9.7
O I	8	6453.640	10.74	-1.30	7.3
Na I	11	6154.230	2.10	-1.56	11.4
Na I	11	5688.210	2.10	-0.42	74.7
Mg I	12	5711.100	4.34	-1.75	38.0 (SS)
Si I	14	6237.330	5.61	-0.53	35.6
Si I	14	5948.550	5.08	-1.22	22.5
S I	16	6757.160	7.87	-0.20	20.7
S I	16	6748.790	7.87	-0.35	10.5
Ca I	20	6102.727	1.88	-0.80	59.7
Ca I	20	6449.820	2.52	-0.62	33.3
Ca I	20	5590.130	2.52	-0.74	26.6
Ca I	20	6439.075	2.53	0.39	116.4
Sc II	21	6604.600	1.36	-1.23	98.6
Sc II	21	5552.240	1.45	-2.08	15.3
Sc II	21	5667.153	1.50	-1.21	68.3
Ti II	22	4798.521	1.08	-2.67	84.5
Ti II	22	6606.980	2.06	-2.85	29.0
Ti II	22	5010.212	3.10	-1.30	76.7
Cr II	24	5510.730	3.83	-2.48	18.2
Cr II	24	5310.700	4.07	-2.28	15.8
Cr II	24	5502.090	4.17	-1.99	22.3
Mn I	25	6021.800	3.07	0.03	39.6
Mn I	25	6016.650	3.07	-0.22	33.1
Fe I	26	5198.711	2.22	-2.14	33.3
Fe I	26	5049.820	2.28	-1.35	80.7
Fe I	26	6421.351	2.28	-2.01	33.4
Fe I	26	6252.555	2.40	-1.72	41.7
Fe I	26	6191.558	2.43	-1.42	60.1
Fe I	26	6136.596	2.45	-1.40	65.5
Fe I	26	6230.723	2.56	-1.28	59.2
Fe I	26	6137.692	2.59	-1.40	47.5
Fe I	26	5281.790	3.04	-0.83	76.9
Fe I	26	5324.179	3.24	-0.10	108.5
Fe I	26	5615.644	3.33	0.05	118.6
Fe I	26	6400.001	3.60	-0.29	66.2
Fe I	26	6411.649	3.65	-0.66	37.7
Fe I	26	5445.042	4.39	0.04	40.0
Fe I	26	6024.058	4.55	-0.06	29.5
Fe I	26	6419.950	4.73	-0.09	15.3
Fe I	26	5572.842	3.40	-0.28	91.9
Fe II	26	5991.368	3.15	-3.56	54.7
Fe II	26	6084.099	3.20	-3.80	48.5
Fe II	26	6147.741	3.89	-2.73	66.1
Fe II	26	6383.721	5.55	-2.14	17.6
Ni I	28	6767.780	1.83	-2.17	11.6
Ni I	28	5035.370	3.63	0.29	35.1
Ni I	28	6772.320	3.66	-0.98	5.2
Ni I	28	5694.990	4.09	-0.61	5.1
Zn I	30	4810.540	4.08	-0.17	72.5 (SS)

Table A.1: continued.

ion	Z	wavelength (Å)	EP (eV)	log gf	EW (mÅ)
Y II	39	5289.815	1.03	-1.85	144.7
Y II	39	5728.890	1.84	-1.12	149.4
Zr II	40	5124.982	1.53	-1.50	117.2
Zr II	40	5477.822	1.83	-1.40	86.2
La II	57	5482.268	0.00	-2.06	158.9
La II	57	5712.391	0.17	-1.96	147.7
La II	57	5936.210	0.17	-2.07	118.5
La II	57	5880.633	0.24	-1.92	158.3
La II	57	6146.523	0.24	-2.47	83.2
La II	57	5062.918	0.77	-1.72	91.9
La II	57	6126.075	1.25	-1.19	120.6
La II	57	5566.925	2.38	-1.00	51.1
La II	57	6399.030	2.65	-0.52	70.2
Ce II	58	5031.986	1.41	-0.90	62.5
Ce II	58	5613.694	1.42	-1.00	67.6
Ce II	58	5459.193	1.62	-0.58	94.4
Ce II	58	5959.688	1.63	-0.84	47.6
Ce II	58	6143.376	1.70	-0.80	70.0
Ce II	58	6098.326	1.77	-0.61	61.3
Ce II	58	5359.508	1.78	-0.78	60.1
Ce II	58	5685.836	1.90	-0.43	54.4
Pr II	59	5135.140	0.95	-0.13	118.6
Pr II	59	5605.642	0.96	-0.65	71.3
Nd II	60	5221.572	0.38	-1.34	120.7
Nd II	60	5934.738	0.75	-1.39	109.7
Nd II	60	6365.540	0.93	-1.37	77.2
Nd II	60	6031.270	1.28	-0.83	103.8
Nd II	60	6803.980	1.44	-0.79	108.2
Nd II	60	6737.763	1.60	-0.78	93.4
Nd II	60	6650.517	1.95	-0.32	105.2
Sm II	62	4791.580	0.10	-1.24	111.2
Sm II	62	6731.813	1.17	-0.52	88.0
Eu II	63	6437.640	1.32	-0.27	87.2 (SS)
Gd II	64	5733.852	1.37	-0.89	26.3 (SS)
Dy II	66	5169.688	0.10	-1.95	68.3 (SS)
Er II	68	5229.319	2.60	-0.39	16.5 (SS)
Yb II	70	5352.954	3.75	-0.34	53.6 (SS)
Lu II	71	6463.107	1.46	-1.05	126.0 (SS)
Hf II	72	4790.708	2.20	-1.11	38.5 (SS)
W II	74	5104.432	2.36	-0.91	46.3 (SS)

Appendix B

Atomic data used for the spectral analysis in Chapter 5

Table B.1: Details of all spectral lines used for the spectral analysis of J051213.81-693537.1 (J051213) and J051848.86-700246.9 (J051848) in Chapter 5. EWs indicated with SS are calculated using synthetic spectra.

				J051213	J051848
ion	wavelength (Å)	EP (eV)	log gf	EW (mÅ)	EW (mÅ)
C I	6002.987	8.65	-2.17	-	30.9
C I	6007.176	8.64	-2.06	-	24.0
C I	6014.834	8.64	-1.58	-	54.0
C I	6587.622	8.50	-1.02	-	124.4
C I	6655.517	8.540	-1.94	40.31	-
O I	6155.971	10.74	-0.67	-	16.3
O I	6300.230	0.00	-9.75	59.6	-
O I	6454.444	10.74	-1.08	-	7.9
Mg I	4057.505	4.35	-1.20	-	76.9
Mg I	4167.271	4.35	-1.00	-	100.9
Mg I	5528.420	4.350	-0.47	172.13	-
Al I	6698.673	3.140	-1.65	38.91	-
Si I	5645.620	4.93	-2.14	26.5	-
Si I	5690.430	4.93	-1.91	46.6	-
Si I	6155.140	5.62	-0.84	75.5	-
Si I	6237.330	5.61	-1.22	42.1	-
S I	6748.790	7.87	-0.35	26.5	-
S I	6757.160	7.87	-0.20	36.5	36.2
Ca I	5512.990	2.93	-0.45	69.5	41.0
Ca I	5581.980	2.52	-0.55	113.7	62.6
Ca I	5590.130	2.52	-0.74	95.6	44.8
Ca I	5601.290	2.52	-0.63	89.2	46.2
Ca I	6102.727	1.88	-0.80	137.5	79.3
Ca I	6122.217	1.89	-0.32	157.6	-
Ca I	6169.560	2.52	-0.57	99.9	-
Ca I	6439.075	2.53	0.39	171.0	124.4
Ca I	6449.820	2.52	-0.62	103.4	48.5
Ca I	6462.567	2.52	0.31	-	131.8
Ca I	6471.670	2.52	-0.88	84.7	-
Ca I	6717.690	2.71	-0.52	95.9	-
Ca II	5021.150	7.510	-1.24	18.86	-
Sc II	5239.820	1.45	-0.80	167.4	-
Sc II	5318.360	1.36	-1.79	-	42.8
Sc II	5552.240	1.45	-2.08	-	22.7
Sc II	5640.990	1.50	-1.02	-	106.5
Sc II	5667.153	1.50	-1.21	134.2	86.9
Sc II	5684.200	1.51	-1.08	144.3	109.2
Sc II	6604.600	1.36	-1.23	-	101.8
Ti I	5113.440	1.44	-0.70	22.1	-
Ti I	5210.384	0.05	-0.82	108.2	-
Ti II	4798.521	1.08	-2.67	136.4	112.1
Ti II	4874.014	3.10	-0.90	122.0	98.2
Ti II	5010.212	3.10	-1.30	108.5	78.2
Ti II	5185.913	1.89	-1.37	174.6	-
Ti II	5211.540	2.59	-1.85	111.2	-
Ti II	5418.751	1.58	-2.11	165.6	117.2
Ti II	6606.980	2.06	-2.85	66.3	-
V I	6119.523	1.06	-0.32	21.0	-
V II	6120.973	2.50	-2.40	21.9	-
V II	6261.087	2.54	-2.39	18.7	-
Cr I	5208.425	0.94	0.16	-	153.1
Cr I	5247.570	0.96	-1.64	-	26.3
Cr I	5296.691	0.98	-1.36	105.0	48.9
Cr I	5297.377	2.90	0.17	-	29.5
Cr I	5300.745	0.98	-2.02	42.6	-
Cr I	5329.138	2.91	-0.06	-	22.8

Table B.1: continued.

				J051213	J051848
ion	wavelength (Å)	EP (eV)	log gf	EW (mÅ)	EW (mÅ)
Cr I	5345.796	1.00	-0.90	141.4	-
Cr I	5348.330	1.00	-1.29	99.9	50.4
Cr II	4812.350	3.86	-1.80	124.7	103.5
Cr II	4884.600	3.86	-2.08	101.3	66.7
Cr II	5246.768	3.71	-2.47	-	51.3
Cr II	5305.870	3.83	-2.08	86.2	75.2
Cr II	5308.430	4.07	-1.81	101.5	85.6
Cr II	5310.700	4.07	-2.28	-	43.6
Cr II	5334.869	4.07	-1.89	-	76.5
Cr II	5407.604	3.83	-2.15	90.4	68.2
Cr II	5420.922	3.76	-2.46	58.3	47.2
Cr II	5502.090	4.17	-1.99	-	51.7
Cr II	5503.240	4.14	-2.25	-	37.6
Cr II	6053.480	4.74	-2.16	29.4	20.5
Mn I	6021.800	3.070	-1.52	2.78	-
Fe I	4918.994	2.87	-0.34	-	129.6
Fe I	4924.770	2.28	-2.20	-	47.6
Fe I	5022.236	3.98	-0.49	112.7	-
Fe I	5083.339	0.96	-2.91	130.5	-
Fe I	5090.774	4.26	-0.36	91.8	-
Fe I	5125.117	4.22	-0.08	104.1	-
Fe I	5150.840	0.99	-3.00	-	72.6
Fe I	5171.596	1.49	-1.76	184.6	127.9
Fe I	5194.942	1.56	-2.06	153.3	-
Fe I	5198.711	2.22	-2.14	96.2	55.0
Fe I	5202.336	2.18	-1.84	127.9	79.8
Fe I	5232.940	2.94	-0.08	-	147.9
Fe I	5242.491	3.63	-0.97	87.9	51.7
Fe I	5266.550	3.00	-0.49	162.4	-
Fe I	5281.790	3.04	-0.83	134.9	88.3
Fe I	5288.525	3.69	-1.51	35.0	-
Fe I	5324.179	3.24	-0.10	174.1	136.5
Fe I	5339.929	3.27	-0.68	144.2	96.4
Fe I	5341.024	1.61	-1.95	-	113.6
Fe I	5364.871	4.45	0.23	-	76.5
Fe I	5367.467	4.42	0.44	139.6	93.1
Fe I	5369.962	4.37	0.54	142.1	97.2
Fe I	5373.709	4.47	-0.71	47.6	-
Fe I	5383.369	4.31	0.65	152.2	113.1
Fe I	5389.479	4.42	-0.25	94.9	-
Fe I	5410.910	4.47	0.40	-	99.1
Fe I	5415.200	4.39	0.50	-	89.4
Fe I	5434.524	1.01	-2.12	-	145.5
Fe I	5445.042	4.39	0.04	110.5	62.8
Fe I	5466.396	4.37	-0.57	60.0	-
Fe I	5506.779	0.99	-2.80	141.1	-
Fe I	5554.895	4.55	-0.38	80.1	-
Fe I	5560.212	4.43	-1.04	33.2	-
Fe I	5563.600	4.19	-0.84	61.4	-
Fe I	5572.842	3.40	-0.28	153.7	-
Fe I	5576.089	3.43	-0.85	126.8	68.3
Fe I	5586.756	3.37	-0.12	181.8	125.2
Fe I	5615.644	3.33	0.05	-	138.5
Fe I	5679.023	4.65	-0.77	40.5	-
Fe I	6003.020	3.88	-1.12	63.3	-
Fe I	6020.169	4.61	-0.21	70.3	-
Fe I	6024.058	4.55	-0.06	101.1	-
Fe I	6027.051	4.08	-1.09	46.5	-
Fe I	6065.482	2.61	-1.53	142.5	67.7

Table B.1: continued.

				J051213	J051848
ion	wavelength (Å)	EP (eV)	log gf	EW (mÅ)	EW (mÅ)
Fe I	6096.665	3.98	-1.78	17.7	-
Fe I	6136.596	2.45	-1.40	154.1	98.5
Fe I	6137.692	2.59	-1.40	141.6	96.2
Fe I	6191.558	2.43	-1.42	159.5	95.2
Fe I	6200.313	2.60	-2.44	67.4	-
Fe I	6230.723	2.56	-1.28	142.0	102.5
Fe I	6254.259	2.28	-2.44	92.4	25.7
Fe I	6265.134	2.18	-2.55	76.2	-
Fe I	6322.686	2.59	-2.43	66.7	21.7
Fe I	6380.743	4.19	-1.32	28.9	-
Fe I	6400.001	3.60	-0.29	149.7	96.1
Fe I	6411.649	3.65	-0.66	105.5	60.6
Fe I	6419.950	4.73	-0.09	69.2	-
Fe I	6421.351	2.28	-2.01	131.7	59.5
Fe I	6430.846	2.18	-2.01	124.5	66.4
Fe I	6592.914	2.73	-1.47	116.2	76.2
Fe I	6593.871	2.44	-2.42	77.4	-
Fe I	6750.153	2.24	-2.62	82.8	-
Fe I	6752.707	4.64	-1.20	21.0	-
Fe II	5120.352	2.83	-4.21	-	56.6
Fe II	5325.559	3.22	-3.17	140.8	-
Fe II	5414.046	3.22	-3.62	-	72.1
Fe II	5425.247	3.20	-3.21	135.0	-
Fe II	5525.125	3.27	-3.95	73.7	39.5
Fe II	5991.368	3.15	-3.56	111.4	68.6
Fe II	6084.099	3.20	-3.80	88.4	57.7
Fe II	6147.741	3.89	-2.73	119.3	104.7
Fe II	6149.258	3.89	-2.72	131.5	98.1
Fe II	6247.545	3.89	-2.34	160.8	111.1
Fe II	6369.464	2.89	-4.19	87.5	-
Fe II	6383.721	5.55	-2.14	36.2	-
Fe II	6416.921	3.89	-2.68	130.1	-
Fe II	6432.682	2.89	-3.71	118.9	104.0
Fe II	6516.030	2.88	-3.27	148.1	-
Ni I	4829.030	3.54	-0.33	-	41.2
Ni I	5035.370	3.63	0.29	-	64.8
Ni I	5081.120	3.85	0.30	-	51.1
Ni I	5084.100	3.68	0.03	-	41.0
Ni I	5099.940	3.68	-0.10	-	38.3
Ni I	5578.730	1.68	-2.64	49.2	-
Ni I	5754.670	1.93	-2.33	-	17.6
Ni I	6378.260	4.15	-0.89	11.9	-
Ni I	6643.640	1.68	-2.30	70.1	19.6
Ni I	6767.780	1.83	-2.17	66.2	26.3
Cu I	5218.197	3.82	0.48	-	6.2
Zn I	4810.528	4.08	-0.14	-	76.9
Zn I	4810.540	4.08	-0.17	118.8	-
Y II	4881.436	0.41	-2.79	122.0	96.4
Y II	5196.422	1.75	-0.88	145.1	132.8
Y II	5289.815	1.03	-1.85	140.6	127.7
Y II	5480.732	1.72	-0.99	-	125.4
Y II	5509.895	0.99	-1.01	-	167.6
Y II	5728.890	1.84	-1.12	139.3	117.7
Y II	6795.414	1.74	-1.19	156.6	-
Zr II	5112.297	1.67	-0.59	153.1	-
Zr II	5124.982	1.53	-1.50	-	74.9
Zr II	5477.822	1.83	-1.40	-	61.1
Zr II	6787.117	2.49	-1.17	53.7	-
La II	4804.039	0.23	-1.49	-	144.7

Table B.1: continued.

				J051213	J051848
ion	wavelength (Å)	EP (eV)	log gf	EW (mÅ)	EW (mÅ)
La II	4826.873	0.17	-2.38	-	102.4
La II	4970.386	0.32	-1.12	-	161.4
La II	4999.461	0.40	-0.75	-	175.7
La II	5290.818	0.00	-1.72	-	161.8
La II	5377.052	2.30	-0.32	103.0	-
La II	5671.528	2.21	-0.80	70.9	-
La II	6067.117	0.77	-2.28	43.9	-
La II	6146.523	0.24	-2.47	74.5	-
La II	6172.721	0.13	-2.25	124.1	-
La II	6320.376	0.17	-1.56	-	172.9
La II	6390.477	0.32	-1.44	-	172.1
La II	6399.030	2.65	-0.52	48.7	-
Ce II	5117.169	1.40	0.01	146.7	-
Ce II	5468.371	1.40	-0.39	134.5	79.2
Ce II	5685.836	1.90	-0.43	-	44.9
Ce II	5695.847	1.63	-0.48	101.3	-
Ce II	5959.688	1.63	-0.84	-	39.6
Ce II	5975.818	1.33	-0.45	128.0	80.3
Ce II	6043.373	1.21	-0.32	137.9	111.9
Ce II	6143.376	1.70	-0.80	82.0	-
Pr II	5219.045	0.80	-0.25	-	92.0
Pr II	5322.772	0.48	-0.46	124.8	-
Pr II	5571.828	0.51	-1.23	-	45.0
Pr II	5623.040	1.33	-0.29	-	50.1
Pr II	5859.676	1.42	-0.30	-	43.3
Pr II	5939.899	1.24	-0.23	-	74.7
Pr II	5951.285	1.20	-0.64	-	34.6
Pr II	5981.205	1.46	-0.38	57.9	40.0
Pr II	6017.767	1.11	-0.36	75.0	-
Pr II	6025.732	1.44	-0.11	74.1	59.4
Pr II	6087.533	1.12	-0.64	56.8	43.2
Pr II	6397.960	1.05	-0.92	-	27.8
Pr II	6656.834	1.82	-0.05	48.7	40.2
Nd II	4989.950	0.63	-0.62	-	145.1
Nd II	5089.832	0.20	-1.10	-	135.8
Nd II	5092.794	0.38	-0.61	-	157.9
Nd II	5130.586	1.30	0.24	-	154.7
Nd II	5212.361	0.20	-0.77	-	166.4
Nd II	5276.869	0.86	-0.39	151.2	-
Nd II	5385.888	0.74	-0.86	139.5	134.5
Nd II	5416.374	0.86	-0.98	103.1	118.3
Nd II	5431.516	1.12	-0.46	-	136.0
Nd II	5442.264	0.68	-0.98	134.6	136.8
Nd II	5592.660	1.16	-1.36	-	57.5
Nd II	5708.271	0.86	-0.58	145.4	-
Nd II	5842.366	1.28	-0.60	125.8	-
Nd II	6031.270	1.28	-0.83	100.2	-
Nd II	6034.228	1.54	-0.66	92.5	99.4
Nd II	6330.151	1.77	-0.87	53.7	62.1
Nd II	6341.492	1.80	-0.68	80.1	-
Nd II	6365.540	0.93	-1.37	68.6	-
Nd II	6637.187	1.45	-1.03	66.3	67.0
Nd II	6650.517	1.95	-0.32	-	98.6
Nd II	6727.695	1.81	-0.76	51.2	-
Nd II	6737.763	1.60	-0.78	69.8	-
Sm II	4791.580	0.10	-1.86	-	63.4
Sm II	6731.813	1.170	-0.52	80.54	84.8
Eu II	6437.640	1.32	-0.27	69.8	71.5
Eu II	6645.064	1.38	0.20	116.8	92.5

Table B.1: continued.

				J051213	J051848
ion	wavelength (Å)	EP (eV)	log gf	EW (mÅ)	EW (mÅ)
Gd II	4059.359	1.73	-0.15	-	43.8
Gd II	5125.555	1.43	-0.75	-	46.3
Gd II	5176.288	1.06	-0.74	-	57.7
Gd II	5583.670	1.06	-1.24	-	33.1
Gd II	5733.852	1.37	-0.67	-	57.1
Gd II	5840.457	1.60	-0.97	-	13.9
Gd II	5855.215	1.60	-1.02	-	21.3
Gd II	5904.046	1.62	-0.71	-	23.4
Gd II	5913.529	2.28	-0.21	-	23.0
Gd II	6752.649	2.33	-0.21	-	16.7
Dy II	4057.442	2.94	0.96	-	75.8
Dy II	4430.997	2.30	-0.11	-	36.6
Dy II	4833.753	1.93	-0.83	-	17.9
Dy II	5279.697	2.42	-0.49	-	20.9
Dy II	5389.581	0.000	-2.47	38.02	-
Dy II	5443.343	2.410	-0.55	15.85	-
Er II	4879.888	1.620	-1.15	21.41	-
Er II	4886.284	0.640	-1.75	41.83	-
Er II	5028.905	0.06	-2.06	-	47.1 (SS)
Tm II	5009.767	2.440	-0.14	-	23.02 (SS)
Lu II	4994.126	1.54	-1.14	-	90.8
Lu II	6221.890	1.54	-0.76	-	123.7
Lu II	6463.107	1.46	-1.05	-	100.1
Hf II	4790.708	2.20	-1.11	-	24.6 (SS)
Pb I	4057.807	1.320	-0.17	96.18 (SS)	36.5 (SS)
Th II	6044.433	0.510	-1.86	20.71 (SS)	-

Appendix C

Pb abundance upper limit determinations of Chapter 6

C.1 Pb line fits

In this appendix, we give an overview of the Pb abundance upper limit determinations in Chapter 6 for the different programme stars together with a brief discussion of the Pb_{up} results.

C.1.1 IRAS 05113+1347

The Pb abundance upper limit determination of IRAS 05113+1347 is presented in Fig. C.1. The determination of the continuum is difficult as the region is dominated by large spectral blends. We use the spectral lines at 4057.5 and 4058.2 Å to optimally estimate the position of the continuum. Thereafter, we adopted a Pb abundance upper limit which fully incorporates the line feature at 4057.807 Å.

The adopted Pb_{up} of IRAS 05113+1347 results in a [Pb_{up}/Fe] which is about 0.2 dex lower than the value for [hs/Fe] (left upper of panel Fig. 6.8) and similar to the element-over-iron ratios of the elements beyond the Ba-peak.

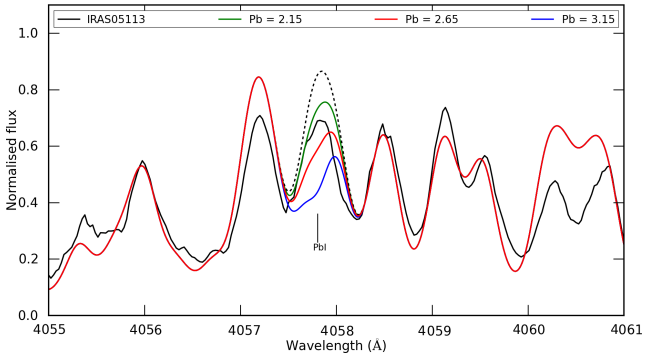

Figure C.1: Spectrum synthesis of the Pb I line at 4057.807 Å for IRAS 05113+1347. The black spectrum is the observed UVES spectrum, the colored spectra represent synthetic spectra with different Pb abundances. The red line represents the adopted Pb abundance upper limit, the green and blue represent the adopted abundance upper limit -0.5 dex and +0.5 dex respectively. The dashed black line shows the synthetic spectrum if no Pb would be present.

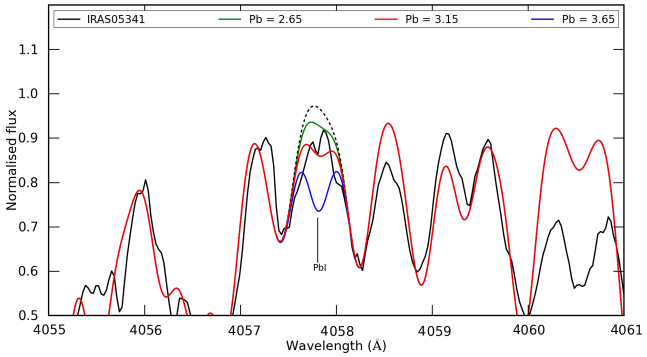

Figure C.2: Spectrum synthesis of the Pb I line at 4057.807 Å for the UVES spectrum of IRAS 05341+0852. Lines and symbols are similar to Fig. C.1.

C.1.2 IRAS 05341+0852

For the strongly *s*-process enriched IRAS 05341+0852, we estimate the position of the continuum by finding a compromise between the spectral blends at 4057.5 and 4058.2 Å in Fig. C.2. We adopt a Pb abundance upper limit which fully includes the small visible line feature.

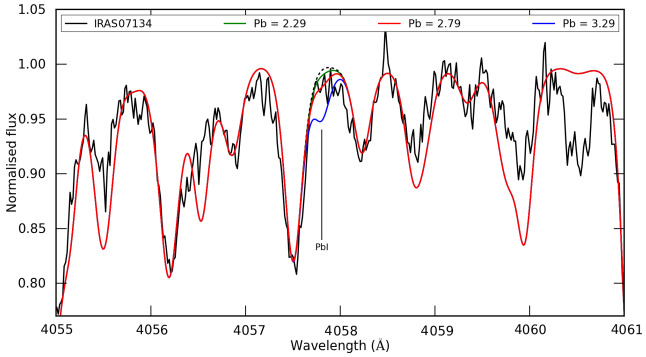

Figure C.3: Spectrum synthesis of the Pb I line at 4057.807 Å for the HERMES spectrum of IRAS 07143+1005. Lines and symbols are similar to Fig. C.1.

Although being one of the most *s*-process enriched Galactic post-AGB stars studied to date, IRAS 05341+0852 displays a [Pb_{up}/Fe] which is about 0.15 dex lower than [hs/Fe] (middle upper panel of Fig. 6.8). Like in IRAS 05113+1347, the [Pb_{up}/Fe] seems similar to the element-over-iron ratios of the elements beyond the Ba-peak.

C.1.3 IRAS 06530-0213

The Pb abundance determination of IRAS 06530-0213 is described in detail in Sect. 6.5. We use the Pb_{up} result of the Pb I line for this strongly *s*-process enriched post-AGB star. The resulting [Pb_{up}/Fe] is about 0.7 dex higher than [hs/Fe] (left upper panel of Fig. 6.9) and the element-over-iron ratios of the elements beyond the Ba-peak.

C.1.4 IRAS 07143+1005

We estimate the position of the continuum of IRAS 07143+1005 by using the spectral blends at 4056.2, 4056.9 and 4057.5 Å at the blue side of the Pb I line, and the blends at 4058.2 and 4059.3 Å at the red side of the Pb I line in Fig. C.3. The spectral region of the Pb I line is dominated by noise and we can not detect any visible contribution from the Pb line. We therefore adopt a Pb abundance upper limit which includes the noise at 4057.807 Å.

The adopted [Pb_{up}/Fe] is about 0.4 dex higher than [hs/Fe] and [ls/Fe], which are both similar in enrichement (middle upper panel of Fig. 6.9).

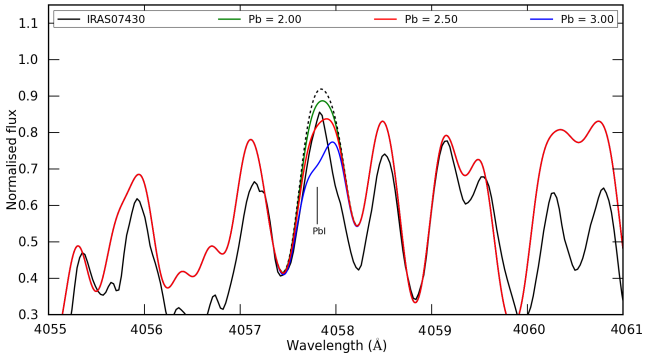

Figure C.4: Spectrum synthesis of the Pb I line at 4057.807 Å for the UVES spectrum of IRAS 07430+1115. Lines and symbols are similar to Fig. C.1.

C.1.5 IRAS 07430+1115

In Fig. C.4, we use the spectral blends at 4057.5 and 4058.8 Å to estimate the position of the continuum. Although not clearly visible, the synthetic spectrum without Pb I line suggests a possible small contribution of Pb at 4057.807 Å. Therefore, we adopt a Pb abundance upper limit which incorporates the peak of the Pb I line feature.

The adopted Pb_{up} of IRAS 07430+1115 gives a [Pb_{up}/Fe] which is significantly lower than [hs/Fe] with a difference of about 0.5 dex (right upper panel of Fig. 6.8).

C.1.6 IRAS 08143-4406

The position of the continuum for IRAS 08143-4406 is estimated using the spectral blends at 4057.5 and 4058.8 Å in Fig. C.5. The spectrum of IRAS 08143-4406 does not show visible contribution of Pb at 4057.807 Å and we see that with the estimated continuum position, the spectral feature at the blue side of the the Pb I line is not even contained within the boundaries of the synthetic spectrum without Pb I line which could be possibly attributed to noise. Due to these uncertainties, we adopt a Pb abundance upper limit which fully incorporates the spectral line peak in the spectral region of the Pb I line.

We find that [Pb_{up}/Fe] is about 0.1 higher than [ls/Fe] and 0.3 dex higher than [hs/Fe] respectively (right upper panel of Fig. 6.9).

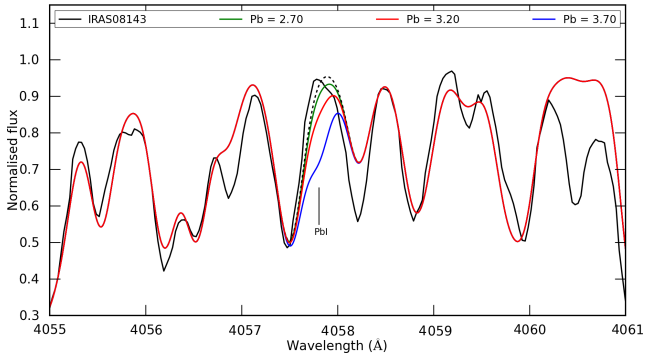

Figure C.5: Spectrum synthesis of the Pb I line at 4057.807 Å for the BLUE437 UVES spectrum of IRAS 08143-4406. Lines and symbols are similar to Fig. C.1.

C.1.7 IRAS 08281-4850

The spectra of IRAS08281-4850 reveal possible Pb line features in both panels of Fig. C.6 but we assume these features are more likely due to noise than a real abundance of Pb. Nevertheless, we adopt a similar Pb abundance upper limit for both Pb lines which fully incorporates the visible spectral features. For the Pb I line, we use the spectral blends at 4056.2, 4057.5 and 4058.8 Å to estimate the position of the continuum. For the Pb II line, we see unidentified spectral lines at 5606.7 and 5607 Å and also at both sides of the Pb II line. These spectral lines are not included in the linelists and we can only use the continuum in the region 5606 - 5606.5 Å and 5611.5 - 5612 Å in combination with the spectral line at 5610.2 Å to estimate the continuum position.

We find a similar Pb_{up} for both the Pb I and Pb II lines. This results in a [Pb_{up}/Fe] which is about 1.2 dex higher than the [hs/Fe] and [ls/Fe] (left lower panel of Fig. 6.9).

C.1.8 IRAS 13245-5036

The Pb abundance determination of IRAS 13245-5036 is described in detail in Sect. 6.5.

For this hottest star in the sample, we only use the Pb II line to determine Pb_{up}. The adopted [Pb_{up}/Fe] is about 0.9 dex higher than [hs/Fe] (left upper panel of Fig. 6.10).

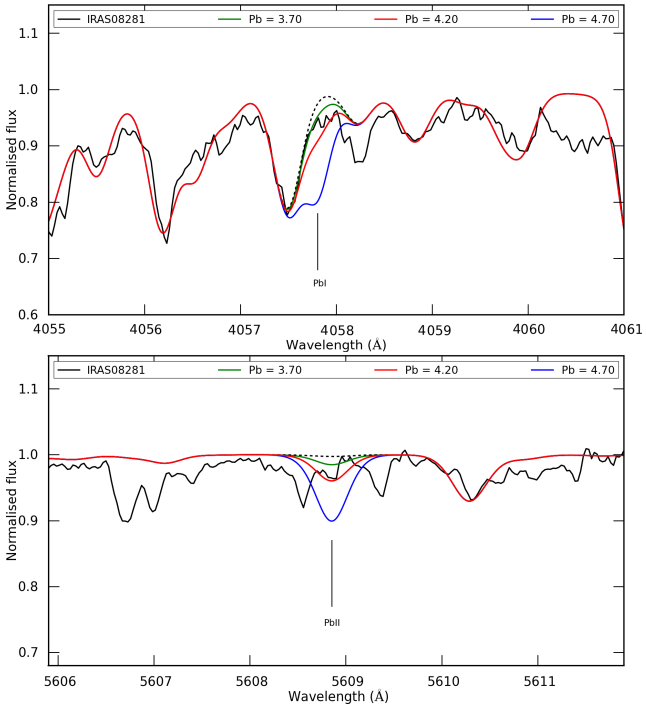

Figure C.6: Spectrum synthesis of the Pb I line at 4057.807 Å (upper panel) and the Pb II line at 5608.853 Å (lower panel) for the UVES spectra of IRAS 08281-4850. Lines and symbols are similar to Fig. C.1.

C.1.9 IRAS 14325-6428

The Pb II line spectral region of IRAS 14325-6428 is dominated by noise and does not show a visible Pb line contribution in Fig. C.7. We estimate the position of the continuum by fitting to the average continuum in the shown spectral region. Around 5610.2 Å, there appears a small line in the synthetic spectra which is not present in the observed spectra so we do not use this line for the continuum estimate. We then adopt a Pb abundance upper limit which incorporates the continuum at 5608.853 Å.

The adopted [Pb_{up}/Fe] is determined only via the Pb II line, and is about 1.3 dex higher than [hs/Fe] (right upper panel of Fig. 6.10).

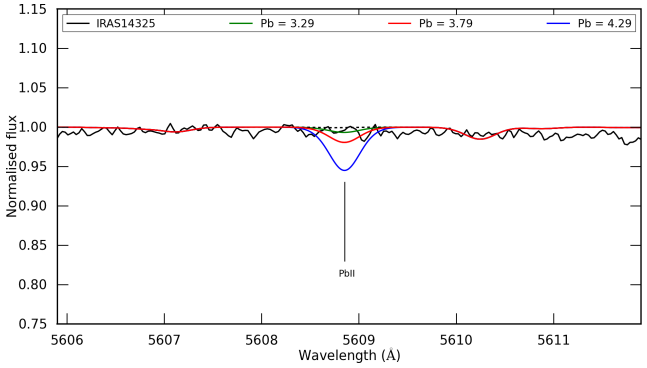

Figure C.7: Spectrum synthesis of the Pb II line at 5608.853 Å for the UVES spectrum of IRAS 14325-6428. Lines and symbols are similar to Fig. C.1.

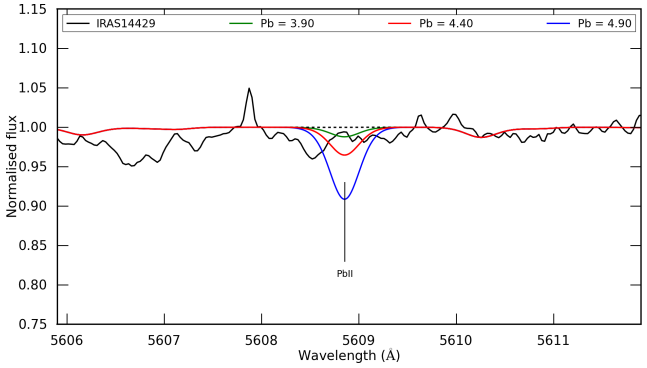

Figure C.8: Spectrum synthesis of the Pb II line at 5608.853 Å for the UVES spectrum of IRAS 14429-4539. Lines and symbols are similar to Fig. C.1.

C.1.10 IRAS 14429-4539

Fig. C.8 shows that the spectral region of the Pb II at 5608.853 Å of IRAS 14429-4539 is totally dominated by noise and that there is no visible contribution of the Pb line. There is a visible line in the spectrum at 5606.6 Å but it is not clear whether this feature is real or due to noise. Nevertheless, it is not included in the linelists. We therefore estimate the position of the continuum by fitting the average continuum in the shown spectral region. We then adopt a Pb abundance upper limit which incorporates the estimated continuum at 5608.853 Å.

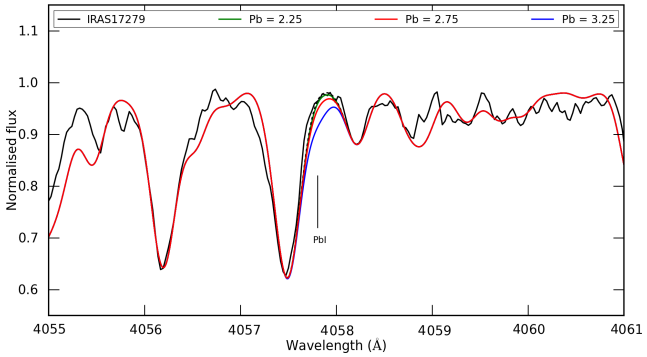

Figure C.9: Spectrum synthesis of the Pb I line at 4057.807 Å for the UVES spectrum of IRAS 17279-1119. Lines and symbols are similar to Fig. C.1.

For the second hottest star in the sample, we only use the Pb II line for the Pb_{up} determination. [Pb_{up}/Fe] exceeds [hs/Fe] by almost 1.4 dex. (left lower panel of Fig. 6.10).

C.1.11 IRAS 17279-1119

The mildly IRAS 17279-1119 does not show any visible Pb line features in Fig. C.9. The local continuum is estimated using the spectral blends at 4056.2, 4057.5 and 4058.2 Å. We adopt a Pb abundance upper limit which fully incorporates the spectral region at 4057.807 Å.

The [Pb_{up}/Fe] for the mildly *s*-process enriched post-AGB star IRAS 17279-1119 is 0.6 dex higher than [hs/Fe] (right lower panel of Fig. 6.9).

C.1.12 IRAS 19500-1709

For the atmospheric parameter set of IRAS 19500-1709, to appear the Pb I line at 4057.807 Å needs a lower Pb abundance than the Pb II line at 5608.853 Å. Therefore, we only use the Pb I line for our analysis. Fig. C.10 shows that the spectral region of the Pb I line has a poor S/N. We use the spectral blend at 4057.5 Å to estimate the position of the continuum and then adopt a Pb abundance upper limit which fully incorporates the noise at 4057.807 Å.

For IRAS 19500-1709, [hs/ls] $\approx$ 0 and the derived [Pb_{up}/Fe] is about 1.35 dex higher than [ls/Fe] and [hs/Fe] (right lower panelof Fig. 6.10).

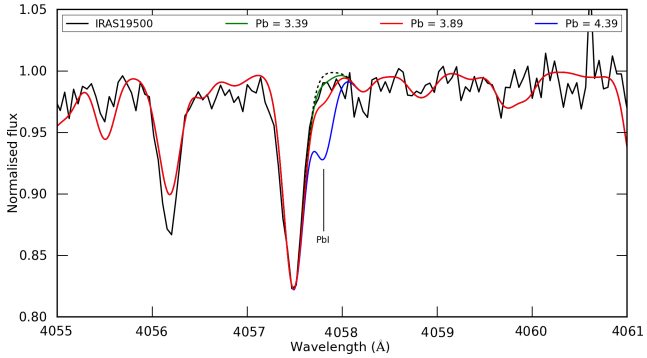

Figure C.10: Spectrum synthesis of the Pb I line at 4057.807 Å for the HERMES spectrum of IRAS 19500-1709. Lines and symbols are similar to Fig. C.1.

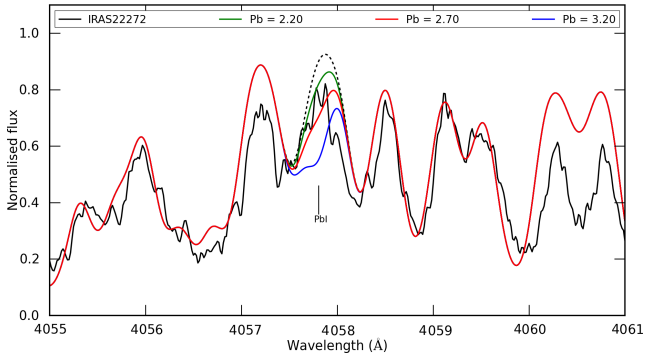

Figure C.11: Spectrum synthesis of the Pb I line at 4057.807 Å for the HERMES spectrum of IRAS 22272+5435. Lines and symbols are similar to Fig. C.1.

C.1.13 IRAS 22223+4327

The Pb abundance determination of IRAS 22223+4327 is described in detail in Sect. 6.5.

For IRAS 22223+4327, the adopted Pb_{up} results in a [Pb_{up}/Fe] which lies about 1.0 dex above [hs/Fe] (left lower panel of Fig. 6.8). For IRAS 22223+4327, the ls elements have higher enrichments than the hs elements and our estimate for [Pb_{up}/Fe] lies about 0.5 dex above [ls/Fe].

C.1.14 IRAS 22272+5435

The spectral region of the Pb I line for IRAS 22272+5435 is dominated by strong blends in combination with low S/N in Fig. C.11. We use the spectral blends at 4057.5 and 4058.8 Å to estimate the position of the continuum. We then adopt a Pb abundance upper limit which fully includes the visible line feature at 4057.807 Å.

The adopted [Pb_{up}/Fe] of IRAS 22272+5435 lies between the results of [hs/Fe] and [ls/Fe] (right lower panel of Fig. 6.8). The element-over-iron ratios of the elements beyond the Ba-peak are also slightly higher than [Pb_{up}/Fe].

Appendix D

Abundance results in Chapter 6 versus previous studies

Here, we present the comparisons of our derived abundance results in Chapter 6 with those of previous abundance studies.

Objects IRAS 05113+1347 and IRAS 22272+5435 have been previously studied by Reddy et al. (2002), the comparisons between the abundance results are presented in Figs. D.1 and D.2. We find similar sets of atmospheric parameters although our derived metallicity for IRAS 05113+1347 is approximately 0.2 dex higher. We find a higher C/O ratio for IRAS 05113+1347 but lower abundances for Y and the heavy s-elements. Especially Pr and Sm differ strongly, by almost 0.8 dex. For Sm, the same occurs with IRAS 22272+5435 for which Reddy et al. (2002) find an abundance which is about 1.25 dex higher than our Sm abundance. For all other elements, the abundance differences are significantly lower.

For IRAS 05341+0852, IRAS 07134+1005, IRAS 19500-1709 and IRAS 22223+4327, we find similar atmospheric parameters as Van Winckel & Reyniers (2000). The strongest difference is the derived temperature of IRAS 05341+0852, which is 250 K hotter in our study. We find similar results for IRAS 05341+0852 (Fig. D.3) and IRAS 07134+1005 (Fig. D.4), only our Sm result differs by about 0.4 dex from that of Van Winckel & Reyniers (2000). For IRAS 19500-1709 (Fig. D.5), all results are similar except for Nd and Eu, for which we find abundances which are about 0.9 dex higher. These large differences are probably attributed to the use of a different set of spectral lines to determine the abundances. Van Winckel & Reyniers (2000) used small lines with an EW $\approx$ 3 mÅ to determine

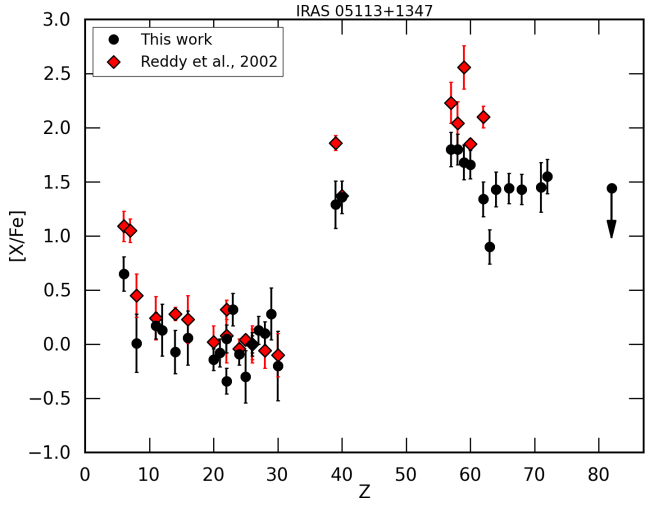

Figure D.1: Comparison between our derived abundances and the results of Reddy et al. (2002) for IRAS 05113+1347.

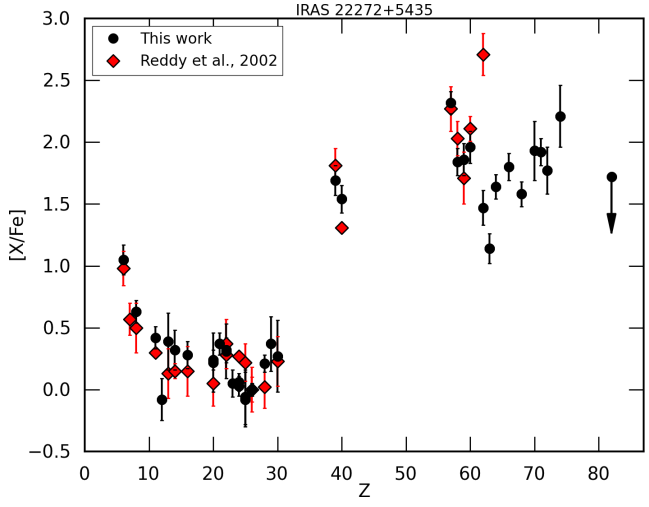

Figure D.2: Comparison between our derived abundances and the results of Reddy et al. (2002) for IRAS 22272+5435.

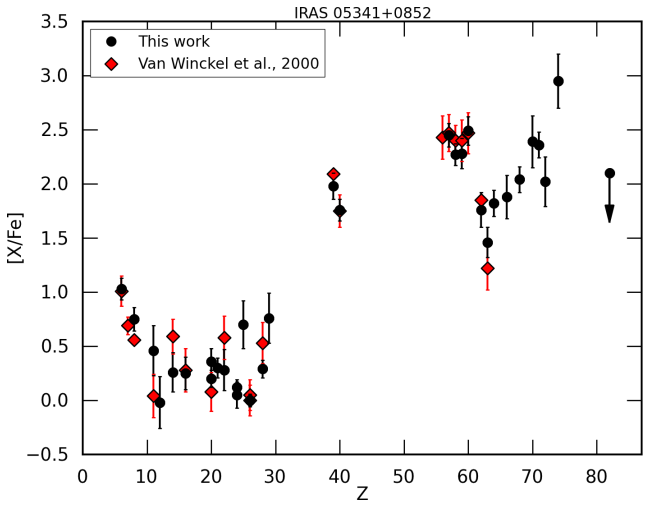

Figure D.3: Comparison between our derived abundances and the results of Van Winckel & Reyniers (2000) for IRAS 05341+0852.

the Nd and Eu abundances, whereas we use five spectral lines with EWs ranging from about 5 up to 24 mÅ to determine the Nd abundance and one line with an EW $\approx$ 16 mÅ to determine the Eu abundance. For these small lines, a small change in EW can result in a large abundance difference which may explain the discrepancy. Our abundance results of IRAS 22223+4327 (Fig. D.6) are similar to the determined abundances from Van Winckel & Reyniers (2000) and Rao et al. (2012). All three independent studies confirm the overabundance of ls elements with respect to the hs elements of IRAS 22223+4327.

Our atmospheric parameter results for IRAS 06530-0213 and IRAS 08143-4406 (Figs. D.7 and D.8) confirm the derived atmospheric parameter sets of Reyniers et al. (2004). Since only the combined [X/Fe] results for the two observational settings for IRAS 08143-4406 are provided in Reyniers et al. (2004), we compare our individual results for the two settings with these combined results. For both stars, our results are similar. The strongest difference is our higher Zr abundance of about +0.3 dex with respect to Reyniers et al. (2004).

For IRAS 07430+1115 (Fig. D.9), we find large abundance differences with respect to Reddy et al. (1999) for almost all *s*-process elements, despite using almost exactly the same atmospheric parameter set. Reddy et al. (1999) find Y and Zr abundances which are respectively $\pm$ 0.5 and $\pm$ 1.0 dex higher than our results. For Sm and Eu, Reddy et al. (1999) find lower abundances of about 0.3 dex. Except for one Eu line, we have used a different set of spectral lines

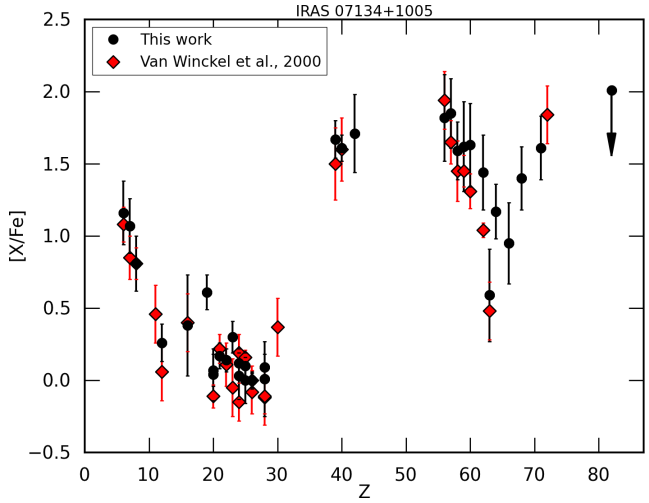

Figure D.4: Comparison between our derived abundances and the results of Van Winckel & Reyniers (2000) for IRAS 07134+1005.

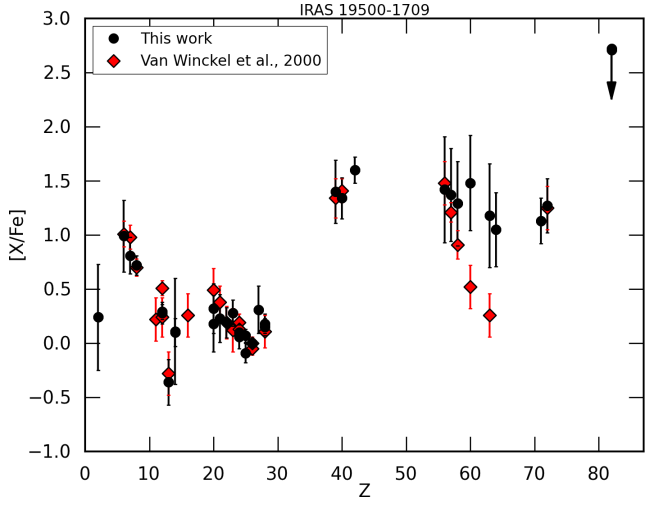

Figure D.5: Comparison between our derived abundances and the results of Van Winckel & Reyniers (2000) for IRAS 19500-1709.

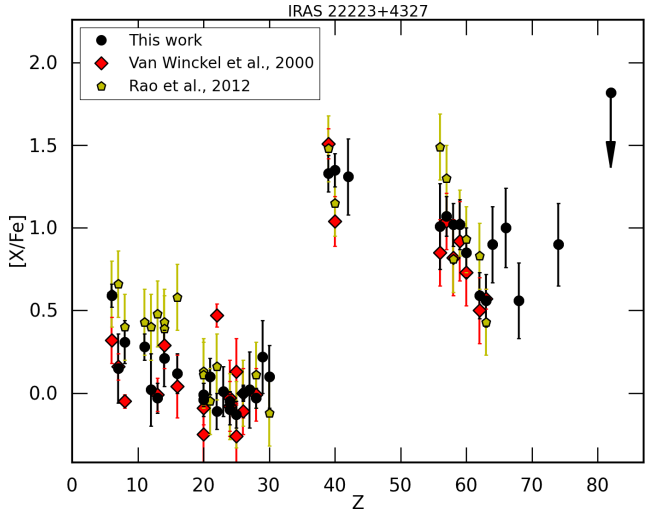

Figure D.6: Comparison between our derived abundances and the results of Van Winckel & Reyniers (2000) and Rao et al. (2012) for IRAS 22223+4327. We adopt a standard deviation of 0.2 dex for all results of Rao et al. (2012).

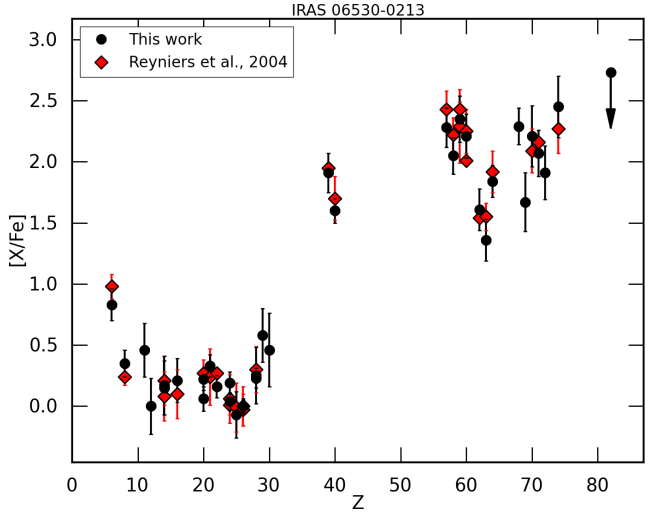

Figure D.7: Comparison between our derived abundances and the results of Reyniers et al. (2004) for IRAS 06530-0213.

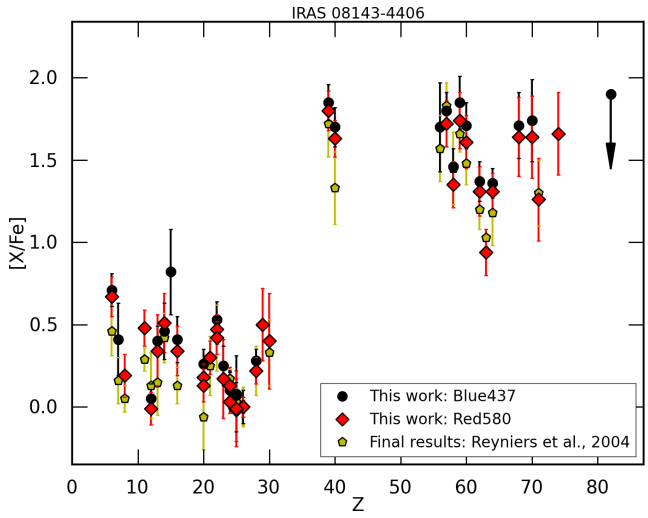

Figure D.8: Comparison between our derived abundances for both observational settings of IRAS08143-4406 and the final results of Reyniers et al. (2004).

than Reddy et al. (1999) for the analysis of Y, Zr, Sm and Eu because many of these lines are part of a spectral blend in our UVES spectra. If these blends are included in the EW calculation, they result in EWs which are much higher than the actual EW which may explain our abundance differences with those of Reddy et al. (1999). For the only common Eu, we find a difference of -0.07 dex between our log gf value and those of Reddy et al. (1999) which may partly explain the abundance difference.

The atmospheric parameter results of Reyniers et al. (2007b) for IRAS 08281-4850 and IRAS 14325-6428 are similar to our results, although they find a microturbulent velocity which is 4 km/s higher than our preferred result for IRAS 14325-6428. We find similar results for IRAS 08281-4850 (Fig. D.10) and also for IRAS 14325-6428, (Fig. D.11) despite the large microturbulence difference.

As discussed above, our results for IRAS 22223+4327 correspond to those of Rao et al. (2012). In case of IRAS 17279-1119 (Fig. D.12), we find similar atmospheric parameters as Rao et al. (2012) except for our $\log g$ which differs by +1.0 dex of that of Rao et al. (2012). We find a stronger enrichment of the hs elements resulting in a mean [hs/Fe] of about 0.9 dex while Rao et al. (2012) find [hs/Fe] $\approx$ 0.6 dex. Nevertheless, we still classify this object as mildly *s*-proces enriched ([s/Fe] < 1) based on our abundance results.

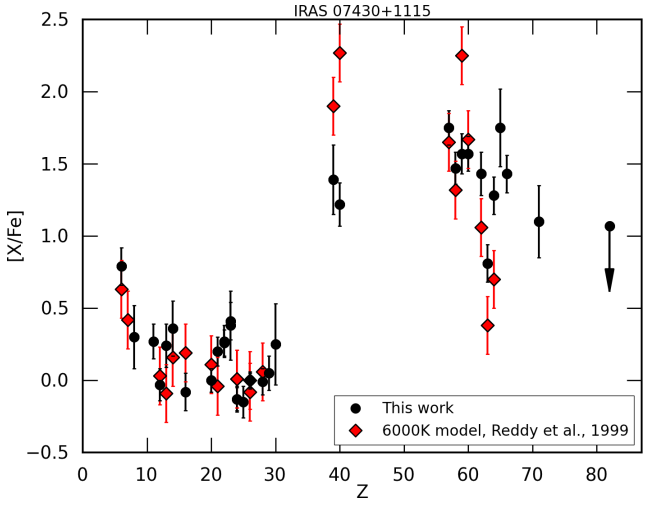

Figure D.9: Comparison between our derived abundances and the results of Reddy et al. (1999) for IRAS 07430+1115. We adopt a standard deviation of 0.2 dex for all results of Reddy et al. (1999).

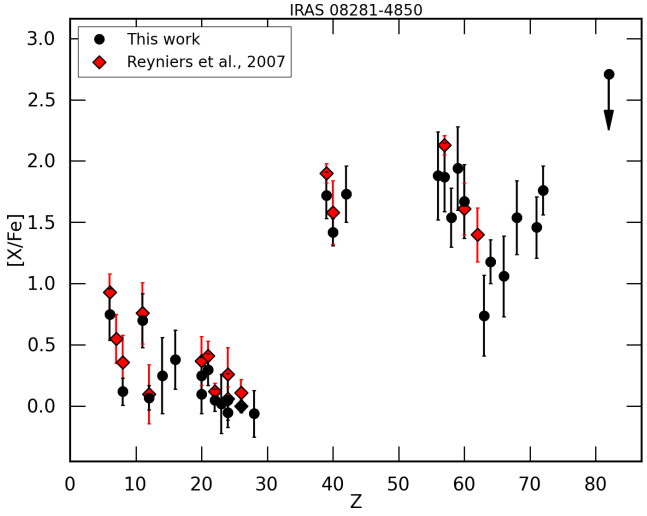

Figure D.10: Comparison between our derived abundances for both observations of IRAS 08281-4850 and the final results of Reyniers et al. (2007b).

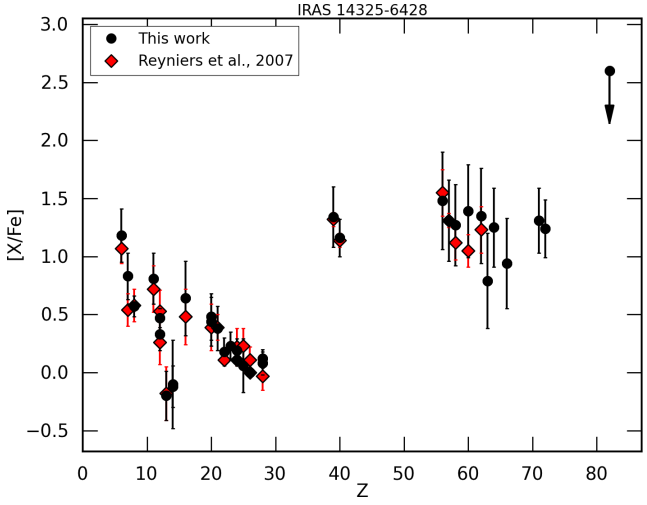

Figure D.11: Comparison between our derived abundances for both observations of IRAS 14325-6428 and the final results of Reyniers et al. (2007b).

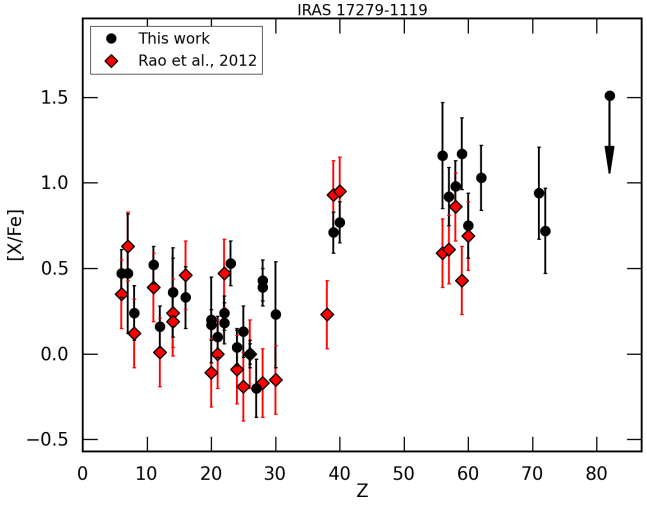

Figure D.12: Comparison between our derived abundances and the results of Rao et al. (2012) for IRAS 17279-1119. We adopt a standard deviation of 0.2 dex for all results of Rao et al. (2012).

Appendix E

Atomic data used for the spectral analyses in Chapter 6

Table E.1: Details of all spectral lines used for the spectral analysis of the Galactic post-AGB stars in Chapter 6. The right part of the table lists the measured EWs, expressed in mÅ, for each individual star. For those elemental abundances that have been determined via spectral synthesis, the listed EW is the theoretical EW corresponding to the derived abundance. The abbreviated names represent respectively: 05113 = IRAS 05113+1347, 05341 = IRAS 05341+0852, 06530 = IRAS 06530-0213, 07134 = IRAS 07134+1005, 07430 = IRAS 07430+1115, 08143B = Blue437 and RED860 spectra of IRAS 08143-4406, 08143R = RED580 spectra of IRAS 08143-4406, 08281 = IRAS 08281-4850, 13245 = IRAS 13245-5036, 14325 = IRAS 14325-6428, 14429 = IRAS 14429-4539, 17279 = IRAS 17279-1119, 19500 = IRAS 19500-1709, 22223 = IRAS 22223+4327, 22272 = IRAS 22272+5435.

ion	λ (Å)	EP (eV)	log gf	05113 08143B 14429	05341 08143R 17279	06530 08281 19500	07134 13245 22223	07430 14325 22272
				-	-	-	-	-
C I	4009.930	7.68	-2.27	-	-	-	-	33.7
				-	-	-	-	-
				-	-	-	55.3	-
C I	4146.264	7.95	-2.02	-	-	-	-	-
				-	42.0	-	-	-
				-	-	-	50.6	-
C I	4228.326	7.68	-2.25	-	-	50.0	-	38.8
				-	31.4	25.7	-	-
				-	-	-	75.8	-
C I	4371.367	7.65	-1.97	-	-	-	-	53.3
				-	72.9	40.9	-	-
				-	-	-	-	-
C I	4734.260	7.95	-2.37	-	-	-	-	25.4
				-	-	-	-	-
				-	-	-	51.7	-
C I	4766.672	7.45	-2.51	85.5	-	-	-	41.7
				-	-	-	-	-
				-	-	-	65.8	-
C I	4770.027	7.46	-2.33	112.2	-	-	-	58.2
				-	-	-	128.4	-
				-	-	-	126.2	-
C I	4771.742	7.46	-1.76	-	-	-	-	131.6
				33.7	-	-	-	-
				-	-	-	80.6	-
C I	4775.897	7.49	-2.19	129.1	-	-	-	-
				-	-	-	132.6	-
				-	-	-	12.2	-
C I	4812.920	7.48	-3.23	19.6	-	-	-	-
				-	-	-	-	-
				-	-	-	23.5	-
C I	4817.373	7.48	-2.89	-	-	-	-	-
				-	20.7	-	50.7	-
				-	-	-	21.8	-
C I	4826.796	7.49	-3.05	-	-	-	-	-
				-	-	-	-	-
				155.1	141.6	-	115.0	-
C I	4932.049	7.68	-1.70	174.8	-	111.1	20.28	88.1
				-	87.6	62.5	172.4	152.7
				-	-	-	24.3	-
C I	5017.090	7.95	-2.43	-	54.9	-	-	-

Table E.1: continued.

ion	λ (Å)	EP (eV)	log gf	05113 08143B 14429	05341 08143R 17279	06530 08281 19500	07134 13245 22223	07430 14325 22272
				-	-	-	-	-
C I	5023.849	7.95	-2.20	- - -	79.5 66.2 37.7	- 37.4 20.1	44.4 - 75.5	- 22.0 -
C I	5024.916	7.95	-2.73	- - -	- - -	- - -	19.3 - -	- - -
C I	5039.057	7.95	-1.77	- - -	121.1 135.9 71.2	133.2 76.2 41.0	82.8 12.39 -	- 62.7 -
C I	5040.123	7.95	-2.30	- - -	- - -	- - -	- - -	- 23.1 -
C I	5040.134	7.95	-2.30	- - -	- - 23.1	- - 12.7	33.8 - -	- - -
C I	5041.639	7.95	-1.70	- - -	- - 80.6	- - -	- - -	- - -
C I	5052.144	7.680	-1.30	- - -	- - -	- - -	- 43.76 -	- - -
C I	5052.167	7.65	-1.30	- - -	195.6 - 131.7	- 192.2 -	155.0 - -	- - -
C I	5380.337	7.68	-1.61	143.5 - -	164.5 - 91.3	161.2 130.2 -	112.5 - 182.7	160.8 - 167.4
C I	5551.018	8.65	-1.63	38.6 - -	- - -	- - -	- - -	- - -
C I	5551.578	8.64	-1.90	- - -	41.2 31.4 18.8	59.4 22.2 12.5	26.2 - 43.4	- - 41.6
C I	5668.940	8.54	-1.47	- - -	- - -	- - -	- - -	- 68.6 -
C I	5793.120	7.95	-2.04	- - -	- - -	- - 23.2	41.6 - 99.0	- - 84.5
C I	5794.473	7.95	-2.77	- - -	- - -	- - -	12.4 - 29.5	- - -
C I	5800.594	7.95	-2.31	- - -	- - -	- - -	25.0 - 64.9	- - -
C I	5805.200	7.95	-2.66	- - -	- - -	- - -	- - 38.9	- - -
C I	6001.118	8.64	-2.06	- - -	35.6 30.7 13.4	- 19.9 -	20.5 - 41.0	- - -
C I	6002.987	8.65	-2.17	- - -	38.7 - -	36.1 - -	17.2 - 40.2	- - -
C I	6007.176	8.64	-2.06	- -	26.6 33.1	41.4 21.6	20.6 -	- -

Table E.1: continued.

ion	λ (Å)	EP (eV)	log gf	05113 08143B 14429	05341 08143R 17279	06530 08281 19500	07134 13245 22223	07430 14325 22272
				-	-	8.0	31.3	-
				-	54.4	-	26.2	50.7
C I	6010.675	8.64	-1.94	-	45.2	23.8	-	-
				-	-	13.7	51.3	-
				21.5	33.1	36.2	21.2	39.9
C I	6012.225	8.64	-2.00	-	29.8	17.3	-	-
				-	-	-	-	29.7
				-	-	131.8	75.4	-
C I	6013.165	8.65	-1.16	-	-	86.1	16.64	69.1
				24.1	-	-	123.2	-
				50.5	63.1	-	48.1	-
C I	6014.834	8.64	-1.58	-	67.7	42.3	-	37.6
				-	29.2	24.6	-	73.0
				-	66.8	53.6	28.3	53.8
C I	6016.444	8.64	-1.83	-	-	-	-	16.0
				-	21.1	12.1	65.6	-
				-	40.4	45.6	20.2	-
C I	6397.961	8.77	-1.78	-	33.4	24.5	-	14.0
				-	-	10.1	-	-
				122.5	137.4	-	107.0	145.4
C I	6587.622	8.50	-1.02	-	-	117.0	-	98.6
				45.0	80.0	67.0	-	152.4
				-	51.0	50.5	21.5	51.6
C I	6655.517	8.54	-1.94	-	43.7	26.8	-	-
				-	15.6	13.6	52.5	-
				-	-	-	58.4	-
C I	6828.115	8.54	-1.39	105.6	-	-	-	-
				-	-	-	112.1	-
				-	-	-	-	-
C I	7087.825	8.65	-1.44	-	-	-	-	46.5
				-	-	-	-	-
				-	-	-	58.9	-
C I	7100.124	8.65	-1.47	83.4	-	-	-	44.2
				-	-	-	-	88.4
				-	-	-	47.2	-
C I	7108.934	8.65	-1.60	74.7	-	-	-	42.3
				-	-	-	-	-
				-	-	-	82.6	-
C I	7111.472	8.65	-1.07	117.3	-	-	-	73.8
				-	-	-	-	122.1
				-	-	-	116.2	-
C I	7113.178	8.65	-0.76	-	-	-	-	-
				-	-	-	-	157.7
				-	-	-	125.5	-
C I	7115.172	8.65	-0.82	-	-	-	-	113.0
				-	-	-	-	151.6
				-	-	-	114.7	-
C I	7116.991	8.65	-0.91	-	-	-	-	106.1
				-	-	-	-	135.7
				-	-	-	91.6	-
C I	7119.656	8.65	-1.15	137.4	-	-	-	89.0
				-	-	-	-	-
				-	-	-	15.4	-
C I	7122.203	8.64	-2.10	-	-	-	-	-
				-	-	-	-	-
				-	-	-	12.5	-
C I	7473.309	8.77	-2.12	20.3	-	-	-	-

Table E.1: continued.

ion	λ (Å)	EP (eV)	log gf	05113 08143B 14429	05341 08143R 17279	06530 08281 19500	07134 13245 22223	07430 14325 22272
				-	-	-	-	-
C I	7476.176	8.77	-1.64	- 55.0 -	- - -	- - -	26.5 - -	- - 44.2
C I	7483.445	8.77	-1.44	- - -	- - -	- - -	48.2 - -	- - -
C I	7848.244	8.85	-1.74	- 34.1 -	- - -	- - -	20.7 - -	- - -
C I	7852.862	8.85	-1.69	- - -	- - -	- - -	22.1 - -	- - -
C I	7860.889	8.85	-1.16	- 99.8 -	- - -	- - -	- - -	- - 80.9
C I	8058.621	8.85	-1.29	- 97.3 -	- - -	- - -	- - -	- - -
N I	6482.699	11.76	-0.51	- - -	- - 4.1	- - -	- - -	- - -
N I	7423.641	10.33	-0.71	- - -	- - -	- - 34.92	30.3 - -	- - -
N I	7442.298	10.33	-0.39	- 40.0 -	- - -	- - 61.68	48.2 - 24.54	- 79.8 -
N I	7468.312	10.34	-0.17	- 57.6 -	- - -	- - 84.47	73.2 - 36.05	- 104.6 -
N I	8200.310	10.33	-1.02	- 8.7 -	- - -	- - -	- - -	- - -
N I	8686.160	10.32	-0.27	- 78.4 -	- - -	- - -	- - -	- 141.5 -
N I	8703.240	10.33	-0.30	- 63.5 -	- - -	- - -	- - -	- 129.8 -
N I	8711.690	10.33	-0.22	- 80.9 -	- - -	- - -	- - -	- 147.8 -
N I	8718.820	10.34	-0.34	- 66.5 -	- - -	- - -	- - -	- 111.2 -
N I	8728.910	10.33	-1.06	- - -	- - -	- - -	- - -	- 32.3 -
O I	4368.242	9.52	-1.71	- - -	- - -	- - 52.2	37.4 - -	- 44.8 -
O I	4968.794	10.74	-1.37	- - 14.0	- - -	- - -	- - -	- 19.0 -
O I	5329.098	10.74	-1.24	-	17.8 -	25.3 17.5	18.5 14.8	- 21.3

Table E.1: continued.

ion	λ (Å)	EP (eV)	log gf	05113 08143B 14429	05341 08143R 17279	06530 08281 19500	07134 13245 22223	07430 14325 22272
				20.7	-	28.1	-	-
				-	-	-	22.6	-
O I	5329.687	10.74	-1.02	-	-	24.7	-	-
				-	-	37.0	22.0	-
				-	-	-	-	-
O I	5330.737	10.74	-0.87	-	-	-	-	44.1
				40.2	-	49.4	-	-
				-	-	-	-	-
O I	5436.862	10.74	-1.40	-	-	-	-	17.6
				-	-	-	-	-
				-	-	-	-	-
O I	6046.436	10.99	-1.46	-	-	-	-	-
				-	-	10.9	-	-
				-	-	40.8	36.9	-
O I	6155.971	10.74	-0.67	-	36.6	33.1	34.0	44.3
				48.3	24.4	66.4	-	16.1
				-	-	65.0	54.6	-
O I	6156.778	10.74	-0.45	-	49.2	52.9	37.2	63.9
				69.9	40.0	86.7	50.4	-
				-	-	-	64.4	-
O I	6158.187	10.74	-0.31	-	57.4	70.5	54.6	98.1
				83.3	-	108.2	55.7	-
				-	-	10.7	-	53.79
O I	6300.230	0.00	-9.75	-	-	-	-	-
				-	-	-	-	-
				18.44	6.7	-	-	19.89
O I	6363.880	0.020	-10.25	-	-	-	-	-
				-	-	-	-	29.6
				-	-	15.9	15.0	-
O I	6453.640	10.74	-1.30	-	-	-	-	15.4
				-	-	-	12.4	-
				-	-	19.1	19.3	-
O I	6454.444	10.74	-1.08	-	-	-	19.3	24.0
				-	-	-	15.9	-
				-	-	-	32.7	-
O I	7002.230	10.99	-0.55	-	-	-	-	-
				-	-	-	-	-
				-	-	-	-	-
Na I	4978.541	2.10	-1.21	-	19.2	-	-	-
				-	-	-	-	-
				111.3	50.8	42.6	-	93.3
Na I	5682.633	2.10	-0.67	-	67.0	-	-	-
				-	45.6	-	84.4	87.3
				-	-	-	-	-
Na I	5688.210	2.100	-0.42	-	-	51.10	-	-
				-	60.6	-	-	-
				26.1	-	-	-	31.6
Na I	6154.230	2.10	-1.56	-	-	-	-	-
				-	-	-	-	18.8
				-	-	-	-	-
Na I	6160.750	2.10	-1.26	-	-	-	-	-
				-	-	-	33.5	-
				-	-	-	-	-
Na I	8183.255	2.100	-0.62	-	-	-	-	11.68
				-	-	-	-	-
				-	-	-	-	-
Mg I	3829.354	2.71	-0.23	-	-	-	108.1	-

Table E.1: continued.

ion	λ (Å)	EP (eV)	log gf	05113 08143B 14429	05341 08143R 17279	06530 08281 19500	07134 13245 22223	07430 14325 22272
				-	-	-	-	-
				-	-	-	-	-
Mg I	3986.753	4.35	-1.06	-	-	49.2	-	-
				-	-	-	-	-
				-	-	-	-	-
Mg I	4057.505	4.35	-0.90	152.6	-	59.5	-	37.9
				-	93.8	-	-	-
				-	-	-	-	-
Mg I	4167.271	4.35	-0.74	-	-	-	-	61.0
				-	-	-	-	-
				-	-	-	95.2	-
Mg I	4703.000	4.35	-0.37	-	-	-	-	107.1
				29.7	-	79.9	-	-
				-	-	-	157.1	-
Mg I	5167.320	2.70	-0.75	-	-	-	58.2	-
				82.0	-	-	-	-
				-	-	-	-	-
Mg I	5172.684	2.71	-0.45	-	-	-	104.4	-
				-	-	-	-	-
				-	-	-	-	-
Mg I	5183.604	2.72	-0.24	-	-	-	126.6	-
				-	-	-	-	-
				-	144.2	146.7	81.9	-
Mg I	5528.420	4.35	-0.47	-	181.2	106.5	16.0	88.7
				21.0	140.8	68.0	-	-
				139.91	-	-	8.2	93.2
Mg I	5711.100	4.340	-1.75	-	36.8	-	-	-
				-	-	-	80.94	58.35
				-	-	-	-	16.0
Mg I	6799.001	5.75	-1.56	-	-	-	-	-
				-	-	-	-	-
				-	-	-	-	-
Mg I	6965.409	5.75	-1.51	8.3	-	-	-	-
				-	-	-	-	-
				-	-	-	-	-
Mg I	7657.603	5.110	-1.27	-	-	-	-	-
				-	-	-	-	39.90
				-	-	-	-	-
Mg I	7659.152	5.110	-1.49	-	-	-	-	-
				-	-	-	-	26.40
				-	-	-	-	-
Mg I	7691.550	5.75	-0.78	35.0	-	-	-	-
				-	-	-	-	-
				-	-	-	-	-
Mg I	8923.569	5.39	-1.68	12.6	-	-	-	-
				-	-	-	-	-
				-	-	-	-	-
Mg II	3848.211	8.86	-1.59	-	-	-	-	57.2
				39.8	-	-	-	-
				-	-	-	-	-
Mg II	4390.580	10.00	-0.53	-	-	-	49.7	-
				64.5	-	84.6	-	-
				-	-	-	-	-
Mg II	4427.990	10.00	-1.20	-	-	-	18.4	29.8
				-	-	28.4	-	-
				-	-	-	-	-
Mg II	4427.994	10.00	-1.21	-	-	-	-	-

Table E.1: continued.

ion	λ (Å)	EP (eV)	log gf	05113 08143B 14429	05341 08143R 17279	06530 08281 19500	07134 13245 22223	07430 14325 22272
				21.8	-	-	-	-
Mg II	4433.990	10.00	-0.90	- - -	- - -	- - 48.5	- - -	- 46.8 -
Mg II	4436.491	11.57	-0.89	- - -	- - -	- - -	- - -	- 15.9 -
Mg II	4739.590	11.57	-0.66	- - -	- - -	- - -	- - -	- 13.0 -
Al I	3944.006	0.000	-0.64	- - 47.4	- - -	- - 92.9	- - -	- 120.42 -
Al I	3961.520	0.010	-0.28	- - 81.6	- - -	- - -	- 66.31 -	- - -
Al I	6696.023	3.14	-1.35	- 18.2 -	- 13.2 -	- - -	- - 16.2	34.3 - -
Al I	6698.673	3.14	-1.65	- - -	- - -	- - -	- - -	27.8 - -
Al I	7835.309	4.02	-0.65	- 16.9 -	- - -	- - -	- - -	- - -
Al I	7836.134	4.02	-0.47	- - -	- - -	- - -	- - 18.7	- - 32.0
Al II	4663.046	10.60	-0.28	- - 20.5	- - -	- - -	- - -	- - -
Si I	3905.523	1.91	-1.04	- - 66.26	- - -	- - 176.1	- 74.0 -	- 146.57 -
Si I	5645.620	4.93	-2.14	33.2 - -	- - -	- - -	- - 24.6	- - -
Si I	5665.560	4.92	-2.04	- - -	- 19.5 -	- - -	- - 27.2	50.2 - -
Si I	5675.417	5.62	-1.23	- - -	- - 10.7	- - -	- - -	- - -
Si I	5690.430	4.93	-1.91	- - -	- 22.0 -	- - -	- - 34.6	- - -
Si I	5772.150	5.08	-1.75	- - -	- - -	- - -	- - 43.2	- - -
Si I	5948.550	5.08	-1.22	- - -	- 61.5 -	- - -	- - 64.7	- - -
Si I	6046.693	5.95	-0.94	- - -	13.4 - -	- - -	- - -	- - -
Si I	6091.920	5.87	-1.33	- -	- -	- -	- -	40.9 -

Table E.1: continued.

ion	λ (Å)	EP (eV)	log gf	05113 08143B 14429	05341 08143R 17279	06530 08281 19500	07134 13245 22223	07430 14325 22272
				-	-	-	17.9	-
				-	-	-	-	-
Si I	6125.030	5.61	-1.51	-	19.7	-	-	-
				-	-	-	25.8	-
				102.6	27.0	-	-	73.7
Si I	6155.140	5.62	-0.84	-	-	12.03	-	-
				-	25.5	-	-	60.0
				-	-	-	-	63.9
Si I	6237.330	5.61	-1.22	-	24.2	-	-	-
				-	18.9	-	38.0	35.6
				-	-	-	-	-
Si I	6243.820	5.61	-1.34	-	23.5	-	-	-
				-	-	-	30.7	-
				-	-	-	-	-
Si I	6244.465	5.62	-1.09	-	-	-	-	-
				-	16.4	-	-	-
				-	32.5	23.7	-	-
Si I	6254.187	5.62	-0.93	-	-	9.83	-	-
				-	20.1	-	-	-
				-	11.6	-	-	-
Si I	6414.990	5.87	-1.11	-	18.8	-	-	-
				-	-	-	-	27.1
				52.3	-	-	-	43.8
Si I	6555.470	5.98	-1.00	-	-	-	-	-
				-	-	-	-	-
				54.8	10.6	8.6	-	-
Si I	6721.840	5.56	-1.26	30.2	-	-	-	-
				-	12.6	-	29.3	-
				-	-	-	-	-
Si I	7034.910	5.87	-0.85	38.7	-	-	-	-
				-	-	-	38.3	37.4
				-	-	-	-	-
Si I	7415.960	5.61	-0.63	-	-	-	-	-
				-	-	-	93.3	-
				-	-	-	-	-
Si I	7423.496	5.62	-0.31	121.9	-	-	-	-
				-	-	-	111.8	-
				-	-	-	-	-
Si I	7932.350	5.96	-0.56	69.9	-	-	-	-
				-	-	-	64.8	-
				-	-	-	-	-
Si II	3853.664	6.86	-1.33	-	-	-	-	-
				-	-	160.1	-	-
				-	-	-	-	-
Si II	4128.050	6.52	-1.56	-	-	-	109.2	136.6
				-	-	168.6	-	-
				-	-	-	-	-
Si II	4130.880	9.80	-0.07	-	-	-	78.2	-
				-	-	-	-	-
				-	-	-	-	-
Si II	5055.984	10.07	0.53	-	-	-	104.9	101.6
				-	-	-	-	-
				-	-	-	-	-
Si II	5056.020	10.030	-0.51	-	-	-	-	-
				35.93	-	-	-	-
				-	-	-	-	-
Si II	6371.350	8.120	-0.10	-	-	-	-	-

Table E.1: continued.

ion	λ (Å)	EP (eV)	log gf	05113 08143B 14429	05341 08143R 17279	06530 08281 19500	07134 13245 22223	07430 14325 22272
				-	144.76	-	-	-
				-	-	179.0	-	-
Si II	6371.371	8.12	-0.04	-	-	-	-	-
				-	-	-	-	-
				-	-	-	-	-
P I	9796.828	6.990	-0.57	15.67	-	-	-	-
				-	-	-	-	-
				-	-	-	-	-
S I	4694.120	6.52	-1.82	33.1	-	-	-	-
				-	-	-	33.1	-
				-	-	-	-	-
S I	4695.440	6.52	-1.96	30.8	-	-	-	-
				-	-	-	-	-
				-	-	-	-	-
S I	4696.250	6.52	-2.19	11.9	-	-	-	-
				-	-	-	17.1	-
				-	23.8	23.4	-	28.0
S I	6743.580	7.87	-0.56	39.9	32.5	14.4	-	-
				-	-	-	32.3	28.7
				-	28.6	29.8	-	-
S I	6748.790	7.87	-0.35	56.0	49.5	20.2	-	-
				-	30.8	-	58.1	-
				58.2	33.3	40.3	14.9	48.4
S I	6757.160	7.87	-0.20	76.9	62.7	28.2	-	-
				-	38.1	-	81.4	51.8
				-	-	-	-	-
S I	8693.960	7.84	-0.41	81.9	-	-	-	-
				-	-	-	-	-
				-	-	-	-	-
S I	9436.967	8.410	-0.72	-	-	-	-	3.33
				-	-	-	-	-
				-	-	-	28.5	-
Ca I	4283.010	1.89	-0.14	-	-	-	-	-
				-	-	-	-	-
				-	-	-	47.9	-
Ca I	4302.528	1.90	0.29	-	-	-	-	-
				-	-	-	-	-
				-	-	-	-	-
Ca I	4318.651	1.90	-0.14	-	-	-	-	18.4
				-	-	-	-	-
				-	-	-	32.0	-
Ca I	4434.957	1.89	-0.01	-	-	-	-	22.1
				-	-	-	-	-
				-	-	-	-	-
Ca I	4454.790	1.90	-0.08	-	-	-	-	-
				-	103.6	-	-	-
				-	-	-	-	-
Ca I	4585.870	2.52	-0.45	68.9	-	-	-	-
				-	-	-	92.9	-
				-	-	-	-	-
Ca I	5265.560	2.52	-0.10	-	89.9	-	-	-
				-	51.7	-	-	-
				-	-	-	-	70.0
Ca I	5512.990	2.93	-0.45	-	30.8	-	-	-
				-	-	-	-	82.7
				-	-	-	-	-
Ca I	5581.980	2.52	-0.55	-	36.9	-	-	-

Table E.1: continued.

ion	λ (Å)	EP (eV)	log gf	05113 08143B 14429	05341 08143R 17279	06530 08281 19500	07134 13245 22223	07430 14325 22272
				-	27.6	-	74.8	-
				-	-	-	28.3	-
Ca I	5588.760	2.52	0.36	-	-	-	-	14.0
				-	-	15.6	-	-
				100.8	-	22.8	-	78.2
Ca I	5590.130	2.52	-0.74	-	30.7	-	-	-
				-	-	-	63.1	80.3
				-	-	29.9	-	98.9
Ca I	5601.290	2.52	-0.63	-	41.6	-	-	-
				-	27.4	-	81.1	89.5
				-	-	-	14.3	-
Ca I	5857.451	2.93	0.24	-	-	-	-	-
				-	-	-	-	-
				-	69.9	46.9	-	-
Ca I	6102.727	1.88	-0.80	-	57.6	14.2	-	-
				-	42.6	-	-	145.6
				-	118.3	100.8	23.0	-
Ca I	6122.217	1.89	-0.32	-	131.3	48.0	-	-
				-	-	-	-	-
				-	140.1	120.1	32.6	-
Ca I	6162.180	1.90	-0.10	-	-	63.2	-	20.7
				-	-	14.6	-	-
				-	-	-	-	-
Ca I	6163.750	2.52	-1.46	-	-	-	-	-
				-	-	-	-	33.0
				-	-	-	-	-
Ca I	6166.440	2.52	-1.14	-	-	-	-	-
				-	-	-	37.6	-
				-	-	29.7	-	-
Ca I	6169.560	2.52	-0.57	-	46.1	-	-	-
				-	-	-	67.9	-
				-	142.3	108.8	30.5	-
Ca I	6439.075	2.53	0.39	-	-	52.1	-	18.5
				-	-	13.0	-	-
				122.3	42.7	22.7	-	92.7
Ca I	6449.820	2.52	-0.62	-	48.6	9.5	-	-
				-	-	-	-	87.7
				-	-	-	28.7	-
Ca I	6462.567	2.52	0.31	-	-	-	-	-
				-	-	-	-	-
				-	-	22.3	-	88.8
Ca I	6471.670	2.52	-0.88	-	32.1	-	-	-
				-	-	-	53.3	92.0
				-	-	-	12.7	-
Ca I	6493.781	2.52	-0.11	-	-	-	-	-
				-	-	-	-	-
				-	57.6	44.7	-	121.5
Ca I	6493.790	2.52	-0.39	-	67.4	-	-	-
				-	48.2	-	-	-
				-	-	18.1	-	-
Ca I	6499.650	2.52	-1.00	-	27.3	-	-	-
				-	-	-	45.6	-
				103.3	39.4	33.4	-	94.6
Ca I	6717.690	2.71	-0.52	62.5	-	-	-	-
				-	23.3	-	-	89.7
				-	-	-	18.4	-
Ca I	7148.150	2.71	0.14	145.2	-	-	-	-

Table E.1: continued.

ion	λ (Å)	EP (eV)	log gf	05113 08143B 14429	05341 08143R 17279	06530 08281 19500	07134 13245 22223	07430 14325 22272
				-	-	-	-	-
				-	-	-	-	-
Ca II	4109.815	7.51	-0.73	-	-	-	-	31.7
				-	-	-	-	-
				-	-	-	25.4	-
Ca II	5001.479	7.50	-0.51	-	-	-	-	-
				-	-	21.5	-	-
				-	88.8	-	44.1	-
Ca II	5019.971	7.51	-0.25	-	122.4	90.2	-	76.2
				-	-	49.3	120.7	81.3
				-	20.7	-	-	-
Ca II	5021.138	7.51	-1.21	-	-	-	-	-
				-	-	-	-	-
				-	-	21.1	-	-
Ca II	5021.150	7.51	-1.24	-	19.4	-	-	-
				-	19.04	-	21.8	-
				-	-	-	-	-
Ca II	5285.266	7.50	-1.15	-	-	-	-	-
				-	-	-	33.6	-
				-	50.8	43.2	13.7	-
Ca II	5307.224	7.51	-0.85	-	55.0	33.8	-	-
				-	-	13.3	-	-
				-	-	-	-	-
Ca II	5339.188	8.44	-0.33	-	40.8	-	-	-
				-	-	-	-	-
				-	-	-	-	-
Sc II	4014.484	0.32	-1.66	-	-	-	-	65.6
				-	-	-	-	-
				-	-	-	-	-
Sc II	4294.781	0.60	-1.27	-	-	-	-	60.1
				-	103.7	46.6	-	-
				-	-	-	-	-
Sc II	4314.083	0.62	-0.10	-	-	-	107.4	-
				130.5	-	-	-	-
				-	-	-	-	-
Sc II	4325.010	0.60	-0.72	-	-	-	50.5	167.3
				59.3	-	133.9	-	-
				-	-	-	-	-
Sc II	4354.610	0.61	-1.48	-	-	-	-	52.4
				-	-	28.3	-	-
				-	-	-	-	-
Sc II	4374.470	0.62	-0.60	-	-	-	-	-
				63.3	-	-	-	-
				-	-	-	-	-
Sc II	4400.389	0.60	-0.54	-	-	-	50.7	-
				57.3	-	-	-	-
				-	-	-	131.2	-
Sc II	4415.560	0.60	-0.54	-	-	-	47.0	-
				-	-	-	-	-
				-	-	-	-	-
Sc II	4670.407	1.36	-0.58	-	-	-	-	120.9
				-	-	-	-	-
				-	-	-	120.8	-
Sc II	5031.020	1.36	-0.31	-	-	-	28.0	124.2
				44.0	-	97.7	-	-
				234.7	-	-	66.1	-
Sc II	5239.820	1.45	-0.80	-	-	122.6	-	61.0

Table E.1: continued.

ion	λ (Å)	EP (eV)	log gf	05113 08143B 14429	05341 08143R 17279	06530 08281 19500	07134 13245 22223	07430 14325 22272
				25.7	99.5	54.2	-	-
				120.3	42.3	50.7	14.2	100.4
Sc II	5318.360	1.36	-1.79	-	-	22.5	-	-
				-	26.0	-	78.8	115.31
				-	-	-	124.0	-
Sc II	5526.820	1.77	0.18	-	-	-	-	-
				61.5	-	-	-	-
				60.1	16.5	23.5	-	70.7
Sc II	5552.240	1.45	-2.08	-	-	-	-	-
				-	14.6	-	37.6	71.02
				184.7	99.1	117.5	49.4	-
Sc II	5640.990	1.50	-1.02	-	-	82.4	-	42.7
				-	61.8	30.2	-	-
				-	-	-	-	-
Sc II	5657.896	1.51	-0.60	-	-	-	19.7	-
				31.3	-	-	-	-
				179.2	94.1	102.1	34.9	-
Sc II	5667.153	1.50	-1.21	-	-	55.8	-	35.0
				-	44.6	23.7	159.4	171.18
				-	-	-	-	-
Sc II	5669.040	1.50	-1.10	-	-	-	-	-
				-	64.8	-	181.6	-
				-	108.2	111.8	50.7	-
Sc II	5684.200	1.51	-1.08	-	-	83.4	-	46.9
				-	-	35.0	-	-
				-	-	-	-	-
Sc II	6245.636	1.51	-1.02	-	135.8	-	-	30.5
				-	-	-	-	-
				-	-	-	-	136.5
Sc II	6279.753	1.50	-1.25	-	-	-	-	-
				-	-	-	-	-
				-	-	-	-	113.2
Sc II	6309.919	1.50	-1.62	-	51.9	-	-	-
				-	-	-	-	-
				183.6	86.3	-	-	-
Sc II	6604.600	1.36	-1.23	-	-	-	-	-
				-	-	-	-	-
				-	-	-	-	104.4
Ti I	4512.733	0.84	-0.40	43.2	-	-	-	-
				-	-	-	-	-
				-	-	-	-	-
Ti I	4617.268	1.75	0.44	37.2	-	-	-	-
				-	-	-	-	68.4
				-	-	-	-	-
Ti I	4840.873	0.90	-0.43	24.5	16.4	-	-	-
				-	-	-	-	-
				196.1	-	-	-	134.3
Ti I	5007.209	0.82	0.17	-	81.8	-	-	-
				-	30.6	-	-	-
				-	-	-	-	-
Ti I	5016.160	0.85	-0.48	-	17.5	-	-	-
				-	-	-	-	-
				123.6	-	-	-	94.7
Ti I	5020.026	0.84	-0.33	-	-	-	-	-
				-	-	-	-	93.7
				-	-	-	-	-
Ti I	5035.903	1.46	0.22	-	32.8	-	-	-

Table E.1: continued.

ion	λ (Å)	EP (eV)	log gf	05113 08143B 14429	05341 08143R 17279	06530 08281 19500	07134 13245 22223	07430 14325 22272
				-	9.6	-	-	-
Ti I	5210.384	0.05	-0.82	199.0 - -	- 34.8 12.9	- - -	- - -	118.2 - -
Ti I	5514.540	1.44	-0.50	- - -	- - -	- - -	- - -	38.6 - -
Ti I	6261.110	1.43	-0.59	37.0 - -	- - -	- - -	- - -	- - -
Ti I	8426.507	0.83	-1.20	- 15.1 -	- - -	- - -	- - -	- - -
Ti I	9675.543	0.84	-0.80	- 21.8 -	- - -	- - -	- - -	- - -
Ti II	3813.388	0.61	-1.89	- - 86.1	- - -	- - -	- - -	- - -
Ti II	3814.580	0.57	-1.68	- - -	- - -	- - -	- 96.6 -	- - -
Ti II	3882.286	1.12	-1.87	- - -	- - -	- - -	- 48.1 -	- - -
Ti II	3987.606	0.61	-2.73	- - 21.5	- - -	- - -	- - -	- - -
Ti II	4025.129	0.61	-2.11	- - -	- - -	- - -	- 48.4 -	- - -
Ti II	4028.338	1.89	-0.92	- - 91.3	- - -	- - -	- 81.2 -	- - -
Ti II	4053.821	1.89	-1.07	- - -	- - -	- - -	- 73.5 -	- - -
Ti II	4163.643	2.59	-0.13	- - 123.7	- - -	- - -	- 104.2 -	- - -
Ti II	4171.903	2.60	-0.30	- - 101.9	- - -	- - -	- - -	- - -
Ti II	4184.311	1.08	-2.49	- - 23.4	- - -	- - -	- - -	- - -
Ti II	4287.873	1.08	-1.79	- - 74.7	- - -	- - -	- 59.9 -	- - -
Ti II	4294.093	1.08	-0.93	- - 149.1	- - -	- - -	- - -	- - -
Ti II	4301.922	1.16	-1.21	- - 117.1	- - -	- - -	- - -	- - -
Ti II	4307.865	1.17	-1.08	- -	- -	- -	- 129.3	- -

Table E.1: continued.

ion	λ (Å)	EP (eV)	log gf	05113 08143B 14429	05341 08143R 17279	06530 08281 19500	07134 13245 22223	07430 14325 22272
				142.9	-	-	-	-
Ti II	4312.860	1.18	-1.12	- - 127.4	- - -	- - -	- 101.3 -	- - -
Ti II	4314.970	1.16	-1.15	- - 133.9	- - -	- - -	- - -	- - -
Ti II	4316.799	2.05	-1.58	- - -	- - -	- 120.8 77.8	- 26.8 164.7	- 78.2 -
Ti II	4330.245	2.05	-1.80	- - 22.7	- - -	- - -	- - -	- - -
Ti II	4330.710	1.18	-2.06	- - 39.7	- - 122.4	- - 92.0	- - -	- - -
Ti II	4350.834	2.06	-1.81	- - -	- - -	- 73.3 53.8	55.1 - -	- 57.5 -
Ti II	4367.659	2.59	-0.87	- - 65.1	- - 145.8	- - 118.1	- - -	- 114.2 -
Ti II	4386.844	2.60	-0.94	- - 47.4	- - 136.5	- - 96.7	- 45.0 -	- 101.9 -
Ti II	4391.031	1.23	-2.24	- - -	- - 110.3	- - 62.5	- - -	- 69.0 -
Ti II	4394.058	1.22	-1.77	- - 57.2	- - -	- - -	- - -	- - -
Ti II	4399.765	1.24	-1.20	- - 124.6	- - -	- - -	- 111.0 -	- - -
Ti II	4407.678	1.22	-2.43	- - 16.4	- - 84.7	- 71.1 34.5	52.3 - -	- 43.2 -
Ti II	4409.516	1.23	-2.57	- - -	- - -	- - 43.6	- - -	- - -
Ti II	4411.080	3.10	-0.67	- - 51.6	- - -	- 126.3 87.9	75.6 - -	- 93.4 -
Ti II	4411.925	1.22	-2.55	- - -	- - 86.6	- 62.5 31.7	52.1 - -	- 33.0 -
Ti II	4418.340	1.24	-1.99	- - 49.5	- - -	- - 88.4	92.4 31.1 -	- - -
Ti II	4421.938	2.06	-1.58	- - 37.0	- - 125.3	- - 72.2	73.3 - -	- 72.8 -
Ti II	4441.734	1.18	-2.27	- - -	- - 118.1	- - 58.5	81.1 - -	- 70.3 -
Ti II	4450.482	1.08	-1.52	- -	- -	- -	- 73.9	- -

Table E.1: continued.

ion	λ (Å)	EP (eV)	log gf	05113 08143B 14429	05341 08143R 17279	06530 08281 19500	07134 13245 22223	07430 14325 22272
				96.0	-	-	-	-
Ti II	4464.450	1.16	-1.81	- - 71.2	- - -	- - 122.2	117.5 - -	- 149.9 -
Ti II	4469.138	1.08	-2.51	- - -	- - -	- - 44.4	- - -	- - -
Ti II	4470.857	1.17	-2.06	- - 36.1	- - -	- - 83.8	- - -	- 101.6 -
Ti II	4488.331	3.12	-0.51	- - 74.2	- - -	- 145.2 104.6	- 43.2 -	- 108.6 -
Ti II	4493.513	1.08	-2.83	- - -	- - 78.9	- 49.5 32.2	48.5 - 150.4	- 33.5 -
Ti II	4501.269	1.12	-0.77	- - 163.1	- - -	- - -	- 156.8 -	- - -
Ti II	4518.327	1.08	-2.64	- - -	- - 104.9	- 71.6 50.7	63.8 - -	- 44.7 -
Ti II	4518.331	1.08	-2.56	- - 22.2	- - -	- - -	- - -	- - -
Ti II	4529.474	1.57	-1.65	- - 45.5	- - -	- - 93.5	104.5 - -	- 112.7 -
Ti II	4544.028	1.24	-2.53	- - -	- - -	- - 43.2	63.1 - 155.5	- 37.7 -
Ti II	4545.133	1.13	-2.46	- - -	- - -	- - 51.8	69.0 - -	- 52.8 -
Ti II	4589.958	1.24	-1.62	- - 89.2	- - -	- - -	- - -	- - -
Ti II	4708.665	1.24	-2.37	- - 25.0	- - -	- - 57.7	65.3 - -	- 54.2 -
Ti II	4763.881	1.22	-2.36	- - 18.4	- - -	- - 51.3	61.2 - -	- 63.5 -
Ti II	4764.526	1.24	-2.77	- - -	- - -	- - -	46.7 - -	- - -
Ti II	4779.985	2.05	-1.26	- - -	- - -	- - 118.1	- - -	- 123.8 -
Ti II	4792.426	1.24	-3.33	- - -	- 68.0 -	- - -	- - -	114.1 - -
Ti II	4798.521	1.08	-2.67	- - -	- 146.7 82.6	112.1 69.3 40.7	56.5 - -	- 41.3 -
Ti II	4805.085	2.06	-0.96	- -	- -	- -	- 71.8	- -

Table E.1: continued.

ion	λ (Å)	EP (eV)	log gf	05113 08143B 14429	05341 08143R 17279	06530 08281 19500	07134 13245 22223	07430 14325 22272
				94.8	-	-	-	-
				-	-	-	-	113.2
Ti II	4806.321	1.08	-3.38	-	-	-	-	-
				-	-	-	-	-
				-	-	-	-	-
Ti II	4849.167	1.13	-2.96	-	123.7	-	-	-
				-	-	-	-	-
				-	-	-	-	-
Ti II	4874.014	3.10	-0.90	-	168.9	103.3	-	80.8
				-	95.6	76.4	-	-
				-	-	-	-	-
Ti II	4911.193	3.12	-0.65	-	-	-	45.1	-
				72.1	-	102.5	-	-
				-	-	-	-	-
Ti II	5010.208	3.10	-1.35	-	-	-	-	-
				14.8	-	-	-	-
				-	-	-	48.1	129.3
Ti II	5010.212	3.10	-1.30	-	120.4	52.6	-	31.3
				-	70.0	40.6	122.2	-
				-	-	-	-	-
Ti II	5013.686	1.58	-2.14	-	-	-	-	-
				15.9	-	-	-	-
				-	-	-	-	-
Ti II	5072.286	3.12	-1.02	-	-	-	-	-
				25.2	-	-	-	-
				-	-	-	118.3	-
Ti II	5129.152	1.89	-1.30	-	-	-	35.3	121.0
				-	-	106.4	-	-
				-	-	180.4	110.4	-
Ti II	5185.913	1.89	-1.37	-	-	-	31.3	112.9
				48.4	137.6	-	-	-
				150.7	-	-	-	158.2
Ti II	5211.530	2.59	-1.41	-	-	-	-	-
				-	-	-	-	-
				-	-	-	-	-
Ti II	5211.540	2.59	-1.85	-	-	-	-	-
				-	75.8	-	-	-
				-	-	-	-	-
Ti II	5226.538	1.57	-1.26	-	-	-	64.0	-
				75.8	-	-	-	-
				-	-	-	115.6	-
Ti II	5336.771	1.58	-1.63	-	-	-	30.3	99.0
				46.3	-	-	-	-
				-	-	-	72.7	-
Ti II	5381.015	1.57	-1.97	-	-	114.8	-	-
				23.4	-	55.5	-	-
				-	127.56	127.9	62.4	-
Ti II	5418.751	1.580	-2.11	-	-	-	-	43.7
				21.3	-	41.4	-	-
				-	-	-	-	41.7
Ti II	5422.494	1.57	-3.71	-	-	-	-	-
				-	-	-	-	-
				-	-	-	-	55.1
Ti II	5454.099	1.57	-3.60	-	-	-	-	-
				-	-	-	-	-
				118.9	-	-	-	134.8
Ti II	5490.692	1.57	-2.66	-	-	-	-	-

Table E.1: continued.

ion	λ (Å)	EP (eV)	log gf	05113 08143B 14429	05341 08143R 17279	06530 08281 19500	07134 13245 22223	07430 14325 22272
				-	-	-	-	-
Ti II	6491.580	2.06	-2.12	123.7	87.08	88.0	-	-
				-	-	-	-	-
				-	-	22.8	-	-
Ti II	6606.980	2.06	-2.85	-	-	31.0	11.1	64.1
				-	-	-	-	-
				-	15.6	-	33.7	75.9
Ti II	6680.133	3.10	-1.89	-	-	-	-	75.8
				-	-	-	-	-
				-	-	-	-	-
V I	6119.523	1.06	-0.32	24.9	-	-	-	19.90
				-	-	-	-	-
				-	-	-	-	-
V I	6199.196	0.29	-1.30	25.4	-	-	-	-
				-	-	-	-	-
				-	-	-	-	-
V I	6251.827	0.29	-1.34	23.2	-	-	-	-
				-	-	-	-	-
				-	-	-	-	-
V II	3787.232	2.52	-0.63	-	-	-	-	-
				-	-	-	-	50.5
				-	-	-	-	-
V II	3863.785	1.80	-1.22	-	-	-	-	-
				-	-	-	-	39.2
				-	-	-	-	-
V II	3899.129	1.80	-0.78	-	-	-	-	-
				-	-	-	-	75.4
				41.3	-	87.4	-	-
V II	3916.411	1.43	-1.05	-	-	-	-	-
				-	-	-	-	-
				-	-	73.9	-	-
V II	3951.960	1.48	-0.78	-	-	-	-	-
				-	-	-	-	104.3
				41.0	-	109.9	-	-
V II	3977.733	1.48	-1.56	-	-	-	-	-
				-	-	-	-	31.5
				-	-	42.9	-	-
V II	3997.117	1.48	-1.23	-	-	-	-	-
				-	-	-	-	-
				-	-	51.4	-	-
V II	4002.936	1.43	-1.45	-	-	-	-	-
				-	-	-	-	-
				-	-	50.9	-	-
V II	4005.705	1.82	-0.52	-	-	-	103.9	-
				-	-	-	28.2	111.1
				53.7	-	93.7	-	-
V II	4008.169	1.79	-2.07	-	-	-	-	-
				-	-	-	-	-
				-	35.7	-	-	-
V II	4023.378	1.80	-0.69	-	-	-	99.3	-
				-	-	-	-	93.6
				-	145.8	91.1	-	-
V II	4035.630	1.79	-0.54	-	-	-	-	-
				-	-	142.3	26.4	91.8
				49.3	-	-	-	-
V II	4036.777	1.48	-1.59	-	-	-	-	-
				-	-	-	-	28.6

Table E.1: continued.

ion	λ (Å)	EP (eV)	log gf	05113	05341	06530	07134	07430
				08143B	08143R	08281	13245	14325
				14429	17279	19500	22223	22272
				-	90.4	31.0	-	-
				-	-	-	28.8	-
V II	4051.054	1.80	-1.75	-	-	-	-	-
				-	49.4	-	-	-
				-	-	-	40.3	-
V II	4183.428	2.05	-1.11	-	-	-	-	28.1
				-	-	39.5	-	-
				-	-	-	41.9	-
V II	4202.355	1.70	-1.52	-	-	-	-	-
				-	-	-	-	-
				-	-	-	-	-
V II	4234.256	1.69	-1.92	-	-	-	-	-
				-	45.8	-	-	-
				-	-	-	-	-
V II	4254.350	1.68	-1.11	-	-	-	-	70.2
				-	-	57.5	-	-
				-	-	-	-	-
V II	4564.579	2.27	-1.39	56.9	-	-	-	-
				-	-	-	97.6	-
				-	-	-	-	-
V II	4965.408	3.80	-1.12	8.1	-	-	-	-
				-	-	-	-	-
				-	-	-	-	-
V II	5785.633	2.49	-2.30	-	-	-	-	-
				-	-	-	13.6	-
				-	-	-	-	-
V II	5819.924	2.52	-1.69	-	-	-	-	-
				-	-	-	24.4	29.0
				-	-	-	-	-
V II	5928.851	2.52	-1.68	-	18.8	-	-	-
				-	-	-	29.1	32.2
				-	-	-	-	24.2
V II	6086.932	2.56	-2.34	-	-	-	-	-
				-	-	-	-	-
				-	-	-	-	21.1
V II	6261.087	2.54	-2.39	-	-	-	-	-
				-	-	-	-	-
				-	-	-	91.3	-
Cr I	4254.350	0.00	-0.11	-	-	-	-	83.5
				-	-	62.0	-	-
				-	-	-	77.9	-
Cr I	4274.810	0.00	-0.23	-	-	-	-	52.6
				-	-	39.1	-	-
				-	-	-	-	-
Cr I	4626.180	0.97	-1.32	36.0	-	-	-	-
				-	-	-	-	99.3
				-	-	-	16.2	-
Cr I	4646.170	1.03	-0.70	102.1	-	-	-	-
				-	-	-	-	-
				-	-	-	-	-
Cr I	4652.170	1.00	-1.03	59.7	-	-	-	-
				-	-	-	88.6	-
				-	-	-	-	-
Cr I	5208.400	0.940	-0.80	-	-	15.74	-	46.7
				-	124.0	36.5	-	-
				126.4	-	-	-	-
Cr I	5247.570	0.96	-1.64	-	19.2	-	-	-

Table E.1: continued.

ion	λ (Å)	EP (eV)	log gf	05113 08143B 14429	05341 08143R 17279	06530 08281 19500	07134 13245 22223	07430 14325 22272
				-	8.8	-	41.7	64.2
				158.8	25.4	21.1	-	93.5
Cr I	5296.691	0.98	-1.36	-	23.1	-	-	-
				-	-	-	-	-
				83.3	-	-	-	-
Cr I	5329.138	2.91	-0.01	-	-	-	-	-
				-	-	-	-	-
				169.0	33.0	22.0	-	101.3
Cr I	5348.330	1.00	-1.29	-	36.4	-	-	-
				-	-	-	69.0	95.8
				-	-	-	-	-
Cr I	5409.800	1.03	-0.72	-	69.2	-	-	-
				-	-	-	115.4	-
				-	-	-	-	-
Cr I	5787.930	3.32	-0.08	-	-	-	-	-
				-	-	-	19.6	-
				-	-	-	-	-
Cr I	7400.190	2.90	-0.11	25.6	-	-	-	-
				-	-	-	33.2	46.9
				-	-	-	-	-
Cr II	3979.504	5.67	-0.86	-	-	-	26.3	-
				24.5	-	-	-	-
				-	-	-	-	-
Cr II	4242.364	3.87	-1.17	-	-	-	84.6	169.7
				86.2	-	146.0	-	-
				-	-	-	73.6	-
Cr II	4252.632	3.86	-1.81	-	-	-	-	69.7
				35.4	-	60.5	145.8	-
				-	-	-	-	-
Cr II	4261.913	3.86	-1.34	-	-	-	54.1	145.6
				76.0	124.0	117.2	-	-
				-	-	-	-	-
Cr II	4269.277	3.85	-2.02	-	-	-	-	-
				-	-	35.6	-	-
				-	-	-	-	-
Cr II	4275.567	3.86	-1.52	-	-	-	39.0	114.8
				58.6	114.2	89.2	-	-
				-	-	-	-	-
Cr II	4284.188	3.85	-1.67	-	-	-	31.9	-
				37.8	-	-	-	-
				-	-	-	-	-
Cr II	4554.988	4.07	-1.28	-	-	-	-	-
				58.3	-	-	-	-
				-	-	-	-	-
Cr II	4565.740	4.04	-1.82	-	-	-	-	-
				30.2	-	-	-	-
				-	-	-	-	-
Cr II	4588.199	4.07	-0.63	-	-	-	-	-
				146.2	-	-	-	-
				-	-	-	-	-
Cr II	4592.049	4.07	-1.22	-	-	-	-	-
				69.8	-	-	-	-
				-	-	-	92.8	-
Cr II	4616.640	4.07	-1.29	-	-	-	-	117.5
				59.4	-	100.9	-	-
				-	-	-	-	-
Cr II	4618.803	4.07	-0.84	-	-	-	-	-

Table E.1: continued.

ion	λ (Å)	EP (eV)	log gf	05113 08143B 14429	05341 08143R 17279	06530 08281 19500	07134 13245 22223	07430 14325 22272
				109.4	-	-	-	-
				-	-	-	-	-
Cr II	4634.070	4.07	-0.99	-	-	-	-	-
				98.8	-	-	-	-
				-	96.8	116.3	61.2	123.8
Cr II	4812.350	3.86	-1.80	139.3	117.4	-	-	56.6
				31.1	78.3	53.1	-	130.6
				-	-	-	-	-
Cr II	4824.127	3.87	-0.97	-	-	-	-	-
				115.6	-	-	-	-
				-	-	-	-	-
Cr II	4836.229	3.86	-1.96	-	-	-	-	64.8
				34.7	-	44.4	-	-
				-	-	-	124.3	-
Cr II	4848.250	3.86	-1.14	-	-	-	74.8	157.8
				100.9	-	-	-	-
				-	-	-	-	-
Cr II	4876.400	3.85	-1.46	-	-	-	46.1	140.1
				82.4	-	127.7	-	-
				-	60.3	89.1	42.0	-
Cr II	4884.600	3.86	-2.08	109.5	95.8	68.3	12.3	41.9
				-	67.0	36.4	136.2	116.1
				-	-	-	-	-
Cr II	5237.330	4.07	-1.39	-	-	-	50.0	126.6
				75.6	118.7	112.5	-	-
				-	52.8	57.9	29.9	-
Cr II	5246.768	3.71	-2.47	-	61.5	37.8	-	23.2
				-	48.8	22.6	-	-
				-	-	-	-	-
Cr II	5249.437	3.76	-2.49	-	-	-	-	21.2
				-	44.7	23.4	-	-
				-	-	-	-	-
Cr II	5274.964	4.07	-1.56	-	-	-	-	-
				46.8	-	-	-	-
				-	71.3	81.3	45.2	98.0
Cr II	5305.870	3.83	-2.08	-	87.8	58.7	-	45.9
				22.8	-	46.0	134.4	103.1
				-	81.2	94.4	45.3	99.6
Cr II	5308.430	4.07	-1.81	-	103.7	69.8	-	-
				25.0	61.7	44.1	137.9	120.9
				-	-	61.1	24.5	-
Cr II	5310.700	4.07	-2.28	-	54.3	35.9	-	21.5
				-	-	27.3	83.9	-
				-	-	-	-	-
Cr II	5313.590	4.07	-1.78	-	126.4	-	20.6	-
				36.8	-	65.4	-	-
				-	80.5	105.1	-	93.2
Cr II	5334.869	4.07	-1.89	-	107.1	79.0	-	59.1
				33.4	71.0	56.4	140.2	98.0
				-	67.6	75.1	-	90.7
Cr II	5407.604	3.83	-2.15	-	84.2	52.1	-	39.6
				16.0	45.7	29.2	107.6	106.4
				-	40.6	62.4	26.8	81.0
Cr II	5420.922	3.76	-2.46	-	51.2	35.3	8.5	25.8
				-	53.4	26.6	99.1	68.0
				-	-	-	-	-
Cr II	5478.365	4.18	-1.97	-	-	-	-	-

Table E.1: continued.

ion	λ (Å)	EP (eV)	log gf	05113 08143B 14429	05341 08143R 17279	06530 08281 19500	07134 13245 22223	07430 14325 22272
				22.2	-	-	-	-
				-	65.3	74.6	39.7	-
Cr II	5502.090	4.17	-1.99	-	67.8	45.9	-	32.5
				18.9	41.8	34.1	102.2	-
				-	-	-	28.7	-
Cr II	5503.240	4.14	-2.25	-	-	36.2	-	21.1
				-	-	28.5	-	61.7
				-	-	-	34.9	-
Cr II	5508.630	4.15	-2.11	-	63.5	39.2	-	26.6
				14.7	40.0	32.3	94.5	-
				-	38.9	53.1	27.6	-
Cr II	5510.730	3.83	-2.48	-	45.0	31.3	-	24.5
				-	-	27.2	77.8	61.7
				-	-	-	-	-
Mn I	4030.750	0.00	-0.49	-	-	-	-	51.0
				-	-	34.3	-	-
				-	-	-	-	-
Mn I	4034.480	0.00	-0.84	-	-	-	-	-
				-	-	18.1	-	-
				-	-	-	11.2	-
Mn I	4754.040	2.28	-0.09	80.0	-	-	-	-
				-	-	-	117.5	125.3
				-	-	-	-	-
Mn I	4765.860	2.94	-0.08	32.5	-	-	-	-
				-	-	-	-	-
				-	-	2.10	16.3	-
Mn I	4783.420	2.300	-1.40	104.1	3.46	-	-	-
				-	-	-	-	-
				-	-	-	-	30.1
Mn I	5420.350	2.14	-1.46	-	-	-	-	-
				-	-	-	-	-
				4.25	-	0.43	-	72.6
Mn I	6021.800	3.070	-1.52	-	0.70	-	-	-
				-	-	-	50.8	-
				-	-	-	-	-
Mn II	4205.377	1.81	-3.44	-	-	-	-	-
				-	-	29.2	-	-
				-	-	-	-	-
Mn II	4238.791	1.83	-3.63	-	-	-	-	-
				-	-	21.5	-	-
				-	-	-	-	-
Mn II	4259.200	5.40	-1.44	-	-	-	-	-
				-	-	11.4	-	-
				-	40.7	-	-	-
Mn II	4292.237	5.38	-1.54	-	-	-	-	-
				-	-	-	-	-
				-	-	-	-	-
Mn II	4326.639	5.40	-1.25	-	-	-	-	-
				12.0	-	16.6	-	-
				-	-	-	15.6	-
Mn II	4755.727	5.40	-1.24	-	-	-	-	-
				13.7	-	14.6	-	-
				-	-	-	-	-
Mn II	4806.822	5.42	-1.57	-	-	-	-	-
				-	17.6	-	-	-
				-	-	-	-	-
Mn II	5559.047	6.18	-1.31	-	7.6	-	-	-

Table E.1: continued.

ion	λ (Å)	EP (eV)	log gf	05113 08143B 14429	05341 08143R 17279	06530 08281 19500	07134 13245 22223	07430 14325 22272
				-	6.5	-	-	-
				-	-	-	11.3	-
Mn II	7387.189	3.71	-2.53	-	-	-	-	-
				-	-	-	-	-
				-	-	-	30.2	-
Mn II	7415.810	3.71	-2.18	-	-	-	-	-
				-	-	-	-	-
				-	-	-	-	-
Mn II	7432.230	3.70	-2.79	25.2	-	-	-	-
				-	-	-	-	26.52
				-	-	-	16.5	-
Mn II	7432.300	3.71	-2.49	-	-	-	-	-
				-	-	-	-	-
				-	-	-	-	-
Fe I	3758.232	0.96	-0.03	-	-	-	-	-
				134.3	-	-	-	-
				-	-	-	-	-
Fe I	3787.880	1.01	-0.86	-	-	-	-	-
				29.9	-	-	-	-
				-	-	-	-	-
Fe I	3805.350	3.30	0.37	-	-	-	-	51.6
				-	-	-	-	-
				-	-	-	-	-
Fe I	3815.839	1.49	0.24	-	-	-	89.3	-
				-	-	-	-	-
				-	-	-	-	-
Fe I	3820.425	0.86	0.12	-	-	-	134.8	-
				-	-	-	-	-
				-	-	-	-	-
Fe I	3821.177	3.27	0.20	-	-	-	23.9	-
				-	-	-	-	-
				-	-	-	-	-
Fe I	3825.880	0.92	-0.04	-	-	-	117.3	-
				-	-	-	-	-
				-	-	-	-	-
Fe I	3846.799	3.25	-0.02	-	-	-	13.8	-
				-	-	-	-	-
				-	-	-	-	-
Fe I	3859.911	0.00	-0.71	-	-	-	96.4	-
				121.9	-	-	-	-
				-	-	-	-	-
Fe I	3865.523	1.01	-0.98	-	-	-	27.0	-
				-	-	-	-	-
				-	-	-	-	-
Fe I	3872.501	0.99	-0.93	-	-	-	34.8	-
				-	-	-	-	-
				-	-	-	-	-
Fe I	3899.707	0.09	-1.53	-	-	-	-	-
				44.3	-	-	-	-
				-	-	-	-	-
Fe I	3922.911	0.05	-1.65	-	-	-	-	-
				26.9	-	-	-	-
				-	-	-	-	-
Fe I	3927.919	0.11	-1.52	-	-	-	24.7	-
				-	-	-	-	-
				-	-	-	-	-
Fe I	4045.812	1.49	0.28	-	-	-	124.6	-

Table E.1: continued.

ion	λ (Å)	EP (eV)	log gf	05113 08143B 14429	05341 08143R 17279	06530 08281 19500	07134 13245 22223	07430 14325 22272
				137.5	-	-	-	-
				-	-	-	-	-
Fe I	4063.593	1.56	0.06	-	-	-	71.1	-
				86.6	-	-	-	-
				-	-	-	-	-
Fe I	4071.737	1.61	-0.02	-	-	-	54.4	-
				73.4	-	-	-	-
				-	-	-	-	-
Fe I	4132.058	1.61	-0.68	-	-	-	-	-
				23.9	-	-	-	-
				-	-	-	-	-
Fe I	4175.640	2.84	-0.67	-	-	53.0	-	-
				-	-	12.7	-	-
				-	-	-	-	-
Fe I	4199.095	3.05	0.15	-	-	-	-	-
				26.9	-	-	-	-
				-	-	-	-	-
Fe I	4235.936	2.42	-0.34	-	-	-	23.0	-
				-	-	-	-	-
				-	-	-	-	-
Fe I	4250.786	1.56	-0.71	-	-	-	-	-
				36.7	-	-	-	-
				-	-	-	-	-
Fe I	4260.473	2.40	0.11	-	-	-	40.3	-
				51.0	-	-	-	-
				-	-	-	-	-
Fe I	4271.153	2.45	-0.35	-	-	-	-	-
				23.0	-	-	-	-
				-	-	-	-	-
Fe I	4271.760	1.49	-0.16	-	-	-	55.2	-
				73.1	-	-	-	-
				-	-	-	-	-
Fe I	4325.761	1.61	0.01	-	-	-	71.5	-
				87.2	-	-	-	-
				-	-	-	-	-
Fe I	4383.544	1.49	0.20	-	-	-	99.7	-
				116.1	-	-	-	-
				-	-	-	-	-
Fe I	4404.750	1.56	-0.14	-	-	-	73.0	160.0
				60.7	-	-	-	-
				-	-	-	-	-
Fe I	4466.550	2.83	-0.59	187.4	-	65.3	-	-
				-	101.0	-	-	-
				-	-	-	-	-
Fe I	4800.649	4.14	-1.03	21.3	-	-	-	-
				-	-	-	40.1	-
				-	-	145.1	-	-
Fe I	4871.320	2.87	-0.41	-	-	88.7	-	32.8
				-	95.0	-	-	-
				-	-	124.0	42.4	-
Fe I	4872.140	2.88	-0.60	166.8	158.7	59.4	-	17.4
				-	90.4	16.6	-	-
				-	-	77.9	23.8	-
Fe I	4878.210	2.88	-1.01	112.0	99.3	28.9	-	-
				-	-	6.6	162.3	-
				-	-	-	59.2	-
Fe I	4890.750	2.88	-0.43	-	169.5	85.8	-	23.7

Table E.1: continued.

ion	λ (Å)	EP (eV)	log gf	05113 08143B 14429	05341 08143R 17279	06530 08281 19500	07134 13245 22223	07430 14325 22272
				-	101.4	23.5	-	-
				-	-	-	74.3	-
Fe I	4891.490	2.85	-0.14	-	-	113.9	16.5	49.7
				-	-	43.9	-	-
				-	-	-	-	-
Fe I	4896.439	3.88	-1.90	-	-	-	-	-
				-	-	-	12.1	-
				-	-	80.1	-	-
Fe I	4903.310	2.88	-0.93	119.3	99.5	38.6	-	10.9
				-	60.4	-	-	-
				-	-	-	-	50.3
Fe I	4907.732	3.43	-1.82	-	-	-	-	-
				-	-	-	-	-
				-	148.0	142.3	60.8	-
Fe I	4918.994	2.87	-0.34	-	170.5	85.0	-	25.4
				14.3	107.4	29.3	-	-
				-	-	-	-	-
Fe I	4920.502	2.83	0.07	-	-	-	28.9	-
				-	-	-	-	-
				-	-	-	91.5	-
Fe I	4920.503	2.83	0.07	-	-	-	-	74.5
				35.0	-	64.4	-	-
				-	-	-	-	-
Fe I	4924.770	2.28	-2.20	37.5	-	-	-	-
				-	-	-	87.5	-
				-	16.4	-	-	-
Fe I	4930.215	3.96	-1.20	-	-	-	-	-
				-	-	-	35.6	-
				-	-	21.8	-	-
Fe I	4939.687	0.86	-3.33	46.4	-	-	-	-
				-	-	-	96.3	-
				-	-	-	-	-
Fe I	4946.388	3.37	-1.01	-	-	-	-	-
				-	36.7	-	111.9	-
				-	-	-	-	-
Fe I	4957.596	2.81	0.23	-	-	-	-	-
				39.2	-	-	-	-
				-	64.8	49.2	10.8	-
Fe I	4966.089	3.33	-0.84	85.0	80.3	18.8	-	-
				-	-	-	132.0	-
				-	-	-	-	-
Fe I	4968.698	3.64	-1.63	-	-	-	-	-
				-	-	-	32.3	-
				-	-	-	-	-
Fe I	4969.918	4.22	-0.75	40.2	-	-	-	-
				-	-	-	63.5	-
				-	-	-	-	-
Fe I	4973.012	3.96	-0.85	-	-	-	-	-
				-	-	-	72.1	-
				-	-	-	-	-
Fe I	4988.950	4.15	-0.79	-	-	-	-	-
				-	19.8	-	60.7	-
				-	-	-	-	-
Fe I	5002.793	3.40	-1.44	-	17.0	7.1	-	-
				-	13.8	-	59.1	-
				-	-	-	14.3	-
Fe I	5014.943	3.94	-0.27	-	77.2	26.5	-	-

Table E.1: continued.

ion	λ (Å)	EP (eV)	log gf	05113 08143B 14429	05341 08143R 17279	06530 08281 19500	07134 13245 22223	07430 14325 22272
				-	61.5	6.8	148.2	-
				-	63.1	36.2	-	-
Fe I	5022.236	3.98	-0.49	-	58.3	18.1	-	-
				-	-	-	-	-
				-	-	-	-	-
Fe I	5029.618	3.42	-1.90	-	-	-	-	-
				-	-	-	28.9	-
				-	-	-	-	-
Fe I	5031.915	4.37	-1.52	-	-	-	-	-
				-	-	-	10.2	-
				-	107.6	81.4	20.8	-
Fe I	5049.820	2.28	-1.35	-	102.8	33.7	-	-
				-	-	-	-	-
				-	-	-	15.9	-
Fe I	5074.748	4.22	-0.16	-	81.9	24.0	-	-
				-	48.6	-	129.6	-
				-	69.1	-	-	-
Fe I	5083.339	0.96	-2.91	-	60.9	11.1	-	-
				-	-	-	128.0	-
				-	57.8	-	-	121.3
Fe I	5090.774	4.26	-0.36	-	52.2	15.6	-	-
				-	33.5	-	105.5	89.8
				-	73.2	-	-	-
Fe I	5110.413	0.00	-3.76	-	-	-	-	-
				-	-	-	159.4	-
				-	-	-	-	-
Fe I	5125.117	4.22	-0.08	-	-	-	-	-
				-	-	-	140.8	-
				-	-	-	-	-
Fe I	5162.273	4.18	0.08	-	110.1	-	-	9.8
				-	64.2	10.2	-	-
				-	124.5	105.2	39.5	-
Fe I	5171.596	1.49	-1.76	-	150.2	50.7	-	-
				-	-	16.5	-	-
				-	-	-	-	-
Fe I	5192.343	3.00	-0.42	-	-	-	-	-
				9.3	-	-	-	-
				-	-	78.1	23.2	-
Fe I	5194.942	1.56	-2.06	-	91.6	23.8	-	-
				-	-	-	-	-
				-	45.4	27.8	-	123.5
Fe I	5198.711	2.22	-2.14	-	44.2	-	-	-
				-	19.0	-	104.9	-
				-	72.8	45.6	-	-
Fe I	5202.336	2.18	-1.84	-	76.5	-	-	-
				-	42.2	-	154.4	162.3
				-	-	-	13.5	-
Fe I	5216.274	1.61	-2.12	-	-	-	-	-
				-	-	-	-	191.1
				-	167.4	174.2	80.8	-
Fe I	5232.940	2.94	-0.08	-	-	111.8	-	-
				-	-	47.4	-	-
				143.3	42.3	27.5	-	114.4
Fe I	5242.491	3.63	-0.97	-	31.1	-	-	-
				-	23.2	-	-	-
				-	126.8	102.8	34.8	-
Fe I	5266.550	3.00	-0.49	-	153.5	68.8	6.5	19.9

Table E.1: continued.

ion	λ (Å)	EP (eV)	log gf	05113 08143B 14429	05341 08143R 17279	06530 08281 19500	07134 13245 22223	07430 14325 22272
				-	-	19.7	-	-
				-	-	-	-	-
Fe I	5269.537	0.86	-1.32	-	-	-	-	79.4
				-	-	-	-	-
				-	-	-	55.7	-
Fe I	5270.360	1.61	-1.51	-	-	69.2	-	-
				-	101.9	19.7	-	-
				-	85.9	73.7	20.7	174.9
Fe I	5281.790	3.04	-0.83	-	96.0	33.8	-	-
				-	-	9.7	168.1	173.6
				-	-	-	-	-
Fe I	5288.525	3.69	-1.51	-	12.6	-	-	-
				-	-	-	35.5	-
				-	-	-	-	-
Fe I	5322.041	2.28	-2.84	-	-	-	-	-
				-	-	-	25.2	-
				-	144.1	139.6	59.1	-
Fe I	5324.179	3.24	-0.10	-	-	77.7	-	31.8
				-	122.8	29.7	-	-
				-	-	-	-	166.8
Fe I	5339.929	3.27	-0.68	-	94.5	-	-	-
				-	60.2	-	173.3	-
				-	-	76.1	22.6	-
Fe I	5341.024	1.61	-1.95	-	114.9	33.7	-	8.5
				-	53.7	-	-	-
				-	77.4	74.8	23.6	143.0
Fe I	5364.871	4.45	0.23	-	100.8	32.7	-	-
				-	65.7	-	145.6	124.8
				-	98.5	87.5	29.3	155.7
Fe I	5367.467	4.42	0.44	-	117.5	44.2	-	15.2
				-	73.7	12.2	180.9	165.5
				-	-	107.6	38.4	-
Fe I	5369.962	4.37	0.54	-	131.6	61.3	-	19.9
				-	93.1	21.3	-	-
				-	-	-	-	-
Fe I	5371.490	0.96	-1.65	-	-	-	-	-
				-	-	29.3	-	-
				-	18.4	12.7	-	61.5
Fe I	5373.709	4.47	-0.71	-	20.2	-	-	-
				-	13.8	-	42.6	-
				-	-	130.3	46.9	-
Fe I	5383.369	4.31	0.65	-	-	77.7	-	26.0
				15.9	-	29.0	-	-
				-	48.3	37.0	7.5	103.6
Fe I	5389.479	4.42	-0.25	-	45.3	12.4	-	-
				-	-	-	93.9	-
				-	-	-	-	-
Fe I	5393.168	3.24	-0.72	-	-	-	-	-
				-	61.6	-	-	-
				-	-	48.8	12.4	-
Fe I	5400.502	4.37	-0.10	-	60.3	19.9	-	7.3
				-	38.1	-	117.3	-
				-	-	135.0	-	-
Fe I	5405.775	0.99	-1.85	-	-	63.2	-	24.2
				-	-	18.3	-	-
				-	-	85.7	23.8	-
Fe I	5410.910	4.47	0.40	-	105.1	-	-	12.9

Table E.1: continued.

ion	λ (Å)	EP (eV)	log gf	05113 08143B 14429	05341 08143R 17279	06530 08281 19500	07134 13245 22223	07430 14325 22272
				7.9	67.7	14.0	163.4	-
				-	107.2	95.0	36.4	-
Fe I	5415.200	4.39	0.50	-	128.5	56.0	-	18.5
				10.0	82.8	20.0	-	-
				-	113.0	116.0	39.6	-
Fe I	5424.068	4.32	0.58	-	145.8	71.5	-	27.4
				13.4	98.6	26.1	-	-
				-	138.9	111.7	-	-
Fe I	5434.524	1.01	-2.12	-	157.7	47.7	-	-
				-	-	12.3	-	-
				178.3	63.5	61.3	16.6	130.8
Fe I	5445.042	4.39	0.04	-	79.7	23.3	-	-
				-	50.1	-	133.0	123.7
				-	148.3	-	-	-
Fe I	5446.917	0.99	-1.91	-	186.8	70.8	-	-
				-	-	16.0	-	-
				131.4	35.5	22.9	-	87.3
Fe I	5466.396	4.37	-0.57	-	28.4	-	-	-
				-	20.9	-	71.9	63.3
				-	-	-	-	79.2
Fe I	5487.746	4.32	-0.65	-	-	-	-	-
				-	-	-	75.1	72.2
				-	90.1	47.3	-	-
Fe I	5506.779	0.99	-2.80	-	61.7	-	-	-
				-	-	-	169.7	-
				-	-	-	-	-
Fe I	5522.447	4.21	-1.40	-	-	-	-	-
				-	-	-	15.0	-
				-	33.9	27.4	-	92.0
Fe I	5554.895	4.55	-0.38	-	35.9	-	-	-
				-	24.0	-	74.5	68.6
				-	-	-	-	38.5
Fe I	5560.212	4.43	-1.04	-	11.8	-	-	-
				-	-	-	23.4	-
				89.9	26.1	13.7	-	69.1
Fe I	5563.600	4.19	-0.84	-	24.7	-	-	-
				-	14.3	-	51.5	45.2
				88.2	-	-	-	-
Fe I	5567.391	2.61	-2.56	-	-	-	-	-
				-	-	-	-	-
				-	-	67.4	24.2	-
Fe I	5569.618	3.42	-0.49	-	100.3	-	-	11.4
				-	60.7	12.0	177.9	-
				-	100.8	99.8	35.0	-
Fe I	5572.842	3.40	-0.28	-	133.5	-	-	21.3
				-	74.0	17.3	-	-
				-	-	44.5	-	139.3
Fe I	5576.089	3.43	-0.85	-	-	-	-	-
				-	47.8	-	-	-
				-	-	-	-	17.1
Fe I	5584.765	3.75	-2.17	-	-	-	-	-
				-	-	-	-	-
				-	128.6	138.3	44.1	-
Fe I	5586.756	3.37	-0.12	-	170.0	-	-	25.9
				-	-	23.5	-	-
				-	146.6	-	56.0	-
Fe I	5615.644	3.33	0.05	-	-	-	-	34.8

Table E.1: continued.

ion	λ (Å)	EP (eV)	log gf	05113 08143B 14429	05341 08143R 17279	06530 08281 19500	07134 13245 22223	07430 14325 22272
				10.9	-	33.4	-	-
				-	-	-	-	35.1
Fe I	5618.633	4.21	-1.26	-	11.0	-	-	-
				-	-	-	24.0	-
				-	-	-	-	-
Fe I	5633.947	4.99	-0.12	-	22.4	-	-	-
				-	-	-	-	44.9
				-	-	-	-	-
Fe I	5638.262	4.22	-0.72	-	24.0	-	-	-
				-	24.1	-	58.7	-
				75.5	-	-	-	47.6
Fe I	5679.023	4.65	-0.77	-	13.3	-	-	-
				-	11.4	-	35.7	-
				-	-	-	-	84.9
Fe I	5686.530	4.55	-0.45	-	24.7	-	-	-
				-	-	-	57.2	-
				-	-	-	-	-
Fe I	5705.465	4.30	-1.36	-	-	-	-	-
				-	-	-	21.1	15.7
				-	-	-	-	-
Fe I	5731.762	4.26	-1.15	-	-	-	-	-
				-	-	-	34.4	-
				-	-	-	-	-
Fe I	5762.992	4.21	-0.41	-	40.8	-	-	-
				-	-	-	93.2	88.8
				-	-	-	-	-
Fe I	5806.725	4.61	-0.90	-	-	-	-	-
				-	-	-	28.1	-
				-	-	-	-	-
Fe I	5809.218	3.88	-1.69	-	-	-	-	-
				-	-	-	22.1	-
				-	-	-	-	-
Fe I	5852.219	4.55	-1.18	-	-	-	-	-
				-	-	-	17.8	-
				-	-	9.0	-	-
Fe I	5883.817	3.96	-1.21	-	15.9	-	-	-
				-	-	-	42.4	-
				-	-	-	-	93.0
Fe I	5934.655	3.93	-1.02	-	26.4	-	-	-
				-	-	-	60.2	-
				100.9	21.6	-	-	85.1
Fe I	6003.020	3.88	-1.12	-	-	-	-	-
				-	-	-	62.1	59.4
				113.1	-	-	6.9	91.2
Fe I	6020.169	4.61	-0.21	-	40.0	10.0	-	-
				-	24.3	-	79.9	68.9
				141.6	39.3	-	-	109.1
Fe I	6024.058	4.55	-0.06	-	56.6	17.2	-	-
				-	34.8	-	95.7	92.4
				-	-	-	-	66.0
Fe I	6027.051	4.08	-1.09	-	-	-	-	-
				-	12.2	-	47.0	45.3
				-	-	19.7	-	63.8
Fe I	6056.005	4.73	-0.40	-	-	5.4	-	-
				-	19.7	-	-	39.6
				-	61.5	39.3	7.6	144.7
Fe I	6065.482	2.61	-1.53	-	50.5	-	-	-

Table E.1: continued.

ion	λ (Å)	EP (eV)	log gf	05113 08143B 14429	05341 08143R 17279	06530 08281 19500	07134 13245 22223	07430 14325 22272
				-	-	-	125.4	140.4
Fe I	6082.711	2.22	-3.58	40.7 - -	- - -	- - -	- - -	- - -
Fe I	6093.644	4.61	-1.35	24.6 - -	- - -	- - -	- - -	- - -
Fe I	6136.596	2.45	-1.40	- - -	77.8 81.7 -	56.5 29.3 6.4	19.1 - -	- - -
Fe I	6137.692	2.59	-1.40	- - -	66.1 73.7 -	46.9 25.2 -	16.0 - -	161.7 - 158.5
Fe I	6151.618	2.18	-3.29	- - -	- - -	- - -	- - 13.4	- - -
Fe I	6165.360	4.14	-1.47	- - -	- - -	- - -	- - 19.7	- - -
Fe I	6170.507	4.79	-0.38	- - -	- - -	- - -	- - 51.7	- - -
Fe I	6187.990	3.94	-1.57	- - -	- 9.4 -	- - -	- - 21.1	- - -
Fe I	6191.558	2.43	-1.42	- - -	- - -	56.2 - -	- - -	- - -
Fe I	6200.313	2.60	-2.44	- - -	- 12.3 -	- - -	- - 41.0	67.9 - -
Fe I	6213.430	2.22	-2.48	156.5 - -	- - -	- - -	- - -	93.1 - 78.9
Fe I	6230.723	2.56	-1.28	- - -	75.2 85.8 -	66.6 20.7 7.2	17.2 - -	165.5 - -
Fe I	6254.259	2.28	-2.44	139.8 - -	- - -	- - -	- - 72.7	95.9 - 81.1
Fe I	6265.134	2.18	-2.55	164.4 - -	21.9 - -	- - -	- - 55.2	96.4 - 70.8
Fe I	6322.686	2.59	-2.43	125.8 - -	14.9 13.8 -	- - -	- - 43.1	60.0 - 45.7
Fe I	6380.743	4.19	-1.32	- - -	- 8.2 -	- - -	- - 24.6	40.6 - -
Fe I	6400.001	3.60	-0.29	- - -	87.4 94.8 -	75.9 - 11.5	21.7 - -	- - -
Fe I	6411.649	3.65	-0.66	- - -	59.9 61.0 37.8	36.7 - -	- - 124.3	127.3 - -
Fe I	6419.950	4.73	-0.09	118.1 -	29.4 30.8	19.9 12.4	5.1 -	84.7 -

Table E.1: continued.

ion	λ (Å)	EP (eV)	log gf	05113 08143B 14429	05341 08143R 17279	06530 08281 19500	07134 13245 22223	07430 14325 22272
				-	31.4	-	88.3	64.8
Fe I	6421.351	2.28	-2.01	- - -	46.1 48.2 -	24.8 - -	- - 126.9	140.5 - 138.8
Fe I	6430.846	2.18	-2.01	- - -	51.6 43.1 -	31.6 - -	- - 115.8	140.5 - -
Fe I	6469.193	4.83	-0.62	- - -	- - -	- - -	- - 32.5	- - -
Fe I	6592.914	2.73	-1.47	- - -	45.6 48.2 -	27.4 - -	- - -	133.8 - -
Fe I	6593.871	2.44	-2.42	147.7 - -	- 14.0 -	- - -	- - 55.2	79.1 - -
Fe I	6597.561	4.79	-0.92	44.9 - -	- - -	- - -	- - 17.0	- - -
Fe I	6609.110	2.56	-2.69	86.8 - -	8.1 - -	- - -	- - -	- - 30.7
Fe I	6750.153	2.24	-2.62	135.3 17.3 -	- 13.8 -	10.7 - -	- - 45.1	81.9 - 50.8
Fe I	6752.707	4.64	-1.20	41.3 6.5 -	- - -	- - -	- - -	- - -
Fe I	6810.263	4.61	-0.99	- 7.7 -	- - -	- - -	- - 19.9	- - 20.3
Fe I	6820.372	4.64	-1.17	- 6.8 -	- - -	- - -	- - -	- - 13.3
Fe I	6841.339	4.61	-0.60	- - -	- - -	- - -	- - 42.2	- - 46.3
Fe I	7130.922	4.22	-0.70	- 36.3 -	- - -	- - -	- - -	- - 69.7
Fe I	7411.162	4.28	-0.33	- 50.9 -	- - -	- - -	- - 81.5	- - 100.6
Fe I	7495.077	4.22	0.18	- 108.8 -	- - -	- - -	18.1 - -	- - 167.7
Fe I	7511.020	4.18	0.10	- 124.6 -	- - -	- - 9.9	20.4 - 165.4	- - -
Fe II	3779.570	2.54	-3.97	- - 28.8	- - -	- - -	- - -	- - -
Fe II	3781.511	4.50	-2.97	- - 17.8	- - -	- - -	- - -	- 25.4 -
Fe II	3783.342	2.28	-3.39	- -	- -	- -	- -	- -

Table E.1: continued.

ion	λ (Å)	EP (eV)	log gf	05113 08143B 14429	05341 08143R 17279	06530 08281 19500	07134 13245 22223	07430 14325 22272
				100.3	-	-	-	-
Fe II	3821.922	2.34	-4.03	- - -	- - -	- - -	- - -	- 55.9 -
Fe II	3827.085	4.73	-2.36	- - -	- - -	- - -	- 34.6 -	- 66.1 -
Fe II	3845.182	4.48	-2.43	- - -	- - -	- - -	- 39.2 -	- 73.0 -
Fe II	3938.293	1.67	-4.07	- - -	- - -	- - -	- 43.8 -	- - -
Fe II	3938.966	5.91	-1.93	- - -	- - -	- - -	- 25.4 -	- - -
Fe II	3945.211	1.70	-4.44	- - 37.9	- - -	- - -	- - -	- - -
Fe II	4032.939	4.50	-2.57	- - 42.3	- - -	- - -	- - -	- - -
Fe II	4119.518	2.54	-4.39	- - -	- - -	- - -	- - -	- 27.9 -
Fe II	4122.658	2.58	-3.30	- - 86.5	- - -	- - -	- 66.5 -	- 125.0 -
Fe II	4124.790	2.53	-4.02	- - 33.4	- - -	- - -	- - -	- - -
Fe II	4128.739	2.58	-3.58	- - 49.9	- - -	- - -	- - -	- - -
Fe II	4173.451	2.58	-2.74	- - 152.3	- - -	- - -	- 128.4 -	- - -
Fe II	4178.860	2.57	-2.53	- - 167.6	- - -	- - -	- 138.9 -	- - -
Fe II	4273.320	2.70	-3.30	- - 82.9	- - -	- - -	- 50.0 -	- 126.1 -
Fe II	4278.151	2.69	-3.95	- - -	- - -	- - -	- - -	- 57.5 -
Fe II	4296.565	2.70	-2.93	- - 122.7	- - -	- - -	- 90.3 -	- - -
Fe II	4303.170	2.70	-2.56	- - 144.1	- - -	- - -	- 127.9 -	- - -
Fe II	4351.761	2.70	-2.02	- - -	- - -	- - -	- 176.4 -	- - -
Fe II	4357.573	6.09	-2.01	- -	- -	- -	- -	- 24.8

Table E.1: continued.

ion	λ (Å)	EP (eV)	log gf	05113 08143B 14429	05341 08143R 17279	06530 08281 19500	07134 13245 22223	07430 14325 22272
				28.4	-	-	-	-
Fe II	4369.400	2.78	-3.58	- - 46.4	- - -	- - -	- 29.8 -	- 72.1 -
Fe II	4385.376	2.78	-2.68	- - 143.0	- - -	- - -	- 103.7 -	- - -
Fe II	4413.600	2.66	-3.69	- 154.1 29.4	- - 114.0	- - -	65.7 - -	- 67.4 -
Fe II	4416.820	2.77	-2.43	- - 146.6	- - -	- - -	- 131.4 -	- - -
Fe II	4451.540	6.14	-1.91	- - 31.6	- - -	- - -	- - -	- 28.7 -
Fe II	4472.922	2.84	-3.53	- - 43.1	- - -	- - -	- - -	- 84.9 -
Fe II	4489.175	2.83	-2.97	- - 102.3	- - -	- - -	- 74.6 -	- - -
Fe II	4491.407	2.85	-2.59	- - -	- - -	- - -	- 100.8 -	- 198.5 -
Fe II	4508.280	2.84	-2.25	- - 179.3	- - -	- - -	- 157.4 -	- - -
Fe II	4515.333	2.84	-2.45	- - -	- - -	- - -	- 117.7 -	- - -
Fe II	4520.218	2.81	-2.60	- - 142.8	- - -	- - -	- 112.6 -	- - -
Fe II	4522.627	2.84	-2.03	- - -	- - -	- - -	- 166.5 -	- - -
Fe II	4541.520	2.84	-2.81	- - 102.9	- - -	- - -	130.6 - -	- 180.0 -
Fe II	4576.332	2.84	-2.92	- - -	- - -	- - -	- - -	- 170.9 -
Fe II	4576.339	2.84	-2.92	- - 100.4	- - -	- - -	118.0 - -	- - -
Fe II	4580.053	2.58	-3.90	- - 39.2	- - -	- - -	- - -	- 65.8 -
Fe II	4582.840	2.83	-3.12	- - 80.1	- - -	- - 138.8	112.7 - -	- 129.6 -
Fe II	4593.822	2.89	-4.55	- - -	- - -	- - -	- - -	- 13.0 -
Fe II	4596.008	6.23	-1.96	- -	- -	- -	- -	- -

Table E.1: continued.

ion	λ (Å)	EP (eV)	log gf	05113 08143B 14429	05341 08143R 17279	06530 08281 19500	07134 13245 22223	07430 14325 22272
				32.0	-	-	-	-
				-	-	-	-	-
Fe II	4601.372	2.89	-4.52	-	-	-	-	9.9
				-	-	-	-	-
				-	-	-	92.4	-
Fe II	4620.520	2.83	-3.23	-	-	-	-	117.4
				66.5	-	120.6	-	-
				-	-	-	-	-
Fe II	4635.316	5.96	-1.65	-	-	-	-	49.9
				48.6	-	-	-	-
				-	-	-	-	-
Fe II	4648.933	2.58	-4.57	-	-	-	-	17.0
				-	-	-	-	-
				-	-	-	-	-
Fe II	4663.704	2.89	-3.89	-	-	-	-	45.0
				-	-	-	-	-
				-	-	-	100.6	-
Fe II	4666.750	2.83	-3.33	-	-	-	-	115.1
				52.0	-	108.6	-	-
				-	-	-	-	-
Fe II	4731.447	2.89	-3.00	-	-	-	-	135.6
				-	-	-	-	-
				-	-	-	-	-
Fe II	4893.812	2.83	-4.27	-	-	-	-	18.5
				-	-	-	-	-
				-	-	19.8	-	-
Fe II	4953.987	5.57	-2.76	20.9	19.9	19.5	-	12.2
				-	13.4	9.7	28.4	-
				-	97.9	137.1	67.6	139.2
Fe II	4993.347	2.81	-3.67	-	150.5	110.5	20.6	68.7
				36.1	104.5	67.3	-	153.8
				-	-	-	-	-
Fe II	5000.730	2.77	-4.56	-	-	-	-	14.3
				6.7	44.4	-	-	-
				-	-	-	-	-
Fe II	5100.660	2.79	-4.19	-	-	-	-	-
				-	-	-	-	94.9
				-	50.3	57.6	27.2	110.8
Fe II	5120.352	2.83	-4.21	-	84.0	54.8	-	24.0
				12.4	48.9	22.7	104.7	78.3
				-	-	-	-	-
Fe II	5132.657	2.81	-4.00	-	-	-	-	33.4
				-	63.0	33.9	154.5	-
				-	-	47.8	20.4	-
Fe II	5136.790	2.83	-4.31	-	-	-	-	20.8
				-	-	16.3	-	-
				-	-	-	-	-
Fe II	5146.117	2.83	-4.08	-	-	-	-	31.4
				-	-	-	-	-
				-	-	-	142.9	-
Fe II	5197.559	3.23	-2.25	-	-	-	111.2	-
				133.7	182.0	-	-	-
				-	-	-	146.8	-
Fe II	5234.619	3.22	-2.24	-	-	-	119.8	-
				155.6	165.5	-	-	-
				-	-	-	-	-
Fe II	5254.920	3.23	-3.34	-	-	-	21.5	70.2

Table E.1: continued.

ion	λ (Å)	EP (eV)	log gf	05113 08143B 14429	05341 08143R 17279	06530 08281 19500	07134 13245 22223	07430 14325 22272
				41.6	-	-	-	-
				-	-	-	-	-
Fe II	5256.931	2.89	-4.18	-	-	-	-	25.6
				14.6	-	-	-	-
				-	-	-	-	-
Fe II	5264.800	3.22	-3.01	-	-	-	-	-
				-	130.1	113.2	-	-
				-	-	38.5	-	-
Fe II	5272.400	5.95	-2.03	-	42.6	42.1	15.0	24.2
				21.7	34.1	25.8	58.6	-
				-	-	-	-	-
Fe II	5275.999	3.20	-1.91	-	-	-	150.1	-
				187.4	-	-	-	-
				-	159.2	-	116.9	-
Fe II	5284.098	2.89	-3.01	-	-	-	53.9	-
				-	139.6	-	-	-
				-	-	-	-	-
Fe II	5284.103	2.89	-2.99	-	-	-	-	153.9
				-	-	-	-	-
				-	127.4	151.1	85.8	162.9
Fe II	5325.559	3.22	-3.17	-	158.5	137.1	33.6	89.2
				49.7	103.5	85.6	-	175.6
				-	-	-	-	-
Fe II	5337.722	3.23	-3.79	-	-	-	-	40.6
				-	-	-	-	-
				-	-	-	-	-
Fe II	5362.861	3.20	-2.62	-	-	-	76.7	177.2
				-	-	-	-	-
				177.4	72.0	107.4	43.8	124.0
Fe II	5414.046	3.22	-3.62	-	115.3	78.2	14.3	42.0
				19.5	64.1	39.6	165.3	120.5
				-	108.8	152.1	75.2	150.6
Fe II	5425.247	3.20	-3.21	-	164.3	128.5	31.1	90.2
				44.6	92.3	87.1	-	164.9
				-	-	-	-	-
Fe II	5432.962	3.27	-3.53	-	-	-	16.9	53.3
				29.8	-	-	-	-
				-	35.4	49.8	21.9	82.2
Fe II	5525.125	3.27	-3.95	-	54.5	42.0	-	22.7
				-	40.0	19.0	100.9	67.5
				-	-	-	112.0	-
Fe II	5534.834	3.25	-2.77	-	-	-	60.2	141.6
				82.6	126.1	-	-	-
				81.3	-	33.7	14.9	-
Fe II	5627.490	3.37	-4.18	-	27.6	-	-	14.0
				-	-	11.6	77.3	-
				-	-	-	-	16.4
Fe II	5725.963	3.42	-4.83	-	-	-	-	-
				-	-	-	20.5	-
				-	8.4	10.2	-	-
Fe II	5732.724	3.39	-4.67	-	10.7	-	-	-
				-	10.0	-	25.2	16.7
				-	-	-	-	-
Fe II	5813.670	5.57	-2.75	-	-	-	-	-
				-	-	8.0	30.3	-
				160.3	85.2	99.5	49.9	128.7
Fe II	5991.368	3.15	-3.56	-	100.8	81.4	-	-

Table E.1: continued.

ion	λ (Å)	EP (eV)	log gf	05113 08143B 14429	05341 08143R 17279	06530 08281 19500	07134 13245 22223	07430 14325 22272
				-	-	49.4	171.0	138.5
				139.5	53.4	72.7	31.5	108.0
Fe II	6084.099	3.20	-3.80	-	74.8	53.9	-	31.5
				16.2	50.9	27.3	125.8	97.9
				126.4	-	-	18.0	-
Fe II	6113.330	3.21	-4.13	-	52.5	33.3	-	14.0
				-	-	14.0	88.3	76.1
				-	-	-	-	-
Fe II	6116.057	3.23	-4.69	-	-	-	-	-
				-	13.9	-	-	29.5
				168.9	91.3	134.0	69.9	158.8
Fe II	6147.741	3.89	-2.73	-	133.5	119.9	36.5	88.5
				47.1	94.4	81.9	182.8	145.9
				189.6	109.4	138.1	68.4	146.8
Fe II	6149.258	3.89	-2.72	-	133.4	126.8	38.0	86.6
				56.8	91.9	86.4	182.2	157.4
				-	-	17.1	-	-
Fe II	6179.388	5.57	-2.59	-	17.2	20.5	-	-
				-	-	11.8	27.2	20.0
				-	-	-	-	-
Fe II	6238.385	3.89	-2.75	-	-	-	38.6	85.7
				-	-	-	-	-
				74.1	25.8	38.4	-	66.3
Fe II	6239.910	3.89	-3.68	-	30.5	36.4	-	-
				-	29.1	-	73.8	50.0
				-	135.3	-	110.9	172.5
Fe II	6247.545	3.89	-2.34	-	-	-	68.9	128.6
				91.8	127.2	-	-	-
				-	-	28.4	-	-
Fe II	6248.898	5.51	-2.70	-	23.9	22.3	-	12.0
				-	-	10.0	34.5	-
				-	52.3	58.4	23.8	107.3
Fe II	6369.464	2.89	-4.19	-	55.5	48.3	-	-
				-	40.6	23.0	119.8	97.2
				62.4	30.0	46.9	23.6	-
Fe II	6383.721	5.55	-2.14	-	46.9	44.7	-	29.6
				-	38.3	27.8	72.6	33.2
				-	-	-	-	-
Fe II	6385.451	5.55	-2.62	-	28.7	26.6	-	12.4
				-	21.6	9.8	36.9	-
				178.4	113.0	142.1	71.3	154.7
Fe II	6416.921	3.89	-2.68	-	-	122.1	38.7	92.0
				-	90.8	-	-	150.8
				-	79.1	106.2	54.4	141.4
Fe II	6432.682	2.89	-3.71	-	126.5	89.1	18.6	56.7
				20.9	60.4	53.3	-	137.3
				-	-	-	-	-
Fe II	6446.430	6.20	-1.98	-	28.6	26.7	-	-
				13.2	17.2	15.2	-	-
				-	160.4	-	-	-
Fe II	6456.380	3.89	-2.12	-	-	-	82.2	-
				-	-	-	-	-
				-	-	43.9	-	-
Fe II	6482.204	6.22	-1.88	-	-	34.4	-	-
				-	22.0	20.3	44.9	-
				-	-	9.4	-	9.8
Fe II	6506.333	5.59	-3.11	-	-	-	-	-

Table E.1: continued.

ion	λ (Å)	EP (eV)	log gf	05113 08143B 14429	05341 08143R 17279	06530 08281 19500	07134 13245 22223	07430 14325 22272
				-	-	-	-	-
				-	125.5	-	85.6	-
Fe II	6516.030	2.88	-3.27	-	-	-	-	-
				-	-	-	-	-
				-	-	-	-	-
Fe II	6516.076	2.89	-3.32	-	-	-	30.3	-
				-	-	-	-	-
				-	-	-	-	-
Fe II	7222.400	3.89	-3.49	-	-	-	-	-
				-	-	-	93.8	63.0
				-	-	-	-	-
Fe II	7301.570	3.87	-3.70	43.9	-	-	-	-
				-	-	-	-	-
				-	-	-	22.1	-
Fe II	7449.340	3.87	-3.44	74.1	-	-	-	-
				-	-	20.2	97.1	-
				-	-	-	49.8	-
Fe II	7462.380	3.87	-2.98	112.2	-	-	-	-
				25.4	-	-	-	122.6
				-	-	-	-	-
Fe II	7479.694	3.89	-3.68	31.8	-	-	-	-
				-	-	12.1	-	42.0
				-	-	-	18.1	-
Fe II	7515.880	3.89	-3.50	51.0	-	-	-	-
				-	-	17.4	88.1	-
				-	-	-	-	-
Fe II	7711.710	3.90	-2.74	127.2	-	-	-	-
				-	-	-	-	163.1
				-	-	-	-	-
Co I	3995.307	0.92	-0.22	-	-	-	-	-
				-	45.9	-	-	-
				-	-	-	-	-
Co I	4121.318	0.92	-0.32	-	-	-	-	-
				-	28.0	-	-	-
				17.0	-	-	-	-
Co I	5647.233	2.28	-1.56	-	-	-	-	-
				-	-	-	-	-
				18.9	-	-	-	-
Co I	6771.034	1.88	-1.97	-	-	-	-	-
				-	-	-	-	-
				-	-	-	-	-
Co II	4160.656	3.410	-1.91	-	-	-	-	-
				-	-	15.90	-	-
				-	-	-	-	-
Co II	4660.633	3.36	-2.35	-	-	-	-	-
				-	-	-	24.1	-
				-	-	-	-	-
Ni I	3858.292	0.42	-0.94	-	-	-	-	49.1
				-	-	50.7	-	-
				-	-	-	-	-
Ni I	4686.220	3.60	-0.64	24.9	-	-	-	-
				-	-	-	35.8	63.1
				-	-	-	17.2	-
Ni I	4714.408	3.38	0.26	-	-	-	-	-
				-	-	-	-	-
				-	-	-	-	-
Ni I	4714.420	3.38	0.23	-	-	-	-	9.5

Table E.1: continued.

ion	λ (Å)	EP (eV)	log gf	05113 08143B 14429	05341 08143R 17279	06530 08281 19500	07134 13245 22223	07430 14325 22272
				-	-	11.1	-	-
				-	-	-	-	-
Ni I	4756.520	3.48	-0.34	57.3	-	-	-	-
				-	-	-	63.9	89.9
				-	-	-	-	-
Ni I	4806.990	3.68	-0.64	-	-	-	-	-
				-	20.8	-	28.6	-
				-	-	-	-	-
Ni I	4829.030	3.54	-0.33	53.9	-	-	-	-
				-	34.8	-	67.9	-
				-	-	-	-	-
Ni I	4831.180	3.61	-0.42	43.5	-	-	-	-
				-	-	-	-	-
				-	64.6	33.9	-	96.1
Ni I	4904.420	3.54	-0.17	60.4	-	-	-	-
				-	-	-	85.2	-
				-	-	-	-	-
Ni I	4913.980	3.77	-0.63	-	-	-	-	-
				-	15.2	-	-	-
				-	-	-	-	-
Ni I	4925.570	3.65	-0.82	22.8	-	-	-	-
				-	-	-	28.1	-
				-	-	-	-	78.6
Ni I	4937.350	3.61	-0.39	39.6	-	-	-	-
				-	23.4	-	52.2	-
				-	-	-	9.6	-
Ni I	4980.166	3.61	0.07	-	-	-	-	-
				-	-	-	-	-
				-	-	73.7	-	132.0
Ni I	5035.370	3.63	0.29	-	-	-	-	-
				-	-	-	115.3	-
				-	-	-	-	-
Ni I	5080.528	3.65	0.33	-	-	-	-	8.1
				-	-	7.1	-	-
				-	77.9	59.6	13.5	-
Ni I	5080.540	3.65	0.13	-	73.6	-	-	-
				-	-	-	-	-
				-	74.5	50.2	9.6	-
Ni I	5081.120	3.85	0.30	-	-	-	-	-
				-	-	-	95.2	-
				-	-	-	-	-
Ni I	5082.350	3.66	-0.54	-	-	-	-	-
				-	-	-	37.6	-
				-	59.5	45.6	-	102.7
Ni I	5084.100	3.68	0.03	-	-	-	-	-
				-	-	-	86.9	104.5
				-	-	-	-	52.7
Ni I	5578.730	1.68	-2.64	-	-	-	-	-
				-	-	-	-	-
				55.7	-	-	-	25.4
Ni I	5694.990	4.09	-0.61	-	9.2	-	-	-
				-	-	-	-	-
				-	-	-	-	100.1
Ni I	5709.555	1.68	-2.17	-	-	-	-	-
				-	-	-	-	-
				-	-	-	-	-
Ni I	5715.090	4.09	-0.21	-	19.2	-	-	-

Table E.1: continued.

ion	λ (Å)	EP (eV)	log gf	05113 08143B 14429	05341 08143R 17279	06530 08281 19500	07134 13245 22223	07430 14325 22272
				-	-	-	-	-
				115.5	-	-	-	53.8
Ni I	5754.670	1.93	-2.33	-	-	-	-	-
				-	-	-	24.4	44.5
				-	-	-	-	42.0
Ni I	6176.820	4.09	-0.53	-	-	-	-	-
				-	-	-	22.3	-
				142.3	20.1	-	-	60.0
Ni I	6643.640	1.68	-2.30	-	17.6	-	-	-
				-	-	-	-	85.5
				136.4	20.0	-	-	59.5
Ni I	6767.780	1.83	-2.17	27.3	-	-	-	-
				-	-	-	-	-
				47.4	-	-	-	-
Ni I	6772.320	3.66	-0.98	13.2	-	-	-	-
				-	-	-	-	27.8
				-	-	-	-	-
Ni I	7122.240	3.54	0.04	86.7	-	-	-	-
				-	-	-	-	-
				-	-	-	5.7	-
Ni I	7422.290	3.63	-0.14	72.5	-	-	-	-
				-	-	-	-	-
				-	-	-	-	-
Ni I	7525.118	3.63	-0.69	34.5	-	-	-	-
				-	-	-	-	49.3
				-	-	-	-	-
Ni I	7574.050	3.83	-0.63	18.3	-	-	-	-
				-	-	-	-	44.5
				-	-	-	-	-
Ni II	3849.554	4.03	-1.88	-	-	-	55.1	-
				60.9	-	-	-	-
				-	-	-	-	-
Ni II	4015.474	4.030	-2.42	-	-	59.43	20.6	51.1
				32.0	82.3	49.4	-	-
				-	-	-	-	-
Ni II	4067.030	4.03	-1.83	-	-	-	55.7	125.6
				73.1	-	-	-	-
				-	-	-	-	-
Ni II	4192.065	4.03	-3.06	-	-	-	-	14.8
				-	31.0	16.8	-	-
				-	-	-	-	-
Ni II	4244.779	4.03	-3.11	-	-	-	-	-
				-	32.1	-	-	-
				-	-	-	-	-
Ni II	4362.099	4.030	-2.70	-	-	35.86	-	-
				-	-	-	-	-
				-	-	-	40.0	-
Ni II	4362.100	4.03	-2.35	-	-	-	16.9	42.1
				22.5	-	-	-	-
				-	-	14.83	-	-
Ni II	5066.328	6.330	-1.85	-	-	-	-	-
				-	15.3	-	-	-
				-	8.84	4.07	-	48.3
Cu I	5218.197	3.820	-0.44	-	4.95	-	-	-
				-	-	-	8.59	11.79
				30.2	-	-	-	10.6
Cu I	5700.237	1.64	-2.58	-	-	-	-	-

Table E.1: continued.

ion	λ (Å)	EP (eV)	log gf	05113 08143B 14429	05341 08143R 17279	06530 08281 19500	07134 13245 22223	07430 14325 22272
				-	-	-	-	-
Zn I	4810.540	4.080	-0.17	189.90 - -	- 85.24 39.57	71.48 - -	- - 109.7	134.6 - 139.4
Zn I	6362.350	5.79	0.27	- - -	- - -	- - -	- - 28.5	- - -
Y II	3950.349	0.10	-0.47	- - 51.6	- - -	- - -	- 71.3 -	- - -
Y II	3982.591	0.130	-0.46	- - 54.3	- - -	- - -	- 70.42 -	- - -
Y II	4177.529	0.410	-0.16	- - -	- - -	- - -	- 85.68 -	- - -
Y II	4204.695	0.00	-1.76	- - -	- - -	- - -	120.0 - -	- - -
Y II	4309.631	0.180	-0.75	- - 54.6	- - 135.2	- - -	- 43.79 -	- - -
Y II	4358.728	0.10	-1.32	- - -	- - -	- - -	- - -	- 94.0 -
Y II	4398.010	0.13	-0.90	- - 33.8	- - -	- - -	- - -	- - -
Y II	4682.324	0.41	-1.51	- - -	- - -	- - -	109.3 - -	- 51.1 -
Y II	4786.580	1.03	-1.29	- - -	- - -	- 155.6 49.4	- - -	- 48.0 -
Y II	4823.304	0.99	-1.11	- - -	- - -	- - 60.2	- - -	- - -
Y II	4881.436	0.41	-2.79	- 128.4 -	102.5 91.4 -	105.2 29.7 -	23.2 - 114.8	- - -
Y II	4883.682	1.080	0.27	- - 72.0	- - -	- - -	- 91.23 -	- - -
Y II	4900.118	1.03	0.10	- - 81.4	- - -	- - -	- 85.6 -	- - -
Y II	5087.416	1.080	-0.17	- - 39.2	- - -	- - -	- 47.65 -	- - -
Y II	5119.112	0.99	-1.36	- - -	- - 52.5	- - 28.5	88.1 - -	- 30.3 -
Y II	5196.422	1.750	-1.27	198.98 - -	179.6 - -	- - 25.2	79.0 - -	- 22.4 -
Y II	5200.406	0.99	-0.57	- -	- -	- -	- 30.2	- -

Table E.1: continued.

ion	λ (Å)	EP (eV)	log gf	05113 08143B 14429	05341 08143R 17279	06530 08281 19500	07134 13245 22223	07430 14325 22272
				24.0	-	-	-	-
Y II	5205.724	1.030	-0.34	- - 30.3	- - -	- - -	- 37.63 -	- - -
Y II	5289.815	1.03	-1.85	- - -	134.8 161.0 -	139.4 - 9.5	- - -	- - 207.7
Y II	5402.774	1.84	-0.51	- - -	- - 62.0	- - 66.5	- - -	- 68.3 -
Y II	5473.388	1.74	-1.02	- - -	- - 34.9	- 130.6 33.3	- - -	- 28.3 -
Y II	5480.732	1.72	-0.99	- - -	- - 43.1	- 121.9 31.4	90.5 - -	- 36.1 -
Y II	5497.408	1.750	-0.58	- - -	- - 60.8	- - 69.2	- 9.05 -	- 72.8 -
Y II	5509.894	0.99	-0.95	- - 9.3	- - -	- - -	- - -	- - -
Y II	5546.009	1.75	-1.10	- - -	- - 41.3	- 129.5 29.9	82.7 - -	- - -
Y II	5662.925	1.94	0.16	- - -	- - -	- - -	- 31.5 -	- 145.9 -
Y II	5728.890	1.840	-1.12	213.21 - -	142.0 - 36.9	- 98.6 -	73.9 - -	- - -
Y II	6338.147	0.990	-3.10	- - -	- - -	- - -	- - -	52.66 - -
Y II	6613.733	1.75	-1.11	- - -	- - 27.0	- - -	84.9 - -	- - -
Y II	6795.414	1.74	-1.19	- - -	- - 28.5	- 103.5 23.2	82.2 - -	- - -
Y II	6832.478	1.75	-1.94	- 84.6 -	- - -	- - -	21.0 - 74.1	- - 125.1
Y II	6858.225	1.74	-1.97	- 84.5 -	- - -	- - -	24.1 - 92.2	- - 109.6
Y II	6895.979	1.75	-1.76	- - -	- - -	- - -	- - -	- - 158.6
Zr II	3817.590	0.530	-0.97	- - 46.7	- - -	- 129.3 -	- 53.02 -	- 87.3 -
Zr II	3843.018	0.36	-0.94	- - 72.8	- - -	- - -	- - -	- - -
Zr II	3915.934	0.530	-0.85	- - -	- - -	- - -	- 65.28	- - -

Table E.1: continued.

ion	λ (Å)	EP (eV)	log gf	05113 08143B 14429	05341 08143R 17279	06530 08281 19500	07134 13245 22223	07430 14325 22272
				-	-	-	-	-
Zr II	3958.220	0.530	-0.32	- - -	- - -	- - -	- 121.94 -	- - -
Zr II	3991.127	0.760	-0.31	- - 91.1	- - -	- - -	- 108.11 -	- - -
Zr II	4018.370	0.960	-0.99	- - -	- - 74.1	- - 71.2	- 32.87 -	- 58.7 -
Zr II	4029.684	0.71	-0.60	- - 58.5	- - 126.1	- - 141.0	- - -	- 120.3 -
Zr II	4034.083	0.800	-1.51	- - -	- - -	- - -	- 14.05 -	- - -
Zr II	4048.666	0.800	-0.53	- - -	- - -	- - -	- 82.62 -	- - -
Zr II	4050.320	0.71	-1.00	- - -	- - -	- - 102.0	- - -	- 94.8 -
Zr II	4090.510	0.760	-1.01	- - 31.6	- - 89.8	- - 96.8	- 40.32 -	- 70.1 -
Zr II	4149.198	0.800	-0.04	- - -	- - -	- - -	- 135.16 -	- - -
Zr II	4150.990	0.800	-0.99	- - 48.9	- - 102.8	- - 99.9	- 40.49 -	- 97.3 -
Zr II	4208.980	0.710	-0.51	- - -	- - -	- - -	- 92.22 -	- - -
Zr II	4211.907	0.530	-1.08	- - -	- - -	- - 114.7	- 46.90 -	- 103.9 -
Zr II	4258.041	0.560	-1.20	- - -	- - -	- - -	- 36.90 -	- - -
Zr II	4277.373	0.80	-1.40	- - -	- - 47.8	- 98.5 -	90.4 - -	- 25.7 -
Zr II	4286.536	0.97	-1.55	- - -	- - 46.2	- 94.6 29.8	74.8 - -	- - -
Zr II	4293.117	1.74	-0.80	- - 18.1	- - -	- - 36.9	82.7 - -	- - -
Zr II	4312.225	1.76	-1.59	- 102.5 -	- - -	- - -	- - -	- - -
Zr II	4317.299	0.71	-1.38	- - -	- - 63.0	- 136.8 51.5	- - -	- - -
Zr II	4323.641	2.49	-1.50	- -	- -	- -	14.4 -	- -

Table E.1: continued.

ion	λ (Å)	EP (eV)	log gf	05113 08143B 14429	05341 08143R 17279	06530 08281 19500	07134 13245 22223	07430 14325 22272
				-	-	-	-	-
Zr II	4359.720	1.24	-0.46	- - 60.8	- - -	- - 130.2	- - -	- 117.3 -
Zr II	4359.730	1.240	-0.51	- - -	- - -	- - -	- 58.66 -	- - -
Zr II	4370.947	1.210	-0.86	- - -	- - -	- - 95.4	- 32.88 -	- - -
Zr II	4379.742	1.530	-0.36	- - 55.0	- - -	- - -	- 55.97 -	- 113.2 -
Zr II	4401.385	0.97	-1.90	- - -	- - -	- - -	46.1 - -	- - -
Zr II	4403.350	1.18	-1.20	- - 15.3	- - 44.5	- 120.9 52.7	- - -	- 39.4 -
Zr II	4414.539	1.24	-1.17	- - -	- - -	- - 61.6	- - -	- 37.0 -
Zr II	4429.346	1.77	-1.40	- - -	- - -	- - 14.9	- - -	- - -
Zr II	4440.450	1.21	-1.13	- - -	- - 64.8	- - 53.5	- - -	- 52.8 -
Zr II	4445.902	1.67	-1.35	- - -	- - -	- 45.6 -	41.3 - -	- - -
Zr II	4457.431	1.18	-0.80	- - -	- - -	- - -	118.5 - -	- - -
Zr II	4494.418	2.41	-0.48	- - 19.3	- - -	- - -	- - -	- - -
Zr II	4495.455	1.21	-1.20	- - -	- - 38.5	- - -	79.4 - -	- 22.1 -
Zr II	4496.980	0.71	-0.86	- - 48.7	- - -	- - 123.6	- - -	- 122.8 -
Zr II	4601.953	2.43	-1.30	- 66.6 -	- - -	- - -	22.1 - -	- - -
Zr II	4613.972	0.97	-1.52	- - -	- - -	- - 32.2	91.5 - -	- - -
Zr II	4685.186	2.42	-0.90	- 126.6 -	- - -	- - -	- - -	- - -
Zr II	4816.500	1.01	-2.00	- 118.9 -	- 94.5 -	- 29.7 10.6	40.3 - -	- - -
Zr II	4962.310	0.97	-2.00	- -	- -	- -	- -	- -

Table E.1: continued.

ion	λ (Å)	EP (eV)	log gf	05113 08143B 14429	05341 08143R 17279	06530 08281 19500	07134 13245 22223	07430 14325 22272
				-	-	18.2	139.6	-
				-	-	-	49.3	-
Zr II	5000.869	1.67	-1.40	-	-	-	-	-
				-	-	-	-	-
				-	-	-	-	-
Zr II	5112.297	1.67	-0.59	-	-	163.1	33.51	48.7
				26.3	-	60.5	-	-
				-	-	-	-	-
Zr II	5124.982	1.53	-1.50	-	-	53.3	-	-
				-	-	-	-	-
				-	-	-	-	-
Zr II	5191.590	1.76	-0.71	-	-	-	-	52.8
				-	-	75.5	-	-
				-	-	82.9	40.0	-
Zr II	5477.822	1.83	-1.40	-	80.0	32.7	-	-
				-	-	-	-	141.3
				104.8	-	-	-	62.0
Zr II	6028.592	2.43	-1.40	-	52.5	19.6	-	-
				-	-	-	63.9	80.7
				-	-	-	-	-
Zr II	6313.574	2.49	-1.40	-	45.2	19.9	-	-
				-	-	-	64.1	-
				67.2	39.5	-	-	-
Zr II	6578.650	2.43	-1.50	-	-	-	-	-
				-	-	-	-	-
				-	-	-	21.2	-
Zr II	6677.924	2.42	-1.36	-	-	20.3	-	-
				-	-	-	-	-
				114.1	55.7	59.2	26.4	65.4
Zr II	6787.117	2.49	-1.17	53.9	-	-	-	-
				-	-	-	-	85.6
				-	-	-	-	-
Mo II	4363.632	3.110	-1.11	-	-	20.29	-	-
				-	-	-	32.7	-
				-	-	-	18.3	-
Mo II	4377.775	3.02	-1.00	-	-	-	-	-
				-	-	10.4	-	-
				-	-	-	-	-
Mo II	4433.510	3.06	-1.00	-	-	-	-	-
				-	-	7.6	-	-
				-	-	-	47.5	-
Ba II	4166.000	2.72	-0.42	-	-	67.85	-	-
				-	40.62	-	126.8	-
				-	-	-	65.1	-
Ba II	4524.925	2.51	-0.36	-	-	-	-	-
				-	-	-	-	-
				-	-	-	-	-
Ba II	5853.668	0.600	-1.00	-	-	-	38.36	74.42
				-	-	62.87	-	-
				-	-	-	-	-
Ba II	8737.763	5.700	-0.09	6.41	-	-	-	-
				-	-	-	-	-
				-	-	-	-	-
La II	3790.820	0.13	-0.08	-	-	-	27.6	30.8
				-	-	-	-	-
				-	-	-	-	-
La II	3871.640	0.13	-0.17	-	-	-	-	33.8

Table E.1: continued.

ion	λ (Å)	EP (eV)	log gf	05113 08143B 14429	05341 08143R 17279	06530 08281 19500	07134 13245 22223	07430 14325 22272
				-	-	34.0	-	-
				-	-	-	-	-
La II	3949.100	0.40	0.48	-	-	-	-	66.0
				19.2	-	-	-	-
				-	-	-	-	-
La II	3988.520	0.40	0.14	-	-	-	27.5	39.8
				16.8	108.7	32.5	-	-
				-	-	-	-	-
La II	3995.750	0.17	-0.09	-	-	-	-	31.4
				-	-	29.6	-	-
				-	-	-	-	-
La II	4025.870	0.32	-1.36	104.1	-	-	-	-
				-	-	-	-	-
				-	-	-	-	-
La II	4031.690	0.32	-0.09	-	-	-	-	-
				7.8	-	-	-	-
				-	-	-	-	-
La II	4042.910	0.93	0.33	-	-	-	-	27.2
				-	-	-	-	-
				-	-	-	-	-
La II	4086.710	0.00	-0.07	-	-	-	24.2	-
				14.5	-	-	-	-
				-	-	-	-	-
La II	4123.230	0.32	0.11	-	-	-	-	35.1
				-	-	-	-	-
				-	-	-	54.4	-
La II	4141.718	0.40	-0.79	-	-	55.0	-	-
				-	37.0	-	-	-
				-	-	-	47.7	-
La II	4286.958	1.95	0.20	123.7	-	-	-	-
				-	-	-	-	-
				-	-	-	65.9	-
La II	4322.503	0.17	-1.05	179.4	-	50.6	-	-
				-	28.0	-	-	-
				-	-	-	109.5	-
La II	4429.905	0.23	-0.37	-	-	127.5	-	-
				-	-	19.1	-	-
				-	-	-	45.1	-
La II	4526.111	0.77	-0.72	-	-	-	-	-
				-	-	-	-	-
				-	-	-	-	-
La II	4559.282	0.77	-1.31	64.2	-	-	-	-
				-	-	-	-	-
				-	-	-	28.5	-
La II	4605.775	0.71	-1.18	78.9	-	-	-	-
				-	-	-	-	-
				-	-	-	35.1	-
La II	4613.385	0.71	-0.78	-	-	-	-	-
				-	-	-	-	-
				-	-	-	35.9	-
La II	4619.874	1.75	-0.12	116.5	-	-	-	-
				-	-	-	-	-
				-	-	-	-	-
La II	4645.280	0.13	-1.79	76.8	-	-	-	-
				-	-	-	-	-
				-	-	-	40.9	-
La II	4655.480	1.95	0.11	-	-	-	-	-

Table E.1: continued.

ion	λ (Å)	EP (eV)	log gf	05113 08143B 14429	05341 08143R 17279	06530 08281 19500	07134 13245 22223	07430 14325 22272
				-	-	-	-	-
				-	-	-	52.9	-
La II	4662.498	0.00	-1.28	-	-	-	-	-
				-	-	-	-	-
				-	-	-	-	-
La II	4671.803	1.96	-0.47	52.3	-	-	-	-
				-	-	-	-	-
				-	-	-	26.4	-
La II	4692.491	1.75	-0.38	77.9	-	-	-	-
				-	-	-	63.6	-
				-	-	-	-	-
La II	4699.620	0.40	-1.78	48.5	-	-	-	-
				-	-	-	-	-
				-	-	-	-	-
La II	4716.443	0.77	-1.13	84.4	-	-	-	-
				-	-	-	50.9	-
				-	-	-	61.7	-
La II	4740.276	0.13	-1.06	-	-	-	-	-
				-	-	-	-	-
				-	-	-	36.9	-
La II	4743.071	1.78	-0.14	114.2	-	-	-	-
				-	-	-	77.5	-
				-	-	-	38.9	-
La II	4748.726	0.93	-0.76	-	-	-	-	-
				-	-	-	114.3	-
				-	-	-	29.0	-
La II	4804.039	0.23	-1.49	105.2	-	24.7	-	-
				-	-	-	-	-
				-	-	-	30.6	-
La II	4808.996	0.23	-1.49	104.6	-	32.8	-	-
				-	-	-	86.3	-
				-	-	-	-	88.0
La II	4826.873	0.17	-2.38	-	-	-	-	-
				-	-	-	-	-
				-	-	-	22.4	-
La II	4946.452	0.23	-1.67	-	-	26.7	-	-
				-	-	-	-	-
				-	167.6	-	46.8	-
La II	4970.386	0.32	-1.12	-	128.6	44.2	-	-
				-	-	-	-	-
				-	-	-	-	-
La II	4986.819	0.17	-1.18	-	-	39.5	-	-
				-	18.7	-	-	-
				-	-	-	65.2	-
La II	4999.461	0.40	-0.75	-	148.5	70.8	-	-
				-	26.3	9.9	-	-
				-	-	-	51.7	-
La II	5114.559	0.23	-1.04	-	144.2	56.5	-	-
				-	25.7	-	-	-
				-	159.2	130.3	-	-
La II	5290.818	0.00	-1.72	-	66.3	21.1	-	-
				-	-	-	66.8	-
				-	-	-	-	-
La II	5303.528	0.32	-1.41	-	86.1	42.9	-	-
				-	-	-	-	-
				157.2	95.1	-	-	-
La II	5377.052	2.30	-0.32	-	-	-	-	-

Table E.1: continued.

ion	λ (Å)	EP (eV)	log gf	05113	05341	06530	07134	07430
				08143B	08143R	08281	13245	14325
				14429	17279	19500	22223	22272
				-	-	-	35.1	-
				-	-	78.1	12.3	136.1
La II	5482.268	0.00	-2.06	-	40.9	11.1	-	-
				-	-	-	35.5	-
				-	50.1	-	-	61.8
La II	5671.528	2.21	-0.80	-	-	-	-	-
				-	-	-	-	103.49
				-	105.0	85.8	-	-
La II	5712.391	0.17	-1.96	-	27.3	-	-	-
				-	-	-	-	-
				-	-	-	38.6	-
La II	5797.565	0.24	-1.38	-	-	-	-	-
				-	-	-	-	-
				-	-	-	38.6	-
La II	5805.773	0.13	-1.59	-	-	-	-	-
				-	-	-	82.4	-
				-	-	-	10.8	-
La II	5808.313	0.00	-2.18	-	-	-	-	-
				-	-	-	-	-
				-	-	-	-	-
La II	5863.691	0.93	-1.39	-	24.5	-	-	-
				-	-	-	-	-
				-	-	-	16.1	-
La II	5880.633	0.23	-1.92	-	-	-	-	-
				-	-	-	49.9	-
				-	-	-	-	-
La II	5936.210	0.17	-2.07	-	31.6	-	-	-
				-	-	-	35.4	-
				93.3	-	-	-	40.6
La II	6067.117	0.77	-2.28	-	-	-	-	-
				-	-	-	-	104.42
				150.2	94.5	76.0	-	108.0
La II	6126.075	1.25	-1.19	-	-	-	-	-
				-	-	-	-	-
				-	-	74.3	-	108.5
La II	6129.556	0.77	-1.49	-	28.6	-	-	-
				-	-	-	-	-
				139.2	54.5	30.5	-	96.0
La II	6146.523	0.24	-2.47	-	-	-	-	-
				-	-	-	-	-
				176.0	79.2	56.6	-	119.3
La II	6172.721	0.13	-2.25	-	20.9	-	-	-
				-	-	-	-	191.62
				-	-	-	31.2	-
La II	6262.287	0.40	-1.21	-	-	50.3	-	-
				-	-	-	121.1	-
				-	-	-	26.8	-
La II	6320.376	0.17	-1.56	-	93.9	24.4	-	-
				-	10.5	-	-	-
				-	-	-	-	78.8
La II	6358.105	0.71	-1.89	-	-	-	-	-
				-	-	-	-	-
				-	-	-	34.7	-
La II	6390.477	0.32	-1.44	-	-	33.7	-	-
				-	-	-	-	-
				91.1	-	-	-	59.6
La II	6399.030	2.65	-0.52	-	-	-	-	-

Table E.1: continued.

ion	λ (Å)	EP (eV)	log gf	05113 08143B 14429	05341 08143R 17279	06530 08281 19500	07134 13245 22223	07430 14325 22272
				-	-	-	-	89.01
				-	-	-	-	36.9
La II	6642.755	2.53	-0.87	-	-	-	-	-
				-	-	-	-	64.41
				-	-	-	26.3	-
La II	6774.268	0.13	-1.71	102.1	89.5	23.4	-	-
				-	-	-	89.9	-
				-	-	-	-	-
La II	6808.885	0.13	-2.32	37.4	22.4	-	-	-
				-	-	-	32.5	-
				-	-	-	-	-
La II	6834.099	0.24	-2.18	33.2	-	-	-	-
				-	-	-	-	-
				-	-	-	-	-
La II	6837.904	0.32	-2.28	25.8	-	-	-	-
				-	-	-	-	-
				-	-	-	-	-
Ce II	3942.745	0.860	-0.10	-	-	-	4.23	-
				-	-	-	-	-
				-	-	-	97.9	-
Ce II	4040.753	0.45	0.24	-	-	-	-	-
				-	86.8	-	-	-
				-	-	-	-	-
Ce II	4073.474	0.480	-0.68	-	-	-	2.00	-
				-	-	-	-	-
				-	-	-	40.2	-
Ce II	4115.371	0.92	-0.02	123.1	-	44.4	-	-
				-	-	-	-	-
				-	-	-	61.0	-
Ce II	4120.827	0.32	-0.13	-	-	77.9	-	-
				-	58.2	-	-	-
				-	-	-	90.6	-
Ce II	4133.802	0.86	0.72	-	-	-	-	5.21
				-	89.2	-	-	-
				-	-	-	-	-
Ce II	4137.645	0.52	0.25	-	-	-	-	-
				-	-	16.3	-	-
				-	-	-	61.9	-
Ce II	4142.397	0.70	0.01	-	-	59.9	-	-
				-	57.5	-	-	-
				-	-	-	38.2	-
Ce II	4144.492	0.48	-0.51	-	-	-	-	-
				-	-	-	-	-
				-	-	-	42.9	-
Ce II	4144.996	0.70	-0.05	-	-	-	-	-
				-	54.0	-	-	-
				-	-	-	-	-
Ce II	4151.969	0.680	-0.37	-	-	-	3.09	4.30
				-	-	-	-	-
				-	-	-	50.1	-
Ce II	4159.031	1.09	0.16	-	-	-	-	-
				-	-	-	-	-
				-	-	-	-	-
Ce II	4165.599	0.91	0.44	-	-	89.2	-	-
				-	-	13.7	-	-
				-	-	-	50.6	-
Ce II	4166.884	1.35	0.55	-	-	-	-	-

Table E.1: continued.

ion	λ (Å)	EP (eV)	log gf	05113 08143B 14429	05341 08143R 17279	06530 08281 19500	07134 13245 22223	07430 14325 22272
				-	-	-	-	-
				-	-	-	43.4	-
Ce II	4176.702	1.12	0.06	-	-	-	-	-
				-	-	-	-	-
				-	-	-	-	-
Ce II	4186.594	0.860	-0.13	-	-	-	4.10	-
				-	-	-	-	-
				-	-	-	32.1	-
Ce II	4193.871	0.55	-0.47	100.0	-	38.2	-	-
				-	-	-	-	-
				-	-	-	29.8	-
Ce II	4194.903	1.12	-0.22	-	-	-	-	-
				-	-	-	-	-
				-	-	-	36.7	-
Ce II	4214.033	0.61	-0.42	-	-	-	-	-
				-	-	-	-	-
				-	-	-	74.7	-
Ce II	4239.910	0.48	-0.14	-	-	81.6	-	-
				-	-	-	-	-
				-	-	-	64.1	-
Ce II	4248.671	0.68	0.11	-	-	62.1	-	-
				-	52.2	-	-	-
				-	-	-	44.3	-
Ce II	4253.362	0.46	-0.56	-	-	-	-	-
				-	25.2	-	-	-
				-	-	-	55.6	-
Ce II	4270.184	0.56	-0.27	-	-	42.2	-	-
				-	-	8.6	-	-
				-	-	-	67.0	-
Ce II	4306.726	0.52	-0.23	-	-	51.2	-	-
				-	-	-	-	-
				-	-	-	44.7	-
Ce II	4349.789	0.70	-0.11	143.0	-	46.8	-	-
				-	-	-	-	-
				-	-	-	54.4	-
Ce II	4352.707	0.60	-0.30	-	-	49.3	-	-
				-	-	-	-	-
				-	-	-	26.3	-
Ce II	4353.361	1.58	0.15	-	-	-	-	-
				-	-	-	-	-
				-	-	-	53.6	-
Ce II	4375.919	0.49	-0.44	-	-	36.3	-	-
				-	-	-	-	-
				-	-	-	56.7	-
Ce II	4382.165	0.68	0.07	-	-	-	-	-
				-	43.4	10.9	-	-
				-	-	-	33.7	-
Ce II	4388.005	0.86	-0.31	86.2	-	-	-	-
				-	-	-	-	-
				-	-	-	-	-
Ce II	4391.659	0.32	-0.11	-	-	-	-	-
				-	55.0	16.1	-	-
				-	-	-	87.3	-
Ce II	4460.207	0.48	0.17	-	-	98.9	-	-
				-	-	15.2	-	-
				-	-	-	34.6	-
Ce II	4463.408	0.96	-0.11	-	-	-	-	-

Table E.1: continued.

ion	λ (Å)	EP (eV)	log gf	05113 08143B 14429	05341 08143R 17279	06530 08281 19500	07134 13245 22223	07430 14325 22272
				-	-	-	-	-
				-	-	-	58.2	-
Ce II	4483.893	0.86	0.01	-	-	51.9	-	-
				-	-	-	-	-
				-	-	-	73.3	-
Ce II	4486.909	0.29	-0.09	-	-	84.6	-	-
				-	-	-	-	-
				-	-	-	36.1	-
Ce II	4497.846	0.96	-0.35	79.3	-	17.4	-	-
				-	-	-	-	-
				-	-	-	-	-
Ce II	4551.291	0.74	-0.58	75.1	-	-	-	-
				-	-	-	80.4	-
				-	-	-	42.9	-
Ce II	4560.958	0.68	-0.16	-	-	-	-	-
				-	-	-	-	-
				-	-	-	89.8	-
Ce II	4562.359	0.48	0.31	-	-	-	-	-
				-	-	-	-	-
				-	-	-	-	-
Ce II	4593.926	0.700	-1.15	-	-	-	-	0.76
				-	-	-	-	-
				-	-	-	45.5	-
Ce II	4606.400	0.91	-0.20	-	-	-	-	-
				-	-	-	-	-
				-	-	-	93.3	-
Ce II	4628.161	0.52	0.22	-	-	-	-	-
				-	-	-	-	-
				-	-	-	-	-
Ce II	4659.417	0.42	-1.59	-	-	-	-	-
				-	-	-	28.0	-
				-	-	-	16.9	-
Ce II	4680.119	1.06	-0.53	-	-	-	-	-
				-	-	-	71.8	-
				-	-	-	21.2	-
Ce II	4684.598	0.90	-0.42	88.3	-	-	-	-
				-	-	-	-	-
				-	-	-	28.9	-
Ce II	4737.271	1.09	-0.20	-	-	-	-	-
				-	-	-	-	-
				-	-	-	-	-
Ce II	5079.682	1.38	0.19	-	-	45.3	-	-
				-	-	7.2	-	-
				-	134.7	124.5	28.7	136.0
Ce II	5117.169	1.40	0.01	-	61.7	-	-	-
				-	17.7	-	-	-
				-	177.4	183.4	55.3	-
Ce II	5187.458	1.21	0.30	-	101.7	51.9	-	-
				-	-	-	-	-
				165.0	-	-	-	-
Ce II	5252.662	1.16	-0.87	-	-	-	-	-
				-	-	-	31.6	-
				-	-	171.6	59.5	-
Ce II	5274.229	1.04	0.30	-	-	56.6	-	-
				-	-	-	-	-
				-	-	-	65.2	-
Ce II	5330.556	0.87	0.28	-	-	-	-	-

Table E.1: continued.

ion	λ (Å)	EP (eV)	log gf	05113 08143B 14429	05341 08143R 17279	06530 08281 19500	07134 13245 22223	07430 14325 22272
				-	-	-	-	-
				-	108.8	84.3	-	116.7
Ce II	5468.371	1.40	-0.39	-	-	14.6	-	-
				-	8.8	-	38.6	-
				133.1	-	37.2	-	57.1
Ce II	5613.694	1.42	-1.00	-	-	-	-	-
				-	-	-	-	84.7
				-	56.0	34.2	-	-
Ce II	5685.836	1.90	-0.43	-	-	-	-	-
				-	-	-	-	79.9
				-	-	40.3	-	-
Ce II	5695.847	1.63	-0.48	-	18.0	-	-	-
				-	-	-	-	-
				142.1	-	39.0	-	-
Ce II	5715.259	1.54	-0.89	-	-	-	-	-
				-	-	-	-	79.8
				-	118.5	70.3	-	114.6
Ce II	5975.818	1.33	-0.45	-	30.2	-	-	-
				-	-	-	-	-
				-	-	100.1	23.2	123.0
Ce II	6043.373	1.21	-0.32	-	33.2	19.0	-	-
				-	-	-	-	-
				111.2	-	-	-	-
Ce II	6143.376	1.70	-0.80	-	-	-	-	-
				-	-	-	-	76.0
				-	-	-	-	-
Pr II	3908.428	0.00	0.16	-	-	-	-	-
				-	43.1	-	-	-
				-	-	-	19.0	-
Pr II	4189.479	0.37	0.17	138.9	-	4.39	-	-
				-	21.1	-	-	-
				-	-	-	-	-
Pr II	4206.716	0.55	0.41	-	-	-	-	-
				-	38.3	-	-	-
				-	-	-	-	-
Pr II	4225.346	0.000	-0.96	-	-	5.51	-	-
				-	-	-	-	-
				-	-	-	-	-
Pr II	4297.765	0.00	-0.58	80.9	-	-	-	-
				-	-	-	-	-
				-	-	-	-	-
Pr II	4405.825	0.55	-0.04	78.6	-	-	-	-
				-	-	-	-	-
				-	-	-	10.5	-
Pr II	4510.153	0.42	-0.30	82.7	-	-	-	-
				-	-	-	61.7	-
				-	-	-	-	-
Pr II	4643.487	0.06	-1.21	26.4	-	-	-	-
				-	-	-	-	-
				-	-	-	-	-
Pr II	5034.406	1.11	-0.09	-	27.9	-	-	-
				-	-	-	-	-
				-	-	-	8.2	-
Pr II	5110.760	1.15	0.29	-	37.6	-	-	-
				-	-	-	-	-
				-	-	-	-	-
Pr II	5135.140	0.95	0.01	-	31.2	-	-	-

Table E.1: continued.

ion	λ (Å)	EP (eV)	log gf	05113 08143B 14429	05341 08143R 17279	06530 08281 19500	07134 13245 22223	07430 14325 22272
				-	-	-	-	-
				-	-	-	13.7	-
Pr II	5173.902	0.97	0.30	-	61.8	-	-	-
				-	-	-	-	-
				-	99.7	63.9	-	96.7
Pr II	5219.045	0.80	-0.25	-	32.5	-	-	-
				-	-	-	28.4	152.2
				-	-	118.0	15.3	157.3
Pr II	5220.108	0.80	0.15	-	59.4	2.26	-	-
				-	-	-	67.2	-
				-	-	-	-	-
Pr II	5292.024	0.63	-0.27	-	-	-	-	-
				-	6.1	-	-	-
				-	-	88.7	-	136.9
Pr II	5322.772	0.48	-0.46	-	43.7	-	-	-
				-	-	-	45.2	-
				78.5	24.6	-	-	36.2
Pr II	5571.828	0.51	-1.23	-	-	-	-	-
				-	-	-	-	60.3
				118.4	36.7	-	-	54.3
Pr II	5756.202	1.00	-0.61	-	-	-	-	-
				-	-	-	-	82.4
				-	-	-	-	-
Pr II	5810.585	1.44	-0.69	-	-	-	-	-
				-	-	-	-	40.6
				-	-	-	-	-
Pr II	5859.676	1.42	-0.30	-	-	-	-	-
				-	-	-	-	82.7
				-	-	-	-	-
Pr II	5868.820	1.05	-0.62	-	9.9	-	-	-
				-	-	-	-	75.2
				-	-	-	-	-
Pr II	5939.899	1.24	-0.23	-	-	-	-	-
				-	-	-	-	91.6
				89.6	22.7	-	-	34.0
Pr II	5981.205	1.46	-0.38	-	-	-	-	-
				-	-	-	-	51.8
				143.6	58.3	41.3	-	72.7
Pr II	6017.767	1.11	-0.36	-	-	-	-	-
				-	-	-	16.2	115.5
				-	42.8	32.6	-	61.3
Pr II	6025.732	1.44	-0.11	-	11.2	-	-	-
				-	-	-	-	90.9
				-	-	-	-	60.1
Pr II	6087.533	1.12	-0.64	-	-	-	-	-
				-	-	-	-	69.6
				-	-	-	-	-
Pr II	6165.940	0.92	-0.20	-	-	-	-	-
				-	5.1	-	-	-
				110.8	-	-	-	45.0
Pr II	6397.960	1.05	-0.92	-	-	-	-	-
				-	-	-	-	62.9
				85.6	29.1	-	-	43.0
Pr II	6656.834	1.82	-0.05	-	-	-	-	-
				-	-	-	-	59.1
				-	-	-	-	-
Pr II	7021.512	1.42	-0.62	11.2	-	-	-	-

Table E.1: continued.

ion	λ (Å)	EP (eV)	log gf	05113 08143B 14429	05341 08143R 17279	06530 08281 19500	07134 13245 22223	07430 14325 22272
				-	-	-	-	-
				-	-	-	-	-
Pr III	5299.993	0.36	-0.72	-	-	-	17.1	-
				-	-	-	-	-
				-	-	-	-	-
Pr III	6090.010	0.36	-0.87	-	-	-	15.5	-
				-	-	-	-	-
				-	-	-	-	-
Nd II	3863.408	0.00	0.16	-	-	-	-	-
				-	-	23.9	-	-
				-	-	-	-	-
Nd II	3951.140	0.180	-1.40	-	-	-	-	0.50
				-	-	15.0	-	-
				-	-	-	-	-
Nd II	3991.741	0.00	-0.51	-	-	-	-	-
				-	20.1	-	-	-
				-	-	-	37.6	-
Nd II	4020.864	0.32	-0.31	-	-	38.8	-	-
				-	19.0	-	-	-
				-	-	-	38.1	-
Nd II	4021.327	0.32	-0.31	-	-	-	-	-
				-	-	-	-	-
				-	-	-	74.3	-
Nd II	4061.080	0.47	0.35	-	-	79.6	-	2.71
				-	49.5	-	-	-
				-	-	-	-	-
Nd II	4135.320	0.63	-0.07	-	-	-	-	-
				-	-	6.5	-	-
				-	-	-	-	-
Nd II	4247.370	0.00	-0.21	-	-	-	-	-
				-	-	12.8	-	-
				-	-	-	30.1	-
Nd II	4327.932	0.56	-0.43	121.0	-	20.3	-	-
				-	14.8	-	88.0	-
				-	-	-	38.3	-
Nd II	4446.384	0.20	-0.58	136.9	-	35.0	-	-
				-	-	-	-	-
				-	-	-	64.0	-
Nd II	4451.563	0.38	0.03	-	-	70.1	-	-
				-	43.3	-	-	-
				-	-	-	15.3	-
Nd II	4451.980	0.00	-1.17	-	-	-	-	-
				-	-	-	-	-
				-	-	-	40.5	-
Nd II	4462.979	0.56	-0.05	-	-	-	-	-
				-	24.9	-	-	-
				-	-	-	15.6	-
Nd II	4516.346	0.32	-0.87	98.3	-	-	-	-
				-	-	-	-	-
				-	-	-	19.1	-
Nd II	4542.600	0.74	-0.47	109.0	-	-	-	-
				-	-	-	87.0	-
				-	-	-	16.7	-
Nd II	4597.014	0.20	-1.03	95.4	-	-	-	-
				-	-	-	-	-
				-	-	-	-	-
Nd II	4706.543	0.00	-0.78	144.8	-	-	-	-

Table E.1: continued.

ion	λ (Å)	EP (eV)	log gf	05113 08143B 14429	05341 08143R 17279	06530 08281 19500	07134 13245 22223	07430 14325 22272
				-	-	-	-	-
				-	-	-	23.6	-
Nd II	4811.342	0.06	-1.01	120.4	76.8	18.3	-	-
				-	8.6	-	90.4	-
				-	150.7	102.6	14.9	-
Nd II	4820.339	0.20	-1.16	80.0	51.8	15.0	-	-
				-	-	-	-	-
				-	-	-	15.4	-
Nd II	4889.102	0.18	-1.17	-	-	-	-	-
				-	-	-	-	-
				-	180.8	137.6	19.2	-
Nd II	4959.119	0.06	-0.92	131.5	89.0	21.3	-	-
				-	-	-	93.7	-
				-	166.0	-	19.8	-
Nd II	4989.950	0.63	-0.62	-	-	17.2	-	-
				-	-	-	89.6	-
				-	142.4	-	-	-
Nd II	5089.832	0.20	-1.10	-	-	-	-	-
				-	-	-	-	-
				-	-	133.4	20.1	172.0
Nd II	5092.794	0.38	-0.61	-	70.2	20.0	-	-
				-	-	-	94.6	-
				-	-	144.7	37.6	-
Nd II	5130.586	1.30	0.24	-	112.5	-	-	-
				-	-	-	86.0	-
				-	-	-	-	-
Nd II	5255.506	0.20	-0.70	-	92.7	-	-	-
				-	-	-	-	-
				-	-	-	39.1	-
Nd II	5273.427	0.68	-0.19	-	-	34.3	-	-
				-	-	4.7	-	-
				-	156.4	123.7	-	158.9
Nd II	5276.869	0.86	-0.39	-	-	-	-	-
				-	-	-	-	-
				-	-	-	40.6	-
Nd II	5293.163	0.82	-0.14	-	136.0	36.6	-	-
				-	18.4	-	-	-
				-	-	-	45.2	-
Nd II	5319.815	0.55	-0.15	-	129.6	45.7	-	-
				-	-	-	-	-
				-	-	-	22.3	-
Nd II	5361.467	0.68	-0.48	-	82.8	24.4	-	-
				-	-	-	-	-
				-	-	71.7	9.0	136.3
Nd II	5385.888	0.74	-0.86	-	29.7	6.3	-	-
				-	-	-	29.5	-
				-	100.3	54.9	-	105.3
Nd II	5416.374	0.86	-0.98	-	17.6	-	-	-
				-	-	-	-	163.1
				-	145.3	81.8	15.0	139.8
Nd II	5431.516	1.12	-0.46	-	38.2	-	-	-
				-	-	-	52.7	-
				-	132.3	75.1	10.9	132.2
Nd II	5442.264	0.68	-0.98	-	31.7	-	-	-
				-	-	-	31.1	-
				-	103.4	-	-	-
Nd II	5485.098	0.55	-1.35	-	-	-	-	-

Table E.1: continued.

ion	λ (Å)	EP (eV)	log gf	05113 08143B 14429	05341 08143R 17279	06530 08281 19500	07134 13245 22223	07430 14325 22272
				-	-	-	-	157.7
				-	-	107.2	17.5	-
Nd II	5485.696	1.26	-0.28	-	56.1	-	-	-
				-	-	-	-	-
				165.6	-	28.3	-	78.7
Nd II	5578.651	0.55	-1.63	-	-	-	-	-
				-	-	-	-	-
				100.3	43.2	-	-	-
Nd II	5592.660	1.16	-1.36	-	-	-	-	-
				-	-	-	-	84.9
				-	130.7	98.8	16.8	-
Nd II	5708.271	0.86	-0.58	-	-	-	-	-
				-	-	-	-	-
				-	-	-	-	-
Nd II	5740.858	1.16	-0.56	-	36.5	-	-	-
				-	-	-	-	-
				-	-	-	15.3	-
Nd II	5804.004	0.74	-0.63	-	-	-	-	-
				-	-	-	47.5	-
				-	-	-	8.9	-
Nd II	5811.572	0.86	-0.87	-	-	-	-	-
				-	-	-	29.2	176.3
				-	-	-	-	120.4
Nd II	5842.366	1.28	-0.60	-	23.7	-	-	-
				-	-	-	33.6	-
				-	-	-	-	-
Nd II	5865.027	1.41	-0.86	-	-	-	-	-
				-	-	-	-	120.5
				166.4	71.7	43.4	-	87.1
Nd II	6031.270	1.28	-0.83	-	18.5	-	-	-
				-	-	-	-	140.5
				152.6	95.3	-	-	98.2
Nd II	6034.228	1.54	-0.66	-	-	-	-	-
				-	-	-	-	-
				-	42.3	-	-	42.8
Nd II	6330.151	1.77	-0.87	-	-	-	-	-
				-	-	-	-	-
				-	71.6	-	-	-
Nd II	6341.492	1.80	-0.68	-	-	-	-	-
				-	-	-	-	-
				145.7	-	31.5	-	60.2
Nd II	6365.540	0.93	-1.37	-	9.5	-	-	-
				-	-	-	-	-
				107.9	45.7	-	-	55.1
Nd II	6637.187	1.45	-1.03	-	-	-	-	-
				-	-	-	-	-
				-	75.7	50.5	-	66.8
Nd II	6650.517	1.95	-0.32	-	20.5	-	-	-
				-	-	-	-	-
				87.5	46.0	-	-	46.9
Nd II	6727.695	1.81	-0.76	14.0	-	-	-	-
				-	-	-	-	72.7
				112.8	57.8	40.1	-	71.6
Nd II	6737.763	1.60	-0.78	20.7	-	-	-	-
				-	-	-	-	-
				-	69.0	-	-	140.6
Nd II	6740.078	0.06	-2.10	-	-	-	-	-

Table E.1: continued.

ion	λ (Å)	EP (eV)	log gf	05113 08143B 14429	05341 08143R 17279	06530 08281 19500	07134 13245 22223	07430 14325 22272
				-	-	-	-	-
				-	31.1	-	-	-
Nd II	6749.270	1.53	-1.14	-	-	-	-	-
				-	-	-	-	-
				-	71.9	-	-	-
Nd II	6790.372	0.18	-2.11	-	-	-	-	-
				-	-	-	-	-
				-	68.6	-	-	-
Nd II	6803.980	1.44	-0.87	-	-	-	-	-
				-	-	-	-	-
				-	-	-	-	-
Nd II	7513.736	0.93	-1.24	28.3	-	-	-	-
				-	-	-	-	-
				-	-	-	-	-
Nd III	4759.526	0.63	-1.15	-	-	-	-	-
				13.2	-	-	-	-
				-	-	-	-	-
Nd III	4911.652	0.14	-1.63	-	-	-	-	-
				10.1	-	-	-	-
				-	-	-	-	-
Nd III	4912.943	0.00	-1.78	-	-	-	13.7	-
				-	-	-	-	-
				-	-	-	-	-
Nd III	4914.094	0.46	-1.10	-	-	-	21.6	-
				16.4	-	-	-	-
				-	-	-	-	-
Nd III	4927.487	0.46	-0.80	-	-	-	37.1	-
				23.3	-	-	-	-
				-	-	-	-	-
Nd III	4942.673	0.63	-1.23	-	-	-	-	-
				10.0	-	-	-	-
				-	-	-	-	-
Nd III	5050.695	0.30	-1.06	-	-	-	30.1	-
				24.5	-	-	-	-
				-	-	-	-	-
Nd III	5102.427	0.30	-0.62	-	-	-	77.5	-
				49.7	-	-	-	-
				-	-	-	-	-
Nd III	5127.044	0.63	-0.40	-	-	-	61.9	-
				42.1	-	-	-	-
				-	-	-	-	-
Nd III	5193.039	0.14	-1.18	-	-	-	28.5	-
				20.5	-	-	-	-
				-	-	-	-	-
Nd III	5203.923	0.14	-0.66	-	-	-	72.3	-
				49.7	-	-	-	-
				-	-	-	-	-
Nd III	5294.113	0.00	-0.69	-	-	-	-	-
				64.9	-	-	-	-
				-	-	-	-	-
Nd III	5410.099	0.14	-1.52	-	-	-	16.6	-
				11.2	-	-	-	-
				-	-	-	-	-
Nd III	5429.794	0.30	-1.24	-	-	-	22.8	-
				-	-	-	-	-
				-	-	-	-	-
Nd III	5987.682	0.46	-1.26	-	-	-	-	-

Table E.1: continued.

ion	λ (Å)	EP (eV)	log gf	05113 08143B 14429	05341 08143R 17279	06530 08281 19500	07134 13245 22223	07430 14325 22272
				13.2	-	-	-	-
Nd III	6145.067	0.30	-1.33	- - 7.9	- - -	- - -	- - -	- - -
Nd III	6327.264	0.14	-1.41	- - -	- - -	- - -	- 24.3 -	- - -
Nd III	6550.231	0.00	-1.49	- - 9.2	- - -	- - -	- 19.5 -	- - -
Sm II	4092.250	0.00	-0.87	- - -	- - 17.3	- - -	- - -	- - -
Sm II	4262.669	0.38	-0.35	- - -	- - -	- - -	26.8 - -	- - -
Sm II	4318.927	0.280	-0.27	- 134.38 -	- - -	- - -	- - -	- - -
Sm II	4329.019	0.18	-0.30	- - -	145.5 - -	122.5 - -	37.2 - -	- - -
Sm II	4424.337	0.48	0.08	- 164.20 -	- - -	- - -	50.5 - -	- - -
Sm II	4452.722	0.28	-0.43	- 113.22 -	- - -	- - -	34.6 - 87.6	- - -
Sm II	4458.509	0.10	-0.66	- 101.22 -	- - -	- - -	31.9 - -	- - -
Sm II	4467.341	0.66	0.30	- - -	- - -	- - -	63.6 - -	- 2.10 -
Sm II	4499.475	0.250	-1.00	- 45.81 -	- - -	- - -	- - -	- - -
Sm II	4523.909	0.43	-0.58	- 74.71 -	- - -	- - -	20.8 - 59.7	- - -
Sm II	4537.941	0.48	-0.23	- 102.3 -	- - -	- - -	33.3 - 66.0	- - -
Sm II	4577.688	0.25	-0.78	- 69.29 -	- - -	- - -	20.9 - 49.9	- - -
Sm II	4642.228	0.38	-0.52	- 89.63 -	- - -	- - -	20.3 - 70.3	- - -
Sm II	4676.902	0.04	-0.86	- 83.28 -	- - -	- - -	18.9 - 61.4	- - -
Sm II	4704.400	0.00	-1.00	- 70.40 -	- - -	- - -	19.8 - 48.3	- - -
Sm II	4745.681	0.10	-0.97	- 76.5	- -	- -	16.2 -	- -

Table E.1: continued.

ion	λ (Å)	EP (eV)	log gf	05113 08143B 14429	05341 08143R 17279	06530 08281 19500	07134 13245 22223	07430 14325 22272
				-	-	-	-	-
				-	-	-	-	-
Sm II	4777.840	0.04	-1.28	-	-	-	-	-
				-	-	-	39.4	-
				-	-	-	-	-
Sm II	4815.800	0.18	-0.82	-	38.5	-	-	-
				-	-	-	-	-
				-	-	-	-	-
Sm II	4829.560	0.38	-1.28	-	14.4	-	-	-
				-	-	-	-	-
				-	-	-	-	-
Sm II	4844.208	0.28	-0.89	-	36.7	-	-	-
				-	-	-	-	-
				158.0	-	-	-	-
Sm II	4938.090	0.25	-1.44	-	-	-	-	-
				-	-	-	-	-
				-	-	-	-	-
Sm II	4948.630	0.54	-0.95	-	24.0	-	-	-
				-	8.7	-	-	-
				-	-	-	-	-
Sm II	5028.450	1.49	-0.25	-	-	-	-	-
				-	7.8	-	-	-
				-	-	-	-	-
Sm II	5103.090	1.17	-0.35	-	31.9	-	-	-
				-	-	-	-	-
				-	-	-	-	96.0
Sm II	5116.690	0.93	-0.72	-	16.1	-	-	-
				-	-	-	-	-
				41.0	-	-	-	-
Sm II	5738.037	1.80	-0.78	-	-	-	-	-
				-	-	-	-	-
				-	-	-	-	42.4
Sm II	6182.890	1.38	-1.14	-	-	-	-	-
				-	-	-	-	-
				-	-	-	-	47.8
Sm II	6267.290	1.17	-1.01	-	-	-	-	-
				-	-	-	-	-
				-	-	-	-	26.0
Sm II	6693.555	1.69	-1.09	-	-	-	-	-
				-	-	-	-	-
				146.4	45.9	30.2	-	-
Sm II	6731.813	1.17	-0.52	31.79	-	-	-	-
				-	-	-	-	118.1
				-	-	-	-	-
Sm II	7042.207	1.080	-0.67	27.87	-	-	-	-
				-	-	-	-	123.3
				-	-	-	-	-
Sm II	7149.565	0.930	-0.78	29.17	-	-	-	-
				-	-	-	-	-
				-	-	-	-	-
Sm II	7928.134	1.610	-0.14	33.83	-	-	-	-
				-	-	-	-	104.2
				-	-	-	-	-
Eu II	4129.725	0.000	-0.77	-	-	6.30	-	1.51
				-	-	-	-	-
				-	-	-	-	-
Eu II	4205.054	0.000	-0.07	-	-	-	-	-

Table E.1: continued.

ion	λ (Å)	EP (eV)	log gf	05113 08143B 14429	05341 08143R 17279	06530 08281 19500	07134 13245 22223	07430 14325 22272
				-	-	16.38	-	-
				-	-	-	9.56	-
Eu II	4435.542	0.210	-0.43	-	-	-	-	-
				-	-	-	-	-
				133.8	46.4	36.9	-	66.6
Eu II	6437.640	1.32	-0.27	-	18.6	-	-	-
				-	-	-	41.2	95.7
				-	100.0	73.2	5.94	116.8
Eu II	6645.064	1.38	0.20	-	42.4	0.91	-	-
				-	-	-	62.5	158.4
				122.5	-	-	-	-
Eu II	6645.094	1.38	-0.16	-	-	-	-	-
				-	-	-	-	-
				-	-	-	-	-
Gd II	3852.461	0.03	-0.10	-	-	-	-	29.7
				-	-	-	-	-
				-	-	-	-	-
Gd II	4013.795	1.37	-0.04	58.8	-	-	-	-
				-	-	-	-	-
				-	-	-	-	-
Gd II	4049.423	0.66	-0.08	-	-	-	-	-
				-	-	5.3	-	-
				-	-	-	43.6	-
Gd II	4049.854	0.99	0.49	-	-	-	-	-
				-	-	-	-	-
				-	-	-	-	-
Gd II	4059.359	1.73	-0.15	27.2	-	-	-	-
				-	-	-	-	-
				-	-	-	-	-
Gd II	4243.837	1.41	-0.44	-	-	-	-	-
				-	-	-	25.0	-
				-	-	-	40.8	-
Gd II	4251.731	0.38	-0.22	139.8	-	41.8	-	-
				-	-	11.8	-	-
				-	-	-	20.9	-
Gd II	4253.358	0.56	-0.52	-	-	-	-	-
				-	-	-	-	-
				-	-	-	15.0	-
Gd II	4316.047	0.66	-0.45	-	-	16.1	-	-
				-	-	-	-	-
				-	-	-	-	-
Gd II	4406.656	1.43	-0.05	44.2	-	-	-	-
				-	-	-	-	141.5
				102.7	-	-	-	-
Gd II	4426.145	0.38	-1.58	-	-	-	-	-
				-	-	-	-	84.1
				-	-	-	9.3	-
Gd II	4436.213	1.73	0.05	-	-	-	-	-
				-	-	-	-	-
				-	-	85.4	-	88.6
Gd II	4438.254	0.66	-0.82	38.5	-	-	-	-
				-	-	-	-	-
				-	-	-	-	-
Gd II	4483.329	1.06	-0.42	39.6	-	-	-	-
				-	-	-	-	144.4
				139.5	-	-	-	-
Gd II	4514.504	1.37	-0.25	-	-	-	-	-

Table E.1: continued.

ion	λ (Å)	EP (eV)	log gf	05113 08143B 14429	05341 08143R 17279	06530 08281 19500	07134 13245 22223	07430 14325 22272
				-	-	-	-	-
				108.1	-	-	-	50.5
Gd II	4521.293	0.56	-1.49	-	-	-	-	-
				-	-	-	-	-
				-	-	39.3	-	-
Gd II	5092.249	1.73	-0.23	-	17.4	-	-	-
				-	-	-	-	73.4
				-	-	44.6	-	-
Gd II	5108.903	1.66	-0.36	-	15.2	-	-	-
				-	-	-	-	76.1
				-	44.3	-	5.0	-
Gd II	5176.288	1.06	-0.74	-	-	-	-	-
				-	-	-	-	-
				-	-	-	-	-
Gd II	5412.632	1.25	-1.70	-	-	-	-	-
				-	-	-	-	21.6
				-	-	-	-	-
Gd II	5500.419	1.37	-1.23	-	-	-	-	-
				-	-	-	-	23.8
				-	40.2	30.7	-	-
Gd II	5733.852	1.37	-0.67	-	-	-	-	-
				-	-	-	-	84.9
				-	-	16.2	-	22.3
Gd II	6080.641	1.73	-0.85	-	-	-	-	-
				-	-	-	-	-
				-	-	-	-	-
Gd II	6752.649	2.33	-0.21	8.5	-	-	-	-
				-	-	-	-	35.0
				-	-	-	-	-
Gd II	7846.361	2.79	0.16	10.0	-	-	-	-
				-	-	-	-	-
				-	-	-	-	32.90
Tb II	4842.760	0.370	-1.49	-	-	-	-	-
				-	-	-	-	-
				-	-	-	57.56	-
Dy II	4000.450	0.100	0.04	-	-	3.51	-	0.67
				-	-	-	-	-
				-	-	-	11.39	-
Dy II	4449.700	0.000	-1.03	-	-	-	-	-
				-	-	-	-	-
				76.0	-	-	-	45.0
Dy II	4503.231	0.93	-1.49	-	-	-	-	-
				-	-	-	-	69.7
				-	-	-	-	-
Dy II	4617.269	0.590	-1.86	-	-	-	-	-
				-	-	-	10.97	69.2
				40.4	13.54	-	-	-
Dy II	4833.753	1.93	-0.83	-	-	-	-	-
				-	-	-	-	32.3
				-	-	-	-	-
Dy II	5389.581	0.00	-2.47	-	-	-	-	-
				-	-	-	-	89.0
				-	19.60	-	-	-
Dy II	5426.700	2.540	-0.16	-	-	-	-	-
				-	-	-	-	-
				-	-	-	-	-
Dy II	6483.590	2.00	-1.06	-	-	-	-	-

Table E.1: continued.

ion	λ (Å)	EP (eV)	log gf	05113 08143B 14429	05341 08143R 17279	06530 08281 19500	07134 13245 22223	07430 14325 22272
				-	-	-	-	31.7
				-	-	-	-	7.9
Dy II	6700.640	1.84	-1.62	-	-	-	-	-
				-	-	-	-	-
				-	-	-	-	-
Dy II	6899.340	1.84	-0.51	-	-	-	-	-
				-	-	-	-	109.4
				-	-	-	-	-
Dy II	7457.050	1.84	-1.22	-	-	-	-	-
				-	-	-	-	26.4
				-	-	-	-	-
Dy II	7729.760	1.85	-0.81	-	-	-	-	-
				-	-	-	-	61.0
				-	-	-	-	-
Dy III	3930.640	0.00	-0.92	-	-	-	29.2	-
				-	-	-	-	-
				-	-	-	-	-
Er II	4630.882	1.95	0.03	-	-	-	-	-
				-	-	-	-	93.2
				-	-	-	23.3	-
Er II	4675.618	1.32	-0.05	-	-	-	-	-
				-	-	-	43.9	157.3
				-	-	104.6	8.5	-
Er II	4820.354	1.40	-0.49	55.96	40.29	10.5	-	-
				-	-	-	-	-
				84.5	-	-	-	-
Er II	4831.154	1.62	-0.62	30.49	-	-	-	-
				-	-	-	-	-
				31.3	16.9	-	-	-
Er II	4879.888	1.62	-1.15	-	-	-	-	-
				-	-	-	-	25.8
				87.5	24.4	33.9	-	-
Er II	4886.284	0.64	-1.75	-	-	-	-	-
				-	-	-	-	-
				31.1	-	-	-	-
Er II	6015.733	2.71	-0.15	-	-	-	-	-
				-	-	-	-	-
				-	-	14.06	-	-
Tm II	4199.918	0.000	-1.72	-	-	-	-	-
				-	-	-	-	-
				-	-	-	-	-
Yb II	4726.074	3.32	-0.61	28.6	-	-	-	-
				-	-	-	-	-
				-	56.57	55.4	-	-
Yb II	5352.953	3.750	-0.34	-	-	-	-	-
				-	-	-	-	-
				-	-	-	-	-
Yb II	5651.988	3.75	-0.80	-	7.2	-	-	-
				-	-	-	-	-
				-	-	-	-	-
Yb II	5837.136	4.010	-0.68	-	-	-	-	-
				-	-	-	-	15.80
				-	-	79.04	15.84	-
Lu II	4994.125	1.540	-1.14	-	-	-	-	-
				-	-	-	-	-
				-	-	-	-	-
Lu II	5476.675	1.76	-0.42	-	-	-	-	12.2

Table E.1: continued.

ion	λ (Å)	EP (eV)	log gf	05113 08143B 14429	05341 08143R 17279	06530 08281 19500	07134 13245 22223	07430 14325 22272
				-	-	8.9	-	-
				-	-	-	19.06	-
Lu II	5983.886	1.460	-1.16	-	-	-	-	-
				-	-	-	-	-
				-	-	-	-	-
Lu II	6199.592	3.650	-0.33	-	-	-	-	-
				-	-	-	-	19.84
				190.19	142.5	128.87	35.62	93.55
Lu II	6221.890	1.540	-0.76	-	44.10	32.86	-	-
				-	16.92	4.6	-	186.58
				164.12	121.5	103.23	24.25	-
Lu II	6463.106	1.460	-1.05	-	-	-	-	-
				-	-	-	-	-
				-	-	-	-	-
Hf II	3923.900	1.600	-0.87	-	-	25.53	-	-
				-	-	-	-	-
				-	-	-	-	-
Hf II	4093.150	0.45	-1.15	-	-	-	-	11.9
				-	-	-	-	-
				-	-	-	-	-
Hf II	4093.155	0.450	-1.09	-	-	86.58	-	-
				12.5	18.2	13.6	-	-
				32.5	17.2	16.8	-	-
Hf II	4790.708	2.20	-1.11	-	-	-	-	-
				-	-	-	-	30.22
				40.0	-	-	-	-
Hf II	6248.920	1.50	-1.93	-	-	-	-	-
				-	-	-	-	-
				-	-	-	-	-
Hf II	6980.900	1.870	-1.73	-	-	-	-	-
				-	-	-	-	21.24
				-	83.6	48.9	-	-
W II	5104.432	2.35	-0.91	-	9.78	-	-	-
				-	-	-	5.57	69.6
				99.28	33.98	61.82	3.67	31.22
Pb I	4057.807	1.320	-0.17	27.08	-	23.38	-	-
				-	5.44	5.7	59.75	64.13
				-	-	2.57	-	-
Pb II	5608.853	7.370	-0.70	-	-	2.22	1.62	1.02
				1.91	-	1.28	-	-

Appendix F

Atomic data used for the spectral analysis in Chapter 7

Table F.1: Details of all spectral lines used for the spectral analysis of J050221.17-691317.2 in Chapter 7. EWs indicated with SS are calculated using synthetic spectra.

ion	wavelength (Å)	EP(eV)	log gf	EW (mÅ)
C I	4932.049	7.680	-1.70	55.20
C I	5052.167	7.650	-1.30	93.92
C I	5551.578	8.640	-1.90	7.83
C I	6012.225	8.640	-2.00	6.11
C I	6014.834	8.640	-1.58	15.03
C I	6587.622	8.500	-1.02	49.27
O I	6155.971	10.74	-0.67	19.8
O I	6156.778	10.74	-0.45	23.2
O I	6158.187	10.74	-0.31	32.5
Na I	5682.633	2.10	-0.67	68.3
Na I	6160.750	2.10	-1.26	26.6
Mg I	5711.100	4.34	-1.75	73.4
Al I	6696.023	3.14	-1.35	18.3
Al I	6698.673	3.14	-1.65	9.3
Si I	5645.620	4.93	-2.14	16.3
Si I	5665.560	4.92	-2.04	17.3
Si I	5690.430	4.93	-1.91	29.1
Si I	6091.920	5.87	-1.33	18.6
Si I	6142.490	5.62	-1.56	16.7
Si I	6145.020	5.61	-1.48	26.3
Si I	6155.140	5.62	-0.84	52.1
Si I	6237.330	5.61	-1.22	40.0
Si I	6243.820	5.61	-1.34	31.4
Si I	6414.990	5.87	-1.11	27.9
Si I	6721.840	5.56	-1.26	29.9
Si II	6371.350	8.12	-0.10	128.9
S I	6743.580	7.87	-0.56	42.4
S I	6748.790	7.87	-0.35	49.5
S I	6757.160	7.87	-0.20	59.2
Ca I	5581.980	2.52	-0.55	78.9
Ca I	5588.760	2.52	0.36	147.2
Ca I	5590.130	2.52	-0.74	66.1
Ca I	5601.290	2.52	-0.63	82.2
Ca I	6102.727	1.88	-0.80	116.5
Ca I	6166.440	2.52	-1.14	40.6
Ca I	6169.560	2.52	-0.57	73.0
Ca I	6449.820	2.52	-0.62	79.2
Ca I	6471.670	2.52	-0.88	62.7
Ca I	6493.790	2.52	-0.39	118.8
Ca I	6499.650	2.52	-1.00	69.0
Ca I	6717.690	2.71	-0.52	97.7
Ca II	5019.971	7.51	-0.25	94.8
Ca II	5021.150	7.51	-1.24	20.1
Ca II	5285.266	7.50	-1.15	28.1
Ca II	5339.188	8.44	-0.33	33.1
Sc II	5239.820	1.45	-0.80	141.2
Sc II	5318.360	1.36	-1.79	52.9
Sc II	5357.190	1.51	-2.12	16.8
Sc II	5552.240	1.45	-2.08	22.3
Sc II	5640.990	1.50	-1.02	108.0
Sc II	5667.153	1.50	-1.21	83.4
Sc II	6604.600	1.36	-1.23	95.1
Ti I	5173.750	0.00	-1.10	46.2
Ti I	6261.110	1.43	-0.59	15.5
Ti II	5418.751	1.58	-2.11	149.5
Ti II	6491.580	2.06	-2.12	117.0
Ti II	6606.980	2.06	-2.85	52.3

Table F.1: continued.

ion	wavelength (Å)	EP (eV)	log gf	EW (mÅ)
V I	4379.240	0.30	0.80	63.3
V I	4389.976	0.28	0.20	34.1
V I	4406.633	0.30	-0.19	20.2
V II	4036.777	1.48	-1.59	81.2
V II	4209.758	1.68	-1.89	50.5
V II	4234.256	1.69	-1.92	49.3
V II	5303.254	2.28	-2.05	19.9
V II	5439.302	2.27	-2.64	7.1
V II	6028.268	2.49	-2.12	12.4
V II	6086.932	2.56	-2.34	6.4
Cr I	4922.270	3.10	0.27	63.9
Cr I	5247.570	0.96	-1.64	54.7
Cr I	5348.330	1.00	-1.29	83.1
Cr I	5409.800	1.03	-0.72	140.4
Cr II	4252.632	3.86	-1.81	111.1
Cr II	4848.250	3.86	-1.14	165.1
Cr II	4884.600	3.86	-2.08	95.6
Cr II	5246.768	3.71	-2.47	77.1
Cr II	5305.870	3.83	-2.08	109.6
Cr II	5308.430	4.07	-1.81	102.4
Cr II	5310.700	4.07	-2.28	74.4
Cr II	5313.590	4.07	-1.78	126.4
Cr II	5334.869	4.07	-1.89	114.6
Cr II	5407.604	3.83	-2.15	100.7
Cr II	5420.922	3.76	-2.46	75.9
Cr II	5502.090	4.17	-1.99	84.9
Cr II	5508.630	4.15	-2.11	79.0
Cr II	5510.730	3.83	-2.48	67.8
Cr II	5671.657	3.83	-3.44	15.1
Mn I	5117.940	3.13	-1.14	7.0
Mn I	5377.610	3.84	-0.39	10.7
Mn I	6021.800	3.07	0.03	53.9
Mn II	5559.047	6.18	-1.31	7.1
Mn II	5578.126	6.19	-1.40	7.3
Fe I	4175.640	2.84	-0.67	144.4
Fe I	4466.550	2.83	-0.59	142.2
Fe I	4494.563	2.20	-1.14	154.3
Fe I	4890.750	2.88	-0.43	157.1
Fe I	4903.310	2.88	-0.93	137.1
Fe I	4907.732	3.43	-1.82	27.3
Fe I	4924.770	2.28	-2.20	81.9
Fe I	4939.687	0.86	-3.33	83.6
Fe I	4946.388	3.37	-1.01	82.4
Fe I	4969.918	4.22	-0.75	39.8
Fe I	4988.950	4.15	-0.79	61.3
Fe I	5002.793	3.40	-1.44	50.8
Fe I	5014.943	3.94	-0.27	96.6
Fe I	5022.236	3.98	-0.49	75.3
Fe I	5029.618	3.42	-1.90	21.0
Fe I	5049.820	2.28	-1.35	134.2
Fe I	5051.635	0.92	-2.78	115.6
Fe I	5074.748	4.22	-0.16	96.6
Fe I	5083.339	0.96	-2.91	108.4
Fe I	5090.774	4.26	-0.36	77.6
Fe I	5110.413	0.00	-3.76	121.7
Fe I	5121.639	4.28	-0.72	51.3
Fe I	5123.720	1.01	-3.07	95.3
Fe I	5125.117	4.22	-0.08	99.6
Fe I	5150.840	0.99	-3.00	114.8
Fe I	5151.911	1.01	-3.32	80.9

Table F.1: continued.

ion	wavelength (Å)	EP (eV)	log gf	EW (mÅ)
Fe I	5159.058	4.28	-0.65	50.7
Fe I	5162.273	4.18	0.08	121.1
Fe I	5171.596	1.49	-1.76	163.7
Fe I	5194.942	1.56	-2.06	136.3
Fe I	5198.711	2.22	-2.14	87.2
Fe I	5202.336	2.18	-1.84	126.7
Fe I	5242.491	3.63	-0.97	73.0
Fe I	5281.790	3.04	-0.83	129.4
Fe I	5288.525	3.69	-1.51	31.2
Fe I	5315.051	4.37	-1.40	8.3
Fe I	5321.108	4.43	-1.19	17.4
Fe I	5322.041	2.28	-2.84	28.3
Fe I	5339.929	3.27	-0.68	120.1
Fe I	5364.871	4.45	0.23	115.3
Fe I	5367.467	4.42	0.44	119.7
Fe I	5369.962	4.37	0.54	128.6
Fe I	5373.709	4.47	-0.71	42.7
Fe I	5389.479	4.42	-0.25	66.7
Fe I	5400.502	4.37	-0.10	96.1
Fe I	5410.910	4.47	0.40	125.8
Fe I	5415.200	4.39	0.50	123.9
Fe I	5445.042	4.39	0.04	94.7
Fe I	5466.396	4.37	-0.57	54.1
Fe I	5487.746	4.32	-0.65	67.7
Fe I	5522.447	4.21	-1.40	20.2
Fe I	5532.747	3.57	-2.00	17.2
Fe I	5554.895	4.55	-0.38	59.2
Fe I	5560.212	4.43	-1.04	29.4
Fe I	5563.600	4.19	-0.84	59.2
Fe I	5567.391	2.61	-2.56	29.6
Fe I	5569.618	3.42	-0.49	136.9
Fe I	5576.089	3.43	-0.85	107.4
Fe I	5633.947	4.99	-0.12	52.8
Fe I	5686.530	4.55	-0.45	56.4
Fe I	5731.762	4.26	-1.15	26.1
Fe I	5916.247	2.45	-2.99	21.4
Fe I	6065.482	2.61	-1.53	109.8
Fe I	6082.711	2.22	-3.58	8.2
Fe I	6093.644	4.61	-1.35	12.3
Fe I	6136.596	2.45	-1.40	129.7
Fe I	6137.692	2.59	-1.40	113.1
Fe I	6151.618	2.18	-3.29	21.7
Fe I	6173.336	2.22	-2.88	40.0
Fe I	6187.990	3.94	-1.57	22.3
Fe I	6191.558	2.43	-1.42	126.1
Fe I	6200.313	2.60	-2.44	41.1
Fe I	6213.430	2.22	-2.48	60.3
Fe I	6230.723	2.56	-1.28	129.1
Fe I	6254.259	2.28	-2.44	63.4
Fe I	6265.134	2.18	-2.55	53.9
Fe I	6322.686	2.59	-2.43	39.1
Fe I	6380.743	4.19	-1.32	22.3
Fe I	6400.001	3.60	-0.29	123.8
Fe I	6411.649	3.65	-0.66	93.2
Fe I	6419.950	4.73	-0.09	66.4
Fe I	6421.351	2.28	-2.01	102.2
Fe I	6430.846	2.18	-2.01	101.1
Fe I	6469.193	4.83	-0.62	26.2
Fe I	6592.914	2.73	-1.47	94.5
Fe I	6593.871	2.44	-2.42	55.5

Table F.1: continued.

ion	wavelength (Å)	EP (eV)	log gf	EW (mÅ)
Fe I	6597.561	4.79	-0.92	18.9
Fe I	6609.110	2.56	-2.69	23.5
Fe I	6750.153	2.24	-2.62	43.2
Fe II	4413.600	2.66	-3.69	122.7
Fe II	4953.987	5.57	-2.76	20.1
Fe II	4993.347	2.81	-3.67	112.2
Fe II	5000.730	2.77	-4.56	53.4
Fe II	5120.352	2.83	-4.21	75.0
Fe II	5132.657	2.81	-4.00	92.9
Fe II	5136.790	2.83	-4.31	66.2
Fe II	5272.400	5.95	-2.03	46.2
Fe II	5284.098	2.89	-3.01	159.6
Fe II	5325.559	3.22	-3.17	127.5
Fe II	5414.046	3.22	-3.62	103.6
Fe II	5425.247	3.20	-3.21	131.2
Fe II	5525.125	3.27	-3.95	52.3
Fe II	5627.490	3.37	-4.18	49.8
Fe II	5725.963	3.42	-4.83	11.8
Fe II	5732.724	3.39	-4.67	23.1
Fe II	5991.368	3.15	-3.56	96.6
Fe II	6084.099	3.20	-3.80	78.4
Fe II	6113.330	3.21	-4.13	56.4
Fe II	6147.741	3.89	-2.73	123.7
Fe II	6149.258	3.89	-2.72	115.2
Fe II	6179.388	5.57	-2.59	18.1
Fe II	6239.910	3.89	-3.68	57.9
Fe II	6248.898	5.51	-2.70	18.6
Fe II	6369.464	2.89	-4.19	82.2
Fe II	6383.721	5.55	-2.14	40.6
Fe II	6385.451	5.55	-2.62	27.6
Fe II	6416.921	3.89	-2.68	125.9
Fe II	6432.682	2.89	-3.71	128.2
Fe II	6446.430	6.20	-1.98	19.1
Fe II	6482.204	6.22	-1.88	35.0
Co I	4121.318	0.92	-0.32	111.5
Co I	5342.700	4.02	0.74	13.8
Ni I	4937.350	3.61	-0.39	45.9
Ni I	5035.370	3.63	0.29	95.3
Ni I	5081.120	3.85	0.30	80.7
Ni I	5082.350	3.66	-0.54	43.2
Ni I	5084.100	3.68	0.03	67.3
Ni I	6111.080	4.09	-0.87	12.6
Ni I	6643.640	1.68	-2.30	40.8
Ni I	6767.780	1.83	-2.17	45.3
Cu I	5105.550	1.39	-1.72	25.5
Cu I	5218.197	3.82	0.36	20.3
Zn I	4810.540	4.08	-0.17	64.8 (SS)
Y II	5119.112	0.99	-1.36	47.3
Y II	5196.422	1.75	-0.88	34.5
Y II	5289.815	1.03	-1.85	27.7
Y II	5402.774	1.84	-0.51	65.2
Y II	5473.388	1.74	-1.02	40.5
Y II	5546.009	1.75	-1.10	37.4
Y II	5728.890	1.84	-1.12	25.3
Y II	6613.733	1.75	-1.11	33.6
Zr II	4050.320	0.71	-1.06	90.8
Zr II	4317.309	0.71	-1.45	49.1
Zr II	4370.948	1.21	-0.77	60.1
Zr II	4414.535	1.24	-1.08	54.8
Zr II	4816.500	1.01	-2.00	12.6

Table F.1: continued.

ion	wavelength (Å)	EP (eV)	log gf	EW (mÅ)
Zr II	5112.270	1.67	-0.85	43.1
Zr II	6114.852	1.67	-1.40	10.2
Ba II	4166.000	2.72	-0.42	49.5 (SS)
La II	4322.503	0.17	-1.05	57.6
La II	4804.039	0.23	-1.49	37.7
La II	4808.996	0.23	-1.49	40.8
La II	4986.819	0.17	-1.18	54.8
La II	4999.461	0.40	-0.75	113.9
La II	5114.559	0.23	-1.04	60.1
La II	5290.818	0.00	-1.72	26.9
La II	5303.528	0.32	-1.41	30.3
La II	5482.268	0.00	-2.06	12.5
La II	6262.287	0.40	-1.21	45.7
La II	6320.376	0.17	-1.56	29.2
La II	6390.477	0.32	-1.44	31.6
La II	6774.268	0.13	-1.71	29.8
Ce II	4144.996	0.70	-0.05	59.2
Ce II	4193.871	0.55	-0.47	48.2
Ce II	4483.893	0.86	0.01	67.4
Ce II	4486.909	0.29	-0.09	94.8
Ce II	5117.169	1.40	0.01	32.5
Ce II	5187.458	1.21	0.30	58.5
Ce II	5252.662	1.16	-0.87	12.2
Ce II	5274.229	1.04	0.30	75.6
Ce II	5695.847	1.63	-0.48	7.6
Ce II	5975.818	1.33	-0.45	20.8
Ce II	6043.373	1.21	-0.32	27.6
Pr II	4510.153	0.42	-0.30	23.2
Pr II	5219.045	0.80	-0.25	15.0
Pr II	5220.108	0.80	0.15	34.6
Pr II	5322.772	0.48	-0.46	15.6
Nd II	4061.080	0.47	0.35	122.1
Nd II	4327.932	0.56	-0.43	64.0
Nd II	4451.563	0.38	0.03	104.2
Nd II	4462.979	0.56	-0.05	74.7
Nd II	4959.119	0.06	-0.92	45.9
Nd II	4989.950	0.63	-0.62	42.7
Nd II	5092.794	0.38	-0.61	51.3
Nd II	5130.586	1.30	0.24	57.4
Nd II	5293.163	0.82	-0.14	67.4
Nd II	5361.467	0.68	-0.48	41.5
Nd II	5385.888	0.74	-0.86	24.4
Nd II	5431.516	1.12	-0.46	23.5
Nd II	5442.264	0.68	-0.98	22.9
Nd II	5485.696	1.26	-0.28	30.1
Nd II	5740.858	1.16	-0.56	19.9
Nd II	5842.366	1.28	-0.60	14.5
Nd II	6034.228	1.54	-0.66	9.9
Nd II	6740.078	0.06	-1.53	22.4
Sm II	4262.669	0.38	-0.35	45.0
Sm II	4323.290	0.10	-0.90	23.2
Sm II	4424.337	0.48	0.08	80.9
Sm II	4452.722	0.28	-0.43	43.0
Eu II	6437.640	1.32	-0.27	25.7
Eu II	6645.064	1.38	0.20	47.5
Gd II	4406.656	1.430	-0.05	18.98 (SS)
Dy II	4449.700	0.000	-1.03	28.31 (SS)
Lu II	6221.890	1.54	-0.76	17.6 (SS)
Th II	4019.129	0.00	-0.23	43.5 (SS)

Bibliography

Abia, C., Cunha, K., Cristallo, S., et al. 2011, ApJ, 737

Abia, C., de Laverny, P., & Wahlin, R. 2008, A&A, 481, 161

Abia, C., Domínguez, I., Gallino, R., et al. 2002, ApJ, 579, 817

Alves-Brito, A., Karakas, A. I., Yong, D., Meléndez, J., & Vásquez, S. 2011, A&A, 536, A40

Angelou, G. C., Church, R. P., Stancliffe, R. J., Lattanzio, J. C., & Smith, G. H. 2011, ApJ, 728, 79

Aoki, W., Ryan, S. G., Norris, J. E., et al. 2001, ApJ, 561, 346

Arnould, M. & Goriely, S. 2006, Nuclear Physics A, 777, 157

Asplund, M., Grevesse, N., & Sauval, A. J. 2005, in Astronomical Society of the Pacific Conference Series, Vol. 336, Cosmic Abundances as Records of Stellar Evolution and Nucleosynthesis, ed. T. G. Barnes III & F. N. Bash, 25

Asplund, M., Grevesse, N., Sauval, A. J., & Scott, P. 2009, ARA&A, 47, 481

Becker, S. A. 1981, ApJ, 248, 298

Becker, S. A. & Iben, Jr., I. 1980, ApJ, 237, 111

Beers, T. C. & Christlieb, N. 2005, ARA&A, 43, 531

Behara, N. T., Bonifacio, P., Ludwig, H.-G., et al. 2010, A&A, 513, A72

Bekki, K. & Tsujimoto, T. 2012, ApJ, 761, 180

Bisterzo, S., Travaglio, C., Gallino, R., Wiescher, M., & Käppeler, F. 2014, ApJ, 787, 10

Blöcker, T. 2001, Ap&SS, 275, 1

Blöcker, T. 1995, A&A, 299, 755

Blum, R. D., Mould, J. R., Olsen, K. A., et al. 2006, AJ, 132, 2034

Bolatto, A. D., Simon, J. D., Stanimirović, S., et al. 2007, ApJ, 655, 212

Bond, H. E. 1991, in IAU Symp. 145: Evolution of Stars: the Photospheric Abundance Connection, Vol. 145, 341+

Boothroyd, A. I. & Sackmann, I.-J. 1999, ApJ, 510, 232

Boothroyd, A. I., Sackmann, I.-J., & Ahern, S. C. 1993, ApJ, 416, 762

Bowen, G. H. 1988, ApJ, 329, 299

Bujarrabal, V., Alcolea, J., Van Winckel, H., Santander-García, M., & Castro-Carrizo, A. 2013, A&A, 557, A104

Bujarrabal, V., Castro-Carrizo, A., Alcolea, J., & Van Winckel, H. 2015, A&A, 575, L7

Busso, M., Gallino, R., Lambert, D. L., Travaglio, C., & Smith, V. V. 2001, ApJ, 557, 802

Busso, M., Gallino, R., & Wasserburg, G. J. 1999, ARA&A, 37, 239

Busso, M., Lambert, D. L., Beglio, L., et al. 1995, ApJ, 446, 775+

Busso, M., Palmerini, S., Maiorca, E., et al. 2010, ApJ, 717, L47

Cardelli, J. A., Clayton, G. C., & Mathis, J. S. 1989, ApJ, 345, 245

Carroll, B. W. & Ostlie, D. A. 1996, An Introduction to Modern Astrophysics

Castelli, F. & Kurucz, R. L. 2004, ArXiv Astro-ph/0405087

Cerrigone, L., Hora, J. L., Umana, G., et al. 2011, ApJ, 738, 121

Charlton, J. & Churchill, C. 2000, Quasistellar Objects: Intervening Absorption Lines, ed. P. Murdin, 2366

Church, R. P., Cristallo, S., Lattanzio, J. C., et al. 2009, PASA, 26, 217

Cignoni, M., Cole, A. A., Tosi, M., et al. 2012, ApJ, 754, 130

Clayton, D. D. 1983, Principles of stellar evolution and nucleosynthesis

Coelho, P., Barbuy, B., Meléndez, J., Schiavon, R. P., & Castilho, B. V. 2005, A&A, 443, 735

Cristallo, S., Piersanti, L., & Straniero, O. 2014, ArXiv e-prints

Cristallo, S., Piersanti, L., Straniero, O., et al. 2011, ApJS, 197, 17

Cristallo, S., Straniero, O., Gallino, R., et al. 2009, ApJ, 696, 797

Cunha, K., Hubeny, I., & Lanz, T. 2006, ApJ, 647, L143

Cutri, R. M., Skrutskie, M. F., van Dyk, S., et al. 2003, VizieR Online Data Catalog, 2246, 0

Cutri, R. M., Wright, E. L., Conrow, T., et al. 2012, Explanatory Supplement to the WISE All-Sky Data Release Products, Tech. rep.

Cyburt, R. H., Amthor, A. M., Ferguson, R., et al. 2010, ApJS, 189, 240

de Laverny, P., Abia, C., Domínguez, I., et al. 2006, A&A, 446, 1107

De Ruyter, S., Van Winckel, H., Maas, T., et al. 2006, A&A, 448, 641

De Smedt, K., Van Winckel, H., Kamath, D., et al. 2014, A&A, 563, L5

De Smedt, K., Van Winckel, H., Karakas, A. I., et al. 2012, A&A, 541, A67

de Vaucouleurs, G. & Freeman, K. C. 1972, Vistas in Astronomy, 14, 163

Dekker, H., D'Odorico, S., Kaufer, A., Delabre, B., & Kotzlowski, H. 2000, in Society of Photo-Optical Instrumentation Engineers (SPIE) Conference Series, Vol. 4008, Society of Photo-Optical Instrumentation Engineers (SPIE) Conference Series, 534–545

Denissenkov, P. A. & Tout, C. A. 2003, MNRAS, 340, 722

Deroo, P., Acke, B., Verhoelst, T., et al. 2007, A&A, 474, L45

Deroo, P., Reyniers, M., Van Winckel, H., Goriely, S., & Siess, L. 2005, A&A, 438, 987

El Eid, M. F. 1994, A&A, 285, 915

Epchtein, N., de Batz, B., Capoani, L., et al. 1997, The Messenger, 87, 27

Fazio, G. G., Hora, J. L., Allen, L. E., et al. 2004, ApJS, 154, 10

Fishlock, C. K., Karakas, A. I., Lugaro, M., & Yong, D. 2014, ApJ, 797, 44

Fouqué, P., Chevallier, L., Cohen, M., et al. 2000, A&AS, 141, 313

Gallino, R., Arlandini, C., Busso, M., et al. 1998, ApJ, 497, 388

Gallino, R., Straniero, O., Zinner, E., et al. 2011, in Astronomical Society of the Pacific Conference Series, Vol. 445, Why Galaxies Care about AGB Stars II: Shining Examples and Common Inhabitants, ed. F. Kerschbaum, T. Lebzelter, & R. F. Wing, 143

Geisler, D., Grocholski, A., Sarajedini, A., Cole, A., & Smith, V. 2009, LMC Cluster Abundances and Kinematics, ed. T. Richtler & S. Larsen, 133

Gezer, I., Van Winckel, H., Bozkurt, Z., et al. 2015, MNRAS, 453, 133

Gielen, C., Bouwman, J., van Winckel, H., et al. 2011, A&A, 533, A99

Gielen, C., Van Winckel, H., Reyniers, M., et al. 2009, A&A, 508, 1391

Giridhar, S., Ferro, A., & Parrao, L. 1997, PASP, 109, 1077

Gonzalez, G. & Wallerstein, G. 1999, AJ, 117, 2286

Gordon, K. D., Clayton, G. C., Misselt, K. A., Landolt, A. U., & Wolff, M. J. 2003, ApJ, 594, 279

Gordon, K. D., Meixner, M., Meade, M. R., et al. 2011, AJ, 142, 102

Goriely, S. & Mowlavi, N. 2000, A&A, 362, 599

Goriely, S. & Siess, L. 2001, A&A, 378, L25

Goriely, S. & Siess, L. 2004, A&A, 421, L25

Goriely, S. & Siess, L. 2005, in IAU Symposium, Vol. 228, From Lithium to Uranium: Elemental Tracers of Early Cosmic Evolution, ed. V. Hill, P. Francois, & F. Primas, 451–460

Gorlova, N., Van Winckel, H., Vos, J., et al. 2013, in EAS Publications Series, Vol. 64, EAS Publications Series, ed. K. Pavlovski, A. Tkachenko, & G. Torres, 163–170

Gorlova, N., Van Winckel, H., Vos, J., et al. 2014, ArXiv e-prints

Gray, D. F. 2005, The Observation and Analysis of Stellar Photospheres

Gustafsson, B., Edvardsson, B., Eriksson, K., et al. 2008, A&A, 486, 951

Habing, H. J. & Olofsson, H., eds. 2003, Asymptotic giant branch stars

Habing, H. J. & Olofsson, H. 2004, Asymptotic Giant Branch Stars (Springer)

Han, Z., Podsiadlowski, P., & Eggleton, P. P. 1995, MNRAS, 272, 800

Harris, J. & Zaritsky, D. 2009, AJ, 138, 1243

Hayashi, C. 1961, PASJ, 13, 450

Heber, U. 2009, ARA&A, 47, 211

Helou, G. & Walker, D. W., eds. 1988, Infrared astronomical satellite (IRAS) catalogs and atlases. Volume 7: The small scale structure catalog, Vol. 7

Henyey, L. G., Lelevier, R., & Levée, R. D. 1955, PASP, 67, 154

Herwig, F. 2000, A&A, 360, 952

Herwig, F. 2005, ARA&A, 43, 435

Herwig, F., Blöcker, T., Langer, N., & Driebe, T. 1999, A&A, 349, L5

Herwig, F., Bloecker, T., Schönberner, D., & El Eid, M. 1997, A&A, 324, L81

Herwig, F., Langer, N., & Lugaro, M. 2003, ApJ, 593, 1056

Hilditch, R. W., Howarth, I. D., & Harries, T. J. 2005, MNRAS, 357, 304

Hill, V. 1997, A&A, 324, 435

Hill, V. 1999, A&A, 345, 430

Hillen, M., Menu, J., Van Winckel, H., et al. 2014, A&A, 568, A12

Hillen, M., Verhoelst, T., Van Winckel, H., et al. 2013, A&A, 559, A111

Hrivnak, B. J., Van Winckel, H., Reyniers, M., et al. 2008a, AJ, 136, 1557

Hrivnak, B. J., Volk, K., Geballe, T. R., & Kwok, S. 2008b, in IAU Symposium, Vol. 251, IAU Symposium, ed. S. Kwok & S. Sandford, 213–214

Hrivnak, B. J., Volk, K., & Kwok, S. 2009, ApJ, 694, 1147

Iben, I. 1984, ApJ, 277, 333

Iben, I. & Renzini, A. 1983, ARA&A, 21, 271

Iben, Jr., I. 1967, ApJ, 147, 624

Ishihara, D., Onaka, T., Kataza, H., et al. 2010, A&A, 514, A1

Jonsell, K., Barklem, P. S., Gustafsson, B., et al. 2006, A&A, 451, 651

Jorissen, A., Van Eck, S., Mayor, M., & Udry, S. 1998, A&A, 332, 877

Kamath, D., Karakas, A. I., & Wood, P. R. 2012, ApJ, 746, 20

Kamath, D., Wood, P., Van Winckel, H., & van Aarle, E. 2011, in 9th Pacific Rim Conference on Stellar Astrophysics, ed. , ASP conference series, in press

Kamath, D., Wood, P. R., Soszyński, I., & Lebzelter, T. 2010, MNRAS, 408, 522

Kamath, D., Wood, P. R., & Van Winckel, H. 2014, MNRAS, 439, 2211

Kamath, D., Wood, P. R., & Van Winckel, H. 2015, ArXiv e-prints

Karakas, A. & Lattanzio, J. C. 2007, PASA, 24, 103

Karakas, A. & Lugaro, M. 2010, in Nuclei in the Cosmos, 42

Karakas, A. I. 2010, MNRAS, 403, 1413

Karakas, A. I., Campbell, S. W., & Stancliffe, R. J. 2010, ApJ, 713, 374

Karakas, A. I., García-Hernández, D. A., & Lugaro, M. 2012, ApJ, 751, 8

Karakas, A. I. & Lattanzio, J. C. 2014, PASA, 31, 30

Karakas, A. I., Lattanzio, J. C., & Pols, O. R. 2002, PASA, 19, 515

Keller, S. C. & Wood, P. R. 2006, ApJ, 642, 834

Kepler, S. O., Fraga, L., Winget, D. E., et al. 2014, MNRAS, 442, 2278

Kharchenko, N. V. 2001, Kinematika i Fizika Nebesnykh Tel, 17, 409

Kippenhahn, R. & Weigert, A. 1994, Stellar Structure and Evolution

Kippenhahn, R., Weigert, A., & Weiss, A. 2012, Stellar Structure and Evolution

Kiselman, D. 2002, Highlights of Astronomy, 12, 429

Kiss, L. L., Szabó, G. M., & Bedding, T. R. 2006, MNRAS, 372, 1721

Klochkova, V. G. 1995, MNRAS, 272, 710

Kobayashi, C., Karakas, A. I., & Umeda, H. 2011, MNRAS, 414, 3231

Kramida, A., Yu. Ralchenko, Reader, J., & and NIST ASD Team. 2013, NIST Atomic Spectra Database (ver. 5.1), [Online]. Available: `http://physics.nist.gov/asd` [2013, November 6]. National Institute of Standards and Technology, Gaithersburg, MD.

Kupka, F., Piskunov, N., Ryabchikova, T. A., Stempels, H. C., & Weiss, W. W. 1999, A&AS, 138, 119

Kurucz, R. L. 1970, SAO Special Report, 309

Kwok, S., Volk, K. M., & Hrivnak, B. J. 1989, ApJ, 345, L51

Lagadec, E., Verhoelst, T., Mékarnia, D., et al. 2011, MNRAS, 417, 32

Lambert, D. L., Luck, R. E., & Bond, H. E. 1983, PASP, 95, 413

Lamers, H. J. G. L. M. & Cassinelli, J. P. 1999, Introduction to Stellar Winds

Langer, N., Heger, A., Wellstein, S., & Herwig, F. 1999, A&A, 346, L37

Lapenna, E., Mucciarelli, A., Origlia, L., & Ferraro, F. R. 2012, ApJ, 761, 33

Lasker, B. M., Lattanzi, M. G., McLean, B. J., et al. 2008, AJ, 136, 735

Lattanzio, J. 2003, in IAU Symposium, Vol. 209, Planetary Nebulae: Their Evolution and Role in the Universe, ed. S. Kwok, M. Dopita, & R. Sutherland, 73

Lattanzio, J. C. & Boothroyd, A. I. 1997, in American Institute of Physics Conference Series, Vol. 402, American Institute of Physics Conference Series, ed. T. J. Bernatowicz & E. Zinner, 85–114

Lau, H. H. B., De Marco, O., & Liu, X.-W. 2011, MNRAS, 410, 1870

Lederer, M. T. & Aringer, B. 2009, A&A, 494, 403

Lobel, A. 2006, in IAU Joint Discussion, Vol. 4, IAU Joint Discussion

Lodders, K., Palme, H., & Gail, H.-P. 2009, Landolt Börnstein, 44

Luck, R. E. & Lambert, D. L. 1992, ApJS, 79, 303

Luck, R. E., Moffett, T. J., Barnes, III, T. G., & Gieren, W. P. 1998, AJ, 115, 605

Lugaro, M., Campbell, S. W., Van Winckel, H., et al. 2015, A&A

Lugaro, M., Karakas, A. I., Stancliffe, R. J., & Rijs, C. 2012, ApJ, 747, 2

Lugaro, M., Ugalde, C., Karakas, A. I., et al. 2004, ApJ, 615, 934

Lugaro, M. & van Raai, M. 2008, Journal of Physics G Nuclear Physics, 35, 014007

Lyubimkov, L. S., Lambert, D. L., Korotin, S. A., et al. 2011, MNRAS, 410, 1774

Maas, T., Van Winckel, H., & Waelkens, C. 2002, A&A, 386, 504

Marigo, P. 2002, A&A, 387, 507

Marigo, P., Bressan, A., Nanni, A., Girardi, L., & Pumo, M. L. 2013, MNRAS, 434, 488

Marigo, P., Girardi, L. ., & Bressan, A. 1999, A&A, 344, 123

Massey, P. 2002, ApJS, 141, 81

Matsuura, M., Bernard-Salas, J., Lloyd Evans, T., et al. 2014, MNRAS, 439, 1472

Meixner, M., Gordon, K. D., Indebetouw, R., et al. 2006, AJ, 132, 2268

Meixner, M., Ueta, T., Dayal, A., et al. 1999, ApJS, 122, 221

Mermilliod, J.-C., Mermilliod, M., & Hauck, B. 1997, A&AS, 124, 349

Mowlavi, N., Jorissen, A., & Arnould, M. 1998, A&A, 334, 153

Mucciarelli, A., Carretta, E., Origlia, L., & Ferraro, F. R. 2008, AJ, 136, 375

Mucciarelli, A., Origlia, L., & Ferraro, F. R. 2010, ApJ, 717, 277

Munari, U., Sordo, R., Castelli, F., & Zwitter, T. 2005, A&A, 442, 1127

Neyskens, P., van Eck, S., Jorissen, A., et al. 2015, Nature, 517, 174

Olszewski, E. W., Suntzeff, N. B., & Mateo, M. 1996, ARA&A, 34, 511

Pace, G., Castro, M., Meléndez, J., Théado, S., & do Nascimento, Jr., J.-D. 2012, A&A, 541, A150

Palacios, A., Charbonnel, C., Talon, S., & Siess, L. 2006, A&A, 453, 261

Piersanti, L., Cristallo, S., & Straniero, O. 2013, ApJ, 774, 98

Pignatari, M., Gallino, R., Heil, M., et al. 2010, ApJ, 710, 1557

Pojmanski, G. & Maciejewski, G. 2004, Acta Astron., 54, 153

Pompéia, L., Hill, V., Spite, M., et al. 2008, A&A, 480, 379

Posch, T., Mutschke, H., & Andersen, A. 2004, ApJ, 616, 1167

Rao, S. S., Giridhar, S., & Lambert, D. L. 2012, MNRAS, 419, 1254

Raskin, G., van Winckel, H., Hensberge, H., et al. 2011, A&A, 526, A69

Reddy, B. E., Bakker, E. J., & Hrivnak, B. J. 1999, ApJ, 524, 831

Reddy, B. E., Lambert, D. L., Gonzalez, G., & Yong, D. 2002, ApJ, 564, 482

Reid, W. A. & Parker, Q. A. 2010, MNRAS, 405, 1349

Reimers, D. 1975, Memoires of the Societe Royale des Sciences de Liege, 8, 369

Reyniers, M. 2002, PhD thesis, Departement Natuurkunde en Sterrenkunde, K.U.Leuven, Celestijnenlaan 200B, 3001 Leuven, Belgium

Reyniers, M., Abia, C., Van Winckel, H., et al. 2007a, A&A, 461, 641

Reyniers, M., van de Steene, G. C., van Hoof, P. A. M., & van Winckel, H. 2007b, A&A, 471, 247

Reyniers, M. & Van Winckel, H. 2003, A&A, 408, L33

Reyniers, M. & Van Winckel, H. 2007, A&A, 463, L1

Reyniers, M., Van Winckel, H., Biémont, E., & Quinet, P. 2002, A&A, 395, L35

Reyniers, M., Van Winckel, H., Gallino, R., & Straniero, O. 2004, A&A, 417, 269

Richter, O.-G., Tammann, G. A., & Huchtmeier, W. K. 1987, A&A, 171, 33

Rieke, G. H., Young, E. T., Engelbracht, C. W., et al. 2004, ApJS, 154, 25

Romano, D., Karakas, A. I., Tosi, M., & Matteucci, F. 2010, A&A, 522, A32

Russell, S. C. & Bessell, M. S. 1989, ApJS, 70, 865

Schlegel, D. J., Finkbeiner, D. P., & Davis, M. 1998, ApJ, 500, 525

Schönberner, D. 1979, A&A, 79, 108

Schönberner, D. 1983, ApJ, 272, 708

Schönberner, D. 2008, in Astronomical Society of the Pacific Conference Series, Vol. 391, Hydrogen-Deficient Stars, ed. A. Werner & T. Rauch, 139

Seeger, P. A., Fowler, W. A., & Clayton, D. D. 1965, ApJS, 11, 121

Sharp, R., Saunders, W., Smith, G., et al. 2006, in Society of Photo-Optical Instrumentation Engineers (SPIE) Conference Series, Vol. 6269, Society of Photo-Optical Instrumentation Engineers (SPIE) Conference Series, 0

Siess, L. 2006, A&A, 448, 717

Siess, L. 2007, A&A, 476, 893

Siess, L. & Arnould, M. 2008, A&A, 489, 395

Siess, L., Dufour, E., & Forestini, M. 2000, A&A, 358, 593

Siess, L., Goriely, S., & Langer, N. 2003, PASA, 20, 371

Siess, L., Goriely, S., & Langer, N. 2004, A&A, 415, 1089

Skrutskie, M. F., Cutri, R. M., Stiening, R., et al. 2006, AJ, 131, 1163

Sloan, G. C., Lagadec, E., Zijlstra, A. A., et al. 2014, ApJ, 791, 28

Smith, V. V., Lambert, D. L., & McWilliam, A. 1987, ApJ, 320, 862

Sneden, C., Cowan, J. J., & Gallino, R. 2008, ARA&A, 46, 241

Sneden, C. A. 1973, PhD thesis, The University of Texas at Austin.

Spite, F., Barbuy, B., & Spite, M. 1993, A&A, 272, 116

Spite, M., Francois, P., Spite, F., Cayrel, R., & Richtler, T. 1986, A&A, 168, 197

Stancliffe, R. J., Dearborn, D. S. P., Lattanzio, J. C., Heap, S. A., & Campbell, S. W. 2011, ApJ, 742, 121

Stancliffe, R. J., Glebbeek, E., Izzard, R. G., & Pols, O. R. 2007, A&A, 464, L57

Storm, J., Gieren, W., Fouqué, P., et al. 2011, A&A, 534, A95

Straniero, O., Gallino, R., Busso, M., et al. 1995, ApJ, 440, L85

Straniero, O., Gallino, R., & Cristallo, S. 2006, Nuclear Physics A, 777, 311

Szymanski, M. K. 2005, Acta Astron., 55, 43

Truran, J. W. & Iben, Jr., I. 1977, ApJ, 216, 797

Udalski, A., Kubiak, M., & Szymanski, M. 1997, Acta Astron., 47, 319

Ueta, T., Meixner, M., & Bobrowsky, M. 2000, ApJ, 528, 861

van Aarle, E., Van Winckel, H., De Smedt, K., Kamath, D., & Wood, P. R. 2013, A&A, 554, A106

van Aarle, E., van Winckel, H., Lloyd Evans, T., et al. 2011, A&A, 530, A90

van der Marel, R. P., Alves, D. R., Hardy, E., & Suntzeff, N. B. 2002, AJ, 124, 2639

Van der Swaelmen, M., Hill, V., Primas, F., & Cole, A. A. 2013, A&A, 560, A44

Van Eck, S., Goriely, S., Jorissen, A., & Plez, B. 2001, Nature, 412, 793

Van Eck, S., Goriely, S., Jorissen, A., & Plez, B. 2003, A&A, 404, 291

van Loon, J. T., Zijlstra, A. A., Whitelock, P. A., et al. 1998, A&A, 329, 169

Van Winckel, H. 2003, ARA&A, 41, 391

Van Winckel, H., Cohen, M., & Gull, T. R. 2002, A&A, 390, 147

Van Winckel, H., Jorissen, A., Gorlova, N., et al. 2010, MemSAI, 81, 1022

Van Winckel, H., Lloyd Evans, T., Briquet, M., et al. 2009, A&A, 505, 1221

Van Winckel, H., Mathis, J. S., & Waelkens, C. 1992, Nature, 356, 500

Van Winckel, H., Oudmaijer, R. D., & Trams, N. R. 1996a, A&A, 312, 553

Van Winckel, H. & Reyniers, M. 2000, A&A, 354, 135

Van Winckel, H., Waelkens, C., Fernie, J. D., & Waters, L. B. F. M. 1999, A&A, 343, 202

Van Winckel, H., Waelkens, C., & Waters, L. B. F. M. 1995, A&A, 293, L25

Van Winckel, H., Waelkens, C., & Waters, L. B. F. M. 1996b, A&A, 306, L37+

Vassiliadis, E. & Wood, P. R. 1993, ApJ, 413, 641

Vassiliadis, E. & Wood, P. R. 1994, ApJS, 92, 125

Venn, K. A. & Lambert, D. L. 1990, ApJ, 363, 234

Volk, K., Hrivnak, B. J., Matsuura, M., et al. 2011, ApJ, 735, 127

Volk, K., Kwok, S., & Hrivnak, B. J. 1999, ApJ, 516, L99

Waters, L. B. F. M., Trams, N. R., & Waelkens, C. 1992, A&A, 262, L37

Werner, K., Rauch, T., Kruk, J. W., & Kurucz, R. L. 2011, A&A, 531, A146

Werner, M. W., Roellig, T. L., Low, F. J., et al. 2004, ApJS, 154, 1

Wesson, R., Cernicharo, J., Barlow, M. J., et al. 2010, A&A, 518, L144

Wood, P. R. 1976, MNRAS, 174, 531

Wood, P. R. 1979, ApJ, 227, 220

Wood, P. R., Kamath, D., & Van Winckel, H. 2013, MNRAS, 435, 355

Woods, P. M., Oliveira, J. M., Kemper, F., et al. 2011, MNRAS, 411, 1597

Wright, E. L., Eisenhardt, P. R. M., Mainzer, A. K., et al. 2010, AJ, 140, 1868

Zaritsky, D., Harris, J., Thompson, I. B., & Grebel, E. K. 2004, AJ, 128, 1606

Zaritsky, D., Harris, J., Thompson, I. B., Grebel, E. K., & Massey, P. 2002, AJ, 123, 855

Zhang, Y., Kwok, S., Nakashima, J.-i., Chau, W., & Dinh-V-Trung. 2013, ApJ, 773, 71

List of publications

Publications in refereed journals

- **Post-AGB stars in the SMC as tracers of stellar evolution: the extreme s-process enrichment of the 21 μm star J004441.04-732136.4**
  2012, A&A, 541, 67. **Chapter 3 in this thesis.**
  De Smedt, K., Van Winckel, H., Karakas, A. I., Siess, L., Goriely, S., Wood, P. R.

- **The orbits of subdwarf B + main-sequence binaries. I. The sdB+G0 system PG 1104+243**
  2012, A&A, 548, 6.
  Vos, J., Østensen, R. H., Degroote, P., **De Smedt, K.**, Green, E. M., Heber, U., Van Winckel, H., Acke, B., Bloemen, S., De Cat, P., Exter, K., Lampens, P., Lombaert, R., Masseron, T., Menu, J., Neyskens, P., Raskin, G., Ringat, E., Rauch, T., Smolders, K., Tkachenko, A.

- **Remarkable spectral variability on the spin period of the accreting white dwarf in V455 And**
  2013, MNRAS, 429, 3433.
  Bloemen, S., Steeghs, D., **De Smedt, K.**, Vos, J., Gänsicke, B. T., Marsh, T. R., Rodriguez-Gil, P.

- **Detailed abundance study of four s-process enriched post-AGB stars in the Large Magellanic Cloud**
  2013, A&A, 554, 106.
  van Aarle, E., Van Winckel, H., **De Smedt, K.**, Kamath, D., Wood, P. R.

- **A search for pulsations in the HgMn star HD 45975 with CoRoT photometry and ground-based spectroscopy**
  2014, A&A, 561, 35.
  Morel, T., Briquet, M., Auvergne, M., Alecian, G., Ghazaryan, S., Niemczura, E., Fossati, L., Lehmann, H., Hubrig, S., Ulusoy, C., Damerdji, Y., Rainer, M., Poretti, E., Borsa, F., Scardia, M., Schmid, V. S., Van Winckel, H., **De Smedt, K.**, Pápics, P. I., Gameiro, J. F., Waelkens, C., Fagas, M., Kaminski, K., Dimitrov, W., Baglin, A., Michel, E., Dumortier, L., Frémat, Y., Hensberge, H., Jorissen, A., Van Eck, S.

- **The lead discrepancy in intrinsically *s*-process enriched post-AGB stars in the Magellanic Clouds**
  2014, A&A, 563, 5. **Chapter 4 in this thesis.**
  De Smedt, K., Van Winckel, H., Kamath, D., Karakas, A. I., Siess, L., Goriely, S., Wood, P.

- **Pulsating red giant stars in eccentric binary systems discovered from Kepler space-based photometry. A sample study and the analysis of KIC 5006817**
  2014, A&A, 564, 36.
  Beck, P. G., Hambleton, K., Vos, J., Kallinger, T., Bloemen, S., Tkachenko, A., García, R. A., Østensen, R. H., Aerts, C., Kurtz, D. W., De Ridder, J., Hekker, S., Pavlovski, K., Mathur, S., **De Smedt, K.**, Derekas, A., Corsaro, E., Mosser, B., Van Winckel, H., Huber, D., Degroote, P., Davies, G. R., Prsa, A., Debosscher, J., Elsworth, Y., Nemeth, P., Siess, L., Schmid, V. S., Pápics, P. I., de Vries, B. L., van Marle, A. J., Marcos-Arenal, P., Lobel, A.

- **Detecting non-uniform period spacings in the Kepler photometry of gamma Doradus stars: methodology and case studies**
  2015, A&A, 574, 17.
  Van Reeth, T., Tkachenko, A., Aerts, C., Pápics, P. I., Degroote, P., Debosscher, J., Zwintz, K., Bloemen, S., **De Smedt, K.**, Hrudkova, M., Raskin, G., Van Winckel, H.

- **Asteroseismic Fingerprints of Rotation and Mixing in the Slowly Pulsating B8 V Star KIC 7760680**
  2015, ApJ, 803, 25.
  Pápics, P. I., Tkachenko, A., Aerts, C., Van Reeth, T., **De Smedt, K.**, Hillen, M., Østensen, R., Moravveji, E.

- **Gravity-mode Period Spacings as a Seismic Diagnostic for a Sample of gamma Doradus Stars from Kepler Space Photometry and High-resolution Ground-based Spectroscopy**

2015, ApJS, 218, 27.
Van Reeth, T., Tkachenko, A., Aerts, C., Pápics, P. I., Triana, S. A., Zwintz, K., Degroote, P., Debosscher, J., Bloemen, S., Schmid, V. S., **De Smedt, K.**, Fremat, Y., Fuentes, A. S., Homan, W., Hrudkova, M., Karjalainen, R., Lombaert, R., Nemeth, P., Østensen, R., Van De Steene, G., Vos, J., Raskin, G., Van Winckel, H.

- **Chemical abundance study of two strongly *s*-process enriched post-AGB stars in the LMC: J051213.81-693537.1 and J051848.86-700246.9**
  2015, A&A accepted **Chapter 5 in this thesis.**
  De Smedt, K., Van Winckel, H., Kamath, D., Wood, P.

- **The WISE view of RV Tauri stars**
  2015, MNRAS, 453, 133.
  Gezer, I., Van Winckel, H., Bozkurt, Z., **De Smedt, K.**, Kamath, D., Hillen, M., Manick, R.

- **KIC 10080943: An eccentric binary system containing two pressure and gravity mode hybrid pulsators**
  2015, A&A accepted
  Schmid, V. S., Tkachenko, A., Aerts, C., Degroote, P., Bloemen, S., Murphy, S. J., Van Reeth, T., Papics, P. I., Bedding, T. R., Keen, M. A., Prsa, A., Menu, J., Debosscher, J., Hrudkova, M., **De Smedt, K.** Lombaert, R., Nemeth, P.

- **Internal rotation of red-giant star KIC 4448777 by means of asteroseismic inversion**
  2015, ApJ, submitted
  Di Mauro, M. P., Ventura, R., Cardini, D., Stello, D., Christensen-Dalsgaard, J., Dziembowski, W. A., Paternò, L., Beck, P. G., Bloemen, S., Davies, G. R., **De Smedt, K.**, Elsworth, Y., García, R. A., Hekker, S., Mosser, B., Tkachenko, A.

- **Post-AGB stars in the Magellanic Clouds and neutron-capture processes in AGB stars**
  2015, A&A accepted
  Lugaro, M., Campbell, S. W., Van Winckel, H., **De Smedt, K.**, A. I., Käppeler, F.

- **Post-AGB stars in the Magellanic Clouds and neutron-capture processes in AGB stars**
  2015, A&A accepted
  Lugaro, M., Campbell, S. W., Van Winckel, H., **De Smedt, K.**, Karakas, A. I., Käppeler, F.

- **Study of Pb abundances in Galactic *s*-process enriched post-AGB stars**
  2015, A&A, submitted. **Chapter 6 in this thesis.**
  De Smedt, K., Van Winckel, H., Kamath, D., Siess, L., Goriely, S., Karakas, A. I., Manick R.

Publications in conference proceedings

- **Post-AGB stars in the LMC and SMC**
  2012, Planetary Nebulae: An Eye to the Future, Proceedings of the International Astronomical Union, IAU Symposium, 283, 235
  Van Winckel, H., van Aarle, E., Wood, P. R., Kamath, D., Evans, T. L., **De Smedt, K.**, Gorlova, N., Gielen, C.

- **Post-AGB stars in the Magellanic Clouds as tracers of the *s*-process nucleosynthesis**
  2014, Why Galaxies Care About AGB Stars III
  De Smedt, K., Van Winckel, H., Kamath D. , Karakas, A. I., Siess, L., Goriely, S., Wood, P. R.

FACULTY OF SCIENCE
DEPARTMENT OF PHYSICS AND ASTRONOMY
INSTITUUT VOOR STERRENKUNDE
Celestijnenlaan 200D box 2401
B-3001 Heverlee